

1222·2022
800
ANNI



UNIVERSITÀ
DEGLI STUDI
DI PADOVA

UNIVERSITÀ DEGLI STUDI DI PADOVA
Department of Industrial Engineering - DII

Ph.D. course in Industrial Engineering
Curriculum in Mechanical Engineering
Cycle XV

**Theoretical development and experimental validation of the Peak Stress
Method for the fatigue design of steel welded structures**

Coordinator: Prof. Ing. Giulio Rosati
Supervisor: Prof. Ing. Giovanni Meneghetti
Co-Supervisor: Prof. Ing. Alberto Campagnolo

Ph.D. Student: Luca Vecchiato

*Considerate la vostra semenza:
fatti non foste a viver come bruti,
ma per seguir virtute e canoscenza.*

Dante Alighieri

Divina Commedia - Inferno: C. XXVI

To my wife

Abstract

Welding undoubtedly represents one of the most efficient and most frequently employed technological processes for efficiently joining metallic components. Unfortunately, it is well known that the safety and structural durability of metallic structures relies on the strength of their joints, since most of their in-service failures are due to fatigue actions occurring in the joints. Furthermore, fatigue failures are also very critical for another reason: they occur apparently without warning at a load level far below the static strength of the structure.

International standards and recommendations suggest design welded joints against fatigue using the nominal stress approach. It consists in evaluating the applied nominal stress by means of standard solid-mechanics-based stress calculations without considering any stress concentration at the weld bead and assuming a linear elastic material behaviour. Then, its value is compared with the fatigue strength of the considered joints, the latter being directly evaluated from the specific S-N design curve chosen from a list of classified structural details. The most significant limitation of this method becomes clear in case of complex joint geometries whose standard fatigue curve for the specific geometry of the welded detail is not available.

However, it has been demonstrated in the literature that this limitation can be overcome by adopting local approaches, i.e. fatigue lifetime evaluation criteria based on local rather than nominal quantities. Among all local approaches, the Peak Stress Method (PSM) is a rapid technique to estimate the Notch Stress Intensity Factors (NSIFs) at the weld toe and weld root, which are idealised and modelled as sharp notches having null tip radius. Essentially, the PSM takes advantage of the singular, linear elastic, opening, sliding, and tearing peak stresses evaluated at the notch tip using coarse free mesh patterns to estimate the mode I, II, and III NSIF-terms, respectively. By adopting the averaged Strain Energy Density (SED) as a fatigue strength criterion, a PSM-based design stress, i.e. the so-called equivalent peak stress, can be defined as a function of the relevant peak stresses. Noteworthy, the equivalent peak stress

according to the PSM allows to assess the fatigue strength of welded joints regardless the joint's geometry, the steel grade, or the testing conditions and the capability and effectiveness of this method have been extensively checked and validated in many publications. Unfortunately, despite the great capability demonstrated by the PSM, there are of course many aspects that still requires to be improved. The aim of the present work was precisely to overcome some of these limitations and to extend the capability of the method.

The main feature that has been analysed in the present manuscript is that the PSM has only been defined and validated under Constant Amplitude (CA) local stresses, i.e. fatigue cyclic stresses with a constant amplitude and a constant mean stress. However, welded structures under real in-service conditions are typically subjected to rather complex load-time histories composed by Variable Amplitude (VA) uniaxial or multi-axial sequence of stresses both deterministic and stochastic in nature.

Another aspect which has been investigated and discussed is that the PSM does not include any prediction of the fatigue limit, i.e. the stress level below which, theoretically, an infinite number of CA load cycles can be applied to the structure without causing fatigue failure, despite the significant implications of this threshold value on practical problems. In light of the above discussed, the present manuscript addresses some theoretical developments of the PSM and the subsequent validation against experimental data.

More in detail, Chapter 1 will introduce the problem and will give the theoretical background on the local approaches used in the rest of the manuscript. In particular, the concepts of Stress Intensity Factor (SIF), the Notch Stress Intensity Factor approach (NSIF), the averaged Strain Energy Density (SED) criterion and the Peak Stress Method (PSM) will be introduced along with their theoretical background, and their application to fatigue lifetime assessment of welded joints.

Then, Chapter 2 will deal with the first extension of the PSM which allows to account for variable amplitude (VA) uniaxial as well as in-phase and out-of-phase multiaxial fatigue loadings applied to steel arc-welded joints. The extension to VA loading situations has been based on Palmgren-Miner's linear damage rule (LDR) to account for cumulative damage. The proposed method has been validated against a large bulk of VA fatigue data taken from the literature proving the PSM as an extremely valid technique to design welded joints against CA or VA uniaxial as well as multiaxial fatigue local stresses. The proposed method has also been checked against new experimental data generated by fatigue testing non-load-carrying (nlc)

fillet-welded double transverse or inclined attachments made of S355 structural steel under pure axial loading.

Later on, another extension of the PSM will be presented in Chapter 3, to estimate the constant amplitude uniaxial fatigue limit of welded structures in the stress-relieved state. To address this topic, a fracture mechanics-based criterion has been used starting from the observation that at the fatigue limit a non-propagating short crack exists in the structure. The chosen criterion adopts the so-called cyclic R-curve analysis for the calculations. More in detail, it simply consists of comparing the driving force for a propagating crack (depending on the geometry, the material and the external loads) with the cyclic R-curve, i.e. the crack size dependence of the fatigue crack propagation threshold in the short crack regime. After an accurate calibration, the method based on the cyclic R-curve analysis has been combined with the PSM obtaining a new procedure that allows to a rapid and effective design of weld toe failures in the infinite life region. The huge advantage given by this new approach is that it works without the need of complex and time-consuming fracture mechanics-based calculations.

Interestingly, results obtained in this chapter move from the assumption that the cyclic R-curve represents a material property measured by means of experimental fracture mechanics fatigue tests using flat specimens like e.g. the single edge notch bend (SENB). However, in the case of small cracks (e.g. the cyclic R-curve), International Standards advise using different specimens' geometry, such as for example single-edge-crack round bars. At the same time, they do not give any give information on how to perform real-time in-situ crack length measurement on such specimens' geometry, this aspect being undoubtedly critical and extremely challenging.

For this reason, the possibility of experimentally determining the cyclic R-curve on complex specimens' geometries has been investigated in the present work. More in detail, Chapter 4 will give an insight on some critical aspects relevant to the experimental determination of the cyclic R-curve and, in general, on experimental fracture mechanics tests dealing with short cracks. In particular, Chapter 4 will discuss how to perform real-time in-situ crack length measurement of a single-edge-crack propagating in round bars adopting the Direct Current Potential Drop (DCPD). In this context, the performances of the DCPD method, in terms of measurability, sensitivity and reproducibility, have been analysed thanks to 3D electrical FE analyses. Numerical results allowed to investigate the effect of the current and the potential probes position on the performances. Finally, the accuracy of the numerical analyses has been checked against experimental results.

Index

CHAPTER 1. Introduction	1
List of symbols	2
1.1. Fatigue of weldments	3
1.2. Notch-Stress Intensity Factors (NSIFs) approach	6
<i>1.2.1. Crack: Stress Intensity Factors (SIFs)</i>	6
<i>1.2.2. Sharp V-Notch: Notch Stress Intensity Factors (NSIFs)</i>	9
<i>1.2.3. Numerical evaluation of the NSIFs</i>	13
<i>1.2.4. The Peak Stress Method: rapid estimation of the NSIFs</i>	15
<i>1.2.5. Fatigue design against pure mode I weld toe using the NSIFs approach</i>	25
<i>1.2.6. Limitations of the NSIFs approach</i>	27
1.3. The averaged Strain Energy Density (SED) criterion	29
1.4. The Peak Stress Method: equivalent peak stress	36
1.5. Conclusions	41
1.6. References	42
CHAPTER 2. Variable amplitude multiaxial local stresses	51
List of symbols	52
2.1. Introduction	54
2.1. The Peak Stress Method for variable amplitude multiaxial local stresses	60

2.2.	Validation with data from the literature.....	71
2.2.1.	<i>Demofonti et al., two-sided full penetration butt-welded joints and transverse nlc full-penetration welded joints.....</i>	<i>76</i>
2.2.2.	<i>Maddox and Zhang, longitudinal stiffeners with full penetration welds.....</i>	<i>83</i>
2.2.3.	<i>Vanrostenberghe et al., longitudinal stiffeners with full penetration welds.....</i>	<i>85</i>
2.2.4.	<i>Yildirim et al., transverse nlc fillet-welded joints.....</i>	<i>87</i>
2.2.5.	<i>Bertini et al., tube-to-flange joints.....</i>	<i>89</i>
2.2.6.	<i>Sonsino et al., tube-to-flange joints.....</i>	<i>93</i>
2.2.7.	<i>Witt et al., tube-to-flange joints.....</i>	<i>95</i>
2.2.8.	<i>Assessment of weld toe and weld root fatigue failures according to the PSM.....</i>	<i>98</i>
2.3.	New experimental fatigue data: non-load-carrying fillet welded joints.....	113
2.3.1.	<i>Introduction.....</i>	<i>113</i>
2.3.2.	<i>Fatigue tests: specimens.....</i>	<i>114</i>
2.3.3.	<i>Fatigue tests: loads and testing parameters.....</i>	<i>117</i>
2.3.4.	<i>Fatigue test results: damage analysis.....</i>	<i>119</i>
2.3.5.	<i>Fatigue test results: nominal stress.....</i>	<i>122</i>
2.3.6.	<i>Fatigue strength assessment according to the PSM.....</i>	<i>123</i>
2.3.7.	<i>Assessment of weld toe and weld root fatigue failures according to the PSM.....</i>	<i>127</i>
2.3.8.	<i>Discussion: comparison with IIW and Eurocode 3 fatigue curves.....</i>	<i>129</i>
2.3.9.	<i>Discussion: effect of angular misalignments.....</i>	<i>134</i>

2.3.10. Discussion: residual stresses.....	137
2.4. Conclusions.....	142
2.5. References.....	144
CHAPTER 3. Cyclic R curve and fatigue limit.....	153
List of symbols.....	154
3.1. Introduction.....	156
3.2. Calibration of the initial crack size a_i: driving force at the fatigue limit.....	161
3.2.1. Specimens.....	161
3.2.2. Experimental determination of the fatigue limit.....	166
3.2.1. Misalignments: effect of a secondary bending.....	168
3.2.2. Experimental determination of the crack shape evolution.....	174
3.2.3. Structural FEA analyses.....	176
3.3. Calibration of the initial crack size a_i: the cyclic R-curve.....	182
3.3.1. Specimens.....	182
3.3.2. Fatigue crack growth tests setup.....	183
3.3.3. Results.....	187
3.3.4. Discussion: a new procedure for determining the cyclic R-curve.....	188
3.4. Calibration of the initial crack size.....	190
3.4.1. Results.....	190
3.4.2. Discussion: effect of the crack shape c/a	192
3.5. Estimating the fatigue limit of welded structures.....	194
3.5.1. Threshold Notch Stress Intensity Factor $\Delta K_{l,th}$	194
3.5.2. The Peak Stress Method: equivalent peak stress at threshold.....	199
3.5.3. Validation with data taken from the Literature.....	201

3.6. Conclusions	204
3.7. References	206
CHAPTER 4. Fatigue crack growth monitoring of short cracks	211
List of symbols	212
4.1. Introduction	213
4.2. Performances of a DCPD measurement	217
4.3. Numerical investigation	221
<i>4.3.1. Structural FE analyses: iso-KI criterion</i>	221
<i>4.3.1. Electrical FE analyses: Effect of current and potential probe location</i>	225
<i>4.3.2. Results of electrical FE analyses</i>	229
4.4. Effect of the temperature	240
4.5. Experimental Tests	248
<i>4.5.1. Procedure and experimental setup</i>	248
<i>4.5.2. Experimental results</i>	253
4.6. Discussion	274
<i>4.6.1. Comparison between experimental data and numerical estimation</i>	274
<i>4.6.2. Application to real components</i>	276
<i>4.6.3. Minimum detectable crack length increment</i>	277
4.7. Conclusions	279
4.8. References	282
CHAPTER 5. Conclusions	289
5.1. Conclusions	290
5.2. List of Publications	293

CHAPTER 1.

Introduction

List of symbols

2α	V-notch opening angle
a	Reference dimension for selecting the maximum FE size d
c_{w1}, c_{w2}, c_{w3}	Mode I, II, and III coefficients accounting for mean stress effect
d	Average FE size
Δ	Range of cyclic quantities (maximum minus minimum)
e_1, e_2, e_3	Mode I, II, and III coefficients for evaluating $\Delta\bar{W}$
E	Young's modulus
f_{w1}, f_{w2}, f_{w3}	Mode I, II, and III coefficients for calculating $\sigma_{eq,peak}$
K_I, K_{II}, K_{III}	Mode I, II, and III Stress Intensity Factors (SIFs)
K_1, K_2, K_3	Mode I, II, and III Notch Stress Intensity Factors (NSIFs)
$K_{FE}^*, K_{FE}^{**}, K_{FE}^{***}$	Non-dimensional NSIF parameters based on PSM
$\lambda_1, \lambda_2, \lambda_3$	Mode I, II, and III stress singularity degrees
λ	Local biaxiality ratio defined according to PSM
ν	Poisson's ratio
ρ	Notch tip radius
R_0	Size of material-structural volume according to SED criterion
r, θ, z	Coordinates of cylindrical reference system at crack/notch tip
$\sigma_{eq,peak}$	Equivalent peak stress based on PSM
$\sigma_{rr}, \sigma_{\theta\theta}, \sigma_{zz}$	Normal stress components in cylindrical coordinate system
$\sigma_{\theta\theta, \theta=0, peak}$	Mode I linear elastic peak stress calculated by FEA according to PSM
$\tau_{r\theta}, \tau_{rz}, \tau_{\theta z}$	Shear stress components in cylindrical coordinate system
$\tau_{r\theta, \theta=0, peak}$	Mode II linear elastic peak stress calculated by FEA according to PSM
$\tau_{\theta z, \theta=0, peak}$	Mode III linear elastic peak stress calculated by FEA according to PSM
\bar{W}	Averaged SED

1.1. Fatigue of weldments

The process of joining different components has a fundamental role in designing high-performance engineering structures. When it comes to metallic materials, welding is undoubtedly one of the most efficient and most frequently employed technological processes in many different industries. Just think, for example, of the automotive industry, where a significant number of structural parts of the frame, the suspensions, the engine, and the transmission are welded. Unfortunately, it is just as well known that the safety and structural durability of metallic structures relies on the strength of their joints, since most in-service failures of metal structural components are due to fatigue actions occurring in the joints (50% to 90% of mechanical assembly failures [1]). Furthermore, fatigue failures are also very critical for another reason: they occur apparently without warning at a load level far below the static strength of the structure.

To make matters worse, beyond the safety aspects, certainly not negligible, there are many other aspects that industries must face, first of all costs. Indeed, metal's fatigue may seem like a niche issue, far from everyday life problems, but some research, even if relatively dated, have shown that in industrialized countries, the cost of in-service component rupture amounts to around 4% of Gross National Product [2–5]. Last but not least, industries must deal with the 2030 Agenda and its 17 global Sustainable Development Goals (SDGs), according to which there is an urgent need for a global solution to stop Climate Change and global warming worst impacts. This turns out in the need of improving not only the safety of industrial structures and components but also in the need of improving their environmental impact expressed in terms of material and energy consumption with the associated production, inspection, and maintenance costs.

Lack of knowledge in the design of welded structures against fatigue leads to the need to oversize components or the unnecessary use of expensive materials and processes. Improving knowledge and technologies in structural components design can help not only save lives through safer structures but also reduce production, inspection, and maintenance times and costs, making industries more competitive and sustainable. This complex scenario makes clear the reasons why the research on fatigue lifetime evaluation of welded joints has always been

(and still is) of great interest from an engineering perspective. Companies involved in the process of designing and manufacturing engineering structures subjected to in-service fatigue loadings are constantly looking for new design criteria.

A huge amount of work has been put into formalizing and validating design criteria against fatigue since a century and a half ago, when metal's fatigue was first recognised as an engineering problem by Wöhler [6]. Nowadays, among all proposed criteria for assessing the fatigue life of welded details, international standards and recommendations [7,8] suggest the nominal stress approach as probably the simplest method. Such a method consists in evaluating the applied nominal stress by means of standard solid-mechanics-based stress calculations without considering any stress concentration at the weld bead and assuming a linear elastic material behaviour. For fatigue assessment, its value is compared with the fatigue strength of the considered joints, the latter being directly evaluated from the specific S-N design curve chosen from a list of classified structural details.

The most significant limitation of this method emerges when either the nominal stresses cannot be computed or the standard fatigue curve for the specific geometry of the welded detail is not available, e.g. in the case of complex joint geometries, whose proper reference design category does not exist. To overcome this issue, the standards and recommendations suggest carrying out dedicated expensive and time-consuming experimental fatigue tests as the only alternative. On the contrary, in the Literature, it has been demonstrated that this limitation can be overcome by adopting local approaches [9]. The idea of adopting fatigue lifetime evaluation criteria based on local rather than nominal quantities comes from experimental observations on the nature of metals fatigue. In fact, it occurs whenever a component is subjected to fluctuating stresses and strains, which may lead to failure due to progressive and localized structural damage accumulation. Metal fatigue being a localized process of damage accumulation, the local geometrical parameters, the local stresses and the material have a major influence on the fatigue strength and service life of structural members. Accordingly, criteria based on local quantities proved reliable for the fatigue lifetime assessment of welded structures [10].

Among all local phenomenological approaches well established in the literature to design welded structures against fatigue, the following deserve to be mentioned (the literature is huge, only few criteria and papers are cited here):

- Notch stress approach [9–13]
- Strain-life approach [9,14–17]
- Notch-Stress Intensity Factors (NSIFs) approach [9,18,19]
- Averaged Strain Energy Density (SED) criterion [20–25]
- Critical plane models [15,26–28]
- Theory of Critical Distances (TCD) [26,28–35]
- Peak Stress Method (PSM) [36–41]
- Fracture Mechanics (FM) [8,42,43]

Moreover, for the sake of completeness, additional well-established literature on phenomenological local approaches applied to non-welded structures can be cited here:

- Notch stress approach [44–46]
- Strain-life approach [47,48]
- Notch-Stress Intensity Factors (NSIFs) approach [49,50]
- Averaged Strain Energy Density (SED) criterion [51,52]
- Critical plane models [53–57]
- Theory of Critical Distances (TCD) [26,58,59]
- Strain energy-based approach [60,61]
- Fracture Mechanics [62]
- Thermodynamics in continuum mechanics [63–68]

In the context of this complicated scenario, the aim of the present chapter is that of giving the theoretical background on the local approaches used in the rest of the manuscript. In particular, the notch stress intensity factor approach (NSIF), the averaged strain energy density (SED) criterion and the peak stress method (PSM) will be introduced together with their theoretical background, and their application to fatigue lifetime assessment of welded joints.

1.2. Notch-Stress Intensity Factors (NSIFs) approach

1.2.1. Crack: Stress Intensity Factors (SIFs)

The need of analysing the local stress distribution has originally been developed in the context of fracture mechanics. It is well known that a crack in a body can be subjected to three different opening modes (or a combination of them) (Figure 1.1):

- Mode I, symmetric in-plane tensile loading.
- Mode II, anti-metric in-plane shear loading.
- Mode III, out-of-plane shear loading.

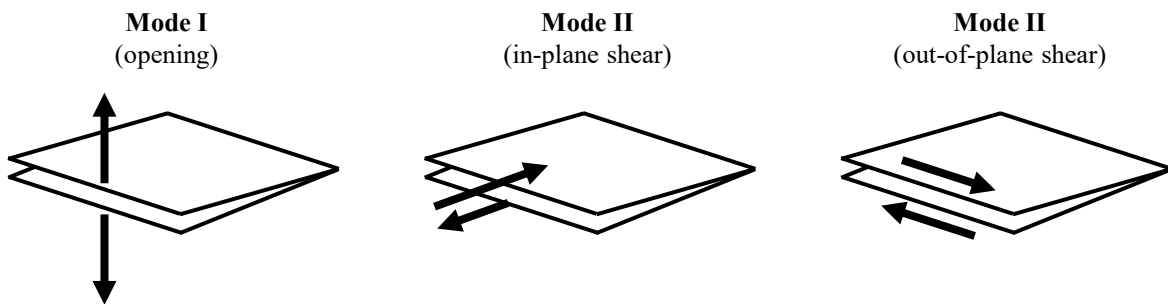


Figure 1.1. The three basic loading modes of a crack.

In the framework of Linear Elastic Fracture Mechanics (LEFM), each local stress mode generates singular stresses at the crack tip (Figure 1.2). Generally speaking, the stress field ahead the crack tip can be described by superimposition of three independent singular stress components corresponding to three independent loading modes of the crack tip (mode I, II and III). For an isotropic linear elastic material behaviour, the singularity is always inversely proportional to the square root of the distance from the crack tip $1/r^{0.5}$ ($\sigma \propto 1/r^{0.5}$, $r \rightarrow 0 \Rightarrow \sigma \rightarrow \infty$) and the asymptotic stress distribution in the vicinity of the crack tip restricted to the first-order terms can be written in closed-form as follow [69–71]:

$$\sigma_{ij} = \frac{1}{\sqrt{2\pi}} K_I \cdot \frac{1}{\sqrt{r}} \cdot f_{I,ij}(\theta) + \frac{1}{\sqrt{2\pi}} K_{II} \cdot \frac{1}{\sqrt{r}} \cdot f_{II,ij}(\theta) \quad (1.1)$$

$$\sigma_{kz} = \frac{1}{\sqrt{2\pi}} K_{III} \cdot \frac{1}{\sqrt{r}} \cdot f_{III,kz}(\theta) \quad (1.2)$$

Where σ_{ij} and σ_{kz} represent the stress components in polar coordinates (Figure 1.2), $f_{I,ij}$, $f_{II,ij}$, and $f_{III,ij}$ are the angular functions and describe the effect of the angular position on the stresses distribution, while K_I , K_{II} and K_{III} are the mode I, mode II, and mode III Stress Intensity Factors (SIFs), respectively, are constant whose values depend on the geometry of the analysed component, the crack length and the applied load and constraint conditions. These equations easily describe the stresses singularity since the stresses are asymptotic to $r = 0$. In particular, they highlight how the stress components near the crack tip vary with $1/r^{0.5}$, regardless of the geometry of cracked body is. Nevertheless, it must be noted that, Eqs. (1.1) and (1.2) are valid for any cracked body when $r \rightarrow 0$, i.e. in the singularity-dominated region of the stress field. Otherwise, far away from the crack type, the stress field is dominated by the boundary conditions instead of the singularity.

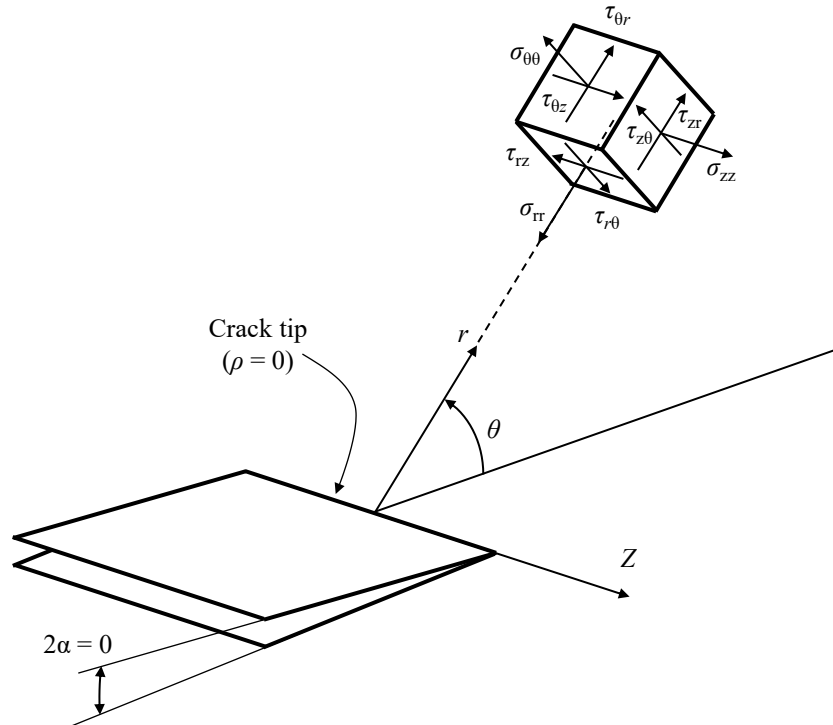


Figure 1.2. Definition of the polar coordinate system at the crack tip ($2\alpha = 0^\circ$, $\rho = 0$) and the corresponding stress components in a generic three-dimensional stress field.

Along the bisector line, the stress components simplify in the following form:

$$\sigma_{\theta\theta}(r, \theta = 0) = \frac{1}{\sqrt{2\pi}} K_I \cdot \frac{1}{\sqrt{r}} \quad (1.3)$$

$$\tau_{r\theta}(r, \theta = 0) = \frac{1}{\sqrt{2\pi}} K_{II} \cdot \frac{1}{\sqrt{r}} \quad (1.4)$$

$$\tau_{\theta z}(r, \theta = 0) = \frac{1}{\sqrt{2\pi}} K_{III} \cdot \frac{1}{\sqrt{r}} \quad (1.5)$$

Such stress components are of fundamental importance in the evaluation of the SIFs K_I , K_{II} and K_{III} , which are defined as follow [70,72,73]:

$$K_I = \lim_{r \rightarrow 0} \sqrt{2\pi} \cdot \sqrt{r} \cdot \sigma_{\theta\theta}(r, \theta = 0) \quad (1.6)$$

$$K_{II} = \lim_{r \rightarrow 0} \sqrt{2\pi} \cdot \sqrt{r} \cdot \tau_{r\theta}(r, \theta = 0) \quad (1.7)$$

$$K_{III} = \lim_{r \rightarrow 0} \sqrt{2\pi} \cdot \sqrt{r} \cdot \tau_{\theta z}(r, \theta = 0) \quad (1.8)$$

These limits exist and are unique. The measurement unit of the SIFs K_I , K_{II} and K_{III} is $\text{MPa}\cdot\text{m}^{0.5}$. They denote the intensity of the asymptotic stress field, since stresses near the crack tip increase homothetically with them, and they completely describe the crack tip conditions. Indeed, once K_I , K_{II} and K_{III} are known, all components of stress, strain, and displacement are known as a function of r and θ . This means the Stress Intensity Factors (SIFs) are capable of completely describing the stress distribution around the singularity dominated region. This description of the crack tip stress fields making use of a single-parameter has been found to be one of the most important concepts in fracture mechanics, since the asymptotic singular stress field distribution in the vicinity of the crack front controls the phenomenon of both fatigue and static fracture.

1.2.2. Sharp V-Notch: Notch Stress Intensity Factors (NSIFs)

The Notch Stress Intensity Factors (NSIFs) approach for welded joints is based on the assumption that conventional arc-welding techniques result in very small values for the weld toe and weld root radius. Accordingly, both the weld toe and the weld root are modelled as sharp V-notches having a null tip radius ($\rho = 0$, worst-case hypothesis) and a certain opening angle 2α (Figure 1.3). It must be noted that this assumption also states when the notch tip radius is small ($\rho \rightarrow 0$) but not null ($\rho \neq 0$), since, as demonstrated by Smith and Miller [74], their fatigue behaviour is the same as that of a sharp V-notch having the same notch depth and opening angle.

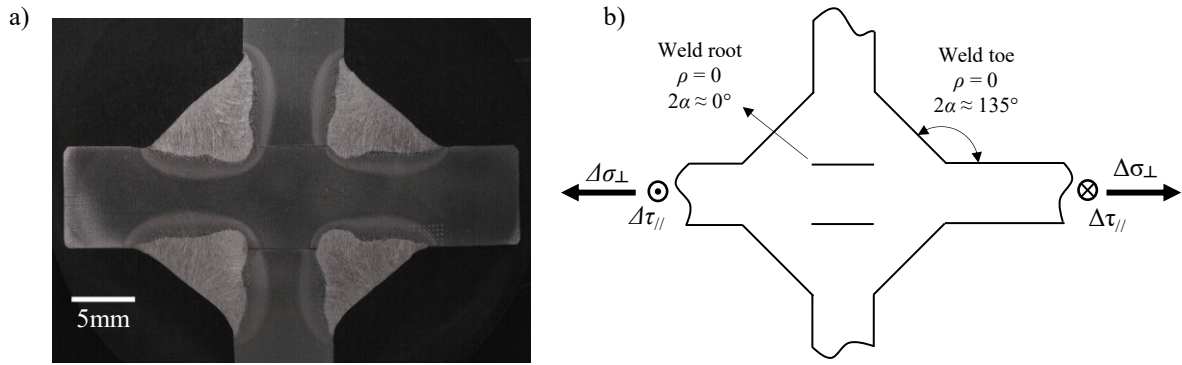


Figure 1.3. Worst case assumption according to the NSIF-based approach in fatigue design of welded joints. (a) example of a fillet welded joints with double attachments and (b) corresponding geometrical model. Typically, the sharp V-notch opening angles are $2\alpha \approx 0^\circ$ for the weld root and $2\alpha \approx 135^\circ$ for the weld toe.

As a consequence of the null radius at the V-notch tip, singular stress fields are produced at the weld toe and at weld root by the external loads acting on the component. In the framework of linear elasticity, similarly to Eqs. (1.1) and (1.2), the stress field in the nearby of a sharp V-notch tip can be described in polar coordinates by the following expressions [75] (Figure 1.4):

$$\sigma_{ij} = \frac{1}{\sqrt{2\pi}} K_1 \cdot \frac{1}{r^{1-\lambda_1}} \cdot f_{1,ij}(\theta) + \frac{1}{\sqrt{2\pi}} K_2 \cdot \frac{1}{r^{1-\lambda_2}} \cdot f_{2,ij}(\theta) \quad (1.9)$$

$$\sigma_{kz} = \frac{1}{\sqrt{2\pi}} K_3 \cdot \frac{1}{r^{1-\lambda_3}} \cdot f_{3,kz}(\theta) \quad (1.10)$$

Where, again, σ_{ij} and σ_{kz} represent the stress components in polar coordinates, $f_{1,ij}$, $f_{2,ij}$, and $f_{3,ij}$ are angular functions which describe the effect of the angular position on the stress values, while K_1 , K_2 and K_3 are the mode 1, mode 2, and mode 3 Notch Stress Intensity Factors (SIFs), which are constant whose values depend on the geometry of the analysed component, the applied load and constraint conditions, the notch size and the notch opening angle 2α . Finally, λ_1 , λ_2 , and λ_3 represent the stress singularity degrees relevant to the corresponding local stress mode (mode 1, 2, and 3 respectively). Just as in the cracked component ($2\alpha = 0$), the complete solution consists in additional non-singular higher-order terms, so Eqs. (1.9) and (1.10) are strictly valid only for $r \rightarrow 0$ since these equations describe an asymptotic distribution of stresses to $r = 0$.

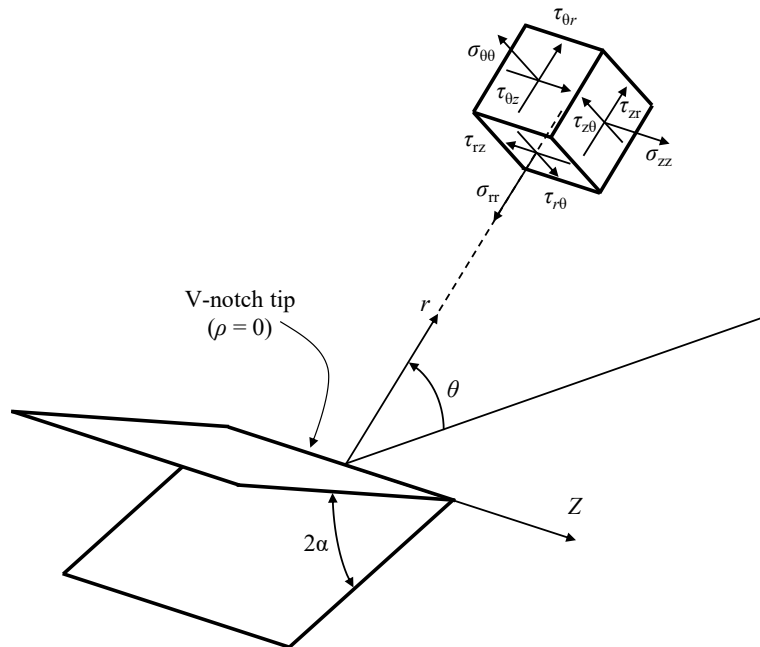


Figure 1.4. Definition of the cylindrical coordinate system (r, θ, z) centered at the sharp V-notch tip ($2\alpha, \rho = 0$) and the corresponding local stress components in a generic three-dimensional stress field.

λ_1 , and λ_2 are the smallest positive eigenvalues in the Williams' solution for the in-plane symmetrical and in-plane anti-metrical stress field, respectively [75]. Similarly, λ_3 is the smallest positive eigenvalue obtained from the solution of the out-of-plane stress field [76].

In more detail, they are the first positive solutions of the following transcendent equations:

$$\sin(2\gamma\lambda_1) + \lambda_1 \cdot \sin(2\gamma) = 0 \quad (1.11)$$

$$\sin(2\gamma\lambda_2) - \lambda_2 \cdot \sin(2\gamma) = 0 \quad (1.12)$$

$$\sin(2\gamma\lambda_3) = 0 \quad (1.13)$$

Where $2\gamma = 2\pi - 2\alpha$. They define the degree of the stress singularity (in simple words, the rate at which the stress field approaches infinity as the distance from the notch tip approaches zero $r \rightarrow 0$) at the notch tip and are function of only the notch opening angle 2α . Table 1.1 reports their values for certain opening angles.

Table 1.1. Stress singularity exponents for certain notch opening angles (values from [21])

2α	λ_1	λ_2	λ_3
[°]	[-]	[-]	[-]
0	0.500	0.500	0.500
90	0.545	0.909	0.667
120	0.616	-	0.750
135	0.674	-	0.800

In a very recent contribution [77] the following parametric expression function of the opening angle 2α has been proposed to compute the stress singularity exponents:

$$1 - \lambda_i = a \cdot (2\alpha)^4 + b \cdot (2\alpha)^3 + c \cdot (2\alpha)^2 + d \cdot (2\alpha) + e \quad (1.14)$$

Where $i = 1, 2$ and 3 , 2α is the V-notch opening angle and must be expressed in degrees [°], while a, b, c, d , and e are coefficients whose values are reported in Table 1.2 as a function of the local stress mode.

Table 1.2. Coefficients of Eq. (1.14) for estimating the stress singularity exponents.

Coefficient	λ_1	λ_2	λ_3
a	$-5.643 \cdot 10^{-10}$	0	0
b	$5.379 \cdot 10^{-8}$	$-9.491 \cdot 10^{-8}$	$-3.768 \cdot 10^{-8}$
c	$-7.777 \cdot 10^{-6}$	$-9.802 \cdot 10^{-6}$	$-1.167 \cdot 10^{-7}$
d	$1.785 \cdot 10^{-4}$	$-2.906 \cdot 10^{-3}$	$-1.525 \cdot 10^{-3}$
e	0.500	0.500	0.500

Eq. (1.14) has been plotted in Figure 1.5 which shows that the singularity exponents for a sharp V-notch ($2\alpha > 0$), expressed in terms of $1 - \lambda_i$ (for $i = 1, 2, 3$), are always smaller than that of cracked components ($2\alpha = 0$). Indeed, in the case of a cracked component, all the singularity exponents collapse into the same value, i.e. 0.5. Interestingly, the mode 2 stress singularity $1 - \lambda_2$ is weaker, i.e. has a smaller value for a fixed notch opening angle 2α , than the mode 3 stress singularity $1 - \lambda_3$, which in turn is blander than $1 - \lambda_1$ (Figure 1.5). Finally, it is important to note that when $1 - \lambda_i$ (for $i = 1, 2, 3$) become null (i.e. the eigenvalue is $\lambda_i = 1$) the corresponding stress field component is no more singular. This happens, i.e. the stress singularity completely disappear, in case of straight edges ($2\alpha = \pi$) for modes 1 and 3 whilst when the opening angle is $2\alpha \geq 102.6^\circ$ for mode 2.

As for the cracked body, the stress components along the bisector line ($\theta = 0$) simplify in the following form:

$$\sigma_{\theta\theta}(r, \theta = 0) = \frac{1}{\sqrt{2\pi}} K_1 \cdot \frac{1}{r^{1-\lambda_1}} \quad (1.15)$$

$$\tau_{r\theta}(r, \theta = 0) = \frac{1}{\sqrt{2\pi}} K_2 \cdot \frac{1}{r^{1-\lambda_2}} \quad (1.16)$$

$$\tau_{\theta z}(r, \theta = 0) = \frac{1}{\sqrt{2\pi}} K_3 \cdot \frac{1}{r^{1-\lambda_3}} \quad (1.17)$$

Somehow, the NSIFs extend the concept of SIFs describing not only the stress singularity at crack tips but also that of sharp V-notches having null tip radius ($\rho = 0$).

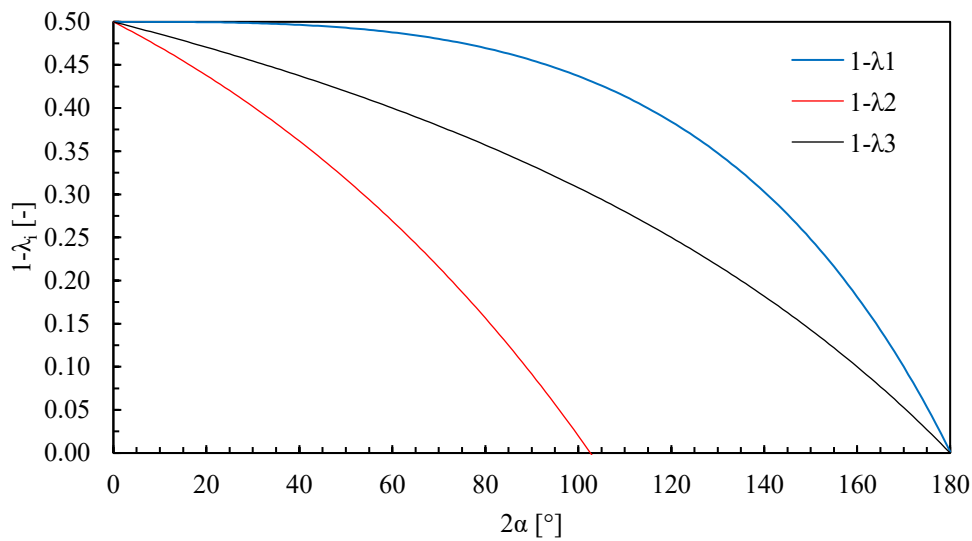


Figure 1.5. Mode I, II and III stress singularity exponents $1 - \lambda_i$ (for $i = 1, 2, 3$) as a function of the opening angle [19].

The definitions of Mode I and Mode II NSIFs (for plane problems) were given by Gross and Mendelson in 1972 [73]:

$$K_1 = \sqrt{2\pi} \cdot \lim_{r \rightarrow 0} \left[\sigma_{\theta\theta, \theta=0} \cdot r^{1-\lambda_1} \right] \quad (1.18)$$

$$K_2 = \sqrt{2\pi} \cdot \lim_{r \rightarrow 0} \left[\tau_{r\theta, \theta=0} \cdot r^{1-\lambda_2} \right] \quad (1.19)$$

while the mode III N-SIF was defined in 1997 [76]:

$$K_3 = \sqrt{2\pi} \cdot \lim_{r \rightarrow 0} \left[\tau_{\theta z, \theta=0} \cdot r^{1-\lambda_3} \right] \quad (1.20)$$

Their dimensions are $\text{MPa} \cdot \text{m}^{1-\lambda_1}$, $\text{MPa} \cdot \text{m}^{1-\lambda_2}$, and $\text{MPa} \cdot \text{m}^{1-\lambda_3}$, respectively. The NSIFs are linear elastic stress parameters applicable to sharp V-shaped notches (having notch tip radius equal to zero) where the linear elastic stress concentration cannot be defined, the stress distributions being singular there. Therefore, the NSIFs take the same role that the SIFs have in the Linear Elastic Fracture Mechanics discipline.

1.2.3. Numerical evaluation of the NSIFs

The most robust and well-known method to compute the NSIFs is by directly applying the NSIFs definition, i.e. evaluating all stress distributions in the vicinity of the V-notch tip along the bisector line ($\theta = 0$ in Figure 1.4 and Figure 1.6) and performing the limit calculation reported in Eqs. (1.18), (1.19), and (1.20). Certainly, the use of finite element analysis (FEA) is a very common and effective tool in calculating the stress distribution. In this case, the element size must be very small, i.e. the mesh must be extremely dense, in order to capture the gradient of the local stress field.

As an example the evaluation of the mode I NSIF, ΔK_1 , at the weld toe of the transverse non-load-carrying welded joint reported in Figure 1.6, the minimum element size in the nearby of

the singularity point (the weld toe) must be in the order of 10^{-5} mm (Figure 1.7) to properly capture the stress distribution in the singularity dominated region (Figure 1.8).

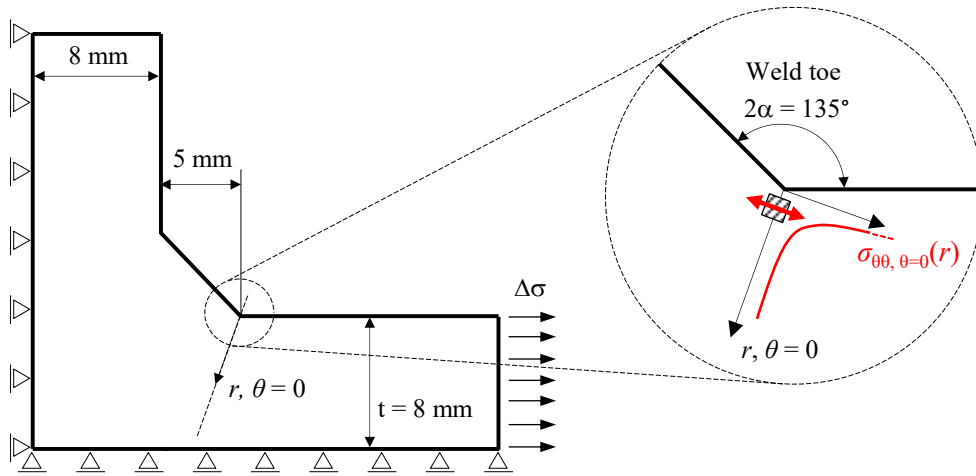


Figure 1.6. Geometry of the transverse non-load-carrying welded joint considered in the example for the calculation of the mode I NSIF at the weld toe according to the NSIF definition (Eqs. (1.18), (1.19), (1.20)). On the right there is a detail of the weld toe modelled as sharp V-notch with highlight the opening (mode I) singular stress distribution along the bisector line $\sigma_{\theta\theta, \theta=0}(r)$.

In particular, the 2D geometry of Figure 1.6 has been modelled exploiting both the planes of symmetry. Then it has been discretized using 2D 4-node quadrilateral plane elements under plane strain conditions. The mesh pattern has been carefully generated so as to obtain a smooth gradient of element size ranging from 10^{-5} mm at the notch tip to 1 mm far away from it. Finally, a uniform tensile nominal stress $\Delta\sigma = 1$ MPa has been applied on the main plate (Figure 1.7).

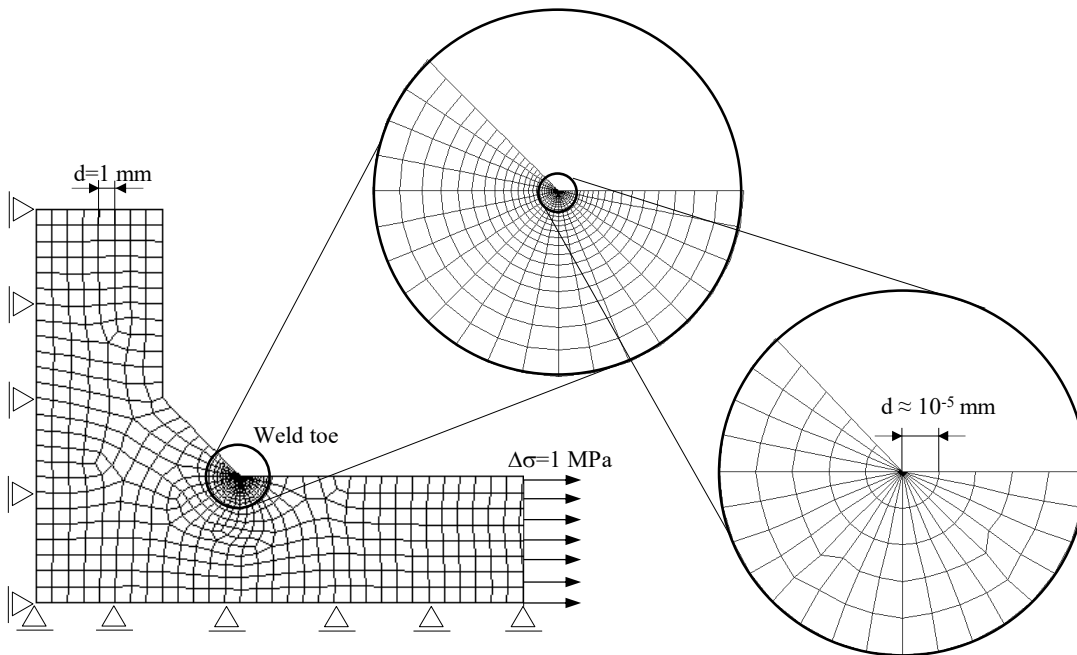


Figure 1.7. FE model adopted for the definition-base calculation of the mode I NSIF at the weld toe of the joint in Figure 1.6.

Eventually, once solved the model, the local stress distribution along the bisector line ($\theta = 0$) has been obtained by the FE model, it has been possible to apply the definition (Eqs. (1.18), (1.19), (1.20)) and obtaining the mode I NSIF range $\Delta K_I = 2.76 \text{ MPa}\cdot\text{mm}^{0.326}$.

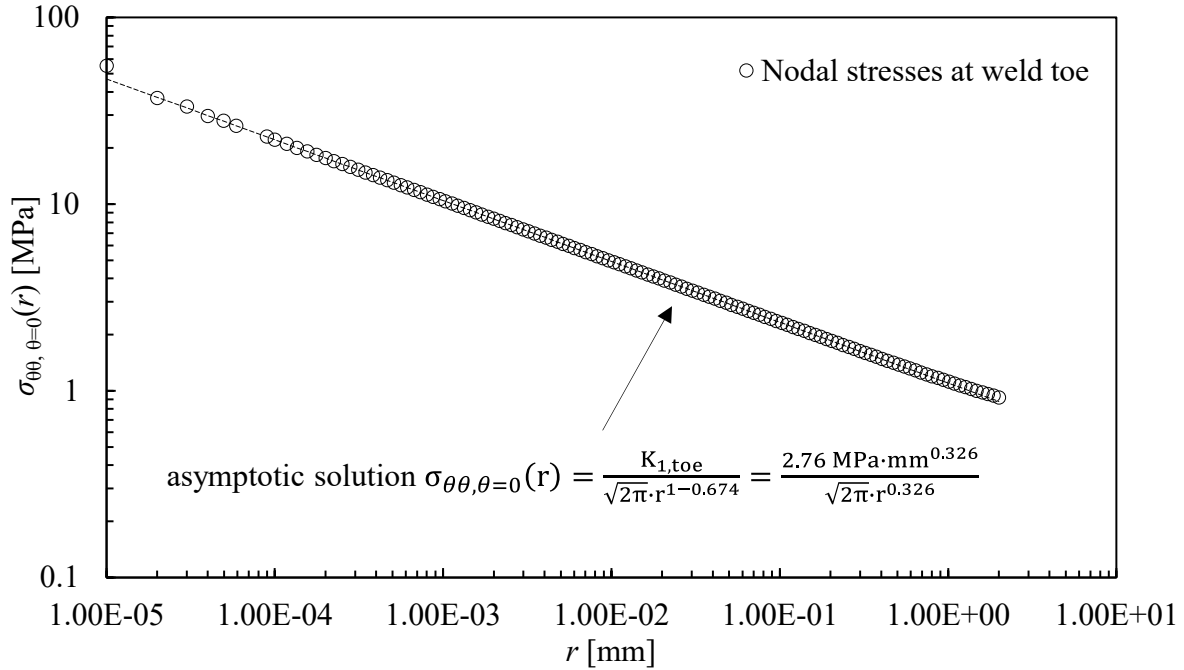


Figure 1.8. Singular linear elastic mode I stress field along the weld toe bisector line of the joint in Figure 1.6 obtained from FEA (Figure 1.7) with applied $\Delta\sigma = 1 \text{ MPa}$ and having very fine mesh ($d \sim 10\text{-}5\text{mm}$) to apply the NSIF definition. The numerical solution is compared with the asymptotic analytical solution showing very good agreement.

1.2.4. The Peak Stress Method: rapid estimation of the NSIFs

It is clear that the definition-based K_I numerical computation approach cannot be easily extended to industrial applications. In fact, the calculations can be very complex and time-consuming, both due to the needed mesh density and the post-processing required in calculating the limit. To overcome this limitation, Meneghetti and Lazzarin [36] proposed the so-called Peak Stress Method (PSM), which is a simplified engineering approach to rapidly estimate the NSIFs using linear elastic FE analyses having rather coarse meshes compared to that required for applying the NSIFs' definition. This numerical method is based on that by Nisitani and Teranishi [78] for the rapid numerical estimation of the SIF of a crack emanating from an ellipsoidal cavity. Under these conditions, they observed that the ratio K_I/σ_{peak} between the mode I SIF K_I and the linear elastic peak stress σ_{peak} calculated at the crack tip by means of FE

analyses depends only on the adopted element size, as long as the mesh pattern has a constant element size. In other words, they showed the linear elastic peak stress σ_{peak} calculated by FEM at the crack tip, can be used to quickly estimate K_I even if the linear elastic analysis does not converge and the finer the mesh is, the higher the linear elastic stress, the linear elastic stresses being singular at the crack tip. The K_I calculation is possible provided that a previous calibration of the adopted mesh pattern has been performed on geometries whose exact K_I are known.

Similarly, the strength of the PSM is exactly to establish a link between the singular linear elastic peak stresses calculated by FEM at the V-notch tip, the finite element size and the relevant NSIF. To rapidly estimate K_1 , K_2 , and K_3 the PSM exploits the opening (mode I), in-plane shear (mode II), and out-of-plane shear (mode III) peak stresses $\sigma_{\theta\theta,\theta=0,\text{peak}}$, $\tau_{r\theta,\theta=0,\text{peak}}$, and $\tau_{\theta z,\theta=0,\text{peak}}$, respectively, obtained from linear elastic FE analyses (see Figure 1.9, Figure 1.10, Figure 1.11, and Figure 1.12). More in detail, $\sigma_{\theta\theta,\theta=0,\text{peak}}$, $\tau_{r\theta,\theta=0,\text{peak}}$, and $\tau_{\theta z,\theta=0,\text{peak}}$ are the peak stresses computed in a local cylindrical coordinate system, which must be centred at the node located at the V-notch tip and have z-direction tangent to the notch tip line and θ -direction aligned with the notch bisector line, r being the radial direction. In such reference system, peak stresses are referred to the notch bisector line identified by the direction $\theta = 0^\circ$, as an example $\sigma_{\theta\theta,\theta=0,\text{peak}}$ is the opening stress acting normal to the notch bisector, as reported in Figure 1.9, Figure 1.10, Figure 1.11, and Figure 1.12.

The PSM has three main advantages compared to the definition-based K_I numerical computation. The first one is that the element size necessary to perform the FE analyses according to the PSM is order of magnitude larger than that required to apply the NSIF definition (see the example in Figure 1.9, Figure 1.10, Figure 1.11, and Figure 1.12). The second is that the free mesh generation algorithm can be used avoiding any time consumption in the pre-processing phase. Finally, the last is that it requires only one nodal stress value, i.e. the peak stresses $\sigma_{\theta\theta,\theta=0,\text{peak}}$, $\tau_{r\theta,\theta=0,\text{peak}}$, and $\tau_{\theta z,\theta=0,\text{peak}}$, instead of the whole stress distribution, greatly simplifying the post-processing of the data.

Then, the NSIFs can be estimated as follow [36–38]:

$$K_1 \cong K_{\text{FE}}^* \cdot \sigma_{\theta\theta,\theta=0,\text{peak}} \cdot d^{1-\lambda_1} \quad (1.21)$$

$$K_2 \cong K_{\text{FE}}^{**} \cdot \tau_{r\theta,\theta=0,\text{peak}} \cdot d^{1-\lambda_2} \quad (1.22)$$

$$K_3 \cong K_{\text{FE}}^{***} \cdot \tau_{\theta z,\theta=0,\text{peak}} \cdot d^{1-\lambda_3} \quad (1.23)$$

where K_{FE}^* , K_{FE}^{**} and K_{FE}^{***} are calibrated non-dimensional constants, d is the average size of the finite elements, λ_i ($i = 1, 2$ and 3) are the stress singularity exponents which depend on the notch opening angle 2α , and $\sigma_{\theta\theta,\theta=0,peak}$, $\tau_{r\theta,\theta=0,peak}$, and $\tau_{\theta z,\theta=0,peak}$ are the opening (mode I), in-plane shear (mode II), and out-of-plane shear (mode III) peak stresses, respectively, obtained from linear elastic FE analyses according to the rules of the PSM.

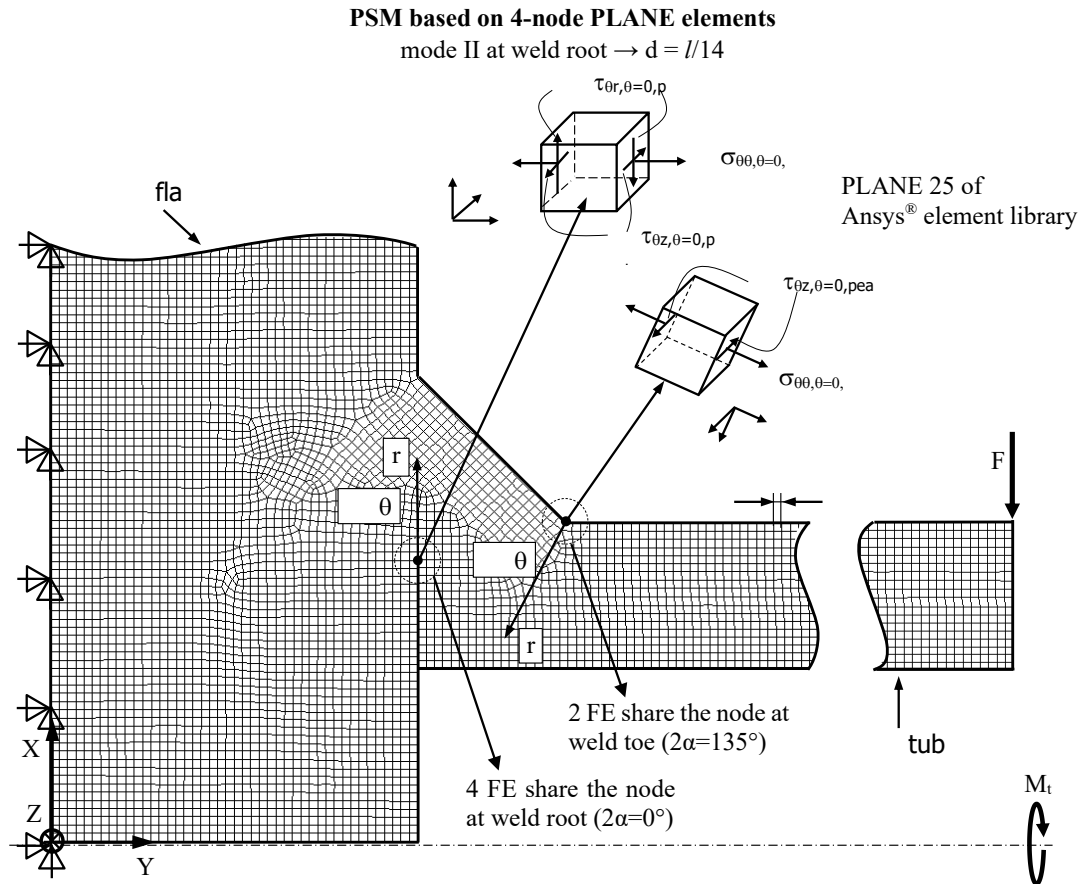
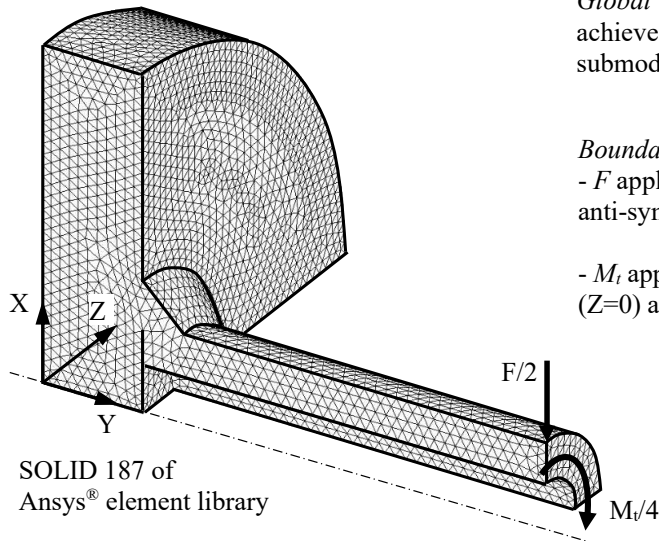


Figure 1.9. FE models to apply the PSM according to Eqs. (1.21), (1.22), and (1.23) for a partial-penetration tube-to-flange welded joint under combined bending and torsion loading using 2D 4-node plane elements. Image taken from [41].

More in detail, K_{FE}^* , K_{FE}^{**} and K_{FE}^{***} (Eqs. (1.21), (1.22), (1.23)) have been calibrated by using 2D as well as 3D finite elements available in several commercial FE codes (Abaqus®, Straus7®, MSC Patran/Nastran®, Lusas®, Ls-dyna®, Optistruct®) [41,79,80] since they depend on the element type and formulation, on the FE mesh pattern and on the employed FE commercial code [79,80]. The calibration for 2D elements has been performed on 4-node quadrilateral plane elements (PLANE 182 with K-option 1 set to 3, activating the ‘simple enhanced strain’ element formulation, of the Ansys® element library) and on 4-node harmonic elements (PLANE 25 of the Ansys® element library) [36–38] (see Table 1.3).

PSM based on 8-node BRICK elements

Main model (10-node TETRA elements)



Global element size: must be chosen to achieve convergence of displacements at submodel cut boundaries

Boundary conditions:

- F applied: symmetry on plane XY ($Z=0$) and anti-symmetry on plane YZ ($X=0$)

- M_t applied: anti-symmetry on both plane XY ($Z=0$) and plane YZ ($X=0$)

Sub model (8-node BRICK elements)

mode II at weld root $\rightarrow d = l/14$

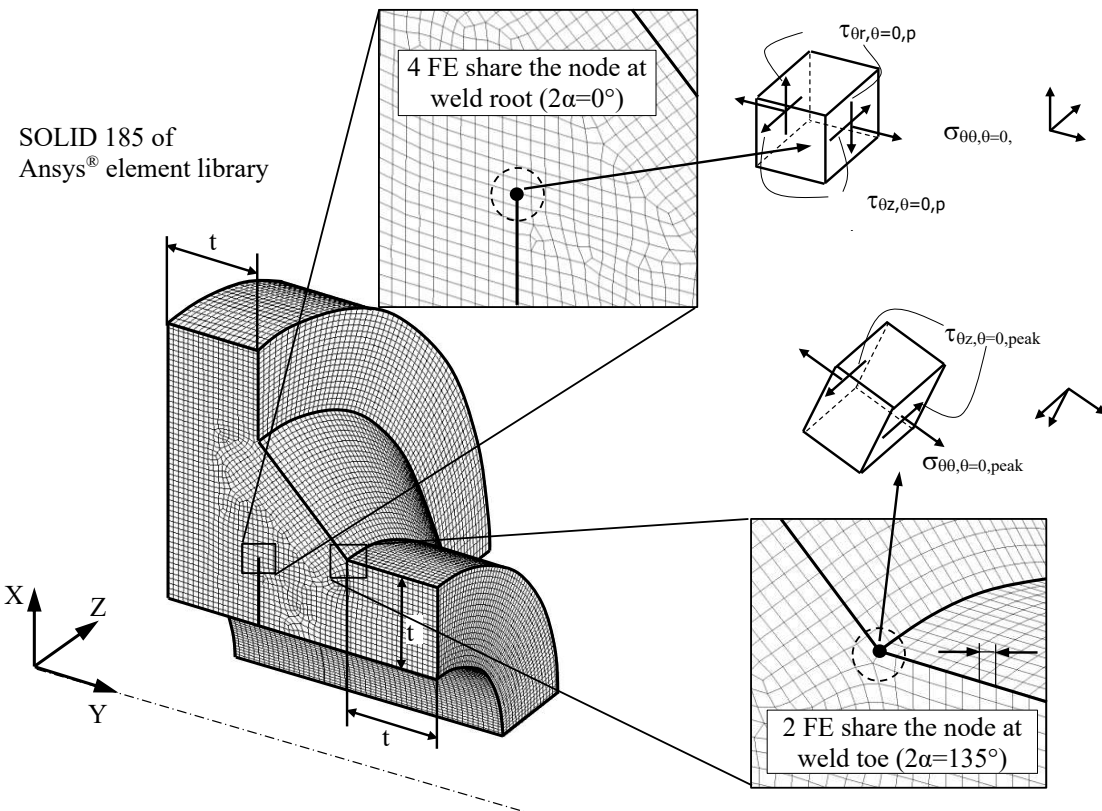


Figure 1.10. FE models to apply the PSM according to Eqs. (1.21), (1.22), and (1.23) for a partial-penetration tube-to-flange welded joint under combined bending and torsion loading using 3D 8-node brick elements. Image taken from [41].

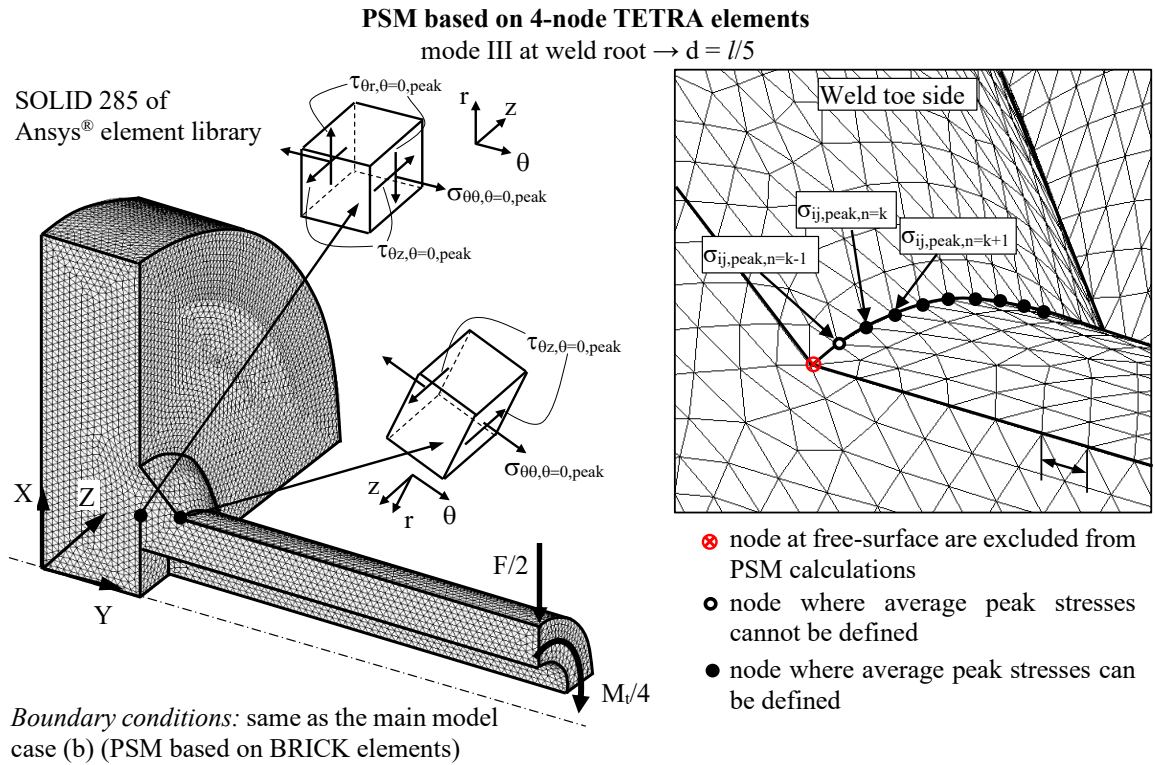


Figure 1.11. FE models to apply the PSM according to Eqs. (1.21), (1.22), and (1.23) for a partial-penetration tube-to-flange welded joint under combined bending and torsion loading using 3D 4-node tetra elements. Image taken from [41].

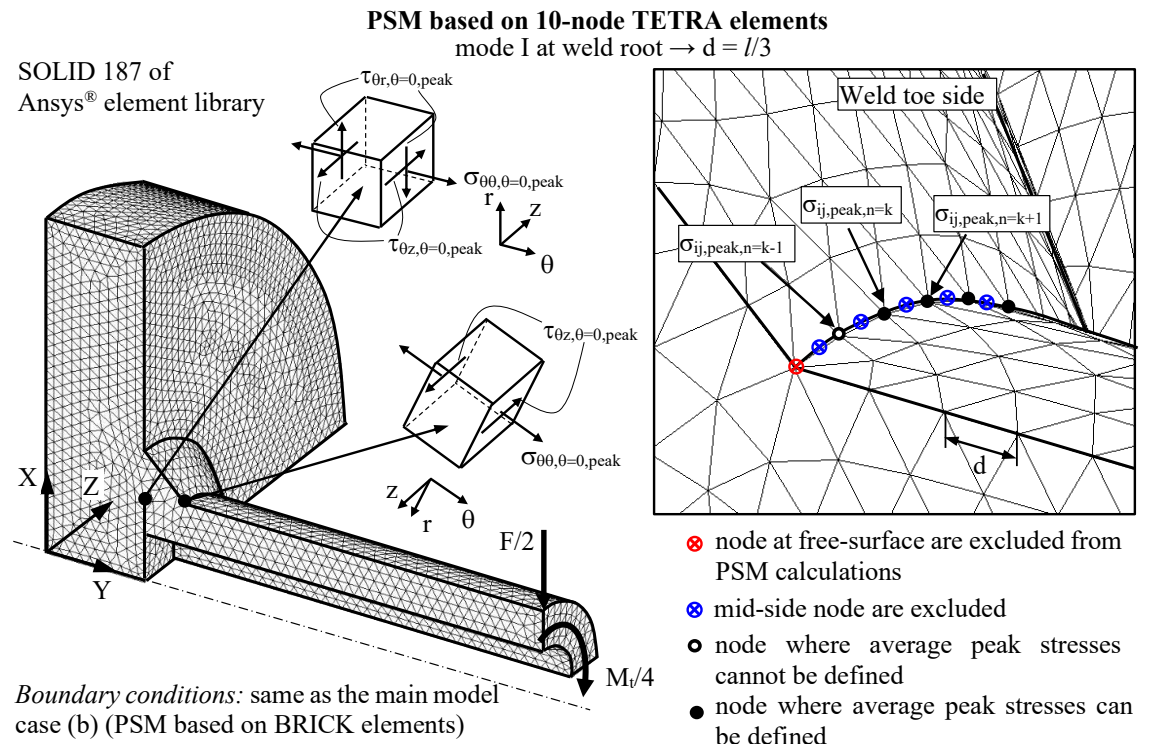


Figure 1.12. FE models to apply the PSM according to Eqs. (1.21), (1.22), and (1.23) for a partial-penetration tube-to-flange welded joint under combined bending and torsion loading using 3D 10-node tetra elements. Image taken from [41].

Instead, the calibration for 3D elements has been performed on 8-node brick elements [81] (SOLID185 with K-option 2 set to 3, activating the ‘simple enhanced strain’ element formulation, of the Ansys® element library) and on both 4-node linear tetra elements (SOLID 285 of the Ansys® element library) and 10-node quadratic tetra elements (SOLID 187 of the Ansys® element library) [40,41]. The corresponding values of K_{FE}^* , K_{FE}^{**} and K_{FE}^{***} calibrated using 2D 4-node plane [36–38], 3D 8-node brick elements [81], and 3D 10-node tetrahedral [40,41] elements of Ansys® software are summarised in Table 1.3.

Table 1.3 also show that some restrictions about the mesh pattern in the nearby of the V-notch tip take place when 2D 4-node plane elements and 3D 8-node brick elements are used. In particular, the PSM requires the node located at the notch tip is shared by four elements when the notch opening angle 2α is smaller than 90° or two elements when the opening angle 2α is greater than 90° [41,79]. This condition can be automatically satisfied by the free mesh generation algorithm available in Ansys® software after having imputed only the ‘global element size’ parameter d , without any further settings, as depicted in Figure 1.13. Figure 1.13 summarizes the requirements on the FE mesh pattern showing some examples of FE mesh patterns according to the PSM taking advantage of the symmetry plane.

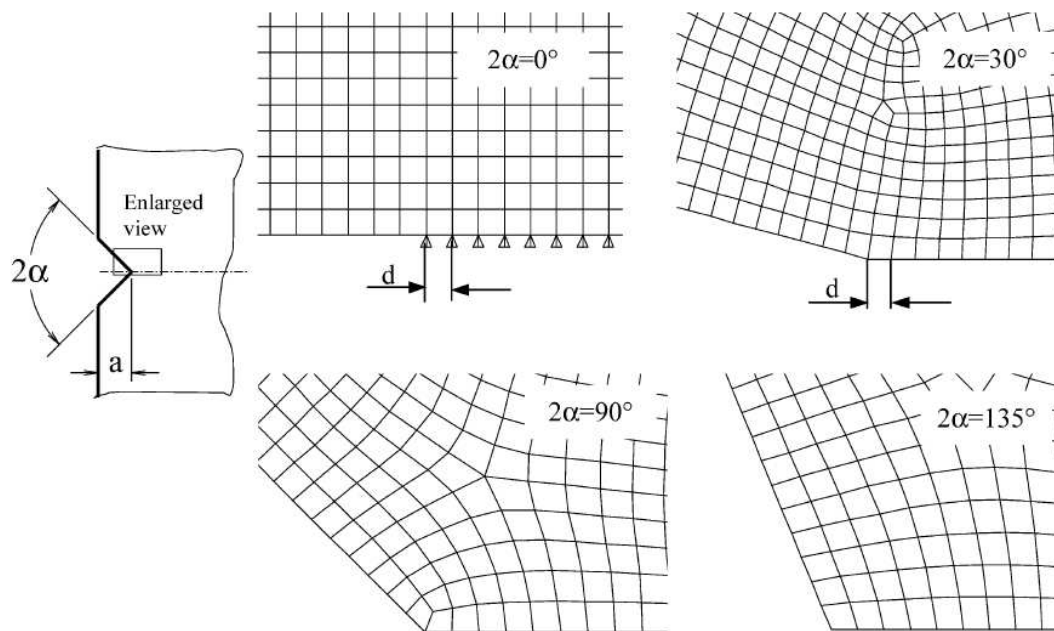


Figure 1.13. Standard FE free mesh pattern according to the PSM for 4-node plane and 8-node brick elements.

Table 1.3. Summary of parameters K^*_{FE} , K^{**}_{FE} and K^{***}_{FE} , mesh density a/d , and FE mesh pattern requirements to apply the PSM with Ansys® [36–41,81,82].

Loading	FE analysis		PSM parameters	$2\alpha = 0^\circ$	$2\alpha = 90^\circ$	$2\alpha = 120^\circ$	$\alpha = 135^\circ$	$a - \text{root side}^\circ$	$a - \text{toe side}^\circ$
	2D/3D	FE type [#]							
Mode I	2D	Plane-4	K^*_{FE}	1.38±3%	1.38±3%	1.38±3%	1.38±3%	min{l, z}	t
			(a/d) _{min}	3	3	3	3		
			FE at notch tip [^]	4	4	2	2		
	3D ⁺	Brick-8	K^*_{FE}	1.38±3%	1.38±3%	1.38±3%	1.38±3%	min{l, z}	t
			(a/d) _{min}	3	3	3	3		
			FE at notch tip [^]	4	4	2	2		
	3D ⁺	Tetra-4	K^*_{FE}	1.75±22%	1.75±22%	1.75±22%	1.75±22%	min{l, z}	t
			(a/d) _{min}	3	3	3	1		
			FE at notch tip [^]	<i>not to be checked</i>					
	3D ⁺	Tetra-10	K^*_{FE}	1.05±15%	1.05±15%	1.05±15%	1.21±10%	min{l, z}	t
			(a/d) _{min}	3	3	3	1		
			FE at notch tip [^]	<i>not to be checked</i>					
Mode II	2D	Plane-4	K^{**}_{FE}	3.38±3%	2.62±10%	-	-	min{l, z}	-
			(a/d) _{min}	14	10	-	-		
			FE at notch tip [^]	4	4	-	-		
	3D ⁺	Brick-8	K^{**}_{FE}	3.38±3%	2.62±10%	-	-	min{l, z}	-
			(a/d) _{min}	14	10	-	-		
			FE at notch tip [^]	4	4	-	-		
	3D ⁺	Tetra-4	K^{**}_{FE}	2.65±15%	2.90±10%	-	-	min{l, z}	-
			(a/d) _{min}	3	1	-	-		
			FE at notch tip [^]	<i>not to be checked</i>					
	3D ⁺	Tetra-10	K^{**}_{FE}	1.63±20%	2.65±10%	-	-	min{l, z}	-
			(a/d) _{min}	1	1	-	-		
			FE at notch tip [^]	<i>not to be checked</i>					
Mode III	2D	Plane-4	K^{***}_{FE}	1.93±3%	1.93±3%	1.93±3%	1.93±3%	min{l, z}	t
			(a/d) _{min}	12	-	-	3		
			FE at notch tip [^]	4	-	-	2		
	3D ⁺	Brick-8	K^{***}_{FE}	1.93±3%	1.93±3%	1.93±3%	1.93±3%	min{l, z}	t
			(a/d) _{min}	12	-	-	3		
			FE at notch tip [^]	4	-	-	2		
	3D ⁺	Tetra-4	K^{***}_{FE}	2.20±15%	2.20±15%	2.20±15%	2.20±15%	min{l, z}	t
			(a/d) _{min}	5	5	5	5		
			FE at notch tip [^]	<i>not to be checked</i>					
	3D ⁺	Tetra-10	K^{***}_{FE}	1.37±15%	1.37±15%	1.70±10%	1.70±10%	min{l, z}	t
			(a/d) _{min}	3	3	3	3		
			FE at notch tip [^]	<i>not to be checked</i>					

⁺ 'Full graphics' option must be activated when calculating peak stresses according to 3D PSM

[#] FE of Ansys® code: Plane-4 = PLANE 182 (K-option 1 set to 3) or PLANE 25, Tetra 10 = SOLID 187

[^] number of finite elements which share the node at the notch tip

[°] l, z, t are defined in Figure 1.14

As for 3D tetra elements, they have no mesh pattern restrictions to comply with when are used [41] (see Figure 1.11 and Figure 1.12). This makes them even more efficient in discretizing very complex 3D geometries compared to brick elements for which the discretization of such geometries would be impossible. Unfortunately, they lead to irregular FE mesh patterns along the notch tip line, which means the nodes located on it share a different number of tetra elements. As a result, such a mesh pattern results in a noisy distribution of the NSIFs, due to a noisy distribution of the peak stresses (see Eqs. (1.21), (1.22), (1.23)) even in 3D geometries where the NSIFs are rigorously constant along the V-notch tip line [39]. To address this issue, Campagnolo et al. [40] suggest smoothing the peak stresses distribution along the V-notch tip line by substituting into Eqs. (1.21), (1.22), (1.23) the peak stresses $\sigma_{\theta\theta,\theta=0,peak}$, $\tau_{r\theta,\theta=0,peak}$, and $\tau_{\theta z,\theta=0,peak}$ with the corresponding average peak stresses $\bar{\sigma}_{\theta\theta,\theta=0,peak}$, $\bar{\tau}_{r\theta,\theta=0,peak}$, and $\bar{\tau}_{\theta z,\theta=0,peak}$ defined as follow:

$$\bar{\sigma}_{ij,peak,n=k} = \frac{\sigma_{ij,peak,n=k-1} + \sigma_{ij,peak,n=k} + \sigma_{ij,peak,n=k+1}}{3} \Bigg|_{n=node} \quad (1.24)$$

Where $\sigma_{ij} = \sigma_{\theta\theta,\theta=0,peak}$, $\tau_{r\theta,\theta=0,peak}$, $\tau_{\theta z,\theta=0,peak}$. In few words, the average peak stresses $\bar{\sigma}_{\theta\theta,\theta=0,peak}$, $\bar{\tau}_{r\theta,\theta=0,peak}$, and $\bar{\tau}_{\theta z,\theta=0,peak}$ are defined as the moving averages of the peak stresses calculated on three adjacent vertex nodes. (1.24) gives the example for calculating the peak stress at node $n = k$ (see Figure 1.11 and Figure 1.12). Moreover, as explained in [40,80], the peak stresses at nodes on a free surface of the investigated structure (red nodes in Figure 1.11 and Figure 1.12) must neglected and not be inputted into Eq. (1.24). An additional restriction comes up when dealing with 10-node tetra elements. It consists in neglecting peak stresses at mid-side nodes (blue nodes in Figure 1.12) and considering only that relevant to vertex node in Eq. (1.24).

Finally, it is important to highlight that the global element size d can be arbitrarily chosen, provided it is within a certain range of applicability, to properly generate a finite element model consistent with the rule of the PSM. In particular, the mesh pattern must satisfy a certain mesh density ratio a/d , where d is the ‘global element size’ to be given as an input to the free mesh generation algorithm of the FE software, while a is a reference dimension defined as a function of the geometrical parameters t , z , l of Figure 1.14. As reported in Table 1.3, the minimum values of a/d depend on the adopted FE type, the local stress mode and the considered notch

opening angle 2α . For example, in the case of a weld toe ($2\alpha = 135^\circ$) under pure mode I loading and modelled using 10-node tetra elements, the minimum mesh density ratio a/d required by the PSM is $a/d \geq 3$ to obtain $K_{FE^*} = 1.21 \pm 10\%$, a being the plate thickness t (Figure 1.14 and Table 1.3). More details on the applicability of the PSM can be found in a recent review [41].

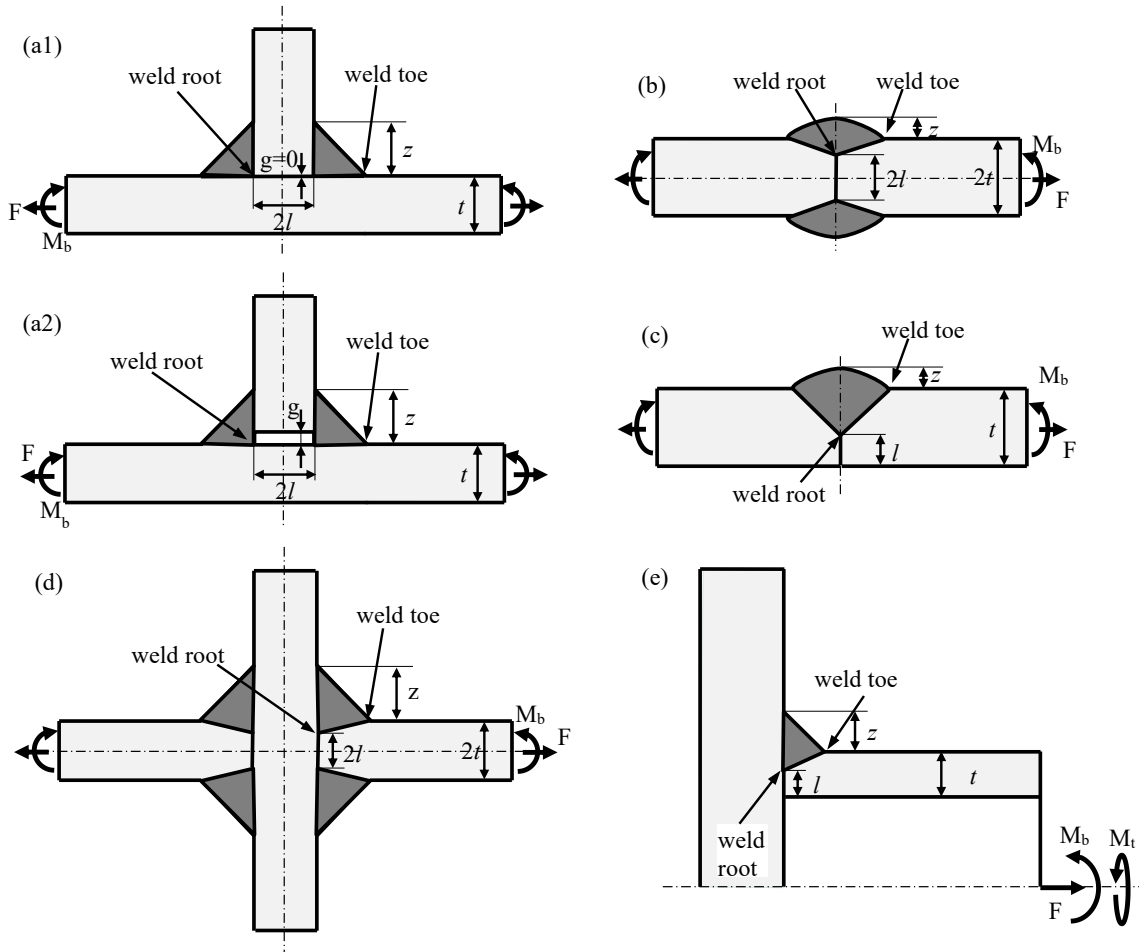


Figure 1.14. Definition of the parameters l , z , t required in the evaluation of the reference dimension a according to Table 1.3. Image taken from [41].

For comparison, the PSM has been applied to the mode I NSIF evaluation at the weld toe of the transverse full penetration welded joint in Figure 1.15 having the same geometry and loading conditions as that reported in Figure 1.6. Again, the FE model has been generated exploiting the two symmetries, and the model has been discretized using 4-node quadrilateral plane elements (PLANE 182 with K-option 1 set to 3, activating the ‘simple enhanced strain’ element formulation, of the Ansys® element library). The minimum mesh density ratio must be $a/d = 3$ to apply the PSM at the weld toe under mode I local stresses, where $a = t = 8$ mm

for considered joint geometry. According, a global element size $d = a/3 = 8/3 = 2.7\text{mm}$ has been given as an input to the free mesh generation algorithm of the Ansys[®] FE software, and it has been obtained the mesh pattern showed in Figure 1.16. After the solution, the maximum principal stress range $\Delta\sigma_{11,\text{peak}} = 1.4097\text{ MPa}$ has been evaluated at the weld toe, since under pure mode I stresses, it approximately corresponds to the opening (mode I) peak stress range $\Delta\sigma_{\theta\theta,\theta=0,\text{peak}}$, but it is easier to be obtained since it is invariant with respect to the reference system. Then, the mode I NSIF range ΔK_I has been evaluated according to Eq. (1.21) obtaining $\Delta K_I = 1.38 \cdot \Delta\sigma_{11,\text{peak}} \cdot d^{3/26} = 1.38 \cdot 1.4097 \cdot 2.7^{0.326} = 2.689\text{ MPa}\cdot\text{mm}^{0.326}$ in very good agreement with the value obtained applying the definition, the percentage error being $(2.689-2.76)/2.76 = -2.6\%$.

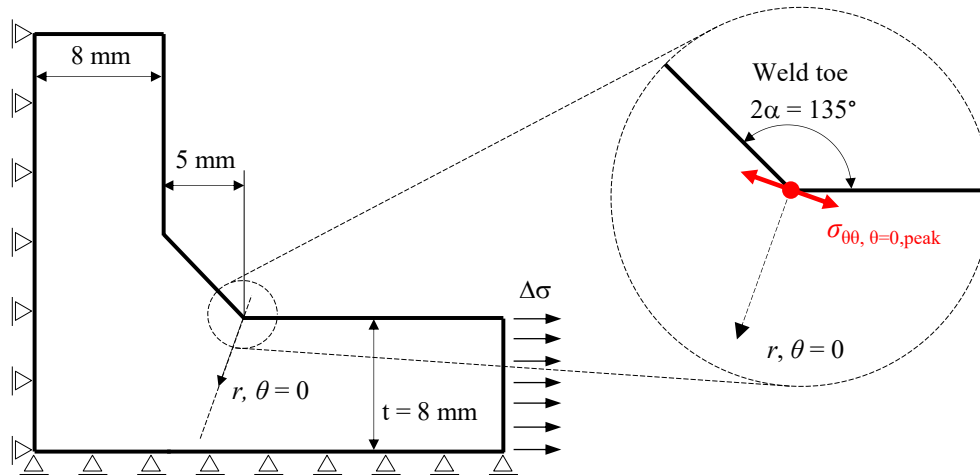


Figure 1.15. Geometry of the transverse non-load-carrying welded joint considered in Figure 1.6 here applied for the calculation of the mode I NSIF at the weld toe according to the PSM (Eqs. (1.21), (1.22), (1.23)). On the right, a detail of the weld toe modelled as sharp V-notch with highlight the opening (mode I) singular peak stress $\sigma_{\theta\theta,\theta=0,\text{peak}}$ evaluated at the FE node laying at the V-notch tip.

By comparing Figure 1.16 with Figure 1.7, it appears clear the advantage of using the PSM instead of the NSIF-definition-based calculation of the NSIFs. Actually, the global element size adopted to apply the PSM ($d = 2.7\text{ mm}$) is extremely greater (i.e. the FE model is computationally extremely faster and more efficient) than that required for the calculation of K_I according to the definition, which locally required element in the order of 10^{-5} mm .

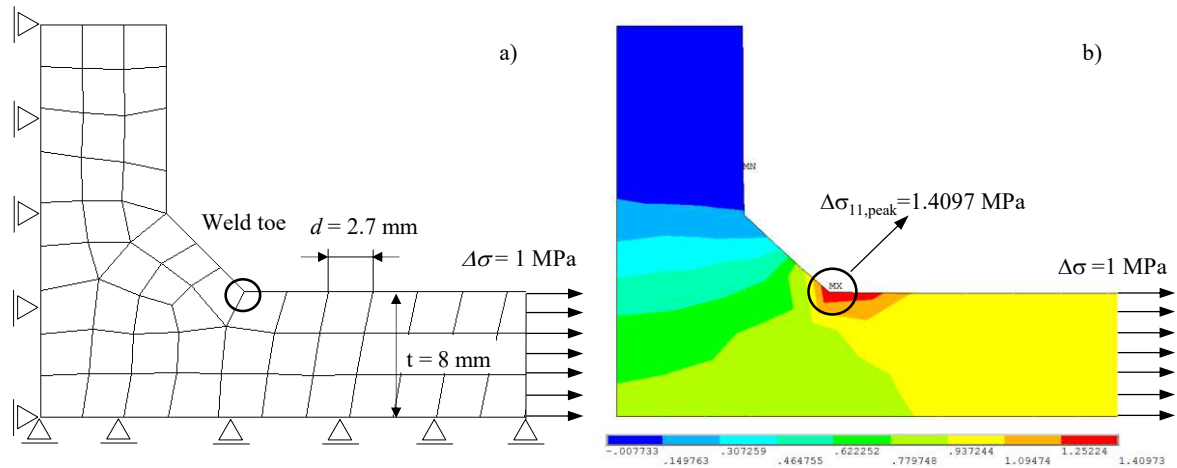


Figure 1.16. a) FE model adopted for the PSM calculation of the mode I NSIF at the weld toe of the joint in Figure 1.15. b) Contour map of the maximum principal stress obtained from FEA according to the PSM with applied $\Delta\sigma = 1$ MPa with highlighted the value at the node laying at the sharp V-notch tip.

1.2.5. Fatigue design against pure mode I weld toe using the NSIFs approach

The NSIFs quantify the intensity of the asymptotic stress distributions at the V-notch tip and they have been shown to be fatigue relevant parameters [9,18,19]. More in detail, in the case of pure mode I loading (there are no mode II and III contributions), the idea behind the NSIF approach for the fatigue lifetime assessment of welded joints is that joints subjected to the same value of the applied NSIF range ΔK_I (calculated maximum value minus minimum value, $K_{\max} - K_{\min}$), will exhibit the same fatigue life (i.e. number of cycles to failure N_f). That because ΔK_I conveys all information on the intensity of the local stress field, regardless the type of loads (as long as they generate only pure mode I local stresses) or the geometry of the component.

A very important application of what has been described is the one reported by Lazzarin and Tovo [18] about welded joints under pure mode I local stresses showing fatigue failure at the weld toe. In this case, they demonstrated the weld toe can be modelled like a sharp V-notch having opening angle $2\alpha = 135^\circ$ (Figure 1.3). They considered the fatigue strength of non-load-carrying fillet welded joints made of structural steel and having different geometry. As expected, they found the experimental data were badly described by a single design scatter band expressed in terms of applied nominal stress range $\Delta\sigma$ versus the cycles to failure N_f , which resulted very wide by virtue of the great variability of the considered geometries (Figure 1.17). Indeed, according to the nominal stress approach [7,8], it is necessary to adopt a different S-N

design curve chosen from a list of classified structural details for each joint geometry rather than including all the data in a single scatter band.

However, by adopting the applied NSIF range ΔK_1 instead of the applied nominal stress range $\Delta\sigma$ all data collapsed within a single scatter band having a much narrower dispersion (Figure 1.17). In other words, similarly to the SIF in the context of the Linear Elastic Fracture Mechanic (LEFM), the NSIF includes all information about the component geometry and the scale effect on the local stress field, properly correlating the fatigue strength of joints having different geometries and different absolute dimensions.

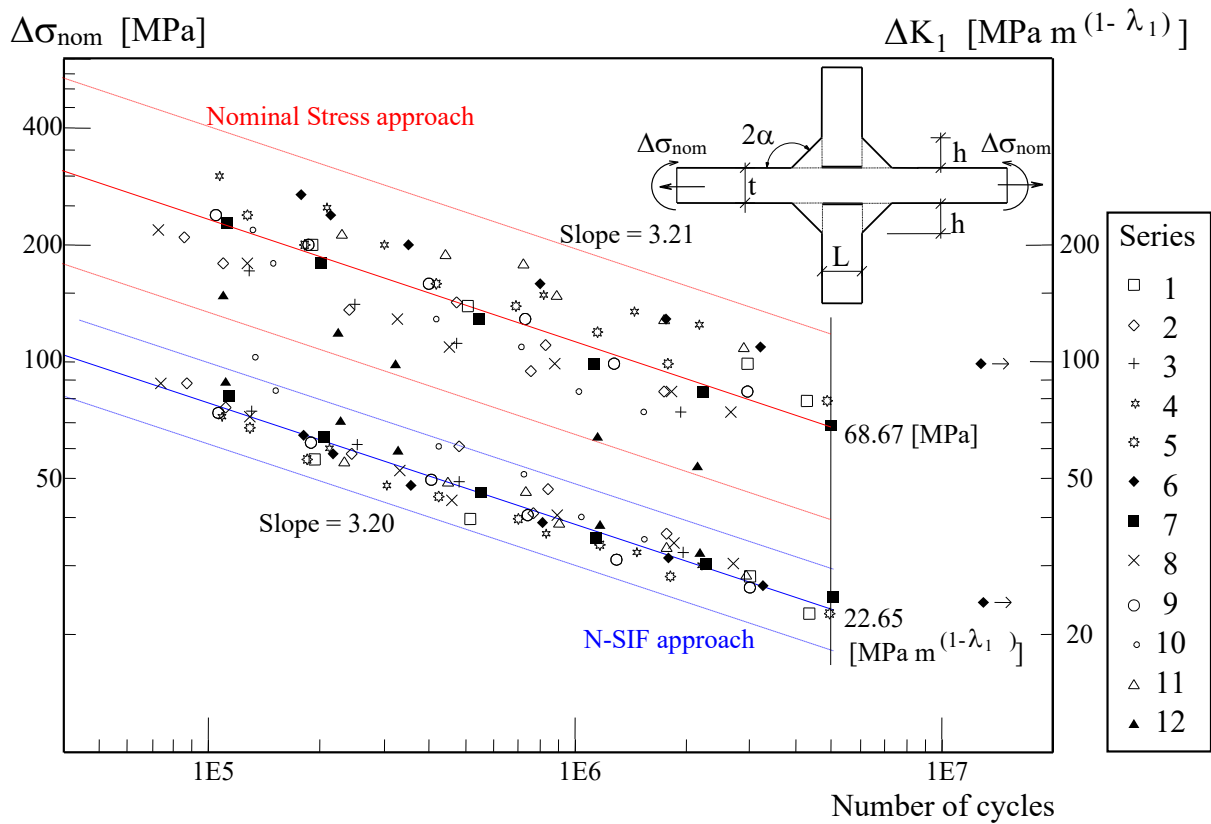


Figure 1.17. Design scatter band for the fatigue lifetime assessment of non-load-carrying fillet welded joints according to the nominal stress approach and to the NSIF based approach [18].

So, summarizing the advantages of the NSIF approach compared to a nominal stress approach are the following:

- It allows to use a single design curve whatever the joint geometry (as long as they have always the same opening angle 2α) for a fixed survival probability (PS). For

example, in case of weld toe failure ($2\alpha = 135^\circ$) the fatigue strength at $N_D = 5 \cdot 10^6$ cycles for PS = 50% (mean value) is $\Delta K_{ID} = 22.65 \text{ MPa}\cdot\text{m}^{0.326} = 211 \text{ MPa}\cdot\text{mm}^{0.326}$ ($2\alpha = 135^\circ \rightarrow 1-\lambda_1 = 0.326$, see Figure 1.5 and Table 1.1).

- It is independent on the complexity of the joint geometry, since it also works in the case of geometries whose proper reference design category does not exist. Indeed, the NSIFs' values can be easily assessed on the analytically, numerically or experimentally.

1.2.6. Limitations of the NSIFs approach

The advantages of the NSIF based approach in designing notched components (welded joints) against fatigue hold true as long as the analysed notches have the same opening angle are subjected only to one of the local stress modes (the other must be null or negligible). Otherwise, the NSIFs K_1 , K_2 , and K_3 can no longer be used as a failure criterion as their size is different and their direct comparison can no longer be done. Unfortunately, many practical/industrial applications relevant to the fatigue of welded joints must deal with components having different notches with different opening angles and subjected to multiaxial loadings, i.e. the notch tip is subjected to not-negligible values of K_1 , K_2 , and K_3 applied at the same time. A typical example is that of a load-carrying fillet-welded cruciform joint (Figure 1.18a) or of a fillet-welded lap joint (Figure 1.18b) in which both the weld toe ($2\alpha = 135^\circ$) and the weld root ($2\alpha = 0^\circ$) are critical point in the structure where fatigue failure can occur. In this case, the mode II at the weld toe is not singular, the opening angle 2α being larger than 102° , while at the weld root both mode I and II are singular. Accordingly, it is no more possible to perform the fatigue lifetime assessment of the welded joints because a criterion would be needed to combine modes I and II and establish the severity of the stress field in the nearby of the notches subjected to mixed mode I+II local stresses.

The NSIF approach cannot be used even in case the mode II component is negligible if compared to mode I (this happens for example in the case of load-carrying fillet-welded cruciform joint, see Figure 1.18a). Indeed, in both the critical points of the structure, i.e. the weld toe and root, the K_1 is a fatigue relevant parameter capable of completely describing the intensity of the local stress field in the nearby of the notches. However, a direct comparison

between K_I for the weld toe and the weld root is not possible, the NSIF measurement units being $\text{MPa}\cdot\text{m}^{0.326}$ for the weld toe ($1-\lambda_1=0.326$ for $2\alpha=135^\circ$) and $\text{MPa}\cdot\text{m}^{0.5}$ for the weld root ($1-\lambda_1=0.5$ for $2\alpha=0^\circ$).

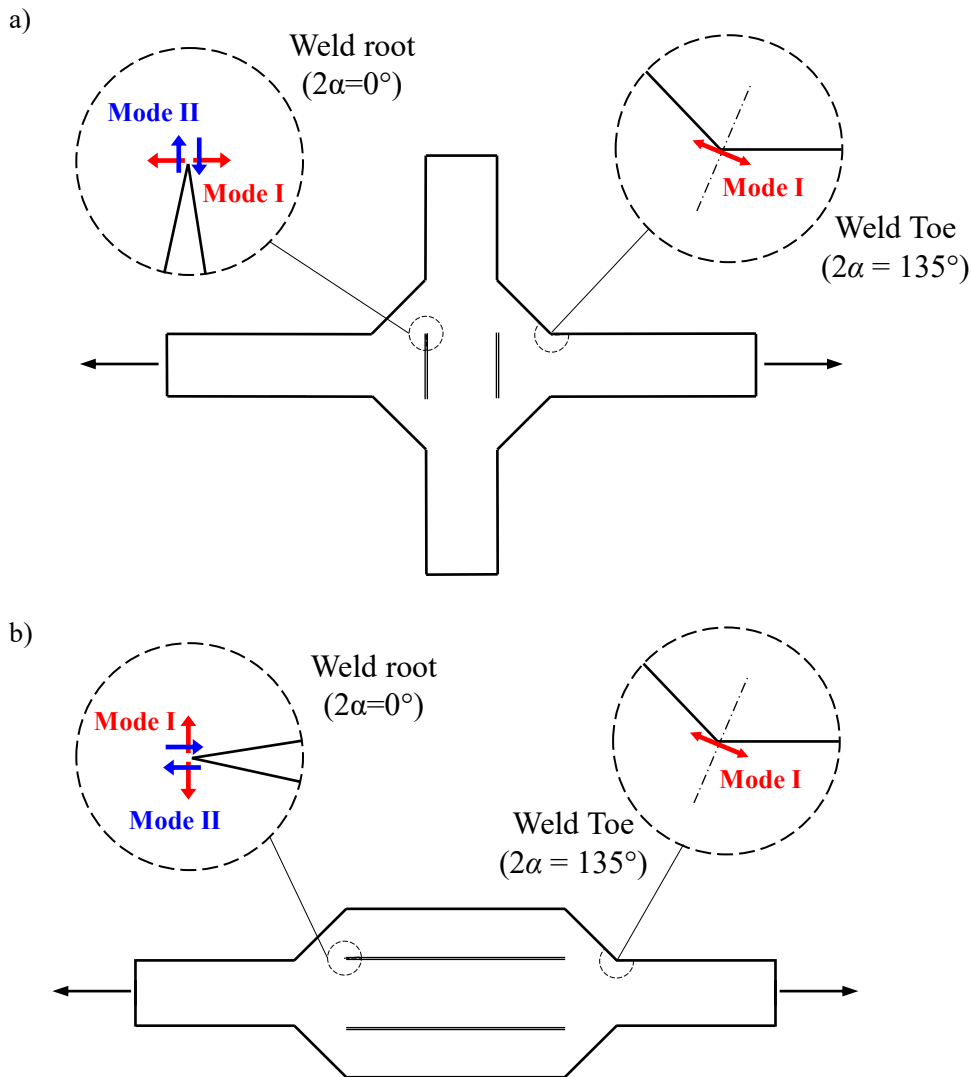


Figure 1.18. Example of welded details exhibiting mode I+II singular local stresses at the weld root ($2\alpha=0^\circ$) and pure mode I singular local stress at the weld toe ($2\alpha=135^\circ$, mode II is not singular at the weld toe). a) load-carrying fillet-welded cruciform joint and b) fillet-welded lap joint.

Noteworthy, the local stress fields relevant to the weld toe and the weld root are not comparable to each other as they are not parallel due to the different stress singularity degree (Figure 1.19). Consequently, it is not possible to establish whether the weld toe or the weld root is the most critical point and performing the fatigue lifetime assessment of the welded joint.

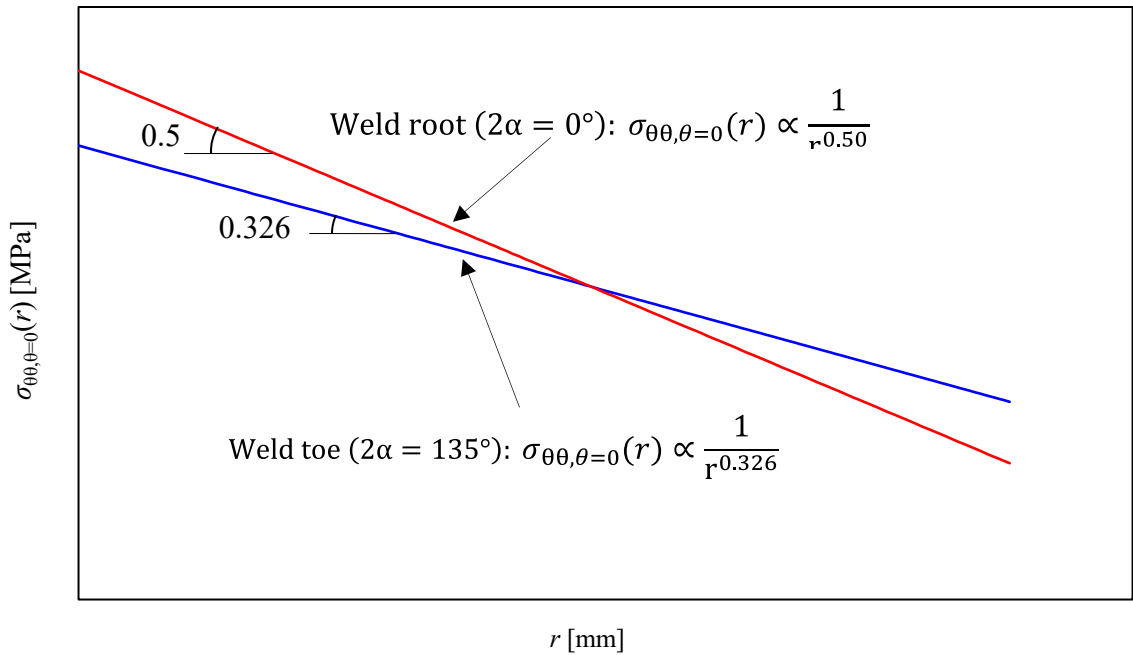


Figure 1.19. Comparison between mode I singular stress field at the weld toe ($2\alpha = 135^\circ$) and at the weld root ($2\alpha = 0^\circ$).

1.3. The averaged Strain Energy Density (SED) criterion

In the context of the NSIF approach and taking advantage of the observations on notch sensitivity moved by Neuber [83], Lazzarin and Zambardi [25] proposed the local Strain Energy Density (SED) approach. The principle behind the method is quite simple. The method is based on the idea of Beltrami [84] who proposed for the first time to adopt the elastic Strain Energy Density W as a strength parameter. The problem in the definition of the SED criterion is that as for the stress components, also the SED is singular in case of sharp V-notches having null tip radius ($\rho = 0$ implies that $\sigma \rightarrow \infty$ and $W \rightarrow \infty$). The solution they found was moved by Neuber's observations [83], according to which both static and cyclic crack initiation at notches is regulated by the average value of the stress over an 'elementary material volume' or 'microstructural support length' instead of the elastic peak stress. Accordingly, as a static and fatigue damage parameter [20–25] they suggest to adopt the average strain energy density (SED) \bar{W} evaluated over a finite material-structural volume close to the notch (or crack) tip. Lazzarin and Zambardi [25] proposed a circular-shaped material-structural volume, surrounding the crack initiation point, i.e., the weld toe or the weld root, and geometrically described by a radius R_0 , the latter being taken as a material property (see Figure 1.20).

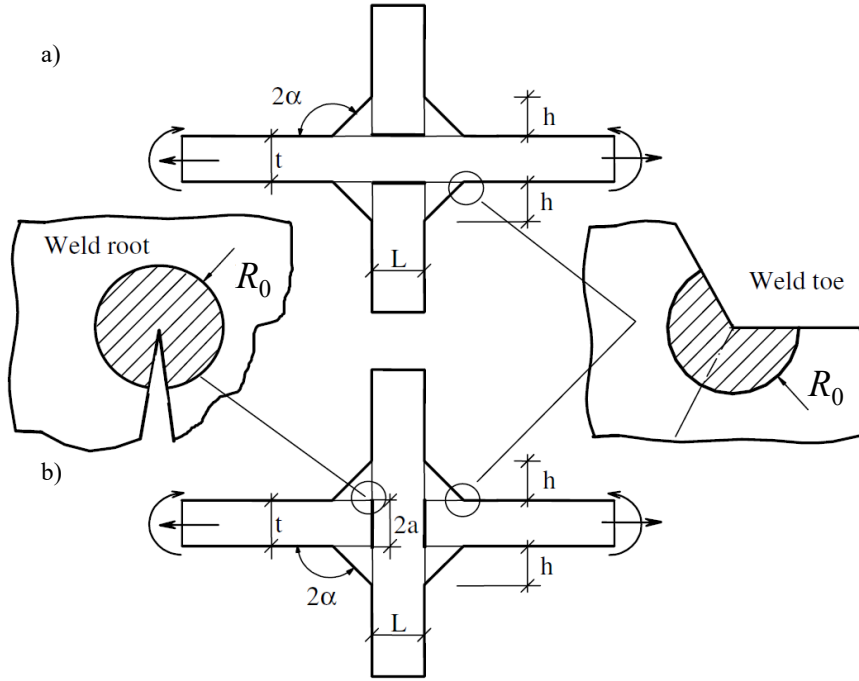


Figure 1.20. Circular-shaped average SED material-structural control volume with radius R_0 surrounding the crack initiation point, i.e., the weld toe or the weld root, of a) a transverse non-load-carrying fillet welded joints and b) a load-carrying fillet welded cruciform joint.

So, according to the SED approach, two components having sharp V-notches with different opening angles 2α (Figure 1.20) subject to a generic combination of loads generating different multiaxial local stresses at the V-notch tips (mode I+II+III), will exhibit the same fatigue life N_f if characterized by the same average SED range $\Delta\bar{W}$. This means the SED criterion overcomes the limitations of the NSIF approach related to the notch opening angle and to the multiaxial load conditions in the fatigue design of welded joints. Indeed, regardless the notch opening angle and the multiaxial stress state, the damage parameter is always an energy density having unit of measurement equal to Nm/m^3 . Furthermore, they observed that in the case of a sharp V-notch under mixed mode I+II+III loading and when high-order non-singular stress terms are negligible inside the structural volume, the SED \bar{W} is directly linked to the NSIFs K_1 , K_2 , and K_3 . In particular, concerning fatigue loading, they proved that the averaged SED $\Delta\bar{W}$ can be written as a function of the ranges of the NSIFs, ΔK_1 , ΔK_2 , and ΔK_3 (i.e. maximum value minus minimum value, $K_{\max} - K_{\min}$) according to the following expression [21]:

$$\Delta\bar{W} = c_{w1} \frac{e_1}{E} \left[\frac{\Delta K_1}{R_0^{1-\lambda_1}} \right]^2 + c_{w2} \frac{e_2}{E} \left[\frac{\Delta K_2}{R_0^{1-\lambda_2}} \right]^2 + c_{w3} \frac{e_3}{E} \left[\frac{\Delta K_3}{R_0^{1-\lambda_3}} \right]^2 \quad (1.25)$$

where E is the Young's modulus of the material, e_1 , e_2 , and e_3 are coefficients depending on the sharp V-notch opening angle 2α and the Poisson's ratio ν [21], while c_{w1} , c_{w2} , and c_{w3} account for the mean stress sensitivity in case of stress-relieved joints. More in detail, the total SED coefficients e_i (for $i = 1, 2, 3$) are defined by the following expressions [25,85]:

$$e_1 = \frac{\int_{-\gamma}^{+\gamma} f_{e_1,ij}(\theta, \nu) d\theta}{4 \cdot \lambda_1 \cdot \gamma} \quad (1.26)$$

$$e_2 = \frac{\int_{-\gamma}^{+\gamma} f_{e_2,ij}(\theta, \nu) d\theta}{4 \cdot \lambda_2 \cdot \gamma} \quad (1.27)$$

$$e_3 = \frac{(1 + \nu) \cdot \int_{-\gamma}^{+\gamma} f_{e_3,ij}(\theta, \nu) d\theta}{6 \cdot \lambda_3 \cdot \gamma} \quad (1.28)$$

Where $f_{e1,ij}$, $f_{e2,ij}$, and $f_{e3,ij}$ are the angular terms of the strain energy (see [25,85] for their explicit expressions). Some notable value relevant to structural steels ($\nu = 0.3$) is reported in Table 1.4 as a function of the opening angle.

Table 1.4. Total SED exponents (Eqs. (1.26), (1.27), (1.28)) for certain notch opening angles of structural steel ($\nu = 0.3$) under plain strain conditions.

2α	e_1	e_2	e_3
[°]	[-]	[-]	[-]
0	0.134	0.341	0.414
90	0.146	0.168	0.310
120	0.130	-	0.276
135	0.117	-	0.259

A parametric polynomial expression which gives the total SED coefficients the total for a generic V-notch opening angle 2α and Poisson's ratio ν is the following [77]:

$$e_i(2\alpha, \nu) = p_{00} + p_{10} \cdot (2\alpha) + p_{01} \cdot (\nu) + p_{20} \cdot (2\alpha)^2 + p_{11} \cdot (2\alpha) \cdot (\nu) + p_{30} \cdot (2\alpha)^3 + p_{21} \cdot (2\alpha)^2 \cdot (\nu) \quad (1.29)$$

1.3 The averaged Strain Energy Density (SED) criterion

Where the p_{jk} are coefficients (their values are reported in Table 1.5) depending on the local stress mode ($i = 1, 2,$ and 3) which subscripts i and j refer to the grades of the variable opening angle 2α and Poisson's ratio ν , respectively.

Table 1.5. Coefficients of Eq. (1.29) for estimating the total SED coefficients (Eqs. (1.26), (1.27), (1.28)).

Coefficient	e_1	e_2	e_3
p_{00}	$2.289 \cdot 10^{-1}$	$3.761 \cdot 10^{-1}$	$3.183 \cdot 10^{-1}$
p_{10}	$6.818 \cdot 10^{-4}$	$-2.973 \cdot 10^{-3}$	$-8.842 \cdot 10^{-4}$
p_{01}	$-3.200 \cdot 10^{-1}$	$-1.154 \cdot 10^{-1}$	$3.183 \cdot 10^{-1}$
p_{20}	$-8.023 \cdot 10^{-6}$	$5.987 \cdot 10^{-6}$	$8.168 \cdot 10^{-15}$
p_{11}	$-3.688 \cdot 10^{-4}$	$1.695 \cdot 10^{-3}$	$-8.842 \cdot 10^{-4}$
p_{30}	$-3.771 \cdot 10^{-9}$	0	0
p_{21}	$1.169 \cdot 10^{-5}$	0	0

Figure 1.21 shows the total SED coefficients dependence on the opening angle 2α in case of structural steels ($\nu = 0.3$) under plain strain conditions. It can be noted that e_3 is always higher than e_1 and e_2 . The latter, in turn, is always larger than e_1 , at least in the region where the mode II SED field (i.e. mode II the stress field) is singular ($2\alpha \leq 102.6^\circ$).

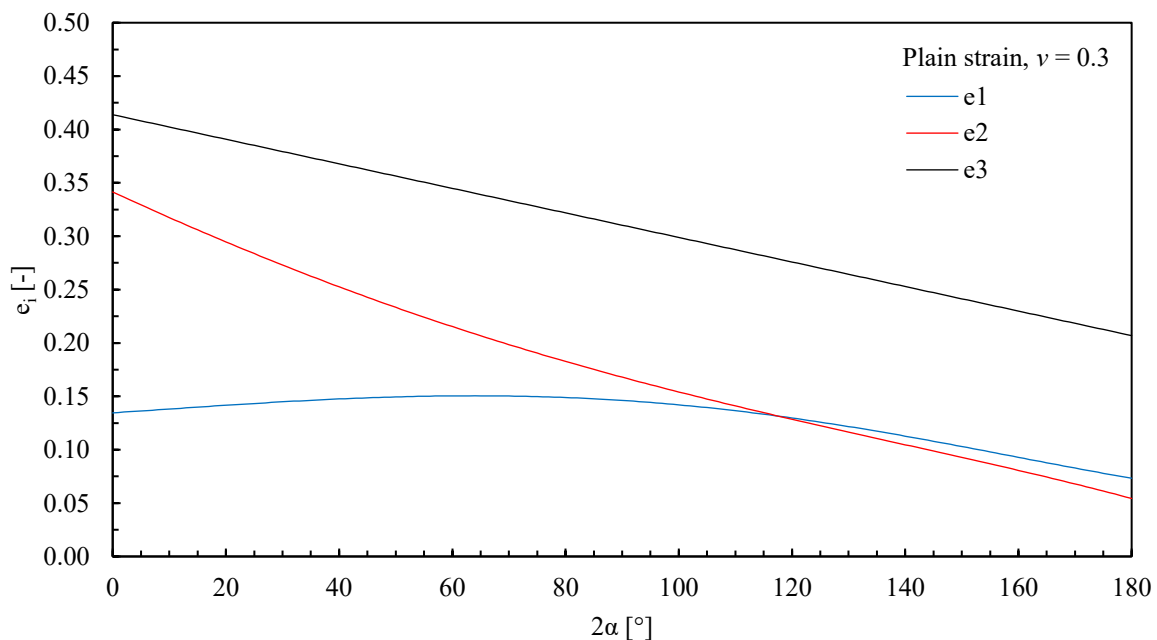


Figure 1.21. Total SED coefficients e_1 , e_2 and e_3 as a function of the notch opening angle 2α for structural steels ($\nu = 0.3$) under plane strain conditions.

Going back to Eq. (1.25), the c_{wi} coefficients are introduced to include the mean stress effect in the averaged SED calculation [41]. Lazzarin et al. [20,21] suggest using the c_w coefficients only in the case of stress-relieved welded joints, forcing $c_w = 1$ for as-welded joints, independently of the residual stress state. This assumption is somehow linked to what suggested in international standards and recommendations [7,8,86] according to which there is no mean stress effect on the fatigue strength of welded joints for $R \geq -0.25$ since the residual stresses are tensile and medium-high if compared to the yield strength of the material. Nevertheless, the c_w coefficients, to be used in case of stress-relieved joints, are defined as a function of the nominal load ratio $R_i = (\sigma_{\min}/\sigma_{\max})_i$ for each local stress mode ($i = 1, 2, 3$) according to the following expression [19]:

$$c_{wi}(R_i) = \begin{cases} \frac{1+R_i^2}{(1-R_i)^2} & \text{if stress-relieved and } -1 \leq R_i \leq 0, \\ \frac{1-R_i^2}{(1-R_i)^2} & \text{if stress-relieved and } 0 \leq R_i < 1, \\ 1 & \text{if as-welded for any } R \text{ value} \end{cases} \quad (1.30)$$

Eq. (1.30) is plotted in Figure 1.22 as a function of the nominal load ratio R . Noteworthy the factor of 2 between the coefficients for pulsating ($R = 0 \rightarrow c_w = 1$) and fully reversed loading ($R = -1 \rightarrow c_w = 0.5$). The last and most important aspect to be discussed is the circular-shaped material-structural volume radius R_0 (Figure 1.20). It must be thought as a material property which value differs from material to material. Interestingly, Lazzarin and Livieri [20] found a unique value of R_0 for all welded joints made of structural steels. They proposed to calibrate the control radius R_0 by equating the range averaged strain energy density at the fatigue limit (or at a reference number of cycles) of a plain specimen to that of a notched one:

$$\Delta \bar{W}_{\text{notch}} = \Delta \bar{W}_{\text{plain}} \quad (1.31)$$

To estimate the range of average strain energy density of the notched component $\Delta \bar{W}_{\text{notch}}$, Lazzarin and Livieri [20] considered the fatigue data relevant to the toe failure of fillet-welded joints in the as-welded state ($c_w = 1$) under pure axial fatigue loading. The V-notch opening angle has been assumed to be $2\alpha = 135^\circ$, this way the averaged mode 2 local SED \bar{W}_2 is

negligible (the stress field being not singular since $2\alpha > 102^\circ$) and only the averaged mode I local SED \bar{W}_I has a significant contribution.

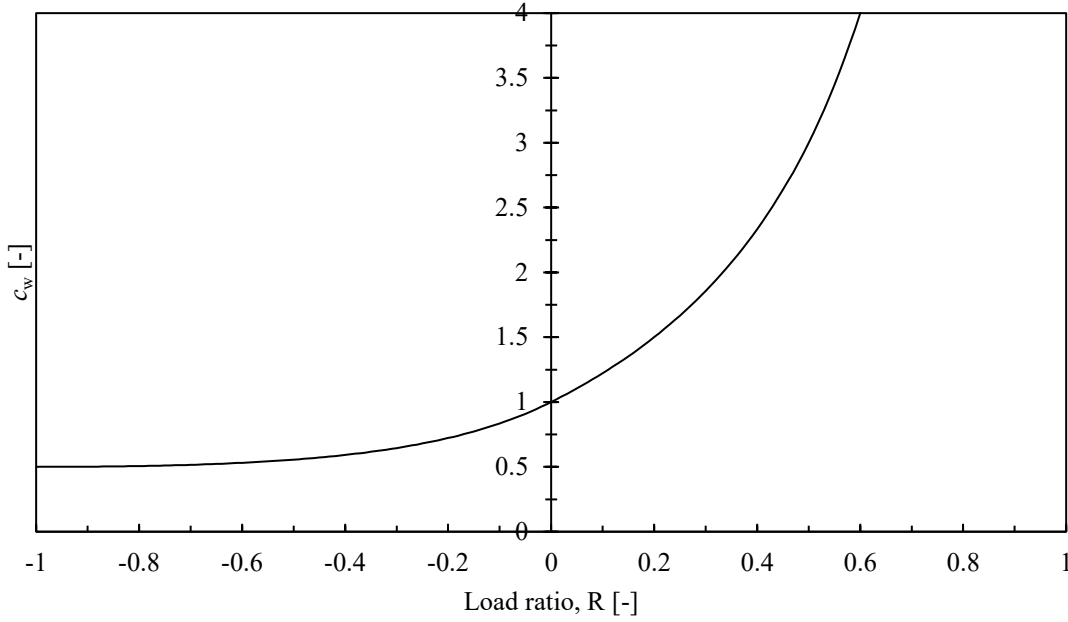


Figure 1.22. Coefficients c_w as a function of the nominal load ratio R .

Accordingly, assuming isotropic and linear-elastic material behaviour under plane strain conditions together with the Beltrami total strain energy criterion [84], the range of the average strain energy density for the notched component $\Delta\bar{W}_{\text{notch}}$ can be written as a function of the mode I NSIF range at the fatigue limit ΔK_{ID} starting from Eq. (1.25) as follow:

$$\Delta\bar{W}_{\text{notch}} \cong \frac{c_1}{E} \left(\frac{\Delta K_{ID}}{R_0^{1-\lambda_1}} \right)^2 \quad (1.32)$$

For the plain material, they chose the fatigue data relevant to a butt weld flush ground to plate since this joint has no notch effect being subjected to a uniform tensile stress field. Therefore, the range of the average strain energy density for the plain specimen $\Delta\bar{W}_{\text{plain}}$ is only function of the applied stress range at the fatigue limit $\Delta\sigma_D$ and can be obtained with the following expression:

$$\Delta\bar{W}_{\text{plain}} \cong \frac{1}{2E} \Delta\sigma_D^2 \quad (1.33)$$

Then, equating Eq. (1.32) with Eq. (1.33) as in Eq. (1.31) and by making the unknown variable R_0 explicit, the following expression can be obtained:

$$R_0 = \left[\sqrt{2e_1} \cdot \frac{\Delta K_{1D}}{\Delta \sigma_D} \right]^{\frac{1}{1-\lambda_1}} \quad (1.34)$$

According to which it is possible to determine the value of the control radius if ΔK_{1D} and $\Delta \sigma_D$ are known. The welded material instead of the base metal fatigue resistance properties must be used in the calculations since it is known that the welding processes locally alter the base material in the nearby of the weld bead (i.e. were the fatigue failure occurs). Lazzarin and Livieri [20] proposed to consider the fatigue data with reference to a number of cycles $N_D = 5 \cdot 10^6$ relevant to a survival probability $PS = 50\%$ (mean value) cycles, and obtained under pulsating loading (nominal load ratio $R = 0$). Thus, by substituting the mode I NSIF range at the fatigue limit relevant to the toe failure of fillet-welded joints in the as-welded state $\Delta K_{1D} = 211 \text{ MPa} \cdot \text{mm}^{0.326}$ (see Figure 1.17) [18] and the nominal stress range at the fatigue limit relevant to a butt weld flush ground to plate $\Delta \sigma_D = 155 \text{ MPa}$ [29] into Eq. (1.34), Lazzarin and Livieri [20] have found the material-structural control volume radius is equal to $R_0 = 0.28 \text{ mm}$ for arc-welded structural steel joints.

Once the R_0 value is known, the SED criterion can be applied to any potential fatigue crack initiation point in a welded structure allowing the comparison between them (both the fatigue strength at the weld toes and the weld roots are expressed in averaged SED range $\Delta \bar{W}$, thus they have the same measurement unit) and the following fatigue strength calculation. Figure 1.23 demonstrates the capability of the averaged SED method in summarizing approximately 900 experimental data relevant to the fatigue failure of welded joints made of structural steel if expressed in terms of average SED versus the number of cycles to failure $\Delta \bar{W} - N_f$.

1.4 The Peak Stress Method: equivalent peak stress

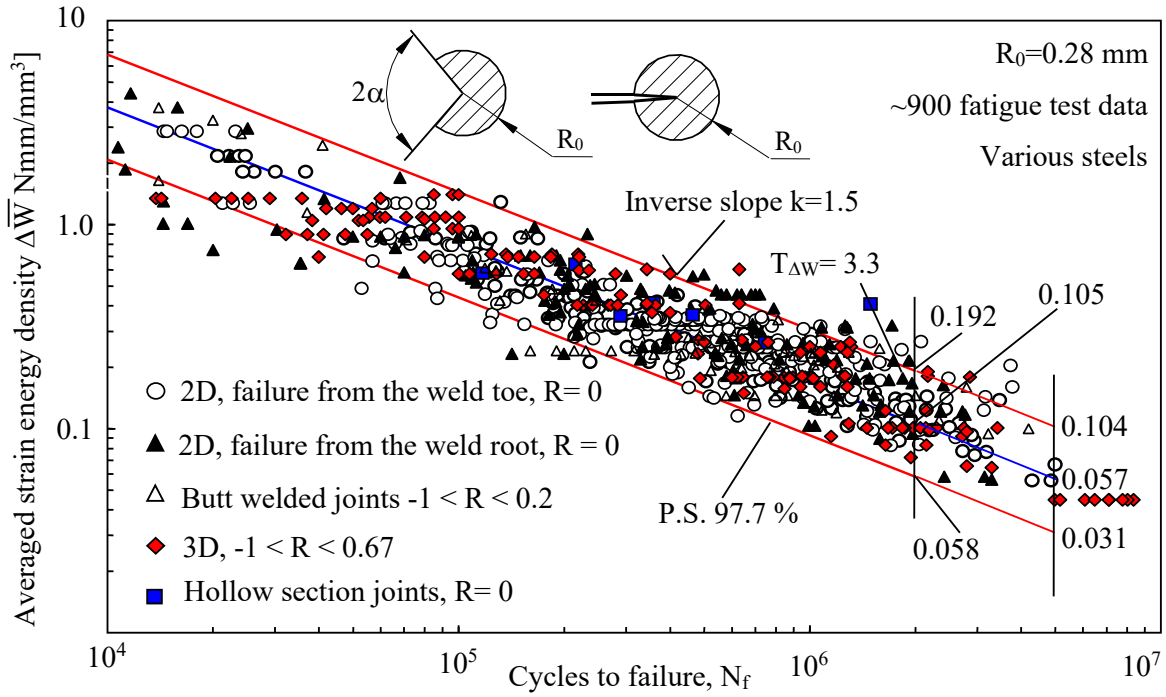


Figure 1.23. Fatigue design scatter band for fatigue weld toe and weld root failures of welded joints made of structural steel according to the averaged SED criterion. Image taken from [87].

1.4. The Peak Stress Method: equivalent peak stress

Taking advantage of the rapid evaluation of the NSIFs by means of the PSM, Meneghetti et al. [88,89] proposed to express Eq. (1.25) as a function of the peak stresses obtained from FE analyses according to the PSM:

$$\Delta\bar{W} = c_{w1} \frac{e_1}{E} \left[K_{FE}^* \cdot \Delta\sigma_{\theta\theta, \theta=0, \text{peak}} \cdot \left(\frac{d}{R_0} \right)^{1-\lambda_1} \right]^2 + c_{w2} \frac{e_2}{E} \left[K_{FE}^{**} \cdot \Delta\tau_{r\theta, \theta=0, \text{peak}} \cdot \left(\frac{d}{R_0} \right)^{1-\lambda_2} \right]^2 + c_{w3} \frac{e_3}{E} \left[K_{FE}^{***} \cdot \Delta\tau_{\theta z, \theta=0, \text{peak}} \cdot \left(\frac{d}{R_0} \right)^{1-\lambda_3} \right]^2 \quad (1.35)$$

Or in case of tetra elements:

$$\Delta\bar{W} = c_{w1} \frac{e_1}{E} \left[K_{FE}^* \cdot \bar{\Delta}\sigma_{\theta\theta, \theta=0, \text{peak}} \cdot \left(\frac{d}{R_0} \right)^{1-\lambda_1} \right]^2 + c_{w2} \frac{e_2}{E} \left[K_{FE}^{**} \cdot \bar{\Delta}\tau_{r\theta, \theta=0, \text{peak}} \cdot \left(\frac{d}{R_0} \right)^{1-\lambda_2} \right]^2 + c_{w3} \frac{e_3}{E} \left[K_{FE}^{***} \cdot \bar{\Delta}\tau_{\theta z, \theta=0, \text{peak}} \cdot \left(\frac{d}{R_0} \right)^{1-\lambda_3} \right]^2 \quad (1.36)$$

The SED value thus obtained, once equated to an equivalent uniaxial plane strain state $\Delta\bar{W} = (1-\nu^2)\Delta\sigma_{eq,peak}^2 / 2E$, allows to define an equivalent peak stress generating the same local SED [88,89]:

$$\Delta\sigma_{eq,peak} = \sqrt{c_{w1} \cdot f_{w1}^2 \cdot \Delta\sigma_{\theta\theta,\theta=0,peak}^2 + c_{w2} \cdot f_{w2}^2 \cdot \Delta\tau_{r\theta,\theta=0,peak}^2 + c_{w3} \cdot f_{w3}^2 \cdot \Delta\tau_{\theta z,\theta=0,peak}^2} \quad (1.37)$$

Or in the case of tetra elements:

$$\Delta\sigma_{eq,peak} = \sqrt{c_{w1} \cdot f_{w1}^2 \cdot \Delta\sigma_{\theta\theta,\theta=0,peak}^{-2} + c_{w2} \cdot f_{w2}^2 \cdot \Delta\tau_{r\theta,\theta=0,peak}^{-2} + c_{w3} \cdot f_{w3}^2 \cdot \Delta\tau_{\theta z,\theta=0,peak}^{-2}} \quad (1.38)$$

where f_{w1} , f_{w2} , f_{w3} are coefficients accounting for the stress averaging inside the material-structural volume with size R_0 defined as follow:

$$f_{w1} = K_{FE}^* \cdot \sqrt{\frac{2e_1}{1-\nu^2}} \cdot \left(\frac{d}{R_0}\right)^{1-\lambda_1} \quad (1.39)$$

$$f_{w2} = K_{FE}^{**} \cdot \sqrt{\frac{2e_2}{1-\nu^2}} \cdot \left(\frac{d}{R_0}\right)^{1-\lambda_2} \quad (1.40)$$

$$f_{w3} = K_{FE}^{***} \cdot \sqrt{\frac{2e_3}{1-\nu^2}} \cdot \left(\frac{d}{R_0}\right)^{1-\lambda_3} \quad (1.41)$$

It is worth highlighting that both the peak stresses $\sigma_{\theta\theta,\theta=0,peak}$, $\tau_{r\theta,\theta=0,peak}$, and $\tau_{\theta z,\theta=0,peak}$ and the parameters f_{wi} depend on the global element size d adopted to generate the free mesh pattern (Eqs. (1.21), (1.22), (1.23) and (1.39), (1.40), (1.41)). On the other hand, the equivalent peak stress is independent of the FE size d , due to the multiplication of the peak stresses by the corresponding f_{wi} parameters (see Eq. (1.37) or Eq. (1.38)).

Similarly to the averaged SED range $\Delta\bar{W}$, the equivalent peak stress range $\Delta\sigma_{eq,peak}$ (Eqs. (1.37) and (1.38)) has been adopted as fatigue damage parameter for the fatigue lifetime assessment of arc-welded details made of structural steels subjected to uniaxial and multiaxial constant amplitude local stresses [41]. In particular, two components having sharp V-notches with different opening angles 2α subject to a generic combination of loads generating different

multiaxial local stresses at the V-notch tips (mode I+II+III), will exhibit the same fatigue life N_f if characterized by the same equivalent peak stress range $\Delta\sigma_{eq,peak}$.

Two different PSM design curve, expressed in terms of equivalent peak stress range $\Delta\sigma_{eq,peak}$ versus the number of cycles to failure $\Delta\sigma_{eq,peak}-N_f$, were obtained for the fatigue design of welded joints made of structural steel under pure mode I and under pure mode III local stresses, respectively [38,41,90]. The design curve relevant to pure mode I local stresses has been defined analysing approximately 180 experimental data relevant to weld toe failure of transverse or cruciform fillet welded joints having different main plate thickness and made of different structural steels [41,90]. All joints were tested in the as-welded conditions under pulsating loadings ($R = 0$). As a result, they obtained scatter band is characterized by a fatigue strength at $N_A = 2 \cdot 10^6$ cycles $\Delta\sigma_{eq,peak,A,50\%} = 214$ MPa for a survival probability $PS = 50\%$, an inverse slope $k = 3$ and scatter index T_σ with reference to survival probabilities of 2.3%-97.7% equal to 1.90. On the other hand, the design curve relevant to pure mode III local stresses has been identified analysing approximately 20 experimental data relevant to weld toe failure of stress relieved full-penetration or fillet-welded tube-to-flange joints having different main plate thickness and made of different structural steels tested under fully-reversed loadings ($R = -1$) [38,41]. The resulting scatter band is characterized by a fatigue strength at $N_A = 2 \cdot 10^6$ cycles $\Delta\sigma_{eq,peak,A,50\%} = 354$ MPa for a survival probability $PS = 50\%$, an inverse slope $k = 5$ and scatter index T_σ with reference to survival probabilities of 2.3%-97.7% equal to 1.90.

The proper PSM design scatter band must be chosen on the basis of a local biaxiality ratio λ which summarizes the relative SED contributions due to mode II/III shear stresses and mode I normal stresses. It can be expressed as a function of the peak stresses according to the following expression:

$$\lambda = \frac{c_{w2} \cdot f_{w2}^2 \cdot \Delta\tau_{r\theta,\theta=0,peak}^2 + c_{w3} \cdot f_{w3}^2 \cdot \Delta\tau_{\theta z,\theta=0,peak}^2}{c_{w1} \cdot f_{w1}^2 \cdot \Delta\sigma_{\theta\theta,\theta=0,peak}^2} \quad (1.42)$$

Or for tetra elements:

$$\lambda = \frac{c_{w2} \cdot f_{w2}^2 \cdot \Delta\tau_{r\theta,\theta=0,peak}^{-2} + c_{w3} \cdot f_{w3}^2 \cdot \Delta\tau_{\theta z,\theta=0,peak}^{-2}}{c_{w1} \cdot f_{w1}^2 \cdot \Delta\sigma_{\theta\theta,\theta=0,peak}^{-2}} \quad (1.43)$$

It is easy to observe that when the considered notch is subjected to a pure mode I local stress state the local biaxiality ratio becomes $\lambda = 0$, whilst it is subjected only to mode II+III local stresses $\lambda \rightarrow \infty$, otherwise the λ assumes a finite value between 0 and ∞ in case of mixed mode I+II+III local stresses. The criterion to choose the proper PSM design curve as a function of the value of λ is the following [41] (Table 1.6): fatigue data relevant to $\lambda = 0$ must be compared with the PSM-based design scatter band having $\Delta\sigma_{eq,peak,A,50\%} = 214$ MPa and $k = 3$, while fatigue data relevant to $\lambda > 0$ must be compared with the PSM-based design scatter band having $\Delta\sigma_{eq,peak,A,50\%} = 354$ MPa and $k = 5$.

Table 1.6. Criterion for selecting the PSM-based fatigue design curves for arc-welded joints made of structural steels [41].

T [mm]	λ Eq. (1.42) [-]	N_A [cycles]	$\Delta\sigma_{eq,peak,A,50\%}$ [MPa]	$\Delta\sigma_{eq,peak,A,97.7\%}$ [MPa]	$\Delta\sigma_{eq,peak,A,2.3\%}$ [MPa]	k	T_G [-]
$T \geq 2$ mm	$\lambda = 0$	$2 \cdot 10^6$	214	156	296	3	1.90
$T \geq 2$ mm	$\lambda > 0$	$2 \cdot 10^6$	354	257	488	5	1.90

The equivalent peak stress has been adopted to re-analyse many experimental data relevant to arc-welded joint made of structural steel subjected to pure axial/pure bending, pure torsion, and in-phase and out-of-phase multiaxial local stresses [41]. Please note that the scatter band have never been updated (in terms of slope and endurable stresses) after the original calibration [38,90]. Subsequently, they have systematically validated by adding new experimental data points and simply checking whether or not the new ones fell inside the pre-existing scatter band.

Figure 1.24 and Figure 1.25 demonstrate the capability of the method in summarizing approximately 860 and 430 experimental data relevant to the weld toe and weld root fatigue failure of welded joints made of structural steel for $\lambda = 0$ (pure mode I) and $\lambda > 0$ (mode I+II+II), respectively, when expressed in terms of equivalent peak stress range $\Delta\sigma_{eq,peak}$ versus the number of cycles to failure $\Delta\sigma_{eq,peak}-N_f$.

Additional details on the PSM for the fatigue strength assessment of welded structures undergoing constant amplitude multiaxial loadings and the conditions of applicability of the method can be found in a recent review [41]. Among recent developments of the PSM, its automated implementation [91,92] for the fatigue assessment of complex welded structures under CA multiaxial loadings and the application of the PSM to the fatigue assessment of welded details included in industrial case studies [93] deserve to be mentioned.

1.4 The Peak Stress Method: equivalent peak stress

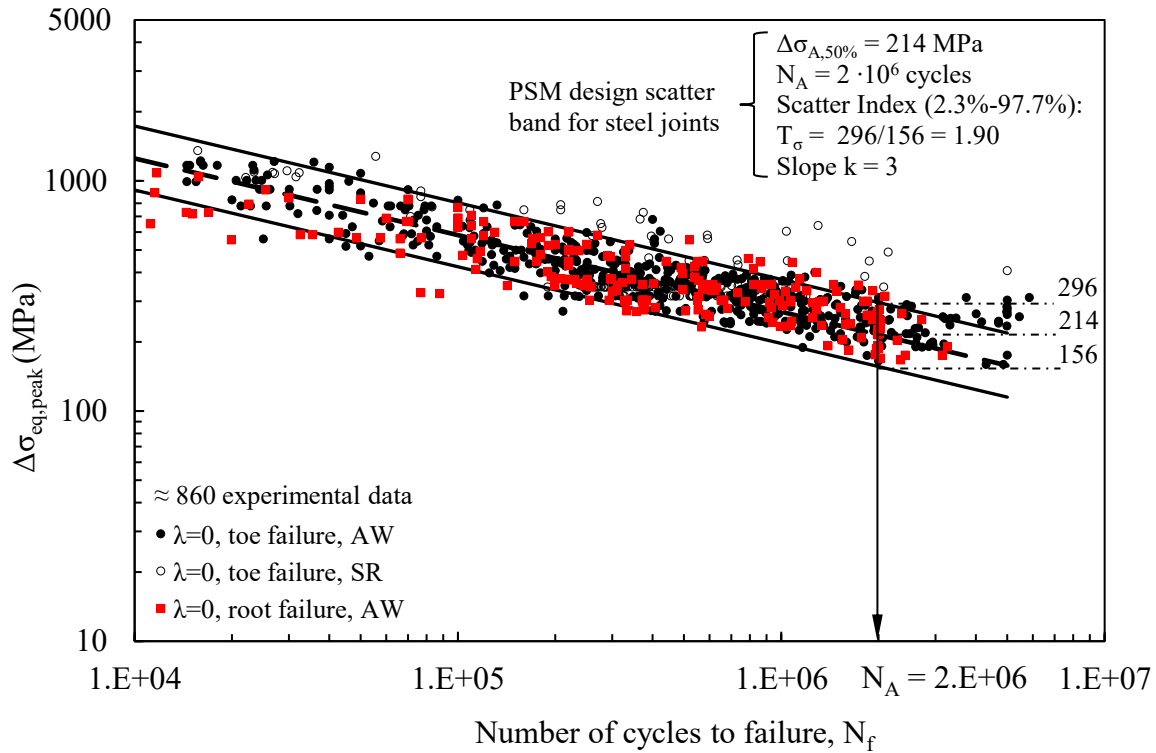


Figure 1.24. Fatigue assessment of pure mode I ($\lambda = 0$) weld toe and weld root failures of welded joints made of structural steels tested in as-welded or stress-relieved conditions according to the PSM. Image taken from [41].

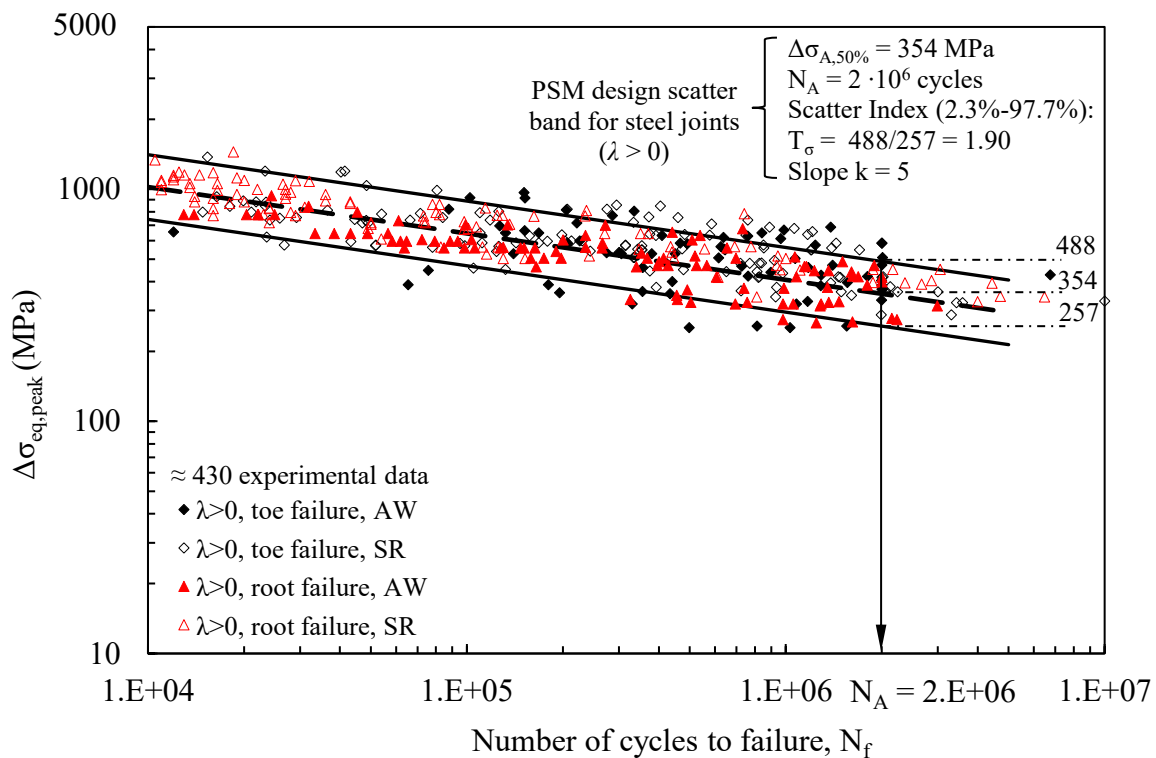


Figure 1.25. Fatigue assessment of pure multiaxial mode I+II+III ($\lambda > 0$) weld toe and weld root failures of welded joints made of structural steels tested in as-welded or stress-relieved conditions according to the PSM. Image taken from [41].

1.5. Conclusions

The aim of the present chapter was introducing the reader to the fatigue of weldments and giving all the theoretical background on the local approaches for the fatigue lifetime assessment of welded joints. What described here will be extensively exploited in the rest of the manuscript especially the concepts of Stress Intensity Factor (SIF), the Notch Stress Intensity Factor (NSIF), the averaged Strain Energy Density (SED) criterion and the Peak Stress Method (PSM).

In Chapter 2 the theoretical framework for developing the Peak Stress Method for the fatigue strength assessment of welded joints subjected to Variable Amplitude (VA) uniaxial as well as in-phase and out-of-phase multiaxial local stresses will be presented. Then, the proposed method will be validated against a large bulk of VA fatigue data taken from the literature proving the PSM as an extremely valid technique to design welded joints against CA or VA uniaxial as well as multiaxial fatigue local stresses. The proposed method will also be checked against new experimental data generated by fatigue testing non-load-carrying (nlc) fillet-welded double transverse or inclined attachments made of S355 structural steel under pure axial loading.

Next, Chapter 3 will address the introduction of a constant amplitude fatigue limit in the mode I PSM design scatter band. Accordingly, a novel approximate approach will be presented to a rapid and effective estimate of the constant amplitude uniaxial fatigue limit of welded structures in the stress-relieved state by using the PSM, without the need of complex and time-consuming fracture mechanics-based calculations. This topic will be addressed exploiting a fracture mechanics-based criterion based on short fatigue crack propagation and on the so-called cyclic R-curve analysis, whose theoretical background will be presented in Chapter 3.

Finally, Chapter 4 will give an insight on some critical aspects relevant to the experimental determination of the cyclic R-curve (used in Chapter 3) and, in general, on experimental fracture mechanics tests dealing with short cracks. In particular, the problem of performing real-time in-situ crack growth monitoring of short cracks will be extensively discussed, this aspect being undoubtedly the most crucial when performing fracture mechanic tests on short cracks.

1.6. References

- [1] Stephens RI, Fatemi A, Stephens RR, Fuchs HO. *Metal Fatigue in Engineering*. 2nd ed. John Wiley & Sons; 2001.
- [2] Reed RP, Smith JH, Christ BW. The economic effects of fracture in the United States. *Natl Bur Stand Spec Publ* 1983;647:1–7. <https://doi.org/10.6028/NBS.SP.647P1>.
- [3] Faria L. The economic effect of fracture in Europe. Final Report of European Atomic Energy Community – study contract no. 320105. Brussels: 1991.
- [4] Milne I. The importance of the management of structural integrity. *Eng Fail Anal* 1994;1:171–81. [https://doi.org/10.1016/1350-6307\(94\)90016-7](https://doi.org/10.1016/1350-6307(94)90016-7).
- [5] Dowling NE. *Mechanical behavior of materials - Engineering methods for deformation, fracture and fatigue*. 4th ed. Pearson; 2013.
- [6] Wöhler A. Tests to determine the forces acting on railway carriage axles and the capacity of resistance of the axles. *Engineering* 1871;11:199.
- [7] EN. Eurocode 3: Design of steel structures – part 1–9: Fatigue 2005.
- [8] Hobbacher AF. *Recommendations for Fatigue Design of Welded Joints and Components*. International Institute of Welding - IIW Collection. Springer International Publishing; 2016. <https://doi.org/10.1007/978-3-319-23757-2>.
- [9] Radaj D, Sonsino CM, Fricke W. *Fatigue assessment of welded joints by local approaches*. 2nd ed. Cambridge, England: Woodhead Publishing; 2006.
- [10] Radaj D, Vormwald M. *Advanced Methods of Fatigue Assessment*. 1st ed. Berlin: Springer Berlin Heidelberg; 2013. <https://doi.org/https://doi.org/10.1007/978-3-642-30740-9>.
- [11] Karakas Ö, Morgenstern C, Sonsino CM. Fatigue design of welded joints from the wrought magnesium alloy AZ31 by the local stress concept with the fictitious notch radii of $r_f = 1.0$ and 0.05 mm. *Int J Fatigue* 2008;30:2210–9. <https://doi.org/10.1016/j.ijfatigue.2008.05.017>.
- [12] Karakas Ö. Consideration of mean-stress effects on fatigue life of welded magnesium joints by the application of the Smith–Watson–Topper and reference radius concepts. *Int J Fatigue* 2013;49:1–17. <https://doi.org/10.1016/j.ijfatigue.2012.11.007>.

- [13] Fricke W. IIW recommendations for the fatigue assessment of welded structures by notch stress analysis: IIW-2006-09. Woodhead Pub; 2012.
 - [14] Radaj D, Sonsino CM. Fatigue assessment of welded joints by local approaches. Cambridge: Abington Publishing; 1998.
 - [15] Sonsino CM. Multiaxial fatigue of welded joints under in-phase and out-of-phase local strains and stresses. *Int J Fatigue* 1995;17:55–70. [https://doi.org/10.1016/0142-1123\(95\)93051-3](https://doi.org/10.1016/0142-1123(95)93051-3).
 - [16] Jakubczak H, Glinka G. Fatigue analysis of manufacturing defects in weldments. *Int J Fatigue* 1986;8:51–7. [https://doi.org/10.1016/0142-1123\(86\)90053-8](https://doi.org/10.1016/0142-1123(86)90053-8).
 - [17] Fiedler M, Vormwald M. Considering fatigue load sequence effects by applying the Local Strain Approach and a fracture mechanics based damage parameter. *Theor Appl Fract Mech* 2016;83:31–41. <https://doi.org/10.1016/j.tafmec.2016.01.003>.
 - [18] Lazzarin P, Tovo R. A Notch Intensity Factor Approach to the Stress Analysis of Welds. *Fatigue Fract Eng Mater Struct* 1998;21:1089–103. <https://doi.org/10.1046/j.1460-2695.1998.00097.x>.
 - [19] Lazzarin P, Sonsino CM, Zambardi R. A notch stress intensity approach to assess the multiaxial fatigue strength of welded tube-to-flange joints subjected to combined loadings. *Fatigue Fract Eng Mater Struct* 2004;27:127–40. <https://doi.org/10.1111/j.1460-2695.2004.00733.x>.
 - [20] Livieri P, Lazzarin P. Fatigue strength of steel and aluminium welded joints based on generalised stress intensity factors and local strain energy values. *Int J Fract* 2005;133:247–76. <https://doi.org/10.1007/s10704-005-4043-3>.
 - [21] Lazzarin P, Livieri P, Berto F, Zappalorto M. Local strain energy density and fatigue strength of welded joints under uniaxial and multiaxial loading. *Eng Fract Mech* 2008;75:1875–89. <https://doi.org/10.1016/j.engfracmech.2006.10.019>.
 - [22] Remes H, Gallo P, Jelovica J, Romanoff J, Lehto P. Fatigue strength modelling of high-performing welded joints. *Int J Fatigue* 2020;135:105555. <https://doi.org/10.1016/j.ijfatigue.2020.105555>.
 - [23] Fischer C, Fricke W, Rizzo CM. Experiences and recommendations for numerical analyses of notch stress intensity factor and averaged strain energy density. *Eng Fract Mech* 2016;165:98–113. <https://doi.org/10.1016/j.engfracmech.2016.08.012>.
 - [24] Fischer C, Fricke W, Rizzo CM. Review of the fatigue strength of welded joints based
-

- on the notch stress intensity factor and SED approaches. *Int J Fatigue* 2016;84:59–66. <https://doi.org/10.1016/J.IJFATIGUE.2015.11.015>.
- [25] Lazzarin P, Zambardi R. A finite-volume-energy based approach to predict the static and fatigue behavior of components with sharp V-shaped notches. *Int J Fract* 2001 1123 2001;112:275–98. <https://doi.org/10.1023/A:1013595930617>.
- [26] Susmel L. *Multiaxial Notch Fatigue*. Cambridge, UK: Woodhead Publishing; 2009.
- [27] Carpinteri A, Spagnoli A, Vantadori S. Multiaxial fatigue life estimation in welded joints using the critical plane approach. *Int J Fatigue* 2009;31:188–96. <https://doi.org/10.1016/j.ijfatigue.2008.03.024>.
- [28] Susmel L. Three different ways of using the Modified Wöhler Curve Method to perform the multiaxial fatigue assessment of steel and aluminium welded joints. *Eng Fail Anal* 2009;16:1074–89. <https://doi.org/10.1016/j.engfailanal.2008.05.016>.
- [29] Taylor D, Barrett N, Lucano G. Some new methods for predicting fatigue in welded joints. *Int J Fatigue* 2002;24:509–18. [https://doi.org/10.1016/S0142-1123\(01\)00174-8](https://doi.org/10.1016/S0142-1123(01)00174-8).
- [30] Susmel L. Modified Wöhler curve method, theory of critical distances and Eurocode 3: A novel engineering procedure to predict the lifetime of steel welded joints subjected to both uniaxial and multiaxial fatigue loading. *Int J Fatigue* 2008;30:888–907. <https://doi.org/10.1016/j.ijfatigue.2007.06.005>.
- [31] Susmel L. The Modified Wöhler Curve Method calibrated by using standard fatigue curves and applied in conjunction with the Theory of Critical Distances to estimate fatigue lifetime of aluminium weldments. *Int J Fatigue* 2009;31:197–212. <https://doi.org/10.1016/j.ijfatigue.2008.04.004>.
- [32] Karakaş Ö, Zhang G, Sonsino CM. Critical distance approach for the fatigue strength assessment of magnesium welded joints in contrast to Neuber's effective stress method. *Int J Fatigue* 2018;112:21–35. <https://doi.org/10.1016/j.ijfatigue.2018.03.004>.
- [33] Baumgartner J, Schmidt H, Ince E, Melz T, Dilger K. Fatigue assessment of welded joints using stress averaging and critical distance approaches. *Weld World* 2015;59:731–42. <https://doi.org/10.1007/s40194-015-0248-x>.
- [34] Susmel L. Estimating fatigue lifetime of steel weldments locally damaged by variable amplitude multiaxial stress fields. *Int J Fatigue* 2010;32:1057–80. <https://doi.org/10.1016/j.ijfatigue.2009.12.004>.
- [35] Susmel L, Askes H. Modified Wöhler Curve Method and multiaxial fatigue assessment
-

- of thin welded joints. *Int J Fatigue* 2012;43:30–42. <https://doi.org/10.1016/j.ijfatigue.2012.01.026>.
- [36] Meneghetti G, Lazzarin P. Significance of the elastic peak stress evaluated by FE analyses at the point of singularity of sharp V-notched components. *Fatigue Fract Eng Mater Struct* 2007;30:95–106. <https://doi.org/10.1111/j.1460-2695.2006.01084.x>.
- [37] Meneghetti G. The use of peak stresses for fatigue strength assessments of welded lap joints and cover plates with toe and root failures. *Eng Fract Mech* 2012;89:40–51. <https://doi.org/10.1016/j.engfracmech.2012.04.007>.
- [38] Meneghetti G. The peak stress method for fatigue strength assessment of tube-to-flange welded joints under torsion loading. *Weld World* 2013;57:265–75. <https://doi.org/10.1007/s40194-013-0022-x>.
- [39] Campagnolo A, Meneghetti G. Rapid estimation of notch stress intensity factors in 3D large-scale welded structures using the peak stress method. *MATEC Web Conf.*, vol. 165, EDP Sciences; 2018. <https://doi.org/10.1051/mateconf/201816517004>.
- [40] Campagnolo A, Roveda I, Meneghetti G. The Peak Stress Method combined with 3D finite element models to assess the fatigue strength of complex welded structures. *Procedia Struct Integr* 2019;19:617–26. <https://doi.org/10.1016/j.prostr.2019.12.067>.
- [41] Meneghetti G, Campagnolo A. State-of-the-art review of peak stress method for fatigue strength assessment of welded joints. *Int J Fatigue* 2020;139:105705. <https://doi.org/10.1016/j.ijfatigue.2020.105705>.
- [42] Madia M, Zerbst U, Th. Beier H, Schork B. The IBESS model – Elements, realisation and validation. *Eng Fract Mech* 2018;198:171–208. <https://doi.org/10.1016/j.engfracmech.2017.08.033>.
- [43] Zerbst U, Madia M, Schork B, Hensel J, Kucharczyk P, Ngoula D, et al. *Fatigue and Fracture of Weldments*. *Fatigue Fract. Weldments*, Cham: Springer International Publishing; 2019, p. 1–130. <https://doi.org/10.1007/978-3-030-04073-4>.
- [44] Radaj D. *Generalised Neuber Concept of Fictitious Notch Rounding*. *Adv. Methods Fatigue Assess.*, Berlin, Heidelberg: Springer Berlin Heidelberg; 2013, p. 1–100. https://doi.org/10.1007/978-3-642-30740-9_1.
- [45] Krzyżak D, Robak G, Łagoda T. Determining fatigue life of bent and tensioned elements with a notch, with use of fictitious radius. *Fatigue Fract Eng Mater Struct* 2014;n/a-n/a. <https://doi.org/10.1111/ffe.12276>.
-

- [46] Robak G. Using a variable value of the fictitious radius to estimate fatigue life of notched elements. *Fatigue Fract Eng Mater Struct* 2020;43:2006–23. <https://doi.org/10.1111/ffe.13280>.
- [47] Manson SS. Behavior of materials under conditions of thermal stress. Report No. NACA TN-2933. 1954.
- [48] Coffin LF. A study of the effect of cyclic thermal stresses on a ductile metal. *Trans ASME* 1954;76:931–50.
- [49] Kihara S, Yoshii A. A strength evaluation method of a sharply notched structure by a new parameter, ‘the equivalent stress intensity factor’. *JSME Int J* 1991;34:70–5.
- [50] Boukharouba T, Tamine T, Niu L, Chehimi C, Pluvinage G. The use of notch stress intensity factor as a fatigue crack initiation parameter. *Eng Fract Mech* 1995;52:503–12. [https://doi.org/10.1016/0013-7944\(94\)00242-A](https://doi.org/10.1016/0013-7944(94)00242-A).
- [51] Berto F, Lazzarin P, Yates JR. Multiaxial fatigue of V-notched steel specimens: a non-conventional application of the local energy method. *Fatigue Fract Eng Mater Struct* 2011;34:921–43. <https://doi.org/10.1111/j.1460-2695.2011.01585.x>.
- [52] Meneghetti G, Campagnolo A, Berto F, Tanaka K. Notched Ti-6Al-4V titanium bars under multiaxial fatigue: Synthesis of crack initiation life based on the averaged strain energy density. *Theor Appl Fract Mech* 2018;96:509–33. <https://doi.org/10.1016/j.tafmec.2018.06.010>.
- [53] Fatemi A, Socie DF. A Critical Plane Approach to Multiaxial Fatigue Damage Including Out-Of-Phase Loading. *Fatigue Fract Eng Mater Struct* 1988;11:149–65. <https://doi.org/10.1111/j.1460-2695.1988.tb01169.x>.
- [54] Gates NR, Fatemi A. Multiaxial variable amplitude fatigue life analysis using the critical plane approach, Part I: Un-notched specimen experiments and life estimations. *Int J Fatigue* 2017;105:283–95. <https://doi.org/10.1016/j.ijfatigue.2017.09.008>.
- [55] Gates NR, Fatemi A. Multiaxial variable amplitude fatigue life analysis using the critical plane approach, Part II: Notched specimen experiments and life estimations. *Int J Fatigue* 2018;106:56–69. <https://doi.org/10.1016/j.ijfatigue.2017.09.009>.
- [56] Carpinteri A, Ronchei C, Scorza D, Vantadori S. Critical Plane Orientation Influence on Multiaxial High-Cycle Fatigue Assessment. *Phys Mesomech* 2015;18:348–54. <https://doi.org/10.1134/S1029959915040074>.
- [57] Carpinteri A, Berto F, Campagnolo A, Fortese G, Ronchei C, Scorza D, et al. Fatigue

- assessment of notched specimens by means of a critical plane-based criterion and energy concepts. *Theor Appl Fract Mech* 2016;84:57–63. <https://doi.org/10.1016/j.tafmec.2016.03.003>.
- [58] Taylor D. The theory of critical distances. *Eng Fract Mech* 2008;75:1696–705. <https://doi.org/10.1016/j.engfracmech.2007.04.007>.
- [59] Susmel L. The theory of critical distances: a review of its applications in fatigue. *Eng Fract Mech* 2008;75:1706–24. <https://doi.org/10.1016/j.engfracmech.2006.12.004>.
- [60] Ellyin F. *Fatigue Damage, Crack Growth and Life Prediction*. Dordrecht: Springer Netherlands; 1996. <https://doi.org/10.1007/978-94-009-1509-1>.
- [61] Ellyin F. *Cyclic strain energy density as a criterion for multiaxial fatigue failure*. Biaxial an. London: EGF Publication; 1989.
- [62] Anderson TL. *Fracture Mechanics, Fundamentals and Applications*. 3rd ed. Boca Raton: CRC Press LLC; 2009.
- [63] Basaran C. *Introduction to Unified Mechanics Theory with Applications*. Switzerland AG: Springer - Nature; 2021.
- [64] Lemaitre J, Chaboche J. *Mechanics of solid materials*. Cambridge University Press; 1998.
- [65] Rosakis P, Rosakis AJ, Ravichandran G, Hodowany J. A thermodynamic internal variable model for the partition of plastic work into heat and stored energy in metals. *J Mech Phys Solids* 2000;48:581–607. [https://doi.org/10.1016/S0022-5096\(99\)00048-4](https://doi.org/10.1016/S0022-5096(99)00048-4).
- [66] Chrysochoos A, Louche H. An infrared image processing to analyse the calorific effects accompanying strain localisation. *Int J Eng Sci* 2000;38:1759–88. [https://doi.org/10.1016/S0020-7225\(00\)00002-1](https://doi.org/10.1016/S0020-7225(00)00002-1).
- [67] Rousselier G. Dissipation in porous metal plasticity and ductile fracture. *J Mech Phys Solids* 2001;49:1727–46. [https://doi.org/10.1016/S0022-5096\(01\)00013-8](https://doi.org/10.1016/S0022-5096(01)00013-8).
- [68] Hansen NR, Schreyer HL. A thermodynamically consistent framework for theories of elastoplasticity coupled with damage. *Int J Solids Struct* 1994;31:359–89. [https://doi.org/10.1016/0020-7683\(94\)90112-0](https://doi.org/10.1016/0020-7683(94)90112-0).
- [69] Westergaard HM. Bearing Pressures and Cracks: Bearing Pressures Through a Slightly Waved Surface or Through a Nearly Flat Part of a Cylinder, and Related Problems of Cracks. *J Appl Mech* 1939;6:A49–53. <https://doi.org/10.1115/1.4008919>.
- [70] Irwin GR. *Analysis of Stresses and Strains Near the End of a Crack Traversing a Plate*.
-

- J Appl Mech 1957;24:361–4. <https://doi.org/10.1115/1.4011547>.
- [71] Williams ML. On the Stress Distribution at the Base of a Stationary Crack. J Appl Mech 1957;24:109–14. <https://doi.org/10.1115/1.4011454>.
- [72] Gross B, Srawley JE, William FBJ. NASA Technical Note D-2395: Stress-intensity factors for a single-edge-notch tension specimen by boundary collocation of a stress function. Cleveland, Ohio: 1964.
- [73] Gross B, Mendelson A. Plane elastostatic analysis of V-notched plates. Int J Fract Mech 1972;8:267–76. <https://doi.org/10.1007/BF00186126>.
- [74] Smith RA, Miller KJ. Prediction of fatigue regimes in notched components. Int J Mech Sci 1978;20:201–6. [https://doi.org/10.1016/0020-7403\(78\)90082-6](https://doi.org/10.1016/0020-7403(78)90082-6).
- [75] Williams ML. Stress singularities resulting from various boundary conditions in angular corners of plates in tension. J Appl Mech 1952;19:526–8.
- [76] Qian J, Hasebe N. Property of eigenvalues and eigenfunctions for an interface V-notch in antiplane elasticity. Eng Fract Mech 1997;56:729–34. [https://doi.org/10.1016/S0013-7944\(97\)00004-0](https://doi.org/10.1016/S0013-7944(97)00004-0).
- [77] Visentin A, Campagnolo A, Meneghetti G. Analytical expressions for rapid estimation of the N-SIFs at V-notch tips using the Peak Stress Method (submitted). Fatigue Fract Eng Mater Struct 2022.
- [78] Nisitani H, Teranishi T. KI value of a circumferential crack emanating from an ellipsoidal cavity obtained by the crack tip stress method in FEM. Proc 2nd Int Conf Fract Damage Mech, Guagliano M, Aliabadi MH, Ed 2001;71:141–6. [https://doi.org/10.1016/S0013-7944\(03\)00035-3](https://doi.org/10.1016/S0013-7944(03)00035-3).
- [79] Meneghetti G, Campagnolo A, Avalle M, Castagnetti D, Colussi M, Corigliano P, et al. Rapid evaluation of notch stress intensity factors using the peak stress method: Comparison of commercial finite element codes for a range of mesh patterns. Fatigue Fract Eng Mater Struct 2018;41:1044–63. <https://doi.org/10.1111/ffe.12751>.
- [80] Meneghetti G, Campagnolo A, Visentin A, Avalle M, Benedetti M, Bighelli A, et al. Rapid evaluation of notch stress intensity factors using the peak stress method with 3D tetrahedral finite element models: comparison of commercial codes. Fatigue Fract Eng Mater Struct 2022;accepted.
- [81] Meneghetti G, Guzzella C. The peak stress method to estimate the mode I notch stress intensity factor in welded joints using three-dimensional finite element models. Eng
-

- Fract Mech 2014;115:154–71. <https://doi.org/10.1016/j.engfracmech.2013.11.002>.
- [82] Visentin A. Automated Fatigue Strength Assessment of V - Notch Structures according to the Peak Stress Method. University of Padova, 2020.
- [83] Neuber H. Kerbspannungslehre. 2nd Ed. Berlin: Springer-Verlag; 1958.
- [84] Beltrami E. Sulle condizioni di resistenza dei corpi elastici (in Italian). Nuovo Cim. 18, 1885, p. 145–55.
- [85] Berto F, Lazzarin P. Recent developments in brittle and quasi-brittle failure assessment of engineering materials by means of local approaches. Mater Sci Eng R Reports 2014;75:1–48. <https://doi.org/10.1016/j.mser.2013.11.001>.
- [86] EN. Eurocode 9: Design of aluminium structures - Part 1-3: Structures susceptible to fatigue 2007.
- [87] Berto F, Lazzarin P. A review of the volume-based strain energy density approach applied to V-notches and welded structures. Theor Appl Fract Mech 2009;52:183–94. <https://doi.org/10.1016/j.tafmec.2009.10.001>.
- [88] Meneghetti G, Campagnolo A, Rigon D. Multiaxial fatigue strength assessment of welded joints using the Peak Stress Method – Part I: Approach and application to aluminium joints. Int J Fatigue 2017;101:328–42. <https://doi.org/10.1016/j.ijfatigue.2017.03.038>.
- [89] Meneghetti G, Campagnolo A, Rigon D. Multiaxial fatigue strength assessment of welded joints using the Peak Stress Method – Part II: Application to structural steel joints. Int J Fatigue 2017;101:343–62. <https://doi.org/10.1016/j.ijfatigue.2017.03.039>.
- [90] Meneghetti G, Lazzarin P. The Peak Stress Method for Fatigue Strength Assessment of welded joints with weld toe or weld root failures. Weld World 2011;55:22–9. <https://doi.org/10.1007/BF03321304>.
- [91] Meneghetti G, Campagnolo A, Visentin A. Automated fatigue strength assessment of arc-welded structures according to the Peak Stress Method. Procedia Struct Integr 2020;28:1062–83. <https://doi.org/10.1016/j.prostr.2020.11.122>.
- [92] Visentin A, Campagnolo A, Babini V, Meneghetti G. Automated implementation of the Peak Stress Method for the fatigue assessment of complex welded structures. Forces Mech 2022;submitted.
- [93] Meneghetti G, Campagnolo A. Fatigue of Welded Components. Ref. Modul. Mater. Sci. Mater. Eng., Elsevier; 2022. <https://doi.org/10.1016/B978-0-12-822944-6.00003-7>.
-

CHAPTER 2.

Variable amplitude multiaxial local stresses

List of symbols

2α	V-notch opening angle
a	Reference dimension for selecting the maximum FE size d
c_{w1}, c_{w2}, c_{w3}	Mode I, II, and III coefficients accounting for mean stress effect
d	Average FE size
Δ	Range of cyclic quantities (maximum minus minimum)
e_1, e_2, e_3	Mode I, II, and III coefficients for evaluating $\Delta\bar{W}$
E	Young's modulus
f_{s1}, f_{s2}, f_{s3}	Mode I, II, and III coefficients accounting for the LDR equivalency
f_{w1}, f_{w2}, f_{w3}	Mode I, II, and III coefficients for calculating $\sigma_{eq,peak}$
K_I, K_{II}, K_{III}	Mode I, II, and III Stress Intensity Factors (SIFs)
K_1, K_2, K_3	Mode I, II, and III Notch Stress Intensity Factors (NSIFs)
$K_{FE}^*, K_{FE}^{**}, K_{FE}^{***}$	Non-dimensional NSIF parameters based on PSM
$\lambda_1, \lambda_2, \lambda_3$	Mode I, II, and III stress singularity degrees
λ	Local biaxiality ratio defined according to PSM
$n_{I,ij}, n_{II,hk}, n_{III,mp}$	Mode I, II and III number of applied cycles from cycle counting
N_I, N_{II}, N_{III}	Mode I, II, and III total number of applied cycles from cycle counting
N_0	Reference number of cycles
ν	Poisson's ratio
$q_{Ii}, q_{IIh}, q_{III,mp}$	Mode I, II and III number of peak stress levels from cycle counting
$q_{Ij}, q_{IIk}, q_{III,p}$	Mode I, II and III number of local load ratios from cycle counting
$R_{I,j}, R_{II,k}, R_{III,p}$	Mode I, II and III local load ratios from cycle counting
R_0	Size of material-structural volume according to SED criterion
ρ	Notch tip radius
r, θ, z	Coordinates of cylindrical reference system at crack/notch tip
...	

2.1 Introduction

...	
$\sigma_{eq,peak}$	Equivalent peak stress based on PSM
$\sigma_{rr}, \sigma_{\theta\theta}, \sigma_{zz}$	Normal stress components in cylindrical coordinate system
$\sigma_{\theta\theta,\theta=0,peak}$	Mode I linear elastic peak stress calculated by FEA according to PSM
$\tau_{r\theta}, \tau_{rz}, \tau_{\theta z}$	Shear stress components in cylindrical coordinate system
$\tau_{r\theta,\theta=0,peak}$	Mode II linear elastic peak stress calculated by FEA according to PSM
$\tau_{\theta z,\theta=0,peak}$	Mode III linear elastic peak stress calculated by FEA according to PSM
\bar{W}	Averaged SED

2.1. Introduction

As discussed in the introduction, most failures of metal structural components are due to fatigue actions occurring in the joints. For this reason, companies involved in the process of designing and manufacturing engineering welded structures subjected to in-service fatigue loadings are constantly looking for new design criteria. Indeed, improving knowledge and technologies in structural components design can help not only save lives through safer structures but also reduce production, inspection, and maintenance times and costs, making industries more competitive and sustainable.

Unfortunately, nowadays a huge lack of knowledge still exists when in-service load conditions are considered and performing a reasonable accurate fatigue lifetime prediction in this design situation is still a challenge for engineers. All fatigue damage criteria have been defined and validated under Constant Amplitude (CA) local stresses, i.e. fatigue cyclic stresses with a constant amplitude and a constant mean stress. A typical example of CA load is that of a sinusoidal load, usually adopted to perform standard fatigue tests for the characterization of materials and components' fatigue properties. However, under real in-service conditions all welded structures are usually subjected to rather complex load-time histories composed by Variable Amplitude (VA) uniaxial or multi-axial sequence of stresses that can be both deterministic and stochastic in nature. Lack of knowledge in the design of welded structures against VA fatigue stresses leads to the need to oversize components or the unnecessary use of expensive materials and processes.

In the Literature, there are many attempts to formulate and validate new criteria for the design of welded structures against VA fatigue, but none of them has reached yet universal acceptance. International standards and recommendations suggest the nominal stress approach as probably the simplest method. As presented in the previous chapter, this method consists in evaluating the applied nominal stress by means of standard solid-mechanics-based stress calculations without considering any stress concentration at the weld bead and assuming a linear elastic material behaviour. The fatigue lifetime assessment is done by comparing the value of the applied nominal stress with the fatigue strength of the considered joints, the latter being

2.1 Introduction

directly evaluated from the specific S-N design curve (see Figure 2.1a) chosen from a list of classified structural details. In case of VA loads, standards and recommendations [1,2] suggest combining the CA design curves with a cumulative damage rule, i.e. the so-called Palmegren-Miner Linear Damage Rule (LDR) [3,4]. According to the original formulation of the LDR by Miner [4], a certain fatigue damage is present in the analysed component when applying n_i loading cycles at the same stress level $\Delta\sigma_i$ (CA), the damage being proportional to the total amount of net work w_i absorbed during the n_i loading cycles. If the component is loaded with the same stress level $\Delta\sigma_i$ until failure, then the number of loading cycles become equal to the corresponding fatigue life endurance $n_i = N_i$ and the absorbed net work become equal to the total work absorbed at failure $w_i = W_i$. Then, assuming the absorbed work w_i is proportional to the applied number of loading cycles n_i , Miner suggested mathematically describing the fatigue damage induced by these n_i loading cycles at the same stress level $\Delta\sigma_i$ as follow:

$$D_i = \frac{w_i}{W_i} = \frac{n_i}{N_i} \quad (1.1)$$

The damage D_i being obviously equal to 1 at failure. Finally, assuming the total amount of net work absorbed at failure W_i is constant with the stress level ($W_i = W$ for any $\Delta\sigma_i$), Miner suggested evaluating the total damage provoked by different loading cycles n_1, n_2, \dots, n_n applied at different load levels $\Delta\sigma_1, \Delta\sigma_2, \dots, \Delta\sigma_n$ by the following expression:

$$D = \sum_{i=1}^n D_i = \sum_{i=1}^n \frac{w_i}{W} = \sum_{i=1}^n \frac{n_i}{N_i} = 1 \quad (1.2)$$

After its first formulation in 1945, many fatigue tests were undertaken with the aim of validating the LDR and, unfortunately, significant differences were experimentally observed in several instances. Although such disagreements encouraged the publication of a huge number of novel theories on VA fatigue [5,6], to date no one has reached yet universal acceptance, the reasons being for example the absence of a physical meaning, a complex mathematical and experimental description or the lack of generality which makes the criteria applicable to some specific conditions only. Consequently, standards and recommendations [1,7] suggest keep using the LDR but in a modified version as proposed by Haibach [8,9].

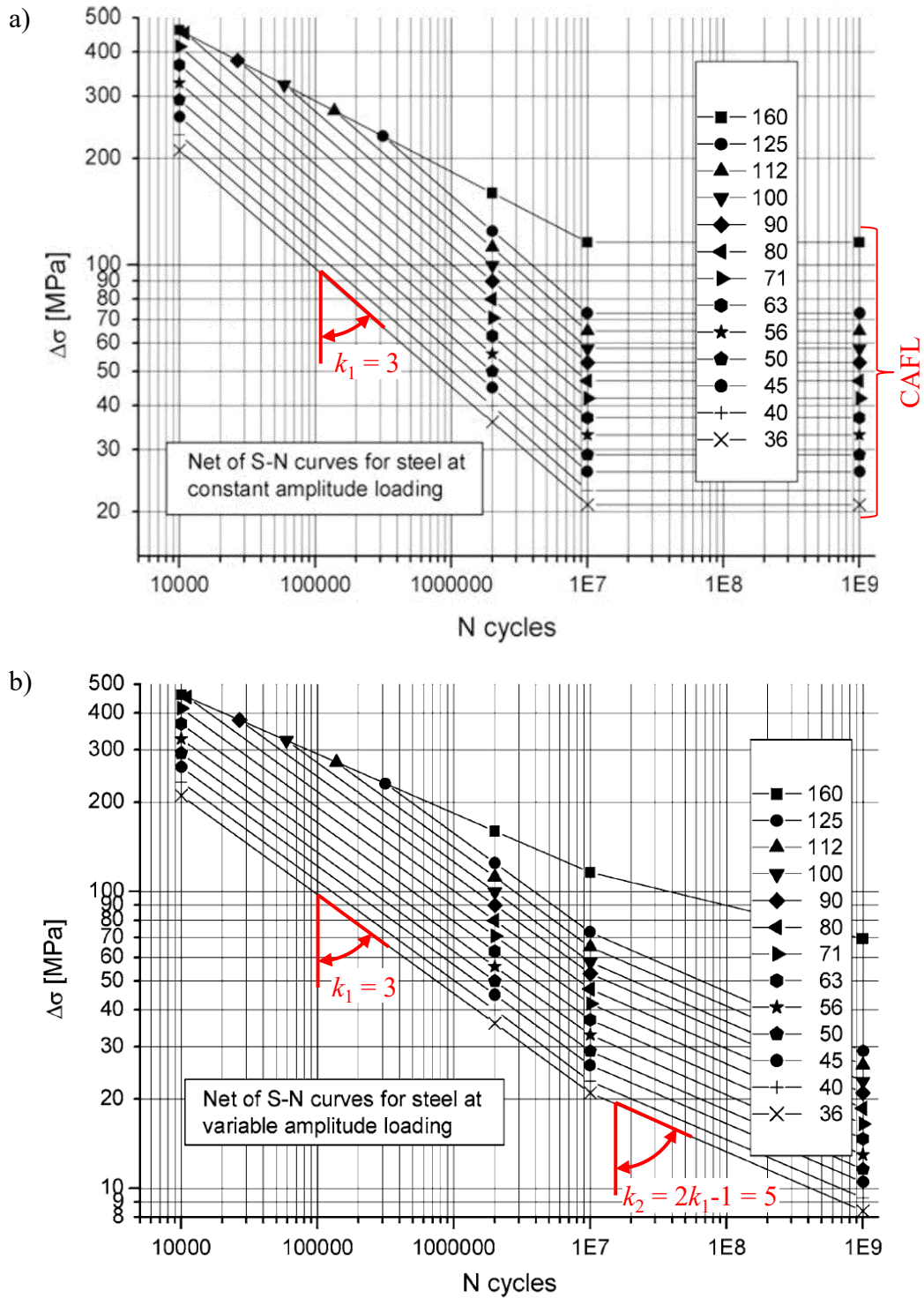


Figure 2.1. a) Fatigue resistance S-N curves for steel welded joints subjected to normal stresses. b) Modified resistance S-N curves of steel welded joints for the Palmgren-Miner summation. Images taken from [2].

According to the standard LDR formulation, all the loading cycles applied at a stress level below the Constant Amplitude Fatigue Limit (CAFL) of the welded details are not damaging,

2.1 Introduction

in this case the number of cycles to failure being theoretically $N_i \rightarrow \infty$ and the consequent fatigue damage $n_i/N_i \rightarrow 0$. In VA fatigue, this observation holds true when all the loading cycles are applied below the fatigue limit. On the contrary, it is well known from experimental observations that loading cycles applied below the CAFL can contribute to increase the fatigue damage when loads are applied both above and below the CAFL during VA fatigue tests. To overcome this limitation of the LDR, standards and recommendations [1,7] indicate extrapolating the S-N curve beyond the fatigue limit with a slope $k_2 = 2 \cdot k_1 - 1$ according to Haibach's modification [8,9] (see Figure 2.1b which shows the modified S-N curves for welded joints under normal stresses taken from the IIW recommendations [2]).

Noteworthy, important differences still exist between available standards and recommendations. The first that needs to be highlighted is the definition of the CAFL. In particular, both Eurocode 3 [1] and IIW recommendations [2] define the CAFL as the stress level corresponding to a certain fixed number of cycles to failure (see the knee points on Figure 2.1 for the case of IIW recommendations), this number being dependent on the considered standard ($5 \cdot 10^6$ cycles for [1] and 10^7 cycles for [2]).

Another fundamental difference relies on the total damage sum to failure D . Indeed, although the Eurocode 3 [1] suggest using a total damage sum $D = 1$ in agreement with the first formulation of the LDR [4], it has been widely demonstrated in the Literature that this parameter can assume significantly smaller values than 1 [10,11]. One reasonable and effective way to overcome the possible unconservative predictions of the LDR was suggested for the first time by Schütz [12] and consists in the use of a relative Palmegren-Miner rule, i.e. introducing a safety factor in the LDR. This results in fixing the total damage sum to failure $D = D_{\text{spec}} < 1$, the value of D_{spec} to be selected by experience on similar components and VA tests. Accordingly, Hobbacher [2] recommends using $D_{\text{spec}} = 0.5$ for standard applications and $D_{\text{spec}} = 0.2$ when considering "spectra with high mean stress fluctuations".

As argued in the previous chapter, most significant limitation of the nominal stress approach appears when considering real components for which either the nominal stresses cannot be computed or the standard fatigue curve for the specific geometry of the welded detail is not available. It has also been discussed that this limitation of the nominal stress approach can be overcome by adopting fatigue approaches based on local quantities instead of global ones [13,14]. Among local approaches, the notch stress approach [13–15], the strain-life approach [13,16–19], those based on the Notch-Stress Intensity Factors (NSIFs) approach [13,20,21], the

averaged Strain Energy Density (SED) criterion [22–27], the critical plane approach [17,28,29], the Theory of Critical Distances (TCD) [28,30,31] or the Peak Stress Method (PSM) [32–37] deserve to be mentioned.

It is worth noting that most of previous local approaches have been extended to account also for variable amplitude fatigue loadings [38–41]. Interestingly, all these methods have been always reformulated in the same way, i.e., by combining their CA formulation with the Palmgren-Miner LDR as cumulative damage rule to account for VA loads. The difference between these methods is the adopted fatigue damage parameter. In particular, Nykänen et al. [38] proposed using the effective notch stress approach [2,13–15,42–44] which in very few words consists in modelling a fictitious notch tip radius r at the weld toe or root of the welded joint ($r = 1$ mm for steel welded joints [2,42]) and evaluating the total stress at the rounded notch tip assuming linear elastic behaviour. Otherwise, Hu et al. [39] suggested adopting the averaged SED [22–27] (see Chapter 1) as fatigue damage parameter and evaluating it by means of the direct approach which requires modelling the material/structural cylindrical volume having radius R_0 ($R_0 = 0.28$ mm for steel welded joints) into FE analyses. Finally, Susmel et al. [40,41] recommended using the Modified Wöhler Curve Method (MWCM) [45,46] together with the Theory of Critical Distances (TCD) [28,30,31,47–52] for evaluating the fatigue damage in welded details. Concisely, the MWCM is a bi-parametrical critical plane approach which assumes the maximum shear stress amplitude as a reference parameter to define the critical plane and assess the fatigue lifetime of welded connections under multiaxial stresses, while the TCD [53], starting from Neuber [54] and Peterson [55] observation on notch sensitivity, indicates either the stress averaged over a line having a certain critical length (Line Method – LM) or the stress evaluated at a certain critical distance from the notch tip (Point Method – PM) as fatigue damage parameter.

Interestingly, although the accuracy and validity of the methods discussed above is unquestionable, their application can certainly be very difficult from a practical/industrial point of view. For example, rounding the weld beads and the weld roots with a fictitious radius $r = 1$ mm as required by the effective notch stress approach, or modelling the material/structural cylindrical volume having radius R_0 ($R_0 = 0.28$ mm for steel welded joints) into FE analyses as suggest by the averaged SED calculation with the direct approach are very difficult and time-consuming operations. On the contrary, both the TCD and the Peak Stress Method (PSM) [32–37] can be easily implemented without the need of modelling complex geometrical feature,

especially when complicated three-dimensional geometries are involved. Moreover, the presented methods require a mesh pattern that tends to be finer than that needed to apply PSM (e.g. when applying the SED direct approach the mesh inside the material/structural volume must be considerably smaller than R_0) significantly increasing the computational effort required to solve the models. Finally, the PSM requires only one nodal stress value rather than the whole stress field at the notch tip, i.e. a set of stress-distance FE data usually which definition usually requires a lot of time in the post processing phase, as required for applying the TCD.

The rapidity and effectiveness of PSM in the pre-processing, solving and post-processing phases make this method very advantageous for industrial applications where the welded structures can assume very complex 3D geometries, with many different critical weld toes and roots, and whose dimensions give rise to huge FE models difficult to solve from a computational point of view. In addition, among recent developments of the PSM, its automated implementation [56,57] for the fatigue assessment of complex welded structures under CA multiaxial loadings is making the PSM application even easier and faster.

Consequently, the aim of the present manuscript was extending for the first time the formulation of the PSM to account also for variable amplitude loading conditions. According to the observations relevant to the available theories on VA fatigue [5,6] and in agreement with main standards and recommendations [1,2] as well as with the other approaches discussed above [38–41], the PSM [37] has been extended to VA loading by combining the existing CA formulation with the Palmgren-Miner LDR [3,4].

In the following paragraph, the procedure for applying the Peak Stress Method in case of uniaxial/multiaxial constant or variable amplitude loads will be presented. Then, the efficacy of the proposed method will be checked against a large set of experimental fatigue data taken from the literature as well as new experimental results generated by fatigue testing non-load-carrying (nlc) fillet-welded joints having double transverse or inclined attachment. The considered fatigue data are relevant to several welded joint geometries, made of different steel grades, and subjected to different types of VA uniaxial and multiaxial fatigue loads.

2.1. The Peak Stress Method for variable amplitude multiaxial local stresses

The physical basis of the PSM, its theoretical background together with the procedure for its applicability and the corresponding limitations have been extensively presented in the previous chapter of this manuscript. As discussed, it is an NSIF-based approach that assume the weld toes and the weld roots can be modelled as sharp V-notches described by a certain opening angle 2α and having a null tip radius ($\rho = 0$, worst-case condition). Owing to this assumption, the external loads generate singular stress fields at the weld toe and at the weld root and in the framework of linear elasticity, the NSIFs have been shown to be fatigue relevant parameters. It is important to note that the effects of loading type, shape and scale of the welded joint are fully accounted for the NSIFs as largely demonstrated in the literature [20,58].

Combining the PSM for the rapid evaluation of the NSIFs with the averaged SED as fatigue damage criterion, Meneghetti et al. [59,60] proposed to define the following equivalent peak stress as fatigue damage parameter to assess the fatigue lifetime of welded joints under CA uniaxial as well as multiaxial local stresses:

$$\Delta\sigma_{eq,peak} = \sqrt{c_{w1} \cdot f_{w1}^2 \cdot \Delta\sigma_{\theta\theta,\theta=0,peak}^2 + c_{w2} \cdot f_{w2}^2 \cdot \Delta\tau_{r\theta,\theta=0,peak}^2 + c_{w3} \cdot f_{w3}^2 \cdot \Delta\tau_{\theta z,\theta=0,peak}^2} \quad (1.3)$$

Where c_{w1} , c_{w2} , c_{w3} account for the mean stress sensitivity (see Chapter 1 and Eq. (1.30)), $\sigma_{\theta\theta,\theta=0,peak}$, $\tau_{r\theta,\theta=0,peak}$, and $\tau_{\theta z,\theta=0,peak}$ are the opening (mode I), in-plane shear (mode II), and out-of-plane shear (mode III) peak stresses, respectively, obtained from linear elastic FE analyses according to the PSM, while f_{w1} , f_{w2} , f_{w3} account for the stress averaging inside the material-structural volume with size R_0 and are defined as follows:

$$f_{w1} = K_{FE}^* \cdot \sqrt{\frac{2e_1}{1-\nu^2}} \cdot \left(\frac{d}{R_0}\right)^{1-\lambda_1} \quad (1.4)$$

2.1 The Peak Stress Method for variable amplitude multiaxial local stresses

$$f_{w2} = K_{FE}^{**} \cdot \sqrt{\frac{2e_2}{1-\nu^2}} \cdot \left(\frac{d}{R_0}\right)^{1-\lambda_2} \quad (1.5)$$

$$f_{w3} = K_{FE}^{***} \cdot \sqrt{\frac{2e_3}{1-\nu^2}} \cdot \left(\frac{d}{R_0}\right)^{1-\lambda_3} \quad (1.6)$$

Noteworthy, Eqs. (1.3), (1.4), (1.5), and (1.6) have been defined and completely described in the previous Chapter. They have been here reported for the sake of clearness but the reader is referred to Chapter 1 for a more detailed description of the PSM CA formulation.

In principle, the suggested method for VA fatigue combines the CA fatigue design curves with the Linear Damage Rule (LDR) by Palmgren-Miner in order to provide a new damage parameter accounting for all types of loadings, i.e. uniaxial/multiaxial and constant/variable amplitude. The new damage parameter is defined in terms of an equivalent peak stress like the CA formulation (see Eq. (1.3)). The mode I, II, and III peak stress spectra at the critical points of the welded structure obtained by a linear elastic FE analysis according to the criteria of the PSM are required as an input for the definition of the new equivalent peak stress. After that, each local stress spectra must be used separately to evaluate a ‘constant amplitude equivalent peak stress’ producing the same fatigue damage as the spectrum according to the LDR, the latter being separately applied for each local stress mode. It should be emphasized that ‘equivalent’ highlights the stress averaging inside the material-structural volume with size R_0 using the f_{wi} coefficients (Eqs. (1.4), (1.5), and (1.6)), while ‘constant amplitude’ emphasizes the synthesis of the spectrum using Palmgren-Miner's law. Then, a single equivalent peak stress accounting also for multiaxiality is obtained by combining the three ‘constant amplitude equivalent peak stresses’ that were previously computed separately for each local stress mode. The resulting damage parameter, i.e. the equivalent peak stress is defined under a CA uniaxial plane strain state in such a way that it generates the same averaged SED existing at the weld toe or the weld root subjected to a general mixed mode I+II+III VA local stress state [59,61–63]. In the end, the equivalent peak stress must be compared to the pertinent PSM design curve, which must be selected using a local biaxiality ratio. More specifically, the procedure is divided into the following steps:

1. The welded joint must be modelled according to the worst-case scenario, i.e. both the weld toe and the weld root are considered as sharp V-notches having a null tip radius ($\rho = 0$) and a certain opening angle 2α as reported in the example of Figure 2.2.

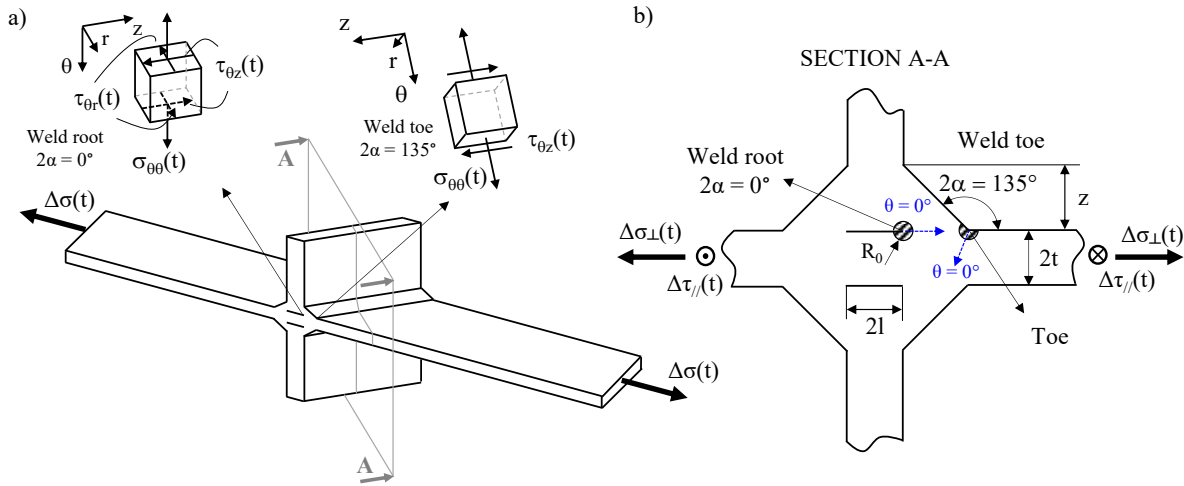


Figure 2.2. Geometry according to the NSIF-based approach and the worst-case hypothesis for the fatigue lifetime assessment of welded joints. (a) example referred to a non-load-carrying fillet-welded double inclined attachments. The sharp V-notch opening angle is typically $2\alpha = 135^\circ$ for the weld toe and $2\alpha = 0^\circ$ for the weld root. Detail on the local cylindrical reference systems (r, θ, z) centred at the weld toe and at the weld root with highlighted the local stress components. (b) the material-structural volume having radius R_0 centred at the weld toe and at the weld root according to the averaged SED criterion.

2. Then, a linear elastic FE analysis should be performed in order to evaluate the mode I, II, and III peak stress time-histories, i.e. $\sigma_{\theta\theta, \theta=0, \text{peak}}(t)$, $\tau_{r\theta, \theta=0, \text{peak}}(t)$ and $\tau_{\theta z, \theta=0, \text{peak}}(t)$, respectively (Figure 2.3a and c), at the critical points in the welded structure, i.e. weld roots and/or weld toes (Figure 2.3a). The modelled geometry must be discretized with linear elastic Finite Elements according to the guidelines of the PSM [37] (see the example in Figure 2.3a). Here, it must be reminded that in case 3D tetra elements are used for the analysis, the peak stresses distribution along the V-notch tip line obtained from the FE analysis $\sigma_{\theta\theta, \theta=0, \text{peak}}$, $\tau_{r\theta, \theta=0, \text{peak}}$, and $\tau_{\theta z, \theta=0, \text{peak}}$ must be smoothed by calculating the average peak stresses $\bar{\sigma}_{\theta\theta, \theta=0, \text{peak}}$, $\bar{\tau}_{r\theta, \theta=0, \text{peak}}$, and $\bar{\tau}_{\theta z, \theta=0, \text{peak}}$ defined as the moving averages of the peak stresses calculated on three adjacent vertex nodes [36]:

$$\bar{\sigma}_{ij, \text{peak}, n=k} = \frac{\sigma_{ij, \text{peak}, n=k-1} + \sigma_{ij, \text{peak}, n=k} + \sigma_{ij, \text{peak}, n=k+1}}{3} \Bigg|_{n=\text{node}} \quad (1.7)$$

2.1 The Peak Stress Method for variable amplitude multiaxial local stresses

Where $\sigma_{ij} = \sigma_{\theta\theta,\theta=0,\text{peak}}$, $\tau_{r\theta,\theta=0,\text{peak}}$, $\tau_{\theta z,\theta=0,\text{peak}}$. Moreover, as explained in the first chapter, the peak stresses at nodes laying on a free surface of the investigated structure (red nodes in Figure 2.3b) must be neglected and not be inputted into Eq. (1.7). Additionally, when dealing with 10-node tetra elements, peak stresses at mid-side nodes (blue nodes in Figure 2.3b) must be neglected, while that obtained from vertex node are the only to be considered for the calculations in Eq. (1.7) [36,64]. It deserves to be highlighted that just one FE analysis can be performed to obtain the peak stress time-histories $\sigma_{\theta\theta,\theta=0,\text{peak}}(t)$, $\tau_{r\theta,\theta=0,\text{peak}}(t)$, and $\tau_{\theta z,\theta=0,\text{peak}}(t)$, as due to the hypothesis of linear elasticity it is possible to scale the obtained value of the peak stresses by multiplying them for the external loads time histories.

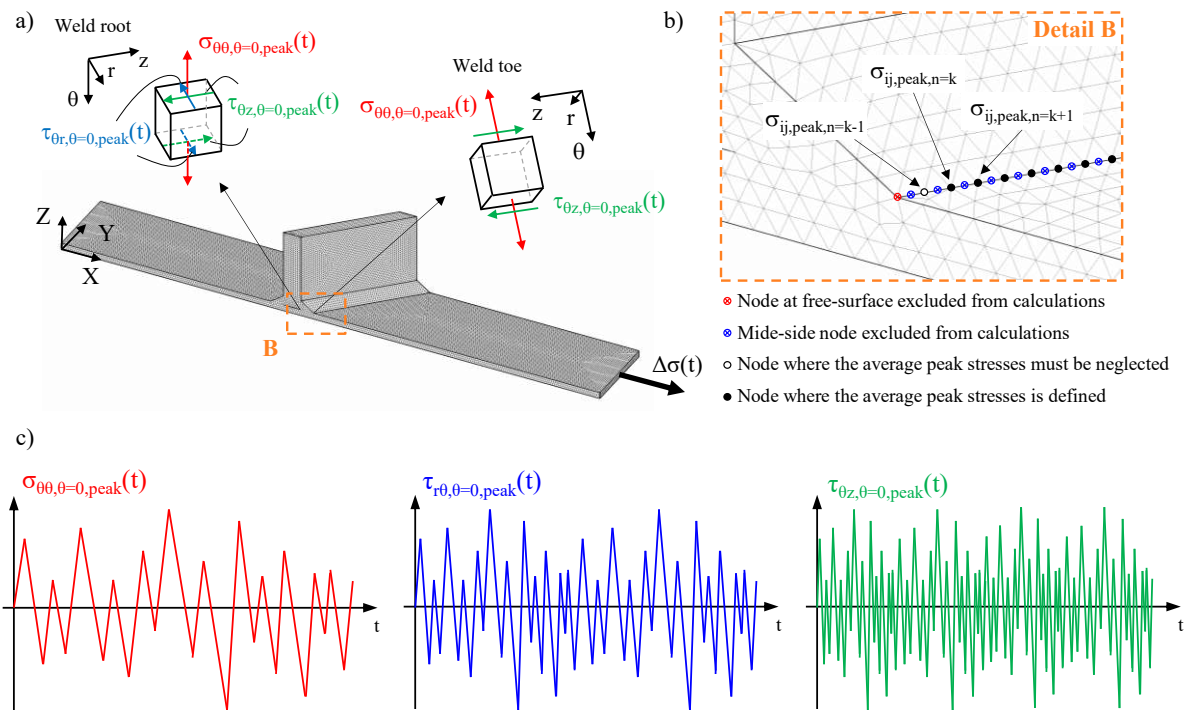


Figure 2.3. Example of application of the PSM to the joint geometry of Figure 2.2. (a) and (b) FE model obtained exploiting the XY symmetry plane and discretized using 10-node tetra elements (SOLID 187 of the Ansys® element library) with detail on the peak stresses evaluated in a cylindrical reference system (r,θ,z) oriented along the V -notch bisector line and located at the node laying at the weld toe or the weld root notch tip. (c) example of mode I, II, and III peak stress time histories at the weld root, output of the FE analysis.

- The next step consists in applying the Rainflow cycle counting algorithm [65–67] to the peak stress time-histories $\sigma_{\theta\theta,\theta=0,\text{peak}}(t)$, $\tau_{r\theta,\theta=0,\text{peak}}(t)$, and $\tau_{\theta z,\theta=0,\text{peak}}(t)$ (or the average peak stress time-histories $\bar{\sigma}_{\theta\theta,\theta=0,\text{peak}}(t)$, $\bar{\tau}_{r\theta,\theta=0,\text{peak}}(t)$, and $\bar{\tau}_{\theta z,\theta=0,\text{peak}}(t)$ in case of tetra elements).

This way, all the information of the time-histories are summarized in the mode I, II and III Rainflow matrices (Figure 2.4a), which give the applied number of cycles for each combination of local load ratio and peak stress range, or in the mode I, II, and III peak stress spectra (Figure 2.4b), which replace the rainflow matrices when all the peak stress ranges are applied at the same mean peak stress, i.e. with the same local load ratio. To clarify what presented and simplify the explanation, it is worthwhile symbolize some parameters as follow (see Figure 2.4):

- $\Delta\sigma_{\theta\theta,\theta=0,\text{peak},i}$, $\Delta\tau_{r\theta,\theta=0,\text{peak},h}$, $\Delta\tau_{\theta z,\theta=0,\text{peak},m}$ are the peak stress range levels relevant to mode I, II, and III, respectively.
- q_{ii} , q_{IIIh} , and $q_{III m}$ are the number of stress levels resulting from the Rainflow cycle counting, referred to mode I, II, and III, respectively.
- $\Delta\sigma_{\theta\theta,\theta=0,\text{peak},\text{max}}$, $\Delta\tau_{r\theta,\theta=0,\text{peak},\text{max}}$, $\Delta\tau_{\theta z,\theta=0,\text{peak},\text{max}}$ denote the maximum applied peak stress range for mode I, II, and III, respectively.
- $R_{I,j}$, $R_{II,k}$, $R_{III,p}$ are the mode I, II, and III local load ratio, respectively. They gather all information about the level of the mean peak stress at which each peak stress range is applied.
- q_{Ij} , q_{IIIk} , and $q_{III p}$ are the corresponding number of local load ratio levels resulting from the Rainflow cycle counting, referred to mode I, II, and III, respectively.
- $n_{I,ij}$, $n_{II,hk}$, $n_{III,mp}$, are the number of applied cycles for each combination of peak stress range levels (i.e. $\Delta\sigma_{\theta\theta,\theta=0,\text{peak},i}$, $\Delta\tau_{r\theta,\theta=0,\text{peak},h}$, $\Delta\tau_{\theta z,\theta=0,\text{peak},m}$) and local load ratios (i.e. $R_{I,j}$, $R_{II,k}$, $R_{III,p}$).
- N_I , N_{II} , N_{III} are the total number of cycles of each loading mode and can be evaluated as follow:

$$N_I = \sum_{i=1}^{q_{ii}} \sum_{j=1}^{q_{Ij}} n_{I,ij} \quad (1.8)$$

2.1 The Peak Stress Method for variable amplitude multiaxial local stresses

$$N_{II} = \sum_{h=1}^{q_{II}} \sum_{k=1}^{q_{IIk}} n_{II,hk} \quad (1.9)$$

$$N_{III} = \sum_{m=1}^{q_{III}} \sum_{p=1}^{q_{IIIp}} n_{III,mp} \quad (1.10)$$

- N_0 identifies a reference number of cycles defined by Eq. (1.11).

$$N_0 = \min \{ N_I, N_{II}, N_{III} \} \quad (1.11)$$

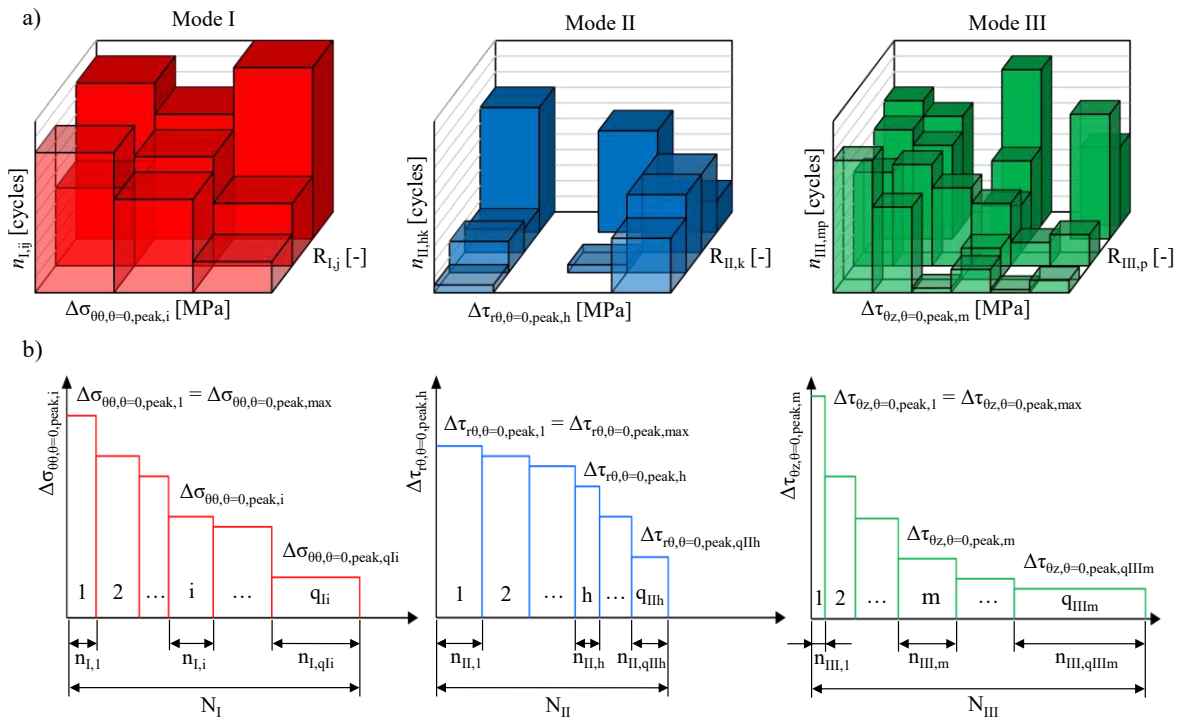


Figure 2.4. Result of the Rainflow cycle counting algorithm applied to the peak stresses time-histories. (a) mode I, II, and III Rainflow matrices giving the applied number of cycles for each combination of local load ratio (gathering all information on the mean peak stresses) and peak stress range. (b) the special case of mode I, II and III peak stress spectra which replace the Rainflow matrices when all the peak stress ranges are applied at the same mean peak stress.

4. Then, the procedure requires to evaluate separately the mode I, mode II, and mode III ‘constant amplitude equivalent peak stresses’, i.e. $\Delta\sigma_{\text{eq,peak,I}}$, $\Delta\sigma_{\text{eq,peak,II}}$, $\Delta\sigma_{\text{eq,peak,III}}$, which give the same fatigue damage (with respect to the design scatter band relevant to each

specific loading mode), induced in accordance with the LDR by the real peak stress time-histories when applied for N_0 cycles. In more detail, this can be done converting the mode I, II and III peak stress Rainflow matrices $(\Delta\sigma_{\theta\theta,\theta=0,\text{peak},i}, R_{I,j}, n_{I,ij})$, $(\Delta\tau_{r\theta,\theta=0,\text{peak},h}, R_{II,k}, n_{II,hk})$, $(\Delta\tau_{\theta z,\theta=0,\text{peak},m}, R_{III,p}, n_{III,mp})$, (or spectra $(\Delta\sigma_{\theta\theta,\theta=0,\text{peak},i}, n_{I,i})$, $(\Delta\tau_{r\theta,\theta=0,\text{peak},j}, n_{II,j})$, $(\Delta\tau_{\theta z,\theta=0,\text{peak},h}, n_{III,h})$, see Figure 2.4) into equivalent peak stress Rainflow matrices (or spectra) by multiplying each peak stress range by the relevant f_{wi} coefficient (Eqs. (1.4), (1.5), and (1.6)). Secondly, the Palmgren-Miner LDR must be applied separately for each loading mode by comparing each equivalent peak stress spectra with the PSM CA fatigue design curve relevant to the same loading mode (see Figure 2.5 and Table 2.1). For the sake of simplicity, the PSM CA fatigue design curves must be taken without any cut-off or slope change. What presented above to obtain the three constant amplitude equivalent peak stresses generating the same fatigue damage (according to the LDR) as the equivalent peak stress spectra when applied for N_0 cycles (see Figure 2.5) is very easily summarized by the following expressions:

$$\Delta\sigma_{\text{eq,peak,I}} = f_{s1} \cdot f_{w1} \cdot \Delta\sigma_{\theta\theta,\theta=0,\text{peak,max}} \quad (1.12)$$

$$\Delta\sigma_{\text{eq,peak,II}} = f_{s2} \cdot f_{w2} \cdot \Delta\tau_{r\theta,\theta=0,\text{peak,max}} \quad (1.13)$$

$$\Delta\sigma_{\text{eq,peak,III}} = f_{s3} \cdot f_{w3} \cdot \Delta\tau_{\theta z,\theta=0,\text{peak,max}} \quad (1.14)$$

where the f_{si} coefficients, which account for the Palmgren-Miner LDR equivalency, are defined by the following expressions:

$$f_{s1} = \left[\sum_{i=1}^{q_{I,i}} \sum_{j=1}^{q_{I,j}} \frac{n_{I,ij}}{N_0} \cdot \left(\sqrt{c_{w1,j}} \cdot \frac{\Delta\sigma_{\theta\theta,\theta=0,\text{peak},i}}{\Delta\sigma_{\theta\theta,\theta=0,\text{peak,max}}} \right)^{k_1} \right]^{1/k_1} \quad (1.15)$$

$$f_{s2} = \left[\sum_{h=1}^{q_{II,h}} \sum_{k=1}^{q_{II,k}} \frac{n_{II,hk}}{N_0} \cdot \left(\sqrt{c_{w2,k}} \cdot \frac{\Delta\tau_{r\theta,\theta=0,\text{peak},h}}{\Delta\tau_{r\theta,\theta=0,\text{peak,max}}} \right)^{k_2} \right]^{1/k_2} \quad (1.16)$$

$$f_{s3} = \left[\sum_{m=1}^{q_{III,m}} \sum_{p=1}^{q_{III,p}} \frac{n_{III,mp}}{N_0} \cdot \left(\sqrt{c_{w3,p}} \cdot \frac{\Delta\tau_{\theta z,\theta=0,\text{peak},m}}{\Delta\tau_{\theta z,\theta=0,\text{peak,max}}} \right)^{k_3} \right]^{1/k_3} \quad (1.17)$$

Wherein, the mean stress effect is taken into account by the c_w coefficients, which definitions are the followings:

$$c_{w1,j}(R_{I,j}) = \begin{cases} 1 & \text{if as-welded for any R value} \\ \frac{1+R_{I,j}^2}{(1-R_{I,j})^2} & \text{if stress-relieved and } -1 \leq R \leq 0, \\ \frac{1-R_{I,j}^2}{(1-R_{I,j})^2} & \text{if stress-relieved and } 0 \leq R < 1, \end{cases} \quad (1.18)$$

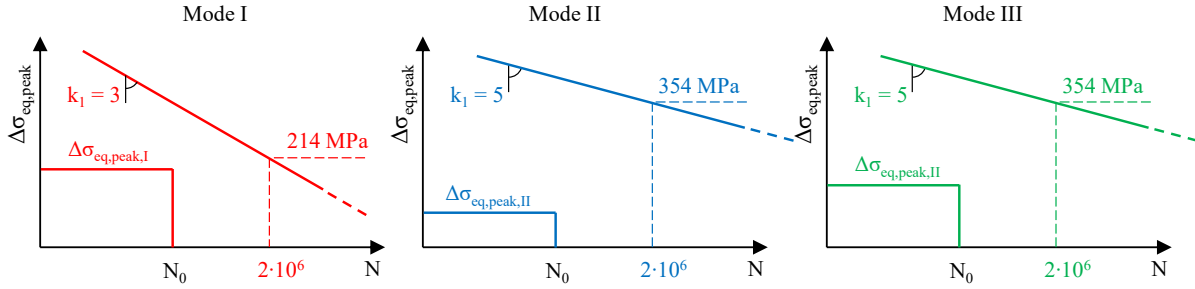
$$c_{w2,k}(R_{II,k}) = \begin{cases} 1 & \text{if as-welded for any R value} \\ \frac{1+R_{II,k}^2}{(1-R_{II,k})^2} & \text{if stress-relieved and } -1 \leq R \leq 0, \\ \frac{1-R_{II,k}^2}{(1-R_{II,k})^2} & \text{if stress-relieved and } 0 \leq R < 1, \end{cases} \quad (1.19)$$

$$c_{w3,p}(R_{III,p}) = \begin{cases} 1 & \text{if as-welded for any R value} \\ \frac{1+R_{III,p}^2}{(1-R_{III,p})^2} & \text{if stress-relieved and } -1 \leq R \leq 0, \\ \frac{1-R_{III,p}^2}{(1-R_{III,p})^2} & \text{if stress-relieved and } 0 \leq R < 1, \end{cases} \quad (1.20)$$

Again, it deserve to be remembered that when using the PSM based on tetra elements, the average peak stresses $\bar{\sigma}_{\theta\theta,\theta=0,peak}$, $\bar{\tau}_{r\theta,\theta=0,peak}$, and $\bar{\tau}_{\theta z,\theta=0,peak}$ must be used in place of the peak stresses $\sigma_{\theta\theta,\theta=0,peak}$, $\tau_{r\theta,\theta=0,peak}$, and $\tau_{\theta z,\theta=0,peak}$, as described in Chapter 1.

Table 2.1. Parameters of the PSM CA fatigue design curves to be used when applying the Palmgren-Miner LDR equivalency.

Mode	N_A	$\Delta\sigma_{eq,peak,A}$	k
[-]	[cycles]	[MPa]	[-]
Mode I	$2 \cdot 10^6$	214	3
Mode II	$2 \cdot 10^6$	354	5
Mode II	$2 \cdot 10^6$	354	5


 Figure 2.5. Mode I, II and III constant amplitude equivalent peak stresses generating the same fatigue damage (according to the LDR) as the equivalent peak stress spectra when applied for N_0 cycles (Eqs.(1.12), (1.13), (1.14), respectively).

5. Finally, the three ‘constant amplitude equivalent peak stresses’ pertinent to the mode I, II, and III, i.e. $\Delta\sigma_{eq,peak,I}$, $\Delta\sigma_{eq,peak,II}$, $\Delta\sigma_{eq,peak,III}$, respectively, must be combined together to provide the ‘multiaxial equivalent peak stress’ $\Delta\sigma_{eq,peak}$ accounting also for multiaxial local stresses. This can be done, as for the constant amplitude formulation, by simply adding together the mode I, II and III averaged SED contributions. This turns out into the following expression:

$$\Delta\sigma_{eq,peak} = \sqrt{\Delta\sigma_{eq,peak,I}^2 + \Delta\sigma_{eq,peak,II}^2 + \Delta\sigma_{eq,peak,III}^2} \quad (1.21)$$

In order to keep the nomenclature concise and consistent with other published work on the PSM, the term ‘multiaxial equivalent peak stress’ (Eq.(1.21)) will be used interchangeably with ‘equivalent peak stress’ throughout the whole manuscript. Noteworthy, when CA local stresses are considered, the equivalent peak stress $\Delta\sigma_{eq,peak}$ (Eq.(1.21)) simplifies to its original formulation for CA loads (Eq. (1.3)) [37]. Indeed, in this case, the application of the Rainflow cycle counting algorithm is not required and the coefficients f_{s1}, f_{s2}, f_{s3} collapse into $\sqrt{c_{w1}}$, $\sqrt{c_{w2}}$, and $\sqrt{c_{w3}}$.

6. Eventually, the fatigue lifetime of the investigated welded joints can be evaluated by entering the equivalent peak stress $\Delta\sigma_{\text{eq,peak}}$ (Eq.(1.21)) into the appropriate PSM design scatter band for steel joints, the latter being chosen based on a local biaxiality ratio λ (Figure 2.6). Like the ('multiaxial') equivalent peak stress, the local biaxiality ratio λ is defined as a function of the mode I, II and III 'constant amplitude equivalent peak stresses', i.e. $\Delta\sigma_{\text{eq,peak,I}}$, $\Delta\sigma_{\text{eq,peak,II}}$, and $\Delta\sigma_{\text{eq,peak,III}}$, respectively:

$$\lambda = \frac{\Delta\sigma_{\text{eq,peak,II}}^2 + \Delta\sigma_{\text{eq,peak,III}}^2}{\Delta\sigma_{\text{eq,peak,I}}^2} \quad (1.22)$$

In particular, the local biaxiality ratio λ summarizes the relative SED contributions due to mode II/III shear stresses and mode I normal stresses. It is easy to observe that $\lambda = 0$ under pure mode I local stresses, $\lambda \rightarrow \infty$ under mode II+III local stresses and $0 < \lambda < \infty$ in case of mixed mode I+II+III local stresses. The criterion to choose the appropriate PSM fatigue design curve as a function of the value of λ is the same as that proposed in [37] (Table 2.2). Fatigue data relevant to $\lambda = 0$ must be compared with the PSM-based design scatter band having $\Delta\sigma_{\text{eq,peak,A,50\%}} = 214$ MPa and $k = 3$, while fatigue data relevant to $\lambda > 0$ must be compared with the PSM-based design scatter band having $\Delta\sigma_{\text{eq,peak,A,50\%}} = 354$ MPa and $k = 5$. Noteworthy, the calculated equivalent peak stress range has to be directly compared against the CA PSM design curve having 50% of survival probability (PS). On the other hand, the CA PSM design curves relevant to $\text{PS} = 2.3\%$ and $\text{PS} = 97\%$ can be used to check if all the analysed fatigue data lie within this scatter band. Interestingly, as observed by Meneghetti et al. [60] correspond to a scatter index $T_\sigma = 1.90$, i.e. the intrinsic scatter of single test series tested un CA loadings (see Haibach [9,68] and Sonsino [17,69] for more details).

Table 2.2. Criterion for selecting the PSM-based fatigue design curves for arc-welded joints made of structural steels.

λ	N_A	$\Delta\sigma_{\text{eq,peak,A,50\%}}$	$\Delta\sigma_{\text{eq,peak,A,97.7\%}}$	$\Delta\sigma_{\text{eq,peak,A,2.3\%}}$	k	T_σ
Eq. (1.22)	[cycles]	[MPa]	[MPa]	[MPa]	[-]	[-]
$\lambda = 0$	$2 \cdot 10^6$	214	156	296	3	1.90
$\lambda > 0$	$2 \cdot 10^6$	354	257	488	5	1.90

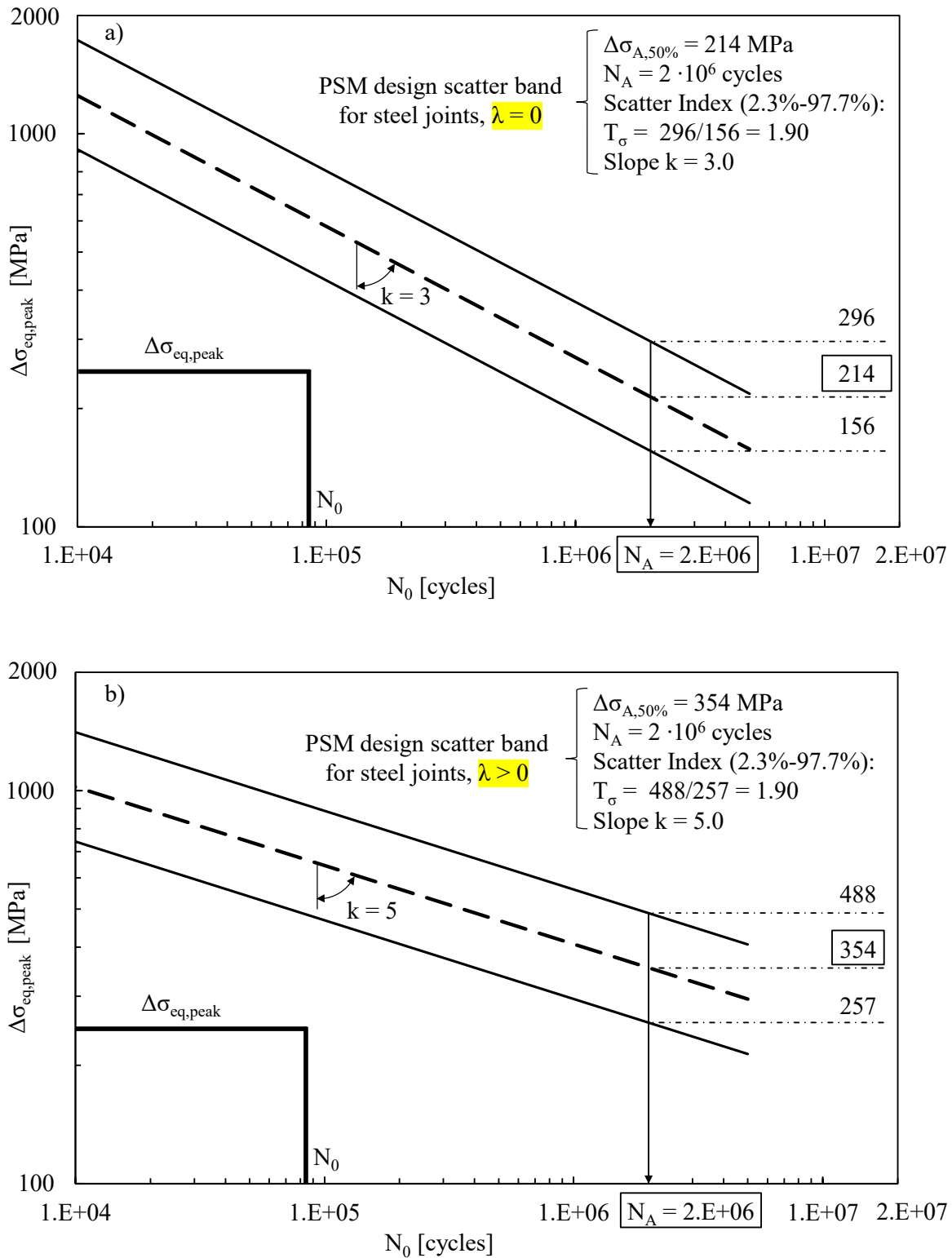


Figure 2.6. Multiaxial equivalent peak stress $\Delta\sigma_{eq,peak}$ (Eq. (1.21)) compared with the proper design curve depending on the local biaxiality ratio λ (Eq. (1.22)). a) the PSM design scatter band for pure mode I local stresses ($\lambda = 0$) and b) the PSM design scatter band for multiaxial local stresses ($\lambda > 0$).

2.2. Validation with data from the literature

A large number of data has been taken from the literature to validate the proposed model against experimental fatigue test results. The analysed data were referred to many different specimens' geometries, materials, and loading conditions [70,71,80,81,72–79]. In particular, the specimens were butt-welded joints, transverse non-load-carrying (nlc) joints, longitudinal stiffeners, and also tube-to-flange welded joints, made of different steel grades, and subjected to different types of uniaxial as well as multiaxial CA and VA fatigue loads. See Table 2.3 for details on materials, welding process, and testing conditions of all the considered steel welded joints.

Table 2.3. Summary of experimental data.

Ref.	Model	Material	f_y	f_u	Welding Process	TCS*	Failure Criterion
[-]	[-]	[-]	[MPa]	[MPa]	[-]	[-]	[-]
Demofonti et al. [70]	(1-4)	S355N	378	560	GMAW/SAW	AW	Complete Separation
		S355M	422	524	GMAW/SAW	AW	Complete Separation
		S690Q	784	868	GMAW/SAW	AW	Complete Separation
		S960Q	998	1072	GMAW	AW	Complete Separation
Maddox and Zhang [71,72]	(5)	BS 4360 Grade 50B	418	554	GMAW	AW	Complete Separation
Vanrostenberghe et al. [73]	(6)	S700MC	-	-	Robot arc-welding	AW	Complete Separation
		S960MC	-	-	Robot arc-welding	AW	Complete Separation
Yildirim et al. [74]	(7)	AH36	423	546	Robot arc-welding	AW	Complete Separation
		S690QL	832	856	Robot arc-welding	AW	Complete Separation
Bertini et al. [75–78]	(8-9)	S355JR	355	520	-	AW	Break Through
Sonsino et al. [79]	(10)	Fe E 460	520	670	GMAW	SR	Break Through
Witt et al. [80,81]	(11)	P 460	520	670	GMAW	SR	Break Through

* Testing Conditions: AW = as-welded; SR = stress-relieved

In the analysed contributions CA and VA pure axial or pure bending loadings were used to test butt-welded joints, transverse non-load-carrying (nlc) joints and longitudinal stiffeners. The applied nominal stress range $\Delta\sigma$ has been calculated with reference to the main plate according to the following expressions:

$$\Delta\sigma = \frac{\Delta F}{A} = \frac{\Delta F}{B \cdot t} \quad \text{axial loading} \quad (1.23)$$

$$\Delta\sigma = \frac{\Delta M_f}{W_f} = \frac{\Delta M_f}{\frac{1}{6} \cdot B \cdot t^2} \quad \text{bending loading} \quad (1.24)$$

wherein ΔF and ΔM_f represent the ranges of the applied axial force and of the bending moment, respectively, whilst A and W_f are the section area and the section modulus, respectively, both defined as a function of the plate width B and the plate thickness t . In the case of tube-to-flange welded joints pure bending, pure torsion and multiaxial CA as well as VA fatigue loadings have been used. The nominal stress ranges have been defined on the tube side according to the following expressions:

$$\Delta\sigma = \frac{\Delta M_f}{W_f} = \frac{\Delta M_f}{\frac{\pi}{32} \cdot \frac{d_e^4 - (d_e - 2t)^4}{d_e}} \quad \text{bending loading} \quad (1.25)$$

$$\Delta\tau = \frac{\Delta M_t}{W_t} = \frac{\Delta M_t}{\frac{\pi}{16} \cdot \frac{d_e^4 - (d_e - 2t)^4}{d_e}} \quad \text{torsion loading} \quad (1.26)$$

where ΔM_f and ΔM_t are the bending and torsional moment ranges, respectively, W_f and W_t are the section moduli, d_e is the tube outer diameter and t is the tube thickness. Moreover, a nominal biaxiality ratio has been defined in the case of combined bending and torsion loadings:

$$\Lambda = \frac{\Delta\tau}{\Delta\sigma} \quad (1.27)$$

In the original publications, the authors provided the experimental fatigue data stated in terms of cycles to failure as a function of the applied nominal stresses. Many different Variable Amplitude (VA) fatigue loadings have been used in the analysed papers (see Table 2.4). Figure

2.2 Validation with data from the literature

2.7 reports a summary of the adopted load spectra expressed in terms of normalized nominal stress range $\Delta\sigma/\Delta\sigma_{\max}$ versus the number of exceedings cycles N , i.e. the number of cycles for which the applied normalized nominal stress ranges are greater than or equal to $\Delta\sigma/\Delta\sigma_{\max}$, whose maximum value is the block length L_s (their main parameters are summarized in Table 2.4).

Table 2.4. Summary of load spectra applied in [70–74,79–81].

Code	Ref.	Spectrum type	L_s	$\Delta\sigma_{\min}/\Delta\sigma_{\max}$
[-]	[-]	[-]	[cycles]	[-]
VA-I	[70][79][80,81]	Gaussian	$5.0 \cdot 10^4$	0
VA-II	[70]	Gaussian + Overloads	$5.0 \cdot 10^4$	0
VA-III	[71,72]	Concave-Up Shape	1042	0.25
VA-IV	[71,72]	Concave-Up Shape	2167	0.20
VA-V	[71,72]	Concave-Up Shape	4982	0.15
VA-VI	[71,72]	Concave-Up Shape	14482	0.10
VA-VII	[73]	Log-Lin	$1.0 \cdot 10^5$	0.15
VA-VIII	[74]	Log-Lin	$2.5 \cdot 10^5$	0.16

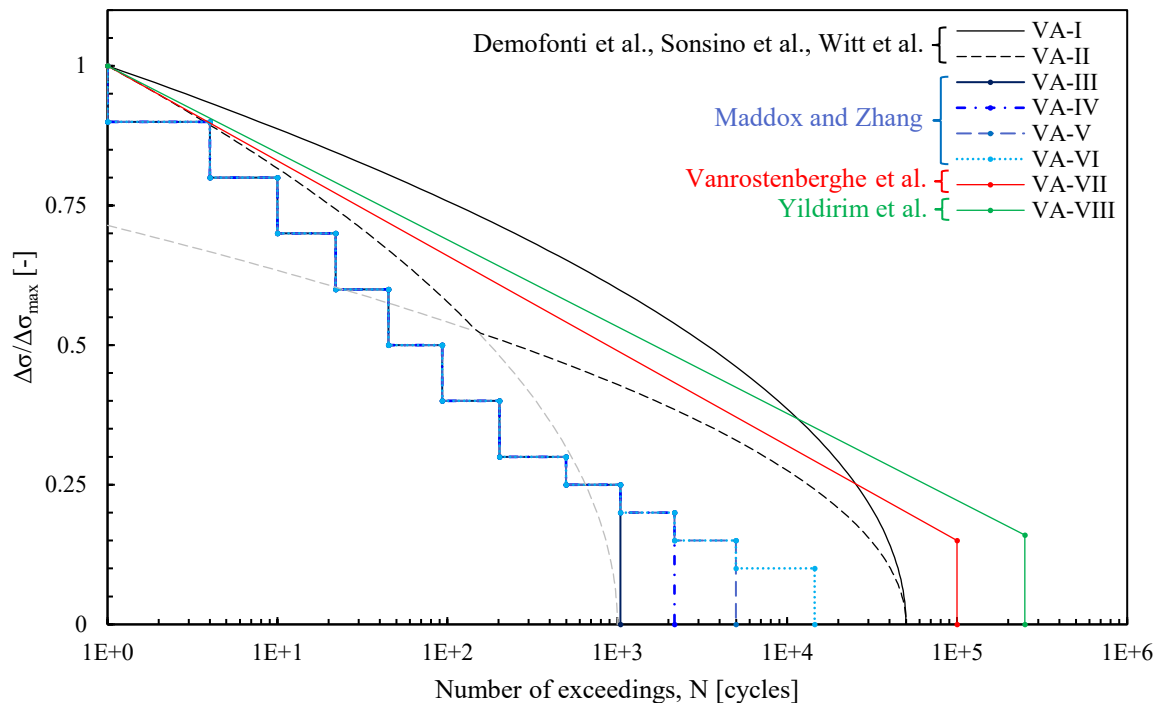


Figure 2.7. Normalized stress range spectra applied in [70–74,79–81] for VA tests. The main parameters are summarized in Table 2.4.

It is worth noting that multiaxial load spectra from VA-IX and VA-XV have been generated by two constant amplitude (CA) loading blocks applied in sequence, e.g. ΔN_1 cycles under pure bending followed by ΔN_2 cycles under pure torsion loadings. The spectra have been reported in Figure 2.8 and Table 2.5 in terms of number of cycles instead of exceedings and the torsional stress range $\Delta\tau$ has been normalized with reference to the maximum bending stress range $\Delta\sigma_{\max}$.

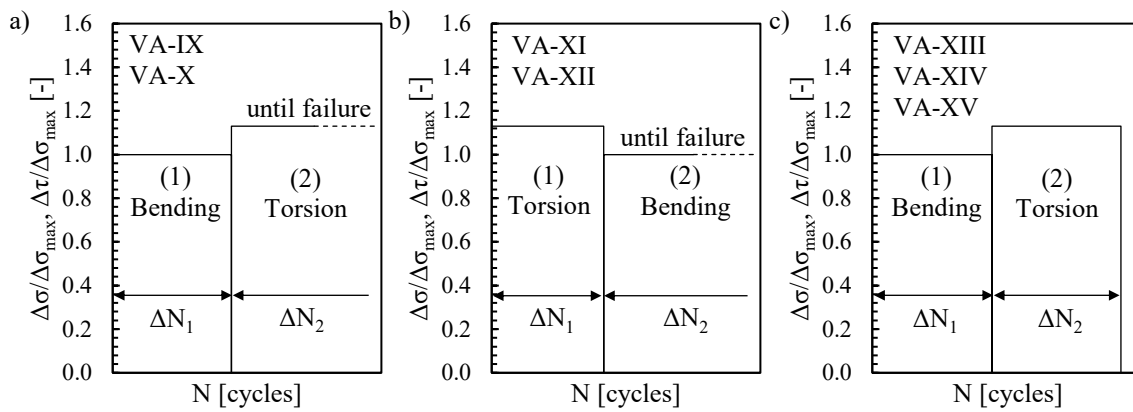


Figure 2.8. Normalized stress range spectra applied for VA tests in Bertini et al. [75–78]. The main parameters are summarized in Table 2.5.

Table 2.5. Summary of load spectra applied in Bertini et al. [75–78]

Code	Ls	i	ΔN_i	$\Delta\sigma/\Delta\sigma_{\max}$	$\Delta\tau/\Delta\sigma_{\max}$
[-]	[cycles]	[-]	[cycles]	[-]	[-]
VA-IX	Undefined	1	276000	1	0
		2	Until Failure	0	1.13
VA-X	Undefined	1	414000	1	0
		2	Until Failure	0	1.13
VA-XI	Undefined	1	306000	0	1.13
		2	Until Failure	1	0
VA-XII	Undefined	1	459000	0	1.13
		2	Until Failure	1	0
VA-XIII	21	1	10	1	0
		2	11	0	1.13
VA-XIV	210	1	100	1	0
		2	110	0	1.13
VA-XV	21000	1	10000	1	0
		2	11000	0	1.13

Depending on the joint geometries, three different element types of Ansys® element library have been adopted to generate the free FE mesh patterns according to the PSM:

- 2D 4-node quadrilateral plane elements (PLANE 182 with K-option 1 set to 3), named ‘PLANE-4’ in the following, have been adopted to generate a 2D free mesh pattern of plane joint geometries, such as butt-welded joints and transverse nlc joints under axial or bending loadings (see models 1-2 in Figure 2.9, models 3-4 in Figure 2.10, and model 7 in Figure 2.17).
- 2D 4-node quadrilateral harmonic elements (PLANE 25), named ‘PLANE-4’ in the following, have been adopted to generate a 2D free mesh pattern of axis-symmetric joint geometries, such as tube-to-flange joints under bending or torsion loadings (see models 8-9 in Figure 2.19, model 10 in Figure 2.21, and model 11 in Figure 2.23). Such element type is applicable to axis-symmetric components subjected to loads expressible through a Fourier series expansion of the angular co-ordinate (it is worth noting that the axis-symmetric loading condition is just a particular case of that). Accordingly, PLANE 25 can be used to simulate 3D axis-symmetric structures subjected to bending or torsion loads, while keeping the advantage of managing 2D FE models.
- 3D 10-node tetrahedral elements (SOLID 187), named ‘TETRA-10’ in the following, have been adopted to generate a 3D free mesh pattern of more complex, non axis-symmetric joint geometries, such as the longitudinal stiffeners under axial loading (see models 5 in Figure 2.13 and model 6 in Figure 2.15).

Additional details relevant to the experimental fatigue tests and the PSM analysis procedure of each test series are reported in Table 2.7 and described in the following sub-sections.

2.2.1. *Demofonti et al. [70], two-sided full penetration butt-welded joints and transverse nlc full-penetration welded joints*

The authors analysed two-sided full penetration butt-welded joints (models 1 and 2 in Figure 2.9) and transverse non-load-carrying (nlc) full-penetration welded joints (models 3 and 4 in Figure 2.10), both specimen geometries having different plate thickness and being made of different steel grades. In particular, the main plates thickness was either $t = 10$ mm or $t = 30$ mm and they were made of structural steels with four different steel grades, i.e. S355N, S355M, S690Q and S960Q. All the specimens were fatigue tested in the as-welded state with different load type depending on the plate thickness. The joints having 30-mm-thick plates were loaded under pure bending (using a 4-point-bending device), whereas those having 10-mm-thick plates were tested under pure axial loading.

The tests were carried out under fully reversed ($R = -1$) or under pulsating ($R = 0$) constant amplitude and under variable amplitude loading. The VA loads consisted in two different spectra applied in random order. The first one was a base Gaussian spectrum [82,83] having a block length $L_s = 5 \cdot 10^4$ cycles (VA-I in Figure 2.7 and Table 2.4). The second one was generated by the superposing of a Gaussian overload spectrum to the base Gaussian spectrum with $L_s = 5 \cdot 10^4$ cycles. More in detail, the Gaussian overload spectrum was obtained by amplifying with a factor of 1.40 the stress ranges of a standard Gaussian spectrum having a block length of 1000 cycles (VA-II in Figure 2.7 and Table 2.4). As expected, the authors reported that failures, i.e. crack initiation and following early fatigue crack propagation, always occurred at the weld toe, the reason of this being the fully penetrated welding execution. The failure condition and the corresponding number of cycles to failure relate to complete specimen's separation.

The experimental fatigue results have been here reported in Figure 2.11 and Figure 2.12 expressed in terms of the number of cycles to failure N_f versus the maximum applied nominal stress range $\Delta\sigma_{\max}$.

The relevant peak stresses have been calculated from 2D free FE mesh patterns of 4-node plane elements (PLANE 182 with K-option 1 set to 3 of Ansys® element library) under plane strain conditions. Only one quarter of the joint geometry was modelled, taking advantage of the double symmetry under axial loading, while the symmetry and anti-symmetry has been exploited under bending loading. It is worth noting that only the weld toe is a potential crack initiation location for these full-penetration joints and the mode II stress field is not singular, 2α being greater than 102° [84]. According to the PSM guidelines [37] for PLANE-4 (see also Table 2.6 here recalled from Chapter 1 for the sake of clarity), the minimum mesh density ratio must be $a/d = 3$ to apply the PSM at the weld toe under mode I loading, where $a = \min\{z, t/2\}$ for the butt-joints, while $a = t/2$ for the double transverse attachments. Therefore, element sizes $d \approx z/3$ and $d \approx (t/2)/3$ have been adopted to generate the free mesh patterns of butt-joints (models 1 and 2 in Figure 2.9) and transverse joints (models 3 and 4 in Figure 2.10), respectively. After having solved the FE model, the maximum principal stress $\Delta\sigma_{11,peak}$ has been evaluated at the weld toe, since under pure mode I stresses, it approximately corresponds to the opening peak stress, $\Delta\sigma_{\theta\theta, \theta=0, peak}$, but it is easier to be obtained since it does not require a polar reference system aligned with the notch bisector line. Then, the equivalent constant amplitude peak stress range has been derived from Eq. (1.21), by assuming $c_{w1} = 1$ in both cases, all specimens having been tested in the as-welded conditions. The local biaxiality ratio λ (Eq. (1.22)) resulted null due to the pure mode I stress state at the weld toe. The resulting opening peak stress $\Delta\sigma_{\theta\theta, \theta=0, peak}$ as well as the factors f_{s1} (Eq. (1.15)) and f_{w1} (Eq. (1.4)) have been reported in Table 2.7. It is worth noting that in the case of butt joints having opening angle 2α at the weld toe in the range between 145° and 155° the coefficient f_{w1} has been calculated by introducing in Eq. (1.4) the parameter $K_{FE}^* = 1.38$, even if it was originally calibrated only in the range $0^\circ \leq 2\alpha \leq 135^\circ$ (Table 2.6), the same extrapolation having been done in Ref. [85].

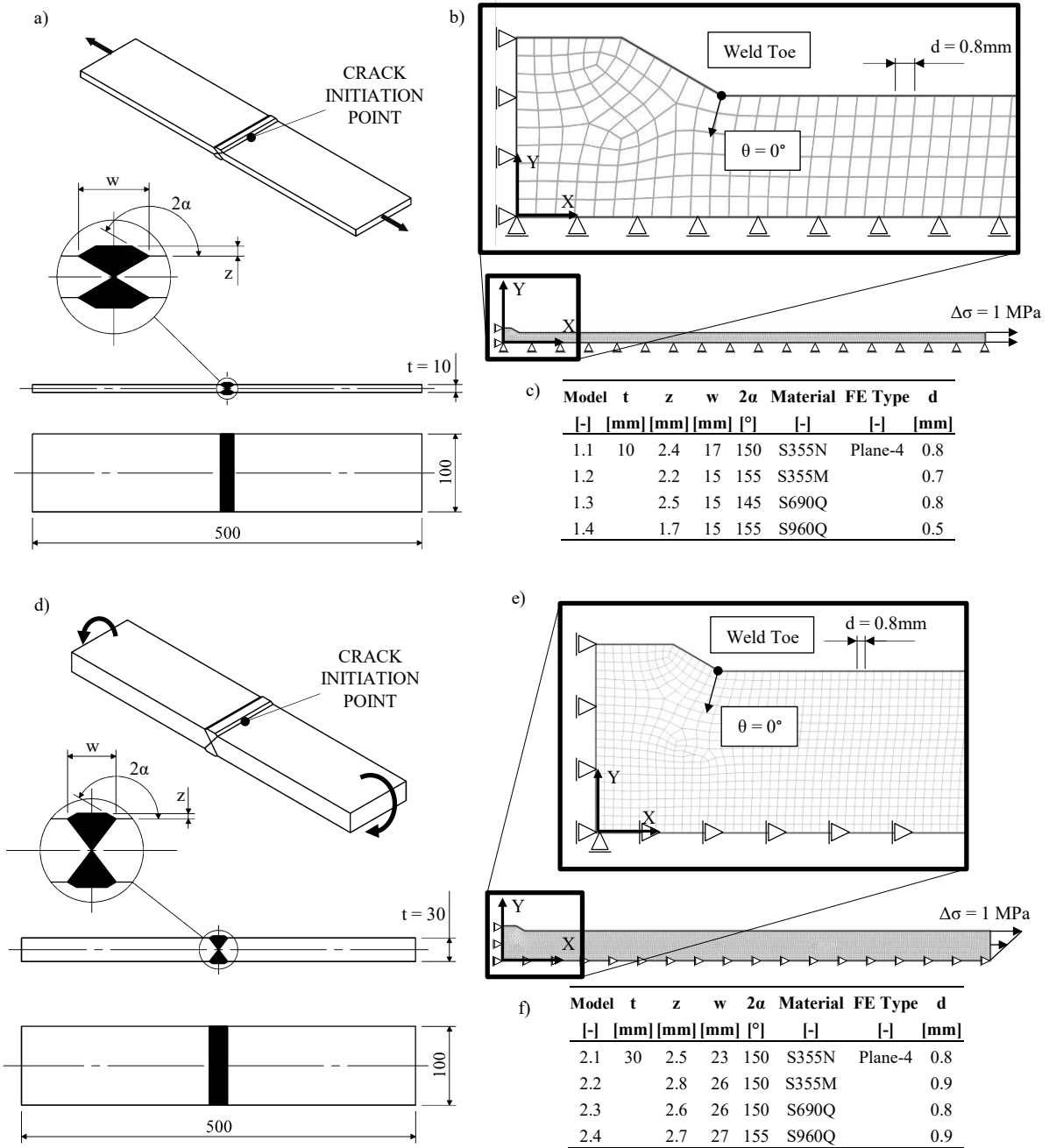


Figure 2.9. Demofonti et al. [70], two-sided full penetration butt-welded joints: a) and d) joint geometry and loading conditions. b) and e) FE model according to the PSM. c) and f) table summarizing the geometrical parameters reported in a) and d).

2.2 Validation with data from the literature

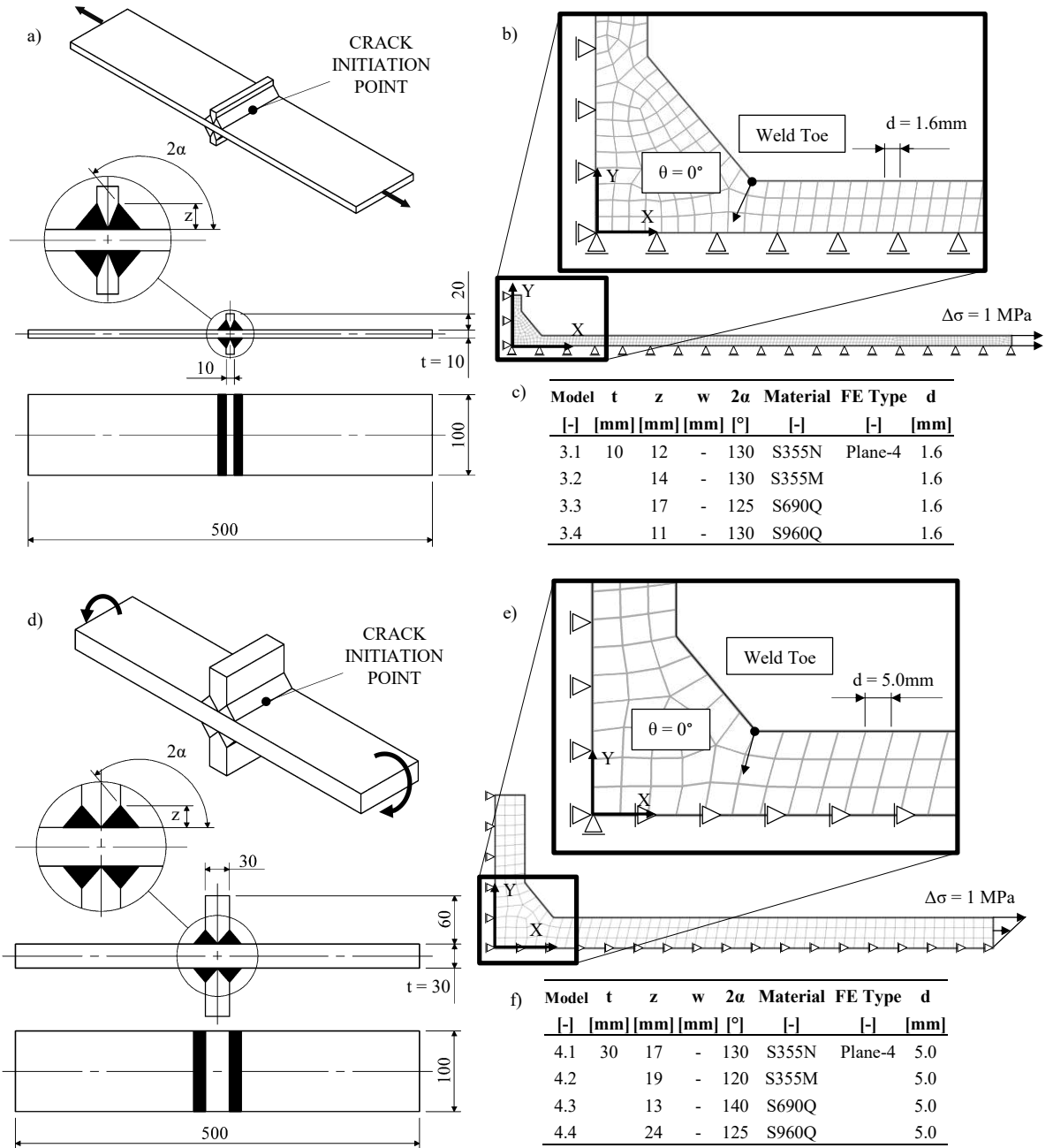


Figure 2.10. Demofonti et al. [70], transverse nlc full-penetration welded joints: a) and d) joint geometry and loading conditions. b) and e) FE model according to the PSM. c) and f) table summarizing the geometrical parameters reported in a) and d).

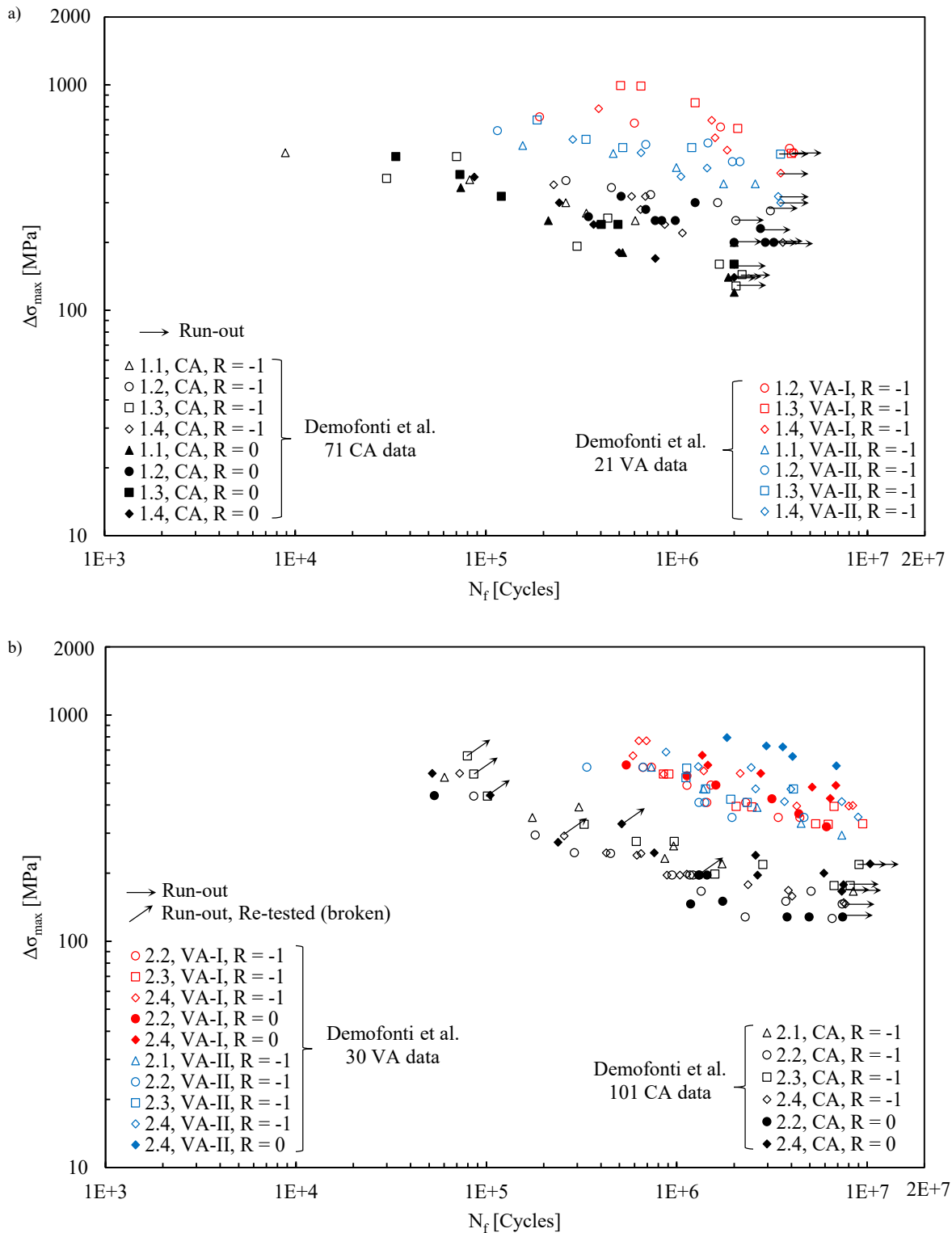


Figure 2.11. Fatigue test results from Demofonti et al. [70] relevant to (a) two-sided full penetration butt-welded joints with $t = 10$ mm (model 1 in Figure 2.9) and (b) two-sided full penetration butt-welded joints with $t = 30$ mm (model 2 in Figure 2.9): data are expressed in terms of maximum applied nominal stress.

2.2 Validation with data from the literature

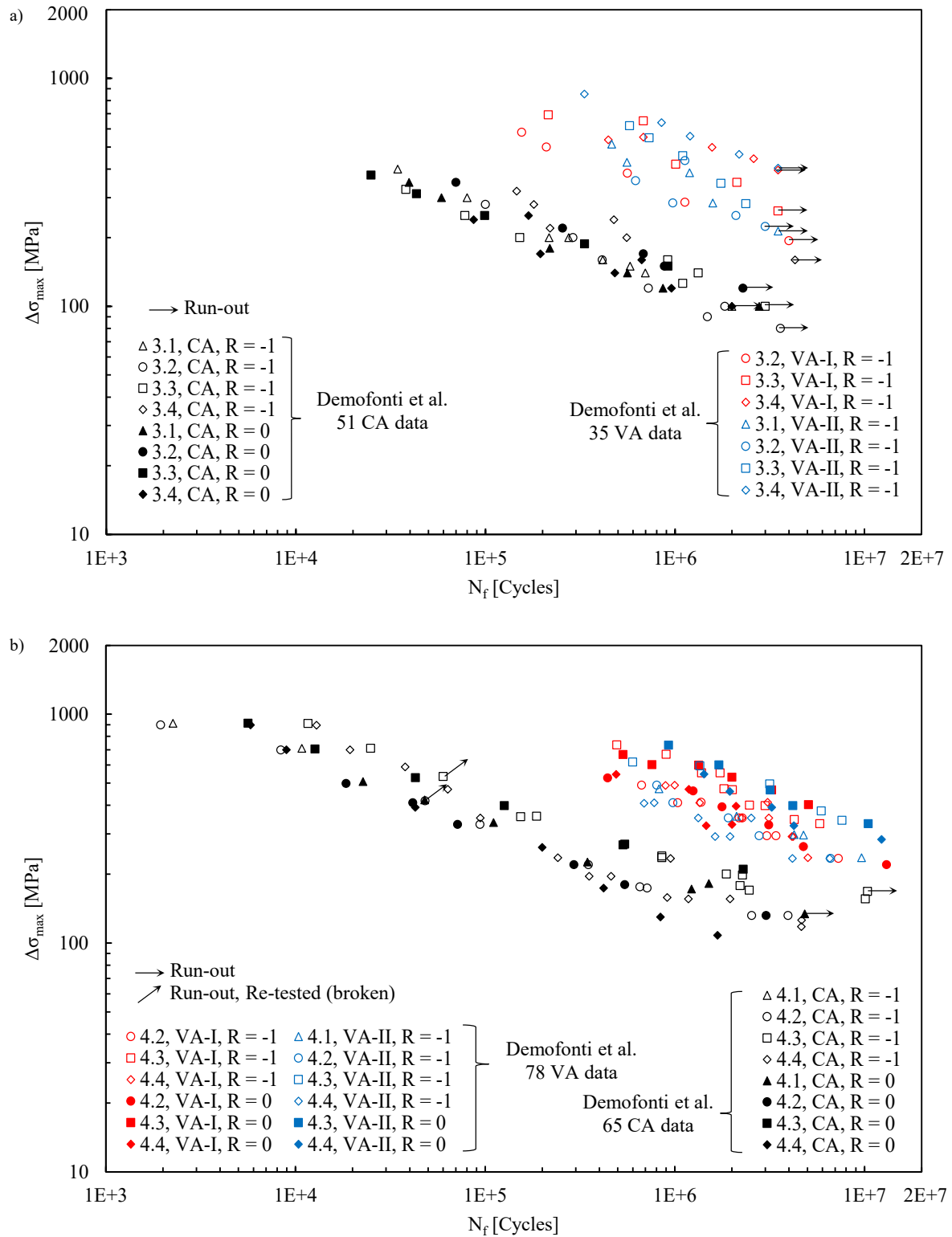


Figure 2.12. Fatigue test results from Demofonti et al. [70] relevant to (a) transverse non-load-carrying (nlc) full-penetration welded joints with $t = 10$ mm (model 3 in Figure 2.10) and (b) transverse non-load-carrying (nlc) full-penetration welded joints with $t = 30$ mm (model 4 in Figure 2.10): data are expressed in terms of maximum applied nominal stress.

CHAPTER 2: Variable amplitude multiaxial local stresses

Table 2.6. Summary of parameters K_{FE}^* , K_{FE}^{**} and K_{FE}^{***} , mesh density a/d , and FE mesh pattern requirements to apply the PSM with Ansys® [32–37,86,87].

Loading	FE analysis		PSM parameters	$2\alpha = 0^\circ$	$2\alpha = 90^\circ$	$2\alpha = 120^\circ$	$\alpha = 135^\circ$	$a - \text{root side}^\circ$	$a - \text{toe side}^\circ$
	2D/3D	FE type [#]							
Mode I	2D	Plane-4	K_{FE}^*	1.38±3%	1.38±3%	1.38±3%	1.38±3%	min{l, z}	t
			$(a/d)_{\min}$	3	3	3	3		
			FE at notch tip [^]	4	4	2	2		
	3D ⁺	Brick-8	K_{FE}^*	1.38±3%	1.38±3%	1.38±3%	1.38±3%	min{l, z}	t
			$(a/d)_{\min}$	3	3	3	3		
			FE at notch tip [^]	4	4	2	2		
	3D ⁺	Tetra-4	K_{FE}^*	1.75±22%	1.75±22%	1.75±22%	1.75±22%	min{l, z}	t
			$(a/d)_{\min}$	3	3	3	1		
			FE at notch tip [^]	<i>not to be checked</i>					
	3D ⁺	Tetra-10	K_{FE}^*	1.05±15%	1.05±15%	1.05±15%	1.21±10%	min{l, z}	t
			$(a/d)_{\min}$	3	3	3	1		
			FE at notch tip [^]	<i>not to be checked</i>					
Mode II	2D	Plane-4	K_{FE}^{**}	3.38±3%	2.62±10%	-	-	min{l, z}	-
			$(a/d)_{\min}$	14	10	-	-		
			FE at notch tip [^]	4	4	-	-		
	3D ⁺	Brick-8	K_{FE}^{**}	3.38±3%	2.62±10%	-	-	min{l, z}	-
			$(a/d)_{\min}$	14	10	-	-		
			FE at notch tip [^]	4	4	-	-		
	3D ⁺	Tetra-4	K_{FE}^{**}	2.65±15%	2.90±10%	-	-	min{l, z}	-
			$(a/d)_{\min}$	3	1	-	-		
			FE at notch tip [^]	<i>not to be checked</i>					
	3D ⁺	Tetra-10	K_{FE}^{**}	1.63±20%	2.65±10%	-	-	min{l, z}	-
			$(a/d)_{\min}$	1	1	-	-		
			FE at notch tip [^]	<i>not to be checked</i>					
Mode III	2D	Plane-4	K_{FE}^{***}	1.93±3%	1.93±3%	1.93±3%	1.93±3%	min{l, z}	t
			$(a/d)_{\min}$	12	-	-	3		
			FE at notch tip [^]	4	-	-	2		
	3D ⁺	Brick-8	K_{FE}^{***}	1.93±3%	1.93±3%	1.93±3%	1.93±3%	min{l, z}	t
			$(a/d)_{\min}$	12	-	-	3		
			FE at notch tip [^]	4	-	-	2		
	3D ⁺	Tetra-4	K_{FE}^{***}	2.20±15%	2.20±15%	2.20±15%	2.20±15%	min{l, z}	t
			$(a/d)_{\min}$	5	5	5	5		
			FE at notch tip [^]	<i>not to be checked</i>					
	3D ⁺	Tetra-10	K_{FE}^{***}	1.37±15%	1.37±15%	1.70±10%	1.70±10%	min{l, z}	t
			$(a/d)_{\min}$	3	3	3	3		
			FE at notch tip [^]	<i>not to be checked</i>					

⁺ 'Full graphics' option must be activated when calculating peak stresses according to 3D PSM

[#] FE of Ansys® code: Plane-4 = PLANE 182 (K-option 1 set to 3) or PLANE 25, Tetra 10 = SOLID 187

[^] number of finite elements which share the node at the notch tip

[°] l, z, t are defined in Chapter 1

2.2.2. Maddox and Zhang [71,72], longitudinal stiffeners with full penetration welds

The fatigue strength of longitudinal stiffeners with full penetration welds made of BS 4360 Grade 50B (model 5 in Figure 2.13) has been investigated in [71,72] under both CA and VA pure axial loadings.

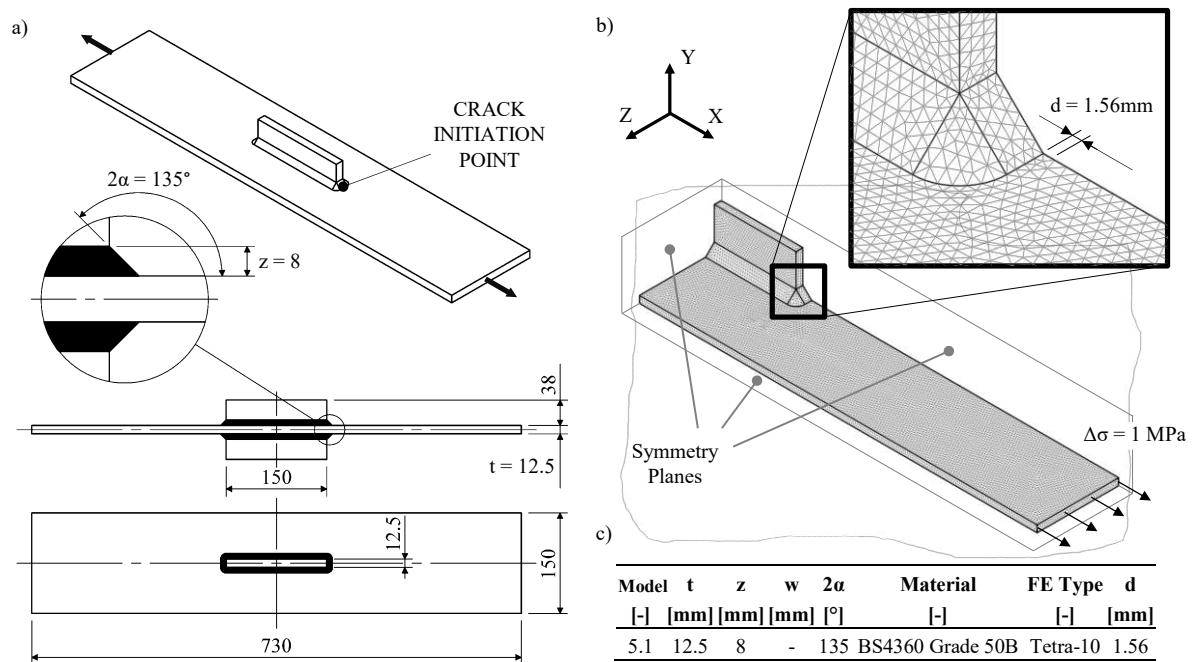


Figure 2.13. Maddox and Zhang [71,72], longitudinal stiffeners with full penetration welds: a) and d) joint geometry and loading conditions. b) and e) FE model according to the PSM. c) and f) table summarizing the geometrical parameters reported in a) and d).

CA fatigue tests were carried out with a constant load ratio $R = 0.1$ or with constant maximum applied stress $\sigma_{\max} = 280$ MPa, with only one exception where $\sigma_{\max} = 135$ MPa was used. On the other hand, VA fatigue tests have been performed by applying concave up spectra (VA-III, VA-IV, VA-V and VA-VI in Figure 2.7 and Table 2.4) in random order and by assuming a block length equal to 1042 cycles for VA-III, 2167 cycles for VA-IV, 4982 cycles for VA-V, 14482 cycles for VA-VI, depending on the omission level, i.e. the smallest applied stress range, which was equal to 25%, 20%, 15%, and 10%, respectively, of the maximum applied stress range. The spectra were applied keeping constant either the maximum stress (σ_{\max}), the mean stress (σ_m) or the minimum stress (σ_{\min}) to investigate the mean stress effect

on the fatigue life. The tested joints being with full penetrated weldment, the fatigue crack initiation location always was the weld toe at the main plate side. The complete separation of the joint was adopted as failure criterion.

The experimental fatigue results have been here reported in Figure 2.14 expressed in terms of the number of cycles to failure N_f versus the maximum applied nominal stress range $\Delta\sigma_{max}$.

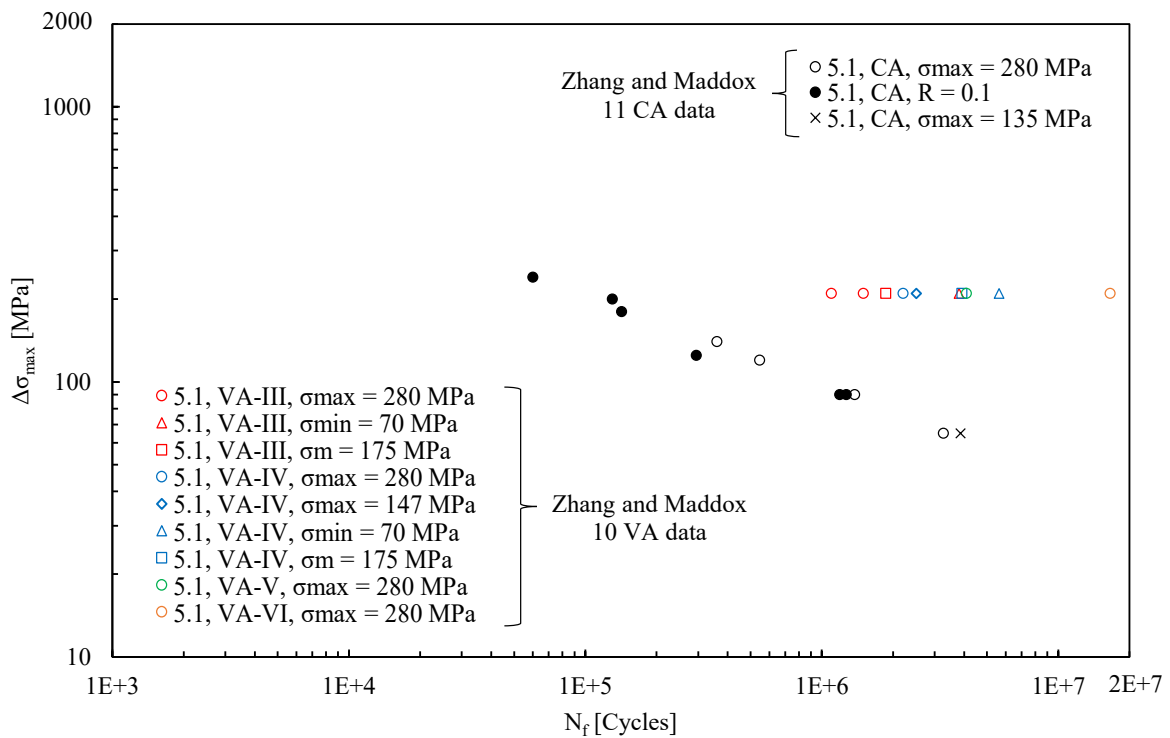


Figure 2.14. Fatigue test results from Maddox and Zhang [71,72] relevant to longitudinal stiffeners with full penetration welds (model 5 in Figure 2.13): data are expressed in terms of maximum applied nominal stress.

A 3D free FE mesh pattern of 10-node tetrahedral elements (SOLID 187 of Ansys® element library) has been defined to calculate the mode I peak stresses at the weld toe, mode II being not singular there. Only one eighth of the joint geometry was modelled, taking advantage of the triple symmetry. A minimum mesh density ratio $a/d = 1$ is necessary to analyse the weld toe ($2\alpha = 135^\circ$) under mode I loading using TETRA-10 finite elements [37] (see also Table 2.6), the characteristic size being $a = t/2 = 6.25$ mm. However, an element size $d = 6.25/1 \approx 6.25$ mm means only a single finite element through the thickness of the longitudinal stiffener and this would not have allowed to apply the PSM at the crack initiation point, the nearest node from a

2.2 Validation with data from the literature

free surface where the average peak stress can be evaluated being the third vertex node according to the PSM based on TETRA-10 (see also Figure 2.3b). Accordingly, a more refined mesh pattern having element size $d = (t/2)/4 \approx 1.56$ mm has been generated (model 5 in Figure 2.13, alternatively one quarter of FE model, instead of one eighth, could have been generated). After solution, the maximum principal stress $\Delta\sigma_{11,\text{peak}}$ has been evaluated at FE nodes located along the weld toe line, then the average peak stress $\Delta\bar{\sigma}_{11,\text{peak}}$ has been calculated from Eq. (1.7), again by taking advantage of the approximate equivalence $\Delta\sigma_{\theta\theta,\theta=0,\text{peak}} \approx \Delta\sigma_{11,\text{peak}}$. Eventually the equivalent peak stress range has been computed from Eq. (1.21), by assuming $c_{w1} = 1$ since all joints have been tested in the as-welded conditions. The maximum value of the equivalent peak stress was found at the weld toe where fatigue cracks experimentally initiated. The local stress state at the critical location being of pure mode I, the local biaxiality ratio is $\lambda = 0$ (Eq. (1.22)). Table 2.7 summarises the resulting opening peak stress $\Delta\bar{\sigma}_{\theta\theta,\theta=0,\text{peak}}$ as well as the factors f_{s1} (Eq. (1.15)) and f_{w1} (Eq. (1.4)).

2.2.3. *Vanrostenberghe et al. [73], longitudinal stiffeners with full penetration welds*

Longitudinal stiffeners with full penetration welds (model 6 in Figure 2.15) having two different plate thicknesses ($t = 5$ or 10 mm) and made of two different steel grades (S700MC and S960MC) were fatigue tested under pure axial loading. The local geometry of the weld bead was not reported in the original reference, but it has been derived from figures of the joint [73]. CA fatigue loadings were applied at load ratios $R = 0.1$ and 0.5 , while VA loadings were applied at $R = -1$ according to a log-linear spectrum applied in random order, having a block length of 10^5 cycles and the smallest stress range equal to the 15% of the largest one (VA-VII in Figure 2.7 and Table 2.4). The fatigue crack initiation always occurred at the weld toe, because of the fully penetrated welding execution, at the main plate side. The fatigue tests have been stopped either at the complete specimen's separation or at a number of cycles equal to 10^7 , which was defined the run-out condition.

The experimental fatigue results have been here reported in Figure 2.16 expressed in terms of the number of cycles to failure N_f versus the maximum applied nominal stress range $\Delta\sigma_{\text{max}}$.

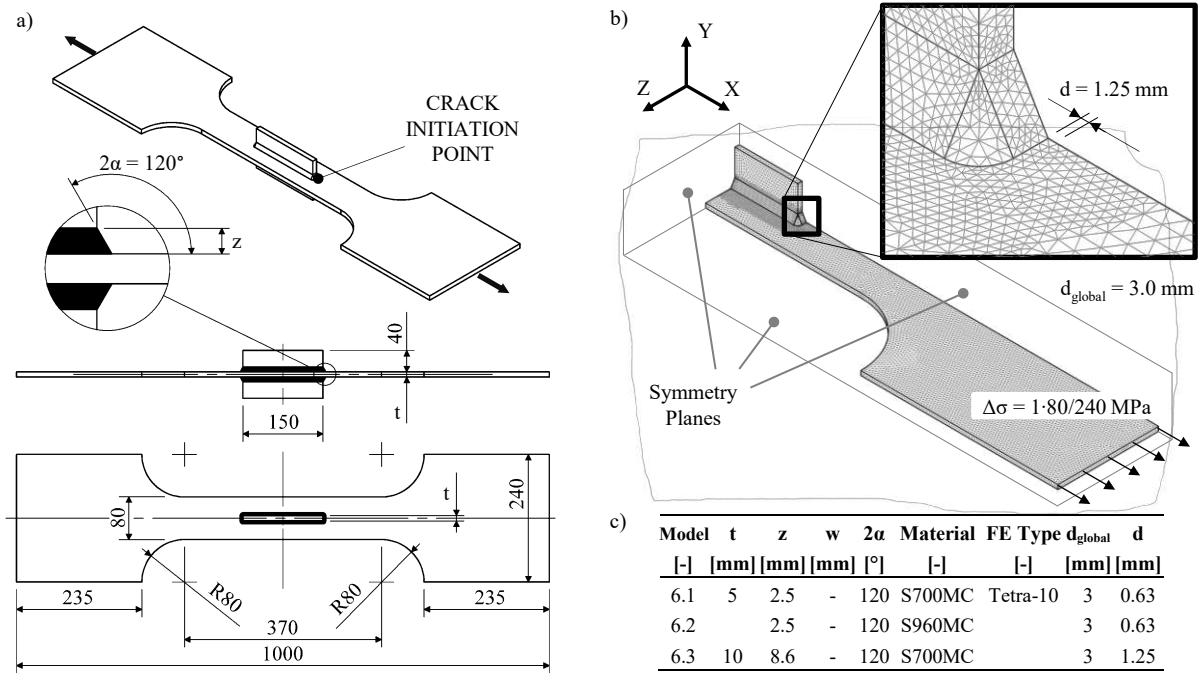


Figure 2.15. Vanrostenberghe et al. [73], longitudinal stiffeners with full penetration welds: a) and d) joint geometry and loading conditions. b) and e) FE model according to the PSM. c) and f) table summarizing the geometrical parameters reported in a) and d).

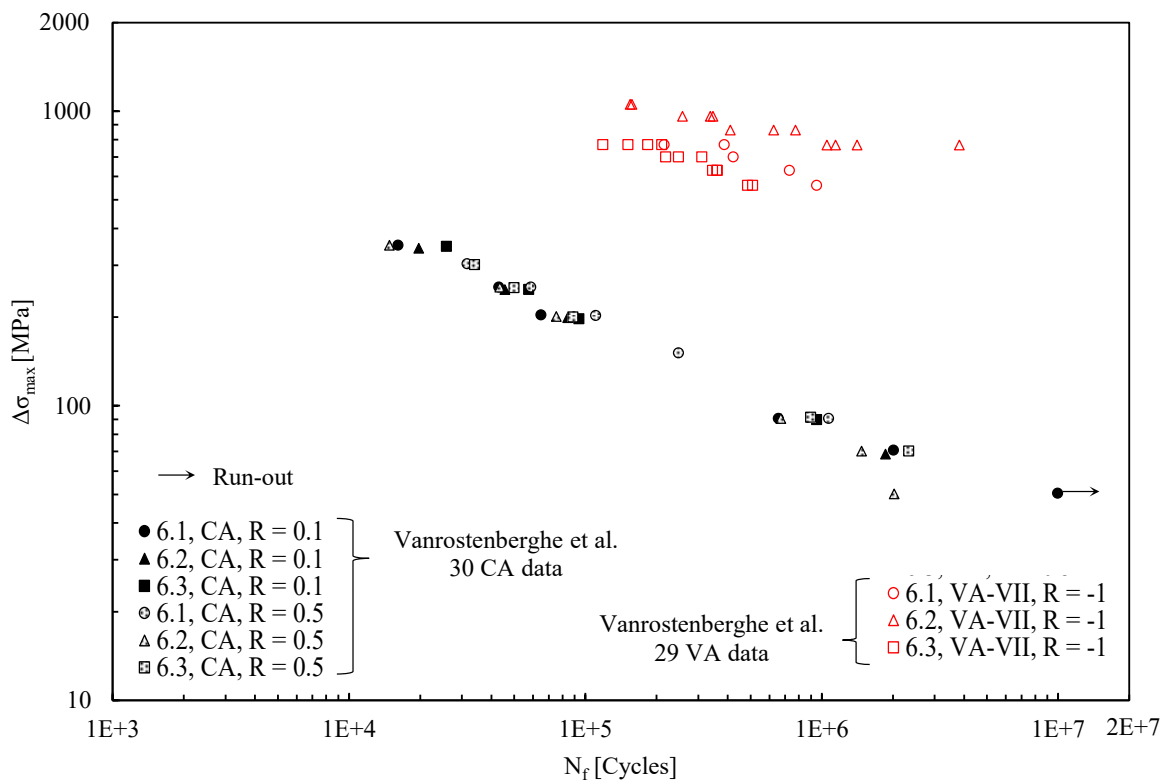


Figure 2.16. Fatigue test results from Vanrostenberghe et al. [73] relevant to longitudinal stiffeners with full penetration welds (model 6 in Figure 2.15): data are expressed in terms of maximum applied nominal stress.

Again, the mode I peak stresses at the weld toe have been calculated from a 3D FE model which has been free-meshed using 10-node tetrahedral elements (SOLID 187 of Ansys® element library). The triple symmetry has been employed to model only one eighth of the joint geometry. The PSM based on TETRA-10 finite elements [37] (see also Table 2.6) requires a minimum mesh density ratio $a/d = 1$ to analyse the weld toe ($2\alpha = 135^\circ$) under mode I loading, where $a = t/2$. However, for the same reason discussed in previous case, a more refined mesh pattern having element size $d_{\text{local}} \approx (t/2)/4$ has been generated by refining locally at the weld toe line a global FE mesh having size $d_{\text{global}} = 3$ mm (model 6 in Figure 2.15). After solution, the maximum principal stress $\Delta\sigma_{11,\text{peak}}$ has been calculated at FE nodes of the weld toe line; afterwards the average peak stress $\Delta\bar{\sigma}_{11,\text{peak}}$ has been evaluated with Eq. (1.7), given that $\Delta\sigma_{\theta\theta,\theta=0,\text{peak}} \approx \Delta\sigma_{11,\text{peak}}$ in the present case. Then the equivalent peak stress range has been calculated with Eq. (1.21), by assuming $c_{w1} = 1$, all joints having been tested in the as-welded conditions. The maximum value of the equivalent peak stress occurred at the weld toe at the main plate side where fatigue cracks experimentally initiated and λ (Eq. (1.22)) is null. The main results, i.e. $\Delta\bar{\sigma}_{\theta\theta,\theta=0,\text{peak}}$, f_{s1} (Eq. (1.15)) and f_{w1} (Eq. (1.4)), have been collected in Table 2.7.

2.2.4. Yildirim et al. [74], transverse nlc fillet-welded joints

The fatigue strength of transverse nlc fillet-welded joints (model 7 in Figure 2.17) made of two different steel grades (AH36 and S690QL) has been investigated under pure axial loading. The CA fatigue tests were performed adopting load ratios $R = -0.43$ and 0.1 , while the VA fatigue tests were carried out at a load ratio $R = -0.43$ by applying a log-linear spectrum in random order and by assuming a block length of $2.5 \cdot 10^5$ cycles with the smallest applied stress range equal to the 16% of the largest one (VA-VIII in Figure 2.7 and Table 2.4). The Authors observed the fatigue crack initiation always at the weld toe and reported the number of cycles to complete separation of the tested joints.

The experimental fatigue results have been here reported in Figure 2.18 expressed in terms of the number of cycles to failure N_f versus the maximum applied nominal stress range $\Delta\sigma_{\text{max}}$.

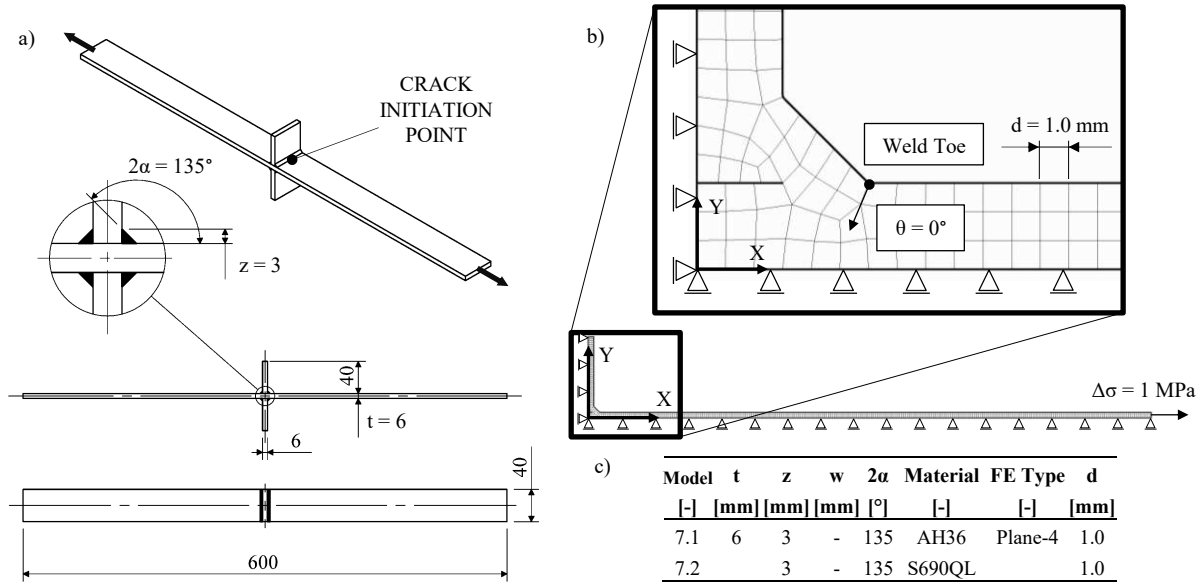


Figure 2.17. Yildirim et al. [74], transverse nlc fillet-welded joints: a) and d) joint geometry and loading conditions. b) and e) FE model according to the PSM. c) and f) table summarizing the geometrical parameters reported in a) and d).

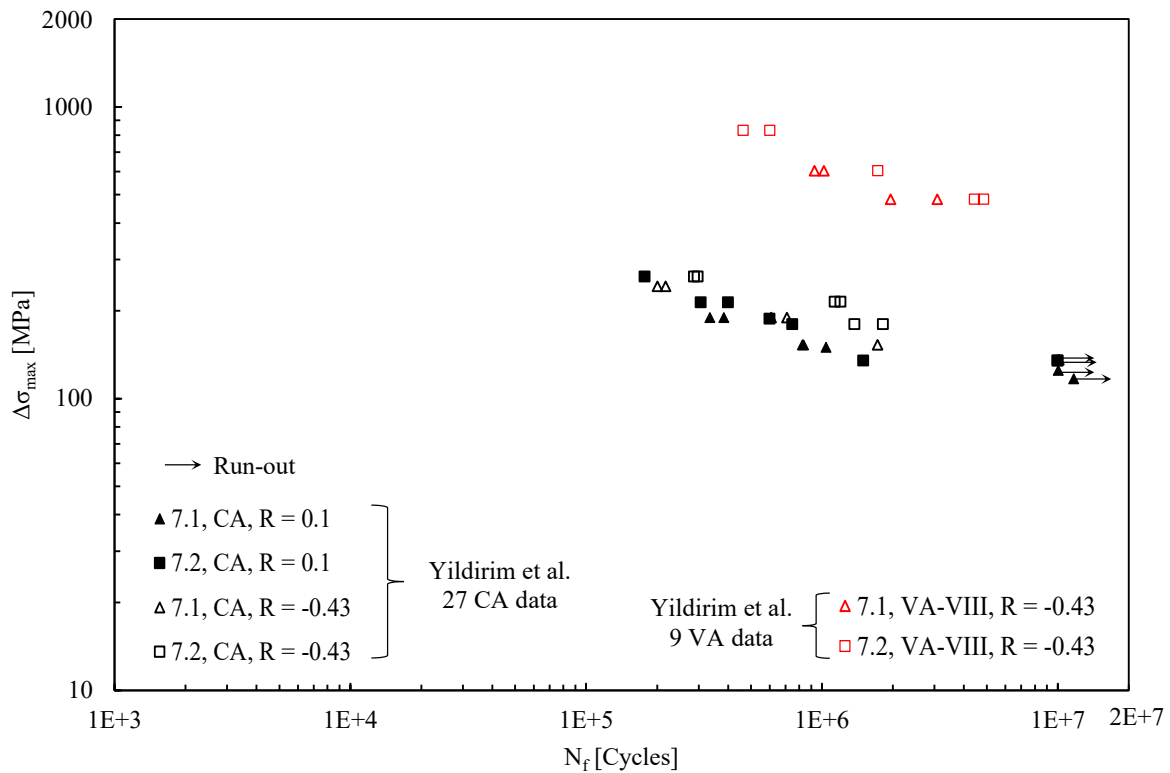


Figure 2.18. Fatigue test results from Yildirim et al. [74] relevant to transverse nlc fillet-welded joints (model 7 in Figure 2.17): data are expressed in terms of maximum applied nominal stress.

A 2D free FE mesh pattern of 4-node plane elements (PLANE 182 with K-option 1 set to 3 of Ansys® element library) under plane strain conditions has been generated to compute the relevant peak stresses. Only one quarter of the joint geometry has been modelled, taking advantage of the double symmetry. Moreover, the PSM has been applied here only to the weld toe, since it is intuitively the crack initiation location of a transverse fillet-welded attachment, even if in principle both the weld root and the weld toe are present in such joint. According to the PSM guidelines for PLANE-4 [37] (see also Table 2.6), a minimum mesh density ratio $a/d = 3$ is required to analyse the weld toe under mode I loading, a being equal to half the plate thickness, i.e. $t/2 = 3$ mm. Therefore, an element size $d \approx 3/3 = 1$ mm has been adopted to generate the free mesh pattern (model 7 in Figure 2.17). The maximum principal stress $\Delta\sigma_{11,peak}$ has been calculated at the weld toe from the FE analysis, again by virtue of the approximation $\Delta\sigma_{\theta\theta,\theta=0,peak} \approx \Delta\sigma_{11,peak}$; then, the equivalent peak stress range has been evaluated from Eq. (1.21), by assuming $c_{w1} = 1$, since all joints were tested in the as-welded conditions. The local biaxiality ratio λ (Eq. (1.22)) resulted null due to the pure mode I stress state at the weld toe. The resulting opening peak stress $\Delta\sigma_{\theta\theta,\theta=0,peak}$ as well as the factors f_{s1} (Eq. (1.15)) and f_{w1} (Eq. (1.4)) have been reported in Table 2.7.

2.2.5. Bertini et al. [75–78], tube-to-flange joints

Two different geometries of tube-to-flange fillet-welded joints (models 8 and 9 in Figure 2.19) made of S355JR structural steel have been fatigue tested. CA fatigue tests were performed under both pulsating ($R = 0$) and fully reversed ($R = -1$) pure bending, pure torsion and combined bending and torsion loadings. Both in-phase ($\phi = 0^\circ$) and out-of-phase ($\phi = 90^\circ$) multiaxial loadings were applied in the fatigue tests, by assuming a nominal biaxiality ratio $\Lambda = 0.31$ or $\Lambda = 1.14$ according to Eq. (1.27). VA fatigue tests have been performed by applying seven different sequences of pulsating ($R = 0$) pure bending and pulsating ($R = 0$) pure torsion loadings (Figure 2.8 and Table 2.5). More in detail, VA-IX and VA-X involved the application of pure bending CA loading for 276000 and 414000 cycles, respectively, and, afterwards, pure torsion CA loading until failure. On the other hand, VA-XI and VA-XII consisted in applying first the pure torsion CA load for 306000 and 459000 cycles, respectively, and then pure

bending CA load until failure. At last, VA-XIII, VA-XIV, and VA-XV included a block of pure bending, made of 10, 100, and 10000 cycles, respectively, followed by a block of pure torsion, made of 11, 110, and 11000 cycles, respectively, applied repeatedly in such a sequence until failure. The authors [75–78] observed the fatigue crack initiation always at the weld root relevant to the outer welding and reported the number of cycles to break-through, which was detected from the air pressure drop in the small volume generated by the sleeve between the tube and the flange (see models 8 and 9 in Figure 2.19). The fatigue results have been reported in the original works [75–78] in terms of bending and torsion nominal stresses calculated in the weld throat as follows [75–78]:

$$\Delta\sigma = \frac{\Delta M_f}{W_f} = \frac{\Delta M_f}{\pi \cdot \left(\frac{(d_e + 2 \cdot s)^3 - d_e^4}{d_e + 2 \cdot s} \right)} \quad \text{bending loading} \quad (1.28)$$

$$\Delta\tau = \frac{\Delta M_t}{W_t} = \frac{\Delta M_t}{\pi \cdot \left(\frac{(d_e + 2 \cdot s)^3 - d_e^4}{d_e + 2 \cdot s} \right)} \quad \text{torsion loading} \quad (1.29)$$

being d_e the tube outer diameter and $s = 10/\sqrt{2}$ the weld throat.

The experimental fatigue results have been here reported in Figure 2.20 expressed in terms of the total number of cycles to failure N_f versus the maximum applied nominal bending stress range evaluated at the tube side $\Delta\sigma_{\max}$ (Eq. (1.25)) in case of pure bending or combined bending and torsion loadings. Pure torsion data have been reported in terms of maximum applied nominal torsion stress range evaluated at the tube side $\Delta\tau_{\max}$ (Eq. (1.26)).

2D axis-symmetric FE models free meshed with 4-node harmonic elements (PLANE 25 of the ANSYS® element library) were employed to apply the PSM. It is worth noting that several potential crack initiation sites are present in each joint geometry (models 8 and 9 in Figure 2.19), however, the most critical ones are intuitively the weld toe at the tube side and the weld root between tube and flange. Moreover, the authors [78] observed that the weld toe on the tube had a significantly large radius, namely on the order of 2 mm. Such large radius reduces the

2.2 Validation with data from the literature

notch severity at the weld toe, therefore only the weld root has been analysed here as a sharp V-notch.

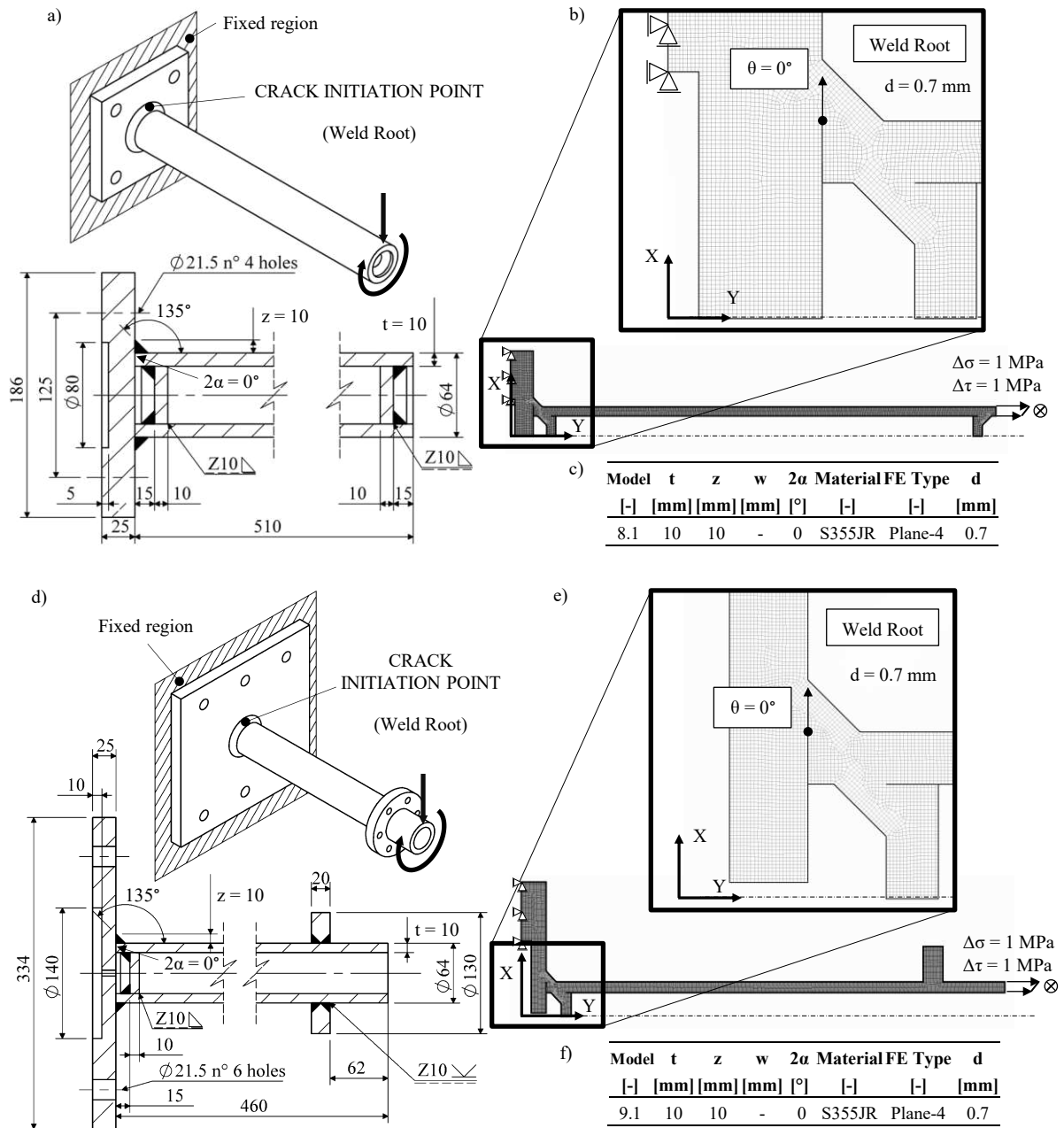


Figure 2.19. Bertini et al. [75–78], tube-to-flange joints: a) and d) joint geometry and loading conditions. b) and e) FE model according to the PSM. c) and f) table summarizing the geometrical parameters reported in a) and d).

The most demanding condition to apply the PSM is the mode II loading at the weld root, which requires a minimum mesh density ratio $a/d = 14$ [37] (see also Table 2.6), a being the tube thickness, i.e. $t = 10$ mm. Therefore, a FE mesh pattern having element size $d = 10/14 = 0.7$ mm has been generated for each considered joint geometry (see models 8 and 9 in Figure 2.19). The connection between the flange and the test bench has been simulated by constraining the back surface of the flange, as indicated in in Figure 2.19 (models 8 and 9). First, the FE models have been solved, after that, the relevant peak stresses $\Delta\sigma_{\theta\theta,\theta=0,\text{peak}}$, $\Delta\tau_{r\theta,\theta=0,\text{peak}}$ and $\Delta\tau_{\theta z,\theta=0,\text{peak}}$ have been calculated; eventually the equivalent peak stress range (Eq. (1.21)) has been evaluated at the weld root, by assuming $c_{w1} = 1$, all joints having been tested in the as-welded conditions. The local biaxiality ratio λ calculated at such location through Eq. (1.22) resulted greater than zero for all considered loading conditions, due to the presence of mode II or mode III stresses (see Table 2.7). Table 2.7 summarises the relevant peak stresses as well as the factors f_{si} (Eqs. (1.15), (1.16), and (1.17)) and f_{wi} (Eqs. (1.4), (1.5), and (1.6)).

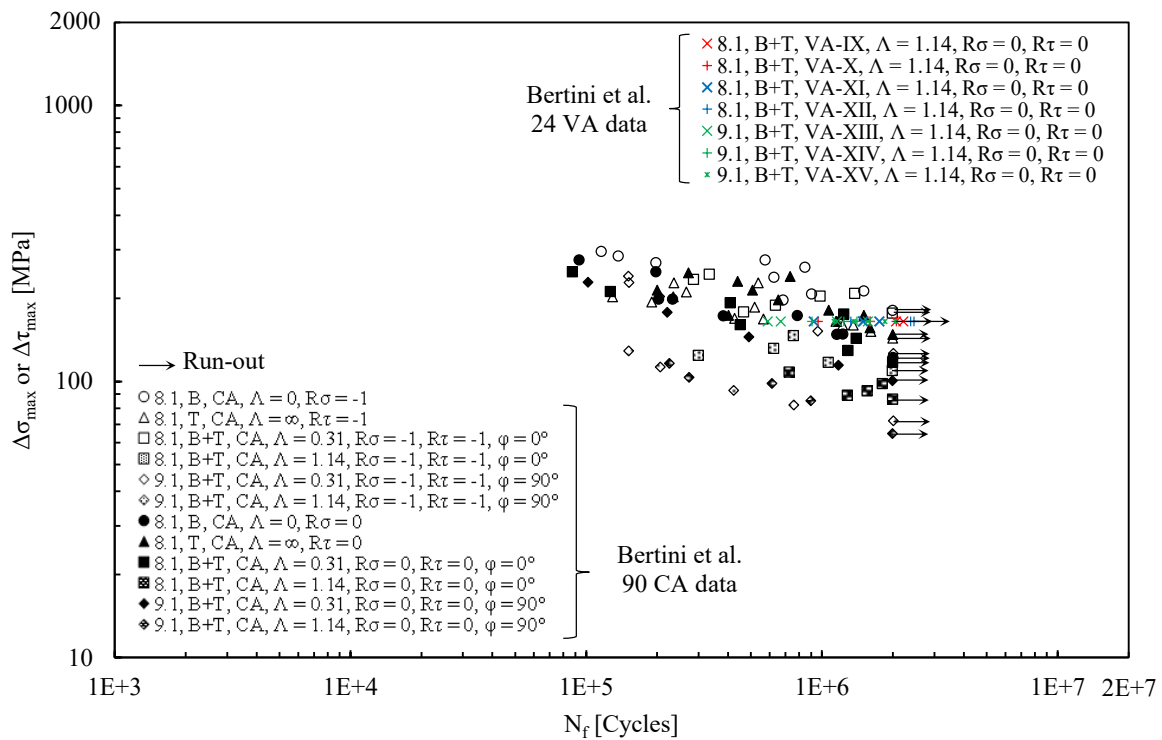


Figure 2.20. Fatigue test results from Bertini et al. [75–78] relevant to two different geometries of tube-to-flange fillet-welded joints (models 8 and 9 in Figure 2.19): data are expressed in terms of maximum applied nominal stress.

2.2.6. *Sonsino et al. [79], tube-to-flange joints*

The fatigue strength of tube-to-flange full-penetration welded joints (model 10 in Figure 2.21) made of Fe E 460 has been investigated under multiaxial loadings. Fully reversed ($R = -1$) both CA and VA pure bending, pure torsion and combined bending and torsion loadings were applied. Multiaxial loadings were applied both in-phase ($\phi = 0^\circ$) and out-of-phase ($\phi = 90^\circ$) by adopting a nominal biaxiality ratio $\Lambda = 0.58$ (Eq. (1.27)). VA loadings followed a standard Gaussian load spectrum [82,83] with a block length of 50000 cycles and were applied in random order (VA-I in Figure 2.7 and Table 2.4). All joints, having a full-penetration weldment, failed at the weld toe. The number of cycles to obtain a through-the-thickness crack has been adopted as failure criterion in the original paper [79].

The experimental fatigue results have been here reported in Figure 2.22 expressed in terms of the total number of cycles to failure N_f versus the maximum applied nominal bending stress range evaluated at the tube side $\Delta\sigma_{\max}$ (Eq. (1.25)) in case of pure bending or combined bending and torsion loadings. Pure torsion data have been reported in terms of maximum applied nominal torsion stress range evaluated at the tube side $\Delta\tau_{\max}$ (Eq. (1.26)).

The mode I and mode III peak stresses have been calculated at the weld toe, mode II being not singular there, by employing a 2D axis-symmetric FE model free meshed with 4-node harmonic elements (PLANE 25 of the ANSYS® element library). According to the PSM guidelines for PLANE-4 [37] (see also Table 2.6), the minimum mesh density ratio must be $a/d = 3$ to apply the PSM at the weld toe under mode I or mode III loading, where $a = t = 10$ mm. Therefore, a mesh pattern having element size $d = 10/3 = 3.33$ mm has been generated (model 10 in Figure 2.21). The peak stresses $\Delta\sigma_{\theta\theta,\theta=0,\text{peak}}$ and $\Delta\tau_{\theta z,\theta=0,\text{peak}}$ have been evaluated at the weld toe from the FE analysis; then, the equivalent peak stress range has been derived from Eq. (1.21), by introducing $c_{w1} = c_{w3} = 0.5$ (Eqs. (1.18) and (1.20) with $R = -1$), all specimens having been tested after stress-relieving treatment. The local biaxiality ratio λ (Eq. (1.22)) resulted null under pure bending loading, while it was greater than zero under pure torsion and combined bending and torsion loading (see Table 2.7). The resulting peak stresses $\Delta\sigma_{\theta\theta,\theta=0,\text{peak}}$ and $\Delta\tau_{\theta z,\theta=0,\text{peak}}$ as well as the factors f_{si} (Eqs. (1.15) and (1.17)) and f_{wi} (Eqs. (1.4) and (1.6)) have been summarised in Table 2.7, for all considered loading conditions.

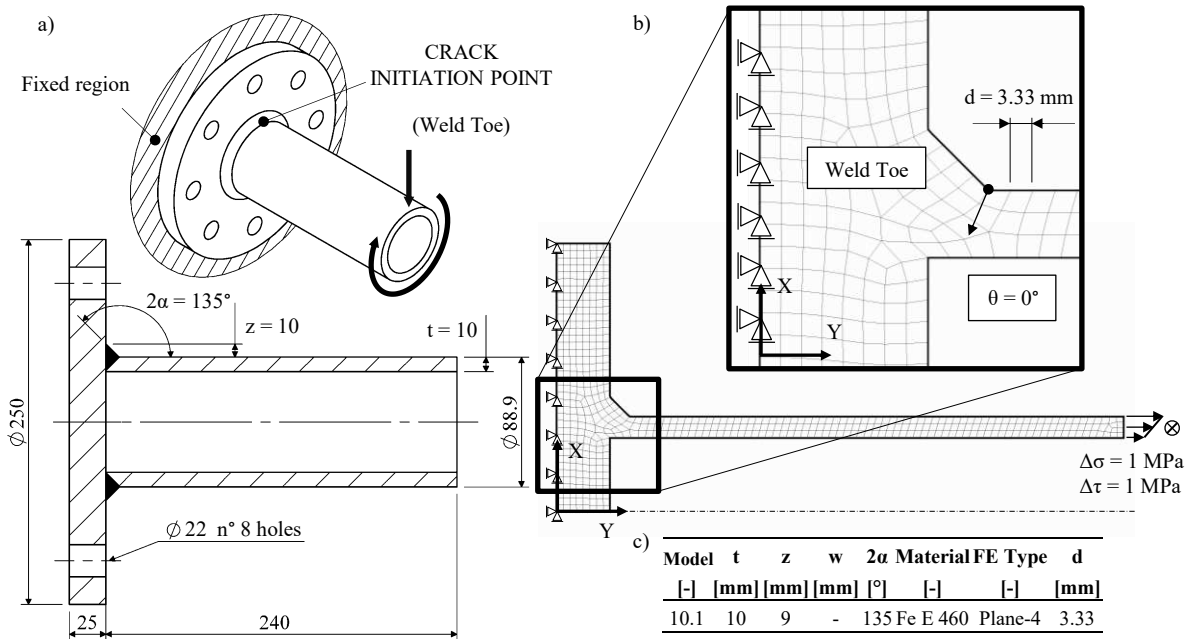


Figure 2.21. Sonsino et al. [79], tube-to-flange joints: a) and d) joint geometry and loading conditions. b) and e) FE model according to the PSM. c) and f) table summarizing the geometrical parameters reported in a) and d).

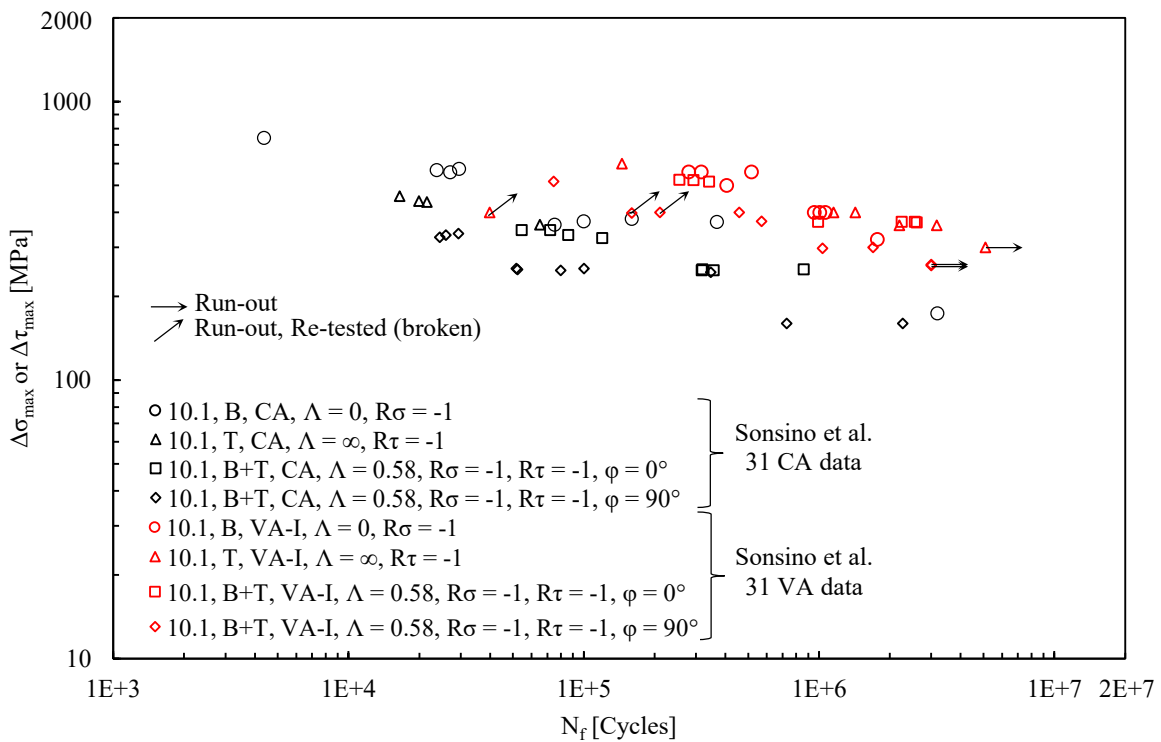


Figure 2.22. Fatigue test results from Sonsino et al. [79] relevant to tube-to-flange full-penetration welded joints (model 10 in Figure 2.21): data are expressed in terms of maximum applied nominal stress.

2.2.7. Witt et al. [80,81], tube-to-flange joints

Tube-to-flange welded joints with partial penetration (model 11 in Figure 2.23) made of fine-grained steel P460 have been fatigue tested under both CA and VA multiaxial loadings. Concerning CA fatigue tests, both pulsating ($R = 0$) and fully reversed ($R = -1$) pure bending, pure torsion and combined bending and torsion loadings were applied. Combined bending and torsion loadings were applied both in-phase ($\phi = 0^\circ$) and out-of-phase ($\phi = 90^\circ$) as well as with different frequency proportions ($f_T = f_B$, $f_T = f_B/5$ or $f_T = 5f_B$), by adopting in all cases a nominal biaxiality ratio $\Lambda = 1$ (Eq. (1.27)). In addition, other combined bending and torsion loading configurations have been generated by superposing a fully reversed ($R = -1$) bending loading with a constant torsional stress and vice versa, i.e. a fully reversed ($R = -1$) torsion loading and a constant bending stress. VA fatigue tests have been performed under almost the same loading configurations as for CA tests, but applied according to a standard Gaussian load spectrum [82,83] of 50000 cycles in random order (VA-I in Figure 2.7 and Table 2.4). In addition to previous loading configurations, VA fatigue tests have also been performed under fully reversed ($R = -1$) combined bending and torsion loadings, applied in an “uncorrelated” manner, i.e. “the load histories for bending and torsion are generated in a different way” as stated in the original works [80,81]. The Authors [80,81] reported the number of cycles to obtain a through-the-thickness crack, which initiated always at the weld toe, tested joints having a very short weld root of depth equal to 1 mm.

The experimental fatigue results have been here reported in Figure 2.22 expressed in terms of the total number of cycles to failure N_f (this being given in the number of cycles of the higher frequency load when bending and torsion were applied simultaneously but at different frequencies) versus the maximum applied nominal bending stress range evaluated at the tube side $\Delta\sigma_{\max}$ (Eq. (1.25)) in case of pure bending or combined bending and torsion loadings. Pure torsion data have been reported in terms of maximum applied nominal torsion stress range evaluated at the tube side $\Delta\tau_{\max}$ (Eq. (1.26)).

A 2D free FE mesh of 4-node harmonic elements (PLANE 25 of the ANSYS® element library) has been generated to compute the mode I and mode III peak stresses at the weld toe, mode II being not singular and weld root being not of interest due to its negligible size. The

most demanding condition to apply the PSM is the mode I or mode III loading at the weld toe, which requires a minimum mesh density ratio $a/d = 3$ [37] (see also Table 2.6), a being the tube thickness, i.e. $t = 8$ mm. Therefore, a FE mesh pattern having element size $d = 8/3 = 2.67$ mm has been generated (model 11 in Figure 2.23). After evaluating the peak stresses $\Delta\sigma_{\theta\theta, \theta=0, \text{peak}}$ and $\Delta\tau_{\theta z, \theta=0, \text{peak}}$ at the weld toe from the FE analysis, the equivalent peak stress range has been derived from Eq. (1.21), by introducing $c_{w1} = c_{w3} = 0.5$ (Eqs. (1.18) and (1.20) with $R = -1$), because of the thermal stress-relieving treatment performed on all specimens before they had been tested. The local biaxiality ratio λ (Eq. (1.22)) resulted null under pure bending loading, while it was greater than zero under pure torsion and all combinations of cyclic bending and torsion loadings (see Table 2.7). Table 2.7 reports the resulting peak stresses $\Delta\sigma_{\theta\theta, \theta=0, \text{peak}}$ and $\Delta\tau_{\theta z, \theta=0, \text{peak}}$ and the factors f_{si} (Eqs. (1.15) and (1.17)) and f_{wi} (Eqs. (1.4) and (1.6)).

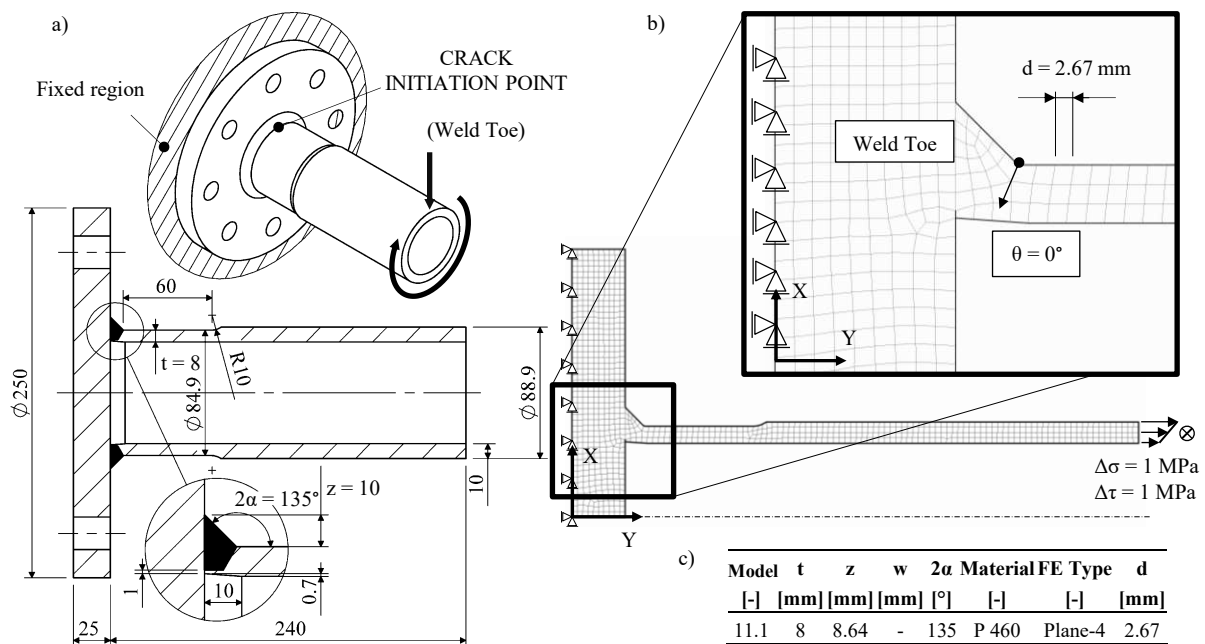


Figure 2.23. Witt et al. [80,81], tube-to-flange joints: a) and d) joint geometry and loading conditions. b) and e) FE model according to the PSM. c) and f) table summarizing the geometrical parameters reported in a) and d).

2.2 Validation with data from the literature

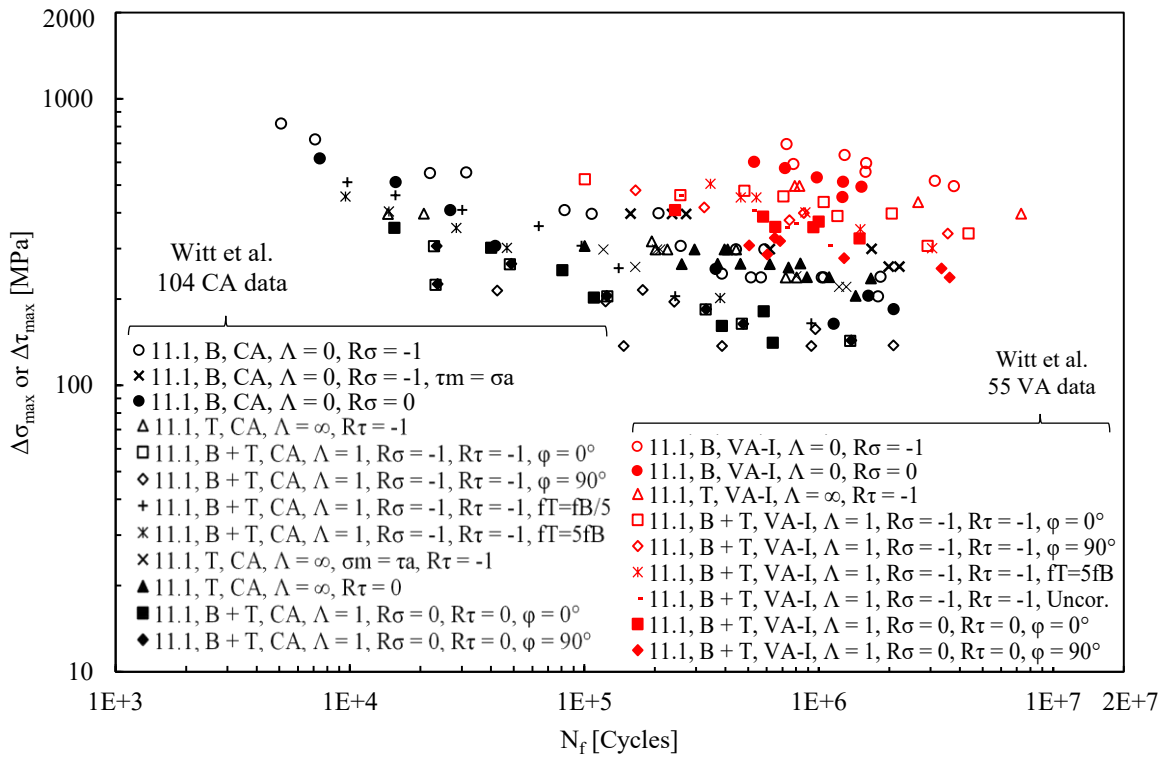


Figure 2.24. Fatigue test results from Witt et al. [80,81] relevant to tube-to-flange welded joints with partial penetration (model 11 in Figure 2.23): data are expressed in terms of maximum applied nominal stress.

2.2.8. Assessment of weld toe and weld root fatigue failures according to the PSM

After having analysed all joint geometries according to the PSM, the experimental data originally expressed in terms of range of nominal stress have been re-converted in terms of range of the equivalent peak stress (Eq. (1.21)) evaluated at the crack initiation location. To do this, Table 2.7 summarises all required parameters to input in Eq. (1.21), i.e. the coefficients f_{wi} (Eqs. (1.4), (1.5), and (1.6)) and f_{si} (Eqs. (1.15), (1.16), and) and the relevant peak stresses evaluated at the critical point, where $\Delta\sigma = \Delta\tau = 1$ MPa have been applied to the FE models. Therefore, the original experimental results have been converted from the nominal stress ranges to the constant amplitude equivalent peak stress ranges of the individual modes I, II and III, by multiplying the nominal stress ranges applied in the original experimental tests by the coefficients f_{si} , f_{wi} and by the relevant peak stress ranges calculated from the FE analyses. Eventually, the equivalent peak stress (Eq. (1.21)) has been evaluated.

Figure 2.25 to Figure 2.32 compare the experimental fatigue results relevant to welded joints made of structural steels with the PSM-based fatigue design scatter bands for steel welded joints as a function of the local biaxiality ratio λ calculated at the crack initiation point according to Eq. (1.22). More in detail, experimental results relevant to $\lambda = 0$ (see Figure 2.25 to Figure 2.29, Figure 2.31a, and Figure 2.32a) have been compared with the PSM-based design scatter band, which has an endurable stress range $\Delta\sigma_{eq,peak,A,50\%} = 214$ MPa, an inverse slope $k = 3$ and a scatter index referred to survival probabilities of 2.3%-97.7%, i.e. the mean value \pm two standard deviations, $T_\sigma = 1.90$ (see Table 2.2). On the other hand, experimental results relevant to $\lambda > 0$ (see Figure 2.30, Figure 2.31b, and Figure 2.32b) have been compared with the PSM-based design scatter band, which has $\Delta\sigma_{eq,peak,A,50\%} = 354$ MPa, $k = 5$ and the 2.3%-97.7% scatter index $T_\sigma = 1.90$ (see Table 2.2). It is worth noting that PSM-based curves referred to a given probability of survival (PS) are iso-damage curves. More precisely, by taking the 50% curves as references with a total damage to failure $D = 1$, the 2.3% and 97.7% curves of the scatter band having $\Delta\sigma_{eq,peak,A,50\%} = 214$ MPa and $k = 3$ are referred to damages $D = 0.39$ and 2.65 , respectively; while the 2.3% and 97.7% curves of the scatter band having $\Delta\sigma_{eq,peak,A,50\%} = 354$ MPa and $k = 5$ are referred to damages $D = 0.20$ and 4.98 , respectively.

2.2 Validation with data from the literature

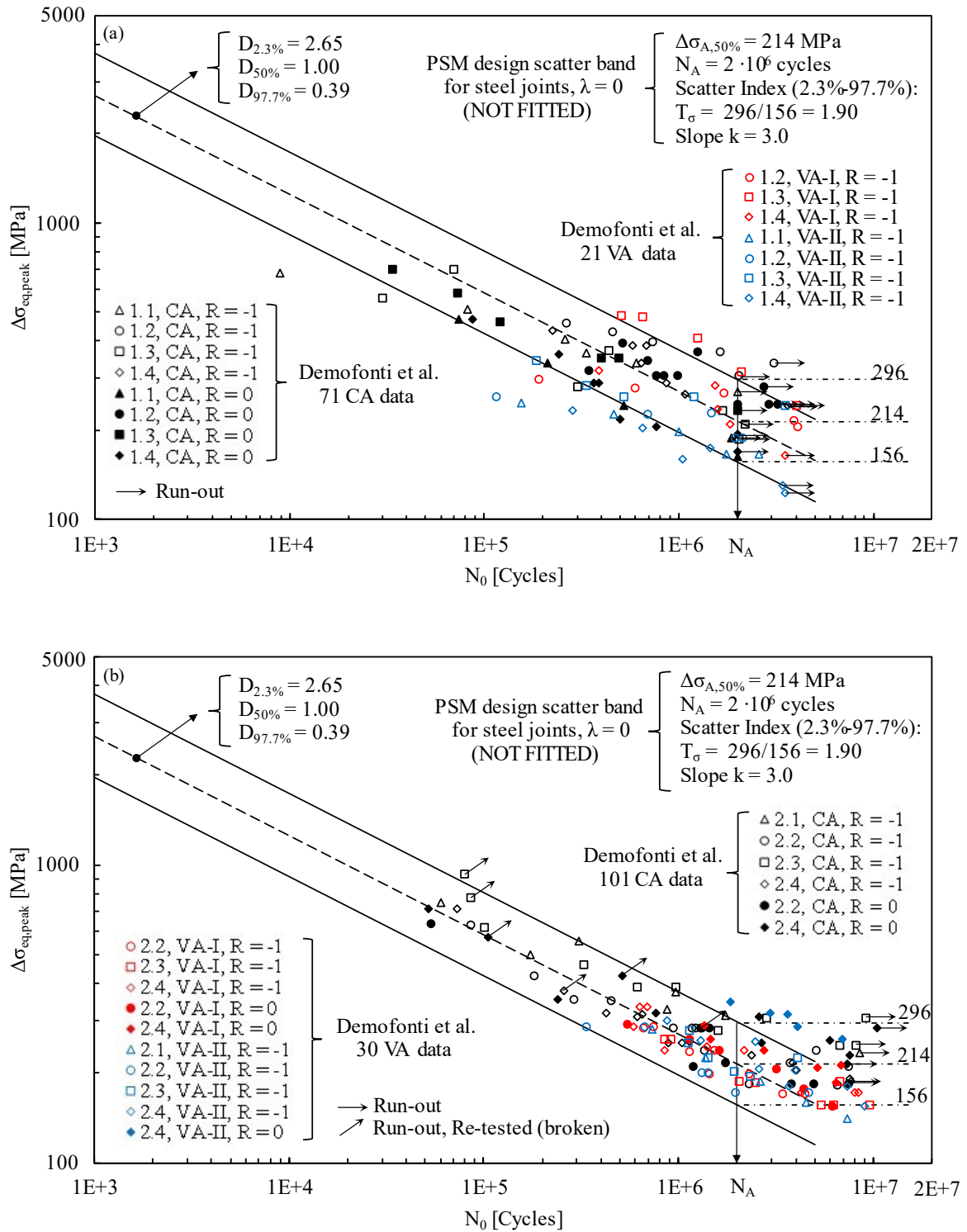


Figure 2.25. Fatigue strength assessment of (a) two-sided full penetration butt-welded joints with $t = 10$ mm (model 1 in Figure 2.9) and (b) two-sided full penetration butt-welded joints with $t = 30$ mm (model 2 in Figure 2.9) adopting the PSM: comparison between the pure mode I ($\lambda = 0$) PSM design scatter band and experimental data from Demofonti et al. [70].

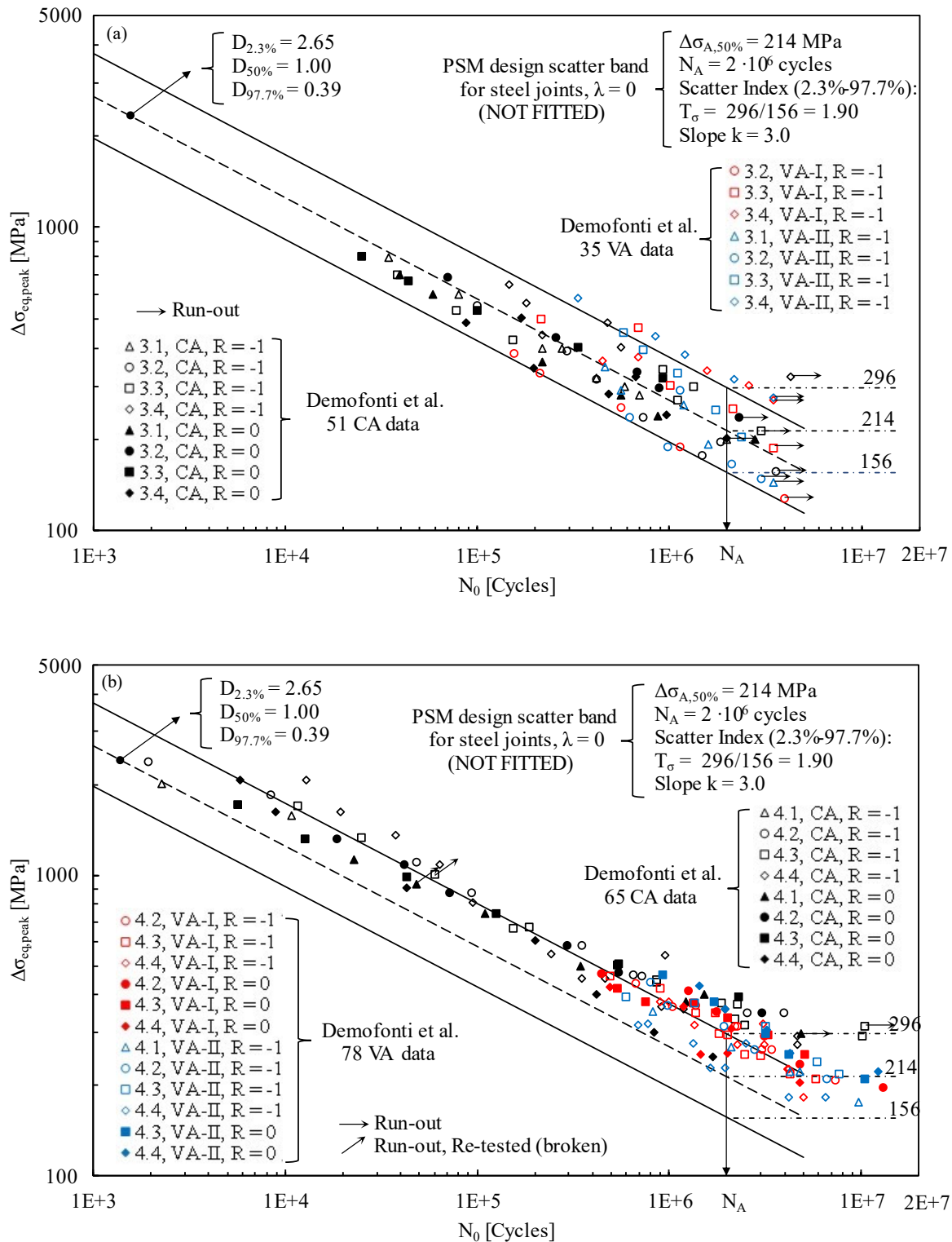


Figure 2.26. Fatigue strength assessment of (a) transverse non-load-carrying (nlc) full-penetration welded joints with $t = 10$ mm (model 3 in Figure 2.10) and (b) transverse non-load-carrying (nlc) full-penetration welded joints with $t = 30$ mm (model 4 in Figure 2.10) adopting the PSM: comparison between the pure mode I ($\lambda = 0$) PSM design scatter band and experimental data from Demofonti et al. [70].

2.2 Validation with data from the literature

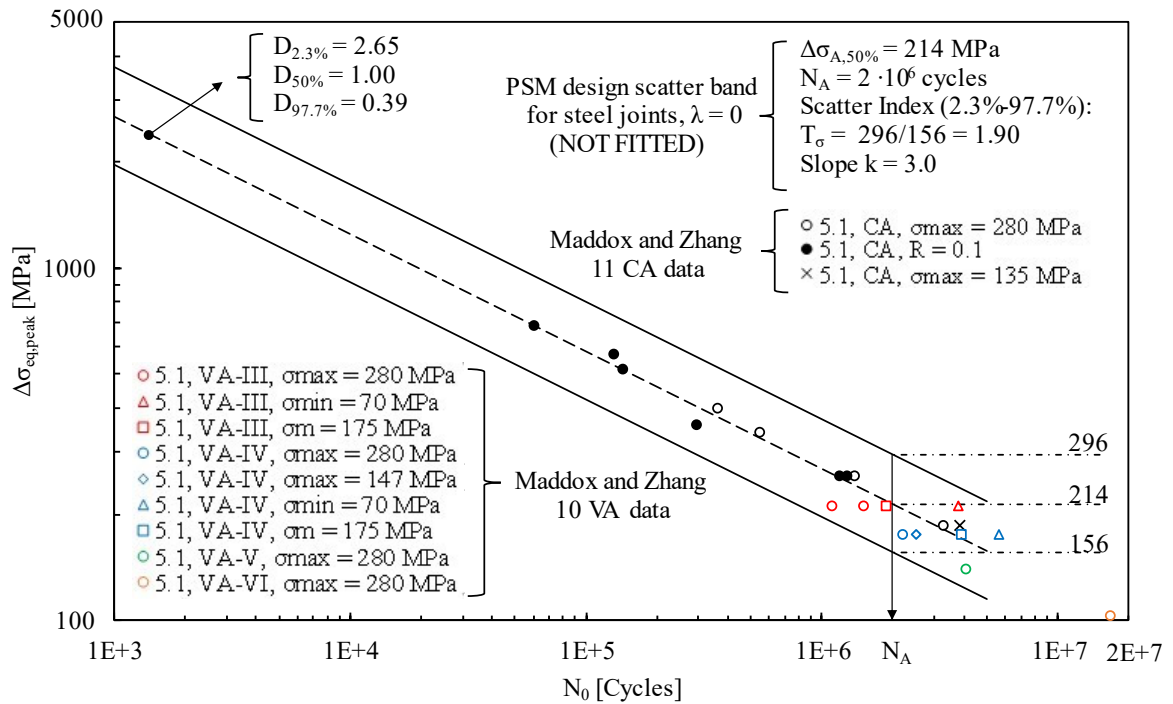


Figure 2.27. Fatigue strength assessment of longitudinal stiffeners with full penetration welds (model 5 in Figure 2.13) adopting the PSM: comparison between the pure mode I ($\lambda = 0$) PSM design scatter band and experimental data from Maddox and Zhang [71,72].

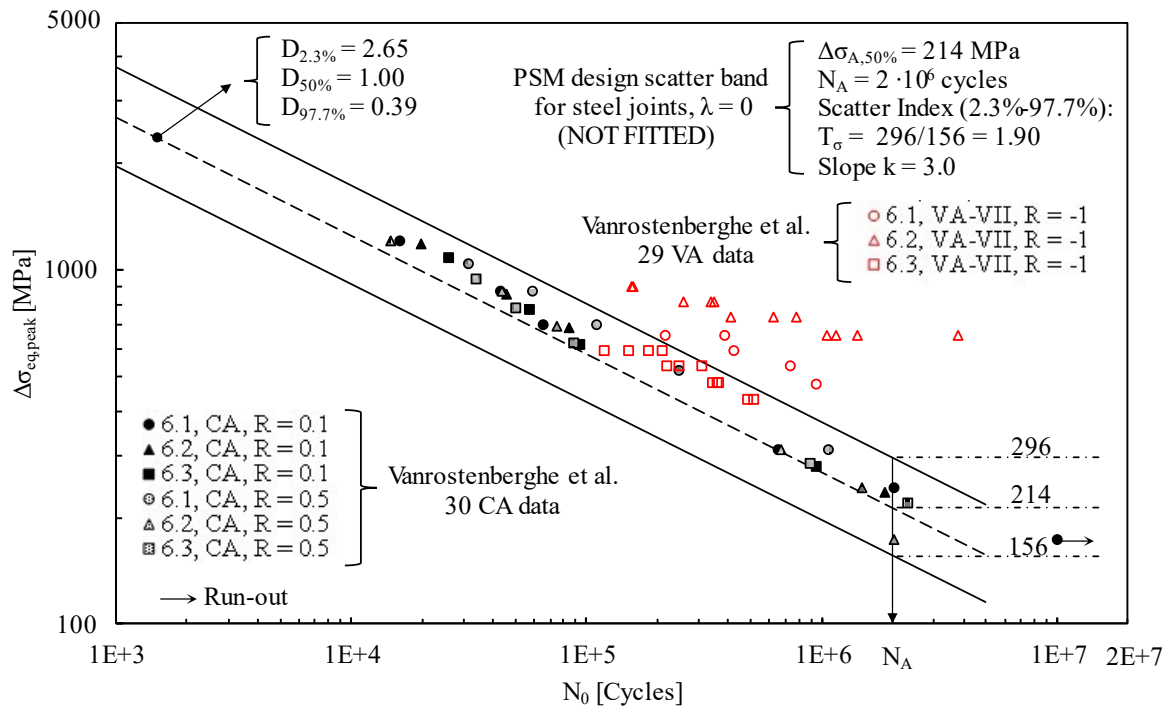


Figure 2.28. Fatigue strength assessment of longitudinal stiffeners with full penetration welds (model 6 in Figure 2.15) adopting the PSM: comparison between the pure mode I ($\lambda = 0$) PSM design scatter band and experimental data from Vanrostenberghe et al. [73].

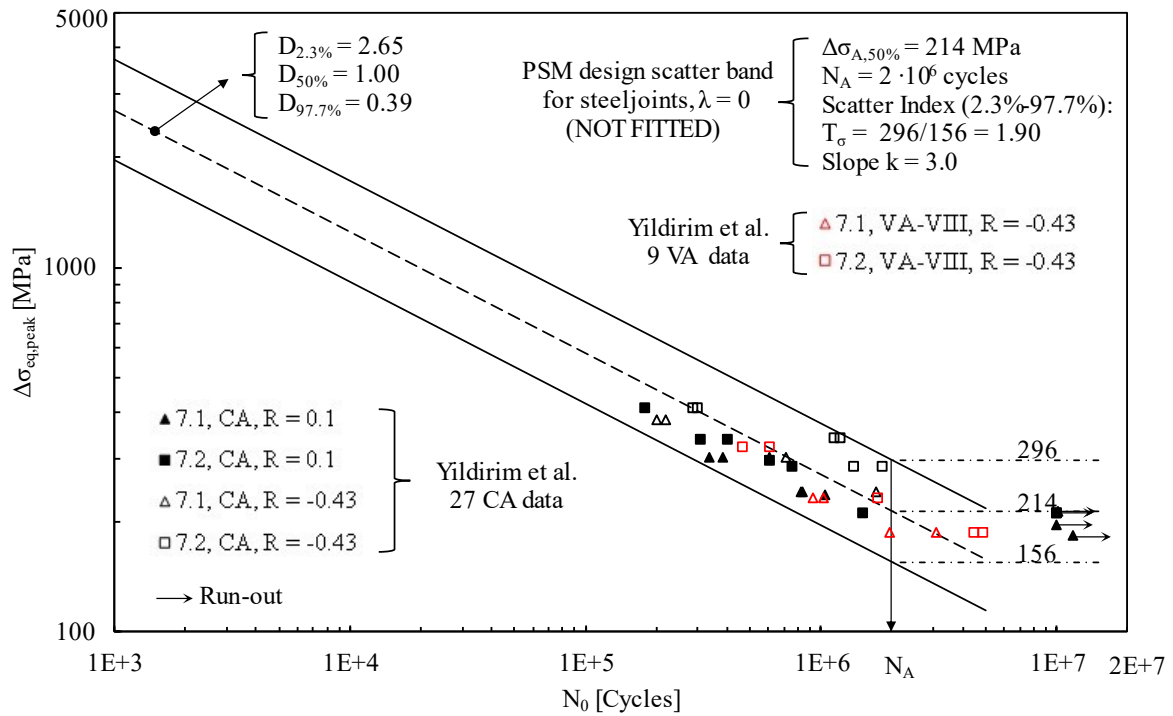


Figure 2.29. Fatigue strength assessment of transverse nlc fillet-welded joints (model 7 in Figure 2.17) adopting the PSM: comparison between the pure mode I ($\lambda = 0$) PSM design scatter band and experimental data from Yildirim et al. [74].

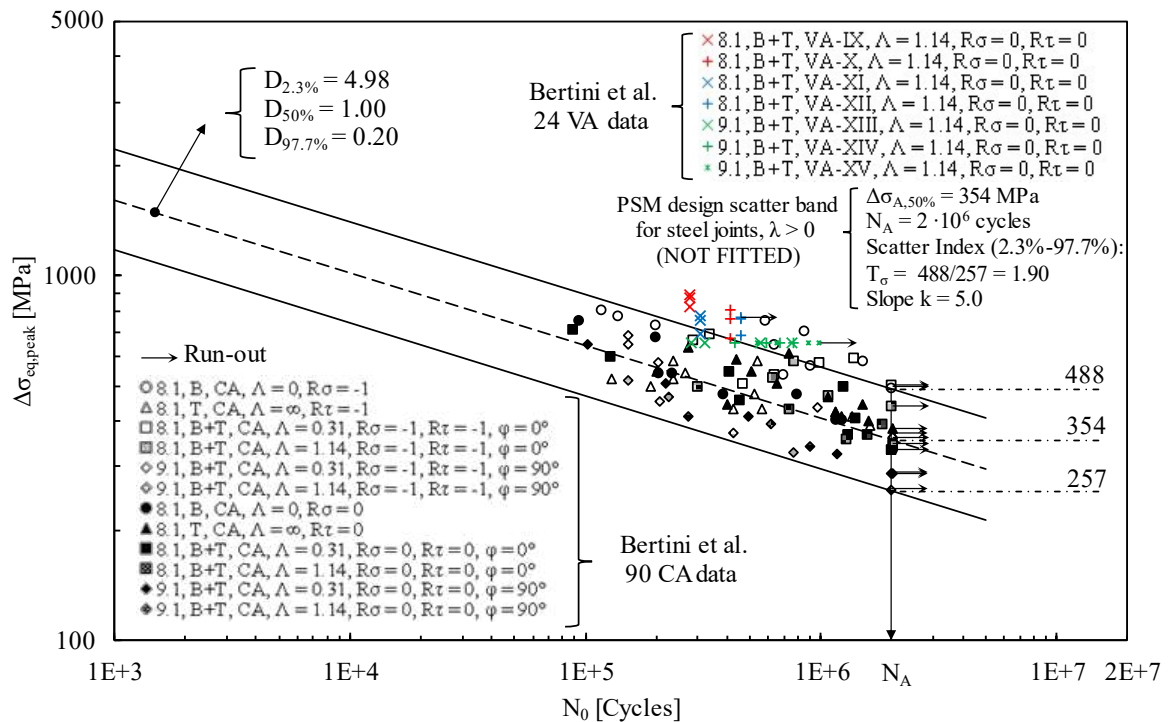


Figure 2.30. Fatigue strength assessment of two different geometries of tube-to-flange fillet-welded joints (models 8 and 9 in Figure 2.19) adopting the PSM: comparison between the multiaxial ($\lambda > 0$) PSM design scatter band and experimental data from Bertini et al. [75–78].

2.2 Validation with data from the literature

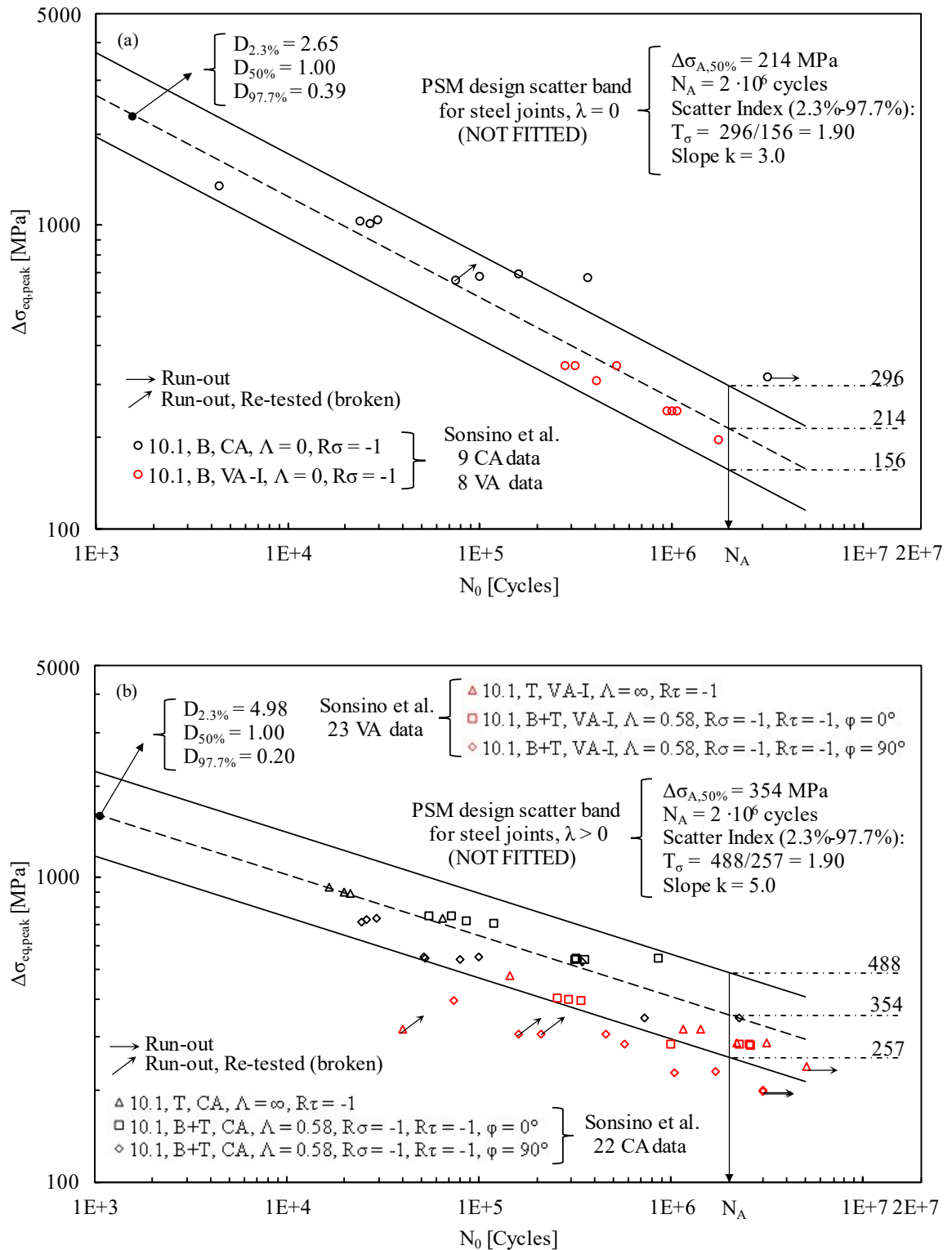


Figure 2.31. Fatigue strength assessment of tube-to-flange full-penetration welded joints (model 10 in Figure 2.21) adopting the PSM: comparison between (a) pure mode I ($\lambda = 0$), and (b) multiaxial ($\lambda > 0$) PSM design scatter bands and experimental data from Sonsino et al. [79].

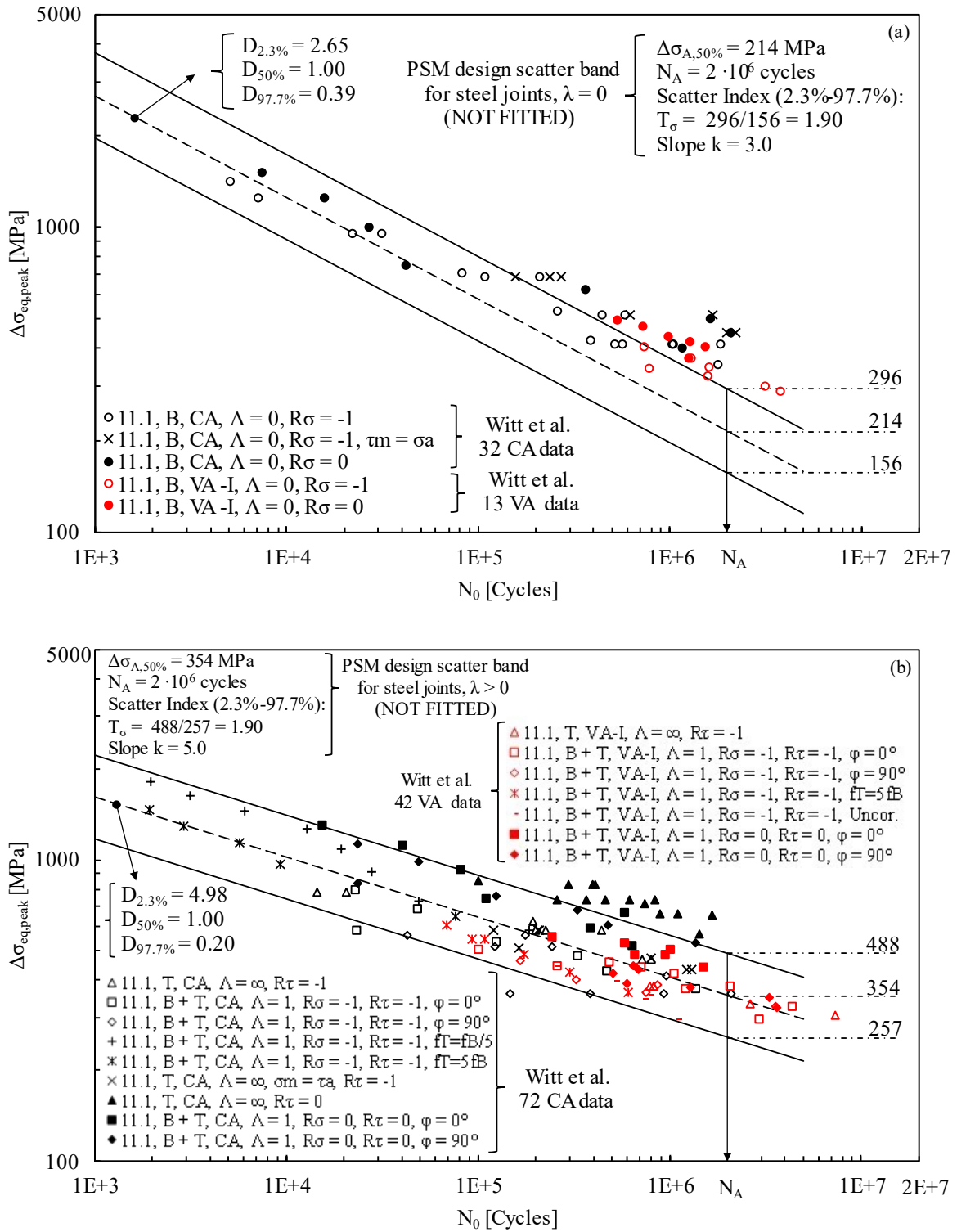


Figure 2.32. Fatigue strength assessment of tube-to-flange welded joints with partial penetration (model 11 in Figure 2.23) adopting the PSM: comparison between (a) pure mode I ($\lambda = 0$), and (b) multiaxial ($\lambda > 0$) PSM design scatter bands and experimental data from Witt et al. [80,81].

Figure 2.25 to Figure 2.32 show that theoretical estimations are in good agreement with the great majority of experimental fatigue results generated under CA uniaxial as well as multiaxial loadings, while theoretical estimations resulted on the safe side with respect to only few data (see Figure 2.26b and Figure 2.32). Such result was expected based on the recent review [37].

Theoretical estimations based on the PSM are in good agreement also with most of experimental fatigue results generated under VA uniaxial as well as multiaxial fatigue loadings, as highlighted by Figure 2.25b, Figure 2.26a, Figure 2.27, Figure 2.29, Figure 2.31a, and Figure 2.32b. Only in few cases, the theoretical estimations based on the PSM do not match the experimental results, since theoretical estimations are either on the unsafe side (see Figure 2.25a, Figure 2.31b) or on the safe side (see Figure 2.26b, Figure 2.28, Figure 2.30, and Figure 2.32a).

The VA cases for which theoretical estimations are on the unsafe side are those relevant to two-sided full penetration butt-welded joints having thickness $t = 10$ mm (Figure 2.25a) and to tube-to-flange joints (Figure 2.31b) tested by Demofonti et al. [70] and Sonsino et al. [79], respectively. Concerning butt-welded joints having thickness $t = 10$ mm, Demofonti et al. [70] obtained an extremely large scatter of the experimental results, documented by values of damage to failure D based on nominal stress curves in the range between 0.06 and 6.0, depending on the spectrum type, the applied axial load level and the steel category. More in detail, lower values of the damage to failure D were obtained when applying the overload spectrum (VA-II in Figure 2.7). Moreover, the results reported in Figure 2.25a are affected by two assumptions: (i) the weld bead of butt-joints showed a strong variability, therefore an average local geometry has been assumed in the FE models, (ii) the effect of misalignments has been neglected, since authors [70] declared that 10-mm-thick joints tested under axial loading were affected by misalignments, but they did not report any value of misalignments or of the induced secondary bending stress. Dealing with tube-to-flange joints, Sonsino et al. [79] observed that joints tested under both CA and VA combined out-of-phase bending and torsion loading exhibited a significant reduction of life by a factor of four as compared to the corresponding in-phase loading, for a given applied stress range. Difference between in-phase and out-of-phase loading is not captured by the approach adopted here, since Eq. (1.21) - on which the PSM is based - does not take into account the phase shift between the different load contributions. However, the experimental outcome obtained by Sonsino et al. [79] is not found

systematically in the literature. In fact, in other investigations it has been observed that the influence of the phase shift between normal and shear stresses can be distinguished but it is not that remarkable [60,88]. In refs [60,88] the PSM has been applied to the fatigue strength assessment of steel welded joints subjected to CA multiaxial loadings taken from the literature [17,75,76,81,89–91].

The VA cases for which theoretical estimations are on the safe side are those referred to transverse nlc welded joints having thickness $t = 30$ mm (Figure 2.26b), longitudinal stiffeners (Figure 2.28) and to tube-to-flange joints (Figure 2.30, and Figure 2.32a) tested by Demofonti et al. [70], Vanrostenberghe et al. [73], Bertini et al. [75–78] and Witt et al. [80,81], respectively. Among these, the most evident is the case of longitudinal stiffeners (Figure 2.28) tested under VA axial fatigue loading, for which the authors [73] observed that the Miner's rule was not accurate for the applied loading spectrum and hence resulted in over conservatism, documented by values of the damage to failure D evaluated on the basis of the nominal stress curves in the ranges between 1.73 and 3.19 for test series 6.1, between 3.16 and 30.04 for test series 6.2, while values between 0.95 and 1.87 were obtained for test series 6.3, which indeed is in good agreement with PSM estimations.

All in all, the PSM-based scatter bands have been validated (not fitted) against a large bulk of fatigue data taken from the literature: approximately 1500 experimental data obtained under pure mode I local stresses ($\lambda = 0$, Figure 2.33a) and 540 experimental data relevant to multiaxial local stresses ($\lambda > 0$, Figure 2.33b). Of all analysed data, approximately 320 are referred to VA tests. Again it should be remembered that a scatter index of 1.90 referred to the 2.3–97.7% survival probabilities corresponds to the intrinsic scatter of single test series tested under CA loadings according to Haibach [9,68] and Sonsino [17,69]. Obtained results (see Figure 2.33) also justify the observation of Gurney [11], according to which it is reasonable, in first approximation, to expect the scatter in variable amplitude tests is almost the same as that in constant amplitude tests.

2.2 Validation with data from the literature

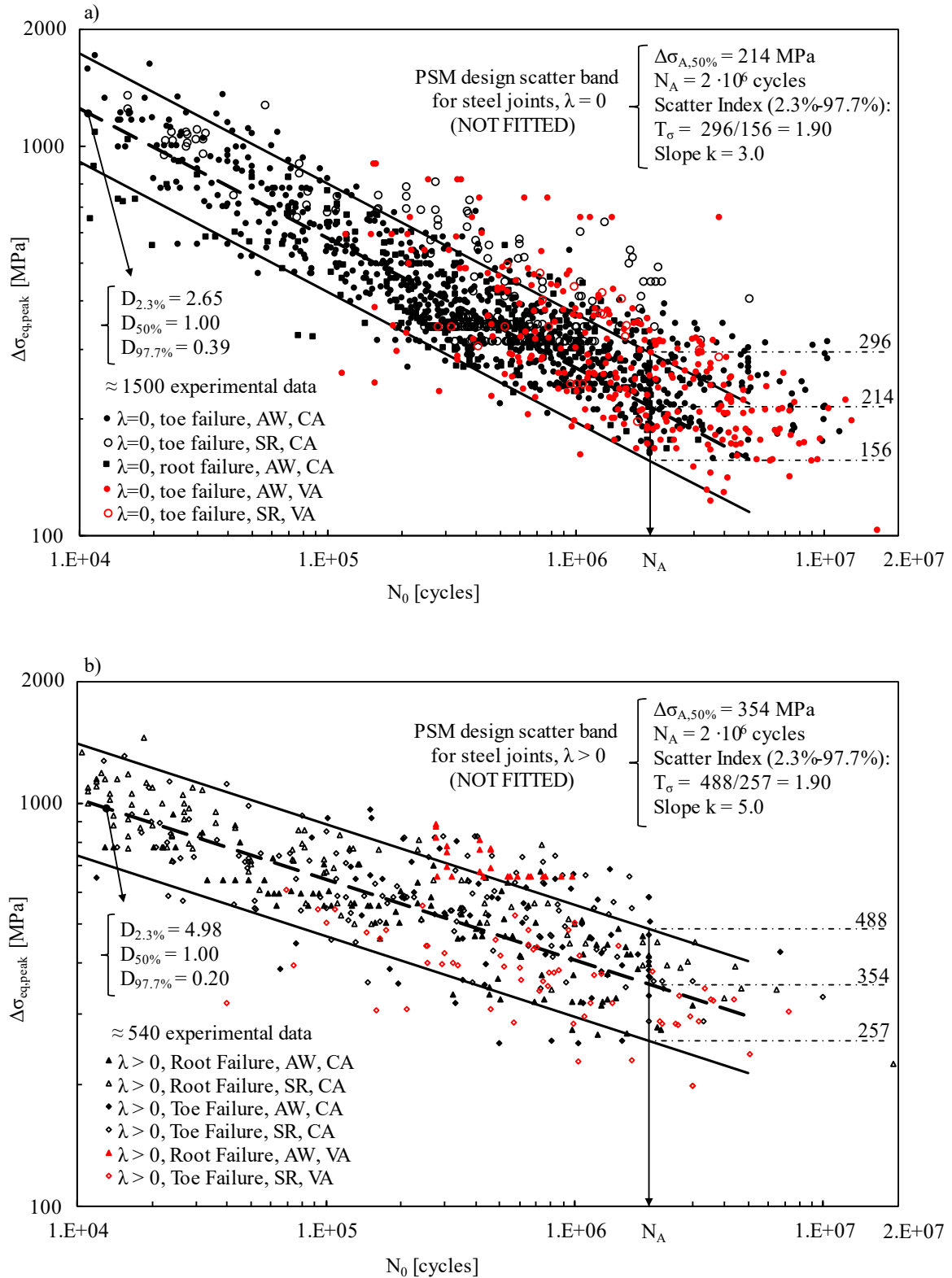


Figure 2.33. PSM-based fatigue assessment of weld toe and weld root failures in welded joints made of structural steels tested in the as-welded or stress-relieved conditions subjected to pure mode I Constant Amplitude (CA) [37] or Variable Amplitude (VA) [63] loadings. a) The design scatter band for pure mode I loading ($\lambda = 0$) has been calibrated in [61], while b) The design scatter band for mixed mode loading ($\lambda > 0$) has been calibrated in [34]. Both are not fitted on the re-analysed experimental data.

CHAPTER 2: Variable amplitude multiaxial local stresses

Table 2.7. Summary of fatigue test results and parameters to apply the PSM on the considered fatigue data taken from the Literature.

Code	Ref.	Load ^o	Spectrum ^{oo}	Λ^{ooo}	R_σ	R_τ	ϕ	$\Delta\sigma_{max}$	$\Delta\tau_{max}$	Failure		Mode I			Mode II			Mode III				
										Toe	Root	f_{s1}	f_{w1}	$\Delta\sigma_1^*$	f_{s2}	f_{w2}	$\Delta\tau_{II}^*$	f_{s3}	f_{w3}	$\Delta\tau_{III}^{**}$		
[-]	[-]	[-]	[-]	[-]	[-]	[-]	[°]	[MPa]	[MPa]	[-]	[-]	[-]	[-]	[MPa]	[-]	[-]	[MPa]	[-]	[-]	[MPa]		
1.1	[70]	A	CA	0	-1	-	-	200-500	-	6	-	1	0.852	1.587	-	-	-	-	-	-	-	
				0	0	-	-	120-350	-	5	-	1	0.852	1.587	-	-	-	-	-	-	-	-
				0	-1	-	-	510-753	-	5	-	0.242	0.852	1.587	-	-	-	-	-	-	-	-
1.2	[70]	A	CA	0	-1	-	-	250-376	-	6	-	1	0.781	1.568	-	-	-	-	-	-	-	
				0	0	-	-	200-320	-	11	-	1	0.781	1.568	-	-	-	-	-	-	-	-
				0	-1	-	-	500-720	-	5	-	0.337	0.781	1.568	-	-	-	-	-	-	-	-
				0	-1	-	-	638-876	-	5	-	0.242	0.781	1.568	-	-	-	-	-	-	-	-
1.3	[70]	A	CA	0	-1	-	-	128-480	-	7	-	1	0.899	1.620	-	-	-	-	-	-	-	
				0	0	-	-	160-480	-	6	-	1	0.899	1.620	-	-	-	-	-	-	-	-
				0	-1	-	-	496-992	-	5	-	0.337	0.899	1.620	-	-	-	-	-	-	-	-
				0	-1	-	-	689-977	-	5	-	0.242	0.899	1.620	-	-	-	-	-	-	-	-
1.4	[70]	A	CA	0	-1	-	-	200-360	-	7	-	1	0.726	1.664	-	-	-	-	-	-	-	
				0	0	-	-	140-390	-	8	-	1	0.726	1.664	-	-	-	-	-	-	-	-
				0	-1	-	-	406-784	-	5	-	0.337	0.726	1.664	-	-	-	-	-	-	-	-
				0	-1	-	-	420-801	-	6	-	0.242	0.726	1.664	-	-	-	-	-	-	-	-
2.1	[70]	B	CA	0	-1	-	-	166-530	-	7	-	1	0.852	1.662	-	-	-	-	-	-	-	
				0	-1	-	-	412-823	-	5	-	0.242	0.852	1.662	-	-	-	-	-	-	-	
2.2	[70]	B	CA	0	-1	-	-	126-438	-	13	-	1	0.877	1.643	-	-	-	-	-	-	-	
				0	0	-	-	128-440	-	9	-	1	0.877	1.643	-	-	-	-	-	-	-	-
				0	-1	-	-	352-588	-	8	-	0.337	0.877	1.643	-	-	-	-	-	-	-	-
				0	0	-	-	320-600	-	6	-	0.337	0.877	1.643	-	-	-	-	-	-	-	-
2.3	[70]	B	CA	0	-1	-	-	176-658	-	11	-	1	0.852	1.656	-	-	-	-	-	-	-	
				0	-1	-	-	328-548	-	8	-	0.337	0.852	1.656	-	-	-	-	-	-	-	
				0	-1	-	-	574-815	-	6	-	0.242	0.852	1.656	-	-	-	-	-	-	-	
2.4	[70]	B	CA	0	-1	-	-	146-552	-	13	-	1	0.824	1.565	-	-	-	-	-	-	-	
				0	0	-	-	166-552	-	11	-	1	0.824	1.565	-	-	-	-	-	-	-	-
				0	-1	-	-	396-768	-	9	-	0.337	0.824	1.565	-	-	-	-	-	-	-	-
				0	0	-	-	428-664	-	6	-	0.337	0.824	1.565	-	-	-	-	-	-	-	-

2.2 Validation with data from the literature

			VA-II	0	-1	-	-	496-960	-	8	-	0.242	0.824	1.565	-	-	-	-	-	-
				0	0	-	-	834-1112	-	5	-	0.242	0.824	1.565	-	-	-	-	-	-
3.1	[70]	A	CA	0	-1	-	-	100-400	-	8	-	1	1.309	1.526	-	-	-	-	-	-
				0	0	-	-	100-350	-	6	-	1	1.309	1.526	-	-	-	-	-	-
			VA-II	0	-1	-	-	300-720	-	5	-	0.242	1.309	1.526	-	-	-	-	-	-
3.2	[70]	A	CA	0	-1	-	-	80-280	-	7	-	1	1.309	1.503	-	-	-	-	-	-
				0	0	-	-	120-350	-	5	-	1	1.309	1.503	-	-	-	-	-	-
			VA-I	0	-1	-	-	194-580	-	5	-	0.337	1.309	1.503	-	-	-	-	-	-
			VA-II	0	-1	-	-	314-610	-	5	-	0.242	1.309	1.503	-	-	-	-	-	-
3.3	[70]	A	CA	0	-1	-	-	100-326	-	7	-	1	1.376	1.552	-	-	-	-	-	-
				0	0	-	-	150-376	-	5	-	1	1.376	1.552	-	-	-	-	-	-
			VA-I	0	-1	-	-	262-692	-	5	-	0.337	1.376	1.552	-	-	-	-	-	-
			VA-II	0	-1	-	-	395-868	-	5	-	0.242	1.376	1.552	-	-	-	-	-	-
3.4	[70]	A	CA	0	-1	-	-	160-320	-	6	-	1	1.309	1.541	-	-	-	-	-	-
				0	0	-	-	100-250	-	7	-	1	1.309	1.541	-	-	-	-	-	-
			VA-I	0	-1	-	-	396-552	-	5	-	0.337	1.309	1.541	-	-	-	-	-	-
			VA-II	0	-1	-	-	566-1196	-	5	-	0.242	1.309	1.541	-	-	-	-	-	-
4.1	[70]	B	CA	0	-1	-	-	710-912	-	2	-	1	1.945	1.136	-	-	-	-	-	-
				0	0	-	-	134-508	-	7	-	1	1.945	1.136	-	-	-	-	-	-
			VA-II	0	-1	-	-	330-661	-	5	-	0.242	1.945	1.136	-	-	-	-	-	-
4.2	[70]	B	CA	0	-1	-	-	132-898	-	9	-	1	2.231	1.188	-	-	-	-	-	-
				0	0	-	-	132-498	-	6	-	1	2.231	1.188	-	-	-	-	-	-
			VA-I	0	-1	-	-	234-490	-	8	-	0.337	2.231	1.188	-	-	-	-	-	-
				0	0	-	-	220-526	-	6	-	0.337	2.231	1.188	-	-	-	-	-	-
			VA-II	0	-1	-	-	328-686	-	5	-	0.242	2.231	1.188	-	-	-	-	-	-
4.3	[70]	B	CA	0	-1	-	-	156-910	-	13	-	1	1.645	1.140	-	-	-	-	-	-
				0	0	-	-	210-912	-	7	-	1	1.645	1.140	-	-	-	-	-	-
			VA-I	0	-1	-	-	332-734	-	10	-	0.337	1.645	1.140	-	-	-	-	-	-
				0	0	-	-	402-666	-	6	-	0.337	1.645	1.140	-	-	-	-	-	-
			VA-II	0	-1	-	-	482-865	-	5	-	0.242	1.645	1.140	-	-	-	-	-	-
				0	0	-	-	465-1025	-	5	-	0.242	1.645	1.140	-	-	-	-	-	-
4.4	[70]	B	CA	0	-1	-	-	118-896	-	14	-	1	2.090	1.104	-	-	-	-	-	-
				0	0	-	-	108-898	-	7	-	1	2.090	1.104	-	-	-	-	-	-
			VA-I	0	-1	-	-	236-490	-	9	-	0.337	2.090	1.104	-	-	-	-	-	-

CHAPTER 2: Variable amplitude multiaxial local stresses

			0	0	-	-	264-546	-	6	-	0.337	2.090	1.104	-	-	-	-	-	-
		VA-II	0	-1	-	-	328-574	-	8	-	0.242	2.090	1.104	-	-	-	-	-	-
			0	0	-	-	398-767	-	5	-	0.242	2.090	1.104	-	-	-	-	-	-
5.1	[71,72]	A	CA	0	0.1	-	-	90-240	-	6	-	1	1.077	2.658	-	-	-	-	-
				0	$\sigma_{max}=280\text{MPa}$	-	-	90-140	-	4	-	1	1.077	2.658	-	-	-	-	-
				0	$\sigma_{max}=135\text{MPa}$	-	-	65	-	1	-	1	1.077	2.658	-	-	-	-	-
		VA-III	0	$\sigma_{max}=280\text{MPa}$	-	-	210	-	2	-	0.350	1.077	2.658	-	-	-	-	-	-
			0	$\sigma_{min}=70\text{MPa}$	-	-	210	-	1	-	0.350	1.077	2.658	-	-	-	-	-	-
		VA-IV	0	$\sigma_m=175\text{MPa}$	-	-	210	-	1	-	0.350	1.077	2.658	-	-	-	-	-	-
			0	$\sigma_{max}=280\text{MPa}$	-	-	210	-	1	-	0.292	1.077	2.658	-	-	-	-	-	-
			0	$\sigma_{max}=147\text{MPa}$	-	-	210	-	1	-	0.292	1.077	2.658	-	-	-	-	-	-
			0	$\sigma_{min}=70\text{MPa}$	-	-	210	-	1	-	0.292	1.077	2.658	-	-	-	-	-	-
			0	$\sigma_m=175\text{MPa}$	-	-	210	-	1	-	0.292	1.077	2.658	-	-	-	-	-	-
		VA-V	0	$\sigma_{max}=280\text{MPa}$	-	-	210	-	1	-	0.233	1.077	2.658	-	-	-	-	-	-
		VA-VI	0	$\sigma_{max}=280\text{MPa}$	-	-	210	-	1	-	0.171	1.077	2.658	-	-	-	-	-	-
6.1	[73]	A	CA	0	0.1	-	-	50-350	-	6	-	1	0.766	4.510	-	-	-	-	-
			0	0.5	-	-	90-303	-	5	-	1	0.766	4.510	-	-	-	-	-	-
		VA-VII	0	-1	-	-	560-770	-	5	-	0.246	0.766	4.510	-	-	-	-	-	-
6.2	[73]	A	CA	0	0.1	-	-	69-342	-	4	-	1	0.766	4.510	-	-	-	-	-
			0	0.5	-	-	50-351	-	5	-	1	0.766	4.510	-	-	-	-	-	-
		VA-VII	0	-1	-	-	768-1056	-	12	-	0.246	0.766	4.510	-	-	-	-	-	-
6.3	[73]	A	CA	0	0.1	-	-	90-347	-	4	-	1	0.996	3.130	-	-	-	-	-
			0	0.5	-	-	70-302	-	6	-	1	0.996	3.130	-	-	-	-	-	-
		VA-VII	0	-1	-	-	560-770	-	12	-	0.246	0.996	3.130	-	-	-	-	-	-
7.1	[74]	A	CA	0	0.1	-	-	117-190	-	7	-	1	1.062	1.489	-	-	-	-	-
			0	-0.43	-	-	136-243	-	6	-	1	1.062	1.489	-	-	-	-	-	-
		VA-VIII	0	-0.43	-	-	483-605	-	4	-	0.245	1.062	1.489	-	-	-	-	-	-
7.2	[74]	A	CA	0	0.1	-	-	135-262	-	8	-	1	1.062	1.489	-	-	-	-	-
			0	-0.43	-	-	180-262	-	6	-	1	1.062	1.489	-	-	-	-	-	-
		VA-VIII	0	-0.43	-	-	483-832	-	5	-	0.245	1.062	1.489	-	-	-	-	-	-
8.1	[75-78]	B	CA	0	-1	-	-	181-295	-	-	10	1	1.184	2.955	1	4.627	0.098	-	-
			0	0	-	-	122-275	-	-	9	1	1.184	2.955	1	4.627	0.098	-	-	-
		T	CA	∞	-	-1	-	144-228	-	13	-	-	-	-	-	-	1	2.911	1.136
			∞	-	0	-	-	148-248	-	13	-	-	-	-	-	-	1	2.911	1.136

2.2 Validation with data from the literature

		B+T	CA	0.31	-1	-1	0	177-245	54-75	-	7	1	1.184	2.955	1	4.627	0.098	1	2.911	1.136
				0.31	0	0	0	117-250	36-77	-	8	1	1.184	2.955	1	4.627	0.098	1	2.911	1.136
				1.14	-1	-1	0	110-147	125-167	-	5	1	1.184	2.955	1	4.627	0.098	1	2.911	1.136
				1.14	0	0	0	86-108	98-123	-	5	1	1.184	2.955	1	4.627	0.098	1	2.911	1.136
			VA-IX	1.13	0	0	-	165	187	-	3	1	1.184	2.955	1	4.627	0.098	1.348-1.477	2.911	1.136
			VA-X	1.13	0	0	-	165	187	-	3	1	1.184	2.955	1	4.627	0.098	1.058-1.320	2.911	1.136
			VA-XI	1.13	0	0	-	165	187	-	3	1.265-1.680	1.184	2.955	1.152-1.365	4.627	0.098	1	2.911	1.136
			VA-XII	1.13	0	0	-	165	187	-	3	1.238-1.633	1.184	2.955	1.136-1.342	4.627	0.098	1	2.911	1.136
9.1	[75-78]	B+T	CA	0.31	-1	-1	90	126-241	39-74	-	5	1	1.184	2.088	1	4.627	0.155	1	2.911	1.321
				0.31	0	0	90	101-229	31-70	-	5	1	1.184	2.088	1	4.627	0.155	1	2.911	1.321
				1.14	-1	-1	90	72-129	82-147	-	5	1	1.184	2.088	1	4.627	0.155	1	2.911	1.321
				1.14	0	0	90	65-116	74-132	-	5	1	1.184	2.088	1	4.627	0.155	1	2.911	1.321
			VA-XIII	1.13	0	0	-	165	187	-	4	1	1.184	2.088	1	4.627	0.155	1.020	2.911	1.321
			VA-XIV	1.13	0	0	-	165	187	-	4	1	1.184	2.088	1	4.627	0.155	1.020	2.911	1.321
			VA-XV	1.13	0	0	-	165	187	-	4	1	1.184	2.088	1	4.627	0.155	1.020	2.911	1.321
10.1	[79]	B	CA	0	-1	-	-	174-742	-	9	-	0.707	1.569	1.645	-	-	-	-	-	-
			VA-I	0	-1	-	-	320-560	-	8	-	0.238	1.569	1.645	-	-	-	-	-	-
		T	CA	∞	-	-1	-	-	362-458	4	-	-	-	-	-	-	-	0.707	2.389	1.209
			VA-I	∞	-	-1	-	-	300-600	7	-	-	-	-	-	-	-	0.276	2.389	1.209
		B+T	CA	0.58	-1	-1	0	248-346	144-200	8	-	0.707	1.569	1.645	-	-	-	0.707	2.389	1.209
				0.58	-1	-1	90	160-336	92-200	10	-	0.707	1.569	1.645	-	-	-	0.707	2.389	1.209
			VA-I	0.58	-1	-1	0	368-524	212-302	7	-	0.238	1.569	1.645	-	-	-	0.276	2.389	1.209
				0.58	-1	-1	90	258-518	150-298	9	-	0.238	1.569	1.645	-	-	-	0.276	2.389	1.209
11.1	[80,81]	B	CA	0	-1	-	-	204-820	-	17	-	0.707	1.460	1.679	-	-	-	-	-	-
				0	-1	$\tau_m = \sigma_a$	-	260-397	-	7	-	0.707	1.460	1.679	-	-	-	-	-	-
				0	0	-	-	164-619	-	8	-	1	1.460	1.679	-	-	-	-	-	-
			VA-I	0	-1	-	-	496-695	-	7	-	0.238	1.460	1.679	-	-	-	-	-	-
				0	0	-	-	453-602	-	6	-	0.337	1.460	1.679	-	-	-	-	-	-
		T	CA	∞	-	-1	-	-	238-397	8	-	-	-	-	-	-	-	0.707	2.286	1.214
				∞	$\sigma_m = \tau_a$	-1	-	-	220-298	7	-	-	-	-	-	-	-	0.707	2.286	1.214
				∞	-	0	-	-	205-306	14	-	-	-	-	-	-	-	1	2.286	1.214
			VA-I	∞	-	-1	-	-	397-496	4	-	-	-	-	-	-	-	0.276	2.286	1.214
		B+T	CA	1	-1	-1	0	143-306	143-306	7	-	0.707	1.460	1.679	-	-	-	0.707	2.286	1.214
				1	-1	-1	90	137-215	137-215	9	-	0.707	1.460	1.679	-	-	-	0.707	2.286	1.214

CHAPTER 2: Variable amplitude multiaxial local stresses

	1	-1	-1	$f_r=f_B/5$	165-512	165-512	8	-	1.209	1.460	1.679	-	-	-	0.707	2.286	1.214
	1	-1	-1	$f_r=5f_B$	202-456	202-456	5	-	0.707	1.460	1.679	-	-	-	0.976	2.286	1.214
	1	0	0	0	140-354	140-354	7	-	1	1.460	1.679	-	-	-	1	2.286	1.214
	1	0	0	90	144-306	144-306	7	-	1	1.460	1.679	-	-	-	1	2.286	1.214
VA-I	1	-1	-1	0	306-524	306-524	9	-	0.238	1.460	1.679	-	-	-	0.276	2.286	1.214
	1	-1	-1	90	338-479	338-479	5	-	0.238	1.460	1.679	-	-	-	0.276	2.286	1.214
	1	-1	-1	$f_r=5f_B$	301-505	301-505	6	-	0.238	1.460	1.679	-	-	-	0.380	2.286	1.214
	1	-1	-1	Uncor.	307-460	307-460	5	-	0.238	1.460	1.679	-	-	-	0.276	2.286	1.214
	1	0	0	0	325-409	325-409	6	-	0.337	1.460	1.679	-	-	-	0.390	2.286	1.214
	1	0	0	90	238-327	238-327	7	-	0.337	1.460	1.679	-	-	-	0.390	2.286	1.214

° Axial (A), Bending (B), Torsion (T).

°° Details are reported in Figure 2.7, Figure 2.8, Table 2.4, and Table 2.5.

°°° According to Eq. (1.27).

* $\Delta\sigma_I = \Delta\sigma_{\theta,0=0,\text{peak}}$ and $\Delta\tau_{II} = \Delta\tau_{r\theta,0=0,\text{peak}}$. In the case of 3D FE models meshed with 10-node tetra elements, values of $\Delta\bar{\sigma}_{\theta,0=0,\text{peak}}$ and $\Delta\bar{\tau}_{r\theta,0=0,\text{peak}}$ have been reported. All values calculated from FE models where $\Delta\sigma = 1$ MPa was applied.

** $\Delta\tau_{III} = \Delta\tau_{\theta z,0=0,\text{peak}}$. In the case of 3D FE models meshed with 10-node tetra elements, values of $\Delta\bar{\tau}_{\theta z,0=0,\text{peak}}$ have been reported. All values calculated from FE models where $\Delta\tau = 1$ MPa was applied.

2.3. New experimental fatigue data: non-load-carrying fillet welded joints

2.3.1. Introduction

The presented equivalent peak stress has been proved to be a fatigue relevant parameter and it has been shown to be capable of summarizing a huge amount of experimental data relevant to constant and variable amplitude uniaxial as well as multiaxial stresses. Indeed, a validation exercise has been done by analysing a huge amount of fatigue data taken from the Literature and relevant to steel joints having different geometries, made of different steel classes, and tested under different uniaxial as well as multiaxial stress spectra.

The same validation exercise has been done on new experimental results, generated by fatigue testing non-load-carrying (nlc) fillet-welded double transverse or 45° inclined attachments made of S355 structural steel under pure axial loading. The choice of fatigue testing such specimens started observing that as fatigue life of joints under multiaxial stresses is concerned, relatively few data are available in the Literature, especially when dealing with multiaxial variable amplitude stresses. To the best of Author's knowledge, the few available fatigue results are relevant only to tube-to-flange joints under combined bending and torsion loads. One possible reason why few data are available is that a complex and dedicated test rig having two independent actuators is generally required to apply combined bending and torsion both in-phase/out-of-phase as well as constant/variable amplitude loadings to tube-to-flange joints [77,79,80], resulting in expensive and time-consuming experiments.

Alternatively, to generate experimental fatigue data under multiaxial in-phase constant/variable amplitude stresses using a standard uniaxial testing machine, which is generally faster and cheaper, a solution was proposed by Booth and Maddox [92], who axially fatigue tested joints having weld bead inclined with respect to the load direction. In this way, the weld toe and the weld root are subjected to in-phase normal as well as shear stresses. However, it is worth noting that such solution does not allow to generate out-of-phase multiaxial local stresses and investigating the effect of different ratios between normal and shear stresses would require different joint geometries having different weld bead inclination. Accordingly, the joints having inclined attachments have been chosen to investigate the effect of a local in-phase multiaxial stress state using a uniaxial testing machine.

In the following paragraph, new experimental results have been generated by fatigue testing non-load-carrying (nlc) fillet-welded steel joints, both with double transverse attachment and with double 45° inclined attachment, under constant amplitude (CA) as well as variable amplitude (VA) axial loadings. The effects of the applied stress range, load ratio, deterministic and stochastic loads, misalignments and welding residual stresses on the fatigue life of the tested joints have been considered and discussed. Finally, the obtained results have been analysed adopting the extension of the PSM, capable of taking into account either uniaxial or multiaxial constant and variable amplitude local stresses.

2.3.2. Fatigue tests: specimens

Fatigue tests were performed using two different joint geometries made from an 8-mm-thick S355J2+N steel plate whose nominal mechanical properties are reported in Table 2.8. Both geometries were non-load-carrying (nlc) fillet-welded joints, one with double transverse attachment (see model 1 in Table 2.9, $\beta = 90^\circ$) and the other with double 45° inclined attachment (see model 2 in Table 2.9, $\beta = 45^\circ$), the latter being chosen to investigate the effect of a local in-phase multiaxial stress state using a uniaxial testing machine. Welding was performed perpendicular to the rolling direction using metal active gas welding (MAG) technique.

Table 2.8. Material properties (nominal values) and welding process of the welded joints.

Joint	Material	f_y	f_U	Welding Process	TCs*	Failure Criterion
[-]	[-]	[MPa]	[MPa]	[-]	[-]	[-]
Transverse (T)	S355J2+N	355	510	MAG	AW	Complete Separation
Inclined (I)	S355J2+N	355	510	MAG	AW	Complete Separation

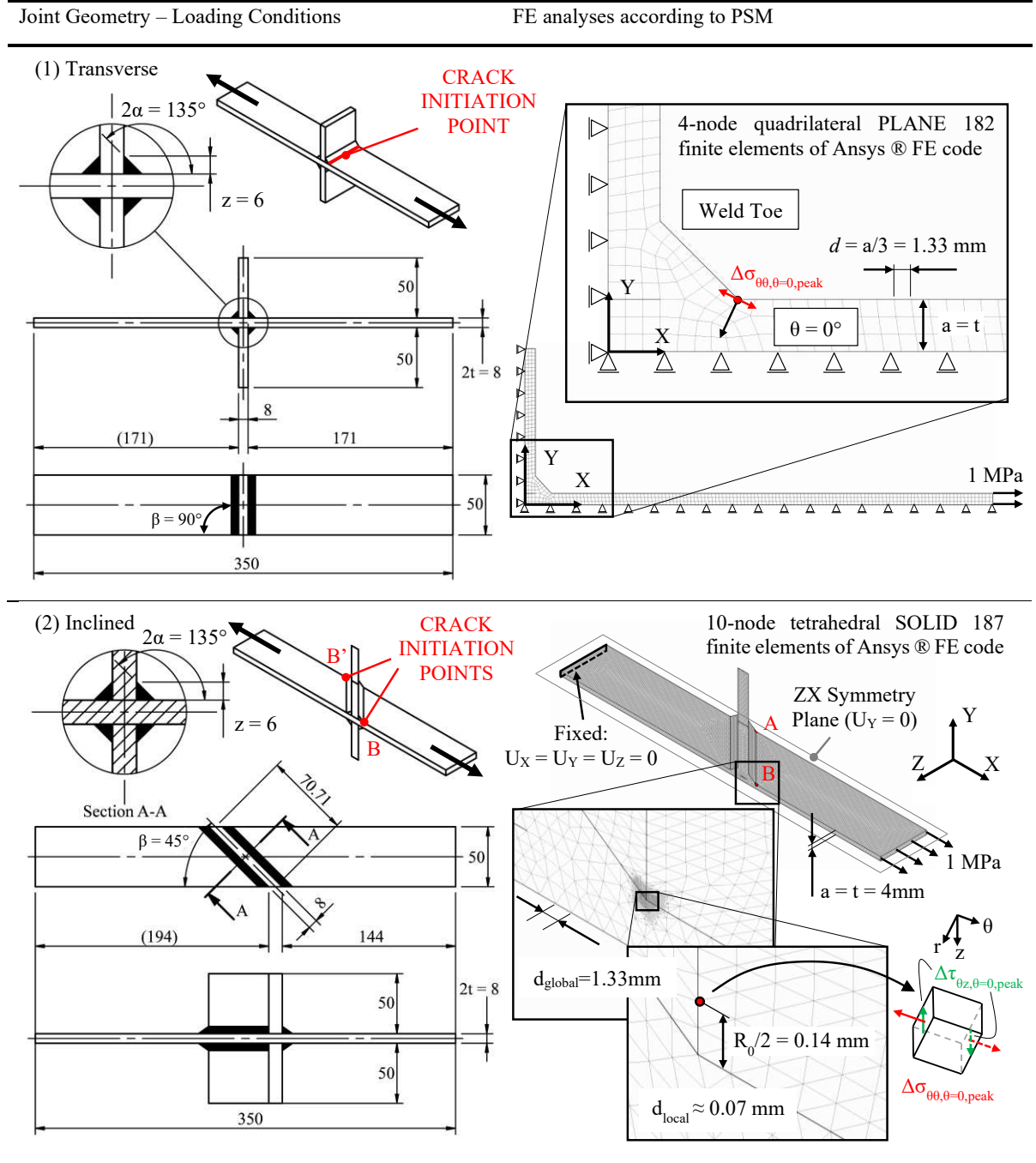
* Testing Conditions: AW = as-welded

Micro-hardness and microstructural analyses have been performed on the specimens. The sample for micro-hardness measurements and microstructural analysis has been extracted by saw cutting a transverse joint which has never been fatigue loaded. The sample was grinded by means of sandpaper with grit P120 up to P1200 and then polished with 6 μm and 1 μm diamond suspensions. Vickers micro-hardness HV0.5 has been measured by using a Leitz™ Durimet indentation machine according to [93], by applying a weight of 0.5 kg. The measurements have been performed:

2.3 New experimental fatigue data: non-load-carrying fillet welded joints

- in a material region close to the weld toe (Figure 2.34a), whose results have been reported in color map mode in the same figure.
- along a straight path starting from the transverse attachment to the main plate through the weld bead (Figure 2.34d), the relevant results having been reported in Figure 2.34b as a function of the coordinate along the path

Table 2.9. Joints geometries and FE analyses according to the PSM.



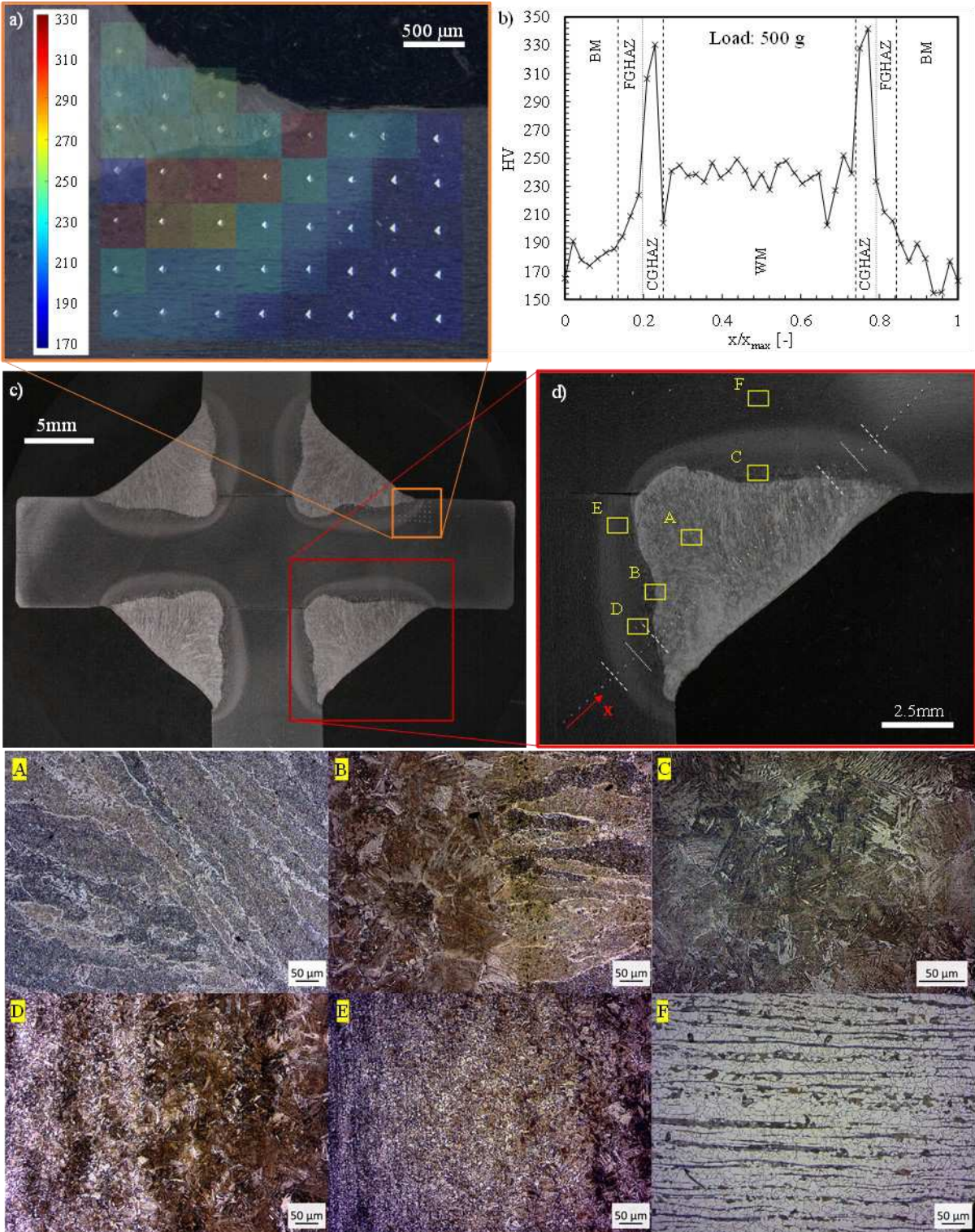


Figure 2.34. Micro-hardness measurements and microstructural analysis of a transverse joint which has not been fatigue tested. (a), (c), and (d) macrographies of the etched sample. (a) and (b) results of micro-hardness measurements. (A)-(F) micrographs of the main microstructures highlighted in (d).

After that, the sample was etched with 4% Nital solution to better highlight the microstructure. Micrographs were taken using an optical microscope and allowed to distinguish three main regions, i.e. the Weld Metal (WM), the Heat Affected Zone (HAZ), and the Base Metal (BM) (see Figure 2.34A-F). The analysis showed that the BM has a microhardness of ~ 175 HV and consists in a typical ferritic-pearlitic microstructure, whose grains are elongated in the rolling direction (see Figure 2.34F). Differently, the maximum values of the hardness (~ 330 - 340 HV) have been measured in the HAZ, which has an inhomogeneous bainitic-martensitic microstructure, divided into two main subregions: the Coarse Grain (CGHAZ, Figure 2.34C) and the Fine Grain (FGHAZ, Figure 2.34E). Figure 2.34 also shows the microstructure of the WM (Figure 2.34A) and the transition in between different microstructures (Figure 2.34B,D).

2.3.3. Fatigue tests: loads and testing parameters

The nominal stress range $\Delta\sigma$ has been calculated with reference to the main plate:

$$\Delta\sigma = \frac{\Delta F}{A} = \frac{\Delta F}{W \cdot t} \quad (1.30)$$

where ΔF is the range of the axial load, while A , W , and t are the cross-section area, the width, and the thickness of the main plate, respectively. All specimens were fatigue tested in the as-welded state under closed loop load-controlled pure axial loading by using a 250 kN MFL servo-hydraulic machine equipped with an MTS TestStar II digital controller. A total of 18 fatigue tests were performed applying CA pulsating ($R = 0.05$) as well as fully reversed ($R = -1$) loading at a frequency ranging between 7 and 20 Hz depending on the applied load level. The same nominal load ratios were used for testing 22 specimens under VA loadings consisting in a p-type spectrum [7,11] (see Figure 2.35) applied repeatedly until failure both as a six-block program (VA-DD) and as a random sequence (VA-Rand). The cycle distribution comes from that of a narrow-band Gaussian random process $\{\sigma(t)\}$, whose probability density

function of the stress amplitudes follows the Rayleigh distribution [94,95]. The cycle distribution can be written as follows [62,83,96,97]:

$$N = e^{\left[1 - \left(\frac{\Delta\sigma}{\Delta\sigma_{\max}}\right)^2\right] \ln L_s} \quad (1.31)$$

where $\Delta\sigma/\Delta\sigma_{\max}$ is the normalized stress range ($0 \leq \Delta\sigma/\Delta\sigma_{\max} \leq 1$), N is the number of cycles for which the applied stress ranges are greater than or equal to $\Delta\sigma/\Delta\sigma_{\max}$, i.e., the number of exceeding cycles, while L_s is the length of the spectrum. Given the exceedance cycle distribution (Eq. (1.31)), the Gaussian spectrum can be converted into the p-type spectrum by amplifying the normalized stress ranges with the following expression [11]:

$$\left(\frac{\Delta\sigma}{\Delta\sigma_{\max}}\right)_p = p + (1-p) \left(\frac{\Delta\sigma}{\Delta\sigma_{\max}}\right)_{Gaussian, p=0} \quad (1.32)$$

where $p = \Delta\sigma_{\min}/\Delta\sigma_{\max}$ is the ratio between the minimum and the maximum stress ranges. In the present work, the length of the spectrum and the p parameter were put equal to $L_s = 10^4$ cycles and $p = 0.25$, respectively (Figure 2.35). The length of the spectrum L_s , shorter than that used by other authors in the Literature [82,98], was chosen to guarantee a sufficiently high number of blocks to failure (> 10) even in the case of relatively short fatigue life tests ($\sim 10^5$ cycles). The six-block program (VA-DD) has been applied in a decreasing/decreasing sequence with test frequencies varying between 0.01 and 20 Hz. Either in the six-block program or in the random sequence, the applied load history was continuously sampled during the test and was systematically compared to the input one to assure that it was applied correctly. The number of cycles to failure corresponded to complete separation of the specimen, while run-out condition was fixed at $2 \cdot 10^6$ cycles, if no failure or crack initiation was detected.

2.3 New experimental fatigue data: non-load-carrying fillet welded joints

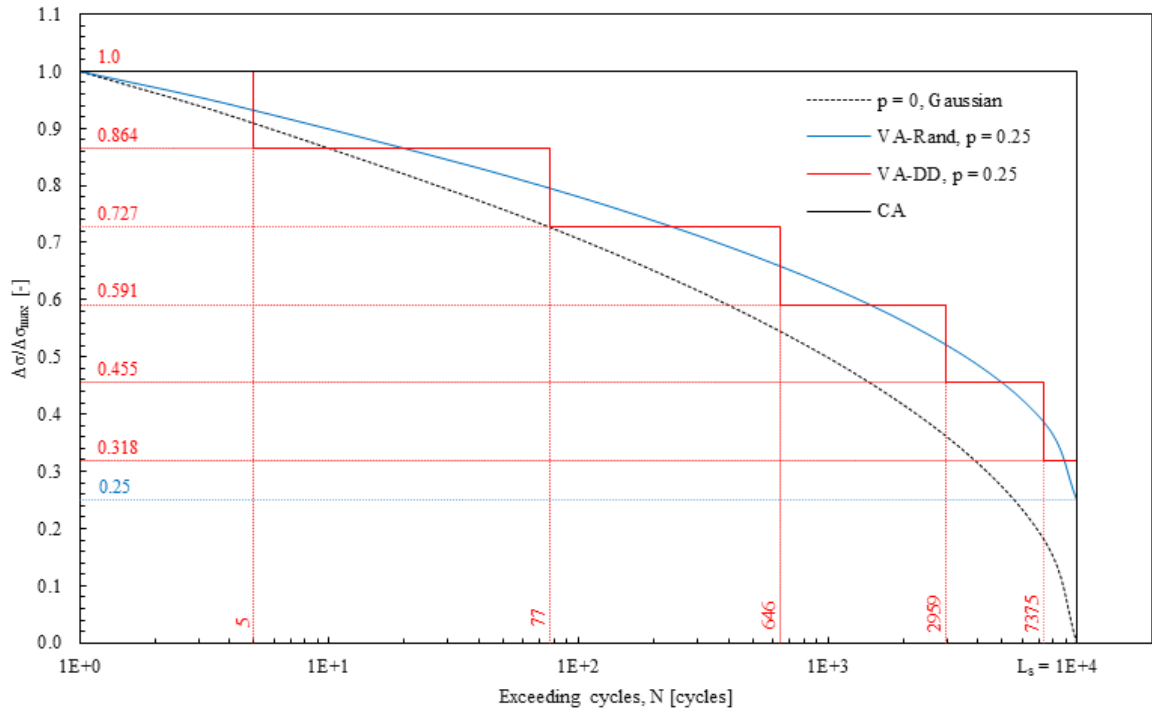




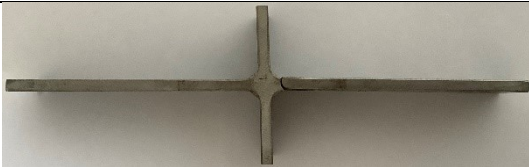
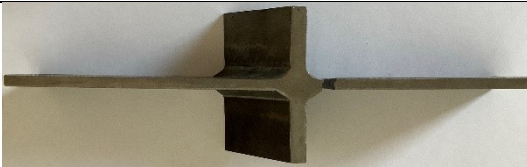





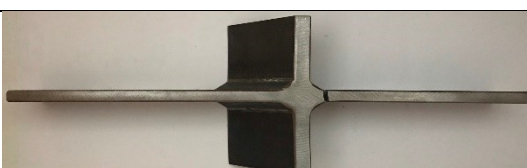




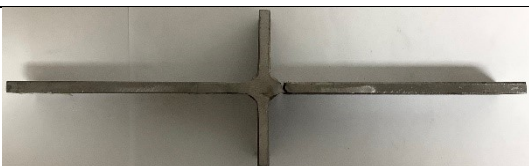

Figure 2.35. Normalized stress range spectra applied in the experimental fatigue tests.

2.3.4. Fatigue test results: damage analysis

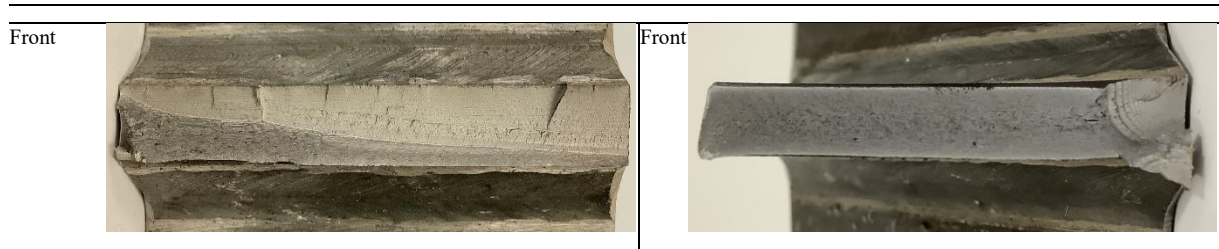
As it was expected, all joints both with transverse and inclined attachments under all types of fatigue loads exhibited fatigue crack initiation at the weld toe on the main plate's side. More specifically, the crack initiation took place at one point or more along the weld toe in case of joints with transverse attachments (see model 1 in Table 2.9 and left side of Table 2.10), while it always occurred at the points of the weld toe at the specimen's edges closer to the machine grips in case of joints with inclined attachments (see point B or B' on model 2 in Table 2.9 and right side of Table 2.10). Then, initiated fatigue crack propagated predominantly through the width, but also through the thickness until final fracture occurred.

CHAPTER 2: Variable amplitude multiaxial local stresses

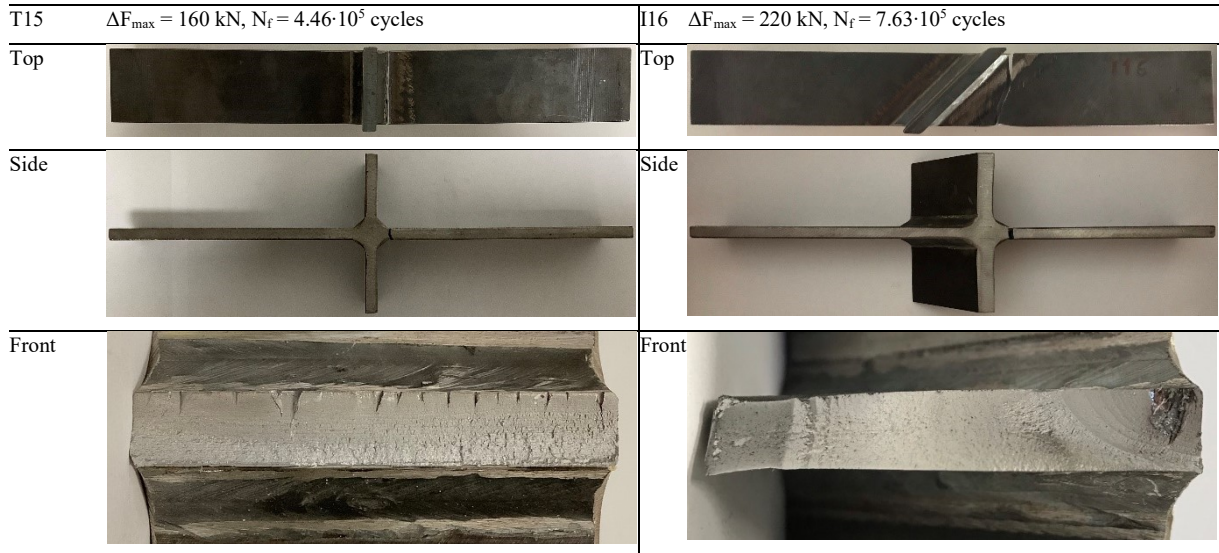
Table 2.10. Fracture surfaces and crack paths.

CA, R = 0.05			
T03	$\Delta F_{\max} = 80 \text{ kN}$, $N_f = 3.44 \cdot 10^5$ cycles	I01	$\Delta F_{\max} = 125 \text{ kN}$, $N_f = 1.72 \cdot 10^5$ cycles
Top		Top	
Side		Side	
Front		Front	
CA, R = -1			
T09	$\Delta F_{\max} = 66 \text{ kN}$, $N_f = 1.44 \cdot 10^6$ cycles	I14	$\Delta F_{\max} = 90 \text{ kN}$, $N_f = 8.82 \cdot 10^5$ cycles
Top		Top	
Side		Side	
Front		Front	
VA_DD, R = 0.05			
T11	$\Delta F_{\max} = 135 \text{ kN}$, $N_f = 1.54 \cdot 10^6$ cycles	I13	$\Delta F_{\max} = 183 \text{ kN}$, $N_f = 5.55 \cdot 10^5$ cycles
Top		Top	
Side		Side	

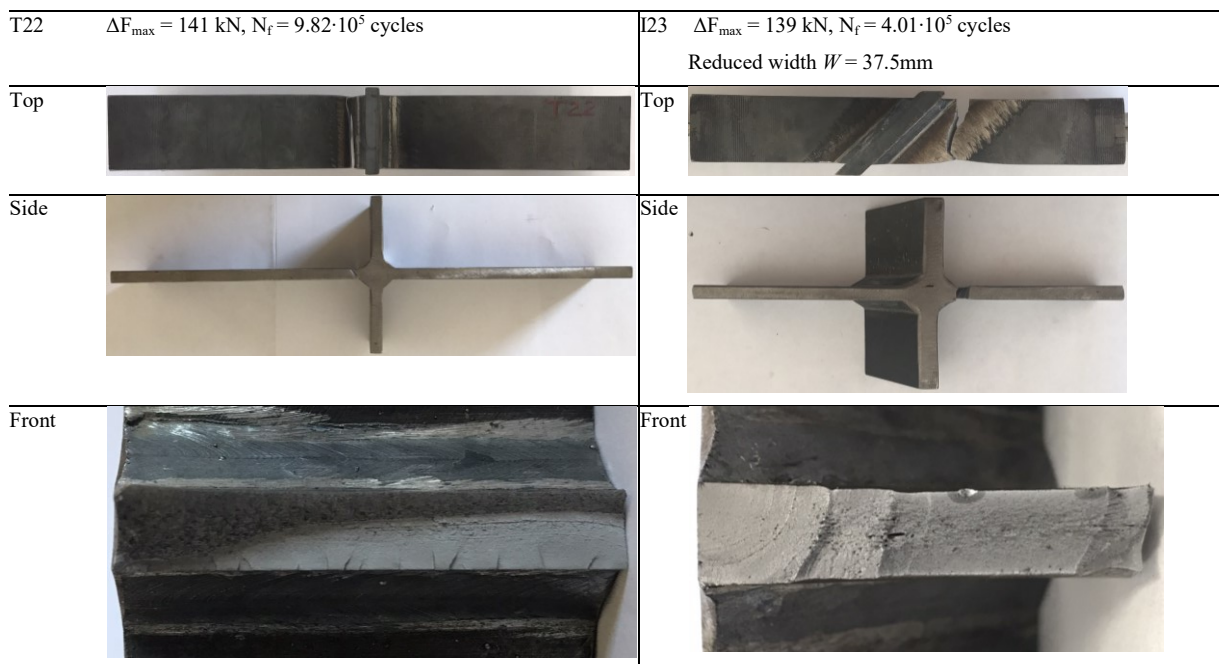
2.3 New experimental fatigue data: non-load-carrying fillet welded joints



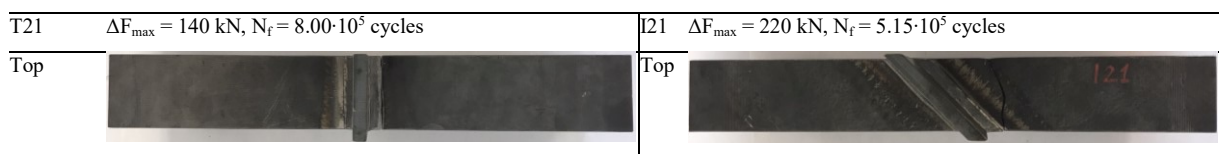
VA_DD, R = -1

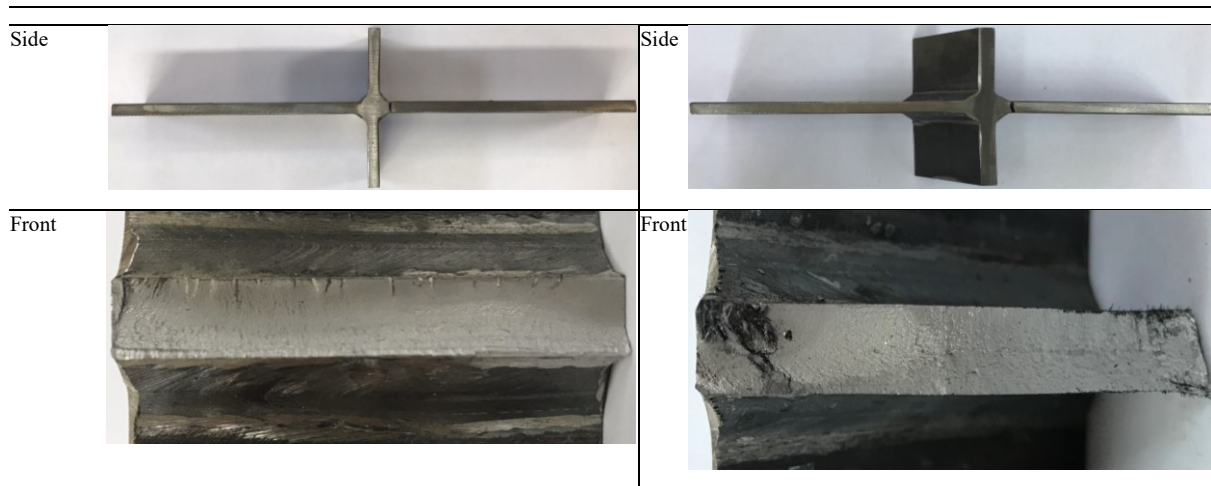


VA_Rand, R = 0.05



VA_Rand, R = -1





2.3.5. Fatigue test results: nominal stress

The experimental fatigue results have been reported in Figure 2.36 in terms of number of cycles to failure N_f versus the maximum applied nominal stress range $\Delta\sigma_{\max}$ along with the uniaxial FAT80 (80 MPa at $2 \cdot 10^6$ cycles) fatigue resistance curve for normal stresses according to IIW recommendations and Eurocode 3 [1,15]. Interestingly, joints with inclined attachments showed longer fatigue lives than joints with transverse attachments for the same applied CA nominal stress range. In other words, fatigue life increases as the inclination angle of the attachments β (see models 1 and 2 in Table 2.9) decreases (compare black triangle markers with circular markers in Figure 2.36). The same experimental outcome is valid for the data generated under VA loads (compare red and blue triangle markers with circular markers in Figure 2.36).

Furthermore, no significant mean stress sensitivity has been observed both under CA loadings (compare black filled and empty markers in Figure 2.36). As VA loads are concerned, transverse joints exhibit no significant mean stress sensitivity as for CA loads (compare red as well as blue filled and empty circular markers in Figure 2.36), while inclined joints showed being slightly sensitive to the load ratio resulting in shorter fatigue under tension-tension nominal stresses ($R = 0.05$) as compared to fully reversed ($R = -1$) loadings at the same nominal stress range (compare red filled and empty triangular markers in Figure 2.36). It must be highlighted that two specimens with transverse weld bead and four specimens with inclined bead have been tested under tension-tension VA nominal stresses ($R = 0.05$) with a maximum nominal stress higher the yield stress of the base material ($\sigma_{\max} \sim 460\text{-}520 \text{ MPa} > \sigma_y \sim 355 \text{ MPa}$,

2.3 New experimental fatigue data: non-load-carrying fillet welded joints

see Figure 2.36). Finally, no significant differences were found between test results relevant to the six-block program (VA-DD) and the random sequence (VA-Rand) of VA loads (compare red and blue markers in Figure 2.36).

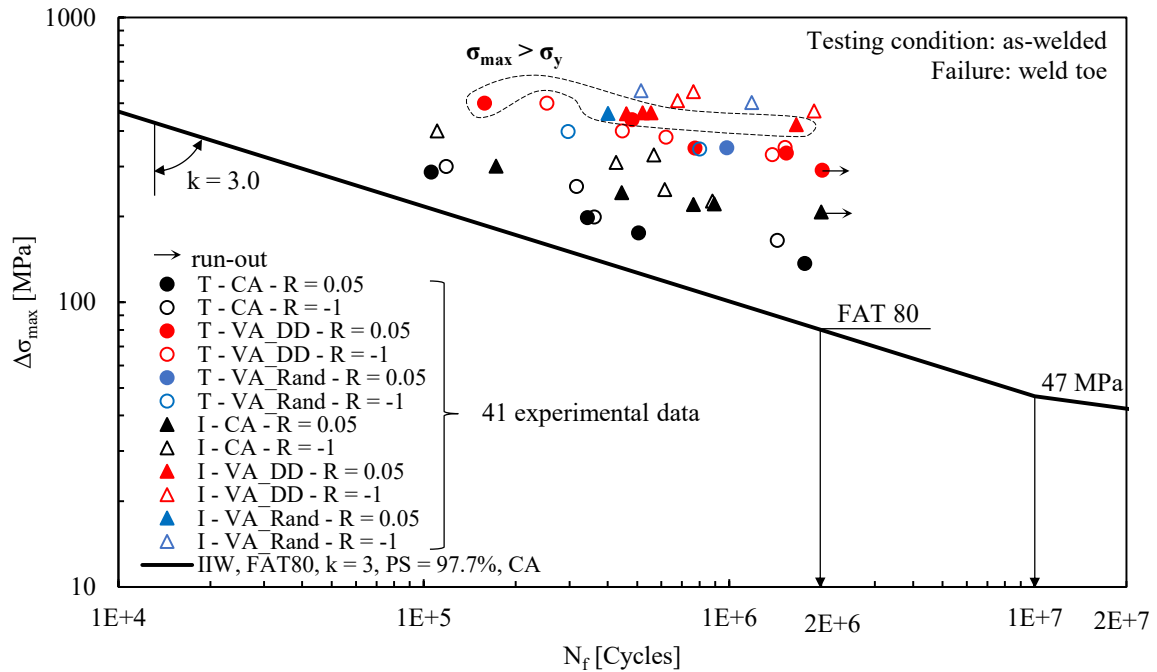


Figure 2.36. Experimental results of fatigue tests performed on non-load-carrying (nlc) fillet-welded joints with double transverse attachments as well as with double 45° inclined attachments. Results are expressed in terms of number of cycles to failure as a function of the maximum applied nominal stress range.

2.3.6. Fatigue strength assessment according to the PSM

The fatigue tested joint geometries have been analysed by adopting the PSM formulation for VA stresses as described above. The nlc fillet-welded joints with double transverse attachment (see model 1 in Table 2.9) have been analysed using a 2D FE model of 4-node plane elements under plane strain conditions (PLANE 182 with K-option 1 set to 3 of Ansys® element library). The weld toe and the weld root were modelled as sharp V-notches ($\rho = 0$, i.e. the worst case) having opening angle $2\alpha = 135^\circ$ and $2\alpha = 0^\circ$, respectively. Only one quarter of the specimen geometry was modelled by taking advantage of the double symmetry and a uniform tensile stress of 1 MPa has been applied to the main plate. The proper finite element size to be adopted

was chosen regardless the weld root, which is not a fatigue critical point, and the mode II stresses at the weld toe, which are not singular, 2α being greater than 102° [84]. Accordingly, the minimum mesh density ratio $a/d = 3$ has been considered, which is the minimum value given by the PSM guidelines [37] for Plane-4 elements (see also Table 2.6) applied at the weld toe under mode I loading. Therefore, being the reference dimension $a = t$ (see Table 2.6) at the weld toe of joints with double transverse attachment [37], the maximum admissible global element size $d \approx t/3 = 4/3 = 1.33$ mm was used as input parameter for the free meshing algorithm in Ansys® (model 1 in Table 2.9). After having solved the FE analysis, the maximum principal stress $\Delta\sigma_{11,\text{peak}}$ has been evaluated at the weld toe instead of the opening peak stress $\Delta\sigma_{\theta\theta,\theta=0,\text{peak}}$ ($\Delta\sigma_{\theta\theta,\theta=0,\text{peak}} \approx \Delta\sigma_{11,\text{peak}}$ under pure mode I stresses), because it is easier to be obtained, the definition of a local coordinate system for stress evaluation being unnecessary. Separately, the coefficients f_{sl} and f_{wl} have been computed thanks to Eq. (1.15) and Eq. (1.4), respectively. More in detail, $c_{wl} = 1$ was assumed in the computation of f_{sl} (Eq. (1.15)) since all joints were tested in the as-welded condition, while $d = 1.33$ mm was input in Eq. (1.4) for the evaluation of f_{wl} . In the present case where pure mode I stresses are involved, the final expression of the equivalent peak stress range $\Delta\sigma_{\text{eq,peak}}$ (Eq. (1.21)) coincides with Eq. (1.12). Regarding the local biaxiality ratio λ (Eq. (1.22)), it resulted null because pure mode I stresses are acting at the weld toe, all shear stress contributions being null.

In the case of nlc fillet-welded joints with double inclined attachment, a 3D FE model has been realized using 10-node tetrahedral elements (SOLID 187 of Ansys® element library), owing to the impossibility of simplifying such geometry in a 2D model. Again, the weld toe and the weld root were shaped as sharp V-notches ($\rho = 0$) having opening angle $2\alpha = 135^\circ$ and $2\alpha = 0^\circ$, respectively, and only half of the joint geometry was modelled exploiting the symmetry in the ZX plane (see model 2 in Table 2.9). The model was fully constrained at one end of the main plate and loaded with a uniform tensile stress of 1 MPa on the opposite side of the main plate. Similarly to the joint with transverse attachment, the weld root was not considered for selecting the proper element size to apply the PSM, the weld toe being the sole critical location. However, in this case the weld toe is subjected to mixed mode I+III local stresses. According to the PSM guidelines relevant to Tetra-10 elements [37] (see also Table 2.6), a/d must be greater than or equal to 1 to analyse the weld toe under mode I stresses, while it has to be greater than or equal to 3 to analyse the weld toe under mode III stresses, a being in any case equal to half the plate thickness, i.e. $t = 4$ mm. Since the most demanding mesh density requirement

comes from mode III, a mesh pattern having element size $d_{global} \approx t/3 = 4/3 = 1.33$ mm has been generated using the free meshing algorithm. However, by adopting multiple local mesh refinements, a more refined mesh with element size $d_{local} = 0.07$ mm has been locally adopted at the outer edges of the weld toe line, i.e. points A and B of model 2 in Table 2.9. In fact, after some preliminary results obtained with a coarser FE mesh, it has been observed that the equivalent peak stress distribution along the weld toe line exhibited a steep gradient at points A and B of the weld toe. Therefore, according to the SED criterion implemented in the PSM, the equivalent peak stresses for steel welded joints must be evaluated in the middle of a 0.28-mm-thick structural volume [88]. As a consequence, the average peak stresses (Eq. (1.7)) must be evaluated at a distance $R_0/2 = 0.14$ mm starting from points A and B along the weld toe line; finally, the local element size $d_{local} = 0.07$ mm was selected for locating the third FE vertex node exactly at 0.14 mm far from points A and B along the weld toe line. After having solved the FE analysis, both the mode I (opening) and mode III (tearing) peak stress distributions, i.e. $\Delta\sigma_{\theta\theta,\theta=0,peak}$ and $\Delta\tau_{\theta z,\theta=0,peak}$, respectively, have been extracted along the weld toe line and the corresponding average peak stresses $\Delta\bar{\sigma}_{\theta\theta,\theta=0,peak}$ and $\Delta\bar{\tau}_{\theta z,\theta=0,peak}$ have been calculated according to Eq. (1.7). FE results are reported in Figure 2.37 as a function of the normalized curvilinear coordinate S/S_{max} running along the weld toe line. Then, the coefficients f_{sI} and f_{s3} have been evaluated for both CA and VA loads entering $c_{wI} = c_{w3} = 1$ into Eqs. (1.15) and (1.17), while the evaluation of coefficients f_{wI} and f_{w3} (Eqs. (1.4) and (1.6)) deserved some attention regarding the element size d to use. The finite element size varied along the weld toe line, because of the mesh refinements applied at points A and B. Therefore, the actual element size d , estimated as the distance between two consecutive vertex nodes along the weld toe line, was used for evaluating the coefficients f_{wI} and f_{w3} (Eqs. (1.4) and (1.6)) at each individual node. Afterwards, the equivalent peak stress ranges $\Delta\sigma_{eq,peak,I}$ and $\Delta\sigma_{eq,peak,III}$ for mode I and mode III, respectively, have been computed thanks to Eq. (1.12) and (1.14) and finally the equivalent peak stress $\Delta\sigma_{eq,peak}$ has been computed by means of Eq. (1.21). The results are reported in Figure 2.37, where the distribution of the equivalent peak stress $\Delta\sigma_{eq,peak}$ is reported versus the normalized curvilinear coordinate S/S_{max} running along the weld toe line for both CA and VA loads in case of a nominal stress range equal to 1 MPa applied to the main plate. Noteworthy, Figure 2.37 shows that the PSM correctly estimates the crack initiation point, the maximum value of the equivalent peak stress range being located at point B, i.e. where fatigue crack initiation experimentally occurred.

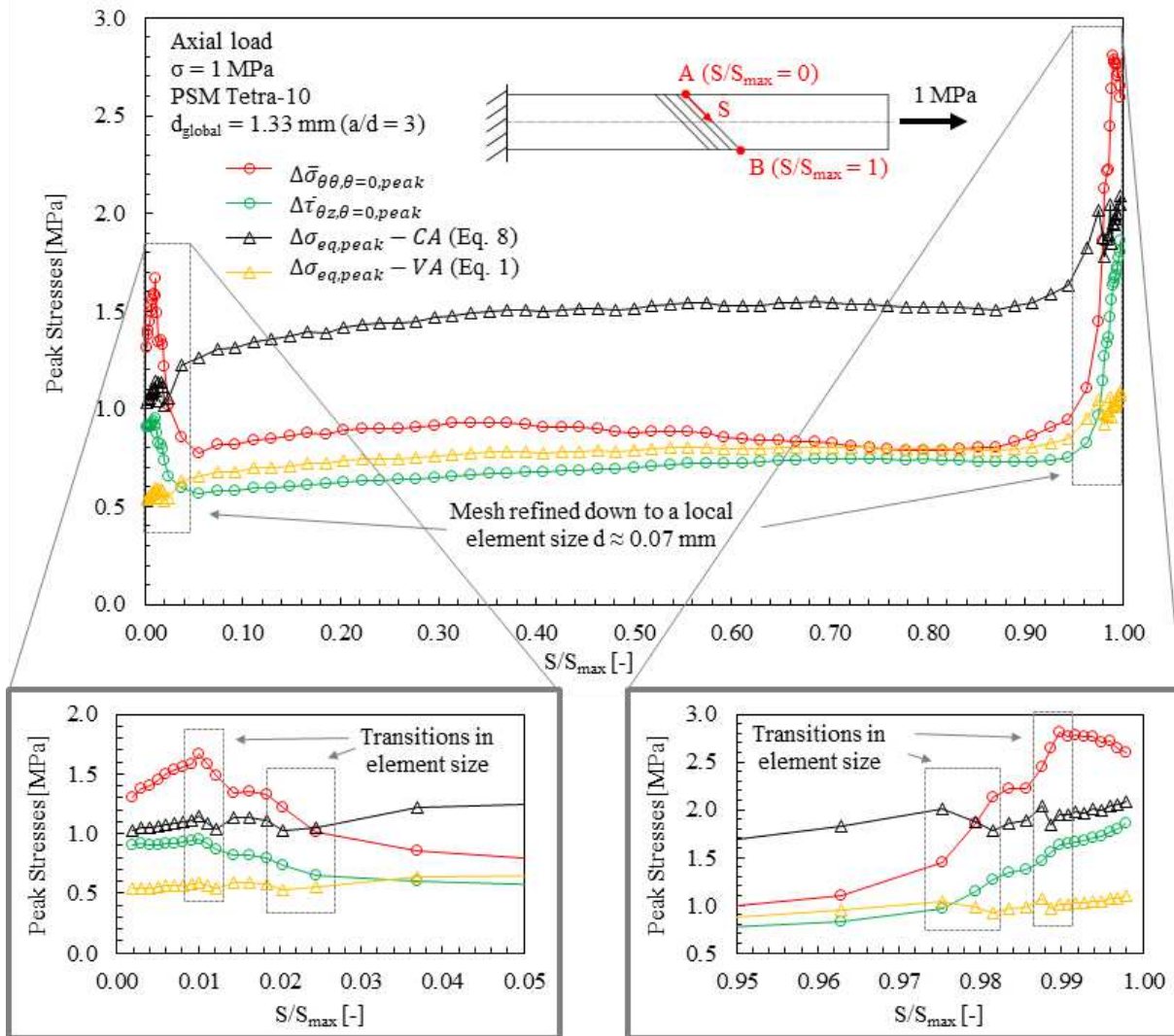


Figure 2.37. Distribution of peak stresses in non-load-carrying (nlc) fillet-welded joints with double 45° inclined attachments (model 2 in Table 2.9) under pure axial loading. Mode I and mode III peak stresses and equivalent peak stresses (Eq. (1.21)) for both CA and VA loadings calculated along the weld toe line by applying the PSM based on Tetra-10 elements.

Differently from the case of the nlc fillet-welded joint with transverse attachments, the existence of mode III stresses resulted in a local biaxiality ratio λ (Eq. (1.22)) greater than zero at all nodes lying on the weld toe line (see Figure 2.38).

2.3 New experimental fatigue data: non-load-carrying fillet welded joints

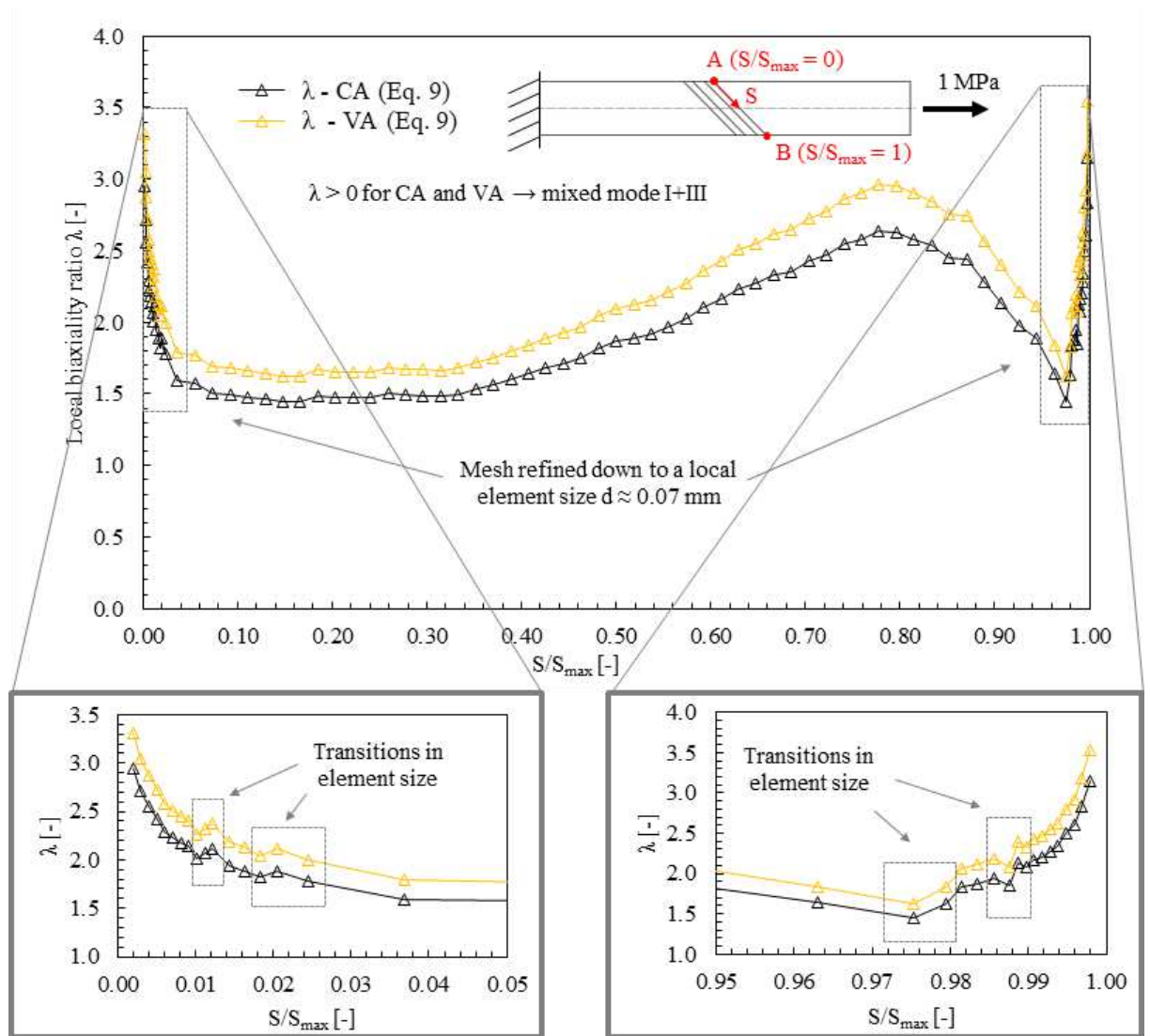


Figure 2.38. Distribution of the local biaxiality ratio λ (Eq. (1.22)) in non-load-carrying (nlc) fillet-welded joints with double 45° inclined attachments (model 2 in Table 2.9) under pure axial loading according to the PSM based on Tetra-10 elements.

2.3.7. Assessment of weld toe and weld root fatigue failures according to the PSM

The PSM-based analyses described above allow to convert the original fatigue data from the maximum nominal stress range ($\Delta\sigma_{\max}$, Figure 2.36) to the equivalent peak stress range $\Delta\sigma_{\text{eq,peak}}$, according to Eq. (1.21) applied where crack initiated in the experimental tests. To do this, the maximum nominal stress ranges applied in the experimental tests have been directly multiplied by the relevant equivalent peak stress range derived in previous section, i.e. from

Eq. (1.21) by giving as inputs the peak stresses calculated from a FE model where $\Delta\sigma = 1$ MPa was applied. Therefore, the linear proportionality between the peak stresses and the applied nominal stress range $\Delta\sigma$ has been exploited, being valid both for transverse and inclined joints under pure axial loading.

Dealing with transverse joints, Figure 2.39 reports the experimental fatigue data expressed in terms of reference number of cycles N_0 (equal to N_f in the present case) as a function of the equivalent peak stress range $\Delta\sigma_{eq,peak}$ along with the PSM-based fatigue design scatter band for steel welded joints relevant to pure mode I loading ($\lambda = 0$). A very good agreement has been observed, since all experimental data fall inside the PSM-based scatter band. It is worth noting that the 2.3% and 97.7% curves of the scatter band imply damages $D = 0.387$ and 2.646 , respectively, if a total damage to failure $D = 1$ is referred to the 50% curve.

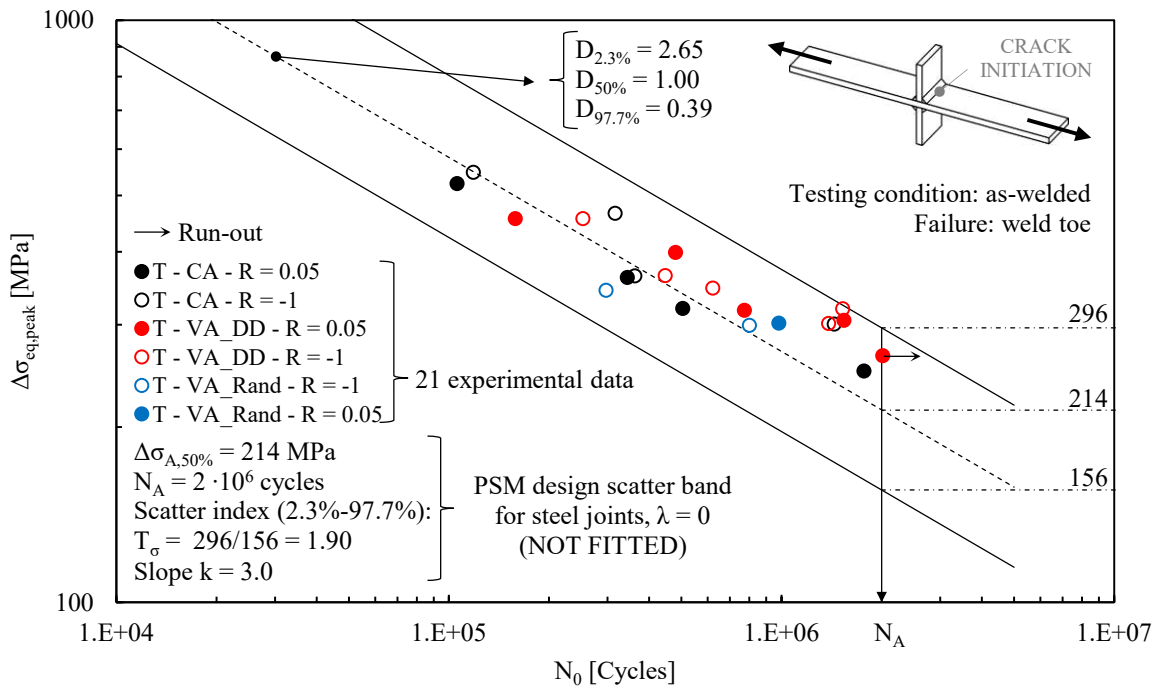


Figure 2.39. Fatigue strength assessment of non-load-carrying (nlc) fillet-welded joints with double transverse attachments (model 1 in Table 2.9) adopting the PSM: comparison between the pure mode I ($\lambda = 0$) PSM design scatter band and experimental data.

Concerning the inclined joints, Figure 2.40 reports the fatigue test data expressed in terms of reference number of cycles N_0 (again equal to N_f) as a function of the equivalent peak stress range $\Delta\sigma_{eq,peak}$ along with the PSM-based fatigue design scatter band for steel welded joints relevant to $\lambda > 0$. Noteworthy, Figure 2.40 shows that, once again, all experimental fatigue data

2.3 New experimental fatigue data: non-load-carrying fillet welded joints

are in good agreement with the theoretical estimations since most of them fall within or slightly on the safe-side of the PSM-based fatigue curves having $k = 5$ and being referred to a 2.3% and 97.7% probability of survival (PS), which correspond to damages $D = 0.202$ and 4.978 , respectively, if a damage $D = 1.0$ is assumed for the curve having 50% probability of survival.

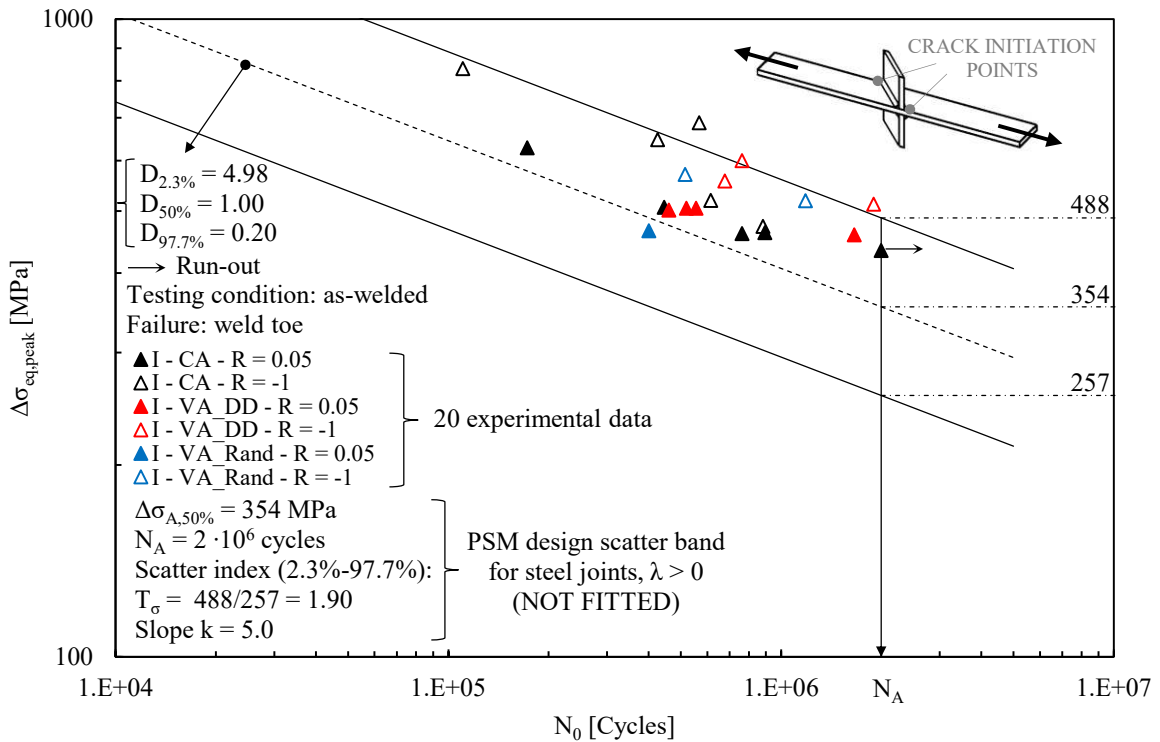


Figure 2.40. Fatigue strength assessment of non-load-carrying (nlc) fillet-welded joints with double 45° inclined attachments (model 2 in Table 2.9) adopting the PSM: comparison between the multiaxial ($\lambda > 0$) PSM design scatter band and experimental data.

2.3.8. Discussion: comparison with IIW and Eurocode 3 fatigue curves

As it has been discussed above, the joints with inclined attachments are subjected to a local in-phase multiaxial stress state even if loaded through a uniaxial testing machine. According to [99], a normal $\Delta\sigma_\perp$ and a shear $\Delta\tau_{//}$ stress components (see Figure 2.2), namely perpendicular and parallel to the weld seam line, respectively, can be derived from the applied nominal stress range $\Delta\sigma$, referred to the cross-sectional area of the main plate (Eq. (1.30)), and the inclination angle β of the attachments with respect to the loading direction:

$$\Delta\sigma_{\perp} = \Delta\sigma \sin^2 \beta \quad (1.33)$$

$$\Delta\tau_{//} = \Delta\sigma \cos \beta \sin \beta \quad (1.34)$$

Existing codes and recommendations [1,2] suggest the adoption of specific procedures for taking into account multiaxial as well as variable amplitude loadings when estimating the fatigue life of welded joints. More in detail, IIW Recommendations [2] suggests the adoption of a Gough-Pollard type equation:

$$\left(\frac{\Delta\sigma_{\perp,eq}}{\Delta\sigma_{R,IIW}} \right)^2 + \left(\frac{\Delta\tau_{//,eq}}{\Delta\tau_{R,IIW}} \right)^2 \leq CV \quad (1.35)$$

wherein $\Delta\sigma_{R,IIW}$ and $\Delta\tau_{R,IIW}$ are the modified FAT classes of the structural detail under normal and shear stresses, respectively, CV is a coefficient called comparison value which is equal to 1.0 for proportional loadings and 0.5 for non-proportional loadings, while $\Delta\sigma_{\perp,eq}$ and $\Delta\tau_{//,eq}$ are equivalent constant amplitude stress ranges evaluated according to the modified Palmgren-Miner rule proposed by Haibach [8]. Dealing with the contribution of normal stress components, when the applied stress ranges $\Delta\sigma_{\perp,i}$ are all above the knee point ($N = 10^7$ cycles, $\Delta\sigma_{\perp} = 47$ MPa), as for the joints tested in the present work, the following expression can be used for evaluating $\Delta\sigma_{\perp,eq}$:

$$\Delta\sigma_{\perp,eq} = \sqrt[m]{\left(\frac{1}{D_{IIW}} \right) \frac{\sum_i n_i \Delta\sigma_{\perp,i}^m}{\sum_i n_i}} \quad (1.36)$$

where n_i is the number of cycles corresponding to the stress range $\Delta\sigma_{\perp,i}$, $m = 3$ is the inverse slope of the fatigue curve above the knee point, and D_{IIW} is the specified Miner sum whose value is equal to 1. The same expression is valid also for computing the equivalent constant amplitude shear stress $\Delta\tau_{//,eq}$ apart from the inverse slope which is $m = 5$, and the knee point, which is located at $N = 10^8$ cycles for $\Delta\tau_{//} = 37$ MPa. By revising Eq. (1.35), an equivalent constant amplitude uniaxial normal stress $\Delta\sigma_{eq,IIW}$ can be expressed as follow [100]:

$$\Delta\sigma_{eq,IIW} = \frac{1}{\sqrt{CV}} \sqrt{\Delta\sigma_{\perp,eq}^2 + \left(\frac{\Delta\sigma_{R,IIW}}{\Delta\tau_{R,IIW}}\right)^2 \Delta\tau_{\parallel,eq}^2} \quad (1.37)$$

All fatigue test data (Table 2.12) have been converted from nominal stress range $\Delta\sigma$ to $\Delta\sigma_{eq,IIW}$ (Eq. (1.37)) and reported in Figure 2.41 along with the uniaxial FAT80 fatigue curve for normal stress ($\Delta\sigma_{R,IIW} = 80$ MPa) which correspond to a survival probability PS = 97.7% [2] (black solid line in Figure 2.41).

The first aspect that deserves to be investigated is the capability of the proposed method to describe the average behaviour of the experimental data. As depicted in Figure 2.41, all experimental fatigue results are in satisfactory agreement with the predictions based on IIW Recommendations, although they all fall largely on the safe side with respect to the design curve, which is referred to a 97.7% probability of survival. A more appropriate comparison can be made with the fatigue resistance curve relevant to a survival probability PS = 50%. The latter being not available in the IIW recommendations [2], it can be estimated by assuming a scatter index $T_{\sigma} = 1.85$ referred to the 2.3–97.7% survival probabilities which corresponds to the intrinsic scatter of single test series tested under CA loadings according to Haibach [9,68] and Sonsino [17,69]. This way the PS = 50% fatigue resistance curve has been obtained scaling that relevant to PS = 97.7% by a factor $\sqrt{1.85}$ (FAT80: $80 \text{ MPa} \cdot \sqrt{1.85} = 109 \text{ MPa}$) and reported in Figure 2.41 as dashed black line. Obviously, fatigue resistance curve with PS = 50% better describes the mean behaviour of experimental data if compared to that having PS = 97.7% (compare experimental data with dashed and solid black lines in Figure 2.41). Nevertheless, this estimate is still slightly on the safety side if compared to that offered by the PSM (Figure 2.39 and Figure 2.40).

Another aspect that deserves to be investigated is the capability of the method to summarize the experimental data in a narrow scatter band. Accordingly, all experimental data reported in Figure 2.41 have been statistically analysed and fitted according to BS ISO 12107:2012 [101]. The obtained scatter band referred to PS = 2.3% - 97.7% (reported as green lines in Figure 2.41) exhibits a scatter index $T_{\sigma} = 2.13$, greater than that of the PSM design scatter bands (Figure 2.39 and Figure 2.40) which is equal to $T_{\sigma} = 1.90$ in very good agreement with the intrinsic scatter according to Haibach [9,68] and Sonsino [17,69].

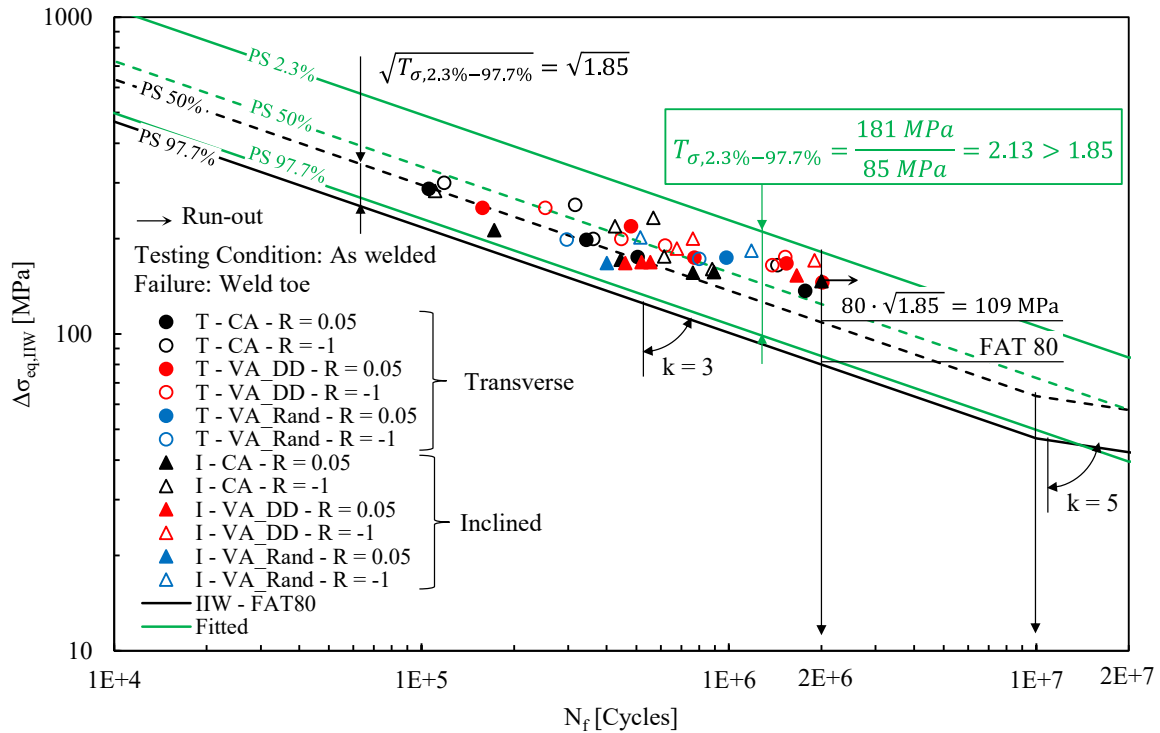


Figure 2.41. Experimental fatigue data re-analyses according to the procedure posed by IIW [2] (Eq. (1.37)). Solid and dashed black lines are not fitted and represent the FAT80 fatigue resistance curves referred to PS = 97.7% and 50%, respectively. Green lines represent the scatter band fitted on experimental data according to [101].

On the other hand, to assess the fatigue life of joints subjected to combined normal and shear stresses, the Eurocode 3 (EC3) suggests a relationship slightly different from Eq. (1.35). More in detail, it proposes to evaluate separately the damages caused by equivalent constant amplitude normal and shear stresses according to Miner's rule and then to simply add them:

$$\left(\frac{\Delta\sigma_{\perp,eq}}{\Delta\sigma_{R,EC3}} \right)^3 + \left(\frac{\Delta\tau_{\parallel,eq}}{\Delta\tau_{R,EC3}} \right)^5 \leq D_{EC3} \quad (1.38)$$

where $\Delta\sigma_{R,EC3}$ and $\Delta\tau_{R,EC3}$ are the uniaxial normal and shear modified fatigue strengths of the considered detail, D_{EC3} is the damage sum which is equal to 1.0, while $\Delta\sigma_{\perp,eq}$ and $\Delta\tau_{\parallel,eq}$ are equivalent constant amplitude stresses. The latter must be evaluated from Eq. (1.36) substituting D_{IIW} with D_{EC3} , provided that all applied stress ranges are above the knee point which corresponds to $N = 5 \cdot 10^6$ cycles and $\Delta\sigma_{\perp} = 59$ MPa for normal stresses and $N = 10^8$ cycles and

2.3 New experimental fatigue data: non-load-carrying fillet welded joints

$\Delta\tau_{//} = 37$ MPa for shear stresses. As above, starting from Eq. (1.38) it is possible to define an equivalent uniaxial constant amplitude normal stress [100]:

$$\Delta\sigma_{eq,EC3} = \sqrt[3]{\Delta\sigma_{\perp,eq}^3 + \left(\frac{\Delta\sigma_{R,EC3}}{\Delta\tau_{R,EC3}}\right)^3 \Delta\tau_{//,eq}^3} \quad (1.39)$$

All fatigue data (Table 2.12) have been converted from nominal stress range $\Delta\sigma$ to $\Delta\sigma_{eq,EC3}$ (Eq. (1.39)) and reported in Figure 2.42 together with the relevant uniaxial normal fatigue curve of the considered detail ($\Delta\sigma_{R,EC3} = 80$ MPa) which correspond to a survival probability PS = 97.7% [1] black solid line in Figure 2.42).

Noteworthy, the procedure according to EC3 gave the same results as that proposed by IIW in the case of joints with transverse attachments subjected to a uniaxial stress state, i.e. the equivalent stresses proposed by EC3 (Eq. (1.39)) and that by IIW (Eq. (1.37)) collapsed into the same expression. Moreover, also in this case experimental data are in satisfactory agreement with the predictions based on EC3, although they all fall largely on the safe side with respect to the design curve, which is referred to a 97.7% probability of survival. Once again, to perform a more appropriate comparison, the fatigue resistance curve relevant to a survival probability PS = 50% has been estimated by assuming a scatter index $T_{\sigma} = 1.85$, the latter being not available in the Eurocode 3 [1]. Accordingly, the PS = 50% fatigue resistance curve has been evaluated scaling that relevant to PS = 97.7% by a factor $\sqrt{1.85}$ ($80 \text{ MPa} \cdot \sqrt{1.85} = 109 \text{ MPa}$) and reported in Figure 2.42 as dashed black line. Similar to what obtained for IIW, fatigue resistance curve with PS = 50% better describes the mean behaviour of experimental data if compared to that having PS = 97.7% (compare experimental data with dashed and solid black lines in Figure 2.42) but the estimate is still remains on the safety side, confirming the PSM method gives a better description of the average behaviour (Figure 2.39 and Figure 2.40).

Finally, to investigate the capability of the method to summarize the experimental data in a narrow scatter band, all experimental data reported have been statistically analysed and fitted according to BS ISO 12107:2012 [101]. The obtained scatter band referred to PS = 2.3% - 97.7% (reported as green lines in Figure 2.42) exhibits a scatter index $T_{\sigma} = 2.31$, greater than that exhibited by the analysis according to the IIW ($T_{\sigma,IIW} = 2.13$, see Figure 2.41), and greater than that of the PSM ($T_{\sigma,PSM} = 1.90$, see Figure 2.39 and Figure 2.40), confirming once again

the PSM offers not only a better description of the average behaviour of the experimental data, but also gives the best summary in terms of scatter index.

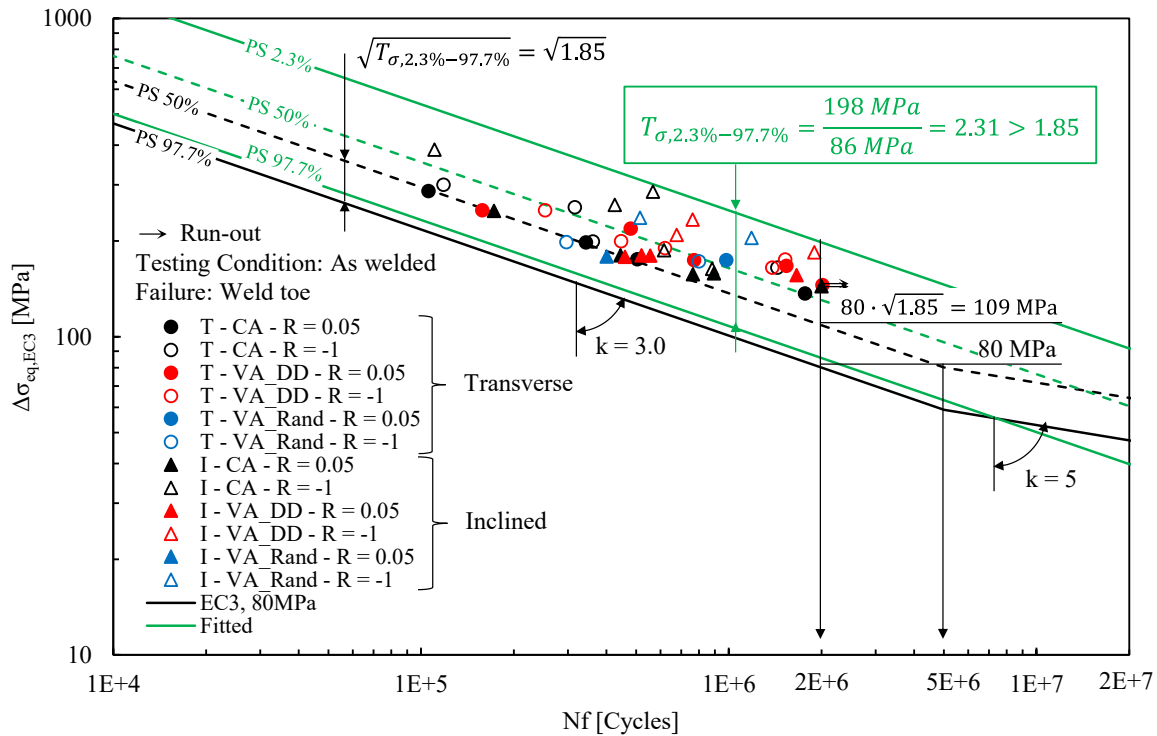


Figure 2.42. Experimental fatigue data re-analyses according to the procedure posed by EC3 [1] (Eq. (1.39)). Solid and dashed black lines are not fitted and represent the FAT80 fatigue resistance curves referred to PS = 97.7% and 50%, respectively. Green lines represent the scatter band fitted on experimental data according to [101].

2.3.9. Discussion: effect of angular misalignments

The angular misalignments (γ in Figure 2.43) were measured in all joints both with transverse and inclined attachments. To do so, each specimen was clamped at one end of the main plate and the vertical positions (Y-coordinate in Figure 2.43) of four points located at a specific axial position on the specimen main plate (points O, A, A', and O' in Figure 2.43) were measured adopting a centesimal dial gauge. The chosen points were located symmetrically with respect to the stiffeners and their vertical position was measured after zeroing the dial gauge at the point O ($Y_O = 0 \text{ mm}$), i.e., the nearest to the clamped side. The measurements have been

2.3 New experimental fatigue data: non-load-carrying fillet welded joints

performed on all test specimens with transverse attachments and inclined attachments, respectively. As a result, it was possible to evaluate their angular misalignments $\gamma = [\arctan((Y_o - Y_A)/80) - \arctan((Y_o - Y_A)/80)]$, which values range between 0.04 and 1.09 degrees for the specimens with transverse attachments and 0.07 and 1.30 degrees for the joints with inclined attachments.

After that, the effect of the secondary bending generated by the misalignments, when the specimens are loaded under nominal pure axial loading, has been investigated by performing strain gauge measurements. Therefore, two specimens, namely T05 and I05, have been chosen among the most misaligned joints with transverse and inclined attachments, respectively, and they have been instrumented with four 3-mm-long grid strain gauges located on the surface of the main plate, where the stress state was theoretically uniform and equal to the nominal applied stress (Eq. (1.30)), on opposite sides with respect to the bending neutral axis of the main plate (1-2 and 3-4 in Figure 2.43). Then, each instrumented specimen has been tested by applying stepwise increasing axial static loads from 0 kN up to 120 kN, which on one side is close to the maximum load applied during the experimental fatigue tests, while on the other side it keeps the nominal stress below yielding, and then unloading to 0 kN, while measuring the corresponding strain gauge signals. The loads have been applied through a servo-hydraulic MFL axial testing machine having a ± 250 kN load capacity and equipped with an MTS TestStar IIIm digital controller, while the IMC Cronos PL-2 data acquisition unit has been adopted to measure the signals from the strain gauges, which have been connected adopting a quarter bridge configuration.

As a result, both the axial ($\varepsilon_{\text{axial},i-j} = (\varepsilon_i + \varepsilon_j)/2$) and bending ($\varepsilon_{\text{bending},i-j} = (\varepsilon_i - \varepsilon_j)/2$) strain components have been measured in two sections (1-2 and 3-4 in Figure 2.43) along the main plate. After that, the axial ($\sigma_{\text{axial},1-2}$, $\sigma_{\text{axial},3-4}$) and bending stress components ($\sigma_{\text{bending},1-2}$, $\sigma_{\text{bending},3-4}$) have been computed by multiplying the strains for the material elastic modulus $E = 206000$ MPa and they have been reported in Figure 2.43 along with the theoretical values of axial stress ($\sigma_{\text{axial,theoretical}}$, Eq. (1.30)) as a function of the applied load level. As expected, the measured axial stresses ($\sigma_{\text{axial},1-2}$, $\sigma_{\text{axial},3-4}$) are in good agreement with the theoretical one ($\sigma_{\text{axial,theoretical}}$) for both specimen geometries. On the other hand, Figure 2.43 shows for both joint geometries and both analyzed sections of the main plate (1-2 and 3-4), that a bending stress component equal to about 40 MPa and 30 MPa for T05 and I05 specimens, respectively, is present even if no axial load is applied to the specimens ($\sigma_{\text{bending},1-2} > 0$ and $\sigma_{\text{bending},3-4} > 0$ when $F = 0$). More

in detail, the bending stress component increases slightly as the applied force increases, leading to a bending stress range ($\Delta\sigma_{\text{bending}}$) of 7 MPa and 5 MPa for specimens T05 and I05, respectively, when the applied load F varies from 0 to 120 kN, while under the same applied load range, the axial stress range ($\Delta\sigma_{\text{axial}}$) results 300 MPa and 316 MPa, respectively.

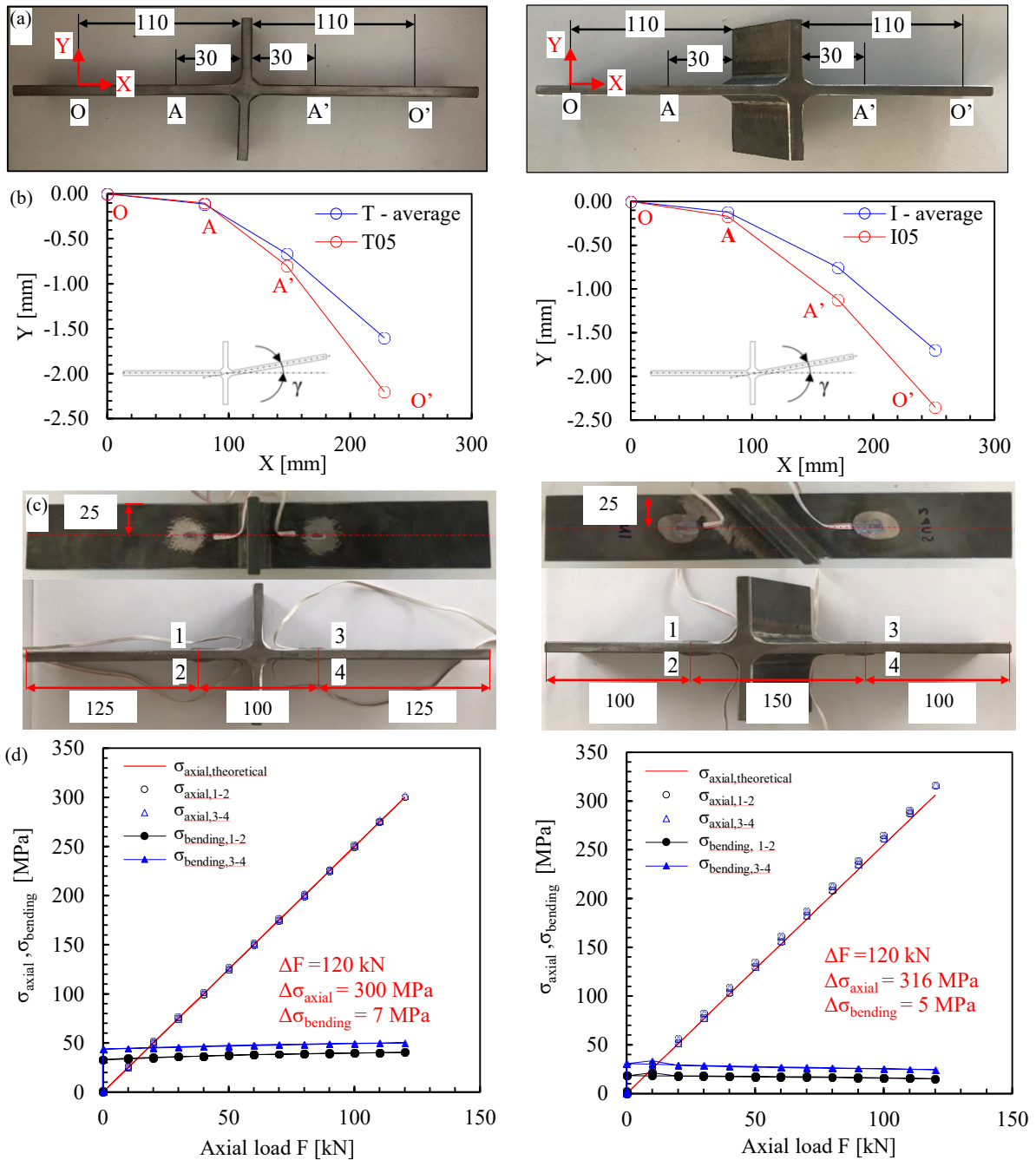


Figure 2.43. Measurement of angular misalignments. (a) Location of the measurement points for determining the angular misalignment γ . (b) Measured vertical positions Y for samples adopted for strain gauge measurements and average values. (c) Position of the strain gauges. (d) Results of the strain gauge measurements.

2.3 New experimental fatigue data: non-load-carrying fillet welded joints

Accordingly, the bending stress ranges being the 2.3% and 1.6% of the axial ones, respectively, it has been concluded that the secondary bending generates a stress component having negligible range under cyclic loading; while it keeps almost constant, therefore it represents a mean stress component. According to International Standards and Recommendations [1,2], the mean stress effect introduced by the bending stresses has been neglected because all joints were tested in the as-welded conditions.

2.3.10. Discussion: residual stresses

Residual stresses have been measured through the X-ray diffraction method applied on one joint with transverse attachments and another one with inclined attachments. Figure 2.44 shows the measurement paths, namely an outer, a mid-plane and one intermediate between the previous ones, all originating from the weld toe, along which the residual stress component σ_{xx} has been measured. The adopted parameters of the X-ray device have been listed in Table 2.11.

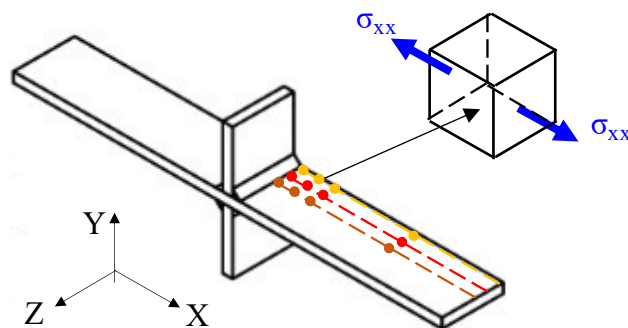


Figure 2.44. Residual stress components and paths for residual stress measurement.

Figure 2.45 reports the measured residual stresses σ_{xx} as a function of the distance from the weld toe. In general, the residual stress components measured at weld toe, i.e. at a distance equal to 0 mm, show no clear trend and have been obtained with low confidence level due to difficulties in the measurement phase. They range from -30 MPa and +30MPa in the welded joint with transverse attachments while from -40 MPa to +155 MPa in the joint with inclined attachments. Differently, the other measures, more reliable due to a higher confidence level,

show that in most cases high tensile residual stresses are present in the material region within a distance of 2 mm and 4 mm from the weld toe, the only exception being the outer path in the joint with transverse attachments, where compressive residual stresses have been measured. More in detail, tensile residual stresses are higher in the joint with inclined attachments, the maximum being 250 MPa, as compared to the joint with transverse attachments, for which the maximum results 105 MPa. Furthermore, far from the weld toe residual stresses become compressive in the case of joint with transverse attachments and reduced but still tensile in the case of joint with inclined attachments.

Table 2.11. Residual stress measurement by the X-ray diffraction method: adopted device and experimental parameters.

Surface preparation	Removal of oxide layer using HCl
X-ray device	GNR Spider X
Radiation	Cr-K α with Vanadium filter, penetration depth 15 μ m
Collimator size	1 mm
Method	$\sin^2 \psi$ – method
Measurement paths	see Figure 2.44
Residual stress components	σ_{xx} (see Figure 2.44)
Acquisition time	500 s/ ψ angle
ψ – angles	7 ψ -angles: $-35^\circ < \psi < 35^\circ$
Elastic constants	E = 206 GPa, $\nu = 0.3$

The obtained results appear to be in agreement with the assumption that as-welded joints are typically subjected to high tensile residual stresses and, therefore, they are typically insensitive to mean stress effect when fatigue tested [1,2,102,103]. However, it is worth noting that the measured residual stress state is the original one, while a significant relaxation of residual stresses after cyclic loading is typically observed [58,59], therefore, the actual residual stress state and its stability during cyclic loading is not known.

2.3 New experimental fatigue data: non-load-carrying fillet welded joints

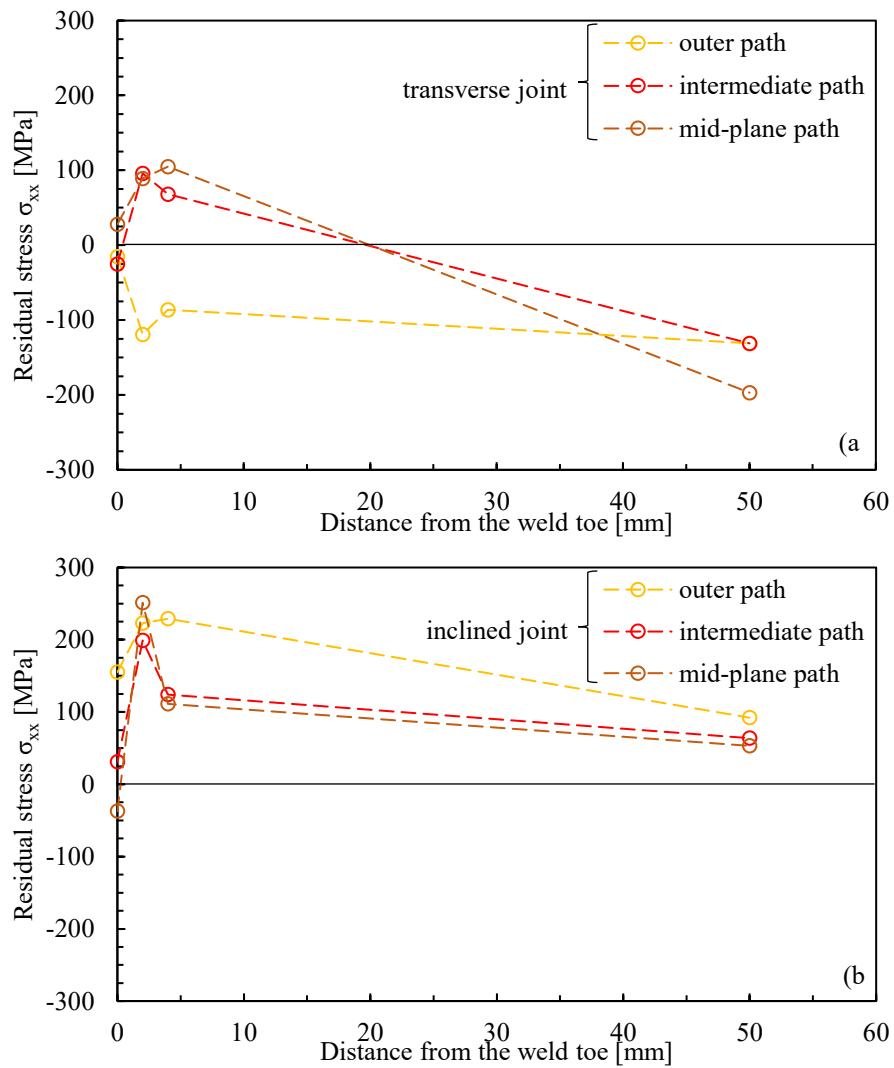


Figure 2.45. Residual stresses along the path shown in Figure 2.44 by the X-ray diffraction method in (a) transverse joint and (b) inclined joint. Dashed lines have been added between measured values only to increase readability, however they do not represent the actual trend of residual stresses.

Table 2.12. Summary of fatigue test results and parameters to apply the PSM.

Test							FE Model			Results						
Geom. [^]	Spectrum ^o	R	Code	γ	$\Delta\sigma_{\max}$	N_f	Type	f_{s1}	f_{w1}	$\Delta\sigma_I^*$	f_{s3}	f_{w3}	$\Delta\tau_{III}^*$	$\Delta\sigma_{eq,peak}$	λ	
[-]	[-]	[-]		[deg]	[MPa]	[cycles]	[-]	[-]	[-]	[MPa]	[-]	[-]	[MPa]	[MPa]	[-]	
T	CA	0.05	T01	1.1	287	$1.06 \cdot 10^5$	2D	1.000	1.166	449	-	-	-	524	0	
			T02	1.0	137	$1.77 \cdot 10^6$		1.000	1.166	214				250	0	
			T03	1.1	198	$3.44 \cdot 10^5$		1.000	1.166	310				362	0	
			T04	0.9	175	$5.05 \cdot 10^5$		1.000	1.166	274				320	0	
		-1	T08	0.9	199	$3.62 \cdot 10^5$		2D	1.000	1.166	312	-	-	-	364	0
			T09	0.9	165	$1.44 \cdot 10^6$			1.000	1.166	258				301	0
			T17	0.2	255	$3.16 \cdot 10^5$			1.000	1.166	399				466	0
			T18	0.4	300	$1.18 \cdot 10^5$			1.000	1.166	470				548	0
	VA-DD	0.05	T06	1.0	291	$2.01 \cdot 10^6$	2D	0.500	1.166	455	-	-	-	265	0	
			T11	0.5	334	$1.54 \cdot 10^6$		0.500	1.166	523				305	0	
			T12	0.4	348	$7.72 \cdot 10^5$		0.500	1.166	545				318	0	
			T13	0.5	437	$4.80 \cdot 10^5$		0.500	1.166	685				399	0	
			T14	0.1	500	$1.58 \cdot 10^5$		0.500	1.166	783				456	0	
		-1	T10	0.3	350	$1.53 \cdot 10^6$	2D	0.500	1.166	548	-	-	-	319	0	
			T15	0.6	399	$4.46 \cdot 10^5$		0.500	1.166	625				364	0	
			T16	0.0	500	$2.53 \cdot 10^5$		0.500	1.166	783				456	0	
			T19	0.3	330	$1.38 \cdot 10^6$		0.500	1.166	517				301	0	
			T23	0.6	380	$6.21 \cdot 10^5$		0.500	1.166	595				347	0	
	VA-Rand	0.05	T22	0.5	349	$9.82 \cdot 10^5$	2D	0.474	1.166	546	-	-	-	302	0	
			T20			$2.96 \cdot 10^5$		0.474	1.166	622	-	-	-	344	0	
T21				$8.00 \cdot 10^5$	0.474	1.166		541				299	0			
I	CA	0.05	I01	1.3	300	$1.73 \cdot 10^5$	3D	1.000	0.396	779	1.000	0.979	547	628	3.14	
			I02	0.6	242	$4.45 \cdot 10^5$		1.000	0.396	629	1.000	0.979	441	507	3.14	
			I04	0.7	221	$7.64 \cdot 10^5$		1.000	0.396	572	1.000	0.979	402	461	3.14	
			I06	0.2	208	$2.00 \cdot 10^6$		1.000	0.396	538	1.000	0.979	378	434	3.14	
			I07	0.1	221	$8.94 \cdot 10^5$		1.000	0.396	574	1.000	0.979	403	463	3.14	

2.3 New experimental fatigue data: non-load-carrying fillet welded joints

	-1	I03	0.3	309	$4.26 \cdot 10^5$	3D	1.000	0.396	802	1.000	0.979	575	647	3.14
		I08	0.7	329	$5.67 \cdot 10^5$		1.000	0.396	853	1.000	0.979	612	687	3.14
		I09	0.9	248	$6.16 \cdot 10^5$		1.000	0.396	645	1.000	0.979	462	520	3.14
		I14	0.3	226	$8.82 \cdot 10^5$		1.000	0.396	587	1.000	0.979	421	473	3.14
		I17	0.6	400	$1.11 \cdot 10^5$		1.000	0.396	1038	1.000	0.979	744	836	3.14
VA-DD	0.05	I10	0.9	231	$5.20 \cdot 10^5$	3D	0.500	0.396	1200	0.530	0.979	860	505	3.53
		I11	0.6	210	$1.66 \cdot 10^6$		0.500	0.396	1089	0.530	0.979	781	459	3.53
		I12	0.6	230	$4.60 \cdot 10^5$		0.500	0.396	1191	0.530	0.979	854	502	3.53
		I13	0.8	231	$5.55 \cdot 10^5$		0.500	0.396	1199	0.530	0.979	859	505	3.53
	-1	I15	0.6	469	$1.90 \cdot 10^6$	3D	0.500	0.396	1217	0.530	0.979	872	513	3.53
		I16	0.6	549	$7.63 \cdot 10^5$		0.500	0.396	1424	0.530	0.979	1020	600	3.53
		I19	0.2	510	$6.78 \cdot 10^5$		0.500	0.396	1323	0.530	0.979	948	557	3.53
VA-Rand	0.05	I23	0.3	460	$4.01 \cdot 10^5$	3D	0.474	0.397	1174	0.499	0.981	837	466	3.44
	-1	I20	0.6	503	$1.18 \cdot 10^6$	3D	0.474	0.396	1305	0.499	0.979	936	519	3.48
		I21	0.8	554	$5.15 \cdot 10^5$		0.474	0.396	1436	0.499	0.979	1029	571	3.48

^ Geometry: T = transverse, I = inclined

° Details are reported in Figure 2.35

° Experimental fatigue strength at $2 \cdot 10^6$ cycles

° Scatter index evaluated as the ratio between fatigue strengths (at $2 \cdot 10^6$ cycles) referred to 2.3% and 97.7% survival probability, respectively.

* $\Delta\sigma_I = \Delta\sigma_{\theta\theta, \theta=0, \text{peak}}$ and $\Delta\tau_{III} = \Delta\tau_{\theta z, \theta=0, \text{peak}}$, $\Delta\bar{\sigma}_{\theta\theta, \theta=0, \text{peak}}$ and $\Delta\bar{\tau}_{\theta z, \theta=0, \text{peak}}$ have been reported in the case of 3D FE models meshed with 10-node tetra elements. All values have been first calculated from FE models where 1 MPa was applied, then they have been reported here multiplied by the maximum nominal stress range $\Delta\sigma_{\text{max}}$.

2.4. Conclusions

The Peak Stress Method (PSM) represent an engineering approach for the fatigue design of welded structures. It allows for a quick and effective estimate of the Notch Stress Intensity Factors (NSIFs) at the weld toe and weld root, idealised and modelled as sharp notches having null tip radius. Basically, the PSM takes advantage of the singular, linear elastic, opening, sliding, and tearing peak stresses evaluated at the notch tip using coarse free mesh patterns to estimate the mode I, II, and III NSIF-terms, respectively. A PSM-based design stress called equivalent peak stress, can be defined as a function of the relevant peak stresses by adopting the averaged Strain Energy Density (SED) as a fatigue strength criterion. In previous papers, the equivalent peak stress has been shown to be a fatigue relevant parameter, capable of assessing the fatigue lifetime of steel arc-welded joints subjected to constant amplitude (CA) uniaxial as well as multiaxial loading conditions.

In the present chapter, a new theoretical formulation of the PSM has been presented discussed in order to account also for uniaxial as well as in-phase and out-of-phase multiaxial variable amplitude fatigue loadings. This has been done combining the constant amplitude formulation of the PSM with the Palmgren-Miner's linear damage rule (LDR) to account for cumulative damage.

Then, the proposed method has been validated against a large bulk of VA fatigue data taken from the literature: approximately 900 experimental data, consisting of 580 CA and 320 VA, grouped into 71 CA and 70 VA test series have been considered all in all. For 4 of the considered 70 VA test series, it has been observed that the PSM-based theoretical predictions were on the unsafe side: in three of four cases extremely low values of fatigue damage to failure were noted (D as low as 0.06) under VA loading with overload spectrum along with lack of information on misalignments-induced secondary bending stresses reported in the original papers, while in the other case it was due to a particularly pronounced detrimental effect of out-of-phase loading, which is not taken into account by the PSM. However, several experimental results generated from steel welded joints under multiaxial loadings show that the effect of the phase shift is distinguishable, but not that remarkable. On the other hand, for 18 of the considered 70 VA test series, the PSM-based theoretical predictions were on the safe side.

2.4 Conclusions

Only in one case, an extreme degree of conservatism was observed and attributed to the poor accuracy of the Palmgren-Miner's LDR in treating the considered loading spectrum, providing values of damage to failure up to 30. Concerning the remaining test series, the PSM-based theoretical estimations resulted in good agreement with the experimental fatigue results. All in all, 671 of the 900 experimental data considered collapsed inside the design scatter bands of the PSM, while 878 among 900 data fell on the safe side of the 97.7% survival probability curve.

Moreover, fatigue tests under both constant and variable amplitude axial loading have been performed on non-load-carrying (nlc) fillet-welded joints, both with double transverse attachment and with double 45° inclined attachments made of S355J2+N structural steel. The latter geometry being chosen as it allows to investigate the effect of a local in-phase mixed mode I+III stress state using a uniaxial testing machine. Two different nominal load ratios, i.e. $R = -1$ and $R = 0.05$, have been adopted. In the case of VA loads, a Gaussian spectrum has been applied either as a six-block program or as a random sequence. Results generated under CA loadings showed that joints with inclined attachments exhibit longer fatigue lives as compared to joints with transverse attachments, for the same applied nominal stress range. Noteworthy, a similar conclusion has been drawn for VA loads. The effects of misalignments and welding residual stresses have been considered and discussed, even if their effects on the fatigue life of the tested joints appeared to be negligible.

Finally, all fatigue data have been re-analysed by adopting the new formulation of Peak Stress Method (PSM). Once again, its effectiveness has been proved not only because it accurately predicted the fatigue crack initiation point and properly described the average behaviour of the experimental data, but also because it perfectly summarized the experimental fatigue results within the PSM-based fatigue design scatter bands for steel welded joints, not fitted on the experimental data. For comparison purposes, the procedures proposed by Eurocode 3 and IIW Recommendations have been also applied. In conclusion, the PSM has proved to be the most accurate and effective criterion in designing steel welded joints against constant as well as variable amplitude multiaxial fatigue loadings.

2.5. References

- [1] EN. Eurocode 3: Design of steel structures – part 1–9: Fatigue 2005.
 - [2] Hobbacher AF. Recommendations for Fatigue Design of Welded Joints and Components. International Institute of Welding - IIW Collection. Springer International Publishing; 2016. <https://doi.org/10.1007/978-3-319-23757-2>.
 - [3] Palmgren AG. Die Lebensdauer von Kugellagern. Zeitschrift Des Vereines Dtsch Ingenieure 1924;68:339–41.
 - [4] Miner MA. Cumulative damage in fatigue. J Appl Mech 1945;12:159–64.
 - [5] Fatemi A, Yang L. Cumulative fatigue damage and life prediction theories: A survey of the state of the art for homogeneous materials. Int J Fatigue 1998;20:9–34. [https://doi.org/10.1016/S0142-1123\(97\)00081-9](https://doi.org/10.1016/S0142-1123(97)00081-9).
 - [6] Yang L, Fatemi A. Cumulative Fatigue Damage Mechanisms and Quantifying Parameters: A Literature Review. J Test Eval 1998;26:89–100. <https://doi.org/10.1520/jte11978j>.
 - [7] Hobbacher A. Cumulative Fatigue by Fracture Mechanics. J Appl Mech 1977;44:769–71. <https://doi.org/10.1115/1.3424173>.
 - [8] Haibach E. Modified linear damage accumulation hypothesis considering the decline of the fatigue limit due to progressive damage (transl.). Lab Für Betriebsfestigkeit, Techn Mitt TM 50/70 1970.
 - [9] Haibach E. Betriebsfestigkeit. Verfahren und Daten zur Bauteilberechnung (German). 3rd ed. Berlin: Springer-Verlag; 2006.
 - [10] Schijve J. Fatigue of Structures and Materials. Springer Netherlands; 2008. https://doi.org/10.1007/978-1-4020-6808-9_1.
 - [11] Gurney T. Cumulative Damage of Welded Joints. Woodhead Publishing; 2006.
 - [12] Schütz W. The prediction of fatigue life in the crack initiation and propagation stages—a state of the art survey. Eng Fract Mech 1979;11:405–21. [https://doi.org/10.1016/0013-7944\(79\)90015-8](https://doi.org/10.1016/0013-7944(79)90015-8).
 - [13] Radaj D, Sonsino CM, Fricke W. Fatigue assessment of welded joints by local approaches. 2nd ed. Cambridge, England: Woodhead Publishing; 2006.
 - [14] Radaj D, Vormwald M. Advanced Methods of Fatigue Assessment. 1st ed. Berlin:
-

- Springer Berlin Heidelberg; 2013. <https://doi.org/10.1007/978-3-642-30740-9>.
- [15] Fricke W. IIW recommendations for the fatigue assessment of welded structures by notch stress analysis: IIW-2006-09. Woodhead Pub; 2012.
- [16] Radaj D, Sonsino CM. Fatigue assessment of welded joints by local approaches. Cambridge: Abington Publishing; 1998.
- [17] Sonsino CM. Multiaxial fatigue of welded joints under in-phase and out-of-phase local strains and stresses. *Int J Fatigue* 1995;17:55–70. [https://doi.org/10.1016/0142-1123\(95\)93051-3](https://doi.org/10.1016/0142-1123(95)93051-3).
- [18] Jakubczak H, Glinka G. Fatigue analysis of manufacturing defects in weldments. *Int J Fatigue* 1986;8:51–7. [https://doi.org/10.1016/0142-1123\(86\)90053-8](https://doi.org/10.1016/0142-1123(86)90053-8).
- [19] Fiedler M, Vormwald M. Considering fatigue load sequence effects by applying the Local Strain Approach and a fracture mechanics based damage parameter. *Theor Appl Fract Mech* 2016;83:31–41. <https://doi.org/10.1016/j.tafmec.2016.01.003>.
- [20] Lazzarin P, Tovo R. A Notch Intensity Factor Approach to the Stress Analysis of Welds. *Fatigue Fract Eng Mater Struct* 1998;21:1089–103. <https://doi.org/10.1046/j.1460-2695.1998.00097.x>.
- [21] Lazzarin P, Sonsino CM, Zambardi R. A notch stress intensity approach to assess the multiaxial fatigue strength of welded tube-to-flange joints subjected to combined loadings. *Fatigue Fract Eng Mater Struct* 2004;27:127–40. <https://doi.org/10.1111/j.1460-2695.2004.00733.x>.
- [22] Remes H, Gallo P, Jelovica J, Romanoff J, Lehto P. Fatigue strength modelling of high-performing welded joints. *Int J Fatigue* 2020;135:105555. <https://doi.org/10.1016/j.ijfatigue.2020.105555>.
- [23] Fischer C, Fricke W, Rizzo CM. Experiences and recommendations for numerical analyses of notch stress intensity factor and averaged strain energy density. *Eng Fract Mech* 2016;165:98–113. <https://doi.org/10.1016/j.engfracmech.2016.08.012>.
- [24] Fischer C, Fricke W, Rizzo CM. Review of the fatigue strength of welded joints based on the notch stress intensity factor and SED approaches. *Int J Fatigue* 2016;84:59–66. <https://doi.org/10.1016/J.IJFATIGUE.2015.11.015>.
- [25] Lazzarin P, Zambardi R. A finite-volume-energy based approach to predict the static and fatigue behavior of components with sharp V-shaped notches. *Int J Fract* 2001 1123
-

- 2001;112:275–98. <https://doi.org/10.1023/A:1013595930617>.
- [26] Livieri P, Lazzarin P. Fatigue strength of steel and aluminium welded joints based on generalised stress intensity factors and local strain energy values. *Int J Fract* 2005;133:247–76. <https://doi.org/10.1007/s10704-005-4043-3>.
- [27] Lazzarin P, Livieri P, Berto F, Zappalorto M. Local strain energy density and fatigue strength of welded joints under uniaxial and multiaxial loading. *Eng Fract Mech* 2008;75:1875–89. <https://doi.org/10.1016/j.engfracmech.2006.10.019>.
- [28] Susmel L. *Multiaxial Notch Fatigue*. Cambridge, UK: Woodhead Publishing; 2009.
- [29] Carpinteri A, Spagnoli A, Vantadori S. Multiaxial fatigue life estimation in welded joints using the critical plane approach. *Int J Fatigue* 2009;31:188–96. <https://doi.org/10.1016/j.ijfatigue.2008.03.024>.
- [30] Baumgartner J, Schmidt H, Ince E, Melz T, Dilger K. Fatigue assessment of welded joints using stress averaging and critical distance approaches. *Weld World* 2015;59:731–42. <https://doi.org/10.1007/s40194-015-0248-x>.
- [31] Susmel L. Modified Wöhler curve method, theory of critical distances and Eurocode 3: A novel engineering procedure to predict the lifetime of steel welded joints subjected to both uniaxial and multiaxial fatigue loading. *Int J Fatigue* 2008;30:888–907. <https://doi.org/10.1016/j.ijfatigue.2007.06.005>.
- [32] Meneghetti G, Lazzarin P. Significance of the elastic peak stress evaluated by FE analyses at the point of singularity of sharp V-notched components. *Fatigue Fract Eng Mater Struct* 2007;30:95–106. <https://doi.org/10.1111/j.1460-2695.2006.01084.x>.
- [33] Meneghetti G. The use of peak stresses for fatigue strength assessments of welded lap joints and cover plates with toe and root failures. *Eng Fract Mech* 2012;89:40–51. <https://doi.org/10.1016/j.engfracmech.2012.04.007>.
- [34] Meneghetti G. The peak stress method for fatigue strength assessment of tube-to-flange welded joints under torsion loading. *Weld World* 2013;57:265–75. <https://doi.org/10.1007/s40194-013-0022-x>.
- [35] Campagnolo A, Meneghetti G. Rapid estimation of notch stress intensity factors in 3D large-scale welded structures using the peak stress method. *MATEC Web Conf.*, vol. 165, EDP Sciences; 2018. <https://doi.org/10.1051/mateconf/201816517004>.
- [36] Campagnolo A, Roveda I, Meneghetti G. The Peak Stress Method combined with 3D finite element models to assess the fatigue strength of complex welded structures.
-

2.5 References

- Procedia Struct Integr 2019;19:617–26. <https://doi.org/10.1016/j.prostr.2019.12.067>.
- [37] Meneghetti G, Campagnolo A. State-of-the-art review of peak stress method for fatigue strength assessment of welded joints. *Int J Fatigue* 2020;139:105705. <https://doi.org/10.1016/j.ijfatigue.2020.105705>.
- [38] Nykänen T, Mettänen H, Björk T, Ahola A. Fatigue assessment of welded joints under variable amplitude loading using a novel notch stress approach. *Int J Fatigue* 2017;101:177–91. <https://doi.org/10.1016/j.ijfatigue.2016.12.031>.
- [39] Hu Z, Berto F, Susmel L. The strain energy density to estimate lifetime of notched components subjected to variable amplitude fatigue loading. *Frat Ed Integrita Strutt* 2019;13:383–93. <https://doi.org/10.3221/IGF-ESIS.47.28>.
- [40] Susmel L, Taylor D. A critical distance/plane method to estimate finite life of notched components under variable amplitude uniaxial/multiaxial fatigue loading. *Int J Fatigue* 2012;38:7–24. <https://doi.org/10.1016/j.ijfatigue.2011.11.015>.
- [41] Susmel L. Four stress analysis strategies to use the Modified Wöhler Curve Method to perform the fatigue assessment of weldments subjected to constant and variable amplitude multiaxial fatigue loading. *Int J Fatigue* 2014;67:38–54. <https://doi.org/10.1016/j.ijfatigue.2013.12.001>.
- [42] FKM-Guideline. Analytical strength assessment of components in mechanical engineering. Frankfurt/M:VDMA: 2003.
- [43] Karakas Ö, Morgenstern C, Sonsino CM. Fatigue design of welded joints from the wrought magnesium alloy AZ31 by the local stress concept with the fictitious notch radii of $r_f = 1.0$ and 0.05 mm. *Int J Fatigue* 2008;30:2210–9. <https://doi.org/10.1016/j.ijfatigue.2008.05.017>.
- [44] Karakas Ö. Consideration of mean-stress effects on fatigue life of welded magnesium joints by the application of the Smith–Watson–Topper and reference radius concepts. *Int J Fatigue* 2013;49:1–17. <https://doi.org/10.1016/j.ijfatigue.2012.11.007>.
- [45] Susmel L. Multiaxial notch fatigue, From nominal to local stress/strain quantities. Woodhead Publishing; 2009.
- [46] Susmel L, Lazzarin P. A bi-parametric Wöhler curve for high cycle multiaxial fatigue assessment. *Fatigue Fract Eng Mater Struct* 2002;25:63–78. <https://doi.org/10.1046/j.1460-2695.2002.00462.x>.
- [47] Taylor D, Barrett N, Lucano G. Some new methods for predicting fatigue in welded
-

- joints. *Int J Fatigue* 2002;24:509–18. [https://doi.org/10.1016/S0142-1123\(01\)00174-8](https://doi.org/10.1016/S0142-1123(01)00174-8).
- [48] Susmel L. The Modified Wöhler Curve Method calibrated by using standard fatigue curves and applied in conjunction with the Theory of Critical Distances to estimate fatigue lifetime of aluminium weldments. *Int J Fatigue* 2009;31:197–212. <https://doi.org/10.1016/j.ijfatigue.2008.04.004>.
- [49] Karakaş Ö, Zhang G, Sonsino CM. Critical distance approach for the fatigue strength assessment of magnesium welded joints in contrast to Neuber's effective stress method. *Int J Fatigue* 2018;112:21–35. <https://doi.org/10.1016/j.ijfatigue.2018.03.004>.
- [50] Susmel L. Three different ways of using the Modified Wöhler Curve Method to perform the multiaxial fatigue assessment of steel and aluminium welded joints. *Eng Fail Anal* 2009;16:1074–89. <https://doi.org/10.1016/j.engfailanal.2008.05.016>.
- [51] Susmel L. Estimating fatigue lifetime of steel weldments locally damaged by variable amplitude multiaxial stress fields. *Int J Fatigue* 2010;32:1057–80. <https://doi.org/10.1016/j.ijfatigue.2009.12.004>.
- [52] Susmel L, Askes H. Modified Wöhler Curve Method and multiaxial fatigue assessment of thin welded joints. *Int J Fatigue* 2012;43:30–42. <https://doi.org/10.1016/j.ijfatigue.2012.01.026>.
- [53] Susmel L. The theory of critical distances: a review of its applications in fatigue. *Eng Fract Mech* 2008;75:1706–24. <https://doi.org/10.1016/j.engfracmech.2006.12.004>.
- [54] Neuber H. *Kerbspannungslehre (Translation: Theory of Notch Stresses)*. 2nd Ed. Berlin: Springer-Verlag; 1958.
- [55] Peterson R. Notch sensitivity. In: Sines G, Waisman J, editors. *Met. fatigue*, New York: McGraw Hill; 1959, p. 293–306.
- [56] Meneghetti G, Campagnolo A, Visentin A. Automated fatigue strength assessment of arc-welded structures according to the Peak Stress Method. *Procedia Struct Integr* 2020;28:1062–83. <https://doi.org/10.1016/j.prostr.2020.11.122>.
- [57] Visentin A, Campagnolo A, Babini V, Meneghetti G. Automated implementation of the Peak Stress Method for the fatigue assessment of complex welded structures. *Forces Mech* 2022;submitted.
- [58] Tovo R, Lazzarin P. Relationships between local and structural stress in the evaluation of the weld toe stress distribution. *Int J Fatigue* 1999;21:1063–78. [https://doi.org/10.1016/S0142-1123\(99\)00089-4](https://doi.org/10.1016/S0142-1123(99)00089-4).
-

2.5 References

- [59] Meneghetti G, Campagnolo A, Rigon D. Multiaxial fatigue strength assessment of welded joints using the Peak Stress Method – Part I: Approach and application to aluminium joints. *Int J Fatigue* 2017;101:328–42. <https://doi.org/10.1016/j.ijfatigue.2017.03.038>.
- [60] Meneghetti G, Campagnolo A, Rigon D. Multiaxial fatigue strength assessment of welded joints using the Peak Stress Method – Part II: Application to structural steel joints. *Int J Fatigue* 2017;101:343–62. <https://doi.org/10.1016/j.ijfatigue.2017.03.039>.
- [61] Meneghetti G, Lazzarin P. The Peak Stress Method for Fatigue Strength Assessment of welded joints with weld toe or weld root failures. *Weld World* 2011;55:22–9. <https://doi.org/10.1007/BF03321304>.
- [62] Vecchiato L, Campagnolo A, Besa B, Meneghetti G. The Peak Stress Method applied to fatigue lifetime estimation of welded steel joints under variable amplitude multiaxial local stresses. *Procedia Struct Integr* 2022;38:418–27. <https://doi.org/10.1016/j.prostr.2022.03.043>.
- [63] Campagnolo A, Vecchiato L, Meneghetti G. Multiaxial variable amplitude fatigue strength assessment of steel welded joints using the peak stress method. *Int J Fatigue* 2022;163:107089. <https://doi.org/10.1016/j.ijfatigue.2022.107089>.
- [64] Meneghetti G, Campagnolo A, Visentin A, Avalle M, Benedetti M, Bighelli A, et al. Rapid evaluation of notch stress intensity factors using the peak stress method with 3D tetrahedral finite element models: comparison of commercial codes. *Fatigue Fract Eng Mater Struct* 2022;accepted.
- [65] ASTM. ASTM E1049-85 - Standard Practices for Cycle Counting in Fatigue Analysis 2017.
- [66] Endo T, Mitsunaga K, Nakagawa H. Fatigue of metals subjected to varying stress - Prediction of fatigue lives. In: The Japan Society of Mechanical Engineers, editor. Prelim. Proc. Chugoku-Shikoku Dist. Meet., 1967.
- [67] Endo T, Mitsunaga K, Nakagawa H, Ikeda K. Fatigue of metals subjected to varying stress – Low cycle, middle cycle fatigue. In: The Japan Society of Mechanical Engineers, editor. Prelim. Proc. Chugoku-Shikoku Dist. Meet., 1967.
- [68] Haibach E. Service fatigue-strength – methods and data for structural analysis. VDI, Dusseld 1989.
- [69] Sonsino CM, Lagoda T, Demofonti G. Damage accumulation under variable amplitude
-

- loading of welded medium- and high-strength steels. *Int J Fatigue* 2004;26:487–95. <https://doi.org/10.1016/j.ijfatigue.2003.10.001>.
- [70] Demofonti G, Riscifuli S, Sonsino CM, Kaufmann H, Sedlacek G, Muller C, et al. High-strength steels in welded state for lightweight constructions under high and variable stress peaks, ECSC Steel Research Programme. European Commission, Report No. 19989. Brussels: 2001.
- [71] Maddox SJ. Improving the fatigue strength of toe ground welds at the ends of longitudinal attachments. *Int Inst Weld* 2007;IIW Doc. X.
- [72] Zhang Y-H, Maddox SJ. Investigation of fatigue damage to welded joints under variable amplitude loading spectra. *Int J Fatigue* 2009;31:138–52. <https://doi.org/10.1016/j.ijfatigue.2008.04.006>.
- [73] Vanrostenberghe S, Clarin M, Shin Y, Driesbeke B, van der Mee V, Doré M, et al. FATWELDHSS - Improving the fatigue life of high strength steel welded structures by post weld treatments and specific filler material, Research Fund for Coal and Steel, Grant Agreement RFSR-CT-2010-00032 Final Report. Brussels: 2015.
- [74] Yıldırım HC, Remes H, Nussbaumer A. Fatigue properties of as-welded and post-weld-treated high-strength steel joints: The influence of constant and variable amplitude loads. *Int J Fatigue* 2020;138:105687. <https://doi.org/10.1016/j.ijfatigue.2020.105687>.
- [75] Bertini L, Cera A, Frenzo F. Experimental investigation of the fatigue resistance of pipe-to-plate welded connections under bending, torsion and mixed mode loading. *Int J Fatigue* 2014;68:178–85. <https://doi.org/10.1016/j.ijfatigue.2014.05.005>.
- [76] Frenzo F, Bertini L. Fatigue resistance of pipe-to-plate welded joint under in-phase and out-of-phase combined bending and torsion. *Int J Fatigue* 2015;79:46–53. <https://doi.org/10.1016/j.ijfatigue.2015.04.020>.
- [77] Bertini L, Frenzo F, Marulo G. Fatigue endurance of welded joints subjected to different blocks of bending and torsion loading. *Procedia Struct Integr* 2016;2:3531–8. <https://doi.org/10.1016/j.prostr.2016.06.440>.
- [78] Frenzo F, Marulo G, Chiocca A, Bertini L. Fatigue life assessment of welded joints under sequences of bending and torsion loading blocks of different lengths. *Fatigue Fract Eng Mater Struct* 2020;43:1290–304. <https://doi.org/10.1111/ffe.13223>.
- [79] Sonsino CM, Kueppers M, Gath N, Maddox SJ, Razmjoo GR. Fatigue behaviour of welded high-strength components under combined multiaxial variable amplitude
-

- loading, ECSC Steel Research Programme, European Commission, Report No. 20050. Brussels: 2001.
- [80] Witt M, Yousefi F, Zenner H. Fatigue strength of welded joints under multiaxial loading: Comparison between experiments and calculations. *ASTM Spec Tech Publ* 2000;191–210. <https://doi.org/10.1520/STP13505S>.
- [81] Yousefi F, Witt M, Zenner H. Fatigue strength of welded joints under multiaxial loading: experiments and calculations. *Fatigue Fract Eng Mater Struct* 2001;24:339–55. <https://doi.org/10.1046/J.1460-2695.2001.00397.X>.
- [82] Haibach E, Fisher R, Schutz W, Huck M. A standard random load sequence of Gaussian type recommended for general application in fatigue testing; its mathematical background and digital generation. *SEE Conf Fatigue Test Des* 1976;2.
- [83] Heuler P, Bruder T, Klätschke H. Standardised load-time histories - A contribution to durability issues under spectrum loading. *Materwiss Werksttech* 2005;36:669–77. <https://doi.org/10.1002/mawe.200500936>.
- [84] Williams ML. Stress singularities resulting from various boundary conditions in angular corners of plates in tension. *J Appl Mech* 1952;19:526–8.
- [85] Meneghetti G, Campagnolo A, Berto F. Fatigue strength assessment of partial and full-penetration steel and aluminium butt-welded joints according to the peak stress method. *Fatigue Fract Eng Mater Struct* 2015;38:1419–31. <https://doi.org/10.1111/ffe.12342>.
- [86] Meneghetti G, Guzzella C. The peak stress method to estimate the mode I notch stress intensity factor in welded joints using three-dimensional finite element models. *Eng Fract Mech* 2014;115:154–71. <https://doi.org/10.1016/j.engfracmech.2013.11.002>.
- [87] Visentin A. Automated Fatigue Strength Assessment of V - Notch Structures according to the Peak Stress Method. University of Padova, 2020.
- [88] Campagnolo A, Vormwald M, Shams E, Meneghetti G. Multiaxial fatigue assessment of tube-tube steel joints with weld ends using the peak stress method. *Int J Fatigue* 2020;135:105495. <https://doi.org/10.1016/j.ijfatigue.2020.105495>.
- [89] Razmjoo G. Fatigue of Load-Carrying Fillet Welded Joints Under Multiaxial Loadings. In: Abington, editor. TWI REF. 7309.02/96/909, Cambridge, UK: 1996.
- [90] Sonsino CM, Łagoda T. Assessment of multiaxial fatigue behaviour of welded joints under combined bending and torsion by application of a fictitious notch radius. *Int J Fatigue* 2004;26:265–79. [https://doi.org/10.1016/S0142-1123\(03\)00143-9](https://doi.org/10.1016/S0142-1123(03)00143-9).
-

- [91] Shams E, Vormwald M. Fatigue of weld ends under combined loading. *Int J Fatigue* 2017;100:627–38. <https://doi.org/10.1016/j.ijfatigue.2016.12.020>.
- [92] Booth GS, Maddox SJ. TWI Research Report no. 93/1979: Influence of various factors on the fatigue strength of steel plates with fillet-welded attachments. 1979.
- [93] ASTM. ASTM E92-17, Standard Test Methods for Vickers Hardness and Knoop Hardness of Metallic Materials 2017. <https://doi.org/10.1520/E0092-17>.
- [94] Rice SO. Mathematical Analysis of Random Noise. *Bell Syst Tech J* 1944;23:282–332. <https://doi.org/10.1002/j.1538-7305.1944.tb00874.x>.
- [95] Bendat JS, Piersol AG. *Random Data, Analysis and Measurement Procedures*. 4th ed. Hoboken, New Jersey: John Wiley & Sons; 2010.
- [96] Gaßner E, Griese FW, Haibach E. Ertragbare Spannungen und Lebensdauer einer Schweißverbindung aus Stahl St 37 bei verschiedenen Formen des Beanspruchungskollektivs. *Arch Für Das Eisenhüttenwes* 1964;35:255–67. <https://doi.org/10.1002/srin.196402317>.
- [97] Hanke M. Eine Methode zur Beschreibung der Betriebslastkollektive als Grundlage für Betriebsfestigkeitsversuche. *ATZ Automob Zeitschrift* 1970;72:91–7.
- [98] Sonsino CM, Kueppers M. Multiaxial fatigue of welded joints under constant and variable amplitude loadings. *Fatigue Fract Eng Mater Struct* 2001;24:309–27. <https://doi.org/10.1046/j.1460-2695.2001.00393.x>.
- [99] Maddox SJ. Fatigue assessment of welds not oriented either normal or parallel to the direction of loading, IIW Doc. JWG XIII/XV-218-10. *Int Inst Weld* 2010.
- [100] Pedersen MM. Multiaxial fatigue assessment of welded joints using the notch stress approach. *Int J Fatigue* 2016;83:269–79. <https://doi.org/10.1016/j.ijfatigue.2015.10.021>.
- [101] ISO. BS ISO 12107:2012 - Metallic materials – Fatigue testing – Statistical planning and analysis data 2013.
- [102] EN. Eurocode 9: Design of aluminium structures - Part 1-3: Structures susceptible to fatigue 2007.
- [103] Sonsino CM. Effect of residual stresses on the fatigue behaviour of welded joints depending on loading conditions and weld geometry. *Int J Fatigue* 2009;31:88–101. <https://doi.org/10.1016/j.ijfatigue.2008.02.015>.
-

CHAPTER 3.

Cyclic R curve and fatigue limit

List of symbols

2α	V-notch opening angle
a	Crack size
a_{CPC}	Crack length after Compression Pre-Cracking (CPC)
a_i	Initial crack size
A	Cross-sectional area of the main plate
c/a	Elliptical crack aspect ratio
c_{w1}	Mode I coefficient accounting for mean stress effect according to PSM
d	Average FE size
Δ	Range of cyclic quantities (maximum minus minimum)
$\Delta a = a - a_{CPC}$	Crack size increment from CPC crack
$\Delta K_{I,th}$	Mode I threshold NSIF
$\Delta K_I(a)$	Driving force, i.e. applied SIF dependence on crack length
$\Delta K_{I,\Delta\sigma_{g,th}}(a)$	Driving force at the fatigue limit
$\Delta K_{th}(\Delta a)$	Fatigue crack propagation threshold dependence on crack size (R-curve)
$\Delta K_{th,LC}$	Long cracks' fatigue crack propagation threshold
$\Delta K_{th,eff}$	Intrinsic component of the fatigue crack propagation threshold
$\Delta\sigma_{g,th}$	Nominal stress range at the fatigue limit
$\Delta\sigma_{eq,peak,th}$	Equivalent peak stress range at the fatigue limit
e_1	Mode I coefficient for evaluating $\Delta\bar{W}$
E	Young's modulus
f_{w1}	Mode I coefficient for calculating $\sigma_{eq,peak}$
K_I	Mode I Stress Intensity Factors (SIFs)
K_1	Mode I Notch Stress Intensity Factors (NSIFs)
K_{FE}^*	Non-dimensional NSIF parameters based on PSM
λ_1	Mode I stress singularity degrees
...	

3.1 Introduction

...	
N_f	Number of cycles to failure
ν	Poisson's ratio
R	Load ratio
R_{ax}	Nominal load ratio without considering any bending component
R_0	Size of material-structural volume according to SED criterion
ρ	Notch tip radius
r, θ, z	Coordinates of cylindrical reference system at crack/notch tip
σ_g	Nominal stress
$\sigma_{g,ax}$	Axial component of the nominal stress
$\sigma_{g,b}$	Bending component of the nominal stress
$\sigma_{g,b,0}$	Bending component of the nominal stress when no axial load is applied
$\sigma_{eq,peak}$	Equivalent peak stress based on PSM
$\sigma_{rr}, \sigma_{\theta\theta}, \sigma_{zz}$	Normal stress components in cylindrical coordinate system
$\sigma_{\theta\theta, \theta=0, peak}$	Mode I linear elastic peak stress calculated by FEA according to PSM
t	Thickness of the main plate
W	Width of the main plate
ζ_b	Ratio between bending and axial nominal stress range

3.1. Introduction

Designing a structure against fatigue is a well-known topic and there are many criteria proposed in the literature, a complete understanding of the phenomenon has not yet been reached. The occurrence of fatigue failure can be avoided making use of one of the design criteria intensely discussed in the previous chapters, thanks to which engineers have to possibility to design welded components against fatigue in the finite life region. In reality, it is not true they completely allow to avoid component's failure but to establish when this will occur. In particular, those criteria let have an estimate of the number of cycles at which the analysed structure will exhibit fatigue failure. The design philosophy behind those criteria is called safe life design and implicitly assumes that at the end of the design life the considered component is removed or dismissed and replaced by a new one.

Unfortunately, there are several practical applications where the fatigue failure as well as the dismissal or substitution of a structural component is undoubtedly unacceptable. Typical examples are that of the nuclear or aerospace industry for which extremely high safety requirements are necessary, as the failure of a component could lead to catastrophic consequences. Noteworthy, for some material classes such as structural steels, there exists a stress level, known as the fatigue limit, below which, theoretically, an infinite number of CA load cycles can be applied to the structure without causing fatigue failure. It is interesting to note that, despite the important and significant implications this concept has on practical problems, there still is a remarkable shortage of knowledge behind this parameter.

As mentioned in the previous chapter, International standards and recommendations [1,2], basing their considerations on the nominal stress approach, suggest defining the Constant Amplitude Fatigue Limit (CAFL) of a welded detail as that stress level corresponding to a fixed number of cycles on the stress-life (S-N) curve of the corresponding reference detail [1,2]. Then the fatigue strength assessment is simply done by comparing the value of the applied nominal stress with the fatigue limit of the considered joints [1,2]: at a stress level below the CAFL no

failure will occur, the number of cycles to failure being $N \rightarrow \infty$, otherwise the calculations must be done accordingly to what discussed in the previous chapters.

It should be noted that the first problem of this procedure is that the number of cycles at which the vertical line has to be fixed depends on the considered standard demonstrating that the knowledge to understand the phenomenon is still lacking. More in detail, while Eurocode 3 [1] identifies the fatigue limit CAFL as the stress level corresponding to $5 \cdot 10^6$ cycles, IIW recommendations [2] fix that number at 10^7 cycles to failure (Figure 3.1).

However, as discussed extensively in the previous chapters, the main problem of the nominal stress approach remains its application in case of more complex joint geometries, for which the proper reference design category does not exist in the list of classified structural details reported in [1,2]. To overcome this issue, standards and recommendations [1,2] suggest carrying out dedicated expensive and time-consuming experimental fatigue tests as the only alternative.

Again, in the Literature, it has been demonstrated that this limitation can be overcome by adopting local approaches [3]. In particular, Frost, Smith and Miller [4,5] observed that when notched component is loaded at a stress level equal to its fatigue limit a crack is present at the notch tip. Accordingly, damage tolerant approaches based on the principles of fracture mechanics [6] have been shown to play a key role in this context [7]: in fact, they postulate the presence of a crack in the structure stating that the crack initiation period is negligible if compared to the propagation phase. So far as the fatigue limit is concerned, its link with fracture mechanics concepts is given by the long crack fatigue propagation threshold $\Delta K_{th,LC}$, which represents the range of Stress Intensity Factor (SIF) ΔK_I below which a crack arrests as it has no more energy to propagate [6,7]. The problem is that at the fatigue limit, notched components exhibit short crack instead of long cracks and their fatigue behaviour can tremendously different. For example, short cracks can grow at rates that are faster than long cracks when loaded with the same crack driving force, i.e. the same SIF range ΔK_I [7–10]. In particular, it has been intensely examined that, if compared with long cracks, they exhibit a much lower fatigue crack propagation threshold ΔK_{th} due to the gradual build-up of the crack closure phenomena [8–10], the latter being completely described by the cyclic R-curve concept, i.e. the crack size dependence of the fatigue crack propagation threshold in the physically/mechanically short crack regime [7,9–15].

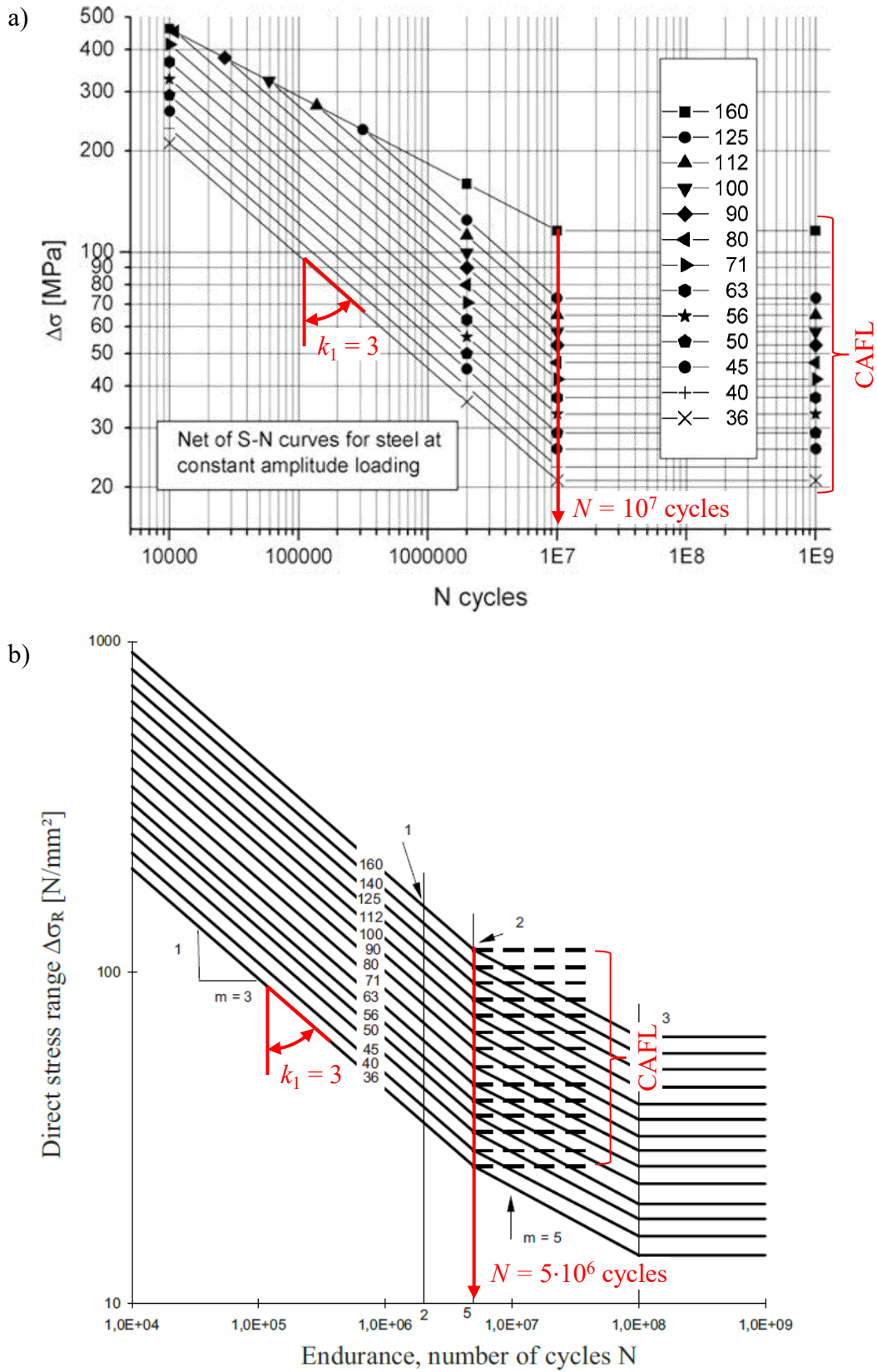


Figure 3.1. Fatigue resistance S-N curves and fatigue limits for steel welded joints subjected to normal stresses taken from: IIW recommendations [2] and b) Eurocode 3 [1].

3.1 Introduction

For determining the fatigue limit of a structure adopting this concept, it is necessary to perform a cyclic R-curve analysis (Figure 3.2) [9,11,14,16]. Similar to the well-established monotonic R-curve analysis, this procedure simply consist in comparing for a propagating crack its driving force (black lines in Figure 3.2), which depends on the geometry, the material and the external loads ($\Delta\sigma_g$ in Figure 3.2), with its resistance curve (red line in Figure 3.2), which is a material property. The crack propagation is promoted whenever the crack driving force assumes higher values than the resistance ones, while the crack is arrested in the opposite case. Consequently, this statement implies the fatigue limit of the component $\Delta\sigma_{g,th}$ is that external stress level at which the crack driving force curve is tangent to the crack resistance (solid black line in Figure 3.2).

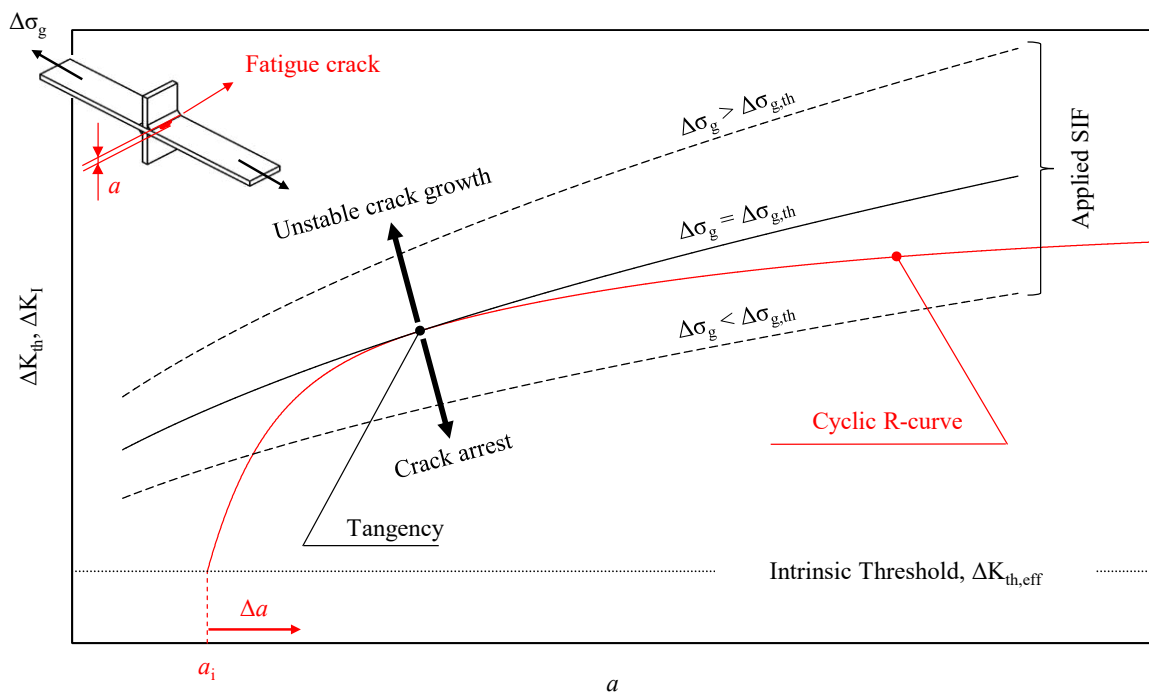


Figure 3.2. Schematic of a cyclic R-curve analysis applied to a welded joint.

However, the most critical aspect of this procedure is that being a fracture mechanics-based approach, it requires the definition of an initial crack size a_i from which starting the computation of the driving and resistance force (Figure 3.2). In the literature, there are different proposals to define the initial crack size (see [17] for a recent review of them), but one of the most promising is the that proposed in the IBESS approach [16–19]: according to this criterion, the initial crack size can be calibrated using a two-criteria concept. In particular, if a large crack-like defect (e.g.

non-metallic inclusions, pores, cavities, shrinkage, weldments defects, microcracks, surface roughness, undercut, corrosion pits or scratches) exists in the structure, they suggest adopting its size as initial crack size a_i . Otherwise, the lower bound of a_i is obtained performing a crack arrest analysis. This procedure consists in comparing the driving force at a stress level equal to the fatigue limit of the plain material $\Delta K_{I,\Delta\sigma_{g,th}}(a)$ with the corresponding resistance curve, i.e. the cyclic R-curve $\Delta K_{th}(a)$. Finally, observing the cyclic R-curve is fixed along the ordinate but not along the abscissa, the initial crack size a_i results from shifting the cyclic R-curve along the abscissa until the tangency condition is found with the driving force (Figure 3.2). The authors suggest evaluating the driving force at the fatigue limit for a semi-circular surface crack propagating normal to the loading plane of a smooth plate specimen under fully reversed ($R = -1$) axial cyclic loading. In particular, they proposed assuming the crack propagates by keeping constant its shape, i.e. the ratio between the its major and minor axes is fixed to $c/a = 1$. Moreover, they suggest using a plasticity corrected driving force, substantially based on elasto-plastic calculations by means of the J-integral. Interestingly, the Zerbst et al. [17–19] declare the value of the initial crack size a_i obtained from the crack arrest analysis represent a material property.

In this chapter the cyclic R-curve analysis has been adopted to estimate the fatigue limit of welded structures. In particular, an accurate experimental calibration of the method based on the crack arrest analysis has been performed by comparing the driving force at the fatigue limit for non-load-carrying (nlc) fillet welded double transverse attachments made of S355J2+N structural steel and the corresponding resistance curve. The cyclic R curve has been experimentally determined by fatigue testing Single Edge Notch in Bending (SENB) on resonant testing machines making use of a new experimental procedure which allows for the determination of the crack propagation threshold from short to long crack regime by means of a single experimental test. The characterization has been carried out for a S355J2+N material and further for the same material but in Heat Affected Zone (HAZ) condition. The specimens in the HAZ condition were obtained from a transverse loaded butt weld ground flush to plate which residual stresses has been removed as much as possible by applying a proper stress relieving thermal treatment.

Once performed the calibration of the initial crack size, its application to the estimation of the fatigue limit of a welded structure has been presented with different degrees of accuracy depending on the available information. In particular, under certain simplifying assumptions it

3.2 Calibration of the initial crack size a_i : driving force at the fatigue limit

was possible to combine the cyclic R-curve analysis with the Peak Stress Method obtaining a new procedure that allows to a rapid and effective design of weld toe failures in the infinite life region, without the need of complex and time-consuming fracture mechanics-based calculations.

3.2. Calibration of the initial crack size a_i : driving force at the fatigue limit

3.2.1. Specimens

As discussed in the introduction, according to Zerbst et al. [17–19] the calibration of the initial crack a_i can be performed with a crack arrest analysis, i.e. by shifting the cyclic R-curve until the tangency with the driving force evaluated at the fatigue limit is found. Interestingly, it has also been discussed the authors assert the obtained initial crack size represent a material property and, as such, its value is independent of the specimen's geometry [17–19]. In other words, this means that, from a theoretical point of view, any specimen's geometry can be used to perform the calibration.

In this work, non-load-carrying (nlc) fillet-welded double transverse attachments specimens have been considered for the calibration. Moreover, instead of a complex elasto-plastic driving force as proposed in [17–19], a linear elastic parameter, i.e. the Stress Intensity Factor Range ΔK_I , has been considered as damage parameter, the non-linear effects being completely included in the cyclic R-curve. Accordingly, the driving force curve at the fatigue limit can be mathematically expressed by the following engineering expression:

$$\Delta K_{I,\Delta\sigma_{g,th}} = \beta \cdot \sqrt{\pi a} \cdot \Delta\sigma_{g,th} \quad (3.1)$$

Where β represents a geometric factor dependent on the crack size a including all information about the specimen's geometry, the loading and constraint conditions and the position, inclination and shape of the propagating crack, while $\Delta\sigma_{g,th}$ is the fatigue limit of the component expressed in terms of nominal stress range. The evaluation of the driving force according to Eq. (3.1) has been done combining together results from both experimental tests and numerical analyses. In particular, the experimental tests has been adopted to evaluate the fatigue

limit $\Delta\sigma_{g,th}$ and investigate the crack's geometry, while the FE analyses have been adopted to compute the geometrical factor β . As mentioned above, the specimens were non-load-carrying (nlc) fillet-welded double transverse attachments made from an 8mm-thickness hot rolled plate of S355J2+N structural steel (EN10025-2 [20]). Welding was performed perpendicular to the rolling direction using Gas Metal Arc Welding (GMAW) technique. A total of 10 specimens have been obtained by band saw-cutting two larger plates. After the cut, the specimens have been heat treated in a muffle furnace to remove the presence of unwanted residual stresses originated during the welding process. The heat treatment consisted in heating up the specimens up to 600 °C with a gradient of 70 °C/h, a maintenance phase at 600 °C for 3h and a cooling ramp down to the laboratory temperature with of about 70 °C/h (Figure 3.3).

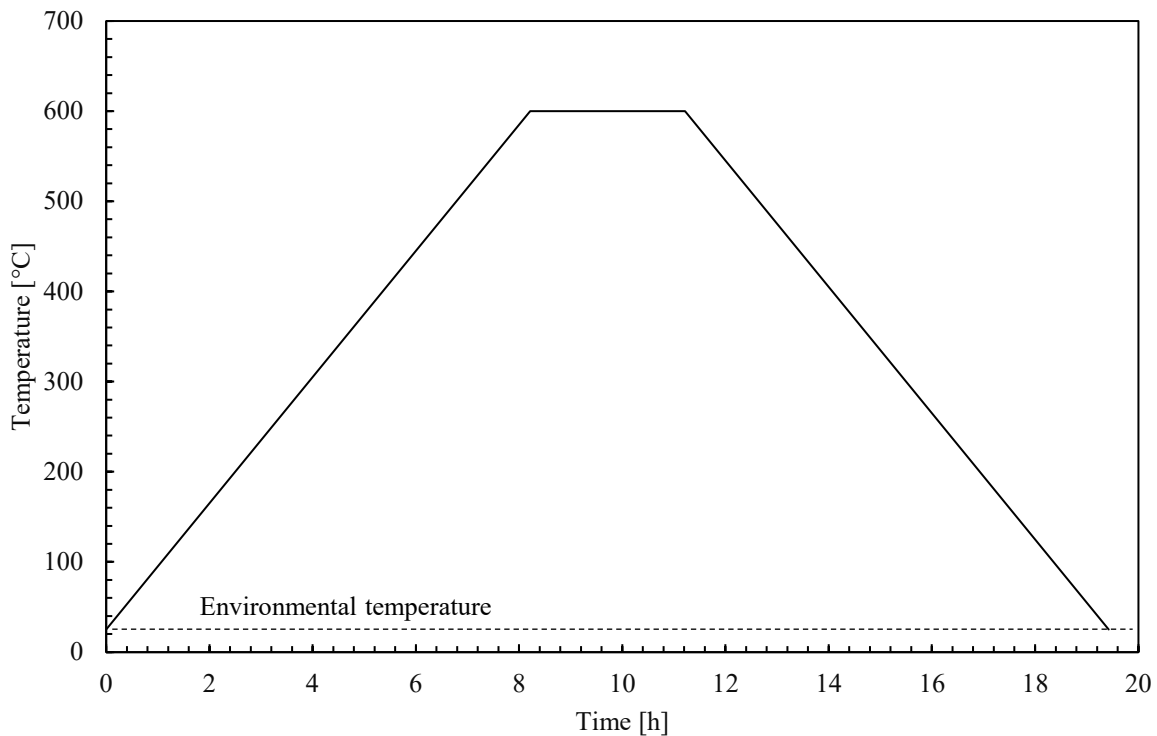


Figure 3.3. Temperature profile adopted for the stress relieving heat treatment.

Finally, the geometry of the tested specimens was that reported in Figure 3.4. The specimens' geometric parameters as well as the local weld bead geometry has been carefully and accurately measured, these parameters having a major influence on the definition of the driving force. In particular, the main plate thickness (t in Figure 3.4) and the width (W in Figure 3.4) have been measured at the specimens' cross sections in the nearby of the weld toe adopting a digital

3.2 Calibration of the initial crack size a_i : driving force at the fatigue limit

caliper. Instead, all other parameters have been measured thanks to image analysis performed with a digital microscope calibrated using graph chart. All the measured parameters have been analysed using basic statistical calculations to obtain their mean values μ and standard deviations δ . The resulting parameters (reported in Table 3.1) have been computed both considering all the specimens together and only that used to obtain the fatigue limit with the staircase procedure (more details about this will be given later on this paragraph).

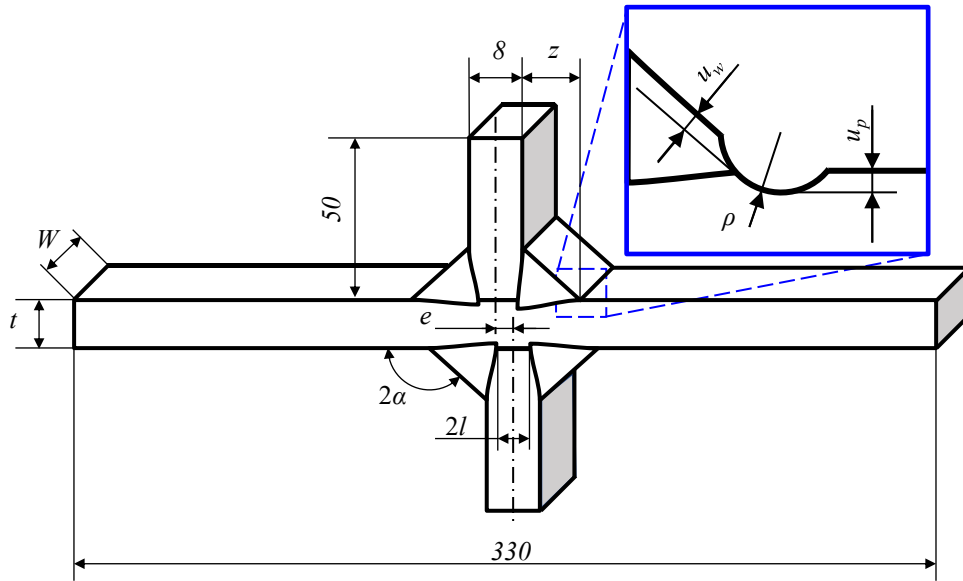


Figure 3.4. Geometry of the tested specimens.

Table 3.1. Measured geometric parameters with corresponding mean value and standard deviations.

Parameter	T25 & T26		Staircase	
	μ	δ	μ	δ
2α [°]	140.45	1.87	140.6*	1.8*
z [mm]	7.36	0.42	7.2*	0.3*
$2l$ [mm]	6.15	0.66	6.17	0.8
ρ [mm]	2.28	1.11	1.3*	0.2*
u_p [mm]	0.09	0.02	0.09*	0.01*
u_w [mm]	0.12	0.05	0*	0*
e [mm]	0.7	0.22	0.9	0.19
t [mm]	8.03	0.01	8.03	0.01
W [mm]	7.15	0.48	7.13	0.47

*Relevant to the weld toe where the fatigue crack initiation always occurred

One of the specimens has been used to perform micro-hardness and microstructural analyses. The sample has been extracted by saw cutting a joint which has never been fatigue loaded. The sample was grinded by means of sandpaper with grit P120 up to P1200 and then polished with 6 μm and 1 μm diamond suspensions. Vickers micro-hardness HV0.5 has been measured according to [21,22], by applying a weight of 0.5 kg for 15s with a Shimadzu hardness tester. The measurements have been performed

- in a material region close to the weld toe (Figure 3.5) where the fatigue failure was expected to occur, whose results have been reported in colour map mode in the e figure.
- along a straight path starting from the transverse attachment to the main plate through the weld bead (Figure 3.5), the relevant results having been reported in Figure 3.5 as a function of the coordinate along the path.

The resulting micro-hardness have been evaluated according to [21,22]:

$$HV = 0.1891 \cdot \frac{P}{d^2} \quad (3.2)$$

Where P is the applied load in newtons N , while d is the average value of the indentation's diagonals in millimetres mm . After that, the sample was etched with 2% Nital solution to better highlight the microstructure. Micrographs were taken using an optical microscope and allowed to distinguish three main regions, i.e. the Weld Metal (WM), the Heat Affected Zone (HAZ), and the Base Metal (BM) (see Figure 3.5). The analysis showed that the BM has a microhardness of ~ 160 HV and consists in a typical ferritic-pearlitic microstructure, whose grains are elongated in the rolling direction (see Figure 3.5). Differently, the maximum values of the hardness (~ 230 - 260 HV) have been measured in the HAZ, which has an inhomogeneous bainitic-martensitic microstructure. Figure 3.5 also shows the average value of microhardness in the WM is ~ 220 HV.

3.2 Calibration of the initial crack size a_i : driving force at the fatigue limit

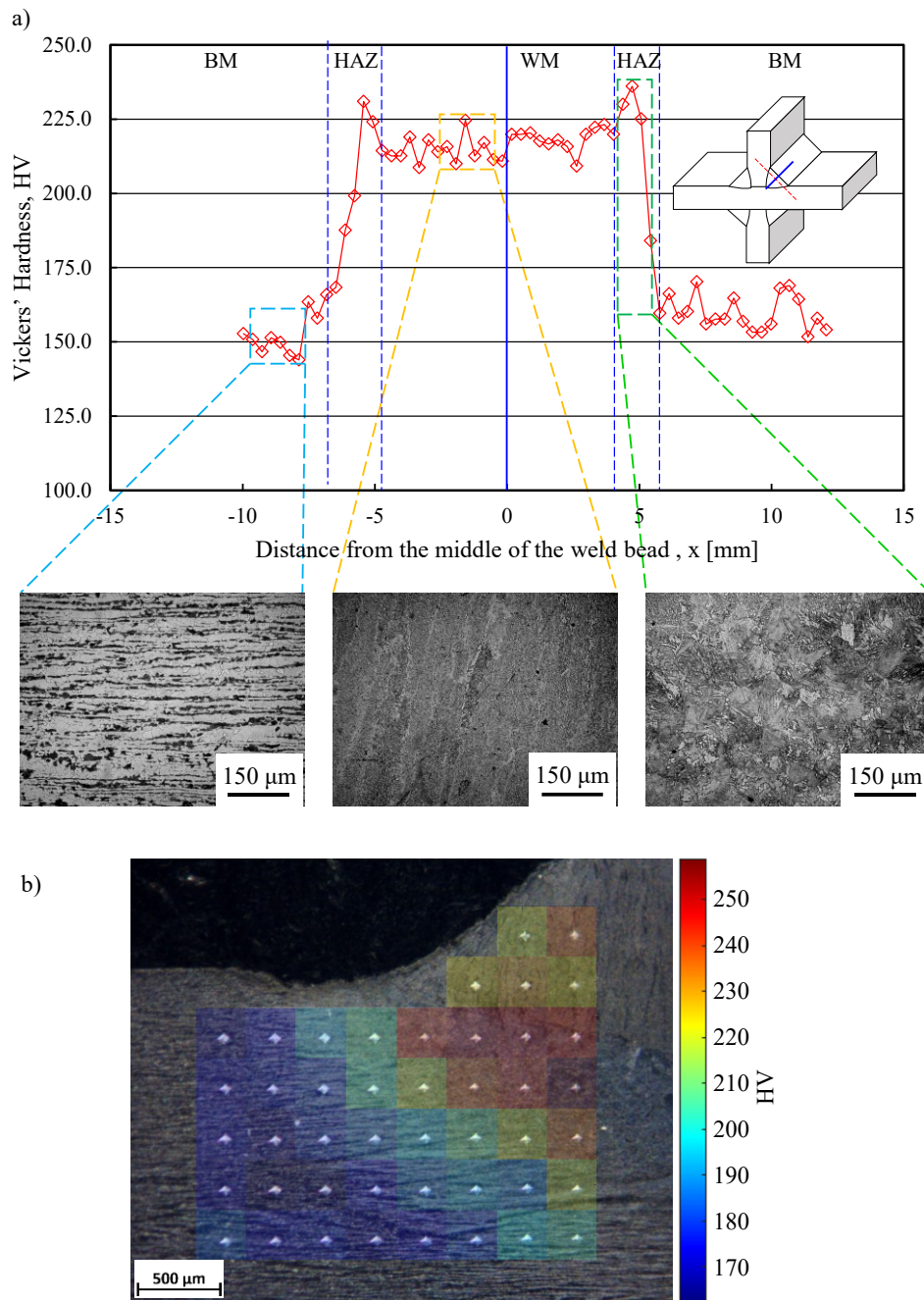


Figure 3.5. Micro-hardness measurements and microstructural analysis of a transverse joint which has not been fatigue tested.

3.2.2. Experimental determination of the fatigue limit

The nominal stress range $\Delta\sigma_{g,ax}$ has been calculated with reference to the main plate:

$$\Delta\sigma_{g,ax} = \frac{\Delta F_{ax}}{A} = \frac{\Delta F_{ax}}{W \cdot t} \quad (3.3)$$

where ΔF_{ax} is the range of the axial load, while A , W , and t are the cross-section area, the width, and the thickness of the main plate, respectively. All specimens were fatigue tested in the stress-relieved state under closed loop load-controlled pure axial loading by using a 100 kN Schenck Hydropulsar PSA 100 servo-hydraulic machine equipped with a Trio Sistemi RT3 digital controller. All fatigue tests were performed applying CA fully reversed ($R_{ax} = -1$) sinusoidal axial loading at a frequency ranging between 25 and 30 Hz depending on the applied load level. The number of cycles to failure N_f corresponded to complete separation of the specimen, while run-out condition was fixed at $10 \cdot 10^6$ cycles, if no failure or crack initiation was detected.

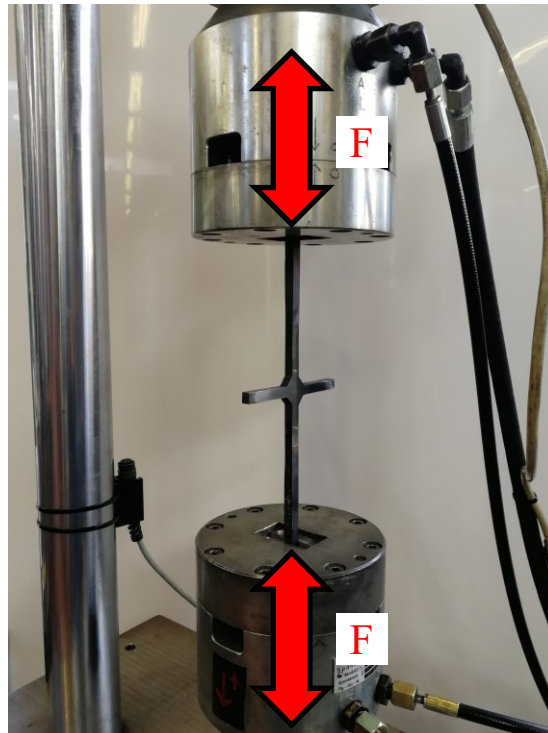


Figure 3.6. Example of specimen tested under fully reversed axial loading using the Schenck Hydropulsar PSA 100 servo-hydraulic machine.

As shown in Figure 3.7 all joints exhibited fatigue crack initiation at the weld toe on the main plate's side. Then crack propagated through the thickness until final brittle fracture.

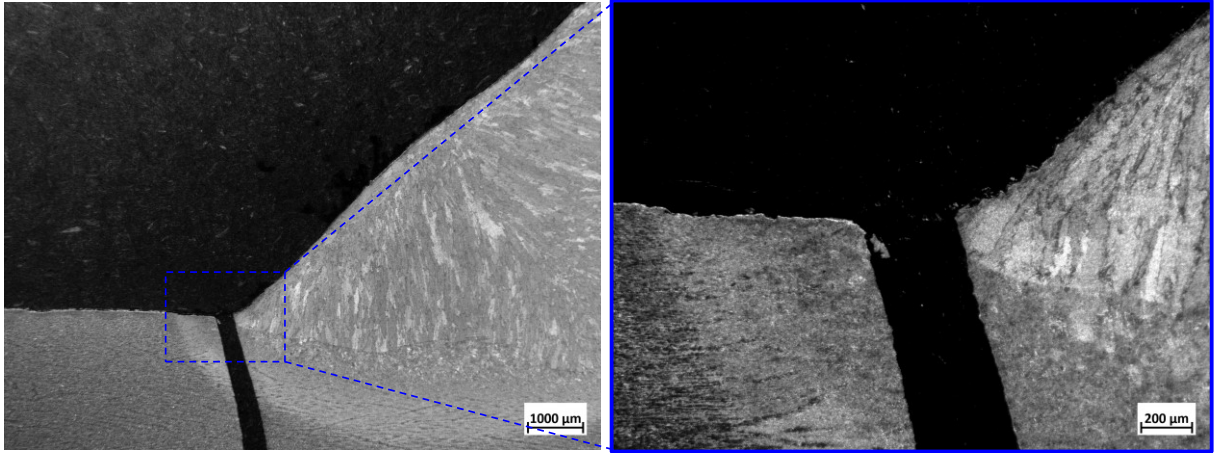


Figure 3.7. Crack propagation plane in the nearby of the weld toe where it initiated.

The experimental fatigue results have been reported in Figure 3.8 in terms of number of cycles to failure N_f versus the applied nominal stress range $\Delta\sigma_{g,ax}$ (Eq. (3.3)) along with the uniaxial fatigue resistance curve for normal stresses according to IIW recommendations [2] (blue line in Figure 3.8). In more detail, as indicated in [2], this curve has been obtained multiplying the FAT80 fatigue resistance curve (80 MPa at $2 \cdot 10^6$ cycles for a Survival Probability $PS = 97.7\%$) by the coefficient $f(R) = 1.6$ to account the mean stress correction, the latter being applicable as the joints were tested in the stress-relieved conditions when subjected to fully-reversed loading ($R_{ax} = -1$) [2].

All experimental data have been statistically analysed and fitted according to BS ISO 12107:2012 [23] by imposing a inverse slope $k = 3$. The obtained design curves referred to $PS = 2.3\%$, 50% , and 97.7% , respectively, have been reported as black lines in Figure 3.8.

More interestingly, the knee point on the fitted curves has been obtained intersecting them with the experimental fatigue limit obtained from the modified staircase procedure as proposed in BS ISO 12107:2012 [23]. The fatigue limit has been evaluated for a Probability of Survival $PS = 50\%$ and it was found to be equal to $\Delta\sigma_{g,th,ax} = 215$ MPa.

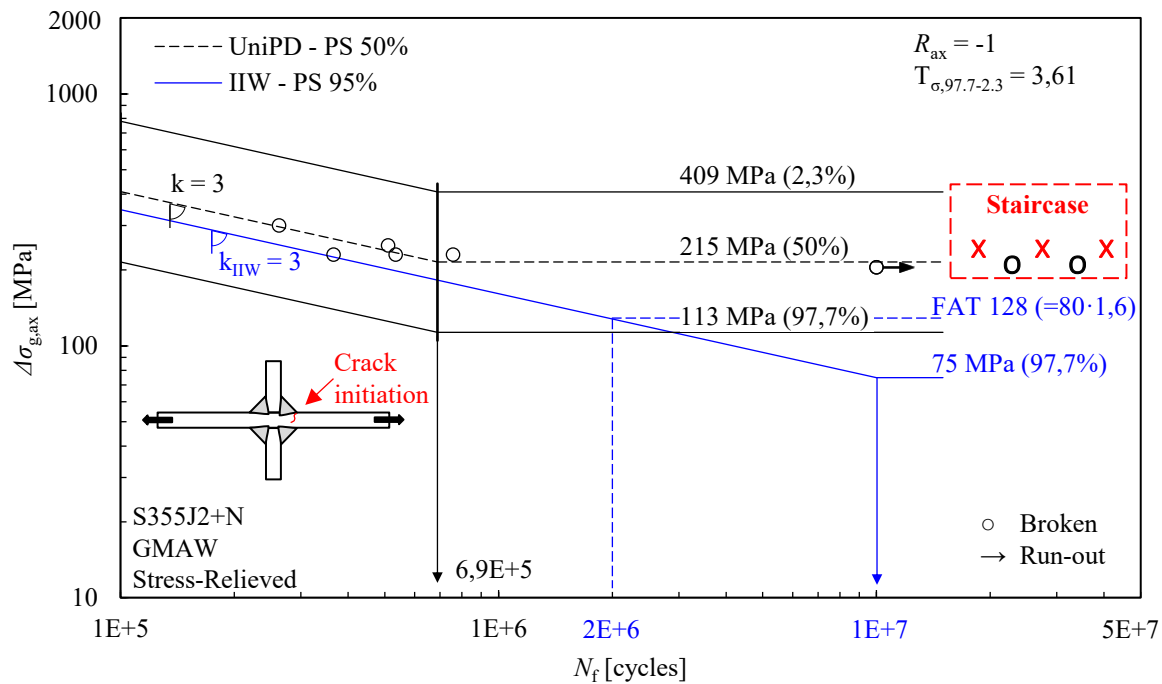


Figure 3.8. Experimental results of fatigue tests performed on non-load-carrying (nlc) fillet-welded joints with double transverse attachments. Results are expressed in terms of number of cycles to failure as a function of the applied nominal stress range according to Eq. (3.3).

3.2.1. Misalignments: effect of a secondary bending

The angular misalignments (γ in Figure 3.9) were measured in all joints. Each specimen was clamped to one end of the main plate on the four-jaw chuck of a lathe machine. Then a centesimal dial gauge has been fixed on the toolholder's table to measure the vertical positions (Y-coordinate in Figure 3.9) of six points located at specific axial positions on the specimen main plate (points A, B, C, C', B', and A' in Figure 3.9). The chosen points were located symmetrically with respect to the stiffeners and their vertical position was measured after zeroing the dial gauge at the point A ($Y_A = 0$ mm). Vertical position of points B and B' was measured not for evaluating the angular misalignment of the joints but for checking the straightness of the main plate in the regions far away from the weld bead. Then, the angular misalignments have been evaluated according to Eq. (3.4) and results reported in Table 3.2.

$$\gamma = abs \left(\arcsin \frac{Y_C - Y_A}{80} - \arcsin \frac{Y_{A'} - Y_{C'}}{80} \right) \quad (3.4)$$

3.2 Calibration of the initial crack size a_i : driving force at the fatigue limit

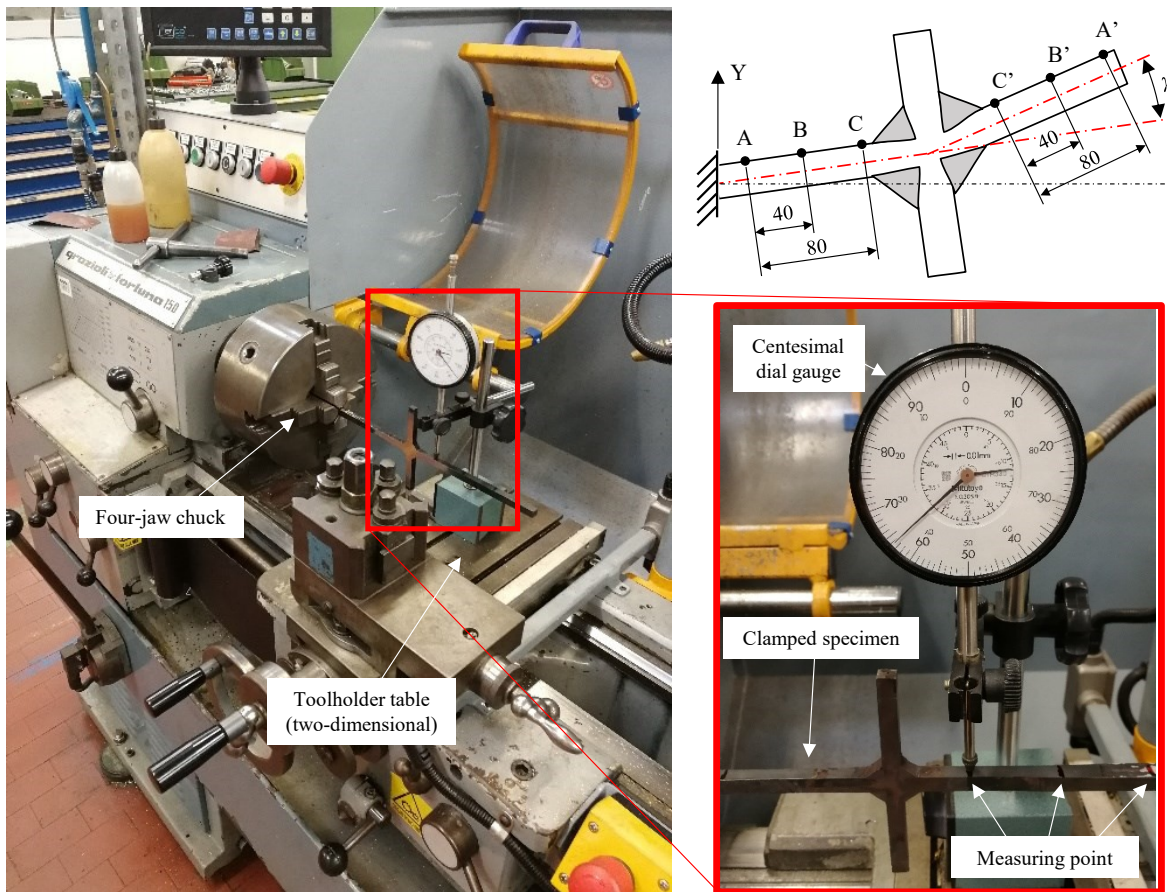


Figure 3.9. Measurement of angular misalignments. (a) Location of the measurement points for determining the angular misalignment γ . Dimensions are in millimetres.

Table 3.2. Measured angular misalignment.

Specimen	Y_A	Y_B	Y_C	$Y_{C'}$	$Y_{B'}$	$Y_{A'}$	γ
[-]	[mm]	[mm]	[mm]	[mm]	[mm]	[mm]	[°]
T25_01	0	0.36	0.69	0.81	0.44	0.03	1.05
T25_02	0	0.07	0.11	-0.32	-1.01	-1.72	1.08
T25_03	0	0.09	0.13	-0.24	-0.86	-1.56	1.04
T25_04	0	0.06	0.12	-0.31	-1.03	-1.74	1.11
T25_05	0	0.16	0.27	-0.05	-0.68	-1.35	1.12
T26_02	0	0.07	0.12	0.84	1.45	2.03	0.77
T26_03	0	0.08	0.12	0.86	1.45	2.04	0.76
T26_04	0	-0.5	-1.04	-1.33	-1.26	-1.22	0.82
T26_05	0	0.98	2.12	4.73	6.51	8.21	0.97

The effects of a secondary bending has been investigated by performing strain gauge measurements. Therefore, the specimen T25_5, i.e. the most misaligned (see Table 3.2), has

been instrumented with four 3-mm-long grid strain gauges. They have been located on the main plate at 30 mm from the stiffeners (see sections 1-2 and 3-4 in Figure 3.9), where the stress state is theoretically uniform and equal to the nominal applied stress (Eq. (3.3)), on opposite sides with respect to the bending neutral axis of the main plate (Figure 3.9).

Then, the instrumented specimen has been gripped in the same testing machine and in the same position as that used for the tested specimens. The testing machine was a servo-hydraulic Schenck Hydropulsar PSA 100 servo-hydraulic machine having a ± 100 kN load capacity and equipped with a Trio Sistemi RT3 digital controller. Finally, once the specimen was gripped, it has been loaded by applying stepwise increasing axial static loads from -7 kN up to +7 kN. At the same time, the corresponding strain gauge signals have been measured by means of a IMC Cronos PL-2 data acquisition unit. By taking advantage of a quarter bridge configuration, it has been possible to evaluate both the axial ($\varepsilon_{ax} = (\varepsilon_i + \varepsilon_j)/2$, $i = 1,3$, $j = 2,4$) and bending ($\varepsilon_b = (\varepsilon_i - \varepsilon_j)/2$, $i = 1,3$, $j = 2,4$) strain components in the two analysed sections (1-2 and 3-4 in Figure 3.9). After that, the axial $\sigma_{g,ax}$ and bending $\sigma_{g,b}$ stress components have been evaluated by multiplying the corresponding strains for the Young's modulus of the material $E = 206000$ MPa.

Results have been reported in Figure 3.10 as a function of the theoretical values of axial stress ($\sigma_{g,ax,theoretical}$), the latter being evaluated as the ratio between the applied load F and the cross-sectional area $A = 56.6 \text{ mm}^2$ (Eq. (3.3)). As expected, the measured axial stresses $\sigma_{g,ax}$ (red lines in Figure 3.10) were in very good agreement with the theoretical one $\sigma_{g,ax,theoretical}$ (black lines in Figure 3.10). On the other hand, Figure 3.10 shows that a bending stress component of $\sigma_{g,b}$ was present in the investigated range of axial stresses. More in detail, a value of $\sigma_{g,b,0,1-2} = 58$ MPa and $\sigma_{g,b,0,3-4} = 74$ MPa was measured at section 1-2 and section 3-4, respectively, when no axial load was applied to the specimens ($\sigma_{g,b,0} = \sigma_{g,b}(\sigma_{g,ax,theoretical}=0) > 0$, see Figure 3.10a). This difference between $\sigma_{g,b,0}$ measured in the two instrumented sections has been explained assuming the presence of a shear load. Accordingly, a linear distribution of the bending stress component $\sigma_{g,b,0}$ has been used and its value at the weld toe locations ($X_A = -7.36$ mm or $X_B = +7.36$ mm in Figure 3.10b) was computed by a simple linear interpolation. Calculations resulted in $\sigma_{g,b,0,A} = 63$ MPa and $\sigma_{g,b,0,B} = 68$ MPa at the weld toe located at an axial coordinate $X_A = -7.36$ mm and $X_B = +7.36$ mm, respectively.

3.2 Calibration of the initial crack size a_i : driving force at the fatigue limit

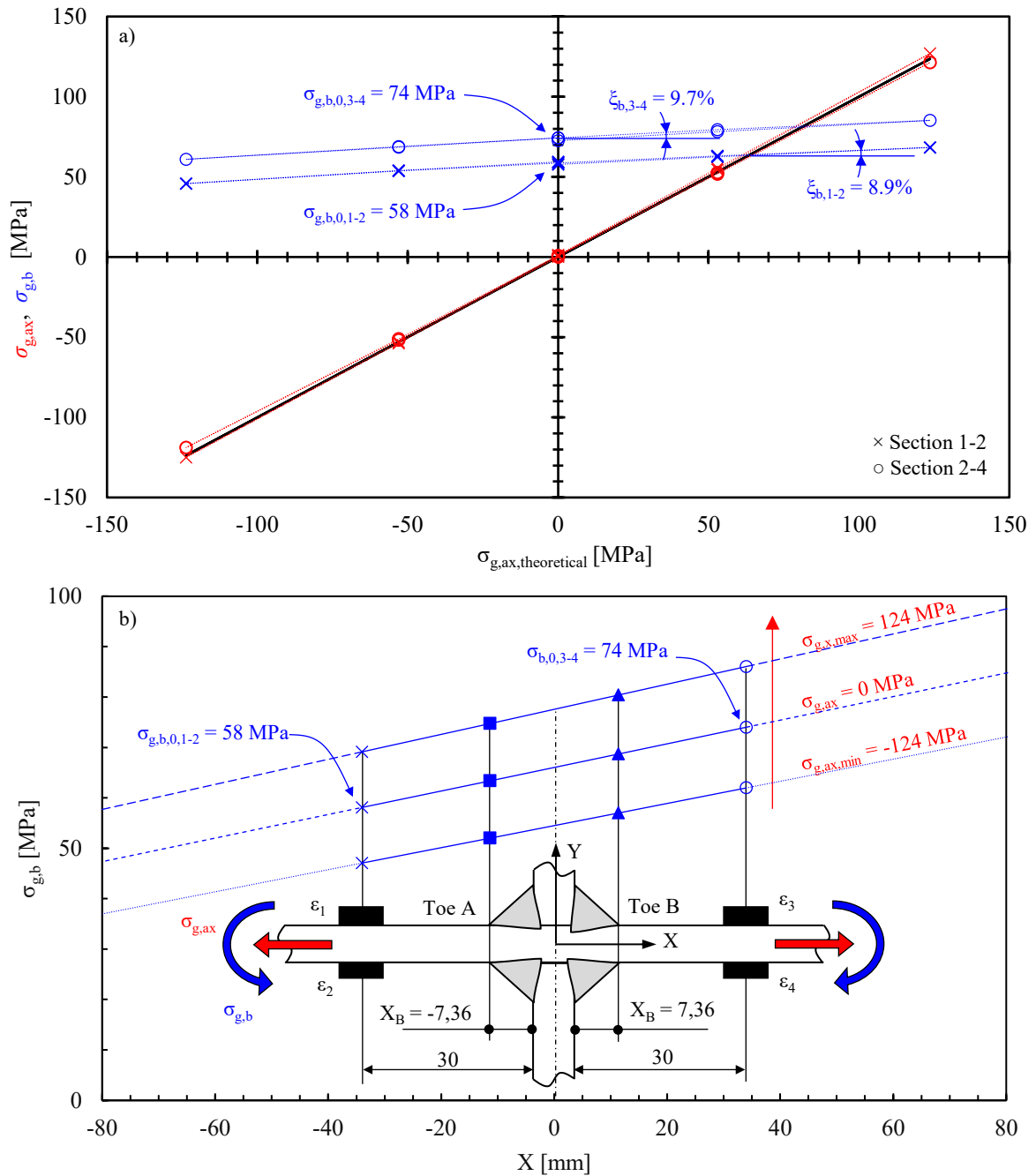


Figure 3.10. Measurement of angular misalignments: a) results of the strains' measurements as a function of the applied theoretical axial stress $\sigma_{ax,theoretical}$ and b) the same results reported as a function of the axial position X along the main plate and for $\sigma_{ax,theoretical} = -124$ MPa, 0 MPa and +124 MPa.

Moreover, Figure 3.10a shows that the measured bending stress $\sigma_{g,b}$ linearly increases with the applied force, this increment being proportional to $\zeta_{b,1-2} = 8.9\%$ and $\zeta_{b,3-4} = 9.7\%$ of the applied theoretical stress $\sigma_{g,ax,theoretical}$ at section 1-2 and 3-4, respectively. Then, the whole

bending stress distribution with the applied force has been evaluated at the weld toes in the same way as done before for the component $\sigma_{b,0}$. Thanks to these, the value $\xi_{b,A} = 9.2\%$ and $\xi_{b,B} = 9.4\%$ have been found at the weld toes having axial location $X_A = -7.36$ mm and $X_B = +7.36$ mm, respectively. Finally, the experimental data reported in Figure 3.8 have been corrected both in terms of applied load ratio R , due to the presence of a mean stress $\sigma_{g,b,0}$ different from zero, and in terms of applied stress range, to account for the bending stress component proportional to the axial one by means of the coefficient ξ_b . Accordingly, the applied stress ranges have been corrected using to the following expression, which defines a new nominal stress range $\Delta\sigma_g$ accounting for both the axial and bending cyclic components of stress:

$$\Delta\sigma_g = \Delta\sigma_{g,ax} + \Delta\sigma_{g,b} = \Delta\sigma_{g,ax} (1 + \xi_b) \quad (3.5)$$

where ξ_b is the rate of change of the bending stress component with the axial one and is equal to $\xi_b = 9.2\%$ and $\xi_b = 9.4\%$ as discussed above. At the same time, the applied load ratio has been corrected according to Eq. (3.6), resulting different for each applied stress range:

$$R = \frac{\sigma_{g,b,0} - \Delta\sigma_g / 2}{\sigma_{g,b,0} + \Delta\sigma_g / 2} \quad (3.6)$$

Fatigue test results in terms of nominal stresses along with the correction factors have been reported in Table 3.3. Results have been reported also in Figure 3.11 expressed in terms of $\Delta\sigma_g$ (Eq. (3.5)) as a function of the number of cycles to failure N_f along with the uniaxial fatigue resistance curve for normal stresses according to IIW recommendations [2] (blue line in Figure 3.11). This time, the IIW curve has been obtained multiplying the FAT80 fatigue resistance curve (80 MPa at $2 \cdot 10^6$ cycles for a Survival Probability $PS = 97.7\%$) by the coefficient $f(R) = 1.31$ (relevant to a load ratio $R = -0.28$, the higher among the tested specimens, see Table 3.3) to account the mean stress correction [2]. Similar to Figure 3.8, all experimental data have been statistically analysed and fitted according to BS ISO 12107:2012 [23] by imposing an inverse slope $k = 3$ and the obtained curves have been reported as black lines in Figure 3.11.

More interestingly, the knee point on the fitted curves has been obtained intersecting the fitted resistance curve having $PS = 50\%$ with the experimental fatigue limit obtained combining the axial and bending components of stress relevant to the staircase procedure (Figure 3.11):

3.2 Calibration of the initial crack size a_i : driving force at the fatigue limit

$$\Delta\sigma_{g,th} = \Delta\sigma_{g,th,ax} + \Delta\sigma_{g,th,b} = 215\text{MPa} + 20\text{MPa} = 235\text{MPa} \quad (3.7)$$

Eventually, the load ratio at the fatigue limit R_{th} has been evaluated entering the stress range at the fatigue limit $\Delta\sigma_{g,th} = 235$ MPa and the mean stress $\sigma_{b,0} = 63$ MPa into Eq. (3.6), obtaining $R_{th} = -0.3$.

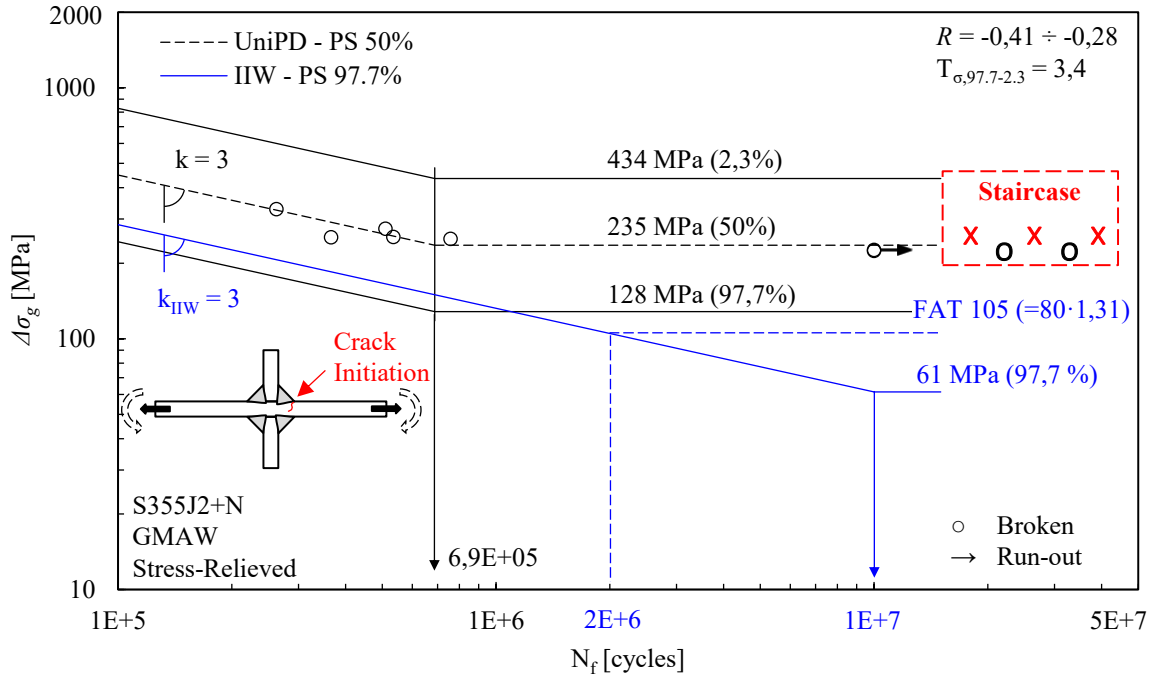


Figure 3.11. Experimental results of fatigue tests performed on non-load-carrying (nlc) fillet-welded joints with double transverse attachments. Results are expressed in terms of number of cycles to failure as a function of the applied nominal stress range $\Delta\sigma$ according to Eq. (3.5). The corresponding load ratio is slightly different for each stress level (Eq. (3.6)).

Table 3.3. Summary of fatigue test results.

Specimen	W	t	ΔF_{ax}	R_{ax}	f	$\Delta\sigma_{g,ax}$	$\Delta\sigma_{g,b}$	$\Delta\sigma_g$	$\sigma_{g,b,0}$	R°	N_f	Toe^+
[-]	[mm]	[mm]	[kN]	[-]	[Hz]	[MPa]	[MPa]	[MPa]	[MPa]	[-]	[cycles]	[-]
T26_02	6.93	8.03	16.70	-1	25	300	28	328	68	-0.41	262496	A
T26_03	7.09	8.03	14.23	-1	27	250	23	273	68	-0.33	510000	A
T26_04*	7.63	8.03	14.10	-1	30	230	21	251	68	-0.30	534480	A
T25_01*	7.47	8.03	13.79	-1	28	230	22	252	63	-0.33	366095	B
T25_02*	6.8	8.03	11.20	-1	30	205	19	224	63	-0.28	10^7	B
T25_03*	6.42	8.03	11.85	-1	27	230	22	252	63	-0.33	757383	B
T25_04*	7.44	8.03	12.25	-1	30	205	19	224	63	-0.28	10^7	B

^oAccording to Eq. (3.6).

*Data obtained in the modified staircase procedure.

⁺ Weld toe were crack initiation and final fatigue failure occurred. 1 and 2 are referred to weld the side according to the scheme reported in Figure 3.10. In case of run-out specimens, failure is referred to the beach marking fatigue tests following the staircase.

3.2.2. Experimental determination of the crack shape evolution

As discussed above, the calibration of the initial crack size requires the driving force (Eq. (3.1)) at the fatigue limit to be known with a high level of accuracy. It has also been discussed that to evaluate the driving force, the calculation of a geometric parameter β (Eq. (3.1)) the inclination and shape of the propagating crack is required. Accordingly, the crack shape evolution during the propagation at a stress level similar to the fatigue limit has been experimentally investigated. To do this, the idea was that of retesting the run-out specimens at a stress level capable of inducing fatigue failure and beach marking the crack front repeatedly in order to recognise post-mortem the complete evolution of the crack shape by image analysis of the fracture surfaces. Accordingly, run-out specimens have been retested at a slightly higher stress level, to induce crack initiation and propagation until failure, under closed loop load-controlled pure axial loading by using a 100 kN Schenck Hydropulsar PSA 100 servo-hydraulic machine equipped with a Trio Sistemi RT3 digital controller, the same used for the fatigue tests. Crack front have been marked adopting a variable amplitude sequence of CA fully reversed ($R_{ax} = -1$) sinusoidal axial loads having the following characteristics (Figure 3.12):

- Block A:
 - Nominal stress range $\Delta\sigma_{g,ax,A} = 270$ MPa
 - Number of cycles $N_A = 10^4$ cycles
 - Frequency $f_A = 20$ Hz
- Block B:
 - Nominal stress range $\Delta\sigma_{g,ax,B} = 200$ MPa
 - Number of cycles $N_B = 4 \cdot 10^4$ cycles
 - Frequency $f_B = 27$ Hz
- Block C:
 - Nominal stress range $\Delta\sigma_{g,ax,C} = 270$ MPa
 - Number of cycles $N_C = 10^4$ cycles
 - Frequency $f_C = 27$ Hz
- Block D:

3.2 Calibration of the initial crack size a_i : driving force at the fatigue limit

- Nominal stress range $\Delta\sigma_{g,ax,D} = 200$ MPa
- Number of cycles $N_D = 4 \cdot 10^4$ cycles
- Frequency $f_D = 37$ Hz

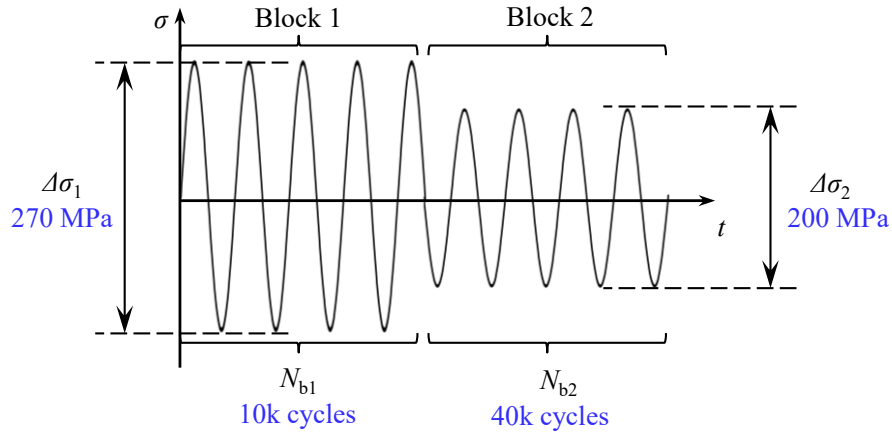


Figure 3.12. Load sequence used for beach marking the run-out specimens.

The sequence AB has been applied repeatedly for a total of 10 times, then the sequence CD has been applied repeatedly until failure. Post-mortem, the fracture surfaces have been captured with a digital microscope and by image analysis has been possible to identify the marked crack front, as shown Figure 3.13. Accordingly, the crack geometry has been obtained analysing the marked crack fronts highlighted with the white lines in Figure 3.13. Then, this crack fronts have been fitted with an elliptical shape having minor axis equal to the crack length a and major axis c (Figure 3.14). The centre of all the ellipses was fixed at the weld toe and located 1 mm away from the side of the specimen (see Figure 3.14).

As a result, the evolution of the ratio c/a as a function of the crack length a has been obtained and reported in Figure 3.14. Figure 3.14 also shows a comparison between the fitted elliptical cracks (in orange) and the corresponding experimental ones (in white). Unfortunately, the smallest crack which has been possible to identify corresponded to $a = 65$ μm . Then, in the following analyses, the ratio c/a has been assumed linearly extrapolating the experimental results when $a < 65$ μm (see dotted line in Figure 3.14).

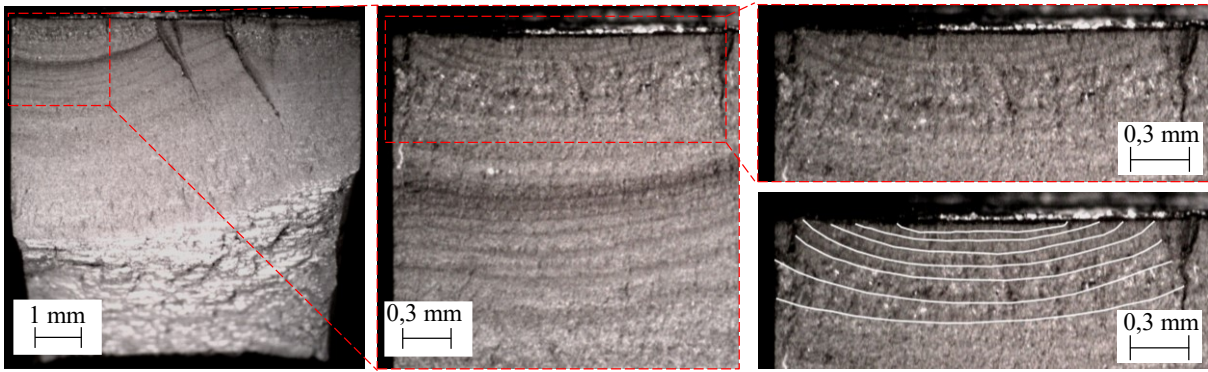


Figure 3.13. Beach marked fracture surface and corresponding crack fronts.

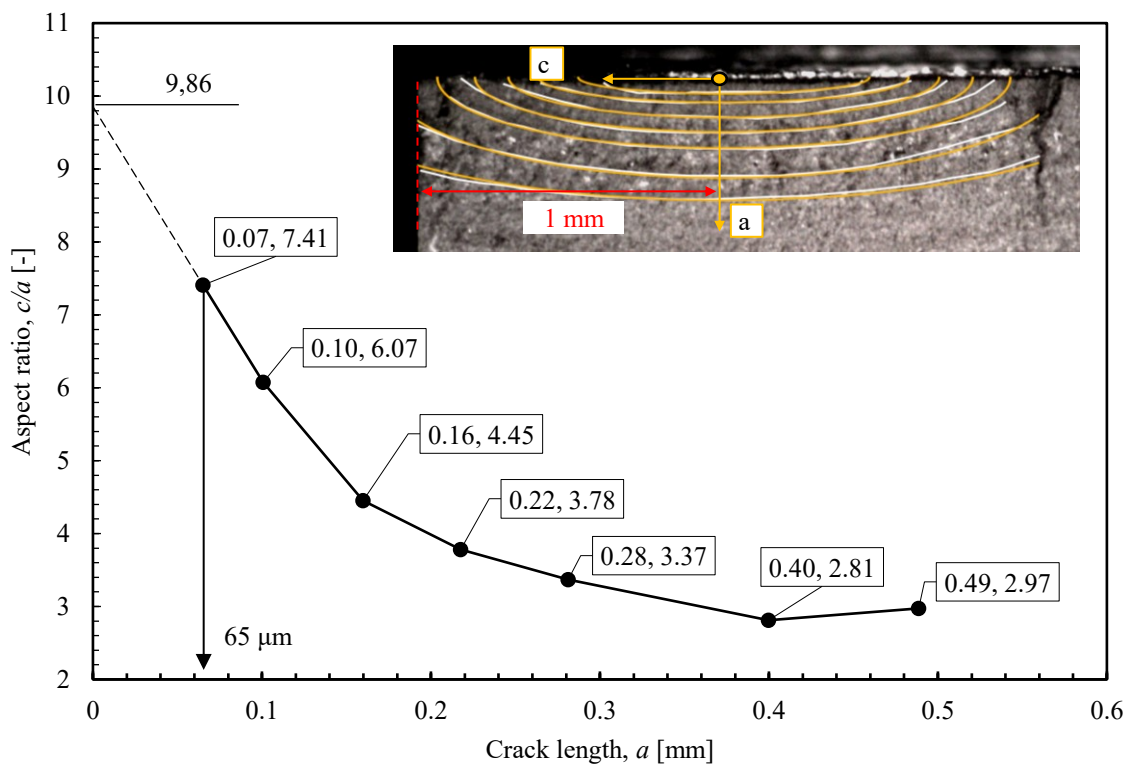


Figure 3.14. Crack shape evolution with the crack length a .

3.2.3. Structural FEA analyses

As discussed in 3.2.1, the analysed joints were subjected to both axial and bending loads. Taking advantage of the linear elasticity hypothesis it was possible to exploit superposition principle and write the applied stress intensity factor range ΔK_I as the sum of two components:

3.2 Calibration of the initial crack size a_i : driving force at the fatigue limit

$$\Delta K_I = \Delta K_{I,ax} + \Delta K_{I,b} = \beta_{ax} \cdot \sqrt{\pi a} \cdot \Delta \sigma_{g,ax} + \beta_b \cdot \sqrt{\pi a} \cdot \Delta \sigma_{g,b} \quad (3.8)$$

Where β_{ax} and β_b are the geometric factors for the axial and bending components of stress, respectively. Their values have been evaluated by means of structural linear elastic FE analyses. In particular, the FEA have been used to estimate the K_I for each loading mode (axial and bending) when applied 1 MPa (this way Eq. (3.8) simplifies and is possible to evaluate the coefficients β_{ax} and β_b). To do this, both the Peak Stress Method (PSM, see chapter 1) [24,25] and the Fracture Tool (FT) implemented in the Ansys® FE commercial software have been used. The numerical model (Figure 3.15) has been generated according to the specimen's geometry of Figure 3.4 whose parameters are reported in Table 3.1. More in detail, the driving force at the fatigue limit $\Delta K_{I,\Delta\sigma_{g,th}}$ (so $K_{I,\Delta\sigma_{g,th}}$) being the aim, the geometrical parameters of the specimens used for the staircase procedure (see the last two columns in Table 3.1) has been adopted in the FE model (Figure 3.15).

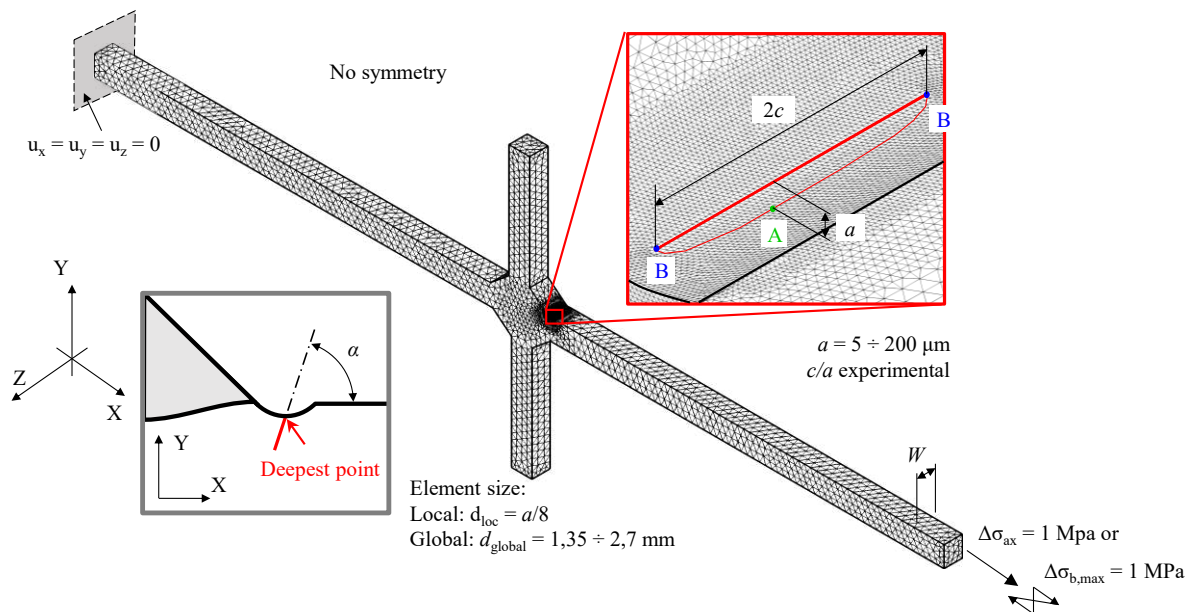


Figure 3.15. Structural linear elastic FE model reproducing the experimental geometry.

The fatigue crack has been introduced as an elliptical crack whose length a was varied between 5 a 200 μm with a gradually increasing step (see Table 3.4) and whose shape c/a was

varied with the crack length a according to what observed experimentally (Figure 3.14). As regard the c/a evolution, its value has been linearly interpolated in between experimental data and linearly extrapolated for $a < 65 \mu\text{m}$ (Figure 3.14). The following hypotheses have been used in modelling the propagating crack (Figure 3.15):

- Planar crack.
- Crack initiation at the deepest point in the weld toe.
- Crack plane parallel to notch bisector line.

The Young's modulus $E = 206000 \text{ MPa}$ and the Poisson's coefficient $\nu = 0.3$ have been used.

Then, the model has been discretized using 3D 10-node tetrahedral elements (SOLID 187 of Ansys® element library) generated thanks to the free mesh generation algorithm present in the Ansys software. The element size has been made varying between $d_{\text{loc}} = a/8$, proportional to the crack size a in the region nearby the crack, up to $d_{\text{global}} = 1.35 - 2.7 \text{ mm}$ far away from it (Figure 3.15). This continuous variation of the element size was made possible by modelling control volumes surrounding the crack region: in particular, within each single volume the element size has been kept constant, while between one volume and the next its value it has been gradually increased. Finally, two different models have been created to investigate separately the effect of the axial and the bending loads. One of the specimen's ends has been constrained imposing a null displacement in all directions ($u_x = u_y = u_z = 0$), while a uniform or linear distribution of stresses has been assigned to the other specimen's end in case of axial or bending stress, respectively. In particular, the loads have been applied in a such a manner to guaranty a stress of 1 MPa was applied both for the axial and bending loads (Figure 3.15).

No symmetry has been exploited in the FE model, as the propagating crack was located in such a manner that no symmetry planes were present in the model (Figure 3.15). In this configuration, the model consisted in approximately $\sim 9 \cdot 10^6$ degrees of freedom, repeated for 30 times as 30 is the number of the different crack size investigated. For this reason, it appears clear why before starting the simulations, a simple sensitivity analysis has been performed to check if the position of the crack could have been changed on the symmetry plane (and consequently exploiting the symmetries of the model) without significantly change the results. Accordingly, a similar model, this time having the crack centred on the weld toe line, i.e. in the middle of the specimen's width ($W/2$ in Figure 3.16) has been generated by exploiting the

3.2 Calibration of the initial crack size a_i : driving force at the fatigue limit

symmetry XY plane (Figure 3.16). Interestingly, an error of less than 3% has been found between the K_I evaluated with the two models (Figure 3.15 and Figure 3.16) in the investigated crack length range, justifying the assumption that the crack position along the weld toe line does not influence the K_I for short cracks. Then, the model exploiting the symmetry (Figure 3.16), whose number of degrees of freedom was more than halved if compared to the model without symmetry, has been adopted and solved for each of the crack length in Table 3.4.

Table 3.4. Crack size analysed with the FE analyses.

a_{\min} [mm]	a_{\max} [mm]	a_{step} [mm]
0.005	0.007	0.002
0.007	0.0125	0.002
0.0125	0.025	0.0025
0.025	0.04	0.0025
0.04	0.06	0.005
0.06	0.1	0.005
0.1	0.15	0.025
0.15	0.2	0.05

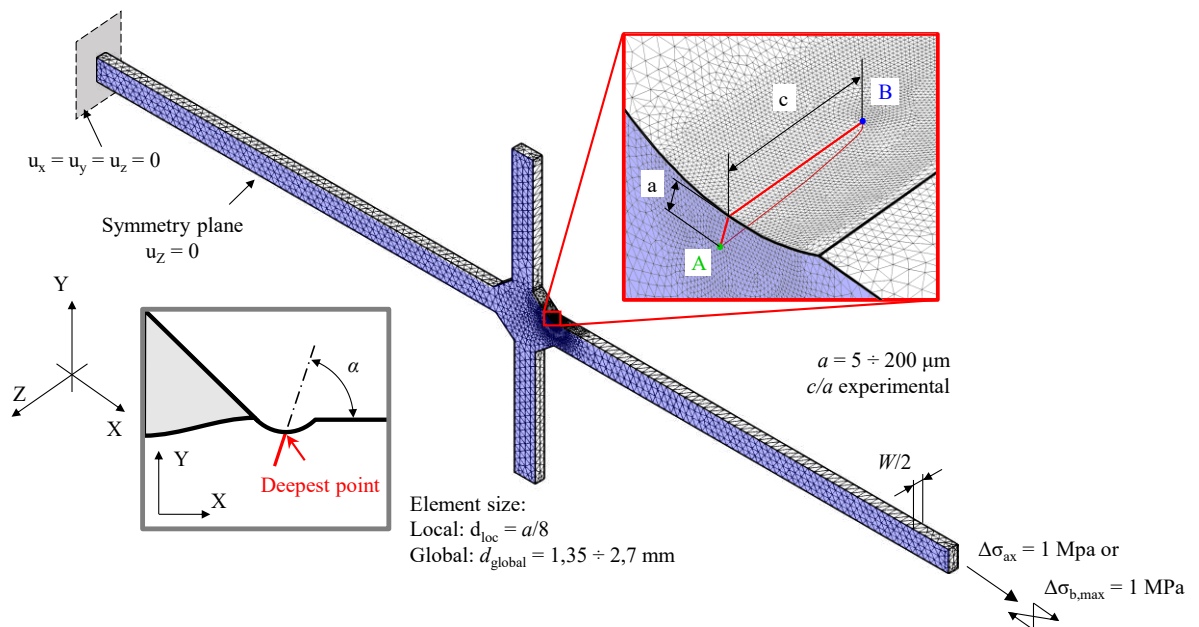


Figure 3.16. Structural linear elastic FE model exploiting the XY symmetry plane.

After the solution, the results have been post-processed and reported in Figure 3.17, which shows the evolution of the K_I with the normalized curvilinear coordinate s/s_{\max} running along the crack front line. Results have been obtained either with the PSM (dotted line in Figure 3.17) or the Fracture Tool (solid line in Figure 3.17) both for the axial and the bending stress components were relevant to a nominal stress of 1 MPa and have reported for the minimum and the maximum crack length, i.e. $a_{\min} = 5 \mu\text{m}$ and $a_{\max} = 200 \mu\text{m}$.

It must be observed that results obtained with the PSM were not taken from nodes lying on the external surfaces of the specimens (point A and point B, green and blue in Figure 3.17, respectively) but on the first available node according to what discussed in chapter 1 regarding the application of the PSM with tetra elements [25]. However, in the light of the very small element size at the crack front and being not a steep gradient of K_I along the crack front, results have been assumed to be perfectly corresponding to that of node at point A and B in Figure 3.17. Results showed that K_I distribution is always monotonically increasing along the crack front line running from the deepest point (point A in Figure 3.17) to the point at the weld toe (point B in Figure 3.17), independently on the crack size, at least within the investigate range of crack lengths ($5 \mu\text{m} < a < 200 \mu\text{m}$). Moreover, results obtained with the PSM (dotted line in Figure 3.17) and the Fracture Tool (solid line in Figure 3.17) were always in very good agreement, the errors between them being always less than 8%. Furthermore, it is interesting to note that the point A always resulted to be that having the highest value of the K_I .

Finally, thanks to the obtained results, it was possible to evaluate the geometrical parameters β in both point A and B according to the following expression:

$$\beta = \frac{K_I}{\sqrt{\pi a} \cdot 1\text{MPa}} \quad (3.9)$$

The obtained evolutions of the coefficients β_{ax} and β_{b} have been reported in Figure 3.18 as a function of the crack length for both the point A and point B.

3.2 Calibration of the initial crack size a_i : driving force at the fatigue limit

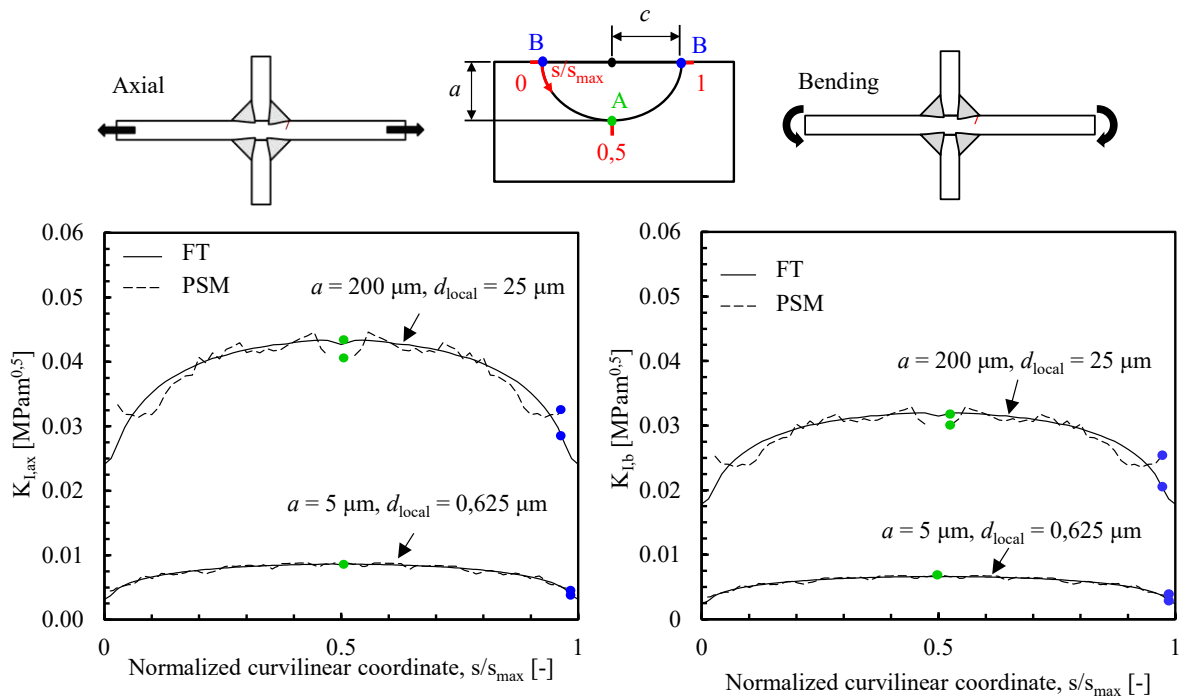


Figure 3.17. K_I distribution along the crack front line for different crack size and different loading conditions. Results have been obtained both using the PSM and the Fracture Tool in Ansys®.

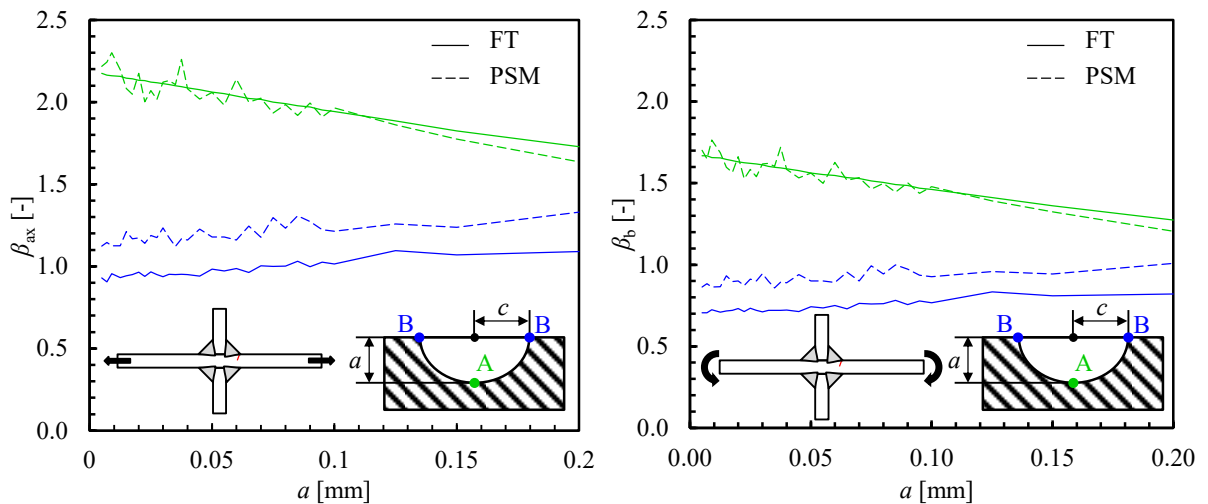


Figure 3.18. Evolution of the factors β_{ax} and β_b with the crack length a .

3.3. Calibration of the initial crack size a_i : the cyclic R-curve

3.3.1. Specimens

The aim was that of performing experimental tests for the characterization of the S355J2+N structural steel mechanical properties, in particular its cyclic R-curve. Starting from the experimental observation that the crack initiation and early crack growth phases in welded joints occur within the Heat Affected Zone (HAZ), the cyclic R-curve has been characterized for both the Base Metal (BM) and in the HAZ. The adopted specimens (Figure 3.19) were Single Edge Notch in Bending (SENB), and made in two different versions, both having the same geometry, but one made of base metal and the other obtained from a transverse loaded butt weld ground flush to plate. In the latter, residual stresses have been reduced as much as possible by applying the proper stress relieving heat treatment. The crack starter notch made by EDM, has been realized within the HAZ so as to promote the propagation within this region and, this way, obtaining the corresponding cyclic R-curve for the HAZ.

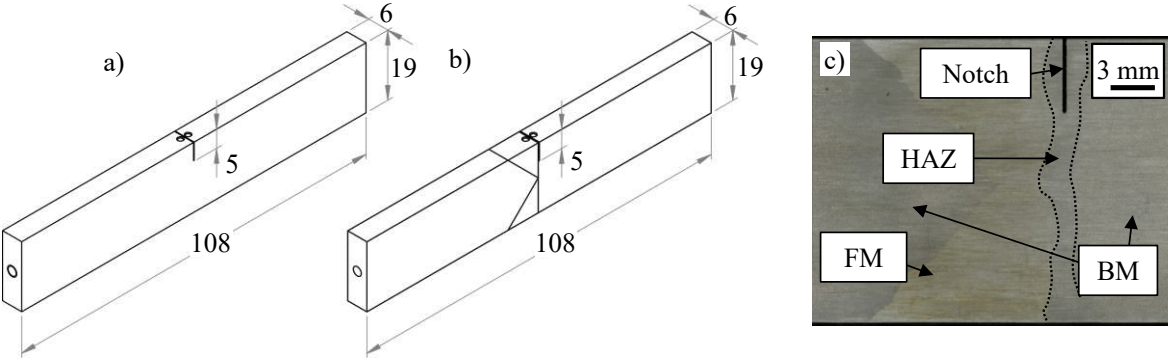


Figure 3.19. SENB geometry. Specimens made of: a) S355J2+N and S690QL; b) welded S355J2+N, with the EDM notch inside the HAZ; c) macrography of one welded specimen showing the EDM notch location

3.3.2. Fatigue crack growth tests setup

The specimens (Figure 3.19) have been loaded in pure bending at two different load ratios, $R = -1$ and $R = 0.1$, thanks to a RUMUL TESTRONIC 100kN or a RUMUL TESTRONIC 20kN resonance-testing machines having working frequency of approximately 60 Hz and 108 Hz, respectively (Figure 3.20b). The negative load ratio was permitted due to the adoption of an eight-point-bending device for SENB specimens allowing the application of fully reversed pure bending cyclic loading (Figure 3.20b,c). In particular, during the fatigue crack growth tests the testing machine has been controlled in terms of applied force or applied Stress Intensity Factor range ΔK_I , the value of which has been calculated adopting the equations reported in the standard ISO12108:2018 [26]:

$$K_I = \frac{F}{B \cdot W^{1/2}} \cdot \frac{S_{\max} - S_{\min}}{2W} \cdot 3 \sqrt{2 \tan \frac{\pi a}{2W}} \cdot \left[\frac{0.923 + 0.199 \left(1 - \sin \frac{\pi a}{2W} \right)^4}{\cos \frac{\pi a}{2W}} \right] \quad (3.10)$$

Where F is the applied force, B and W are the width and the height of the specimen, respectively (Figure 3.20), a is the crack length, while S_{\max} and S_{\min} are major and minor span of the 8-point-bending fixtures, respectively (Figure 3.20).

In-situ real-time crack growth monitoring has been performed by means of a non-destructive evaluation (NDE) technique based on the Direct Current Potential Drop (DCPD) method [12,27] (Figure 3.20b,d). In few words, this technique is based on the principle that the electrical resistance of the tested specimen increases due to crack growth (electrons are "forced" through the uncracked cross-sectional area that become smaller as the crack propagates); therefore, if the specimen is subjected to a constant electrical current flow, the increase of the electrical resistance translates in an increase of the potential drop. The crack depth can be estimated by entering the experimentally measured potential drop in a proper calibration curve. In case of SENB specimens, an analytical expression for the DCPD calibration curve is available [28]:

$$a = \frac{2W}{\pi} \cos^{-1} \left\{ \frac{\cosh(\pi y / 2W)}{\cosh \left[\frac{V}{V_0} \cdot \cosh^{-1} \left(\frac{\cosh(\pi y / 2W)}{\cos(\pi a_0 / 2W)} \right) \right]} \right\} \quad (3.11)$$

where a refers to the crack-length, V to the measured potential, W to the specimen height, y to the distance between the potential probes and the crack plane and V_0 is the measured potential drop at notch depth $a_0 = a_{notch}$, before applying fatigue loads (Figure 3.20). The reader is referred to chapter 4 for a more detailed description of the DCPD method. The effects of temperature variations on the measured potential drop have been compensated by measuring in real-time also the temperature of the specimen. Then, the measured signal has been corrected taking advantage of the linear correlation between the electrical resistivity of the material and the temperature (a detailed description of the problem will be given in chapter 4). For injecting the electrical current into the specimen, a DC Power Supply HP6033A with a pole-switcher for changing the direction of the current and compensating the thermoelectric effects [28] has been used, while the measure of the potential drop signal has been performed thanks to a Keithley 2182A Nanovoltmeter.

The procedure for evaluating the cyclic R-curve (Figure 3.21) has been that one adopted by Tabernig and Pippan [12] and recently updated by Pourheidar et al. [15]. Initially the notches have been sharpened thanks to a special razor blade polishing technique, performed using a customised semiautomatic device (Figure 3.22), which allowed to get extremely sharp notches (Figure 3.22). The reason behind the need for a sharper notch is due to the need of reducing the load level in the compression pre-cracking phase (the following phase), indeed the smaller the notch tip radius, the smaller the load to initiate a pre-crack and the smaller the required length of the pre-crack to avoid notch effects [12,15].

Then, a closure free crack has been generated at the notch tip by applying in force control mode a standard compression pre-cracking procedure at a load ratio $R = 20$ and an initial $\Delta K_I = 16 \text{ MPa}\cdot\text{m}^{0.5}$, these values being chosen based on the experience of the author (Figure 3.21). After the compression pre-cracking, the specimen has been initially loaded in traction by applying constant amplitude fatigue loadings at a stress level which generates a driving force very close to the intrinsic threshold $\Delta K_{th,eff}$ (Figure 3.21). If no propagation occurred, the load level has been increased with increments of about $0.5 - 1 \text{ MPa}\cdot\text{m}^{0.5}$ ($\sim 0.1 \cdot \Delta K_{th,LC}$ [12,15]).

3.3 Calibration of the initial crack size a_i : the cyclic R-curve

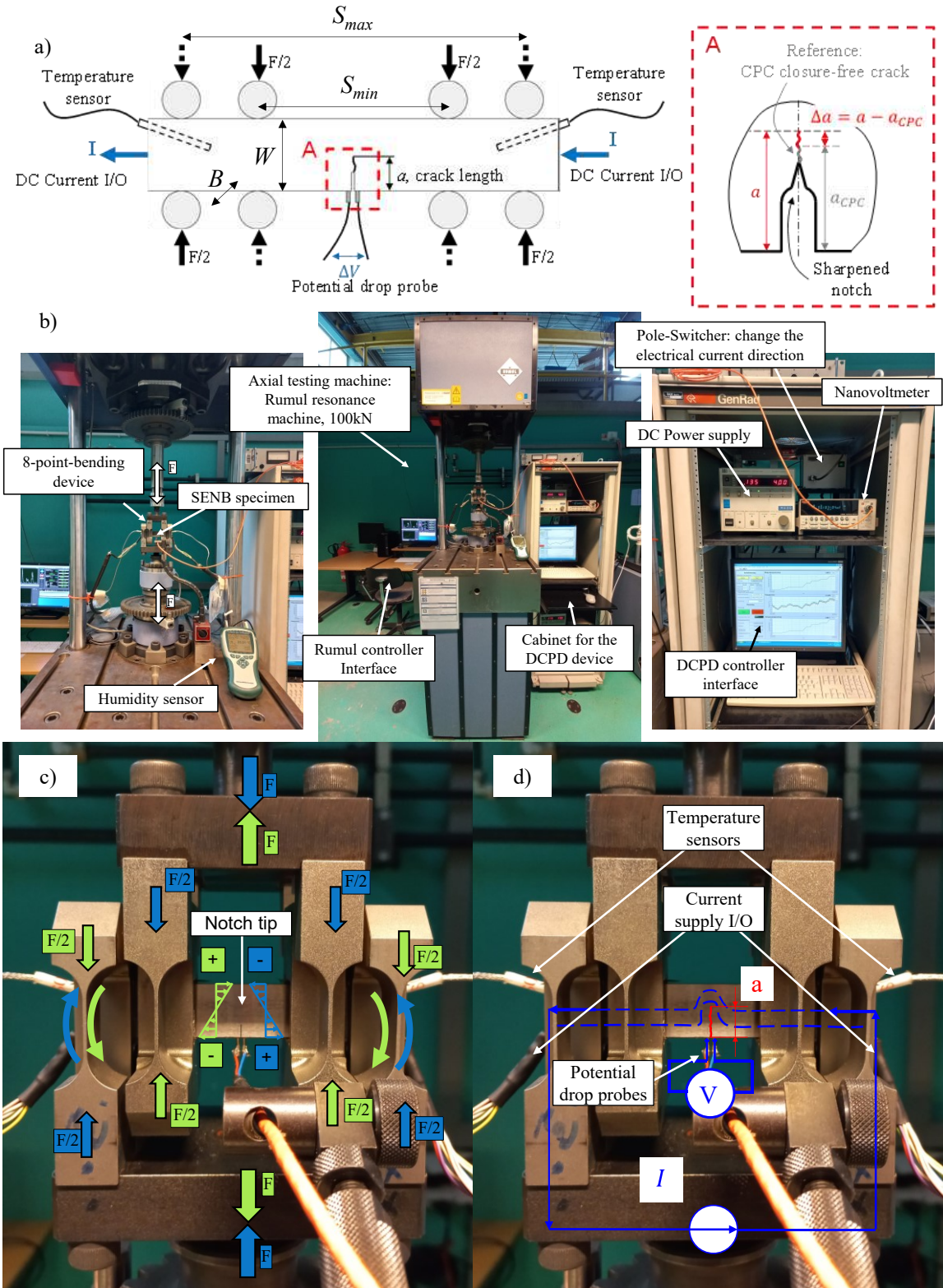


Figure 3.20. Experimental setup: a) schematic illustrating the experimental setup containing the 8-point bending fixture and the DCPD elements. The region A, zoomed in the right-hand side, details the sharpened notch performed before conducting the experiments. b) Experimental setup with detail on the testing machine and on the DCPD device. c) working principle of the 8-point-bending fixture. d) details on the application of the DCPD method.

Whenever the stress level was high enough for the crack to propagate, closure phenomena built up and the crack arrested, reaching again the threshold condition (Figure 3.21). Then the load level has been increased again, and this procedure repeated until no more arrest has been found (Figure 3.21). At this point the control mode of the machine has been switched from controlling the applied force range ΔF to the applied Stress Intensity Factor range ΔK_I , the value of which has been kept constant during the propagation, i.e. the load has been automatically and in real time decreased by the controller in order to keep constant the applied SIF range ΔK_I . Also with this control mode, after each arrest the SIF range ΔK_I level has been increased repeatedly until no more arrest has been found (Figure 3.21).

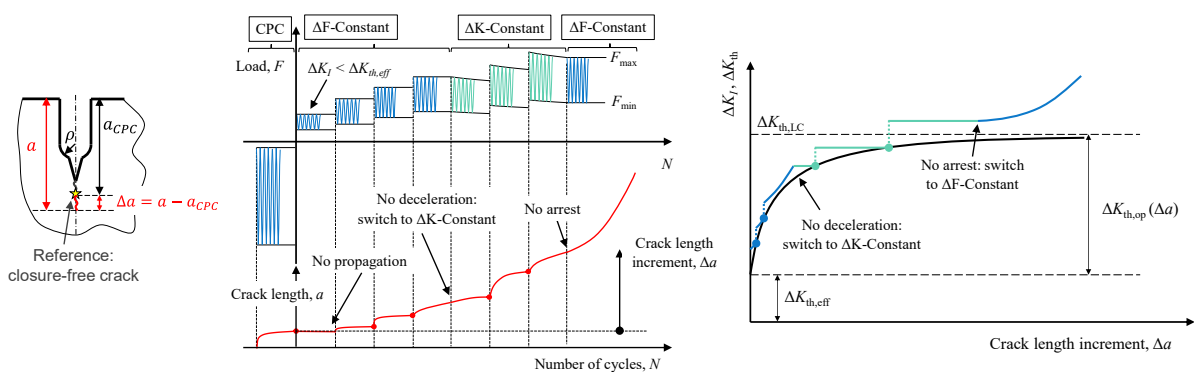


Figure 3.21. Schematic illustrating the experimental procedure for the determination of the cyclic R-curve. Load-cycle history and corresponding crack length evolution, on the left; corresponding cyclic R-curve with the driving force evolution, on the right.

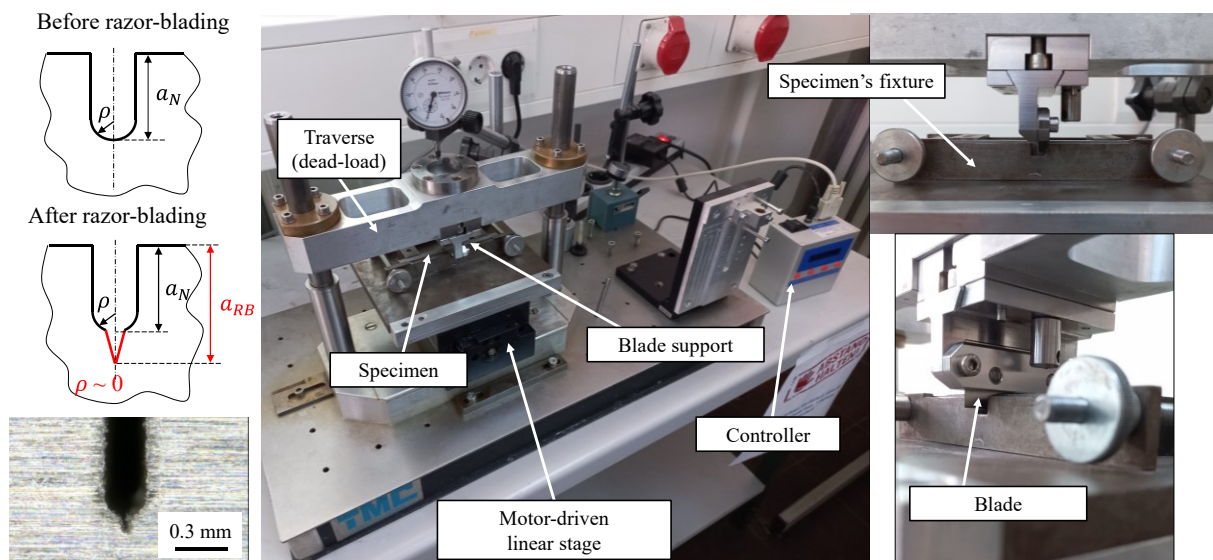


Figure 3.22. Device used to perform the razor blade polishing technique.

3.3.3. Results

The cyclic R-curve has been obtained by reporting in a chart the values of the crack increment from the initial crack size Δa and corresponding stress intensity factor range ΔK_{th} corresponding at the arrest point (Figure 3.21). Results of the performed test have been reported in Figure 3.23 both for the BM and the HAZ along with results obtained in the IBESS project [18,19] on a similar steel, i.e. an S355NL structural steel. The first thing to note is that, apparently, the obtained experimental results follow the cyclic R-curve obtained in IBESS, even though they display a slightly higher resistance probably due to the different material specification (actual J2+N compared to NL in IBESS). Secondly, Figure 3.23 highlights there are no significant differences between the cyclic R-curve relevant to the BM and that relevant to the HAZ conditions at least in the very short crack regime ($\Delta a < 0.5$ mm). On the other hand, this difference became evident for the longer crack regime ($\Delta a > 0.5$ mm, Figure 3.23).

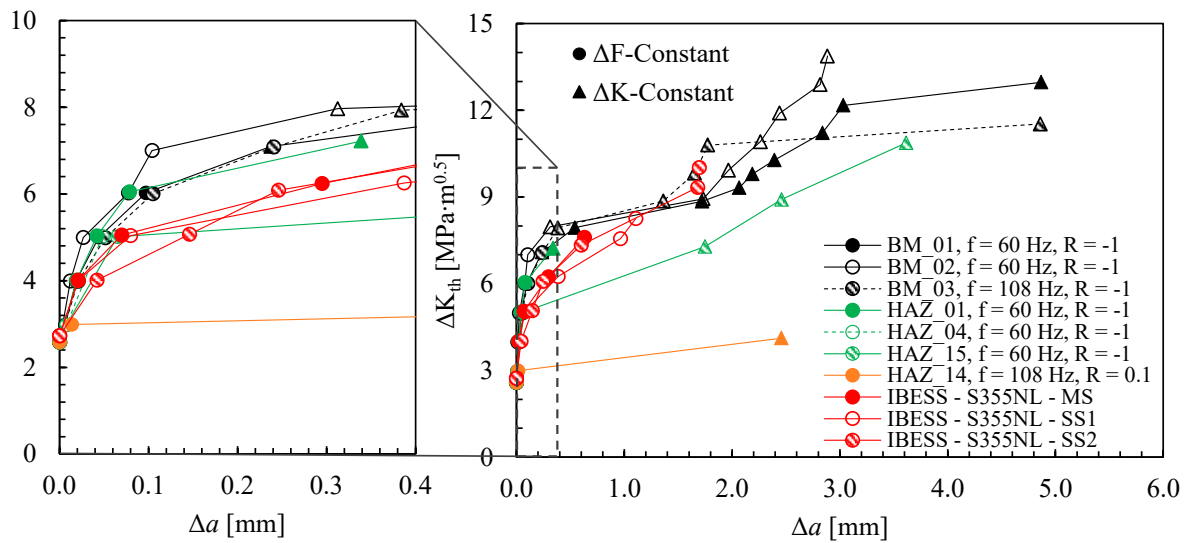


Figure 3.23. Summary of the cyclic R-curves obtained with specimens made of S355J2+N compared to that taken from the Literature and relevant to an S355NL structural steel [18,19]. Results are relevant to different materials/microstructure (Base Metal-BM/Heat Affected Zone-HAZ), different testing frequencies (60 Hz and 108 Hz), and different load ratios ($R = -1$ and $R = 0.1$).

Then, according to Maierhofer et al. [29], the experimental data have been fitted using the following expression:

$$\Delta K_{th} = \Delta K_{th,eff} + (\Delta K_{th,LC} - \Delta K_{th,eff}) \cdot \left[1 - \sum_{i=1}^n v_i \cdot e^{-\frac{\Delta a}{l_i}} \right] \quad (3.12)$$

Where $\Delta K_{I,th,eff}$ and $\Delta K_{I,th,LC}$ represent the intrinsic component of the fatigue crack propagation threshold and the fatigue crack propagation threshold for long crack, respectively, while v_i and l_i are coefficient to be found with best fit on the experimental data, provided that the following constraint condition is satisfied:

$$\sum_{i=1}^n v_i = 1 \quad (3.13)$$

The best fit has been performed taking advantage of the curve fitting tool implemented in Matlab[®] by imposing $i = 2$. The resulting parameters for the cyclic R-curve of the HAZ relevant to $R = -1$, i.e. $\Delta K_{th,eff} = 2.58 \text{ MPam}^{0.5}$, $\Delta K_{th,LC} = 10 \text{ MPam}^{0.5}$, $v_1 = 0.495$, $l_1 = 0.046 \text{ mm}$, $v_2 = 1 - v_1 = 0.505$, $l_2 = 1.913 \text{ mm}$, have been used in the following paragraphs.

3.3.4. Discussion: a new procedure for determining the cyclic R-curve

Although it is not the aim of this chapter to argue about the limits of the procedure used to experimentally derive the R-cyclic curve, in this paragraph a further step forward in the experimental procedure will be discussed. In 2022, Pourheidar et al. [15] proposed an update of the standard procedure for determining the cyclic R-curve [12] consisting in the introduction of Constant- ΔK steps (aqua green steps in Figure 3.21) after the tangency condition between the driving force and the resistance curve when applying Constant- ΔF steps (blue steps in Figure 3.21). The aim of this modification was that of better describing the upper part of the cyclic R-curve, i.e. determine Δa - ΔK_{th} values close to the long crack fatigue crack propagation threshold $\Delta K_{th,LC}$, this being impossible with the Constant- ΔF procedure that provides undesirably conservative threshold values (see Figure 3.21). The latter aspect can be better understood by comparing the experimental data obtained with the Constant- ΔF + Constant- ΔK

3.3 Calibration of the initial crack size a_i : the cyclic R-curve

with that in the IBESS project [18,19] obtained using only the Constant- ΔF technique (see Figure 3.23 for the comparison). Having in mind the need of better describing the long crack regime, in this work it has been proposed to definitely improve the procedure by adding Decreasing- ΔK steps, applied according to the main standards [26,30], when the Constant- ΔK steps can no more intersect the cyclic R-curve (Figure 3.24). This way, with just one single experimental test it is possible to have a complete description of the fatigue crack growth propagation threshold from the short to the long crack regime.

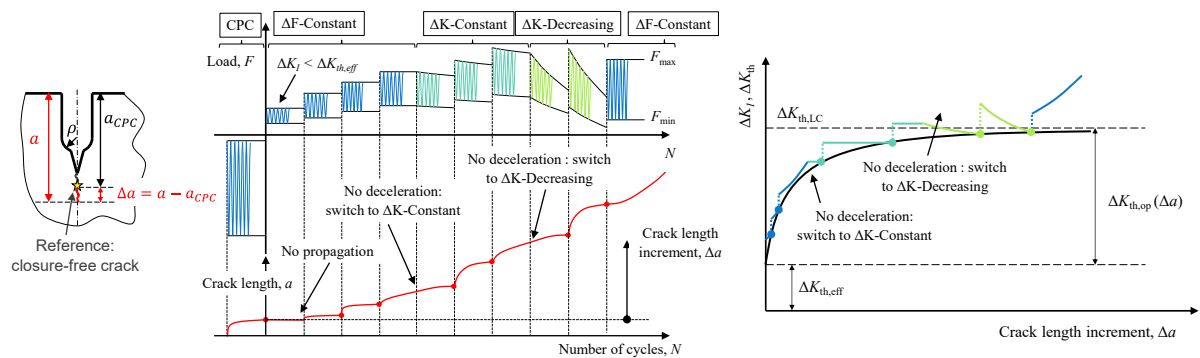


Figure 3.24. Schematic illustrating the proposed experimental procedure for the determination of the cyclic R-curve aimed at better describing the transition from the short to the long crack regime. Load-cycle history and corresponding crack length evolution, on the left; corresponding cyclic R-curve with the driving force evolution, on the right.

Accordingly, data reported in Figure 3.23 has been tested not only by applying the Constant- ΔF + Constant- ΔK procedure, but also adding Decreasing- ΔK steps, according to the procedure described in Figure 3.24. The results of these tests are reported in Figure 3.25. Noteworthy, the proposed procedure gave successfully results despite the a high scatter in the long crack regime, the latter being generated by high sensitivity to extrinsic crack closure phenomena in the long crack regime, for example the presence of environmental effects [31–34]. Accordingly, experimental results highlighted that higher frequency resulted in reduced $\Delta K_{th,LC}$, while no significant effects have been found in the short crack regime. At the same time a higher load ratio R , results in higher reproducibility, i.e. lower scatter (maybe because the crack is kept opened and there is less contact between the fracture surface affected by corrosion, etc..., i.e. there is a lower sensitivity to extrinsic crack closure phenomena). Finally, it is worth noting that, in general, the cyclic R-curves are influenced by the ΔK increase between each step. For smaller increases (e.g. $0.5 \text{ MPa}\cdot\text{m}^{0.5}$ when $R = -1$), less energy is provided to the crack to

overcome the oxide barriers resulting in crack closure. Therefore, a smaller crack extension is usually observed.

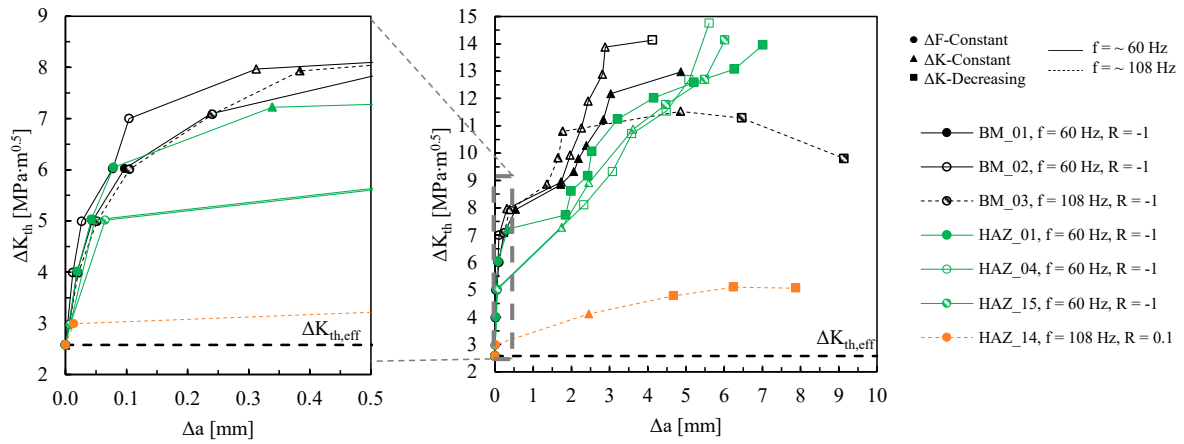


Figure 3.25. Summary of the cyclic R-curves obtained with specimens made of S355J2+N according to the proposed experimental procedure (Figure 3.24). Results are relevant to different materials/microstructure (Base Metal-BM/Heat Affected Zone-HAZ), different testing frequencies (60 Hz and 108 Hz), and different load ratios ($R = -1$ and $R = 0.1$).

3.4. Calibration of the initial crack size

3.4.1. Results

The calibration of the initial crack size a_i according to the crack arrest analysis [17–19] has been made possible by the comparison of the driving force at the fatigue limit (paragraph 3.2) and the corresponding resistance curve (paragraph 3.3). Unfortunately, the comparison has to be made for the same load ratio R but in this work the driving force has been obtained for $I = -0.3$ while the cyclic R-curve for $R = -1$. Accordingly, the driving force at the fatigue limit has been corrected assuming that all the parameter like the crack position, inclination and shape c/a as well as the geometrical factors β were independent of the mean stress but for the fatigue limit expressed in nominal stress range. To take into account the mean stress effect, it has been used an equation based on the Goodman equation [35,36]:

$$\frac{\Delta\sigma_{g,th,R}}{2} = \frac{\Delta\sigma_{g,th,R=-1}}{2} \left(1 - \frac{\sigma_m}{\sigma_{UTS}} \right) \quad (3.14)$$

3.4 Calibration of the initial crack size

where the $\Delta\sigma_{g,th,R}$ and $\Delta\sigma_{g,th,R=-1}$ are the fatigue limit for $R \neq -1$ and $R = -1$, respectively, σ_m is the mean stress, while σ_{UTS} is the ultimate tensile strength of the material. To maintain the dependency of $\Delta\sigma_{g,th,R}$ only from $\Delta\sigma_{g,th,R}$ and R , the tensile strength σ_{UTS} has been replaced with the known relation accounting for the fatigue ratio for steels (~ 0.5):

$$\frac{\Delta\sigma_{g,th,R=-1}}{2} \approx 0.5 \cdot \sigma_{UTS} \quad (3.15)$$

Then, by replacing the mean stress σ_m with:

$$\sigma_m = \frac{\Delta\sigma_{g,th,R}}{2} \cdot \left(\frac{1+R}{1-R} \right) \quad (3.16)$$

it was possible to define the following expression:

$$\frac{\Delta\sigma_{g,th,R}}{\Delta\sigma_{g,th,R=-1}} \approx 2 \frac{1-R}{3-R} \quad (3.17)$$

which allows the mean stress correction of the fatigue limit of a component made of steel once the load ratio R its fatigue limit at load ratio $R = -1$ are known. Accordingly, the driving force at the fatigue limit has been written in the following final version:

$$\Delta K_{I,th,R=-1} = \left(\beta_{ax} \cdot \sqrt{\pi a} \cdot \Delta\sigma_{g,th,R,ax} + \beta_b \cdot \sqrt{\pi a} \cdot \Delta\sigma_{g,th,R,b} \right) \cdot \frac{1}{2} \frac{3-R}{1-R} \quad (3.18)$$

Where β_{ax} and β_b are the geometric factor for the axial and bending load condition at the point A (see paragraph 3.2.3), respectively, $\Delta\sigma_{g,th,ax}$ and $\Delta\sigma_{g,th,b}$ represent the axial and bending stress components of the fatigue limit for a load ratio $R_{th} = -0.3$ (see paragraph 3.2.1). The obtained driving force at the fatigue limit has been reported as black solid line in Figure 3.26 along with the corresponding cyclic R-curve (green solid line). Finally, the latter has been shifted along the crack length axis according to [17–19] until the tangency, or better the

‘initiation’, condition has been found. As a result, an initial crack size equal to $a_i = 5 \mu\text{m}$ has been found for an S355J2+N structural steel subjected to fully reversed cyclic loading ($R = -1$).

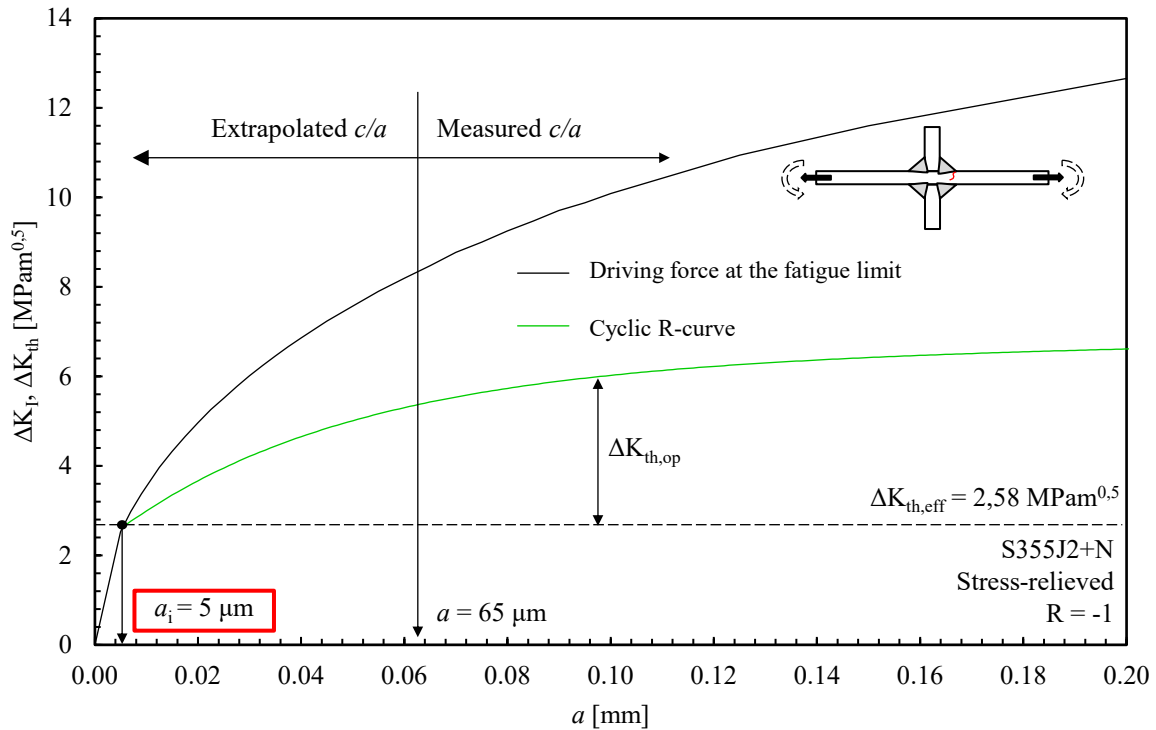


Figure 3.26. Crack arrest analysis and definition of the initial crack size a_i .

3.4.2. Discussion: effect of the crack shape c/a

Another important aspect deserving to be mentioned and discussed is the effect of the aspect ratio c/a . In particular, in this work, the calibration of the initial crack size has been performed introducing the experimental evolution of the c/a into the FE analyses. Unfortunately, the values for very small crack length have been extrapolated as it was not possible to identify on the fracture surface of the tested specimen any marked crack having smaller size than $a < 65 \mu\text{m}$. At the same time several authors in the Literature [17–19,37] assume a semi-circular crack fixing $c/a = 1$. For these reasons, the present paragraph aims at investigating the effect of the aspect ratio c/a on the driving force. Taking advantage of the parametric model presented above (Figure 3.16), the same crack lengths (see Table 3.4) have been investigated this time by imposing a constant aspect ratio $c/a = 1, 5, 10 \text{ e } \infty$ (the latter corresponding to a through-the-

3.4 Calibration of the initial crack size

thickness crack having a straight front). The obtained results have been reported in Figure 3.27 expressed as $\beta \cdot (\pi a)^{0.5}$ versus the crack length a for the case of pure axial loading with applied 1 MPa. Figure 3.27 shows that for a fixed specimen geometry, external load and crack length, an increased aspect ratio c/a results in an increase of the SIF K_I (i.e. $\beta \cdot (\pi a)^{0.5}$) at point A and in a reduction of the K_I at point B. For example, according to what reported in [18], in the case of $c/a = 1$ the point B is the critical one, while the opposite happens when $c/a = 10$ (Figure 3.27). Noteworthy, the highest driving force is that relevant to through-the-thickness crack having a straight front ($c/a = \infty$, in Figure 3.27). Interestingly, the results obtained imposing the experimental evolution of c/a (solid black line in Figure 3.27) are almost overlapped to that of a through-the-thickness crack having a straight front ($c/a = \infty$) when $a < 75 \mu\text{m}$.

Then, the exercise of calibrating the initial crack size a_i (similar to Figure 3.26) assuming the driving force at the fatigue limit of a crack having $c/a = 1$, as suggested in [17–19], has been done. Again, an initiation condition, instead of a tangency condition has been found and the output of this analysis was an initial crack size $a_i = 15 \mu\text{m}$, this value being in very good agreement with $a_i = 17 \mu\text{m}$ obtained in [17–19] with the crack arrest analysis applied to the case of a smooth specimen with a semi-circular surface crack ($c/a = 1$) and adopting a complex elastoplastic driving-force calculation.

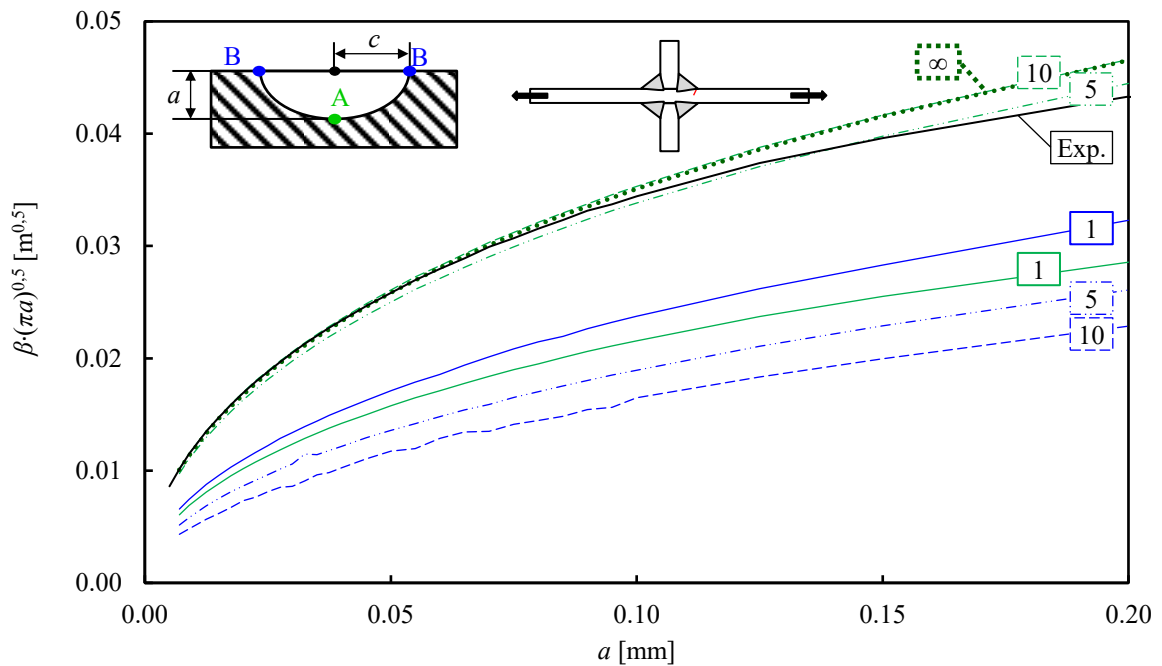


Figure 3.27. Evolution of the normalized driving force for different aspect ratios c/a of the propagating crack.

3.5. Estimating the fatigue limit of welded structures

3.5.1. Threshold Notch Stress Intensity Factor $\Delta K_{I,th}$

As intensively discussed in the introduction, the cyclic R-curve can be adopted to estimate the fatigue limit of notched components like welded structures. Indeed, once the initial crack size a_i along with the resistance curve $\Delta K_{th}(a)$ (both material properties according to [17–19]) are known, the fatigue limit $\Delta\sigma_{g,th}$ can be found by scaling the driving force $\Delta K_I(a)$ until the tangency (or initiation) condition is found with the resistance curve, the position of the latter being fixed by a_i . In the context of welded joints, the rigorous application of the method requires that not only the local weld bead geometry (weld bead leg size z , weld toe and root radius ρ , opening angle 2α , etc.) but also the location, inclination and shape of the propagating crack must be known with a high degree of accuracy to evaluate the driving force and estimate the fatigue limit.

Undoubtedly, the efficacy of the method can be very high when all those information are known, and its application can be of interest in contexts where the maximum precision in the estimation is required (e.g. in the aerospace or nuclear industries). However, there are many other practical industrial applications in which there is no the possibly to carry out accurate and time-consuming measurements and calculations like those required for applying a damage tolerant criterion based on the cyclic R-curve. Not only that, the rigorous application of the method to the case of complex and very large geometries (see the example reported in Figure 3.28) could become so complicated and time-consuming to be substantially unreasonable and/or unfeasible. For these reasons, it is easy to understand how the use of a damage tolerant approach based on fracture mechanics and the use of the cyclic R curve can be, in certain circumstances, somehow prohibitive, this statement being truer the larger the analysed structure, the higher the number of welded connections present in the structure and the more complex the geometry of the joints. Finally, it happens that during the design phase of welded connections many parameters relevant to the local weld bead geometry (for example the weld leg size z) are not known in advance, indeed, they are the output the designer is looking for, or their value depends on the process parameters.

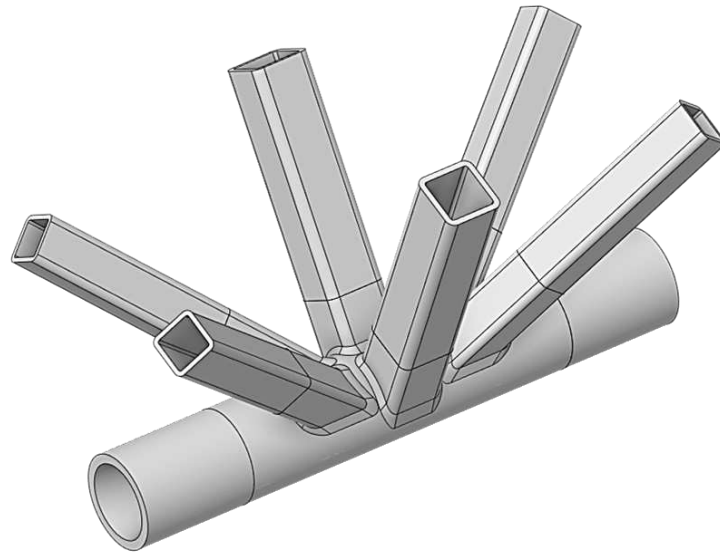


Figure 3.28. Welded detail taken from an example of industrial interest.

In light of what discussed above, there is the need of an efficient procedure to estimate the fatigue limit of welded structures without the need of complex and time-consuming fracture mechanics-based calculations. In this work, to do this, the following simplifying assumptions are made:

- Null weld toe and weld root radius, $\rho = 0$ (worst case hypothesis, see chapter 1). Similar assumption have been proposed yet in the Literature [3,10,24,25,38–42]
- Planar crack having straight front, $c/a = \infty$. This is assumption allows for estimations on the safe side, the corresponding normalized driving force being the highest as discussed in the previous paragraph.
- Crack propagating along the V-notch bisector line.

As discussed in depth in chapter 1, the sharp V-notch hypothesis results in singular stress distribution ahead the V-notch tip, the latter being modelled as V-notch having null tip radius ($\rho = 0$) and described by a certain opening angle 2α (see Figure 3.29). The singular stress distribution is proportional to $1/r^{1-\lambda_1}$ [43], where r is radial the distance from the V-notch tip, while the singularity degree $1-\lambda_1$ is a function of the opening angle [43,44]. Accordingly, the singular stress field is proportional to the external loads and its intensity is quantifies by the

Notch Stress Intensity Factor (NSIF) K_1 [45], which, in few words, represent the natural extension of the SIF K_I concept to notches having opening angle $2\alpha > 0^\circ$. It has also been abundantly highlighted that the NSIF K_1 , or better the range ΔK_1 , represents a fatigue relevant parameter [3,38–41] and that its value can be easily estimated using FE analyses having rather coarse meshes [24,25] (see chapter 1 for a more complete and detailed description).

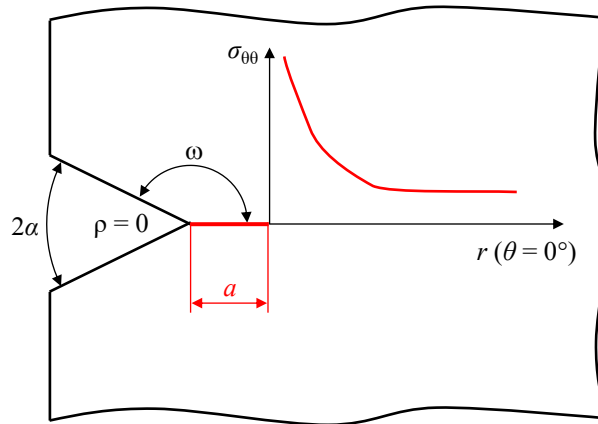


Figure 3.29. Simplified model with the corresponding main parameters and highlighted the distribution of the singular stress component normal to the crack bisector line.

Interestingly, the NSIF concept can be very useful in determining the SIF K_I of short cracks propagating along the bisector line of a sharp V-notch. In fact, in these conditions, the stress field to which the propagating crack is subjected can be completely described by NSIF K_1 . Therefore, many authors in the Literature [46–52] have shown it is possible to write an engineering formula giving the SIF K_I of a crack propagating from a V-notch once the intensity of stress field ahead the V-notch tip without the crack is known, i.e. the NSIF K_1 is known:

$$\Delta K_I = \beta_{NSIF} \cdot \sqrt{\pi} \cdot a^{\lambda_1 - 0.5} \cdot \Delta K_1 \quad (3.19)$$

Where β_{NSIF} is a constant which value depends on the V-notch opening angle 2α , a is the length of the propagating crack measured from the V-notch tip (see Figure 3.29), λ_1 is the Williams' coefficient [43,44] and ΔK_1 is the NSIF quantifying the intensity of the asymptotic stress distribution ahead the sharp V-notch tip evaluated without the crack.

The geometric factor β_{NSIF} can be evaluated using FE simulations or using some analytical expressions available in the Literature, the latter being valid in case of a through the thickness

3.5 Estimating the fatigue limit of welded structures

planar crack propagating along the bisector line of a sharp (or rounded) V-notch [46–52]. For example, Carpinteri et al. [49] proposed the following expression:

$$\beta_{NSIF} = \frac{1}{\pi} \left[\tilde{f}(\omega) B\left(\lambda_1, \frac{1}{2}\right) + \tilde{g}(\omega) B\left(\lambda_1 + 1, \frac{1}{2}\right) + \tilde{h}(\omega) B\left(\lambda_1 + 2, \frac{1}{2}\right) \right] \quad (3.20)$$

Where, $\omega = \pi - \alpha$ (see Figure 3.29), while $\tilde{f}(\omega)$, $\tilde{g}(\omega)$, $\tilde{h}(\omega)$ and B (the latter being called Beta function, also known as the Euler integral of the first kind) are defined as follow:

$$B(x, y) = \int_0^1 t^{x-1} (1-t)^{y-1} dt \quad (3.21)$$

$$\tilde{f}(\omega) = \sqrt{\frac{\pi}{2}} \sqrt{\frac{2\omega + \sin 2\omega}{\omega^2 + \sin^2 \omega}} \quad (3.22)$$

$$\tilde{g}(\omega) = -1 - 3\tilde{f}(\omega) + \tilde{f}_1(\omega) \quad (3.23)$$

$$\tilde{h}(\omega) = 2 + 2\tilde{f}(\omega) - \tilde{f}_1(\omega) \quad (3.24)$$

Wherein:

$$\tilde{f}_1(\omega) = \frac{6.142 + 2.040\omega^2 - 0.1290\omega^3}{\omega^{3/2}} \quad (3.25)$$

At this point, the cyclic R-curve analysis has been applied according to the hypotheses introduced here above for a fixed V-notch opening angle. Having known both the initial crack size a_i and the cyclic R-curve, the driving force at the fatigue limit $\Delta K_{I, \Delta\sigma_{g, th}}$ has been the output of the cyclic R-curve analysis. The driving force has been evaluated thanks to Eq. (3.19), the NSIF at threshold $\Delta K_{1, th}$ being the scaling parameter to be found with the cyclic R-curve analysis. Noteworthy, the fatigue limit expressed in terms of a threshold NSIF $\Delta K_{1, th}$ is only function of the V-notch opening angle 2α , the material and the load ratio R . At the same time,

its value is completely independent on the specimen geometry or the constrain and loading conditions (e.g. axial o bending, provided that only mode I stresses are considered).

In this work, the case of weld toe failure of a stress relieved welded joint made of S355J2+N structural steel under pure mode I fully reversed ($R = -1$) cyclic loading has been considered and the opening angle has been fixed equal to $2\alpha = 135^\circ$ ($\lambda_1 = 0.674$ [43,44]). The resulting cyclic R-curve analysis have been reported in Figure 3.30. The outcome of this analysis was a threshold NSIF equal to $\Delta K_{1,th, 2\alpha=135^\circ, R=-1} = 32,0 \text{ MPam}^{0.326}$. The obtained parameter represents a threshold value against which the applied NSIF ΔK_1 can be compared to investigate if the welded joint will exhibit fatigue failure or not when subjected to CA loadings. More in detail, if $\Delta K_1 > \Delta K_{1,th, 2\alpha=135^\circ, R=-1}$ the applied stress is higher than the fatigue limit of the structure (i.e. the driving force will never meet the resistance curve), otherwise if $\Delta K_1 \leq \Delta K_{1,th, 2\alpha=135^\circ, R=-1}$, then the applied stress is lower, or at most equal to the component's fatigue limit.

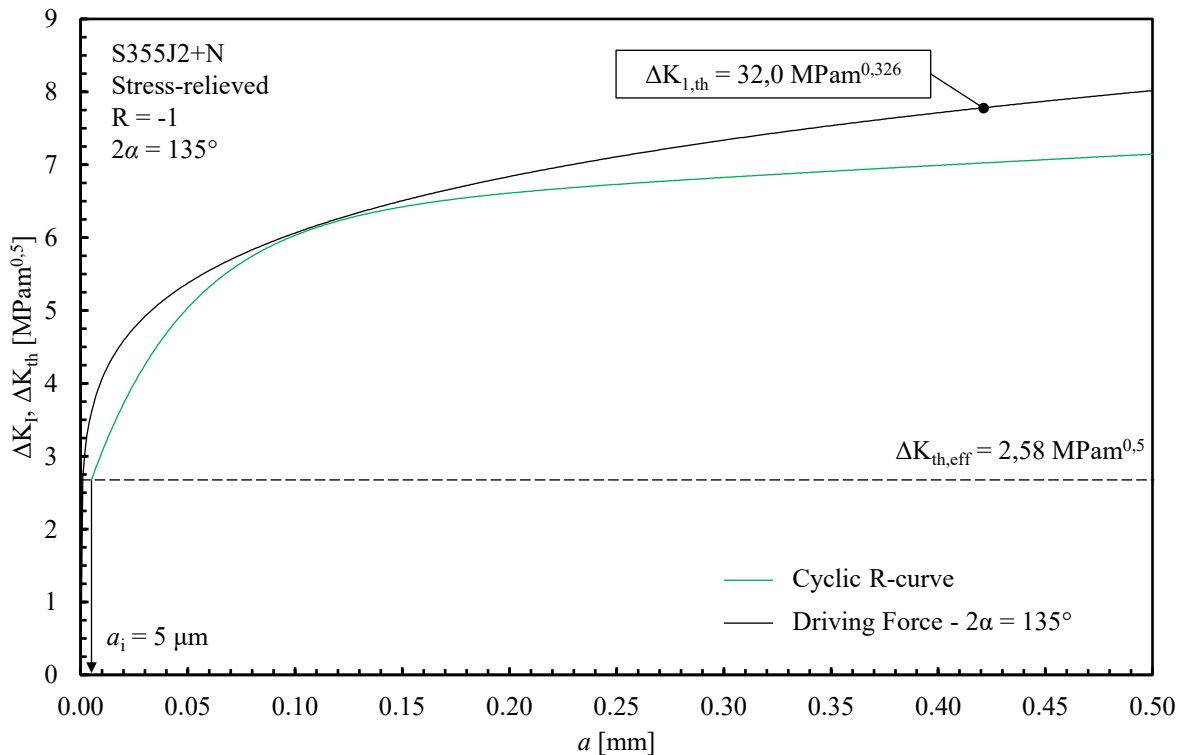


Figure 3.30. Cyclic R-curve analysis: driving force relevant to the case of a planar crack propagating along the bisector line of a sharp V-notch ($\rho = 0$) having opening angle $2\alpha = 135^\circ$ (weld toe).

3.5.2. The Peak Stress Method: equivalent peak stress at threshold

As argued above, the NSIF based approach allows to a rapid and effective design of welded structures against fatigue, without the need of complex and time-consuming fracture mechanics-based calculations. Its most significant advantage lies in the fact that it allows to estimate the fatigue strength of complex structures using the NSIF ΔK_I range, which summarizes all information on geometry, dimensions and applied loadings and boundary conditions into a single design parameter. On the other hand, in chapter 1 it has been demonstrated that evaluating the NSIF according to its definition by using FEA can be very time-consuming and resulting in FE mesh patterns having extremely fine meshes at the V-notch tip. In chapter 1 it also been intensively discussed about the advantages given by the Peak Stress Method and by the use of the equivalent peak stress $\Delta\sigma_{eq,peak}$, whose definition is here reported for the sake of clarity (Eq. (3.26)), as a fatigue damage parameter [24,25]:

$$\Delta\sigma_{eq,peak} = \sqrt{c_{w1}} \cdot K_{FE}^* \cdot \sqrt{\frac{2e_1}{1-\nu^2}} \cdot \left(\frac{d}{R_0}\right)^{1-\lambda_1} \cdot \Delta\sigma_{\theta\theta,\theta=0,peak} \quad (3.26)$$

Where c_{w1} is a coefficient accounting for the mean stress sensitivity; K_{FE}^* is a calibrated non-dimensional constant; e_1 is a constant of integration depending on the opening angle 2α ; ν is the Poisson's coefficient ($\nu = 0.3$); d is the average size of the finite elements is a calibrated constant; R_0 is the material-structural volume with size according to the averaged SED criterion ($R_0 = 0.28$ mm for structural steel welded joints) and $\Delta\sigma_{\theta\theta,\theta=0,peak}$ is the mode I peak stress range evaluated at the V-notch tip by means of linear elastic FEA according to the PSM. The reader is referred to chapter 1 and to the relevant Literature [24,25] for more details on the application of the PSM and of the equivalent peak stress concept.

Going back to the threshold conditions, the concept of equivalent peak stress $\Delta\sigma_{eq,peak}$ can be adopted to rapidly and efficiently estimate the CAFL of weld toe failure observing that in case of pure mode I loading it is possible to write the following relationship:

$$\Delta\sigma_{eq,peak,th} = \sqrt{c_{wl}} \cdot \sqrt{\frac{2e_1}{1-\nu^2}} \cdot \left(\frac{1}{R_0}\right)^{1-\lambda_1} \cdot \Delta K_{1,th} \quad (3.27)$$

Which can be easily obtained by entering the relation $\Delta K_{1,th} = K_{FE}^* \cdot \Delta\sigma_{\theta\theta,0=0,peak} \cdot d^{1-\lambda_1}$ into Eq. (3.26). In paragraph 3.5.1, the case of weld toe failure ($2\alpha = 135^\circ$) has been considered. In this case $e_1 = 0.117$, while $c_{wl} = 0.5$ if fully reversed loads ($R = -1$) are applied to stress relieved welded joints, which threshold NSIF is equal to $\Delta K_{1,th, 2\alpha=135^\circ, R=-1} = 32,0 \text{ MPam}^{0.326}$. By entering those values into Eq. (3.27), a threshold value $\Delta\sigma_{eq,peak,th} = 165 \text{ MPa}$ has been found for a survival probability $PS = 50\%$ (see Figure 3.31), this parameter being valid in case of weld toe failure ($2\alpha = 135^\circ$) of a stress relieved welded joint made of S355J2+N structural steel under pure mode I fully reversed ($R = -1$) cyclic loading. The CAFL expressed in terms of the equivalent peak stress at threshold has been compared to the PSM-based fatigue design scatter bands for steel welded joints relevant to $\lambda = 0$ which has an endurable stress range $\Delta\sigma_{eq,peak,A,50\%} = 214 \text{ MPa}$, an inverse slope $k = 3$ and a scatter index referred to survival probabilities of 2.3%-97.7%, i.e. the mean value \pm two standard deviations, $T_\sigma = 1.90$ (see Figure 3.31). As shown in Figure 3.31, the CAFL correspond to a number to cycles to failure equal to $N_{th} \approx 4.4 \cdot 10^6$ cycles, this value being quite close to that proposed by the Eurocode3 ($5 \cdot 10^6$ cycles) [1].

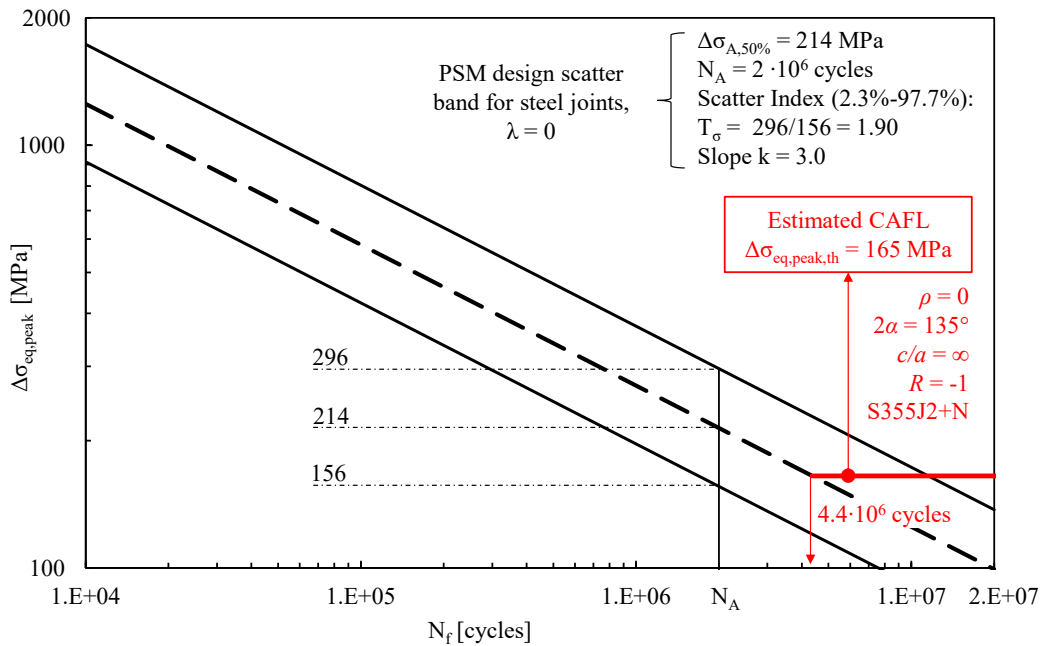


Figure 3.31. PSM design scatter band updated with the introduction of the CAFL relevant to weld toe failure under fully reversed loading.

3.5.3. Validation with data taken from the Literature

The validity of the obtained fatigue limit, expressed in terms of an equivalent peak stress at threshold, has been checked against some experimental data taken from the Literature [53]. Sonsino et al. [53] fatigue tested under fully reversed ($R = -1$) pure axial CA loading longitudinal fillet welded stiffeners (Figure 3.32) having two different plate thicknesses ($t = 12$ or 20 mm) and made of St 52-3 (old nomenclature relevant to the DIN17100 for the S355J2+N EN10025-2 [20]). The authors reported the fatigue crack initiation always occurred at the weld toe at the main plate side. The complete separation of the joint was adopted as failure criterion. The experimental fatigue results have been here reported in Figure 3.33 expressed in terms of the number of cycles to failure N_f versus the applied nominal stress range $\Delta\sigma$ (calculated with reference to the main plate according Eq. (3.3)).

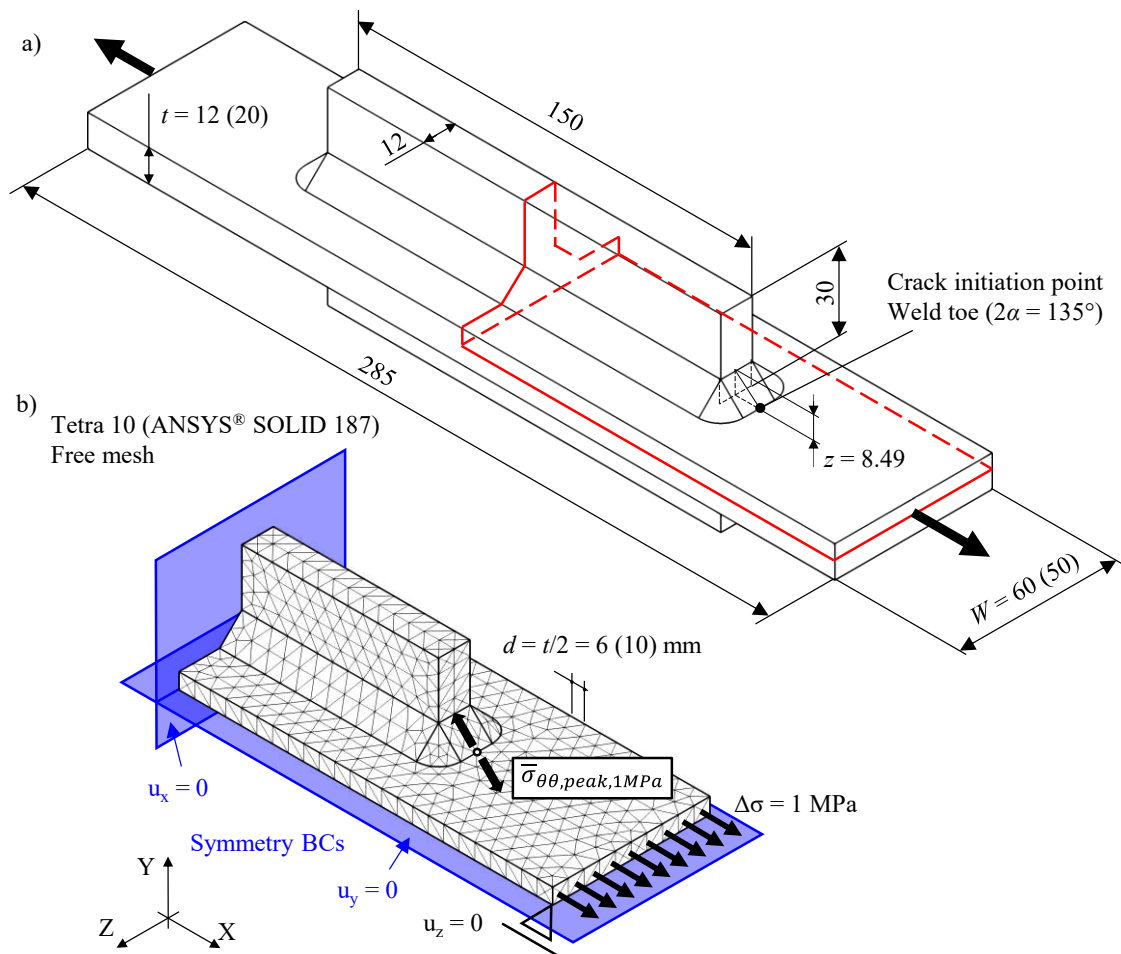


Figure 3.32. Specimens' geometry and corresponding FE model according to the PSM guidelines.

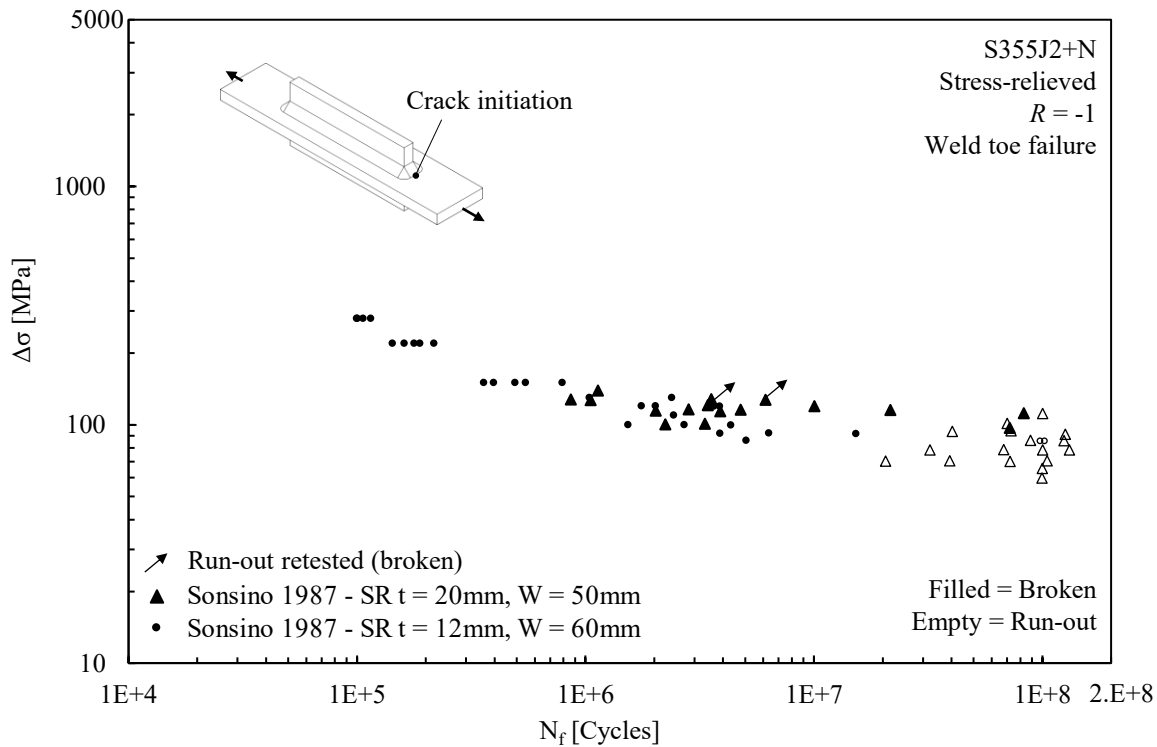


Figure 3.33. Fatigue test results expressed in terms of applied nominal stress range. Data taken from Sonsino et al. [53].

A 3D free FE mesh pattern of 10-node tetrahedral elements (SOLID 187 of Ansys® element library) has been defined to calculate the mode I peak stresses at the weld toe, mode II being not singular there. Only one quarter of FE model, instead of one eighth, have been generated taking advantage of the YZ and ZX double symmetry. According to the PSM guidelines, a minimum mesh density ratio $a/d = 1$ is necessary to analyse the weld toe ($2\alpha = 135^\circ$) under mode I loading using TETRA-10 finite elements [25] (see also chapter 1), the characteristic size being $a = t/2 = 6$ mm (this means only one element in the half thickness of the main plate, see Figure 3.32). A quarter of the specimen instead of exploiting the triple symmetry has been modelled to avoid the need of a mesh refinement at weld toe. In fact, an element size $d = 6/1 \approx 6$ mm would have meant only a single finite element through the thickness of the longitudinal stiffener, and this would not have allowed applying the PSM at the crack initiation point, the nearest node from a free surface where the average peak stress can be evaluated being the third vertex node according to the PSM based on 10-node tetrahedral elements (see chapter 1). Then the symmetry boundary conditions have been applied to the YZ and ZX symmetry planes and a uniform tensile stress of 1 MPa has been applied to the main plate (see Figure 3.32).

3.5 Estimating the fatigue limit of welded structures

After solution, the maximum principal stress $\Delta\sigma_{11,\text{peak}}$ has been evaluated at FE nodes located along the weld toe line, then the average peak stress $\Delta\bar{\sigma}_{11,\text{peak}}$ (see chapter 1), by taking advantage of the approximate equivalence $\Delta\sigma_{\theta\theta,\theta=0,\text{peak}} \approx \Delta\sigma_{11,\text{peak}}$. Eventually the equivalent peak stress range has been computed from Eq. (3.26), by assuming $c_{w1} = 0.5$ since all joints have been tested in the stress-relieved conditions. The maximum value of the equivalent peak stress was found at the weld toe where fatigue cracks experimentally initiated and corresponded to $\Delta\sigma_{\text{eq,peak},1\text{Mpa}} = 2.09$ MPa and $\Delta\sigma_{\text{eq,peak},1\text{Mpa}} = 2.23$ MPa for the joints having $t = 12$ mm and $t = 20$ mm, respectively, when applying 1 MPa nominal stress range at the main plate. The local stress state at the critical location being of pure mode I, the local biaxiality ratio is $\lambda = 0$ (see chapter 1). Finally, the experimental data originally expressed in terms of range of nominal stress have been re-converted in terms of range of the equivalent peak stress (Eq. (3.26)) evaluated at the crack initiation location and compared to the PSM-based fatigue design scatter bands for steel welded joints relevant to $\lambda = 0$ (not fitted on the experimental data) including the threshold equivalent peak stress $\Delta\sigma_{\text{eq,peak,th}} = 165$ MPa (see Figure 3.34).

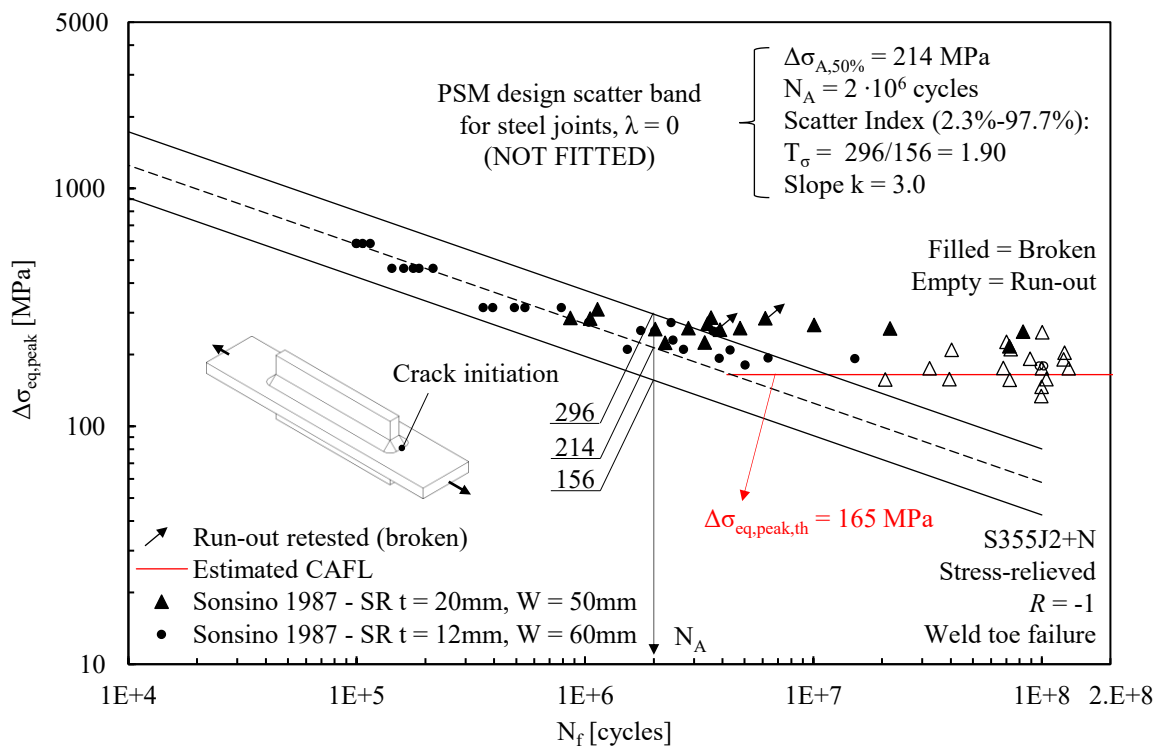


Figure 3.34. Validation with experimental data from the Literature. Comparison with the PSM design scatter band relevant to pure mode I loading ($\lambda=0$) and the corresponding CAFL for weld toe failure under fully reversed loading ($R = -1$).

It is interesting to note that the experimental data are quite well described both in the finite life region and at the fatigue limit, the broken specimens (filled markers in Figure 3.34) and the run-out ones (empty markers in Figure 3.34) being divided with good agreement by the threshold value of the equivalent peak stress $\Delta\sigma_{eq,peak,th}$ (horizontal solid red line in Figure 3.34)

3.6. Conclusions

In the context of fatigue design of welded structures, the fatigue limit represents a fundamental concept around which there still is lack of knowledge. International standards and recommendations, basing their considerations on the nominal stress approach, supply a value for this parameter, which is engineering defined as that stress level corresponding to a fixed number of cycles (typically $5 \cdot 10^6$ or 10^7 cycles) on the stress-life (S-N) curve of the corresponding reference detail. The main problem is related to its application in case of more complex joint geometries, for which the proper reference design category does not exist.

Starting from the experimental observation that the first stage of the fatigue failure are the crack initiation and the early short crack growth, in this work, a damage tolerant criterion based on the linear elastic fracture mechanics and on the cyclic R-curve, i.e. the crack size dependence of the fatigue crack propagation threshold in the physically short crack regime, has been considered to investigate the concept of fatigue limit. Similar to the well-established monotonic R-curve analysis, the cyclic R-curve analysis consists in comparing for a propagating crack its driving force (i.e. the applied SIF - Stress Intensity Factor range ΔK_I), which depends on the geometry, the material and the external loads, with the cyclic R-curve, a material property. The crack propagation is promoted whenever the crack driving force assumes higher values than the resistance ones, while the crack is arrested in the opposite case. Therefore, the fatigue limit is given by that stress level at which the crack driving force curve is tangent to the crack resistance.

One of the most critical aspects in applying this criterion is that being a fracture mechanics-based approach, it requires the definition of an initial crack size from which starting the calculations. According to the Literature, one way to calibrate this parameter is the crack arrest analysis, which consists in evaluating the driving force at the fatigue limit and shifting the resistance curve, i.e. the cyclic R-curve, along the abscissa until the tangency condition with

3.6 Conclusions

the driving force is reached. In this work an accurate experimental calibration has been performed by comparing the driving force at the fatigue limit for nlc fillet welded double transverse attachments made of S355 structural steel and the corresponding resistance curve. The cyclic R curve has been experimentally determined by fatigue testing Single Edge Notch in Bending (SENB) on resonant testing machines making use of a new experimental procedure which allows for the determination of the crack propagation threshold from short to long crack regime by means of a single experimental test. The characterization has been carried out for a S355J2+N material and further for the same material but in Heat Affected Zone (HAZ) condition. The specimens in the HAZ condition were obtained from a transverse loaded butt weld ground flush to plate which residual stresses has been removed as much as possible by applying a proper stress relieving thermal treatment.

Once performed the calibration of the initial crack size, its application to the estimation of the fatigue limit of a welded structure has been discussed with different degrees of accuracy depending on the available information. In particular, under certain simplifying assumptions it was possible to combine the cyclic R-curve analysis with the Peak Stress Method obtaining a new procedure that allows to a rapid and effective design of weld toe failures in the infinite life region, without the need of complex and time-consuming fracture mechanics-based calculations. The proposed method has been successfully checked against experimental data from the Literature and in the future its application will be extended to different material, opening angles (e.g. weld root failures), load ratio and to multiaxial loading conditions.

3.7. References

- [1] EN. Eurocode 3: Design of steel structures – part 1–9: Fatigue 2005.
- [2] Hobbacher AF. Recommendations for Fatigue Design of Welded Joints and Components. International Institute of Welding - IIW Collection. Springer International Publishing; 2016. <https://doi.org/10.1007/978-3-319-23757-2>.
- [3] Radaj D, Sonsino CM, Fricke W. Fatigue assessment of welded joints by local approaches. 2nd ed. Cambridge, England: Woodhead Publishing; 2006.
- [4] Frost NE. Non-Propagating Cracks in Vee- Notched Specimens Subject to Fatigue Loading. *Aeronaut Q* 1957;8:1–20. <https://doi.org/10.1017/S0001925900010362>.
- [5] Smith RA, Miller KJ. Prediction of fatigue regimes in notched components. *Int J Mech Sci* 1978;20:201–6. [https://doi.org/10.1016/0020-7403\(78\)90082-6](https://doi.org/10.1016/0020-7403(78)90082-6).
- [6] Anderson TL. Fracture Mechanics, Fundamentals and Applications. 3rd ed. Boca Raton: CRC Press LLC; 2009.
- [7] Zerbst U, Vormwald M, Pippan R, Gänser H-P, Sarrazin-Baudoux C, Madia M. About the fatigue crack propagation threshold of metals as a design criterion – A review. *Eng Fract Mech* 2016;153:190–243. <https://doi.org/10.1016/j.engfracmech.2015.12.002>.
- [8] Minakawa K, Newman JC, McEvily AJ. A critical study of the crack closure effect on near-threshold fatigue crack growth. *Fatigue Fract Eng Mater Struct* 1983;6:359–65. <https://doi.org/10.1111/j.1460-2695.1983.tb00351.x>.
- [9] McEvily AJ, Endo M, Murakami Y. On the $(\text{area})^{0.5}$ relationship and the short fatigue crack threshold. *Fatigue Fract Eng Mater Struct* 2003;26:269–78. <https://doi.org/10.1046/j.1460-2695.2003.00636.x>.
- [10] Chapetti MD, Belmonte J, Tagawa T, Miyata T. Integrated fracture mechanics approach to analyse fatigue behaviour of welded joints. *Sci Technol Weld Join* 2004;9:430–8. <https://doi.org/10.1179/136217104225021634>.
- [11] Tanaka K, Akiniwa Y. Resistance-curve method for predicting propagation threshold of short fatigue cracks at notches. *Eng Fract Mech* 1988;30:863–76. [https://doi.org/10.1016/0013-7944\(88\)90146-4](https://doi.org/10.1016/0013-7944(88)90146-4).

3.7 References

- [12] Tabernig B, Pippan R. Determination of the length dependence of the threshold for fatigue crack propagation. *Eng Fract Mech* 2002;69:899–907. [https://doi.org/10.1016/S0013-7944\(01\)00129-1](https://doi.org/10.1016/S0013-7944(01)00129-1).
 - [13] Endo M, McEvily AJ. Prediction of the behavior of small fatigue cracks. *Mater Sci Eng A* 2007;468–470:51–8. <https://doi.org/10.1016/j.msea.2006.09.084>.
 - [14] Maierhofer J, Kolitsch S, Pippan R, Gänser H-P, Madia M, Zerbst U. The cyclic R-curve – Determination, problems, limitations and application. *Eng Fract Mech* 2018;198:45–64. <https://doi.org/10.1016/j.engfracmech.2017.09.032>.
 - [15] Pourheidar A, Patriarca L, Madia M, Werner T, Beretta S. Progress in the measurement of the cyclic R-curve and its application to fatigue assessment. *Eng Fract Mech* 2022;260:108122. <https://doi.org/10.1016/j.engfracmech.2021.108122>.
 - [16] Zerbst U, Madia M, Vormwald M. Applying fracture mechanics to fatigue strength determination – Some basic considerations. *Int J Fatigue* 2019;126:188–201. <https://doi.org/10.1016/j.ijfatigue.2019.05.009>.
 - [17] Zerbst U, Madia M. Fracture mechanics based assessment of the fatigue strength: approach for the determination of the initial crack size. *Fatigue Fract Eng Mater Struct* 2015;38:1066–75. <https://doi.org/10.1111/ffe.12288>.
 - [18] Zerbst U, Madia M, Schork B, Hensel J, Kucharczyk P, Ngoula D, et al. *Fatigue and Fracture of Weldments: The IBESS Approach for the Determination of the Fatigue Life and Strength of Weldments by Fracture MEchanics Analysis*. Cham: Springer International Publishing; 2019. https://doi.org/10.1007/978-3-030-04073-4_1.
 - [19] Madia M, Zerbst U, Th. Beier H, Schork B. The IBESS model – Elements, realisation and validation. *Eng Fract Mech* 2018;198:171–208. <https://doi.org/10.1016/j.engfracmech.2017.08.033>.
 - [20] UNI. UNI EN 10025-2:2019 - Prodotti laminati a caldo di acciai per impieghi strutturali - Parte 2: Condizioni tecniche di fornitura di acciai non legati per impieghi strutturali 2019.
 - [21] ASTM. ASTM E92-17, Standard Test Methods for Vickers Hardness and Knoop Hardness of Metallic Materials 2017. <https://doi.org/10.1520/E0092-17>.
 - [22] ASTM. ASTM E384-17: Standard Test Method for Microindentation Hardness of Materials 2017:1–40. <https://doi.org/10.1520/E0384-17>.
 - [23] ISO. BS ISO 12107:2012 - Metallic materials – Fatigue testing – Statistical planning and
-

analysis data 2012.

- [24] Meneghetti G, Lazzarin P. Significance of the elastic peak stress evaluated by FE analyses at the point of singularity of sharp V-notched components. *Fatigue Fract Eng Mater Struct* 2007;30:95–106. <https://doi.org/10.1111/j.1460-2695.2006.01084.x>.
- [25] Meneghetti G, Campagnolo A. State-of-the-art review of peak stress method for fatigue strength assessment of welded joints. *Int J Fatigue* 2020;139:105705. <https://doi.org/10.1016/j.ijfatigue.2020.105705>.
- [26] ISO. ISO 12108:2018 Metallic materials - Fatigue testing - Fatigue crack growth method 2018.
- [27] Si Y, Rouse JP, Hyde CJ. Potential difference methods for measuring crack growth: A review. *Int J Fatigue* 2020;136. <https://doi.org/10.1016/j.ijfatigue.2020.105624>.
- [28] Johnson HH. Calibrating the electric potential method for studying slow crack growth. *Mater Res Stand* 1965.
- [29] Maierhofer J, Pippan R, Gänser H-P. Modified NASGRO equation for physically short cracks. *Int J Fatigue* 2014;59:200–7. <https://doi.org/10.1016/j.ijfatigue.2013.08.019>.
- [30] ASTM. ASTM E647 - 15e1, Standard Test Method for Measurement of Fatigue Crack Growth Rates 2015. <https://doi.org/10.1520/E0647-15E01.2>.
- [31] Taylor D. *Fatigue thresholds*. London, UK: Butterworths; 1989.
- [32] Taylor D. *A compendium of fatigue thresholds and growth rates*. London, UK: 1985.
- [33] Madia M, Vojtek T, Duarte L, Zerbst U, Pokorný P, Jambor M, et al. Determination of fatigue crack propagation thresholds for steel in presence of environmental effects. *Int J Fatigue* 2021;153:106449. <https://doi.org/10.1016/j.ijfatigue.2021.106449>.
- [34] Duarte L, Schönherr JA, Madia M, Zerbst U, Geilen MB, Klein M, et al. Recent developments in the determination of fatigue crack propagation thresholds. *Int J Fatigue* 2022;164:107131. <https://doi.org/10.1016/j.ijfatigue.2022.107131>.
- [35] Goodman J. *Mechanics Applied to Engineering*. London, UK: Longmans, Green and Company; 1899.
- [36] Haigh BP. Experiments on the fatigue of brasses. *J Inst Met* 1917.
- [37] Chapetti M. Fatigue propagation threshold of short cracks under constant amplitude loading. *Int J Fatigue* 2003;25:1319–26. [https://doi.org/10.1016/S0142-1123\(03\)00065-3](https://doi.org/10.1016/S0142-1123(03)00065-3).
- [38] Karakas Ö, Morgenstern C, Sonsino CM. Fatigue design of welded joints from the

3.7 References

- wrought magnesium alloy AZ31 by the local stress concept with the fictitious notch radii of $r_f = 1.0$ and 0.05 mm. *Int J Fatigue* 2008;30:2210–9. <https://doi.org/10.1016/j.ijfatigue.2008.05.017>.
- [39] Karakas Ö. Consideration of mean-stress effects on fatigue life of welded magnesium joints by the application of the Smith–Watson–Topper and reference radius concepts. *Int J Fatigue* 2013;49:1–17. <https://doi.org/10.1016/j.ijfatigue.2012.11.007>.
- [40] Fricke W. IIW recommendations for the fatigue assessment of welded structures by notch stress analysis: IIW-2006-09. Woodhead Pub; 2012.
- [41] Radaj D, Vormwald M. *Advanced Methods of Fatigue Assessment*. 1st ed. Berlin: Springer Berlin Heidelberg; 2013. <https://doi.org/10.1007/978-3-642-30740-9>.
- [42] Chapetti MD. Fracture mechanics for fatigue design of metallic components and small defect assessment. *Int J Fatigue* 2022;154:106550. <https://doi.org/10.1016/j.ijfatigue.2021.106550>.
- [43] Williams ML. Stress singularities resulting from various boundary conditions in angular corners of plates in tension. *J Appl Mech* 1952;19:526–8.
- [44] Visentin A, Campagnolo A, Meneghetti G. Analytical expressions for rapid estimation of the N-SIFs at V-notch tips using the Peak Stress Method (submitted). *Fatigue Fract Eng Mater Struct* 2022.
- [45] Gross B, Mendelson A. Plane elastostatic analysis of V-notched plates. *Int J Fract Mech* 1972;8:267–76. <https://doi.org/10.1007/BF00186126>.
- [46] Hasebe N, Iida J. A crack originating from a triangular notch on a rim of a semi-infinite plate. *Eng Fract Mech* 1978;10:773–82.
- [47] Philipps AG, Karuppanan S, Churchman CM, Hills DA. Crack tip stress intensity factors for a crack emanating from a sharp notch. *Eng Fract Mech* 2008;75:5134–9. <https://doi.org/10.1016/j.engfracmech.2008.08.002>.
- [48] Livieri P, Tovo R. The use of the JV parameter in welded joints: Stress analysis and fatigue assessment. *Int J Fatigue* 2009;31:153–63. <https://doi.org/10.1016/j.ijfatigue.2008.06.007>.
- [49] Carpinteri A, Cornetti P, Pugno N, Sapora A, Taylor D. A finite fracture mechanics approach to structures with sharp V-notches. *Eng Fract Mech* 2008;75:1736–52. <https://doi.org/10.1016/j.engfracmech.2007.04.010>.
-

- [50] Carpinteri A, Cornetti P, Pugno N, Sapora A. On the most dangerous V-notch. *Int J Solids Struct* 2010;47:887–93. <https://doi.org/10.1016/j.ijsolstr.2009.11.017>.
- [51] Carpinteri A, Cornetti P, Sapora A. Brittle failures at rounded V-notches: a finite fracture mechanics approach. *Int J Fract* 2011;172:1–8. <https://doi.org/10.1007/s10704-011-9640-8>.
- [52] Sapora A, Cornetti P, Carpinteri A. Cracks at rounded V-notch tips: an analytical expression for the stress intensity factor. *Int J Fract* 2014;187:285–91. <https://doi.org/10.1007/s10704-014-9932-x>.
- [53] Sonsino CM, Böhme D, Kulka C, Helwig R. Slope of the S-N-Curve and high-cycle fatigue behaviour of longitudinal stiffeners in the as-welded and stress-relieved states, IIW Doc. XIII - 1242-87. *Int Inst Weld* 1987.

CHAPTER 4.

Short fatigue cracks growth monitoring

List of symbols

a	Crack depth
a/D	Normalized crack depth
$2c$	Major axis of the elliptical crack
c/a	Crack aspect ratio
D	Specimen net-section diameter
E	Young's modulus
F	Axial load
I	Electrical current
K_I	Mode 1 Stress Intensity Factor (SIF)
ΔV_{PD}	Potential drop geometrical factor of the active channel
θ_I	Angular position of the current probes
θ_{PD}	Angular position of the active channel potential probes
θ_T	Angular position of the potential probes for temperature compensation
ρ	Electrical resistivity
S	Curvilinear coordinate along the semi-elliptical crack tip profile
ΔV_{PD}	Potential drop of the active channel
ΔV_T	Potential drop of the reference channel for temperature compensation
Y_I	Distance of the current probe from crack plane
Y_{PD}	Distance of the active channel potential probe from crack plane
Y_T	Distance of the reference channel potential probe from crack plane

4.1. Introduction

As deeply discussed in the previous chapter, the material's resistance to crack propagation is typically expressed by the fatigue crack propagation threshold, when dealing with the threshold condition, or the Paris's curve concerning the crack growth rate under continuous propagation [1]. However, it has also been observed that small fatigue cracks could be of great interest in structural reliability since they can grow at rates that are faster than long cracks when loaded with the same crack driving force. In particular, it has been intensely examined that, if compared with long cracks, they exhibit a much lower fatigue crack propagation threshold due to the gradual build-up of the crack closure phenomena [2–4], the latter being completely described by the cyclic R-curve concept [3–10]. Noteworthy, all contributions present in the Literature suggest evaluating the cyclic R curve, i.e. the crack size dependence of the fatigue crack propagation threshold in the physically/mechanically short crack regime, by means of experimental fracture mechanics fatigue tests using flat specimens like the compact tension (CT), the centre cracked tension (CCT), single edge notch tension (SENT) and the single edge notch bend (SENB) [3–10].

On the other hand, the ASTM E647 [11] recommend employing such specimens geometries for fatigue long crack testing, while it advise using a different specimens' geometry, such as the rectangular surface-crack, the corner-crack, and single-edge-crack round bars, when dealing with fracture mechanics fatigue tests of small cracks. At the same time, there is the need to evaluate the cyclic R-curve on such specimen's geometries in order to better understand the effect of a different specimen geometry, and the consequent differences in loading and constraint conditions, on the build-up of the crack closure phenomena.

The problem is that performing fracture mechanics tests to obtain the cyclic R-curve requires the crack size to be measured during the tests, this aspect being very difficult when dealing with those specimens' geometry. Indeed, it is worth noting that standard specimens for fatigue long crack tests are all characterised by a through the thickness crack which allows to adopt several methods for crack size measurement, e.g. visual or non-visual techniques. On the other contrary, all specimens for fatigue small crack tests include a surface crack whose size can be measured

by visual techniques only on the specimen surface, while the crack depth inside the material can be measured only by non-visual techniques. Among non-visual and non-destructive evaluation (NDE) techniques, International standards [12] suggest the compliance method and the electric potential difference (or Potential Drop method).

Certainly, the Potential Drop (PD) method represents one of the most used non-visual techniques for real-time in-situ non-destructive evaluation (NDE) of the crack size in cracked components. This approach is widely cited and suggested by numerous standards in the field of fracture mechanics, both for static [13,14] and fatigue tests [11,12]. In few words, the potential drop is an indirect measurement technique relying upon the passage of a constant electrical current flow through the tested specimen and the subsequent measurement of the voltage between two points located over and under the cracked area of the specimen itself (Figure 4.1). The potential drop method is available in two different versions, depending on the used power supply, the latter being either a small ($\sim 1\text{A}$) alternating electrical current flow in case of the Alternate Current Potential Drop (ACPD) method or a large ($\sim 30\text{A}$ or even larger values) direct electrical current flow for the Direct Current Potential Drop (DCPD) method. The resulting change in voltage comes from the increase in resistance (for DCPD) or impedance (for ACPD) of the specimen under test as a consequence of the crack length increment. To put it simply, electrons are "forced" through the uncracked cross-sectional area, which is smaller than the gross one, therefore, the specimen being subjected to a constant electrical current flow, the increase of the electrical resistance translates in an increase of the potential drop. The resulting change in voltage is used to calculate the crack length by entering in a proper calibration curve (Figure 4.1) which can be derived on experimental, analytical, or numerical basis [15]. However, among all available calibration techniques, the numerical way has the advantage to be easier as well as less time-consuming, giving also the opportunity to investigate the effects of many parameters, e.g. complex specimen geometries, crack shape, and the location of the potential and current probes, on the calibration curves [16].

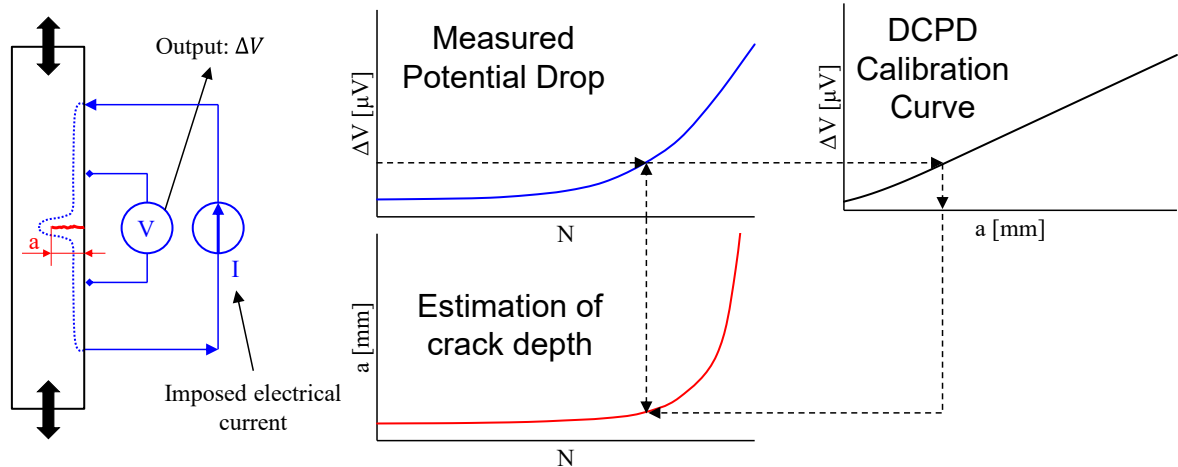


Figure 4.1. Schematic representation of the working principle of a DCPD system.

In DCPD, the current flow is forced through the bulk specimen, while in ACPD, due to the so called “skin effect”, it mainly flows near the specimen surface. As a result, in principle, ACPD could be more sensitive to surface cracks, whereas DCPD, even though it is still employed mainly in this role, has the potential capability to detect also subsurface cracks. DCPD has also the advantage of a relatively inexpensive and easy-to-use setup compared to the one required for ACPD.

As a result of its operating principle, the DCPD is an integral method that gives as an output the estimate of the cracked area [11], but not of the actual crack shape, path and location. For this reason, the DCPD represents one of the most robust and widespread method in the Literature [15,17–19] for standard fracture mechanics fatigue tests for long cracks, but not for complex specimen’s geometries. Indeed, the crack location as well as the crack path and shape are usually known a priori in the case of standard fracture mechanics fatigue tests for long cracks (CT, CCT, SENT or SENB specimens), for which a resolution in the order of tens of microns in crack length can be normally obtained [11]. Noteworthy, a resolution in the order of at least ten microns is required when the cyclic R-curve has to be determined.

In contrast, its application can be extremely difficult in case of specimens having complex geometries (e.g. that suggested by ASTM E647 for small crack testing [11]) or real components, the crack location, path, and shape being not known in advance. For the sake of completeness, it must be reminded that in the literature there are solutions that allow to partially overcome some of these limitations. For example, a multi-probe DPCD method [16,19–22] can be employed in place of a single probe system to get over this limitation. Precisely, the more

potential probes used, the more accurate the crack location is going to be. Moreover, in the case of real components having large size [23–27], a reduced sensitivity is typically observed, because for a fixed input current, the current density is lower [15]. In real components, crack growth resolution is typically on the order of hundreds of microns or even millimetres [23–27].

So far as short cracks are concerned, some applications of the DCPD method to monitor the propagation of short cracks have been performed by Cerny et al. [28–30] and by Funk and Bär [20], who obtained a sensitivity of approximately 0.1 mm in specimens having constant rectangular cross section by locating the potential probes at a distance between 2 and 5 mm from the crack plane and the current probes on the specimen's ends. A similar resolution was obtained by Saka et al. [31] who proposed locating the potential probes and the current probes at a distance of 2.5 mm and 3 mm, respectively, from the crack plane (Closely Coupled Probes Potential Drop - CCPPD).

Unfortunately, in the Literature there exist few example of applications to the specimen's geometries suggested by ASTM E647 [11] for fracture mechanics tests of small fatigue cracks under axial fatigue loading. Some authors have applied the DCPD to cylindrical plain or notched bars under fatigue axial loadings [16,19,32–35], but none of them has never tried understand in which way the performances of the DCPD measurement could have been improved to reach higher resolutions (e.g. that required for determining the cyclic R-curve) in terms of crack size. Accordingly, the present chapter addresses the DPCD applications to laboratory fatigue specimens for investigating the material cracking behaviour and, in particular, for calibrating the method in fatigue crack growth monitoring of single-edge-crack round bar specimens, this specimen's geometry being suggested by ASTM E647 [11] for fracture mechanics tests of small fatigue cracks under axial fatigue loading. In more detail, the purpose of this chapter is to improve the technical performances of the DCPD method by identifying the most influencing parameter and the best way to arrange both the current and potential probes on such specimen's geometry. In particular, the purpose is to improve the technical performances of the DCPD method by a proper arrangement of current and potential probes. Therefore, 3-dimensional finite element electrical analyses have been performed owing to their versatility in evaluating the effects of different geometrical, operational and environmental parameters [16]. Eventually, the accuracy of the numerical analyses' results has been checked against new generated experimental data.

4.2. Performances of a DCPD measurement

Previous research [15] focused heavily on applying the DCPD to standard specimens for fatigue long crack testing (e.g. CT, SENB, ...), by examining ways to enhance the measurements on such specimens. Four factors (Table 4.1) were proposed by Aronson et Ritchie [36] to fully characterize the technical performances of a DCPD measurement:

1. *Measurability*, which represent the ability to measure the output voltage signal. The measurability of a DCPD signal has to be always maximized and this can be achieved increasing the output voltage signal's absolute magnitude, $|\Delta V_{PD}|$ (see Figure 4.2a).
2. *Sensitivity*, which is related to the lowest increase in crack size that can be detected by the measurement system. This parameter can be mathematically represented by derivative of the potential drop with respect to the crack size, which value has to be always maximized (see Figure 4.2b).
3. *Reproducibility*, representing the reliability of the DCPD measurements when repeated and somehow its insensitivity to minimal inaccuracies in the placement of the probes, the latter being one of the most significant sources of error. One way to mathematically describe this parameter is the derivative of the potential drop with respect to the probes' positions, which must be minimized in order to maximize the reproducibility of the measurements (see Figure 4.2c).
4. *Accuracy*, which describes how closely measured crack size and shape correspond to actual value (see Figure 4.2d).

There are essentially two approaches to increase the DCPD performances. One option is to improve the quality of the employed experimental DCPD device, the other instead consist in altering the experimental setup, e.g by carefully selecting the current and potential probe

positions, so as to have a different calibration curve. For example, as the enhancing in the sensitivity of the measure is considered (see Figure 4.2b), it is possible either by acquire an experimental DCPD device with a greater resolution in terms of the smallest observable potential drop change or by choosing the position of the potential probes so as to detect smaller crack size increments for the same change in the potential drop signal. Again, the second approach can also be useful to find a position of the potential probes in a region where the potential drop value is high (increasing the measurability, see Figure 4.2a) and where little errors in their placement might result in negligible inaccuracies in the recorded potential drop value (maximizing this way the reproducibility, see Figure 4.2d).

Table 4.1. Summary of optimization parameters according to Aronson et Ritchie [36].

Parameter	Limiting consideration	Mathematical statement
Measurability	Magnitude of output voltage signal	Maximize $ \Delta V $
Sensitivity	Slope of calibration curve	Maximize $d\Delta V/da$
Reproducibility	Ability to locate potential probes	Minimize $d\Delta V/dx$
Accuracy	Accuracy of calibration curve	-

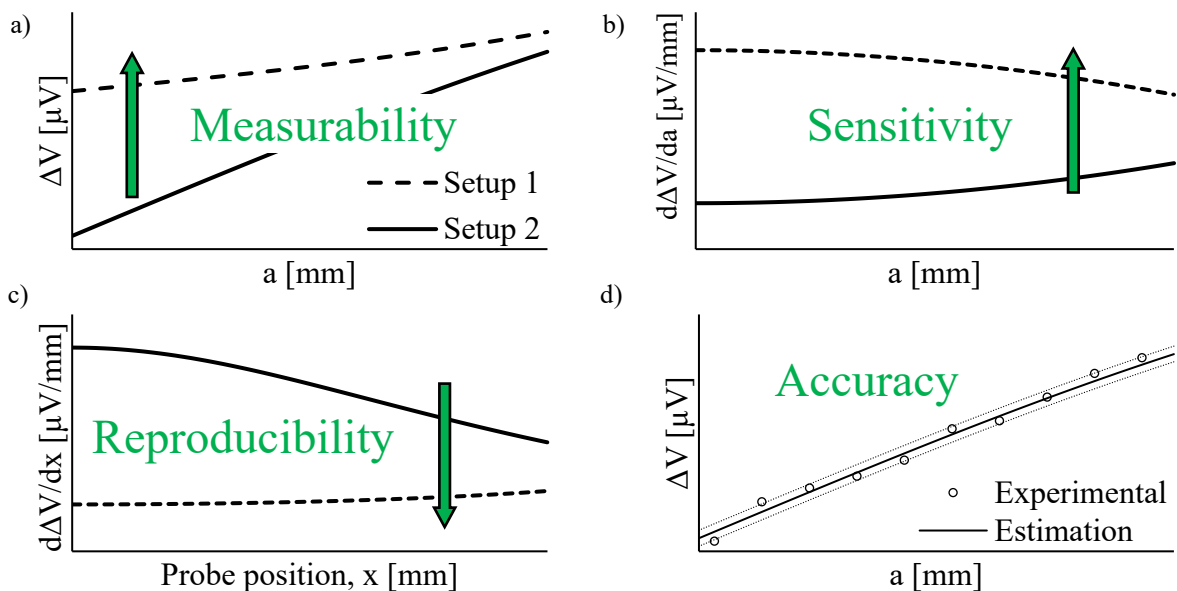


Figure 4.2. Performances of a DCPD setup: a) measurability (4.1), b) sensitivity (4.2), c) reproducibility (4.3), and d) accuracy. Example of comparison between two different DCPD arrangements.

It is handy to write Ohm's law and highlight the factors influencing the potential drop in order to illustrate and better describe the four qualities mentioned above:

$$\Delta V_{PD} = \rho I \Delta v_{PD} \quad (4.1)$$

Eq. (4.1) makes it clear that, generally speaking, the electrical resistivity ρ , the magnitude of the input electrical current I , and a geometrical factor that contains all the details of the electrical current density vector field Δv_{PD} are the three parameters affecting the potential drop value ΔV_{PD} . The first mentioned parameter, the electrical resistivity (or specific electrical resistance) ρ , is a fundamental material property that measures how strongly it resists to the passage of an electric current. Standard applications of the DCPD technique are relevant to specimens made of conductive material, e.g. metals, which electrical resistivity at room temperature ranges from 10^{-5} to $10^{-3} \Omega \cdot \text{mm}$. Nevertheless, it must be mentioned that in the literature can be found some non-conventional applications making use of the DCPD method also with composite materials [37,38] or even non-conductive materials [39]. Other variables that affect this parameter include temperature [35], which effect will be discussed later in this chapter, large deformations, and plasticity at the crack tip [40–45].

Eq. (4.1) easily clarifies that the measurability increases with increasing electrical resistance ρ . The same conclusion may be drawn regarding the magnitude of the electrical current I although its value should be restricted to prevent overheating brought on by the Joule effect. Its value is commonly chosen between 0.5 A and 50 A, even if in some cases much higher values have been adopted [26,46]. Instead, the geometrical factor Δv_{PD} , which includes all geometrical information, depends on a number of variables, including the full specimen geometry, the crack shape, morphology and location, and the entire DCPD setup, including the placement of the current and potential probes as well as geometrical changes generated by mechanical straining of the specimen [36,42,43,45]. Moreover, it can be noted that for a given specimen geometry and a fixed crack size a and shape c/a , this parameter depends only on the position of both current and potential probes if the effect of mechanical straining of the specimen is neglected.

To analyse the sensitivity of the measure, it is convenient to compute the derivative of Eq. (4.1) with respect to the crack size a . To do this, a couple of simplifying hypotheses are necessary, i.e. that both the resistivity ρ and the current I do not change as the crack length a changes during propagation. It is important to say that while the condition on the electric current I is always satisfied, this is not necessarily always true for the assumption made on the electric resistivity ρ , the latter being sensitive to changes in crack tip plasticity as mentioned above. Nevertheless, assuming these conditions are satisfied, it is possible to write the following expression:

$$\frac{d\Delta V_{PD}}{da} = \rho I \frac{d\Delta v_{PD}}{da} \quad (4.2)$$

Eq. (4.2) clearly states that high resistivity and electrical current help to increase the measure's sensitivity. More complex is the dependency on the rate of change of geometrical factor with crack size $d\Delta v_{PD} / da$ which requires to be adequately investigated, e.g. by means of FE analyses.

Finally, the derivative of Eq. (4.1) with respect to the location of the potential probes can be used to analyse the repeatability of the measurement:

$$\frac{d\Delta V_{PD}}{dX_{PD}} = \rho I \frac{d\Delta v_{PD}}{dX_{PD}} \quad (4.3)$$

wherein the generalized coordinate X_{PD} designates the location of the potential probes. This parameter must be as little as feasible, in contrast to measurability and sensitivity [36]. Concluding, it is crucial to identify the current and potential probe locations for a given specimen shape in order to maximize measurability, sensitivity, and repeatability. Accordingly, as declared above, the purpose of this work was to improve the technical performances of the DCPD method by a proper arrangement of current and potential probes when applied to single-edge-crack round bar specimens under fatigue axial loadings.

4.3. Numerical investigation

The whole geometry of the cracked component, including the specimen geometry and the evolution of the crack shape during propagation, is required for the numerical calculations intended to derive the DCPD calibration curves.

4.3.1. Structural FE analyses: iso- K_I criterion

The iso- K_I criterion, firstly formulated in [47,48], postulates that the crack shape changes during the propagation so that constant distribution of the stress intensity factor K_I is provided along the crack front. A single-edge-crack round bar under axial fatigue loading made of steel having elastic modulus equal to 206000 MPa and Poisson's ratio equal to 0.3 has been considered (Figure 4.3). It is a widespread assumption in the Literature to schematize the crack front as a semi-elliptical arch having the centre laying on the specimen surface, one axis corresponding to the crack's depth a , and the other described by the aspect ratio c/a .

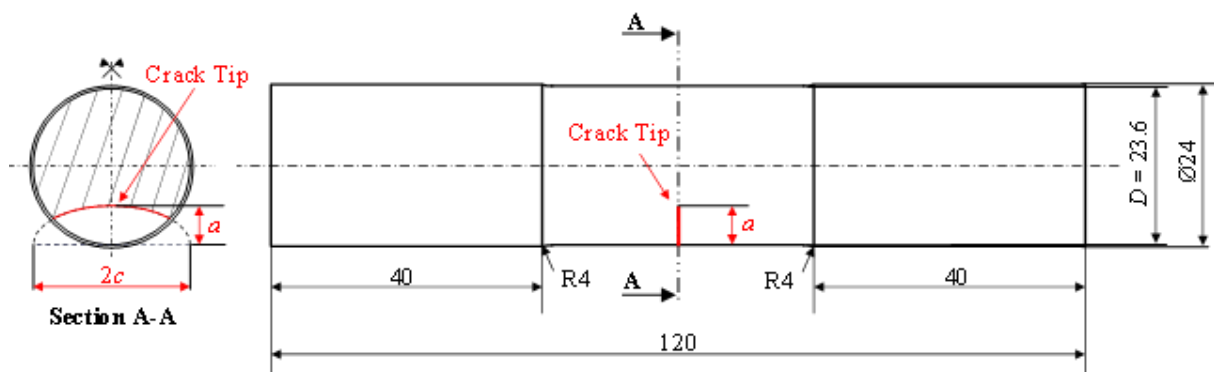


Figure 4.3. Geometry of the single-edge semi-elliptical cracked specimen used in the numerical analyses (dimensions are in millimetres).

By using structural linear elastic FE models, the aspect ratio c/a matching the iso- K_I criterion was determined. In particular, K_I was estimated throughout the whole crack front for various combinations of the normalized crack depth a/D and the aspect ratio c/a (Figure 4.3 and Table

4.2) by means of the Peak Stress Method [49,50]. See Chapter 1 for more details on the application and the conditions of the applicability of the PSM.

Only one quarter of the specimen in Figure 4.4 was modelled by exploiting the XY and ZX symmetry planes (Figure 4.4). The crack has been introduced with a normalized depth a/D ranging from 0.1 and 0.5 stepped by 0.1 and with the aspect ratio c/a in the range 1.0 - 2.5.

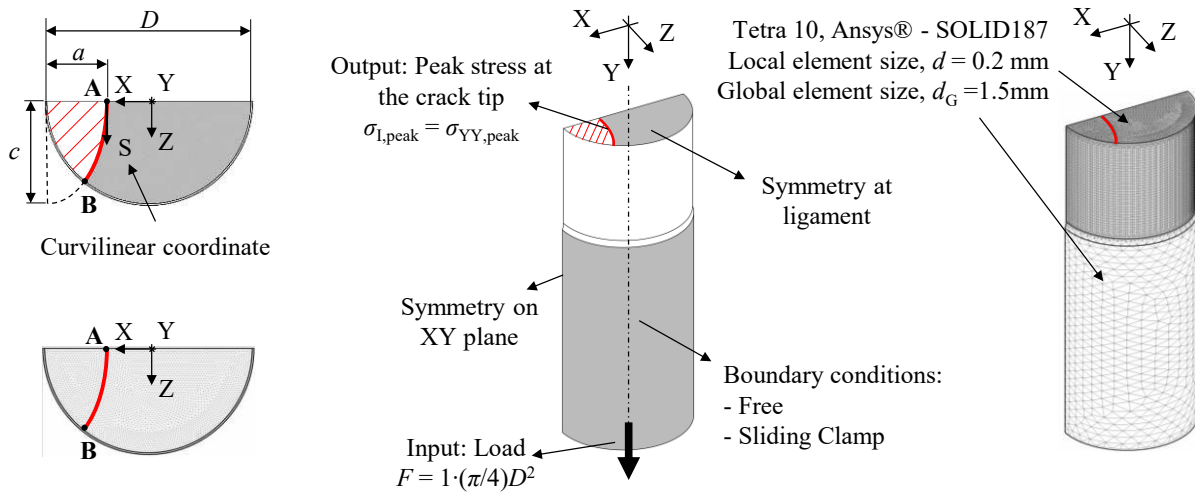


Figure 4.4. 3D structural FE model for evaluating the mode I SIF at the crack tip by means of the PSM based on 10-node tetra elements.

A 3D free FE mesh pattern of 10-node tetrahedral elements (SOLID 187 in the ANSYS® Mechanical APDL element library) has been defined to calculate the mode I stress intensity factor at the crack front line. According to the PSM guidelines for Tetra-10 elements [51,52], the average element size must be $d \leq a/3$, a being the crack length, to properly estimate the stress intensity factor K_I of a crack under pure mode I loading. This turns out in a maximum element size $d_{max} = 2.36/3 \approx 0.78$ mm for the analysed crack having the minimum depth, i.e. the most critical case ($a = 2.36$ mm). However, such a coarse element size would have resulted in a coarse description of the SIF along the crack front. Therefore, a more refined mesh pattern having element size $d \approx 0.2$ mm has been generated by successive local refinements of the free mesh pattern having global element size $d_G = 1.5$ mm.

For the gripped region of the specimen, two sets of boundary conditions have been taken into consideration to investigate the effect of different constrains on the SIF: (1) "free" condition, in which the specimen ends were allowed to freely rotate and translate when axially loaded; (2) "sliding clamp" for emulating machine grips having infinite stiffness, in which the

4.3 Numerical investigation

nodes of the gripped cylindrical surface were constrained in such a manner that only their axial displacements were allowed. Finally, a tensile normal stress of 1 MPa has been applied to the specimen's gross section to simulate the axial load. An overview of the FE analyses performed is presented in Table 4.2.

Table 4.2. Summary of the structural FE analyses carried out to derive the iso- K_I crack propagation pattern.

a/D [-]	D [mm]	c/a [-]	Boundary conditions
0.1	23.6	1.0, 1.1, ..., 1.5	Free, Sliding clamp
0.2		1.0, 1.1, ..., 2.0	
0.3		1.5, 1.6, ..., 2.5	
0.4		1.5, 1.6, ..., 2.5	
0.5		1.5, 1.6, ..., 2.5	

After solution, the opening peak stress, $\sigma_{YY,peak}$ stress distributions have been evaluated at FE nodes located along the crack front, then the average peak stresses $\Delta\bar{\sigma}_{YY,peak}$ have been calculated for computing K_I (see Chapter 1 for more details on the application of the PSM with 10-node tetra elements). The results are reported in Figure 4.5, which depicts the SIF distribution as a function of the normalized curvilinear coordinate running along the crack front line, S/S_{max} , and parametrically with respect to both the normalized crack depth, a/D , and the aspect ratio, c/a . The K_I -distributions for the "free" boundary condition are reported in Figure 4.5a, whereas those for the "sliding clamp" boundary condition are reported in Figure 4.5b.

As expected, results demonstrate that, for a constant crack depth a , the maximum value of K_I and its position along the crack front rely on both the constraint conditions and the aspect ratio c/a . According to Shin et Cai [53], when considering the influence of the constraint condition while keeping fixed the aspect ratio c/a , the "free" condition always results in higher values of K_I than the "sliding clamp" one, this difference being greater as the crack depth increases. Regarding the effect of the aspect ratio c/a , Figure 4.5 demonstrates that, regardless of the constraint condition, the position of the maximum K_I corresponds to the center of the specimen (point A in Figure 4.5) if c/a assumes relatively high values. In this case, the K_I distribution is monotonically decreasing with S/S_{max} . On the contrary, its position is located at the intersection between the crack front and the specimen's external cylindrical surface (point B in Figure 4.5) and the K_I distribution is monotonically increasing with S/S_{max} for low values of c/a . This observation made it possible to identify the values of aspect ratio c/a leading to an

almost constant K_I distribution along the crack front, i.e. the aspect ratios c/a according to the iso- K_I criterion (Figure 4.6).

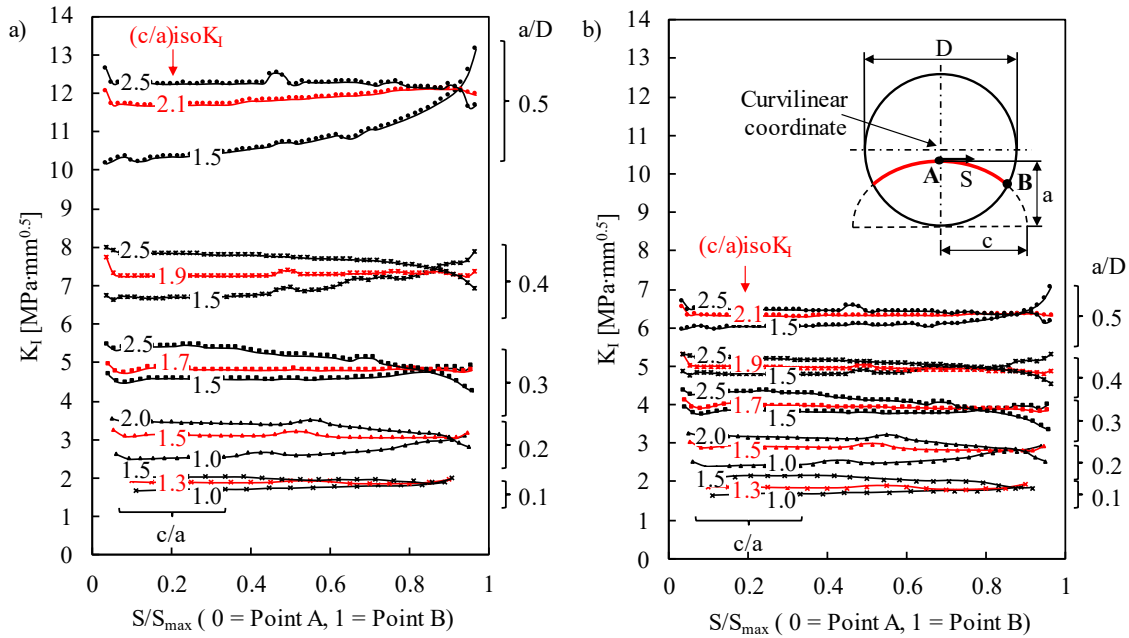


Figure 4.5. Results of the 3D structural FE analysis: mode I SIF profiles as a function of the position along the crack tip (S/S_{max}), the crack depth (a/D), and the aspect ratio (c/a) for the (a) ‘free’ and (b) ‘sliding clamp’ constraint conditions.

Figure 4.6 reports the obtained iso- K_I aspect ratios $(c/a)_{iso-K_I}$ as a function of the normalized crack depth a/D ranging between 0.1 and 0.5. Interestingly, while the constraint conditions significantly affect the K_I values, on the other hand, they do not have any considerable effect on the crack shape evolution. Furthermore, a linear interpolation of the data appeared to be a reasonable characterization of the dependency of $(c/a)_{iso-K_I}$ on the normalized crack depth a/D :

$$(c/a)_{iso-K_I} = 1.15 + 1.85 \cdot (a/D) \quad (4.4)$$

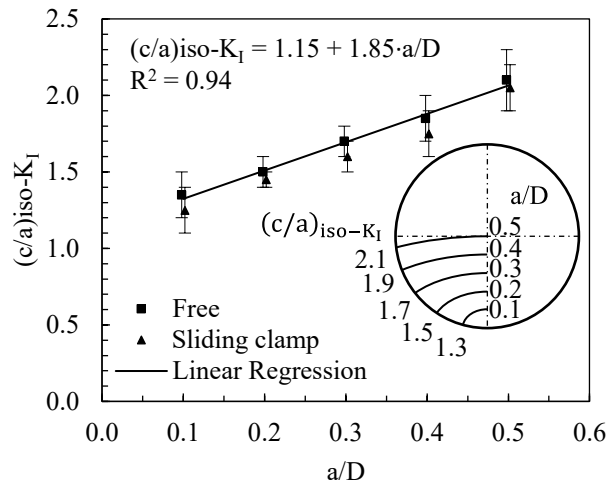


Figure 4.6. Elliptical crack aspect ratio (c/a) according to the iso-KI criterion as a function of the normalised crack depth (a/D) . The figure includes also error bars reporting the range of aspect ratio for which mode I SIF values are approximately constant along the crack front.

4.3.1. Electrical FE analyses: Effect of current and potential probe location

Previously it has been shown that, the electrical resistivity ρ , electrical current I , and geometrical factor ΔV_{PD} are the three basic parameters that determine the DCPD calibration curves. It is important to note that this work only addresses the pure electrical problem, as the effect of mechanical straining is not taken into account. Accordingly, it is clear that for a given specimen geometry and a fixed crack size a and shape c/a , the latter depends only on the positions of both current and potential probes if the effect of mechanical straining of the specimen is neglected. Knowing the whole geometry of the cracked component in Figure 4.3, including the specimen geometry and the evolution of the crack shape during propagation, it was possible to evaluate the DCPD calibration curves for that specimen. The calibration curves have been obtained employing 3D electrical FE analyses in view of their great flexibility in analysing different configurations with relatively little effort. In these analyses, the normalised

crack depth a/D ranged between 0.1 and 0.5 and the aspect ratio c/a has been assumed in accordance with the iso- K_I criterion (Figure 4.6 and Eq. (4.4)) for all crack depths.

A cylindrical coordinate system centred on the axis of the specimen has been used to identify the positions of the current and potential probes (see Figure 4.7, Figure 4.8, Figure 4.9, and Figure 4.10). Accordingly, the position of the current probe was identified by the (θ_I, Y_I) , i.e. the angular and axial coordinate respectively, while the location of the potential probe was represented by the coordinates (θ_{PD}, Y_{PD}) . Four different current injection locations were taken into consideration in order to examine the impact of the current probe position on the DCPD sensitivity in cylindrical specimens:

- 1) A “remote” current input to generate a uniform current density vector field on the gross section of the specimen far away from the crack plane has been simulated by locating the current probe on the specimen’s ends ($Y_I \rightarrow \infty$) (Figure 4.7).

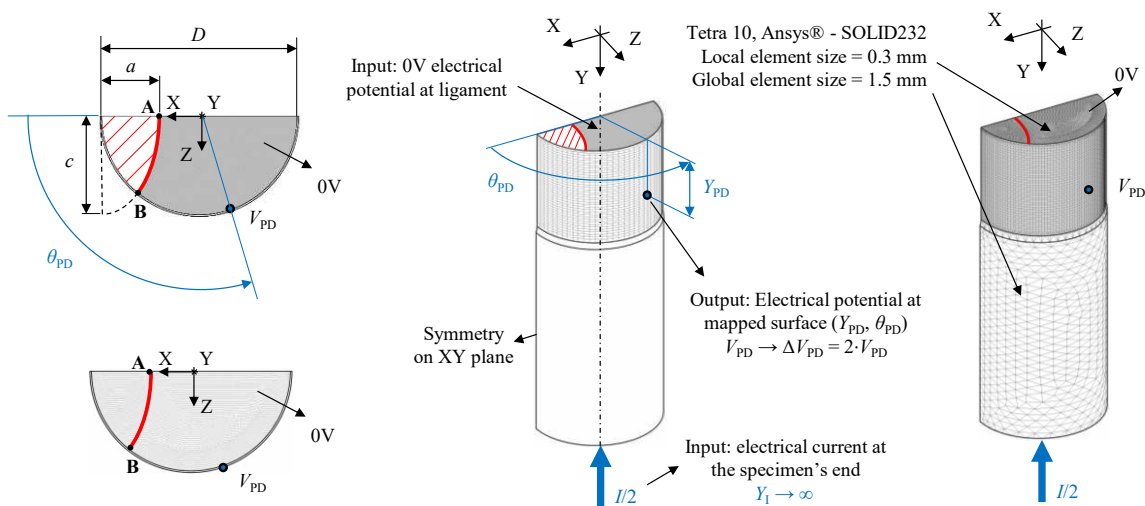


Figure 4.7. 3D electrical FE model: remote current input ($Y_I = \infty$).

- 2) A “local” current input to generate an increased current density close to the crack plane, as suggested by Saka et al. [31] or by Ritchie et al. [54] in case of flat specimens, has been analysed by modelling the current probe on the XY symmetry plane ($\theta_I = 0^\circ$) at an axial coordinate $Y_I = 11.5\text{ mm}$ (Figure 4.8).

4.3 Numerical investigation

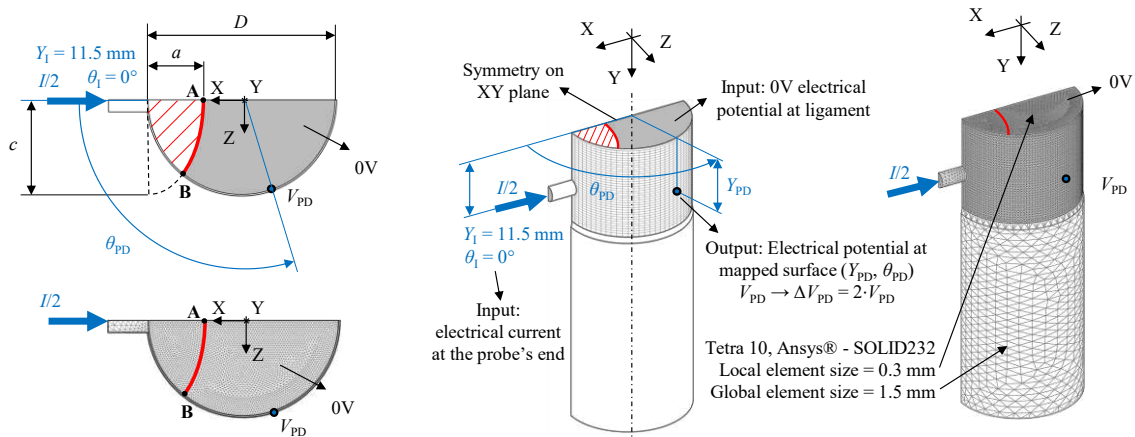


Figure 4.8. 3D electrical FE model: local current input ($Y_1 = 11.5 \text{ mm}$, $\theta_1 = 0^\circ$).

- 3) A “local” current input on the XY symmetry plane ($\theta_1 = 0^\circ$) with a reduced axial distance of the current probe from the crack plane ($Y_1 = 4 \text{ mm}$) (Figure 4.9).

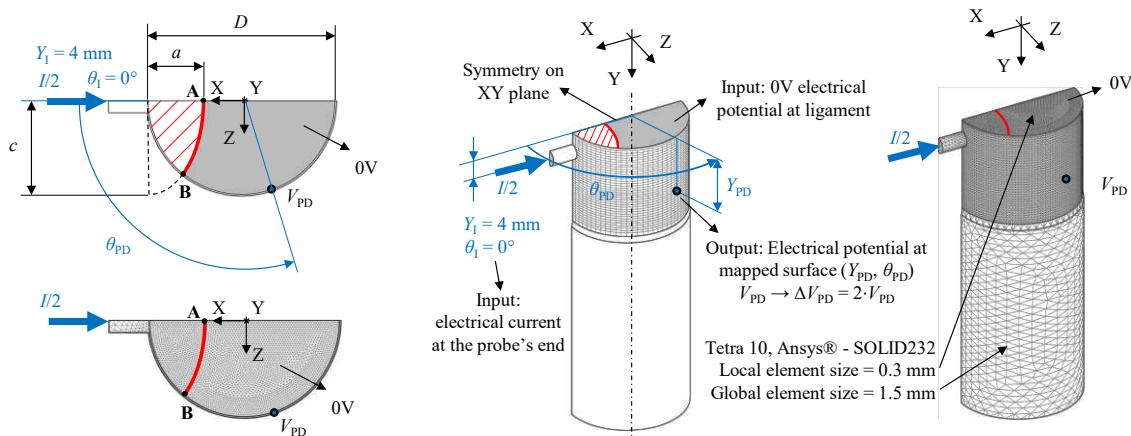


Figure 4.9. 3D electrical FE model: local current input ($Y_1 = 4 \text{ mm}$, $\theta_1 = 0^\circ$).

- 4) A “local” current input configuration having the current probe located at the same axial distance as in case 2) ($Y_1 = 11.5 \text{ mm}$), but at a different angular position ($\theta_1 = 50^\circ$) which roughly corresponds to the angular coordinate of the intersection between the crack tip and the external cylindrical surface of the specimen when the crack is approximately at half the analysed crack depth range ($a/D \sim 0.3$) (Figure 4.10).

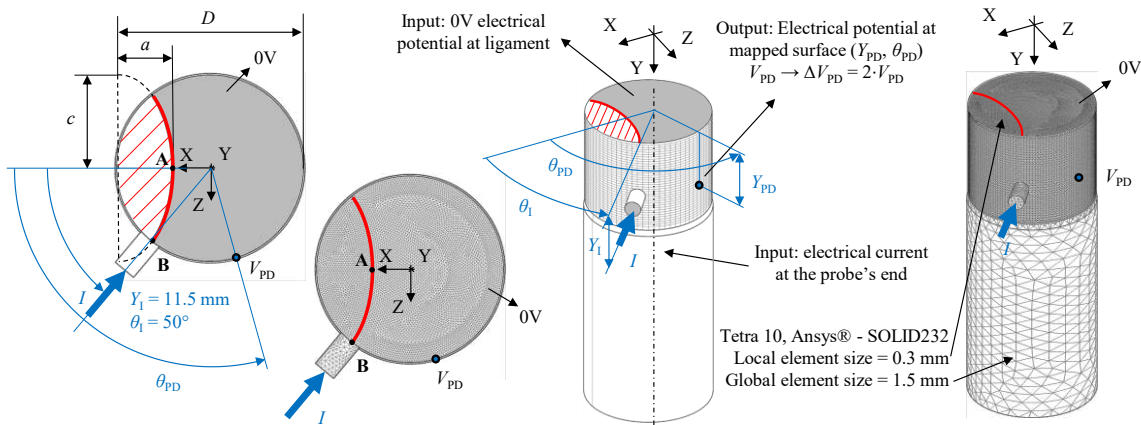


Figure 4.10. 3D electrical FE model: local current input ($Y_I = 11.5$ mm, $\theta_I = 50^\circ$).

The current probe has always been modelled as a 3 mm-diameter cylinder made of medium carbon steel (electrical resistivity $\rho = 20 \cdot 10^{-5} \Omega\text{mm}$, i.e. the same material of the specimen) perfectly in touch with the specimen itself, thus assuming no contact resistance between them. Moreover, the position of both the current and potential probes were symmetrically placed in relation to the crack plane (ZX in Figure 4.7, Figure 4.8, Figure 4.9, and Figure 4.10). Finally, the cylindrical surface between the crack plane and the gripped region was divided into sub-areas, stepped by 0.5 mm in the axial direction and by 5° in the angular direction, in order to evaluate the influence of the position of the potential probes, the latter being assumed to be point-like (see Figure 4.7, Figure 4.8, Figure 4.9, and Figure 4.10). The models have been generated by taking advantage of all available symmetry planes whenever it was possible: in configurations 1, 2, and 3 only one-quarter of the specimen was modelled by exploiting both the ZX anti-symmetry plane and the XY symmetry plane (see Figure 4.7, Figure 4.8, and Figure 4.9). While only the ZX anti-symmetry plane has been used in configuration 4, the latter showing no more symmetry with respect to the XY plane (see Figure 4.10).

A pattern of 10-node tetrahedral electric solid elements (SOLID232 of the Ansys element library) having a global element size of 1.5 mm has been adopted to build up the FE model. A more refined mesh of approximately 0.7 mm has been employed in the region of the specimen where the potential drop values had to be evaluated, while an element size of nearly 0.3 mm has been used in the proximity of the crack plane, where the gradient of the electric field is very steep (see Figure 4.7, Figure 4.8, Figure 4.9, and Figure 4.10). In all the analysed configurations, the magnitude of input current I was fixed to 50 A and a electric potential equal to 0 V was

4.3 Numerical investigation

forced to nodes situated in the ligament area in order to guarantee the anti-symmetry constraint condition on the ZX plane (see Figure 4.7, Figure 4.8, Figure 4.9, and Figure 4.10).

4.3.2. Results of electrical FE analyses

After the solution it was possible to extract the value of the electric potential V_{PD} as a function of potential probe angular and the axial position (θ_{PD}, Y_{PD}) , the crack depth a , and the current probe configuration (θ_I, Y_I) . Having assumed a symmetrical position with respect to the crack plane (ZX in Figure 4.7, Figure 4.8, Figure 4.9, and Figure 4.10) for both the current and potential probes, it was possible to compute the potential drop as $\Delta V_{PD} = 2 \cdot V_{PD}$.

These results let evaluate all the factors characterizing the technical performances of the DCPD measurement, i.e. measurability, sensitivity, and reproducibility (Table 4.1), as a function of the position of both the potential and the current probes.

As a starting point, it is convenient to fix the crack size and evaluate how the position of the potential probes affects the measurability. Accordingly, Figure 4.11 reports the measurability, mathematically represented by the potential drop ΔV_{PD} , relevant to $a/D = 0.3$ (on the left side) and $a/D = 0.4$ (on the right side), for all the analysed current input configurations, as a function of the potential probe location (θ_{PD}, Y_{PD}) . The first thing to observe is that, in general, the potential drop, i.e. the measurability, increases with increasing potential probe distance Y_{PD} , regardless of the crack size or the current input. At the same time, the measurability is higher when the potential probes are close to the crack plane (ZX), i.e. small Y_{PD} , but at an angular position $\theta_{B'} \leq \theta_{PD} \leq \theta_B$, i.e. within the cracked surface (see Figure 4.11). Moreover, by comparing the left and right side of Figure 4.11 it can be noted that an increase of the crack depth always results in an increase of the potential drop. Furthermore, using a local current input, instead of a remote one, substantially change the shape of the potential drop field by markedly increasing its values in the nearby of the current probe i.e. the black area in the contour plots. In particular, by comparing Figure 4.11b with Figure 4.11c it can be seen that the nearer the current probe to the crack plane the higher the measurability in the region within the cracked area ($\theta_{B'} \leq \theta_{PD} \leq \theta_B$) and close to the crack plane ($Y_{PD} \rightarrow 0$). In addition, by changing the angular position of the current probe, the electric potential field shows no more a symmetrical

distribution with respect to the XY symmetry plane and the region having an enhanced measurability turns out to be slightly shifted on the side of the current probe (compare Figure 4.11b and Figure 4.11d). As a conclusion, the measurability can be maximized by locating both the current and the potential probe at an angular position underlying the cracked area, i.e. $\theta_{B'} \leq \theta_I$, $\theta_{PD} \leq \theta_B$, and as close as possible to the crack plane, i.e. $Y_I \rightarrow 0$, $Y_{PD} \rightarrow 0$. The choice of locating the potential probe close to the crack plane ($Y_{PD} \rightarrow 0$) seems in contrast with what has been discussed above about the measurability, which values diminish as the axial distance of the probe gets smaller. To understand the reasons behind this choice, it must be considered that standard practical applications of the DCPD method guarantee a minimum distance between potential probes of roughly 1 mm, as a technical feasibility limit, which could correspond to a magnitude of the measured potential drop in the order of hundreds or thousands of microvolts, therefore easily measurable by a commercial DCPD device. Nevertheless, the magnitude the measurability must always be checked against the resolution of the experimental device used for measuring the potential drop signal, especially when testing low resistivity materials, i.e. copper or aluminum, or in the case of low input current, both the resistivity and the current being directly proportional to measurability (see Eq. (4.1)).

The sensitivity of the measure $d\Delta V_{PD}/da$ has been evaluated by computing the derivative of the potential drop ΔV_{PD} with respect to the crack depth a thanks to the forward difference method. Similar to the measurability, this parameter has been evaluated as a function of the potential probe angular and axial position (θ_{PD} , Y_{PD}) for all the analysed current input configurations and reported for the cases $a/D = 0.3$ (on the left side) and $a/D = 0.4$ (on the right side) in Figure 4.12.

Interestingly, locating the potential probes at an angular position subtended by the cracked area ($\theta_{B'} \leq \theta_{PD} \leq \theta_B$) results in the highest value of the sensitivity, independently of both the crack size a and the current probe position (θ_I , Y_I). Moreover, in the same region, the closer the potential probe to the crack plane ($Y_{PD} \rightarrow 0$) the higher the sensitivity (Figure 4.12). On the contrary, by placing the potential probe at an angular position not subtended by the cracked area, i.e. $\theta_{PD} \leq \theta_{B'}$ or $\theta_{PD} \geq \theta_B$, there is a significant decrease in sensitivity, the latter less and less significant as the distance of the pins from the plane of the crack increases.

4.3 Numerical investigation

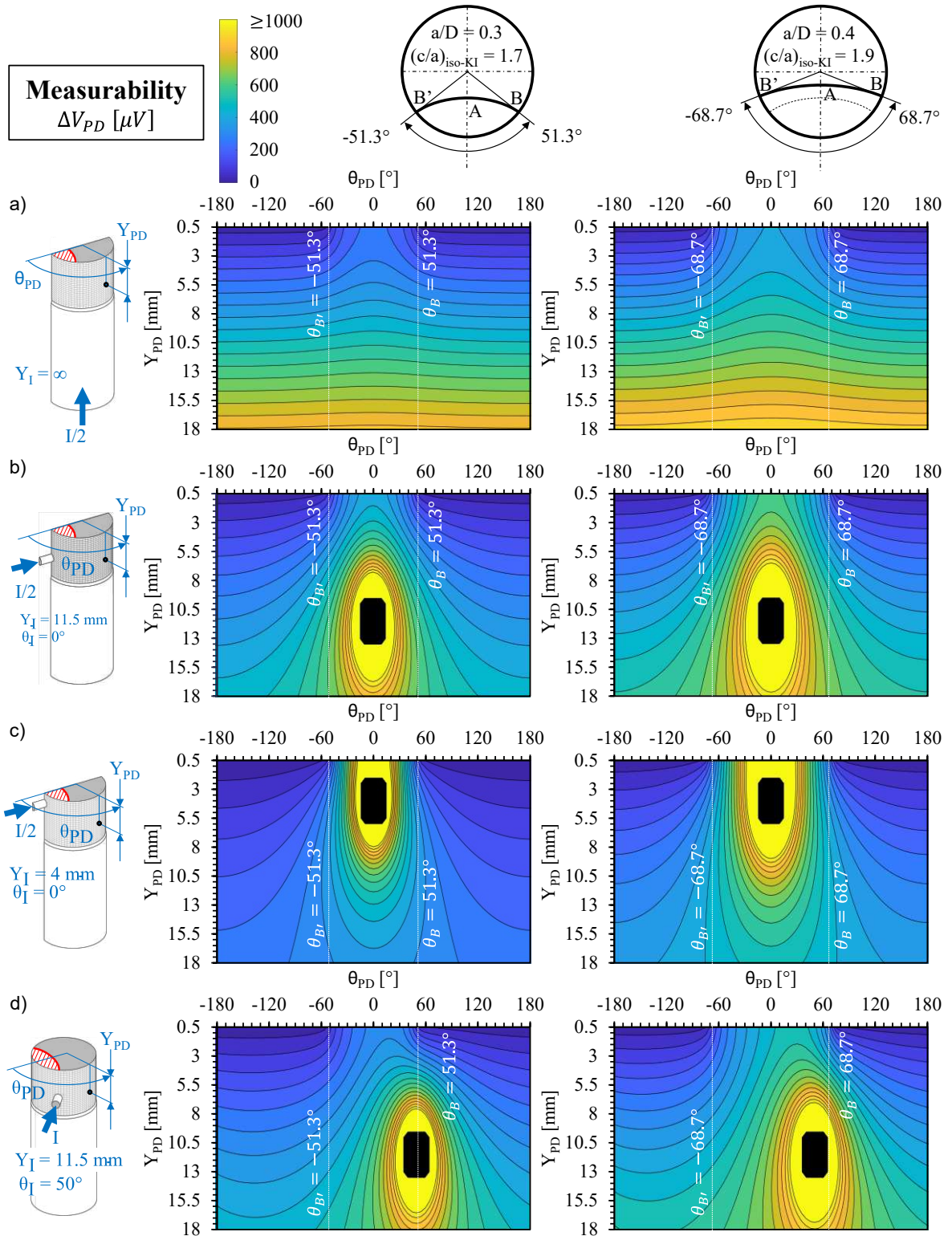


Figure 4.11. Results of the FE analyses: measurability.

Furthermore, similarly to what reported in [36,41,54] for the case of flat specimens, the maximum sensitivity is reached by locating the potential probe as close as possible to the crack tip but on the cracked area side, namely $Y_{PD} \rightarrow 0$ and $\theta_{PD} \rightarrow \theta_B$ or $\theta_{PD} \rightarrow \theta_{B'}$ with $\theta_{B'} \leq \theta_{PD} \leq \theta_B$. This means that the point having maximum sensitivity is always changing with the crack length (compare left and right side of Figure 4.12).

The effect of the current probe position can be understood by comparing Figure 4.12a, b, c, d. At first, the introduction of a local current input (Figure 4.12b) results in a general increase of the sensitivity, which means not only higher peak values but also a more extended region having on average a higher value of the sensitivity, if compared to the remote current input configuration (Figure 4.12a). The same conclusions can be drawn by comparing the local current input in Figure 4.12b with the one having the current probe closer to the crack plane (Figure 4.12c); the nearer the electrical current probe to the crack plane the higher the sensitivity and the larger the area having on average a higher value of the sensitivity.

Finally, similarly to the measurability, locating the local current probe out of the crack symmetry plane (Figure 4.12d) results in a skewed distribution of the sensitivity over the analysed region if compared to the local current input having the current probe on the symmetry plane (Figure 4.12b). In this case, the maximum sensitivity can be reached by locating the potential probe close the crack tip closest to the current input probe ($\theta_{PD} \rightarrow \theta_I \rightarrow \theta_B$). As a conclusion, in the same way as the measurability, the sensitivity can be maximized by locating both the current and the potential probes as close as possible to the crack tip, expressly, $Y_I, Y_{PD} \rightarrow 0$ and $\theta_I, \theta_{PD} \rightarrow \theta_B$.

The measurement's reproducibility is the last parameter to be analysed. It should consider all the possible sources of error in the measurement, among all, that resulting from inaccuracies in the placement of the current and the potential probes. The effect of the potential probe position on reproducibility can be mathematically described by the magnitude of the derivative of the potential drop with respect to the position of the potential probe $|d\Delta V_{PD}/dX_{PD}|$. In this case, the probe position being investigated on a cylindrical surface, the derivative must be evaluated with respect of both the angular and the axial position of the probe, i.e. $|d\Delta V_{PD}/d\theta_{PD}|$ and $|d\Delta V_{PD}/dY_{PD}|$, respectively. Figure 4.13 shows the results relevant to the derivative with respect to the angular position of the potential probe, while Figure 4.14 those relevant to their axial position.

4.3 Numerical investigation

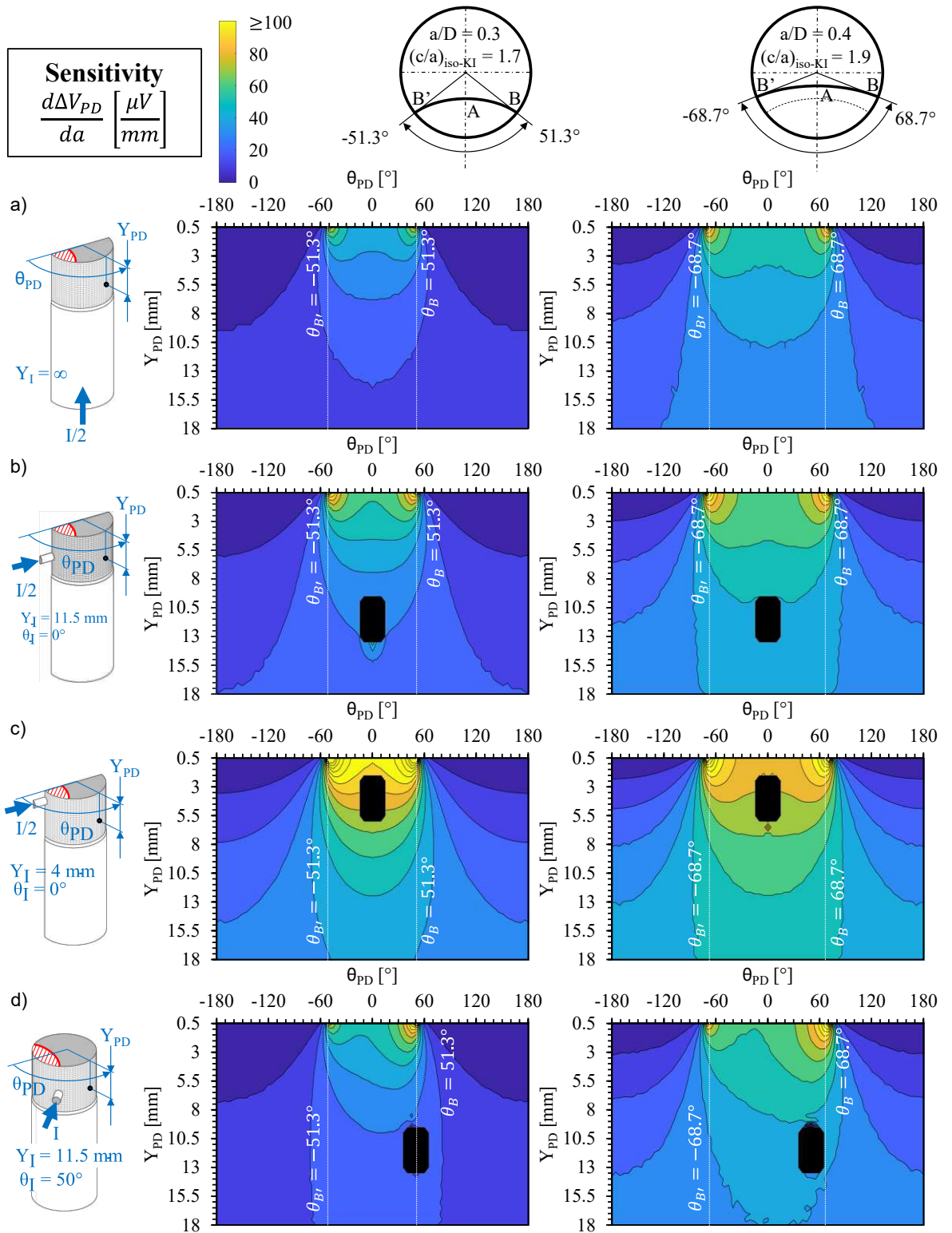


Figure 4.12. Results of the FE analyses: sensitivity.

Starting from Figure 4.13a, it can be noted that the lowest reproducibility, i.e. the highest $|d\Delta V_{PD}/d\theta_{PD}|$, is obtained by locating the potential probe close to the crack tip ($Y_{PD} \rightarrow 0$ and $\theta_{PD} \rightarrow \theta_{B^*}$, θ_B). Unfortunately, the lowest reproducibility is found in the same region that exhibits the maximum of the sensitivity (Figure 4.12). These conclusions, in good agreement with results shown in [36,41,54] for flat specimens, can be explained thinking about the electric potential gradient, which has quite a steep trend in those areas. Reproducibility also decreases as the crack length a increase (compare left and right side of Figure 4.13). Things get worse by introducing a local current input (Fig. XXb) and get even worse by placing the current probe closer to the crack plane (Figure 4.13c) or by aligning its angular position to the crack tip (Figure 4.13d). However, a high-reproducibility region is found by placing the potential probe as close as possible to the crack plane and close to the plane of symmetry ($Y_{PD} \rightarrow 0$ and $\theta_{PD} \rightarrow 0^\circ$). This region being slightly shifted on the side of the current probe if the latter is positioned non-symmetrically with respect to the crack symmetry plane (Figure 4.13d). Also the region described from an angular position that does not subtend the cracked area, i.e. $\theta_{PD} \leq \theta_{B^*}$ or $\theta_{PD} \geq \theta_B$, shows very small $|d\Delta V_{PD}/d\theta_{PD}|$, but it is not of interest due to its quite small measurability (Figure 4.11) and sensitivity (Figure 4.12).

Finally, the effect of the probe position on $|d\Delta V_{PD}/dY_{PD}|$ is shown in Figure 4.14. The highest reproducibility is obtained by locating the probe as close as possible to the crack plane and close to the plane of symmetry ($Y_{PD} \rightarrow 0$ and $\theta_{PD} \rightarrow 0^\circ$). On the contrary, the reproducibility decreases if they are positioned in the region subtending the ligament, i.e. $\theta_{PD} \leq \theta_{B^*}$ or $\theta_{PD} \geq \theta_B$ (Figure 4.14). Similarly to what happens for the derivative with respect to the angular position of the probe $|d\Delta V_{PD}/d\theta_{PD}|$, also that relevant to their axial position $|d\Delta V_{PD}/dY_{PD}|$ increase, i.e. the reproducibility gets worse, both increasing the crack length a (compare left and right side of Figure 4.14) and using a local current input (Figure 4.14b). The same result is obtained locating the current probe closer to the crack plane (Figure 4.14c). This time, if the current probe is located at angular position different from the crack symmetry plane (Figure 4.14d), the reproducibility lower in proximity of the crack tip closest to the current probe ($\theta_{PD} \rightarrow \theta_B$ in Figure 4.14d) and the region showing higher reproducibility moves toward the opposite crack tip (θ_{B^*} in Figure 4.14d).

4.3 Numerical investigation

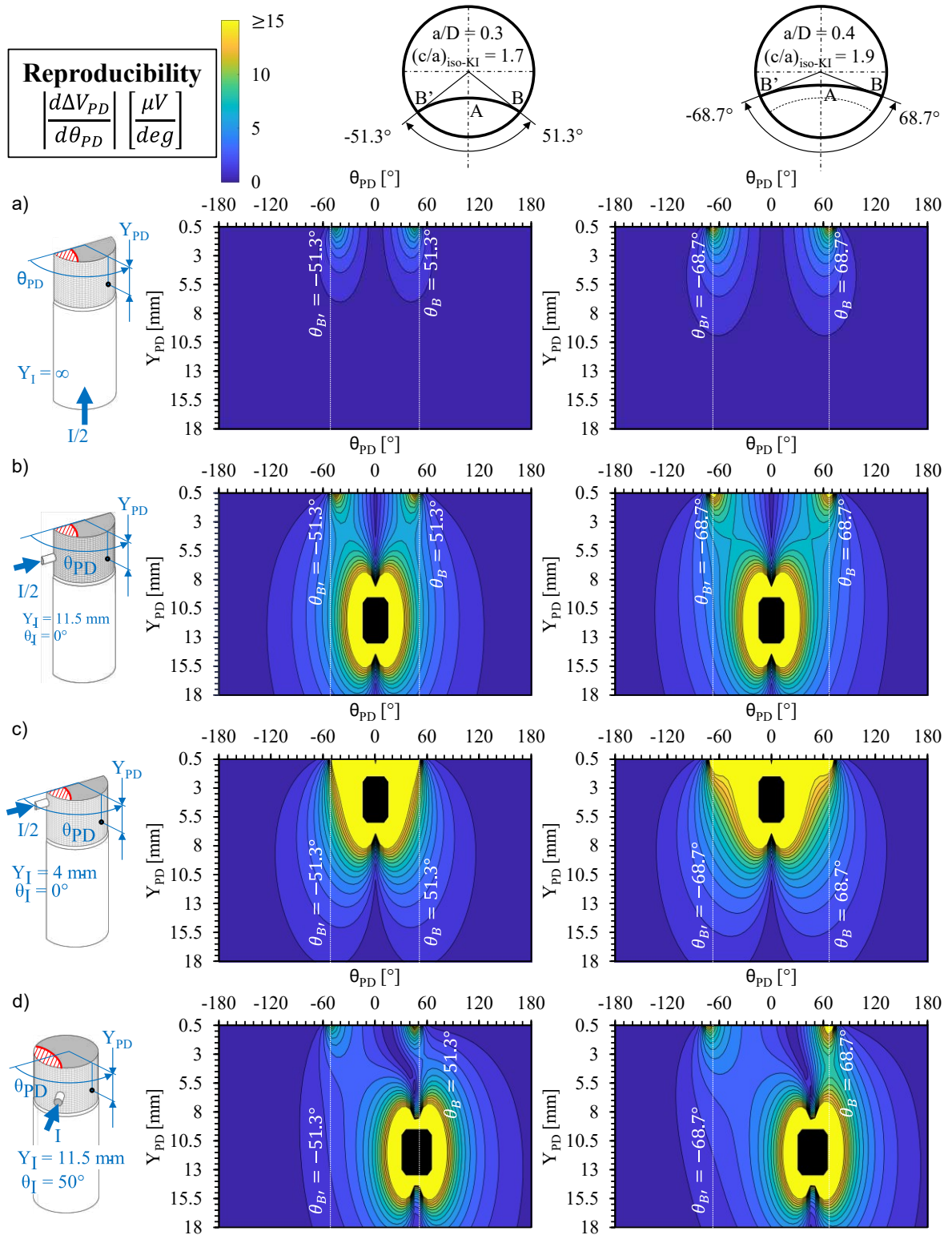


Figure 4.13. Results of the FE analyses: reproducibility 1.

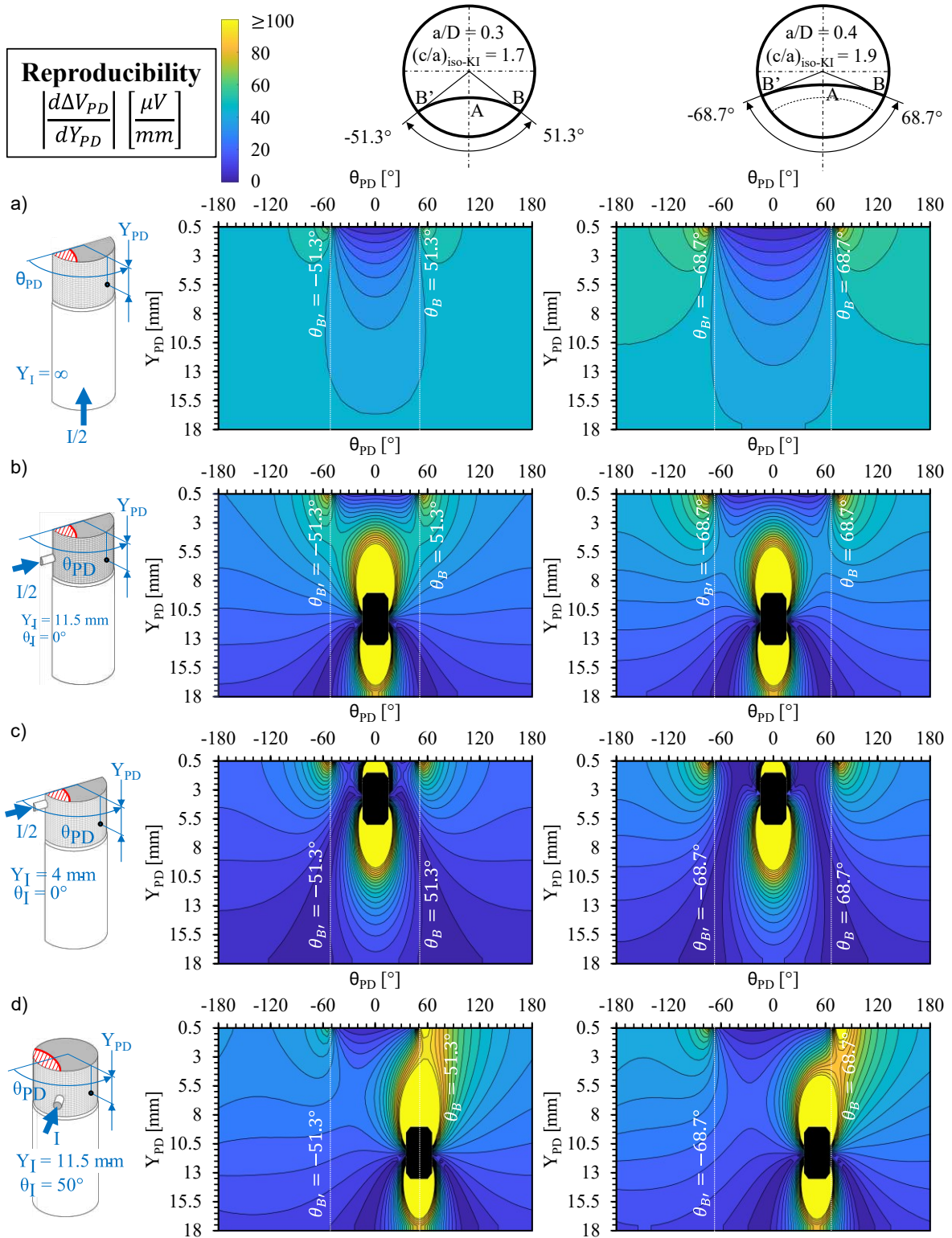


Figure 4.14. Results of the FE analyses: reproducibility 2.

Once qualitatively understood the effect of both the potential and current probe location, it was convenient to keep them fixed and analyse how the measurability, the sensitivity and the reproducibility evolved with the crack length a . Indeed, this is what happens in practical application of the DCPD method, where the probes are obviously kept fixed during the propagation. Thanks to the observation made on Figure 4.11, Figure 4.12, Figure 4.13, and Figure 4.14, it was possible to highlight two different interesting configurations. Both are obtained by placing the potential probe as close as feasible to the crack plane ($Y_{PD} \rightarrow 0$), but one at an angular position corresponding to the crack symmetry plane ($\theta_{PD} = 0^\circ$) in order to maximize the reproducibility, while the other at the same angular position as the crack tip ($\theta_{PD} \rightarrow \theta_B$) to maximize the sensitivity of the measure.

In this work, an axial coordinate $Y_{PD} = 0.5$ mm, corresponding to a spacing between the potential wires of 1 mm, is considered. About the angular position, it has been chosen to compare the configuration having $\theta_{PD} = 0^\circ$ with one having $\theta_{PD} = 50^\circ$, which approximately coincides with the position of the crack tip when the crack length is equal to $a/D = 0.3$. In Figure 4.15 are reported the measurability ΔV_{PD} (Figure 4.15a), the sensitivity $d\Delta V_{PD}/da$ (Figure 4.15b), and the reproducibility $|d\Delta V_{PD}/dX_{PD}|$ (Figure 4.15c and d) as a function of the crack length for the chosen position of the potential probe, the most reproducible on the left and the most sensitive on the right, and for all the analysed current probe configurations (1, 2, 3, and 4 in Figure 4.15). As expected, if the most reproducible configuration is considered (left side of Figure 4.15a), the measurability curves, i.e. the calibration curves (ΔV_{PD} VS a), show that the order of magnitude of the potential drop is always between hundreds and thousands of microvolts, and its value is always monotonically increasing with the crack length a/D . This applies to all current probe positions analysed although, as discussed above, measurability increases as the current probe approaches the crack plane ($Y_I \rightarrow 0$). On the other hand, in case of the most sensitive configuration (right side of Figure 4.15a), the same curves appear to be significantly different. They are still monotonically increasing with the crack length a/D , but this time the potential drop is much lower for $a/D < 0.3$, in the order of tens of microvolts, and rapidly increase up to hundreds of microvolts once the crack tip reaches the position of the probe ($\theta_B \rightarrow \theta_{PD} = 50^\circ$), i.e. $a/D \sim 0.3$.

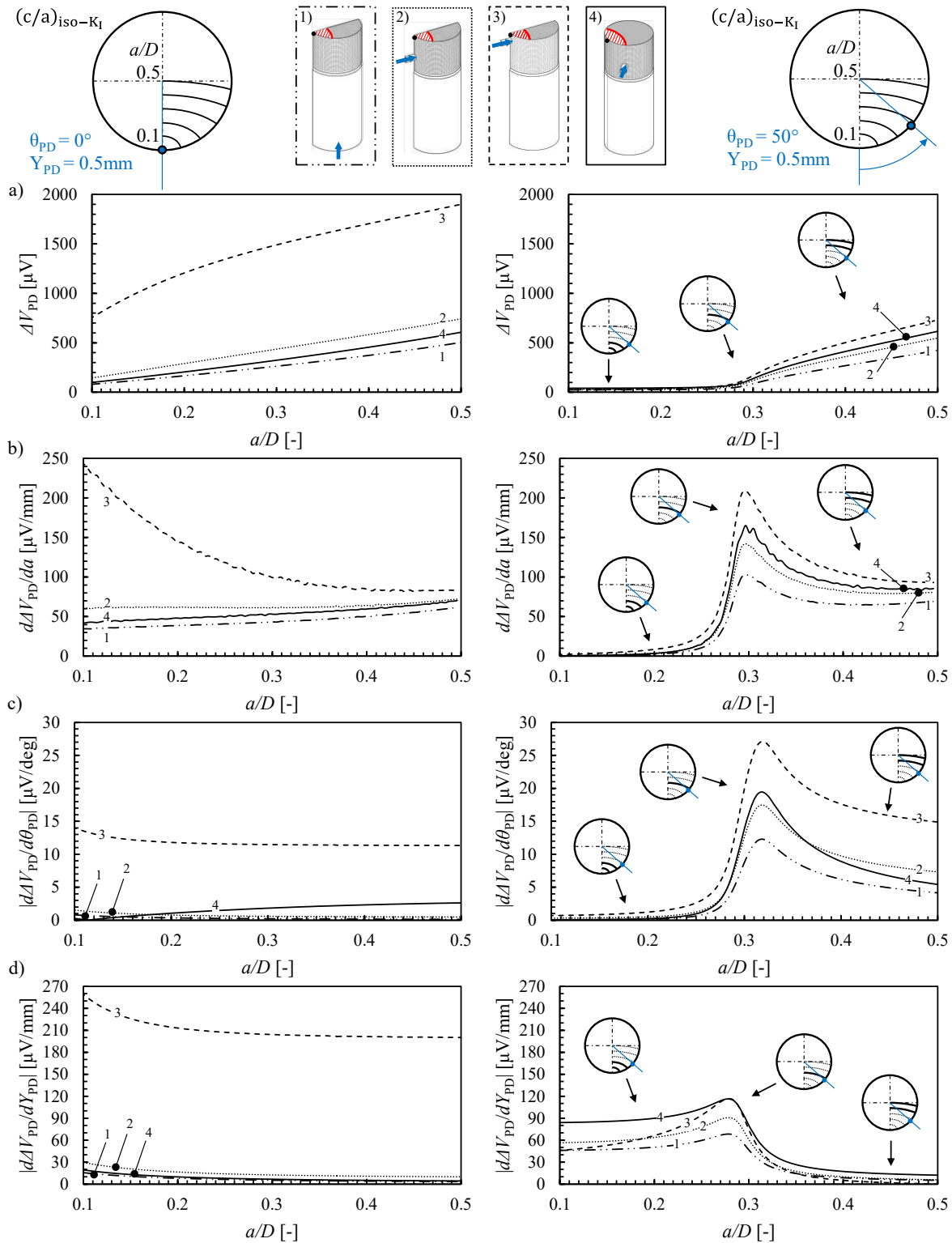


Figure 4.15. Results of the FE analyses: a) measurability, b) sensitivity, and c), d) reproducibility as a function of the normalized crack depth a/D for two different fixed positions of the potential probes as a function of the four current input configurations.

The reasons behind this quick increase in the measurability can be better explained analysing the sensitivity curves (Figure 4.15b), which describe how the slope of the calibration curves $d\Delta V_{PD}/da$ evolves with the crack length a/D . Starting from the configuration having $\theta_{PD} = 0^\circ$ (on the left), in case of current input configurations 1, 2, and 4, the sensitivity of the measure has roughly the same monotonically increasing trend and values ranging within $30 \mu\text{V}/\text{mm}$ to $60 \mu\text{V}/\text{mm}$.

Differently, the current probe configuration 3 has much higher sensitivity when the crack is small ($\sim 250 \mu\text{V}/\text{mm}$ for $a/D = 0.1$). However, it suddenly decreases as the crack length increases asymptotically tending to the other current probe configurations. This aspect may be explained by noting that both the current and the potential probe are located extremely close to the crack tip for a small crack depth ($a/D = 0.1$). Accordingly, as was previously noted, the sensitivity rises as the current and the potential probe get closer to the crack tip, namely $Y_I, Y_{PD} \rightarrow 0$ and $\theta_I, \theta_{PD} \rightarrow \theta_B$. A similar behaviour is shown by the sensitivity curves in case of potential probe located at $\theta_{PD} = 50^\circ$ (right side of Figure 4.15b), although some more considerations are required to analyse them. In this case, the sensitivity initially shows extremely low levels independently of the current probe position (less than $10 \mu\text{V}/\text{mm}$ for $a/D < 0.2$), then immediately increases as the crack tip approaches the angular position of the potential probe ($\theta_B \rightarrow \theta_{PD} = 50^\circ, a/D = 0.3$), and finally tends asymptotically to the values corresponding to the most reproducible configuration, i.e. $70 \mu\text{V}/\text{mm}$ for case 1 and $90 \mu\text{V}/\text{mm}$ for case 3 (the one the left side of Figure 4.15b).

The maximum value of the sensitivity, i.e. the maximum slope in the measurability, is higher when the current probe is closer to the crack tip ($Y_I \rightarrow 0$ and $\theta_I \rightarrow \theta_B$) ranging from $100 \mu\text{V}/\text{mm}$ of case 1 to $210 \mu\text{V}/\text{mm}$ of case 3 (see right side of Figure 4.15b). Noteworthy, these values are almost doubled if compared to that relevant to the most reproducible configuration ($\theta_{PD} = 50^\circ$) for the same crack length (compare left and right side of Figure 4.15b when $a/D \sim 0.3$) demonstrating how advantageous it can be to place both the potential and the current probe close to the crack tip ($Y_I, Y_{PD} \rightarrow 0$ and $\theta_I, \theta_{PD} \rightarrow \theta_B$).

Things go differently when analysing the reproducibility of the measurement, regardless of whether it is evaluated with respect to the angular coordinate $|d\Delta V_{PD}/d\theta_{PD}|$ (Figure 4.15c) or the axial one $|d\Delta V_{PD}/dY_{PD}|$ (Figure 4.15d). In general, injecting the current locally, close to the crack, always involves a worsening of the reproducibility which correspond to an increase in

the derivative either $|d\Delta V_{PD}/d\theta_{PD}|$ or $|d\Delta V_{PD}/dY_{PD}|$. Starting from the sensitivity to the angular position of the potential probe $|d\Delta V_{PD}/d\theta_{PD}|$, it can be noted how the worst

Finally, it can be concluded that for maximizing the measurability and the sensitivity it is convenient to locate both the current and the potential probes as close as possible to the crack plane ($Y_I, Y_{PD} \rightarrow 0$) and within the crack angular extension ($\theta_{B'} < \theta_{PD}, \theta_I < \theta_B$). More in detail, as the current probe is considered, it should be noted that as it approaches the crack plane ($Y_I \rightarrow 0$), on one hand the measurability and the sensitivity increase (see Figure 4.11, Figure 4.12, and Figure 4.15), but on the other hand the reproducibility becomes smaller and therefore both current and potential probes must be positioned very accurately (see Figure 4.13, Figure 4.14, and Figure 4.15).

Regarding the potential probes, provided that measurability requirements are met (i.e. the magnitude of the potential drop signal is high enough to be detected by the adopted DCPD device), while their axial distance should be always minimized, while their angular position is a matter of choice: by locating them in the crack symmetry plane ($\theta_{PD} = 0^\circ$) the measure would be more reproducible but less sensitive, while locating them as close as possible to the crack tip ($\theta_{PD} \rightarrow \theta_B, \theta_{B'}$) the measure would be more sensitive but less reproducible. The latter configuration is promising for monitoring the initiation and early propagation of small cracks from the crack starter because it reduces let reducing the time consumption for determining a given crack growth rate or to reduce reducing the measurable crack growth rates. This latter configuration could be promising for monitoring the initiation and early propagation of small crack from the crack starter.

4.4. Effect of the temperature

As discussed above, the electrical resistivity is a material property whose value could vary due to many parameters. Of all these parameters, the temperature is certainly the most important. The relationship between resistivity and temperature is usually described by Eq. (4.5):

4.4 Effect of the temperature

$$\frac{d\rho}{\rho} = \alpha \cdot dT \quad (4.5)$$

Where ρ represent the electrical resistivity, $d\rho$ is its variation originated by a temperature change dT , and α is another material property called temperature coefficient of resistance. Experimentally it is observed that the temperature dependence of resistivity in conductive material is very well described by a linear relation so that Eq. (4.5) can be simplified into Eq. (4.6):

$$\rho = \rho_0 \cdot (1 + \alpha(T - T_0)) \quad (4.6)$$

Where ρ is the electrical resistivity at temperature T and ρ_0 is the electrical resistivity measured at a reference temperature T_0 (e.g. $T_0 = 0$ °C or 20 °C). Generally, the unit of measurement of the temperature coefficient of resistance α is $1/^\circ\text{C}$, this parameter being the inverse of a temperature.

A change in the resistivity of the specimen, originated from a change in its temperature, results in a shift in the measured potential drop ΔV_{PD} even if no crack growth occurred. To understand how much the temperature can affect the measurement, it is useful to substitute Eq. (4.6) into Eq. (4.1) and derive it by the temperature:

$$\frac{d\Delta V_{PD}}{dT} = \frac{d\rho}{dT} I \Delta V_{PD} = \alpha \cdot \rho_0 I \Delta V_{PD} \quad (4.7)$$

Eq. (4.7) has been obtained assuming the effect of any change in geometry originated by temperature variations (e.g. expansions or contractions of the specimen) are negligible. Moreover, this relation clearly highlights how the temperature sensitivity of the signal $d\Delta V_{PD}/dT$ increases with the temperature coefficient α and with the measured potential drop at temperature T_0 , i.e. $\Delta V_{PD}(T_0) = \rho_0 I \Delta V_{PD}$. In other words, the higher the measurability ΔV_{PD} the higher the signal variations due to temperature changes.

It is worth remembering that the aim of a DCPD measure is that of indirectly evaluating the dimension of the crack size a by the measure of the potential drop ΔV_{PD} . So, it is of more interest to evaluate the effect of a temperature change on the crack length a instead of the variation of

potential drop itself. This means that instead of analysing $d\Delta V_{PD}/dT$ it is better to evaluate the following parameter:

$$\frac{da}{dT} = \frac{d\Delta V_{PD}}{dT} \bigg/ \frac{d\Delta V_{PD}}{da} = \frac{\alpha \Delta v_{PD}}{(1 + \alpha(T - T_0)) \cdot (d\Delta v_{PD}/da)} \quad (4.8)$$

Eq. (4.8) gives information about the fictitious crack length increment caused by a change the specimen's temperature and highlights the way in which it is possible to minimize the effects of temperature on a DCPD measurements. In particular, it can be noted that there is no more the dependence on the electrical resistivity and applied current, instead the geometrical factor Δv_{PD} , including the placement of the current and potential probes, plays the main role. In more detail, the effect of temperature on the estimate of the crack size can be minimized by choosing an arrangement of the potential and current probe which minimize the measurability ($\Delta v_{PD} \rightarrow 0$) and maximize the sensitivity ($d\Delta v_{PD}/da \rightarrow 0$). The physical meaning of this is that, as shown by the parameter $d\Delta V_{PD}/dT$, higher measurability ($\Delta v_{PD} \propto \Delta V_{PD}$) results in a higher change of the measured potential drop for a certain fixed change in the specimen's temperature. On the other hand, a higher measurement sensitivity ($d\Delta V_{PD}/da \propto d\Delta v_{PD}/da$) means that for a fixed change in potential drop, the corresponding change in the estimated crack size is smaller, i.e. the DCPD arrangement has an higher resolution. To better understand in a quantitative way how important is the effect of temperature, the parameters $d\Delta V_{PD}/dT$ (Eq. (4.7)) and da/dT (Eq. (4.8)) have been computed for the configurations analysed in Figure 4.15 and reported in Figure 4.16a and Figure 4.16b, respectively. As expected, the parameter $d\Delta V_{PD}/dT$ has the same behaviour of the measurability Δv_{PD} , as it represents the measurability scaled by a factor $\alpha = 0.003 \text{ } ^\circ\text{C}^{-1}$ (compare Figure 4.15a with Figure 4.16a), the latter being the temperature coefficient of resistance α for a medium carbon steel. Figure 4.16a clearly explains that the measured potential drop would change its value of about ± 1 to $6 \text{ } \mu\text{V}$ for a change of $1 \text{ } ^\circ\text{C}$ in the specimen's temperature, the particular value depending on the current input configuration, the potential probe location and the crack size (Figure 4.16Figure 4.15a).

More interestingly, Figure 4.16b shows the evolution of the parameter da/dT (Eq. (4.8)) with the normalized crack length a/D . It is interesting to note the changes in potential drop estimated in Figure 4.16a would translate in fictitious crack length changes ranging from lower than $10 \text{ } \mu\text{m}$ up to more than $250 \text{ } \mu\text{m}$ depending on the chosen configuration (Figure 4.16b).

4.4 Effect of the temperature

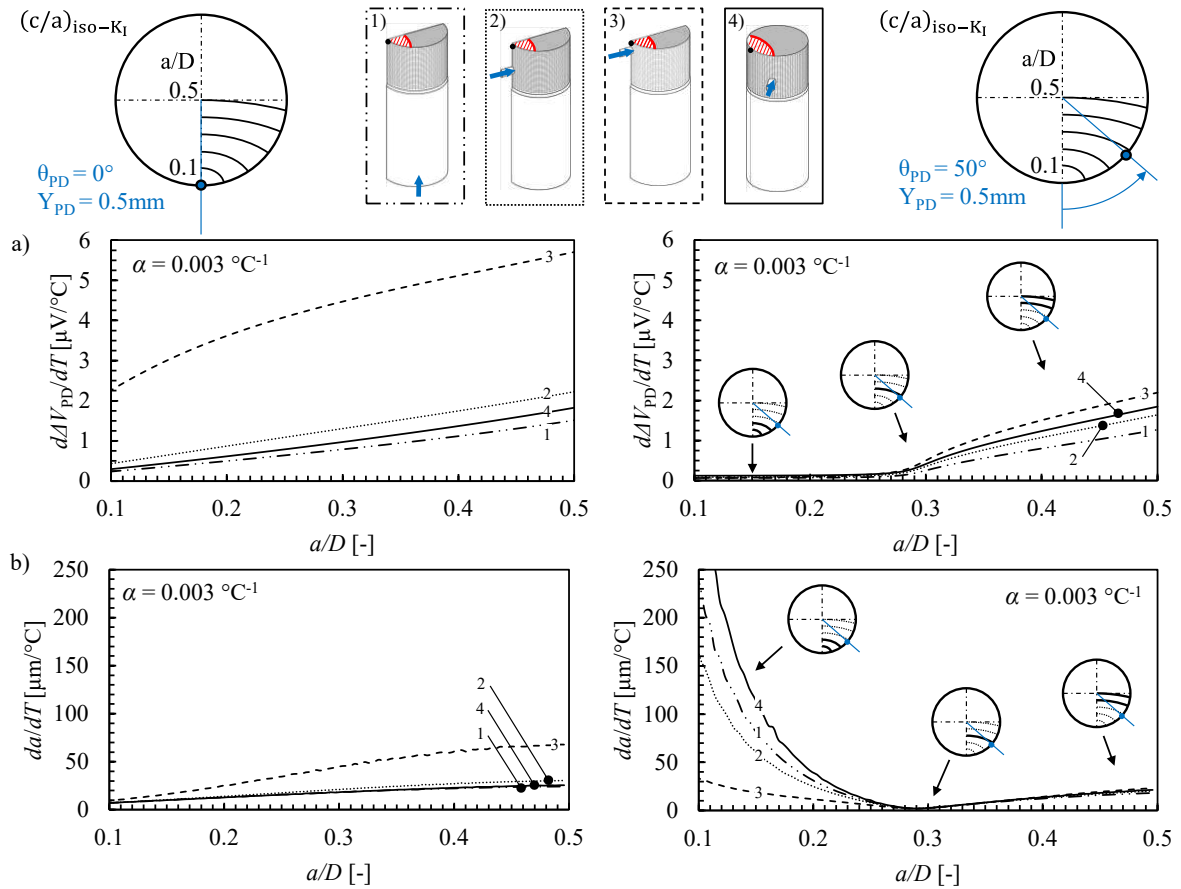


Figure 4.16. Effect of temperature on a DCPD arrangement having no temperature compensation. a) $d\Delta V_{PD}/dT$ and b) da/dT as a function of the normalized crack depth a/D for the configurations analysed in Figure 4.15.

These considerations, together with those related to the measurability, sensitivity and reproducibility can be helpful in case the experimental set up does not allow for any temperature compensation. Otherwise, it is fundamental to find a way to compensate for any signal variations originated by temperature fluctuations. Among all the possibilities there are:

- Single channel technique with temperature sensor (Figure 4.17b). The compensation is made possible by calibrating the temperature coefficient of resistance α of the specimen and the measuring the specimen's temperature T during the test. This way, it is possible to relate each measured potential drop with the corresponding temperature value and evaluate the following temperature compensated signal, referred to the initial temperature T_0 :

$$\frac{\Delta V_{PD}}{1 + \alpha(T - T_0)} \quad (4.9)$$

The advantage of this technique is that it requires no complex and expensive multi-probe DCPD acquisition system, only one single channel being required. On the other hand, it requires customized data acquisition systems capable of evaluating in real time the compensated signal by acquiring at the same time both the potential drop and temperature signal, usually coming from different sensors and having different control software. Otherwise, the temperature compensation can only be performed after the test.

- Dual channel technique with a twin specimen (Figure 4.17c). In this configuration, the potential drop active channel ΔV_{PD} , measured across the cracked section of the tested specimen, is compared to a reference channel ΔV_T , measured on a twin specimen, having the same nominal geometry of the tested specimen but located outside the testing machine. The two specimens are connected in series and the electric current I is made to flow through them. Accordingly, the effect of environmental temperature fluctuations can be compensated normalizing the active channel ΔV_{PD} with the reference channel ΔV_T , i.e. evaluating the ratio:

$$\frac{\Delta V_{PD}}{\Delta V_T} = \frac{\rho I \Delta v_{PD}}{\rho I \Delta v_T} = \frac{\Delta v_{PD}}{\Delta v_T} \quad (4.10)$$

This relation shows how the ratio between the active and the reference channel become both material (resistivity) and current independent. Instead, it only depends on the geometry of the specimens and on the position of the current and potential probes. The advantage of this method is that the temperature compensation is made in real time, without the need of a customized DAQ system integrating both potential drop and temperature signal, however, it requires a multi-probe DCPD system. Another limitation is related to the possibility that the tested specimen can experience a different temperature evolution from the twin specimen. In particular, this technique perfectly compensates for drift of the potential drop signals coming from fluctuations of the environmental temperature (e.g. day and night

temperature differences) but it is not effective against temperature differences between the tested and the twin specimen. For example, the latter can be generated by plastic strain energy dissipation on the tested specimen or localized heat dissipation from the fatigue testing machine.

- Four-probe dual channel technique (Figure 4.17d). Differently from the dual channel technique with a twin specimen, in this case the reference channel ΔV_T is measured between two points of the tested specimen. This configuration surely overcome the problems related to the possibility of having different temperatures between the tested and the twin specimen. This technique can be adopted provided that the temperature is uniform within the specimen [43,55].
- Three-probe dual channel technique (Figure 4.17e). Similarly, to the four-probe configuration, the reference channel ΔV_T is measured on the tested specimen but between one probe of the active potential channel and another probe located on the same specimen. This offers the possibility to reduce the number of wires required and of course the required space for performing the measurement with a dual channel technique. This application is useful in the case of very small specimens, or to limit the overall dimensions. Finally, it is worth to note that even if from a theoretical point of view any position on the specimen is suitable for positioning the third probe, some considerations deserve to be made. For example, the third probe should be located adequately far away from the current probe to prevent any effects of the local current distribution in the nearby of the contact region between the current probe and specimen itself. Furthermore, it should be sufficiently far from the active channel probe so as to have a relatively high measurability and located in a region having low sensitivity to probe positioning errors, i.e. high reproducibility.

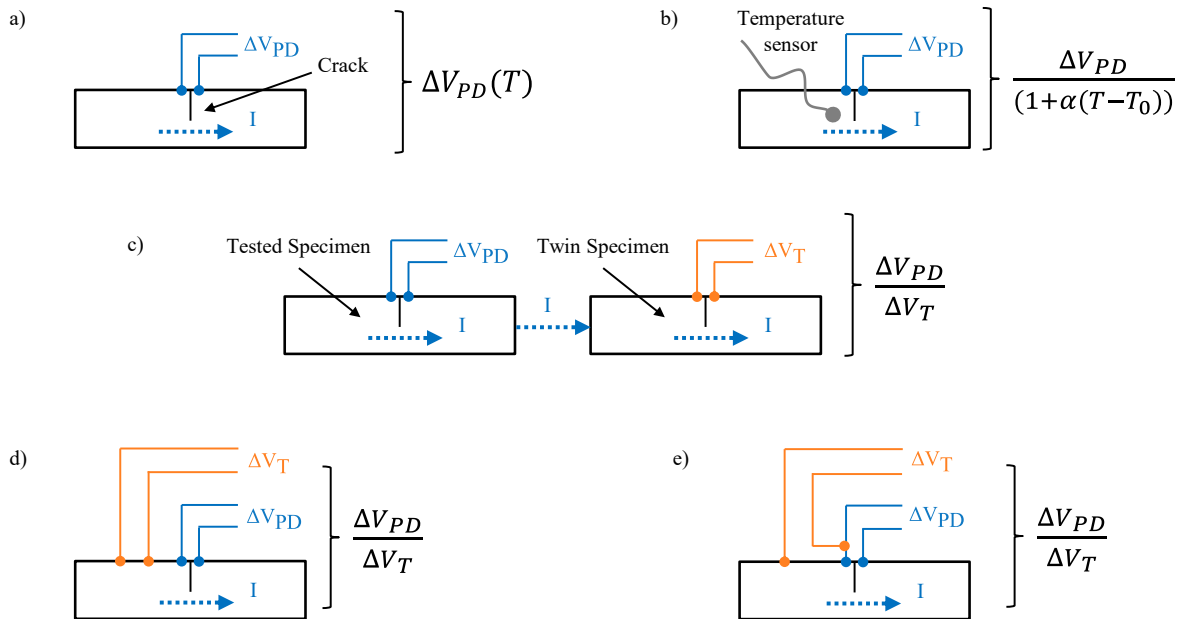


Figure 4.17. Different configurations for temperature compensation. a) Single channel technique with no temperature compensation. b) Single channel technique with temperature sensor. c) Dual channel technique with a twin specimen. d) Four-probe dual channel technique. e) Three-probe dual channel technique.

In this work, the three-probe dual channel technique has been considered. The third probe was positioned at an axial distance from the crack plane $Y_T = 5$ mm and at an angular coordinate equal to that of the potential probe ($\theta_T = \theta_{PD}$). This position has been chosen on the base of qualitative considerations on measurability and reproducibility without any quantitative analyses to establish the optimal position of the third probe. Starting from the results of previous electric FE analyses, the reference potential drop ΔV_T has been calculated as the difference between the electrical potential measured at $Y_{PD} = 5$ mm ($V_{PD,5\text{mm}}$) and that measured at $Y_{PD} = 0.5$ mm ($V_{PD,0.5\text{mm}}$) so that $\Delta V_T = V_{PD,5\text{mm}} - V_{PD,0.5\text{mm}}$. The results of this calculation have been reported in Figure 4.18b together with the calibration curves relevant to the active channel ΔV_{PD} (Figure 4.18a) as a function of the normalized crack depth and parametric for all the analysed current input/output configurations. In the same figure are reported also the normalized calibration curves $\Delta V_{PD}/\Delta V_T$ (Figure 4.18c) which depended only on the specimen geometry, the crack shape and size, and the current and potential probe locations.

4.4 Effect of the temperature

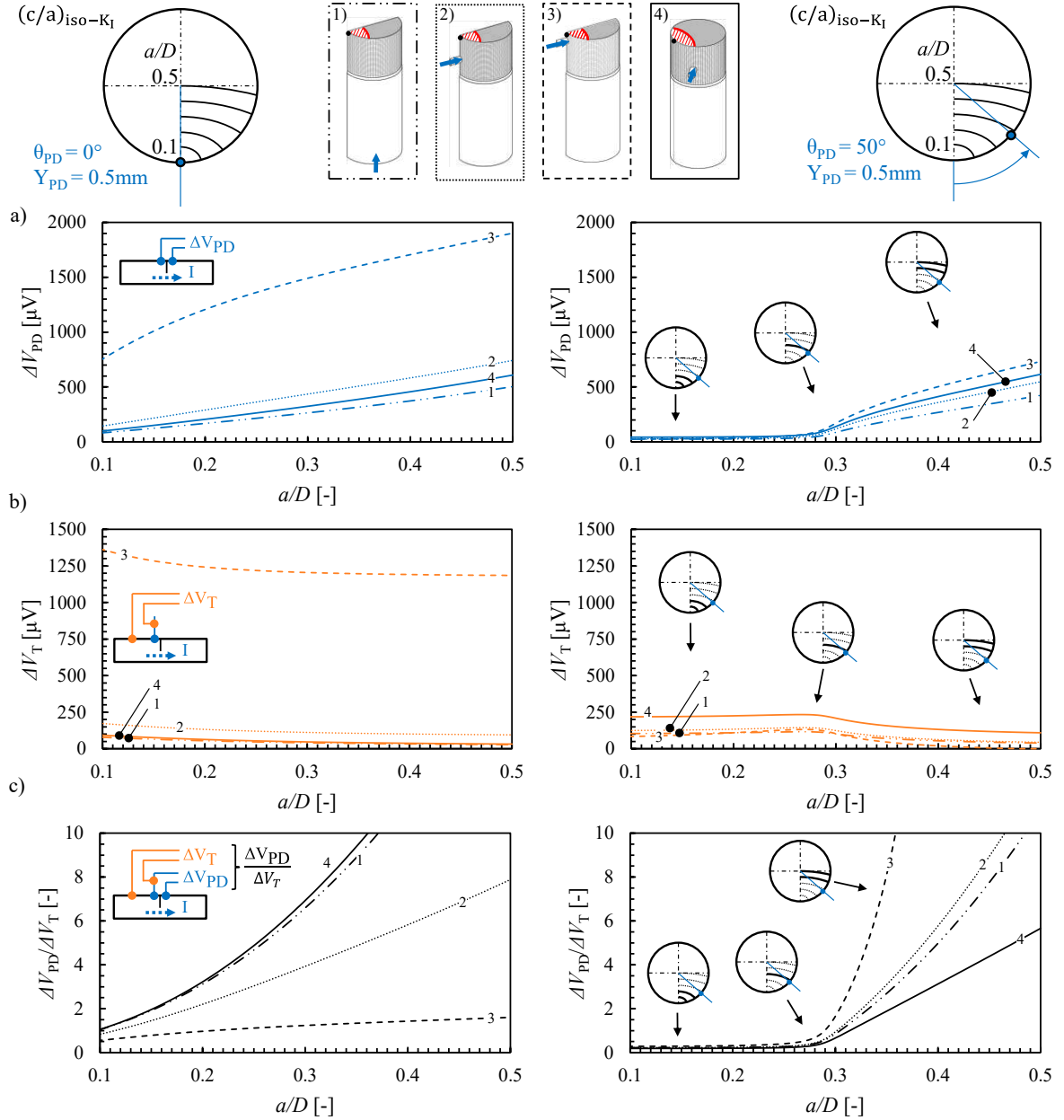


Figure 4.18. Calibration curves for three-probe dual channel technique with potential and temperature probe located at $Y_{PD} = 0.5$ mm, $Y_T = 5$ mm and $\theta_{PD} = \theta_T = 0^\circ$ (on the left) or $\theta_{PD} = \theta_T = 50^\circ$ (on the right). a) calibration curves relative to the active channel (ΔV_{PD}) and the reference channel (ΔV_T); b) normalized calibration curves ($\Delta V_{PD}/\Delta V_T$).

4.5. Experimental Tests

4.5.1. Procedure and experimental setup

Some experimental fatigue tests were conducted in order to verify the applicability of the above-mentioned DCPD configurations as well as the accuracy of the electrical FE analyses, that is, their capacity to accurately describe the relationship between the electrical potential drop and the crack size (Figure 4.2). Accordingly, the validation of the electrical FE analyses being the aim, and not the validation of a structural FE simulation to predict the crack shape evolution and crack path, the real crack shapes measured post-mortem on fracture surfaces of the specimens were reproduced in FE electrical simulations. Therefore, the crack fronts involved in the simulation are not necessarily iso- K_I and could not be so, the initial crack starter notch being straight and not elliptical, as it will be presented later on. Then, as summarized in Figure 4.19, the experimental procedure simply consisted in fatigue testing some single-edge crack round bars under fatigue axial loading while measuring at the same time the fatigue crack growth applying the DCPD method using one or more of the configurations discussed in the previous chapter.

The tested specimens, whose geometry is reported in Figure 4.20, were made of medium carbon steel. i.e. C45. The crack starter notch was machined by hand saw cutting. Axial fatigue tests were performed by means of an MFL axial servo-hydraulic testing machine, with a load capacity of 250 kN and equipped with MTS TestStar II digital controller. The fatigue crack was propagated by a constant-amplitude sinusoidal load cycle under closed-loop load control with a nominal load ratio $R = 0.05$, load range, ΔF , between 60 kN and 80 kN, and a load frequency 18 Hz. The crack front was marked on the crack propagation plane every 24990 cycles by beach marking consisting of 10 overload cycles with load ratio $R_{OL} = 0.6$, load range $\Delta F_{OL} = 50$ kN and a load frequency 0.5 Hz (Figure 4.21).

The crack growth was monitored by using the DCPD method according to the experimental setup sketched in Figure 4.22a: based on the idea of Saka et al. [31], a prototype clip-on-gauge-like (Figure 4.22d) device was designed and realized to both locally inject the current and

4.5 Experimental Tests

measure the potential drop. More in detail, the current probes were made by two 3-mm-diameter cylindrical copper electrodes, 118° cone head positioned at distance of 11.5 mm between each other. Concerning the potential probes, they were three needle point spring probes fixed on a JST VH connector. The use of such connector let being free to make small adjustments to the position of the needle point spring probes. The three-probe dual channel technique (Figure 4.17e) has been adopted to compensate for temperature variations during the fatigue tests. Five micro-notches (two of 0.6 mm depth for the current probes, two of 0.1 mm depth for the potential probes, and another one of 0.1 mm depth for the temperature compensation probe) were milled on the specimen by means of a centre drill bit with a point angle of 118° to allow attachment of the clip-on gauge and to ensure the right positioning of the probes by fitting the probes' head into them. To examine the effect of the current and probe location, three different current input and potential drop measurement positions were investigated.

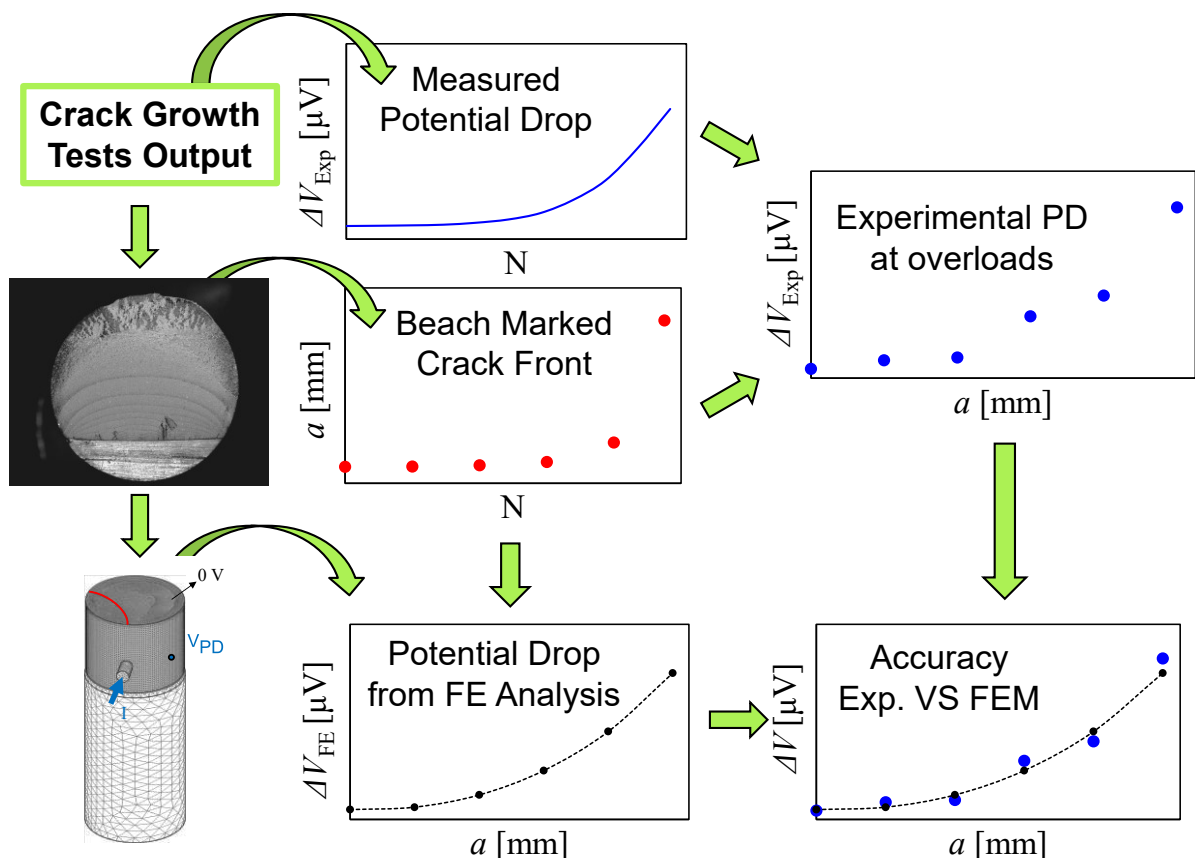


Figure 4.19. Schematic of the experimental procedure used for the experimental aiming at the determination of the accuracy of the DCPD method.

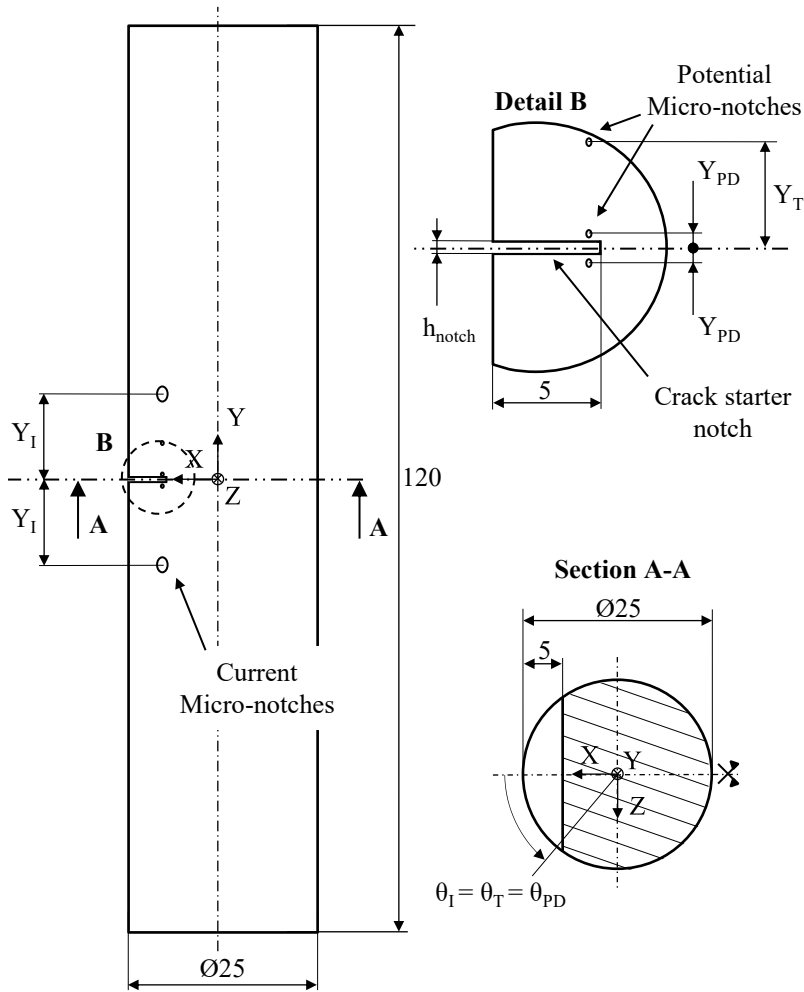


Figure 4.20. Geometry of the single-edge-notch round bar specimen (dimensions are in millimeters).

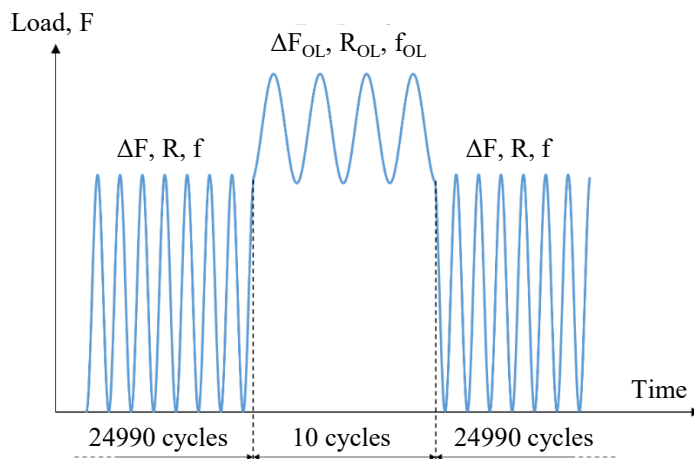


Figure 4.21. Schematic of the applied loads and overloads during the experimental tests.

4.5 Experimental Tests

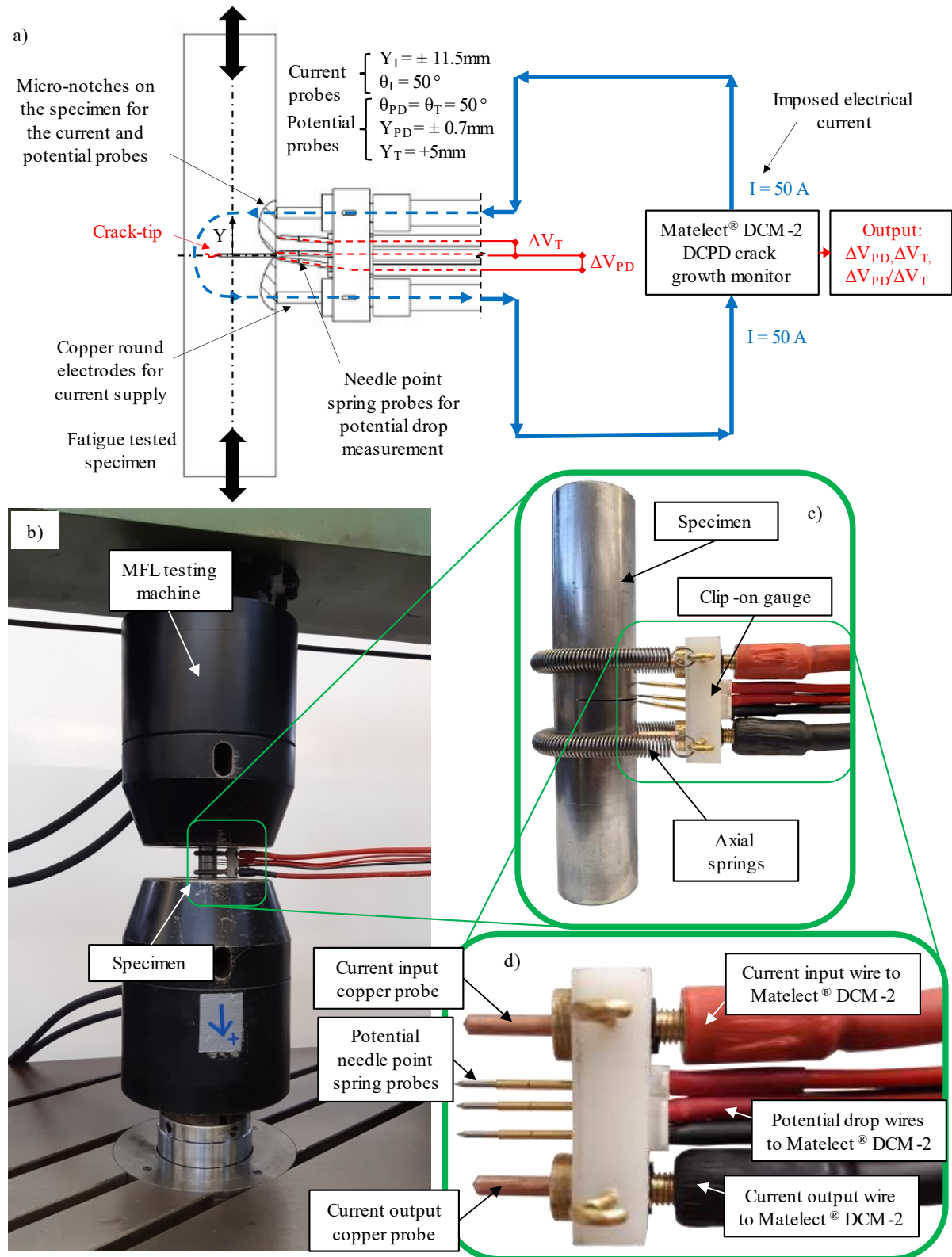


Figure 4.22. Experimental setup: a) scheme of the adopted electrical potential drop arrangement, b), c), and d) MFL servo-hydraulic testing machine adopted for pure axial fatigue tests with details on the specimens and on the clip-on-gauge device for the local configuration of the DCPD method.

In all cases, the potential probes (and the corresponding micro-notches) were positioned symmetrically to the crack plane, precisely at an axial distance $Y_I = 11.5$ mm whilst the latter at $Y_{PD} \sim 0.7 - 0.8$ mm, while the temperature compensation probe was positioned at $Y_T = 5$ mm. On the contrary, their angular position and the position of the current probe was changed as follow:

- All micro-notches were nominally located at an angular position of $\theta_I = \theta_{PD} = \theta_T = 50^\circ$ with the current probes located at an axial distance $Y_I = 11.5$ mm (Figure 4.23a).
- All micro-notches were nominally located symmetrically with respect to the angular position of the notch $\theta_I = \theta_{PD} = \theta_T = 0^\circ$ (Figure 4.20), with the current probes located at an axial distance $Y_I = 11.5$ mm (Figure 4.23b).
- All micro-notches were nominally located symmetrically with respect to the angular position of the notch $\theta_I = \theta_{PD} = \theta_T = 0^\circ$ (Figure 4.20), with the current probes located at the specimens' ends ($Y_I = 11.5$ mm) to investigate the effect of a remote current input (Figure 4.23c).

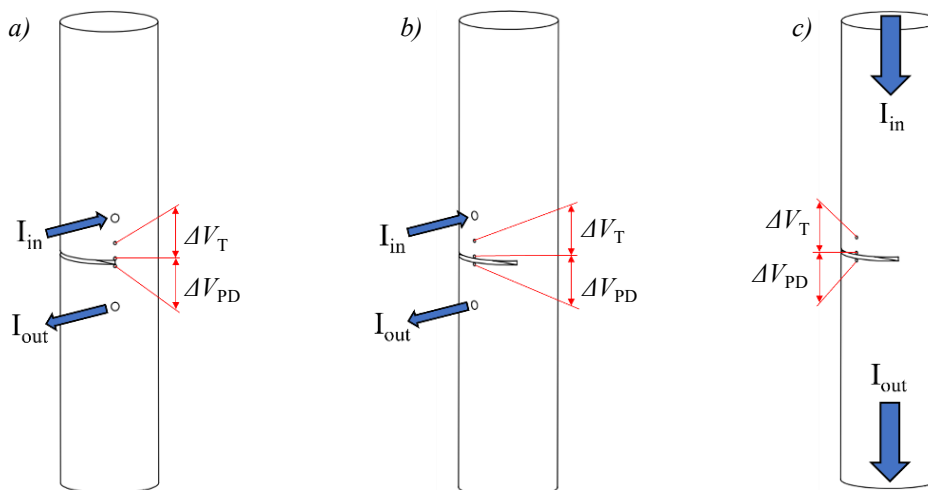


Figure 4.23. The three different configurations investigated with the experimental tests.

Eventually, the actual position of the micro-notches was measured by means of an optical microscope with an uncertainty of about ± 0.2 mm (a summary of the measures is reported in

4.5 Experimental Tests

Table 4.3). The clip-on-gauge-like device was then attached mechanically to the specimen by using two springs. Eventually, it was connected to the measurement system Matelect® DCM-2. A constant current of 50 A was flown through the specimen and the corresponding potential drop signals, ΔV_{PD} and ΔV_T , were measured at a sampling rate in the range of 0.08-1 Hz.

4.5.2. Experimental results

Fracture surfaces have been analysed by optical microscopy and it has been observed that multiple cracks were initiated at different points at the notch tip in all specimens. If the different cracks initiated at different locations were to be studied, then multi-probe DCPD configurations should be adopted [16,19–22]. However, subsequently the multiple cracks, coalesced assuming roughly an elliptical shape, as shown in Table 4.3, therefore the adopted single probe arrangement was appropriate. By image analysis, it was possible to relate the beach marked crack front to the corresponding overload (starting from the last overload before final brittle fracture of the specimen) and consequently to the measured potential drop signal (Figure 4.24).

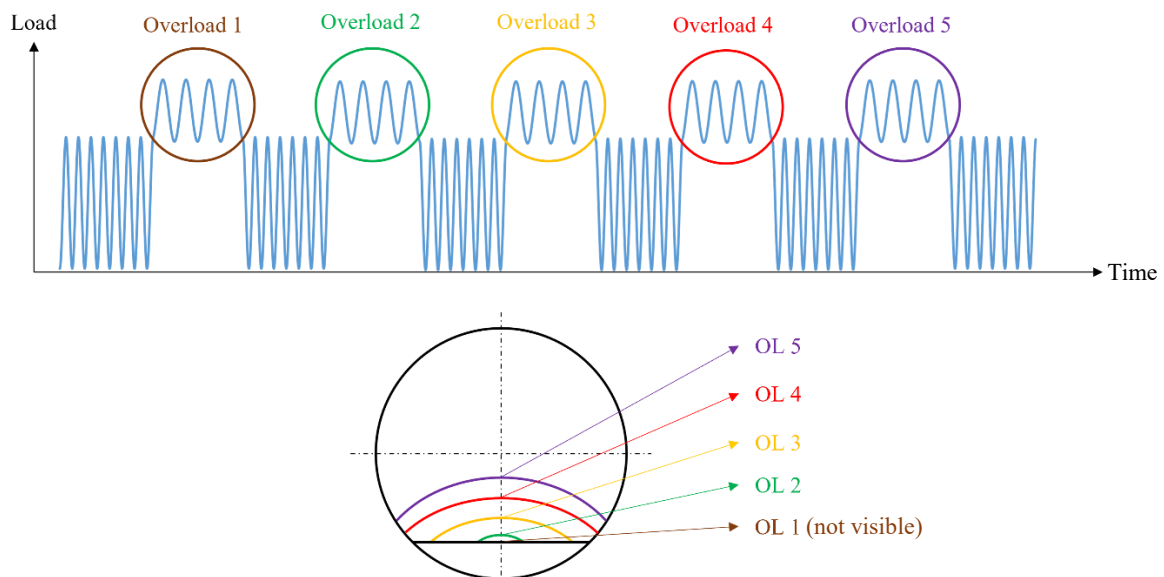


Figure 4.24. Correlation between overloads and the corresponding beach marked crack fronts visible on the fracture surface.

Each one of the beach marked cracks shown in Table 4.3 was approximated by an elliptical arc whose semi-axes were evaluated by means of the curve fitting tool available in MATLAB® according to Figure 4.25. Table 4.3 gives a summary of the fracture surfaces and the geometric parameters of each specimen.

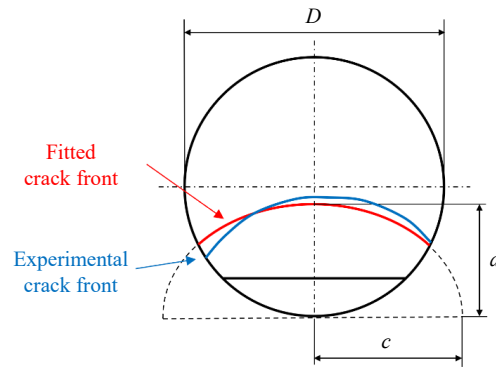


Figure 4.25. Geometric schematization of the beach marked crack fronts.

The corresponding approximated crack fronts are reported in Table 4.3. Accordingly, it was possible to report the following experimental results as a function of the normalized crack depth, a/D : the aspect ratio, c/a , the potential drop signal, ΔV_{PD} , the temperature compensation signal, ΔV_T , and the normalized potential drop signal, $\Delta V_{PD}/\Delta V_T$, as depicted in Figure 4.26 for results relevant to a local DCPD having $\theta_I = \theta_{PD} = \theta_T = 50^\circ$, in Figure 4.27 for results relevant to a local DCPD having $\theta_I = \theta_{PD} = \theta_T = 0^\circ$, or in Figure 4.28 for results relevant to a remote current input DCPD having $\theta_{PD} = \theta_T = 0^\circ$.

Table 4.4 gives a summary of all the obtained experimental results.

4.5 Experimental Tests

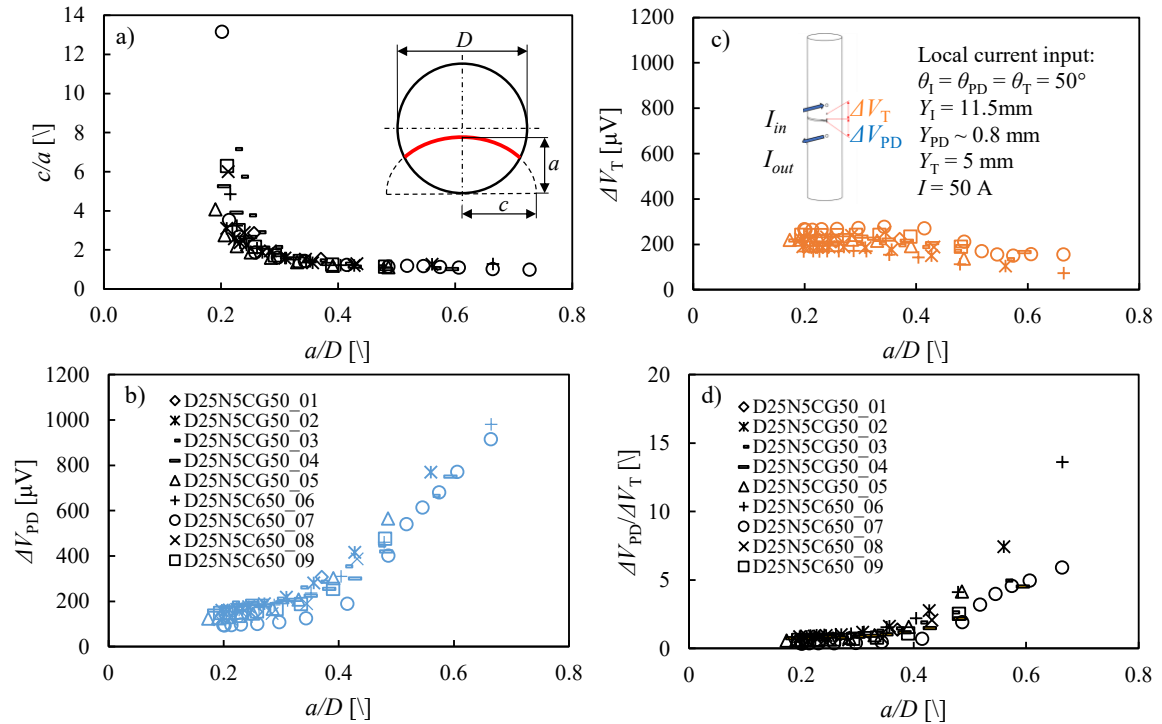


Figure 4.26. Experimental results for specimens tested using a DCPD setup having $\theta_I = \theta_{PD} = \theta_T = 50^\circ$, $Y_I = 11.5$ mm, $Y_{PD} \sim 0.8$ mm, $Y_T = 5$ mm: a) experimental aspect ratio c/a , b) active channel potential drop signal ΔV_{PD} , c) reference potential drop signal ΔV_T , and d) normalized potential drop signal $\Delta V_{PD}/\Delta V_T$ as a function of the normalized crack depth a/D .

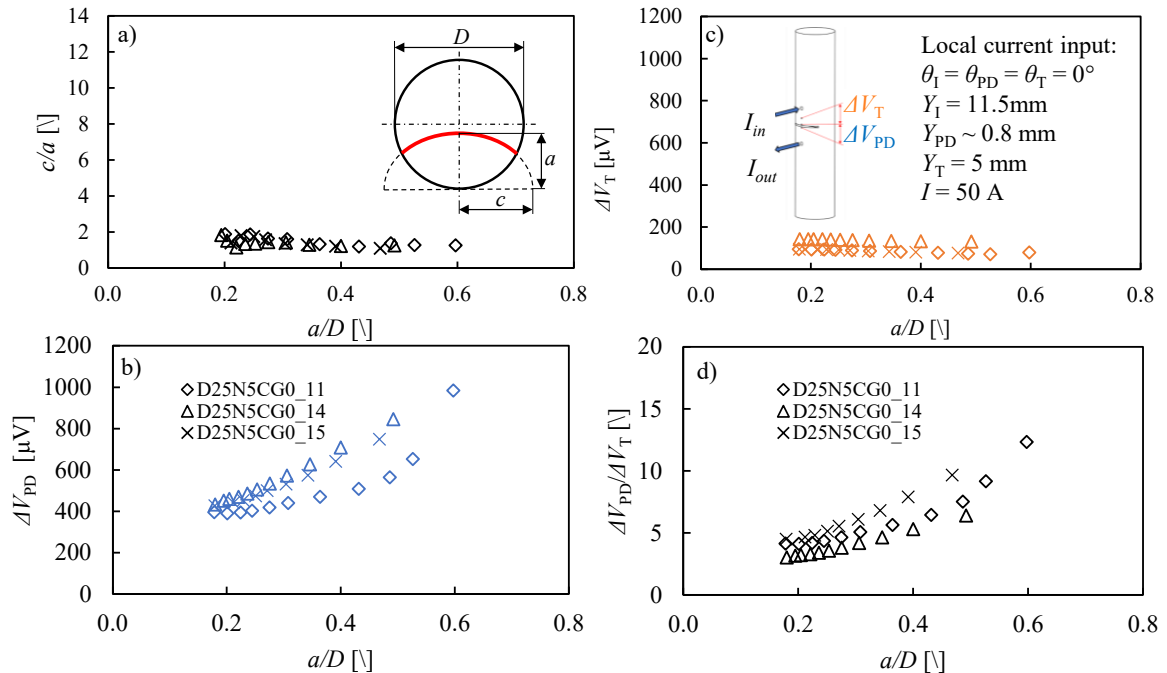


Figure 4.27. Experimental results for specimens tested using a DCPD setup having $\theta_I = \theta_{PD} = \theta_T = 0^\circ$, $Y_I = 11.5$ mm, $Y_{PD} \sim 0.8$ mm, $Y_T = 5$ mm: a) experimental aspect ratio c/a , b) active channel potential drop signal ΔV_{PD} , c) reference potential drop signal ΔV_T , and d) normalized potential drop signal $\Delta V_{PD}/\Delta V_T$ as a function of the normalized crack depth a/D .

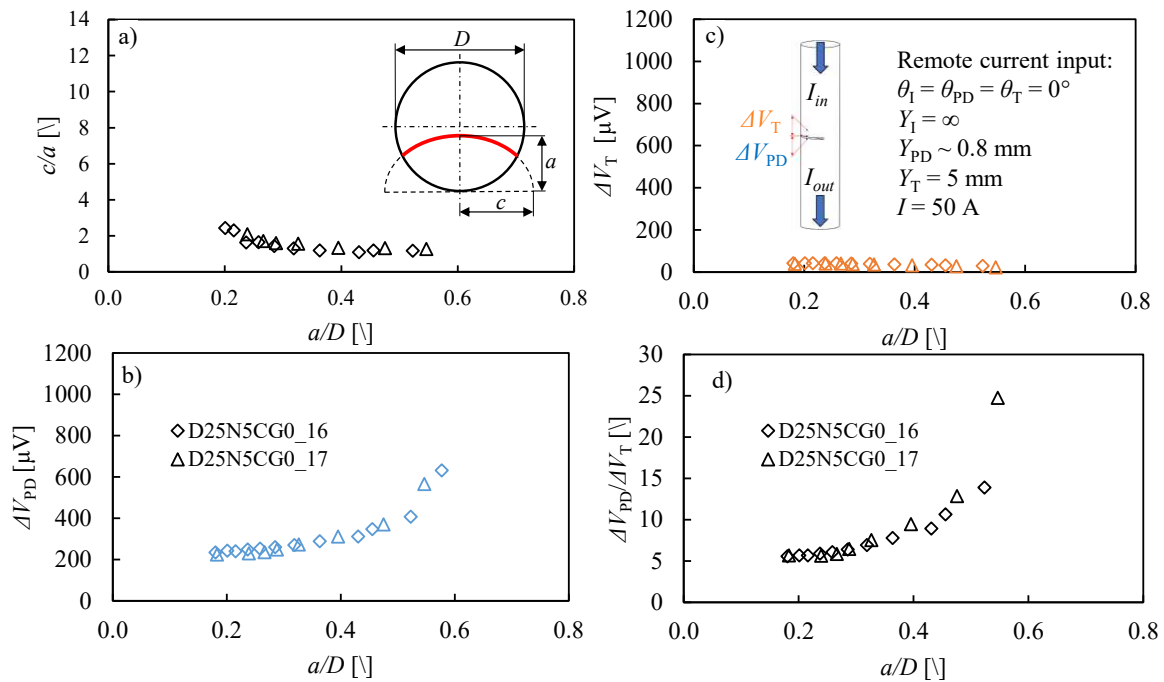


Figure 4.28. Experimental results for specimens tested using a DCPD setup having $\theta_I = \theta_{PD} = \theta_T = 0^\circ$, $Y_I = \infty$, $Y_{PD} \sim 0.8 \text{ mm}$, $Y_T = 5 \text{ mm}$: a) experimental aspect ratio c/a , b) active channel potential drop signal ΔV_{PD} , c) reference potential drop signal ΔV_T , and d) normalized potential drop signal $\Delta V_{PD}/\Delta V_T$ as a function of the normalized crack depth a/D .

Afterwards, the FE analyses were carried out by modelling the cracked configurations observed experimentally. In particular, it was possible since the whole geometry of the cracked component, including the specimen geometry (Figure 4.20), the local geometry of the notch with the micro notches for the local application of the DCPD (Table 4.3), and the corresponding evolution of the crack shape during propagation (Figure 4.26a, Figure 4.27a, Figure 4.28a, and Table 4.4).

The models have been generated without exploiting any symmetry planes, this time being not available to the asymmetric positions of the current and potential probe which have been measured experimentally (Figure 4.30). The current probe has always been modelled as a 3 mm-diameter cylinder made of medium carbon steel (electrical resistivity $\rho = 20 \cdot 10^{-5} \Omega\text{mm}$, i.e. the same material of the specimen) perfectly in touch with the specimen itself, thus assuming no contact resistance between them (Figure 4.30). The cracked section has been modelled dividing the whole plain specimen's geometry into two segments with the crack's plane. Then, once modelled the crack on the two new generated surfaces, that relevant to the ligament have

4.5 Experimental Tests

been merged, while those corresponding to the cracked area have been left separate, just sharing the crack front line (Figure 4.30).

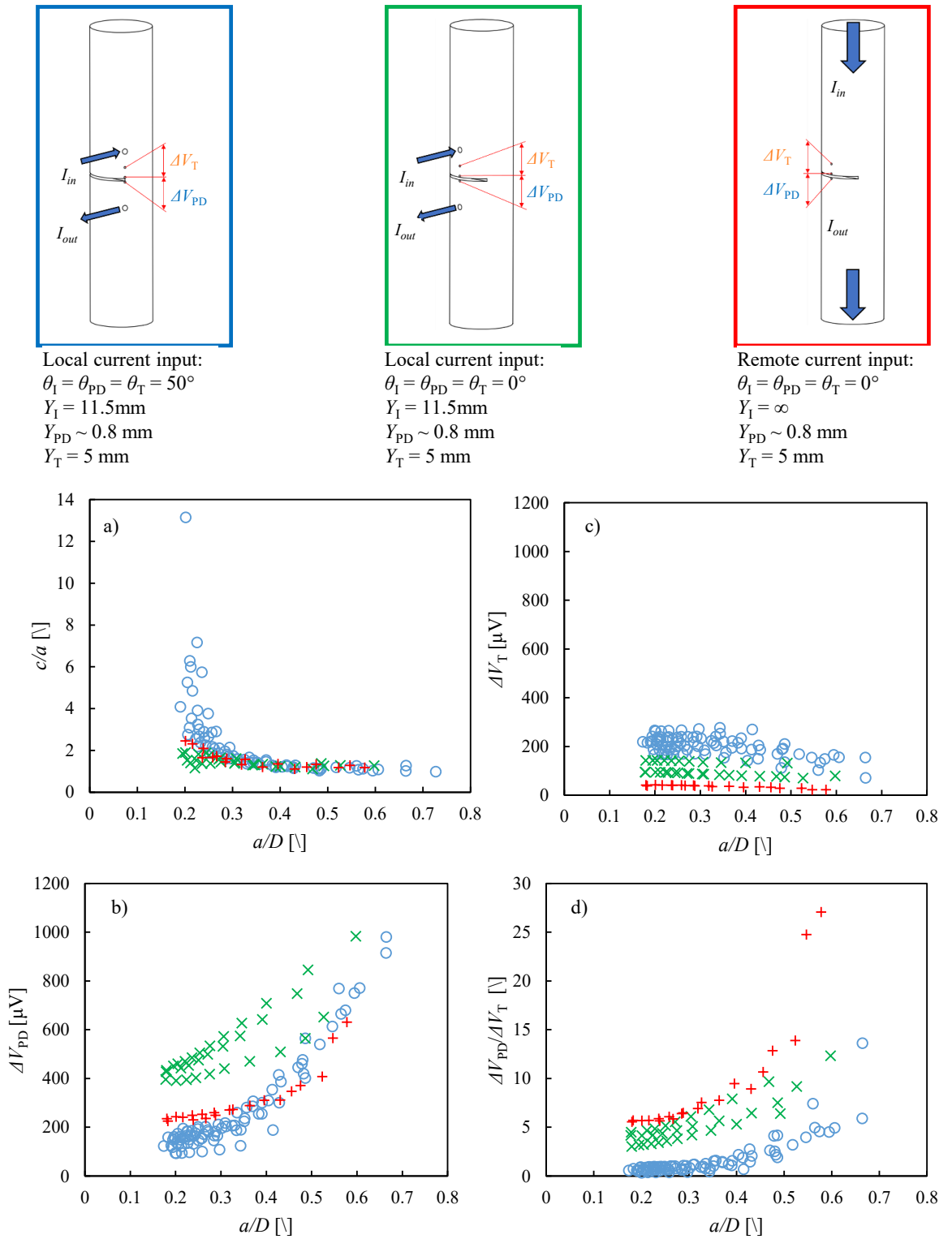


Figure 4.29. Experimental results: comparison between all experimental data.

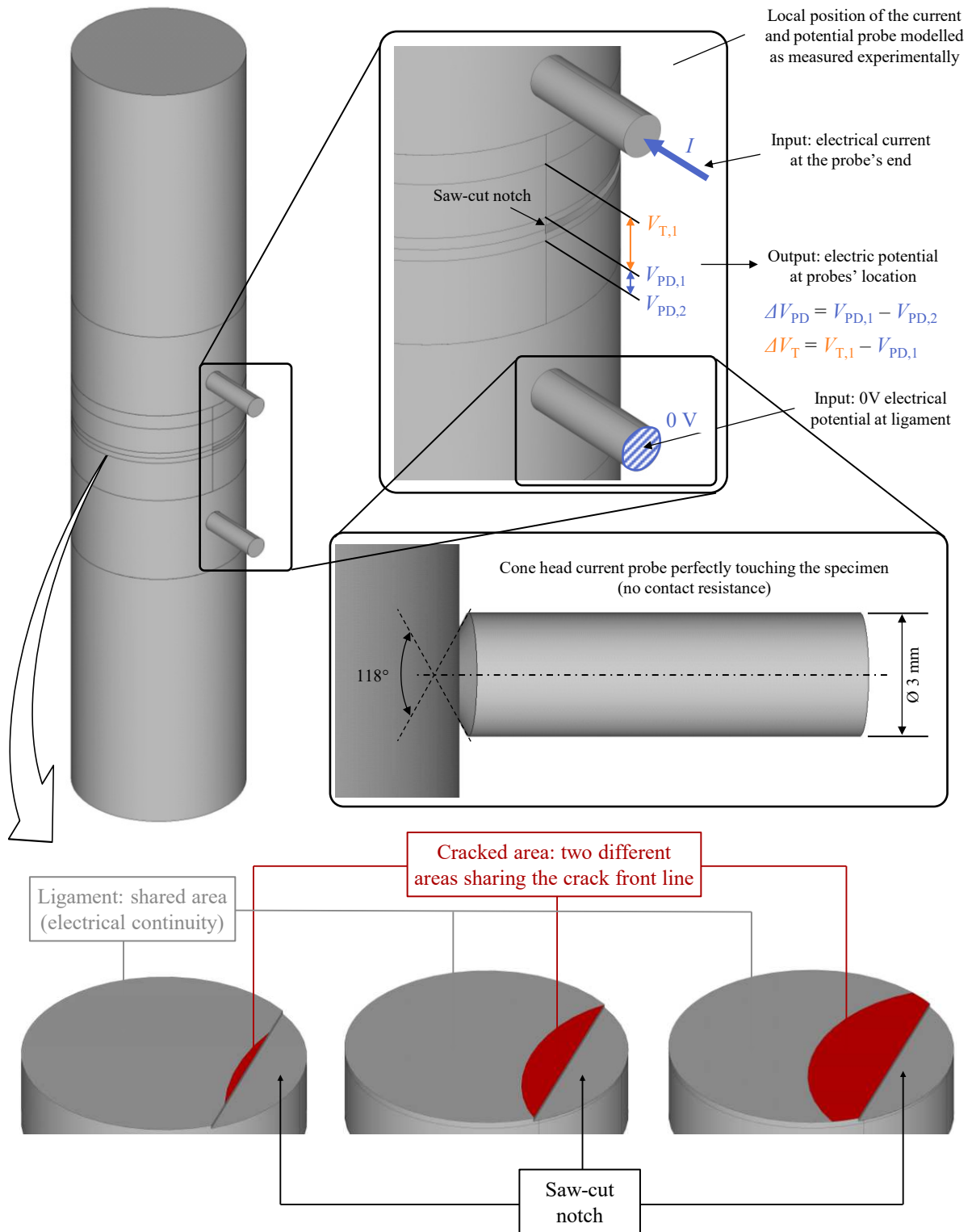


Figure 4.30. FE model reproducing the experimental configuration: example of a local current current input having $\theta_1 = \theta_1 = \theta_1 = 50^\circ$ with details on the modelled current probes and the cracked section. The symmetry planes were not always exploitable due to slightly asymmetric angular and axial position of the probes (different for each specimen).

4.5 Experimental Tests

A pattern of 10-node tetrahedral electric solid elements (SOLID232 of the Ansys element library) having a global element size of 3 mm has been adopted to build up the FE model. A more refined mesh of approximately 0.9 mm has been employed in the region interested by the current probes, and an element size of nearly 0.2 mm and 0.1 mm has been used in the proximity of the notch and crack front, respectively (Figure 4.31). In all the analysed configurations, the magnitude of input current $I = 50$ A was given as an input to one current probe, together with an electric potential equal to 0 V at nodes located in the opposite current probe (Figure 4.31).

After the solution it was possible to extract the value of the electric potentials $V_{PD,1}$, $V_{PD,2}$, and $V_{T,1}$. Then, the corresponding potential drop have been calculated both for the active channel $\Delta V_{PD} = V_{PD,1} - V_{PD,2}$, and for the reference channel $\Delta V_T = V_{T,1} - V_{PD,1}$ (Figure 4.30).

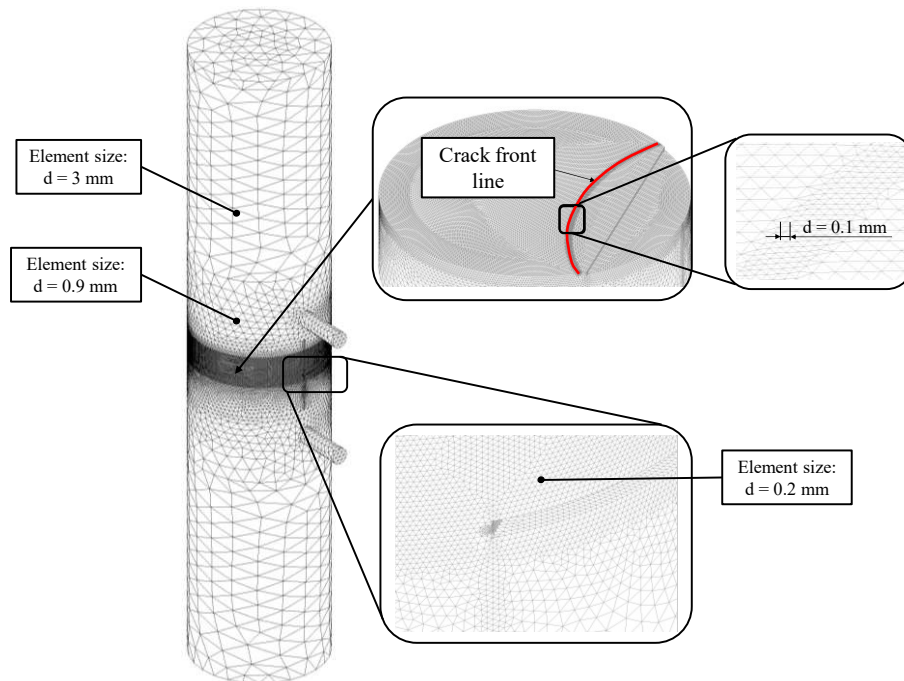


Figure 4.31. Example of FE mesh pattern generated from model reported in Figure 4.30.

Eventually, the obtained values of the potential drop, ΔV_{PD} , temperature compensation signal, ΔV_T , and normalized potential drop signal, $\Delta V_{PD}/\Delta V_T$, were checked against their corresponding experimental results. Results have been reported in Figure 4.32 in terms of normalized error evaluated between the estimated value and the experimental one, for fixed values of a/D , according to the following expressions:

$$Error\% = \frac{X_{FEA} - X_{exp.}}{X_{exp.}} \cdot 100 \quad (4.11)$$

Wherein X represent the potential drop active channel ΔV_{PD} , or the potential drop reference channel ΔV_T , or the normalized one $\Delta V_{PD}/\Delta V_T$.

In general, results showed a discrete agreement between experimental and numerical values, in general, the deviations being always approximately $\pm 20\%$ and $\pm 40\%$ for the potential drop signal ΔV_{PD} (Figure 4.32a), and the normalized potential drop signal $\Delta V_{PD}/\Delta V_T$ (Figure 4.32c), respectively. Although such deviations can seem very high, it must be highlighted that only slightly higher than those in previous works by other authors dealing with much easier specimens' geometries and experimental setups, i.e. SENB, SENT, CT or CCT specimens [45,55–57] or circumferentially notched bars [16,34]. However, certain specimens exhibited larger deviations ranging from -40% and $+70\%$ for the potential drop signal ΔV_{PD} (Figure 4.32a), and from -40% and $+100\%$ for the normalized potential drop signal $\Delta V_{PD}/\Delta V_T$ (Figure 4.32c). Moreover, in general, slightly higher deviations are found for when the crack size is $a/D > 0.3$. Furthermore, it is interesting to note that if each single test is considered individually, all the evaluated errors, i.e. the difference between the experimental and FE data, seem like being bias errors as they always exhibited a certain trend (compare data having the same markers shape and colour in Figure 4.32). On the other hand, when specimens tested with the same DCPD configuration (i.e. for a fixed position of the current and potential probe) are considered, no clear trend can be defined for the errors, them being apparently random distributed from one specimen to another (compare data having the same colour in Figure 4.32). Interestingly, even if there are only few data available, it can be easily noted how the scatter between specimens tested with the same DCPD configuration (data having the same colour in Figure 4.32) is gradually reduced from the local current input with $\theta_I = \theta_{PD} = \theta_T = 50^\circ$ (blue data in Figure 4.32), to the local current input having $\theta_I = \theta_{PD} = \theta_T = 0^\circ$ (green data in Figure 4.32) and finally to the remote current input (red data in Figure 4.32). The latter observation can be justified thinking about the different effects of the current and probe location on the sensitivity and reproducibility, the latter parameter being higher (consequently also the scatter between data should be higher) the closer to the crack tip the current is injected and the potential drop is measured (Figure 4.12, Figure 4.13, Figure 4.14, and Figure 4.15).

4.5 Experimental Tests

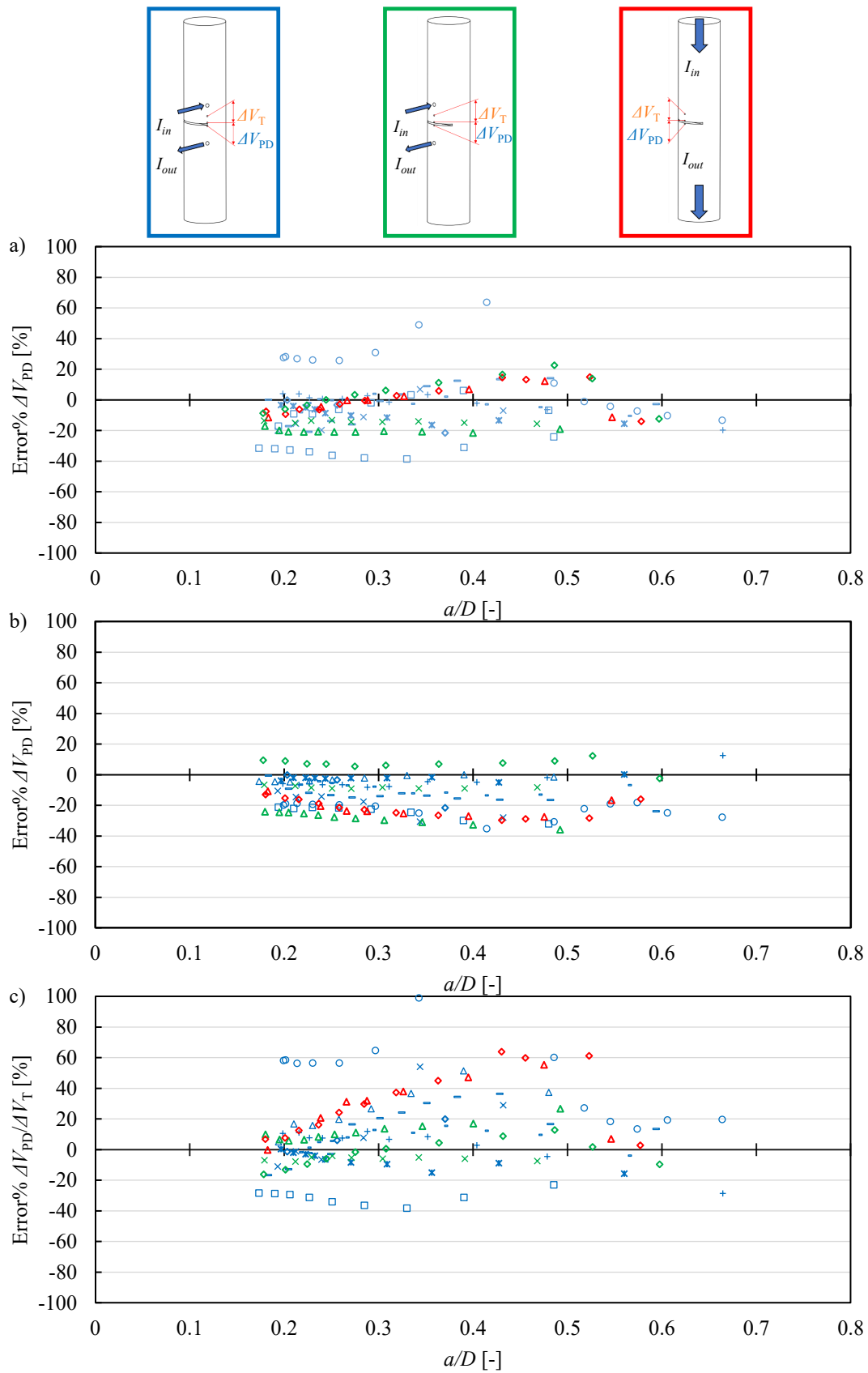
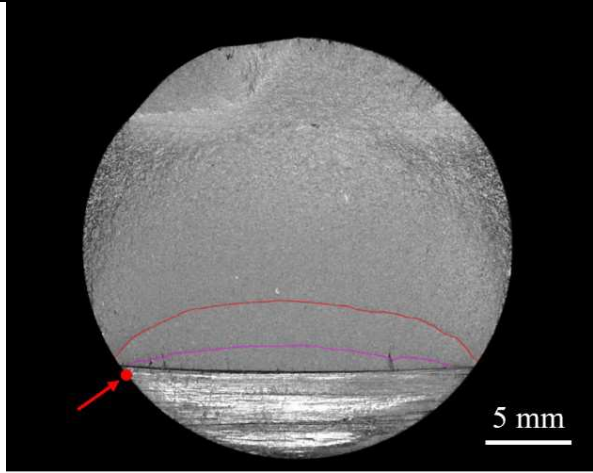
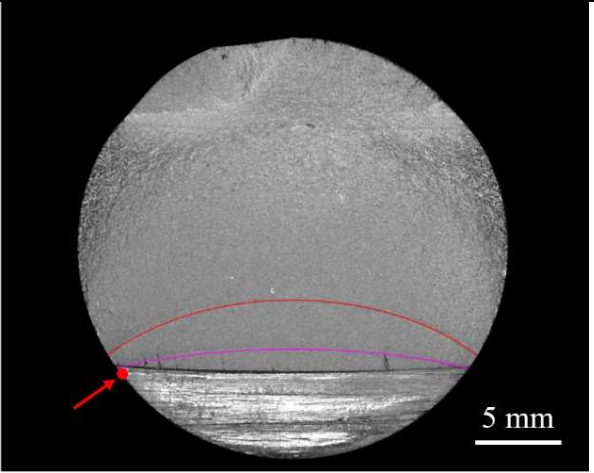
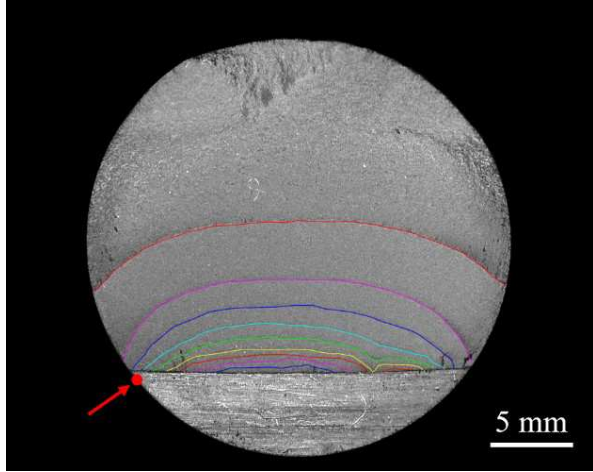
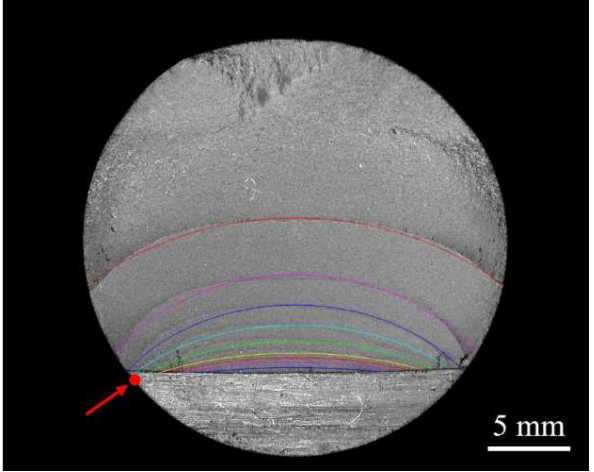
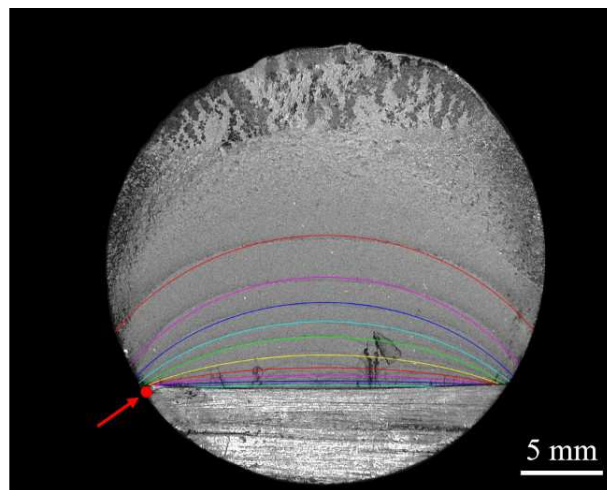
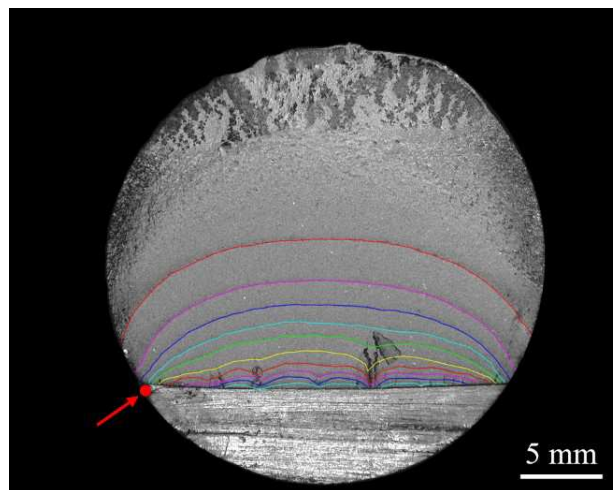


Figure 4.32. Percentage errors between experimental results and FE estimation.

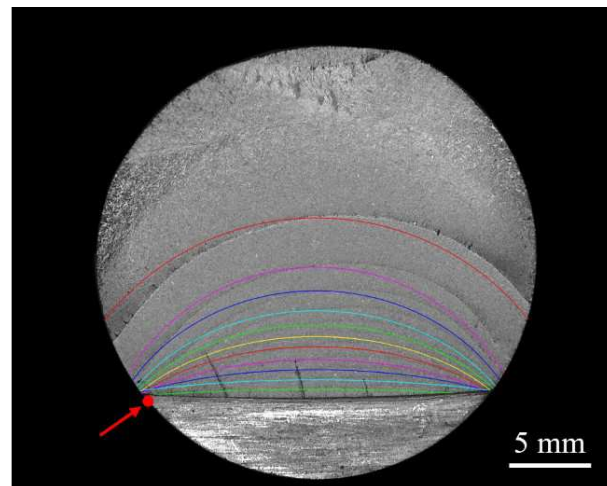
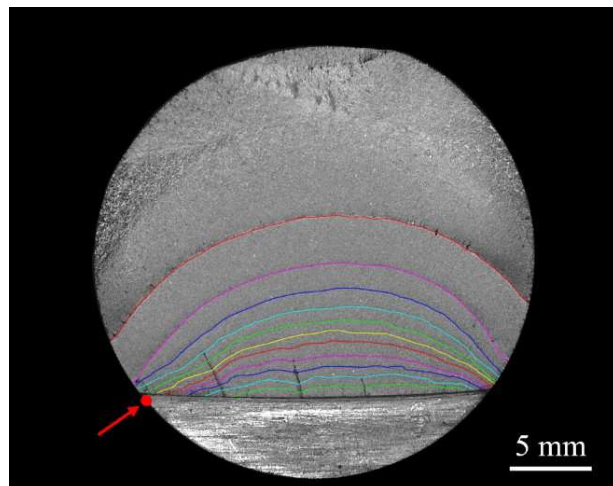
Table 4.3. Fracture surfaces of the tested specimens with main geometric and testing parameters. Real cracks on the left side and fitted cracks on the right side.

Experimental cracks and fitted cracks		Specimen's parameters
		<p>D25N5CG50_01</p> <p>$a_{\text{notch}} = 5.1 \text{ mm}$ $h_{\text{notch}} = 0.6 \text{ mm}$ $\theta_I = \theta_{\text{PD}} = \theta_T = 51^\circ$ $Y_{I,1} = + 11.5 \text{ mm}$ $Y_{I,2} = - 11.5 \text{ mm}$ $Y_{\text{PD},1} = + 0.8 \text{ mm}$ $Y_{\text{PD},2} = - 0.8 \text{ mm}$ $Y_T = + 5.4 \text{ mm}$ $\Delta F = 80 \text{ kN}$ $R = 0.05$ $\Delta F_{\text{OL}} = 50 \text{ kN}$ $R_{\text{OL}} = 0.6$ $N_f = 72627 \text{ cycles}$</p>
		<p>D25N5CG50_02</p> <p>$a_{\text{notch}} = 5.0 \text{ mm}$ $h_{\text{notch}} = 0.7 \text{ mm}$ $\theta_I = \theta_{\text{PD}} = \theta_T = 49^\circ$ $Y_{I,1} = + 11.5 \text{ mm}$ $Y_{I,2} = - 11.5 \text{ mm}$ $Y_{\text{PD},1} = + 0.8 \text{ mm}$ $Y_{\text{PD},2} = - 0.8 \text{ mm}$ $Y_T = + 5.1 \text{ mm}$ $\Delta F = 60 - 70 \text{ kN}$ $R = 0.05$ $\Delta F_{\text{OL}} = 50 \text{ kN}$ $R_{\text{OL}} = 0.6$ $N_f = 383318 \text{ cycles}$</p>

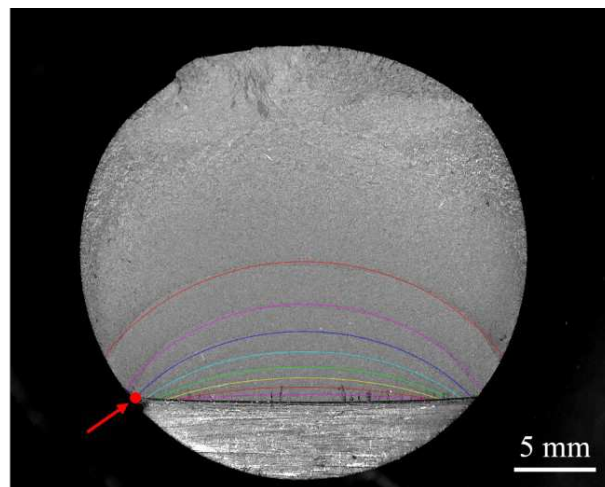
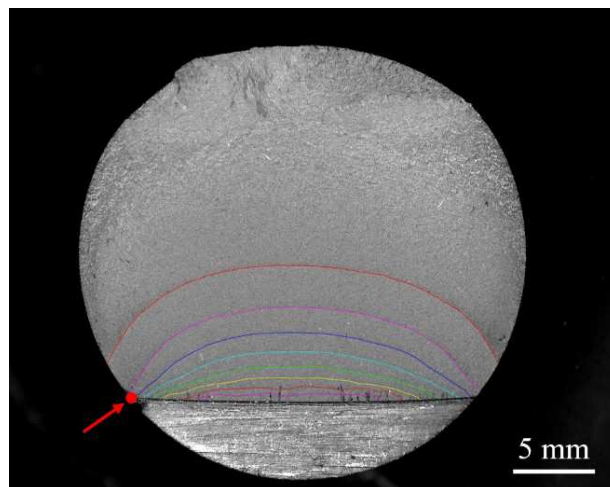
4.5 Experimental Tests



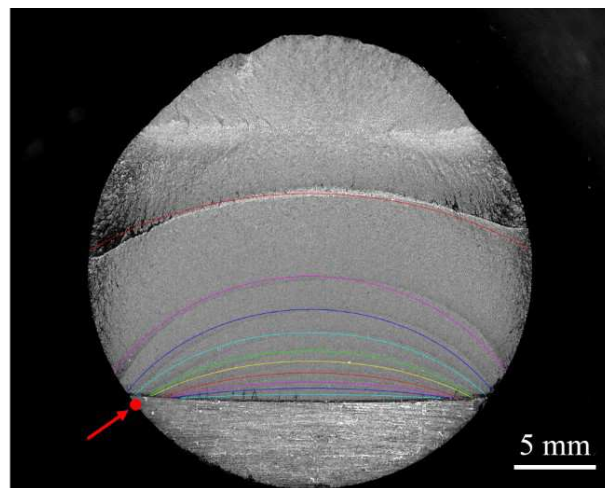
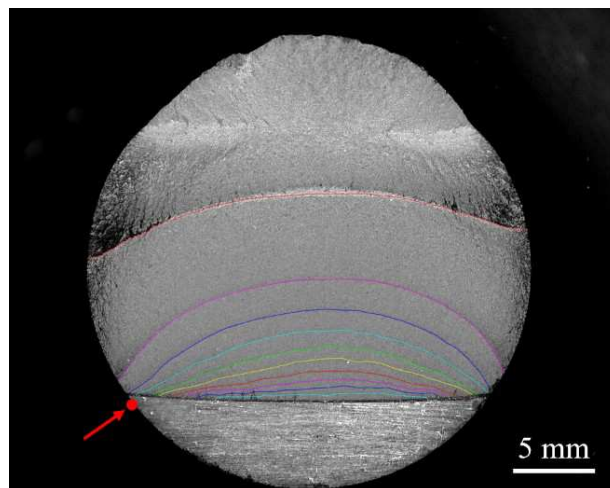
D25N5CG50_03
 $a_{\text{notch}} = 5.4 \text{ mm}$
 $h_{\text{notch}} = 0.6 \text{ mm}$
 $\theta_I = \theta_{\text{PD}} = \theta_T = 50^\circ$
 $Y_{I,1} = + 11.5 \text{ mm}$
 $Y_{I,2} = - 11.5 \text{ mm}$
 $Y_{\text{PD},1} = + 0.9 \text{ mm}$
 $Y_{\text{PD},2} = - 0.9 \text{ mm}$
 $Y_T = + 5.4 \text{ mm}$
 $\Delta F = 70 - 65 \text{ kN}$
 $R = 0.05$
 $\Delta F_{\text{OL}} = 50 \text{ kN}$
 $R_{\text{OL}} = 0.6$
 $N_f = 263584 \text{ cycles}$



D25N5CG50_04
 $a_{\text{notch}} = 4.6 \text{ mm}$
 $h_{\text{notch}} = 0.7 \text{ mm}$
 $\theta_I = \theta_{\text{PD}} = \theta_T = 48^\circ$
 $Y_{I,1} = + 11.5 \text{ mm}$
 $Y_{I,2} = - 11.5 \text{ mm}$
 $Y_{\text{PD},1} = + 0.8 \text{ mm}$
 $Y_{\text{PD},2} = - 0.8 \text{ mm}$
 $Y_T = + 5.5 \text{ mm}$
 $\Delta F = 70 - 65 \text{ kN}$
 $R = 0.05$
 $\Delta F_{\text{OL}} = 50 \text{ kN}$
 $R_{\text{OL}} = 0.6$
 $N_f = 290224 \text{ cycles}$

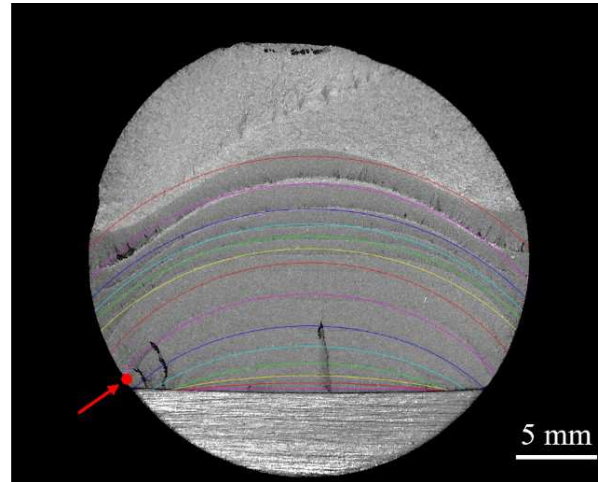
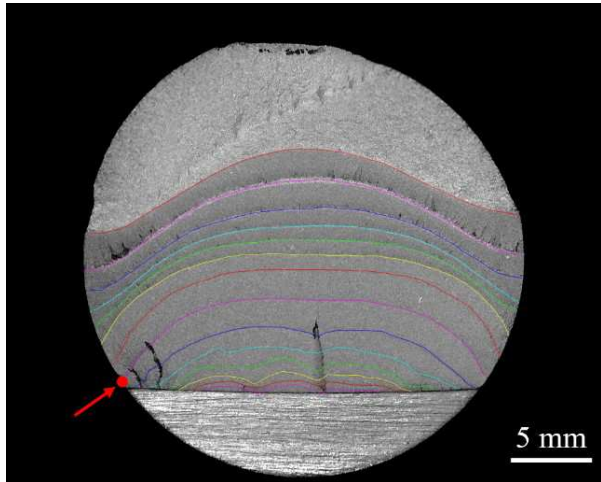


D25N5CG50_05
 $a_{\text{notch}} = 4.34 \text{ mm}$
 $h_{\text{notch}} = 0.67 \text{ mm}$
 $\theta_I = \theta_{PD} = \theta_T = 51^\circ$
 $Y_{I,1} = + 11.48 \text{ mm}$
 $Y_{I,2} = - 11.62 \text{ mm}$
 $Y_{PD,1} = + 0.74 \text{ mm}$
 $Y_{PD,2} = - 0.85 \text{ mm}$
 $Y_T = + 5.09 \text{ mm}$
 $\Delta F = 70 \text{ kN}$
 $R = 0.05$
 $\Delta F_{OL} = 50 \text{ kN}$
 $R_{OL} = 0.6$
 $N_f = 216359 \text{ cycles}$

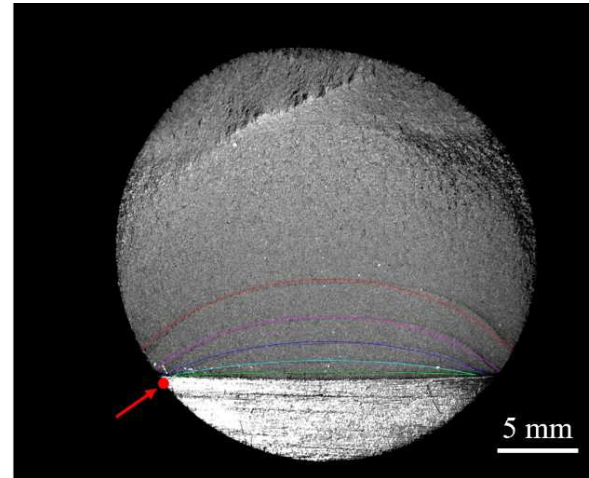
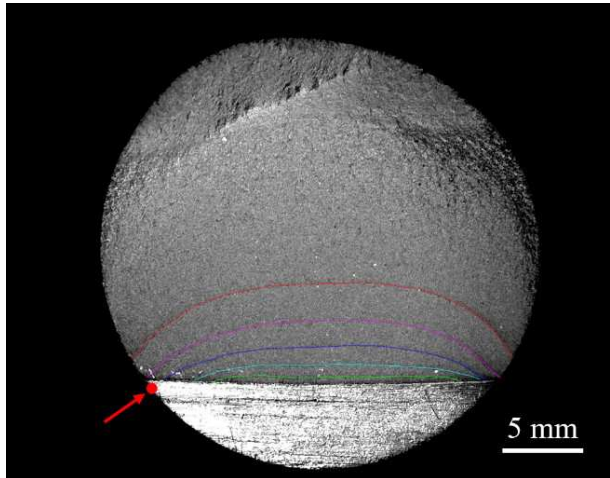


D25N5CG50_06
 $a_{\text{notch}} = 4.97 \text{ mm}$
 $h_{\text{notch}} = 0.69 \text{ mm}$
 $\theta_I = \theta_{PD} = \theta_T = 49^\circ$
 $Y_{I,1} = + 11.53 \text{ mm}$
 $Y_{I,2} = - 11.97 \text{ mm}$
 $Y_{PD,1} = + 0.95 \text{ mm}$
 $Y_{PD,2} = - 1.24 \text{ mm}$
 $Y_T = + 4.73 \text{ mm}$
 $\Delta F = 70 \text{ kN}$
 $R = 0.05$
 $\Delta F_{OL} = 50 \text{ kN}$
 $R_{OL} = 0.6$
 $N_f = 253768 \text{ cycles}$

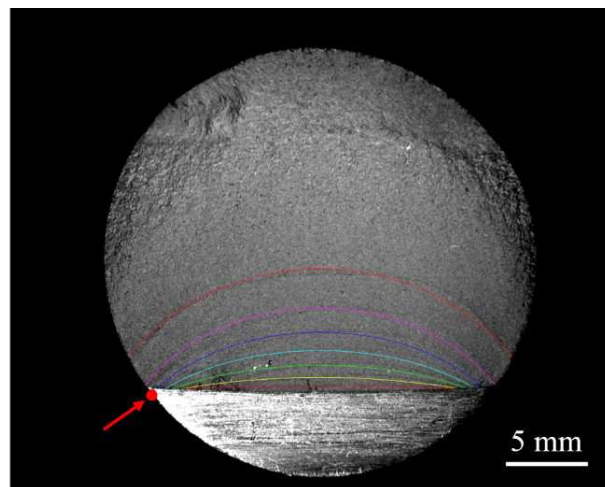
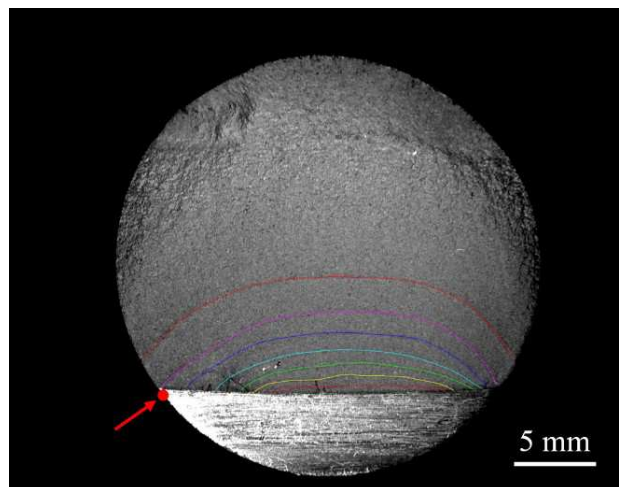
4.5 Experimental Tests



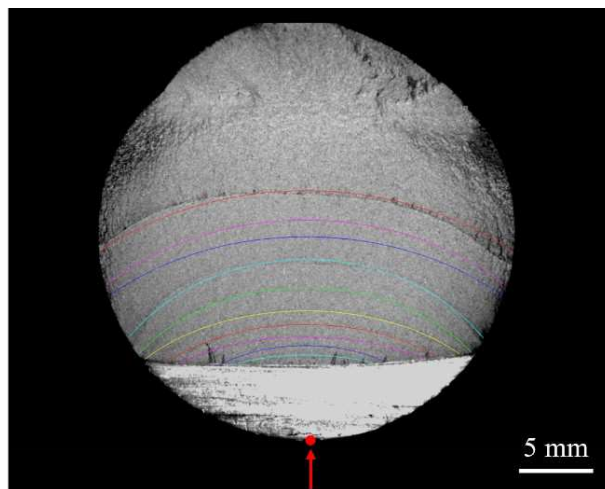
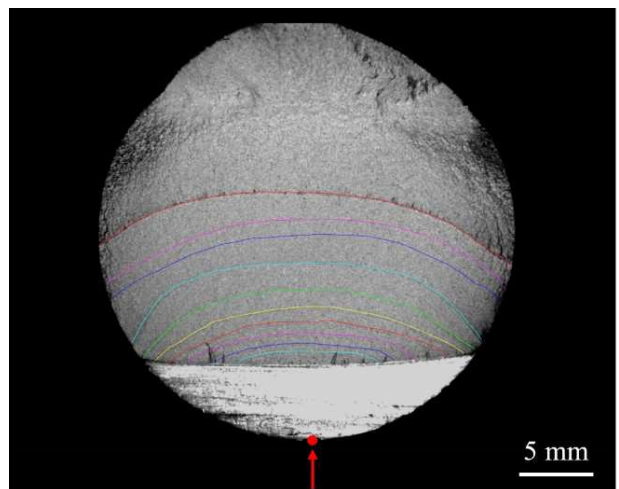
D25N5CG50_07
 $a_{\text{notch}} = 4.98 \text{ mm}$
 $h_{\text{notch}} = 0.58 \text{ mm}$
 $\theta_i = \theta_{\text{PD}} = \theta_T = 51^\circ$
 $Y_{I,1} = + 11.88 \text{ mm}$
 $Y_{I,2} = - 10.97 \text{ mm}$
 $Y_{\text{PD},1} = + 0.81 \text{ mm}$
 $Y_{\text{PD},2} = - 0.58 \text{ mm}$
 $Y_T = + 5.54 \text{ mm}$
 $\Delta F = 70 - 50 \text{ kN}$
 $R = 0.05$
 $\Delta F_{\text{OL}} = 50 \text{ kN}$
 $R_{\text{OL}} = 0.6$
 $N_f = 324992 \text{ cycles}$



D25N5CG50_08
 $a_{\text{notch}} = 4.83 \text{ mm}$
 $h_{\text{notch}} = 0.56 \text{ mm}$
 $\theta_i = \theta_{\text{PD}} = \theta_T = 51^\circ$
 $Y_{I,1} = + 11.35 \text{ mm}$
 $Y_{I,2} = - 11.66 \text{ mm}$
 $Y_{\text{PD},1} = + 0.52 \text{ mm}$
 $Y_{\text{PD},2} = - 0.81 \text{ mm}$
 $Y_T = + 4.81 \text{ mm}$
 $\Delta F = 70 \text{ kN}$
 $R = 0.05$
 $\Delta F_{\text{OL}} = 50 \text{ kN}$
 $R_{\text{OL}} = 0.6$
 $N_f = 148808 \text{ cycles}$

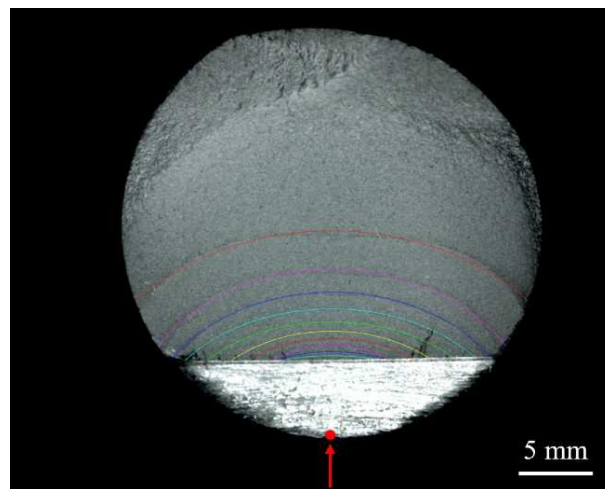
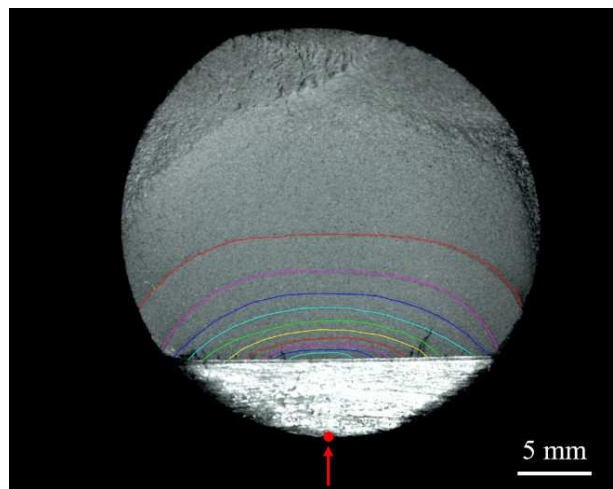


D25N5CG50_09
 $a_{\text{notch}} = 4.85 \text{ mm}$
 $h_{\text{notch}} = 0.61 \text{ mm}$
 $\theta_I = \theta_{PD} = \theta_T = 49^\circ$
 $Y_{I,1} = + 11.63 \text{ mm}$
 $Y_{I,2} = - 11.33 \text{ mm}$
 $Y_{PD,1} = + 0.87 \text{ mm}$
 $Y_{PD,2} = - 0.56 \text{ mm}$
 $Y_T = + 5.14 \text{ mm}$
 $\Delta F = 70 \text{ kN}$
 $R = 0.05$
 $\Delta F_{OL} = 50 \text{ kN}$
 $R_{OL} = 0.6$
 $N_f = 194140 \text{ cycles}$

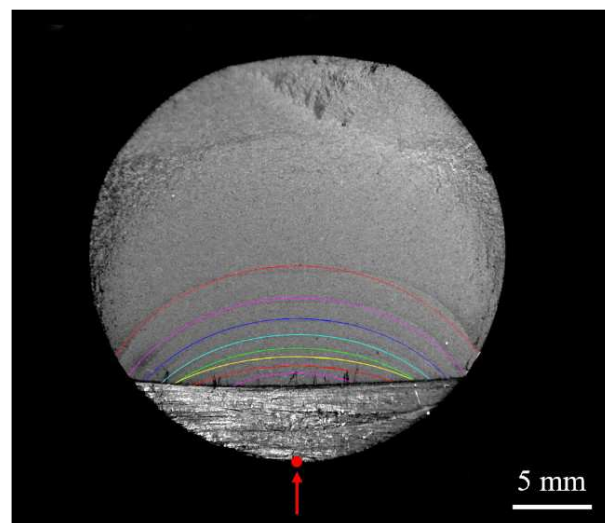
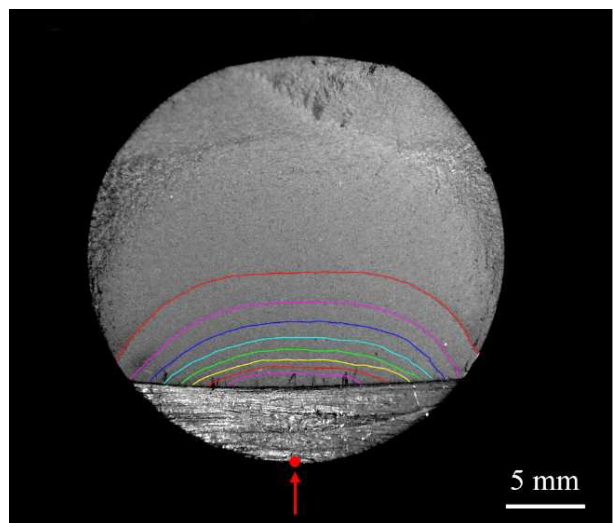


D25N5CG0_11
 $a_{\text{notch}} = 4.44 \text{ mm}$
 $h_{\text{notch}} = 0.96 \text{ mm}$
 $\theta_I = \theta_{PD} = \theta_T = 0^\circ$
 $Y_{I,1} = + 11.42 \text{ mm}$
 $Y_{I,2} = - 11.45 \text{ mm}$
 $Y_{PD,1} = + 0.96 \text{ mm}$
 $Y_{PD,2} = - 1.03 \text{ mm}$
 $Y_T = + 4.93 \text{ mm}$
 $\Delta F = 70 \text{ kN}$
 $R = 0.05$
 $\Delta F_{OL} = 50 \text{ kN}$
 $R_{OL} = 0.6$
 $N_f = 254843 \text{ cycles}$

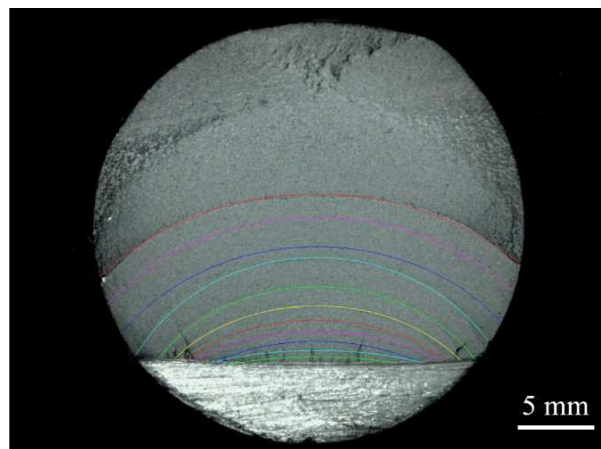
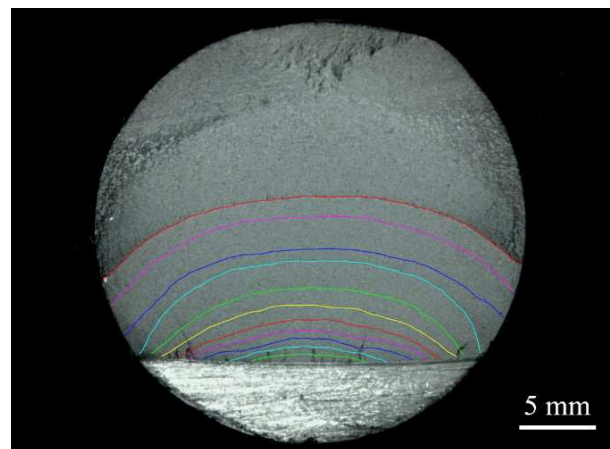
4.5 Experimental Tests



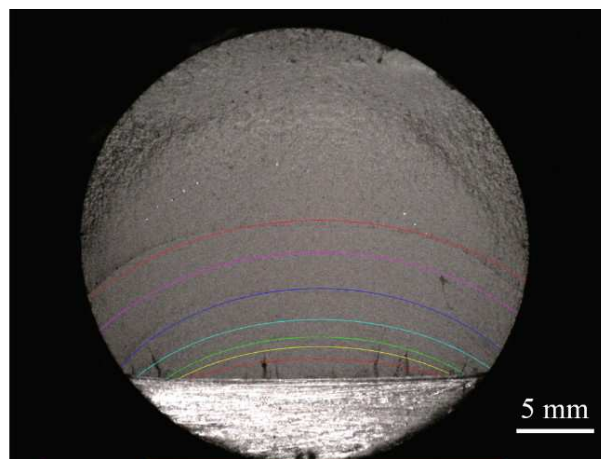
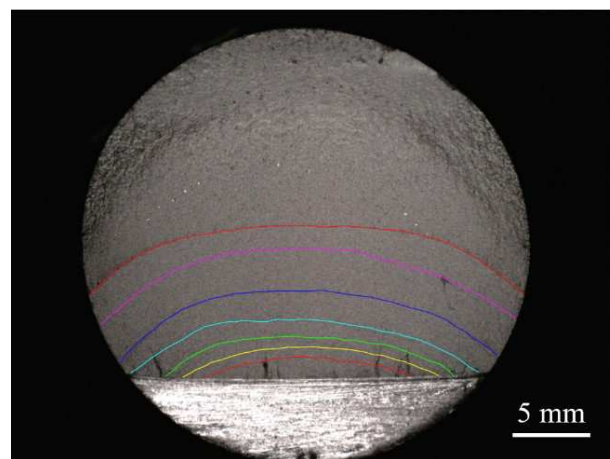
D25N5CG0_14
 $a_{\text{notch}} = 4.49 \text{ mm}$
 $h_{\text{notch}} = 0.87 \text{ mm}$
 $\theta_I = \theta_{PD} = \theta_T = 0^\circ$
 $Y_{I,1} = + 11.48 \text{ mm}$
 $Y_{I,2} = - 11.41 \text{ mm}$
 $Y_{PD,1} = + 0.83 \text{ mm}$
 $Y_{PD,2} = - 1.16 \text{ mm}$
 $Y_T = + 5.01 \text{ mm}$
 $\Delta F = 70 \text{ kN}$
 $R = 0.05$
 $\Delta F_{OL} = 50 \text{ kN}$
 $R_{OL} = 0.6$
 $N_f = 288997 \text{ cycles}$



D25N5CG0_15
 $a_{\text{notch}} = 4.47 \text{ mm}$
 $h_{\text{notch}} = 1.09 \text{ mm}$
 $\theta_I = \theta_{PD} = \theta_T = 0^\circ$
 $Y_{I,1} = + 11.51 \text{ mm}$
 $Y_{I,2} = - 11.48 \text{ mm}$
 $Y_{PD,1} = + 0.98 \text{ mm}$
 $Y_{PD,2} = - 1.07 \text{ mm}$
 $Y_T = + 4.69 \text{ mm}$
 $\Delta F = 70 \text{ kN}$
 $R = 0.05$
 $\Delta F_{OL} = 50 \text{ kN}$
 $R_{OL} = 0.6$
 $N_f = 321154 \text{ cycles}$



D25N5CG0_16
 $a_{\text{notch}} = 4.51 \text{ mm}$
 $h_{\text{notch}} = 0.95 \text{ mm}$
 $\theta_I = \theta_{PD} = \theta_T = 0^\circ$
 $Y_{I,1} = +\infty$
 $Y_{I,2} = -\infty$
 $Y_{PD,1} = +1.43 \text{ mm}$
 $Y_{PD,2} = -0.5 \text{ mm}$
 $Y_T = +5.09 \text{ mm}$
 $\Delta F = 70 \text{ kN}$
 $R = 0.05$
 $\Delta F_{OL} = 50 \text{ kN}$
 $R_{OL} = 0.6$
 $N_f = 306000 \text{ cycles}$



D25N5CG0_17
 $a_{\text{notch}} = 4.57 \text{ mm}$
 $h_{\text{notch}} = 0.89 \text{ mm}$
 $\theta_I = \theta_{PD} = \theta_T = 0^\circ$
 $Y_{I,1} = +\infty$
 $Y_{I,2} = -\infty$
 $Y_{PD,1} = +0.81 \text{ mm}$
 $Y_{PD,2} = -1.01 \text{ mm}$
 $Y_T = +4.85 \text{ mm}$
 $\Delta F = 70 \text{ kN}$
 $R = 0.05$
 $\Delta F_{OL} = 50 \text{ kN}$
 $R_{OL} = 0.6$
 $N_f = 182000 \text{ cycles}$

4.5 Experimental Tests

Table 4.4. Summary of the experimental results.

Specimen [-]	N_f [cycles]	ΔF [kN]	N° OL [-]	N [10 ³ cycles]	a/D [-]	c/a [-]	ΔV_{PD} [μV]	ΔV_T [μV]	$\Delta V_{PD}/\Delta V_T$ [-]	
D25N5CG50_01	72627	\	\	0	0.20	\	134.9	210.4	0.64	
			80	1	25	0.26	2.86	153.4	212.9	0.72
				2	50	0.37	1.53	306.7	222.6	1.38
D25N5CG50_02	383318	\	\	0	0.20	\	160.6	189.1	0.85	
			≤ 65	1	175	0.21	3.09	161.7	185.9	0.87
			65	2	200	0.22	2.56	164.5	186.2	0.88
				3	225	0.23	2.37	167.9	186.6	0.90
			70	4	250	0.24	2.24	175.6	187.6	0.94
				5	275	0.27	1.86	188.7	187.2	1.01
				6	300	0.31	1.58	217.3	184.8	1.18
				7	325	0.36	1.34	280.6	175.8	1.60
				8	350	0.43	1.21	415.0	150.3	2.76
	9	375	0.56	1.26	768.8	103.7	7.41			
D25N5CG50_03	263584	\	\	0	0.22	\	194.0	206.0	0.94	
			70	1	25	0.23	7.16	183.2	199.1	0.92
				2	50	0.24	5.74	185.4	199.5	0.93
				3	75	0.25	3.76	192.3	201.2	0.96
				4	100	0.27	2.90	202.3	202.7	1.00
				5	125	0.29	2.14	211.5	201.9	1.05
				6	150	0.33	1.67	260.3	205.0	1.27
			65	7	175	0.37	1.46	285.8	195.2	1.46
				8	200	0.41	1.29	354.4	187.4	1.89
				9	225	0.47	1.15	445.6	170.1	2.62
	10	250	0.56	1.07	664.5	134.3	4.95			
D25N5CG50_04	290224	\	\	0	0.18	\	158.3	216.0	0.73	
			70	1	25	0.20	5.25	173.2	235.2	0.74

CHAPTER 4: Short fatigue cracks growth monitoring

			2	50	0.23	3.91	182.1	235.6	0.77
			3	75	0.25	2.65	201.4	237.8	0.85
			4	100	0.27	2.10	181.9	240.6	0.76
			5	125	0.30	1.74	196.0	233.4	0.84
		65	6	150	0.32	1.56	205.9	223.7	0.92
			7	175	0.35	1.42	223.9	220.7	1.01
			8	200	0.38	1.28	254.7	215.5	1.18
			9	225	0.43	1.15	300.3	204.7	1.47
			10	250	0.48	1.02	419.7	191.5	2.19
			11	275	0.59	1.02	750.3	166.0	4.52
D25N5CG50_05	216 359	70	\	0	0.17	\	123	219	0.559
			1	25	0.19	4.07	125	220	0.568
			2	50	0.20	2.75	129	220	0.587
			3	75	0.22	2.18	135	221	0.611
			4	100	0.25	1.87	146	221	0.659
			5	125	0.28	1.59	166	220	0.754
			6	150	0.33	1.36	207	215	0.963
			7	175	0.39	1.18	301	192	1.568
			8	200	0.48	1.11	565	136	4.154
D25N5CG50_06	253 768	70	\	0	0.19	\	153	168	0.911
			1	25	0.21	4.85	156	169	0.923
			2	50	0.22	3.23	161	168	0.958
			3	75	0.24	2.58	165	170	0.970
			4	100	0.26	2.07	172	170	1.012
			5	125	0.28	1.80	183	171	1.070
			6	150	0.31	1.57	203	169	1.201
			7	175	0.35	1.40	236	154	1.532
			8	200	0.40	1.21	310	142	2.183
			9	225	0.47	1.10	460	112	4.107

4.5 Experimental Tests

			10	250	0.66	1.27	980	72	13.611
D25N5CG50_07	324 992	70	\	0	0.19	\	94	266	0.354
			1	25	0.20	13.14	94	263	0.356
			2	50	0.21	3.52	95	264	0.359
			3	75	0.23	2.66	97	266	0.365
			4	100	0.25	1.86	100	268	0.375
			5	125	0.29	1.60	108	272	0.396
			6	150	0.34	1.42	124	277	0.449
			7	175	0.41	1.23	188	270	0.696
			8	200	0.48	1.14	402	211	1.904
		65	9	225	0.51	1.18	540	169	3.200
		60	10	250	0.54	1.17	613	155	3.964
			11	275	0.57	1.12	680	149	4.558
			12	300	0.60	1.08	771	156	4.945
			13	325	0.66	1.01	915	155	5.910
D25N5CG50_08	148 808	70	\	0	0.19	\	122.8	219.5	0.559
			1	25	0.21	5.99	124.9	219.8	0.568
			2	50	0.23	2.88	129.5	220.4	0.587
			3	75	0.28	1.95	135	221	0.611
			4	100	0.34	1.51	146	221.5	0.659
			5	125	0.43	1.28	166	220	0.754
D25N5CG50_09	194 140	70	\	0	0.19	\	149	241	0.617
			1	25	0.21	6.28	149	240	0.619
			2	50	0.23	3.00	150	239	0.626
			3	75	0.25	2.15	155	241	0.644
			4	100	0.29	1.71	165	242	0.684
			5	125	0.33	1.43	187	241	0.776
			6	150	0.39	1.24	255	234	1.088
			7	175	0.48	1.13	476	189	2.520

CHAPTER 4: Short fatigue cracks growth monitoring

D25N5CG0_11	254 843	70	\	0	0.17	\	396	95	4.161
			1	25	0.20	1.89	390	94	4.137
			2	50	0.22	1.51	395	94	4.193
			3	75	0.24	1.87	403	92	4.359
			4	100	0.27	1.64	418	90	4.651
			5	125	0.30	1.60	440	87	5.085
			6	150	0.36	1.33	470	83	5.657
			7	175	0.43	1.19	509	79	6.454
			8	200	0.48	1.37	565	75	7.527
			9	225	0.52	1.28	652	71	9.177
			10	250	0.59	1.27	984	80	12.326
D25N5CG0_14	288 997	70	\	0	0.180	/	433	143	3.028
			1	25	/	/	447	143	3.118
			2	50	0.19	1.85	452	143	3.164
			3	75	0.20	1.53	460	143	3.215
			4	100	0.22	1.15	470	143	3.289
			5	125	0.23	1.36	485	142	3.410
			6	150	0.25	1.37	505	141	3.588
			7	175	0.27	1.44	534	140	3.828
			8	200	0.30	1.43	572	136	4.201
			9	225	0.34	1.31	627	135	4.660
			10	250	0.40	1.24	708	133	5.307
D25N5CG0_15	321 154	70	\	0	0.18	/	436	96	4.560
			1	25	/	/	427	95	4.485
			2	50	/	/	429	95	4.505
			3	75	/	/	431	95	4.526
			4	100	/	/	435	95	4.565
			5	125	0.21	1.39	442	95	4.666

4.5 Experimental Tests

			6	150	0.23	1.81	453	94	4.828
			7	175	0.25	1.76	475	92	5.153
			8	200	0.27	1.57	499	90	5.551
			9	225	0.30	1.37	532	87	6.104
			10	250	0.34	1.29	575	84	6.805
			11	275	0.39	1.22	642	81	7.905
			12	300	0.47	1.11	748	77	9.676
D25N5CG0_16	306 000	70	\	0	0.18	/	235	42	5.561
			1	25	/	/	239	43	5.524
			2	50	0.20	2.45	243	43	5.667
			3	75	0.22	2.31	241	42	5.694
			4	100	0.24	1.65	249	42	5.887
			5	125	0.26	1.66	253	42	6.069
			6	150	0.28	1.44	260	41	6.411
			7	175	0.32	1.31	271	39	6.928
			8	200	0.36	1.20	289	37	7.775
			9	225	0.43	1.11	312	35	8.930
			10	250	0.46	1.20	347	33	10.661
			11	275	0.52	1.18	407	29	13.892
			12	300	0.58	1.18	631	23	27.063
D25N5CG0_17	182 000	70	\	0	0.18	/	225	39	5.694
			1	25	0.24	2.09	230	41	5.654
			2	50	0.27	1.72	236	40	5.865
			3	75	0.29	1.61	249	39	6.469
			4	100	0.33	1.57	273	36	7.545
			5	125	0.40	1.35	311	33	9.483
			6	150	0.48	1.33	371	29	12.842
			7	175	0.55	1.28	566	23	24.754

4.6. Discussion

4.6.1. Comparison between experimental data and numerical estimation

Regarding the comparison between experimental results and electrical FE analyses, several aspects deserve further investigations. Firstly, the reconstruction of the actual specimen geometry is crucial for the resulting accuracy of the numerical simulations. More in detail, great attention has to be given to the real position of the probes when modelling the specimen's geometry. Indeed, the use of micro-notches on the specimen limited the positioning errors, although small errors in measuring their location could significantly affect the results, this latter aspect being enhanced when the probe is located in a region where the reproducibility is very low, i.e. where the potential drop is extremely sensitive to the probe position. Most of times, this was the case of the temperature compensation probe, which was in a region where the potential drop changes significantly with the probe position (see Figure 4.14). Secondly, while in the present paper pure electric FE analyses were carried out to calibrate the adopted DCPD setup, Tarnowski et al. [44,45] has recently argued that numerical DCPD calibration curves should be derived from coupled structural-electric FE analyses in order to include the effect of strain on the crack length estimations, especially when potential probes are located in highly strained regions, such as close to the crack tip. Indeed, the effect of strain can affect the estimation of the crack length providing errors up to 30% [44,45,56,57].

Moreover, in the previous section the numerical DCPD calibration curves were validated against experimental results by comparing the potential drop values for fixed cracked configurations, i.e. those measured from specimens' fracture surfaces. However, if the DCPD setup of Figure 4.22 is applied for crack growth monitoring in fracture mechanics testing, the accuracy of the numerical calibration curves should be checked against experimental results in terms of crack size estimation. Figure 4.33 allows to compare estimated and actual crack size for a fixed potential drop, i.e. that is experimentally measured at each overload. In most cases, the crack size estimated by the numerical calibration curve deviated from the actual one of less than 10%. However, for small crack sizes ($a/D < 0.3$), deviations were higher and approximately

4.6 Discussion

$\pm 20\%$ and $\pm 30\%$ when referring to calibration curves in terms of ΔV_{PD} or $\Delta V_{PD}/\Delta V_T$, respectively. These results are related to the adopted specimen geometry and DCPD setup which translate into flat slopes of the calibration curves in Figure 4.29 for small crack sizes ($a/D < 0.3$) and result in high scatter of the estimated crack size within this region, i.e. small deviations in the potential drop value lead to increased deviations in the estimated crack size. Similar conclusions can be drawn analysing the other experimental results, not reported in Figure 4.33 for the sake of brevity.

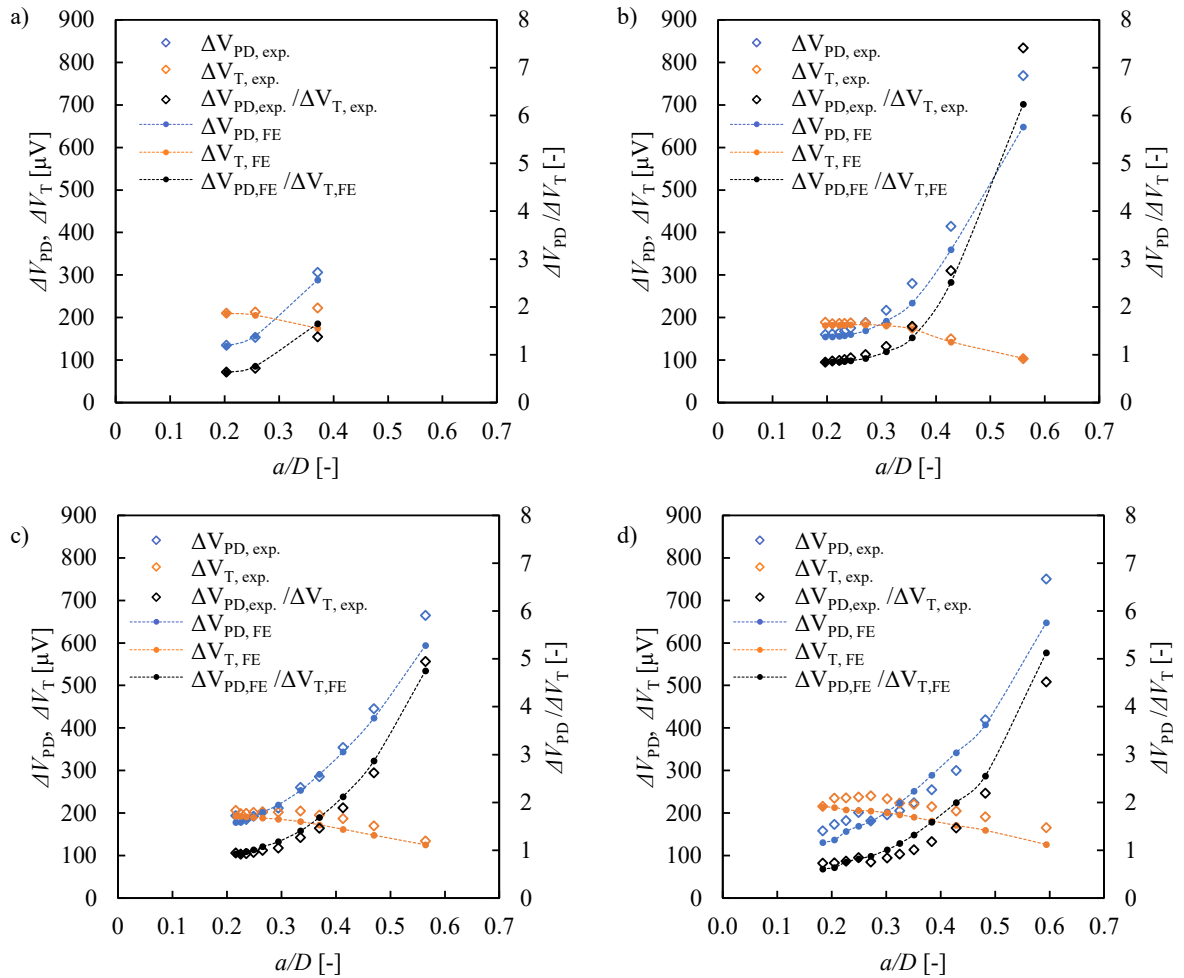


Figure 4.33. Example of comparison between experimental results ('exp.') and numerical simulations for the specimens D25N5CG50_01, D25N5CG50_02, D25N5CG50_03, D25N5CG50_04 tested using a local DCPD configuration with $\theta_1 = \theta_2 = \theta_3 = 50^\circ$.

4.6.2. *Application to real components*

Finally, even if relatively high errors have been found in this investigation, the proposed procedure could be of great interest for future developments and applications of the DCPD method in the field of structural health monitoring [58,59]. For example, in welded structures, crack initiation can always occur at weld defects, but also at stress concentrators like the weld toe or root. All these situations are undesirable, but they cannot always be avoided. The so-called damage tolerance approach assumes that crack initiation and growth are acceptable, but the occurrence of the failure must be prevented by periodic inspections using proper NDE techniques. Applying the DCPD method to a huge and complex welded structure is tremendously different from standard applications for fracture mechanics fatigue test, since crack location and shape are not known a priori in real components, a crack being not introduced on purpose. In this context, the PDM can be effectively applied to detect crack initiation only in components where potential crack initiation locations are present, such as stress concentration features, weldments or notches. As a matter of fact, current and potential probes can be located as close as possible to these critical locations and possibly a multi-probe PDM configuration [16,19–22] can be adopted to monitor multiple critical location of the real component at the same time. As an example, To et al. [23], Lecsek et al. [24] and Cerny [25,26] applied the PDM to monitor the crack initiation at the toe side of welded structures, while recently Meneghetti et al. [34] applied the PDM to monitor the crack initiation at the notch tip of round bars under multiaxial loading conditions, adopting also a multi-probe configuration to detect the crack initiation location [16] along the notch tip line. Accordingly, the proposed local DCPD configuration, making use of the clip-on-gauge device (Figure 4.22) represent a little advancement in this direction.

Unfortunately, as discussed in the introduction, the estimation of the crack shape and location is not the only problem when applying the DCPD method to real components. In fact, most real engineering structures are characterized by having large size which translate into a reduced sensitivity of the PDM, due to the fact that for a fixed input current, the current density is lower [15] (see Eq. (4.2)). To overcome this issue, DCPD configurations require high currents, even greater than 100 A, this current level being not always achievable due to safety reasons or technological limitations. Again, a partial solution to this problem can be given by

adopting the local DCPD configuration and the corresponding clip-on-gauge device (Figure 4.22) which allows for a very localized current input that helps keeping a high resolution even if a lower value of the input current is used.

However, when a component without any preferential crack initiation location is investigated, the application of PDM to detect crack initiation becomes trickier. Only a rough assessment of crack existence from the qualitative viewpoint could be performed by adopting a PDM configuration having current and potential probes located in fixed positions far away from each other to cover a large portion of the component. Other solutions allow to obtain crack depth data in the field without the need to provide permanent contact or micro-notches into the component. As an example, a commercial solution is ‘Mat-3 handheld probe’ [60] from Matelect LTD, which is based on ACPD configuration and allows to locate current and potential probes as close as possible to each other in order to increase the sensitivity, at the expense of a very small investigated area which should be moved along the surface of the component until a crack initiation is detected. Unfortunately, these solutions allow to obtain crack growth resolutions on the order of millimetres [60], due to the poor contact between current/potential probes and the surface of the component.

Concerning instead a real component where a crack has initiated and its location has been identified by a previous PDM-based rough estimation or the application of other NDE techniques, an optimised application of PDM is still applicable to monitor the crack propagation phase, since current and potential probes can be located as close as possible to the initiated crack and micro-notches or permanent connections can be arranged to improve the electric contact. As an example, Cerny [27] monitored the propagation of a crack initiated in a full scale railway axle loaded by rotating bending by locating the current and potential probes close to the initiated crack.

4.6.3. Minimum detectable crack length increment

In some practical applications of the DCPD method it could be of interest to have an estimate of the resolution of a certain DCPD setup. One possibility is to evaluate the minimum detectable crack increment da_{\min} for a given DCPD device resolution, the latter to be intended as the smallest appreciable potential drop change the DCPD device can detect.

For the sake of simplicity, consider an ideal single channel DCPD setup perfectly reproducible and completely insensitive to any measuring error. This way all reading errors (fluctuations in electrical resistivity originating from both temperature and plasticity, or ripple and noise in the electric current flux, or any incorrect positioning of the probes) are assumed to be zero. These hypotheses suggest that the minimum detectable crack size increment da_{\min} is only dependent on the sensitivity of the setup $d\Delta V_{PD}/da$ and on the resolution of the DCPD device in terms of minimum detectable potential drop change $d\Delta V_{\min}$. Accordingly, the minimum detectable crack increment da_{\min} , i.e. that crack increment relevant to the resolution of the DCPD device, can be estimated by the following expression:

$$da_{\min} = \frac{d\Delta V_{\min}}{d\Delta V_{PD} / da}$$

The minimum detectable potential drop change $d\Delta V_{\min}$ depends on the employed experimental DCPD device and on the measurement chain, therefore its value is potentially different from time to time. Nevertheless, in standard application of the DCPD method, a common value can be $d\Delta V_{\min} = 1 \mu\text{V}$, the output voltage being usually at the microvolt level [11,36]. Figure 4.34 shows of an example relevant to the configuration with $\theta_{PD} = 0^\circ$ and $Y_{PD} = 0.5 \text{ mm}$ and the one with $\theta_{PD} = 50^\circ$, $Y_{PD} = 0.5 \text{ mm}$ of Figure 4.15. It can be observed that, an increment of $1 \mu\text{V}$ of the measured potential drop signal would correspond to an increment of the crack depth on the order of tens of microns. Similar to what observed for the sensitivity on the right side of Figure 4.15, Figure 4.34b shows that this value significantly changes with the crack size: for small crack depth ($a/D < 0.3$), the measuring system is rather insensitive to crack growth, but it improves for increasing crack depths thanks to the rapid increase in the sensitivity, as soon as the crack surface tip reaches the probes angular position ($a/D \sim 0.3$). This means that by locating the potential probes at an angular coordinate $\theta_{PD} \neq 0^\circ$ can be advantageous if small crack size increments are to be measured close to the probes position θ_{PD} . In fact, supposing to measure crack propagation from a depth of $a/D \sim 0.3$, the minimum detectable crack size increment when the potential probes are located at the crack tip ranges from 5 to 10 microns (Figure 4.34b), which is half the value in the case $\theta_{PD} = 0^\circ$ reported in Figure 4.34a. If the current probe position is concerned, it is always convenient to put the current probes as close as possible to the crack plane. Unfortunately, it has been shown that the closer

4.7 Conclusions

is the current probe to the crack plane, the lower is the reproducibility due to the high sensitivity to probes positioning errors. For this reason, adopting a local current input involves much more attention in positioning the probes correctly.

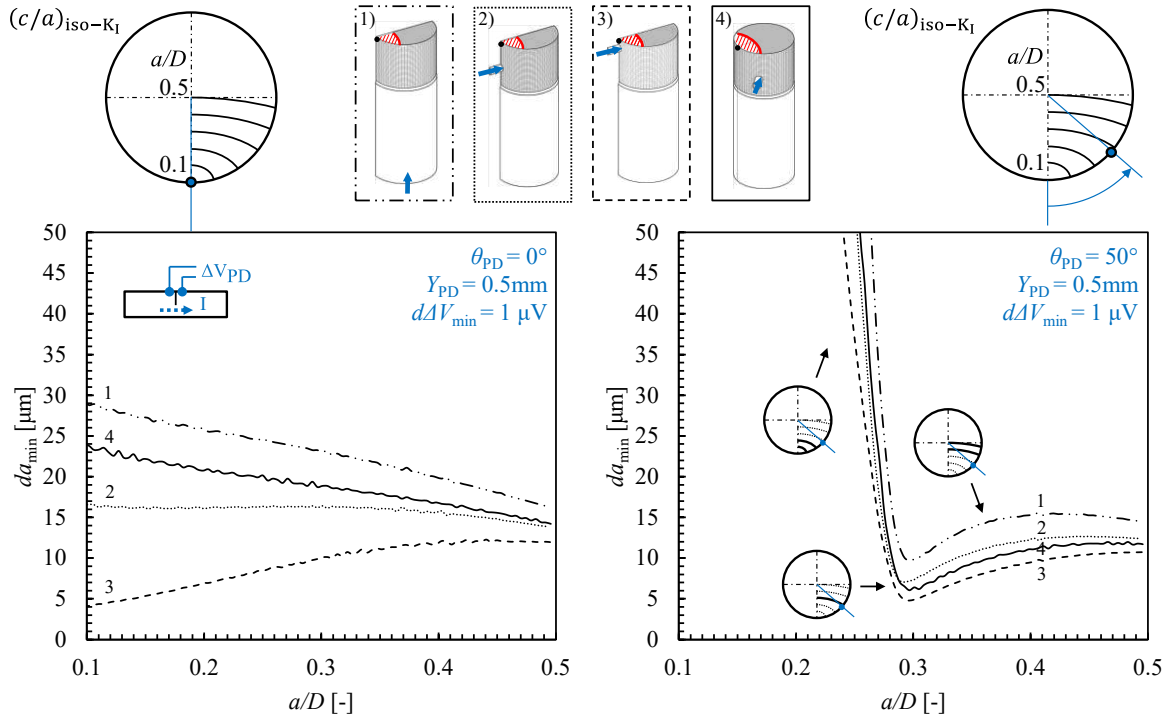


Figure 4.34. Minimum detectable crack length increment da_{min} : effect of the current and potential probes' location.

4.7. Conclusions

In the present chapter it has been discussed the application of the Direct Current Potential Drop (DCPD) method to complex geometry and the way in which it is possible to optimize the experimental arrangement. In particular, the DCPD method has been applied to a single-edge-crack round bars subject to axial fatigue.

Firstly, 3D electrical FE analyses have been adopted to investigate the effect of the current and the potential probes position on the efficiency of the DCPD monitoring technique. To this aim elliptical-shaped crack fronts with aspect ratio and crack depth according to the iso- K_I

criterion have been assumed. Then, almost 10^6 possible combinations grouped into 4 distinct current probe location, 96 crack depth, and 73 angular and 36 axial different position of the potential drop probes, have been considered in the electrical FE analyses. The efficiency of the DCPD setup has been evaluated in terms of measurability, sensitivity and reproducibility.

From the FE results it was possible to conclude that the measurability and the sensitivity of the measure can be maximized by locating both the current and the potential probes as close to the crack plane as possible and within the crack angular extension. More in detail, as the current probes approach the crack plane, on one hand the measurability and the sensitivity increase, but on the other hand the reproducibility becomes smaller. Therefore, the current probes require to be positioned very accurately. Regarding the potential probes, provided that measurability requirements are met (i.e. the signal to noise ratio of the adopted DCPD device is acceptable), their axial distance should be always minimized and their position should be accurately assessed, similarly to the current probes. Their angular position is a matter of choice: by locating them in the crack symmetry plane the measure will be more reproducible but less sensitive, while locating them as close to the crack tip as possible the measure is more sensitive but less reproducible. The latter configuration is favourable for monitoring the initiation and early propagation of small cracks from the crack starter because it appreciates smaller crack growth rates.

Secondly, experimental fatigue tests were conducted in order to verify the applicability of the above-mentioned DCPD configurations as well as the accuracy of the electrical FE analyses, that is, their capacity to accurately describe the relationship between the electrical potential drop and the crack size. The propagating fatigue crack has been monitored with the DCPD technique by means of a compact clip-on gauge device seating both current and potential probes that has been designed and manufactured specifically for the application of the DCPD according to the configurations investigated with the numerical analyses. Fracture surfaces were examined by optical microscopy and by image analysis it was possible to relate the beach marked crack fronts to the corresponding overload and consequently to the measured potential drop signal. All beach marked cracks were approximated by an elliptical arc and given as an input to dedicated electrical 3D FE analyses. Eventually, the resulting numerical values of the potential drop were checked against their corresponding experimental results, showing a quite good agreement, the deviation in most cases being similar to that observed in the previous literature

4.7 Conclusions

even for simpler specimens' geometries and crack configurations, such as SENB specimens or circumferentially notched bars.

The outcomes of this research will be the basis for future applications like the experimental determination of the cyclic R-curve on specimen's geometries different from that one usually adopted in the Literature (SENB), or the introduction of the DCPD as a method for structural health monitoring in real engineering structures.

4.8. References

- [1] Anderson TL. Fracture Mechanics, Fundamentals and Applications. 3rd ed. Boca Raton: CRC Press LLC; 2009.
 - [2] Minakawa K, Newman JC, McEvily AJ. A critical study of the crack closure effect on near-threshold fatigue crack growth. *Fatigue Fract Eng Mater Struct* 1983;6:359–65. <https://doi.org/10.1111/j.1460-2695.1983.tb00351.x>.
 - [3] McEvily AJ, Endo M, Murakami Y. On the $(\text{area})^{0.5}$ relationship and the short fatigue crack threshold. *Fatigue Fract Eng Mater Struct* 2003;26:269–78. <https://doi.org/10.1046/j.1460-2695.2003.00636.x>.
 - [4] Chapetti MD, Belmonte J, Tagawa T, Miyata T. Integrated fracture mechanics approach to analyse fatigue behaviour of welded joints. *Sci Technol Weld Join* 2004;9:430–8. <https://doi.org/10.1179/136217104225021634>.
 - [5] Tanaka K, Akiniwa Y. Resistance-curve method for predicting propagation threshold of short fatigue cracks at notches. *Eng Fract Mech* 1988;30:863–76. [https://doi.org/10.1016/0013-7944\(88\)90146-4](https://doi.org/10.1016/0013-7944(88)90146-4).
 - [6] Tabernig B, Pippan R. Determination of the length dependence of the threshold for fatigue crack propagation. *Eng Fract Mech* 2002;69:899–907. [https://doi.org/10.1016/S0013-7944\(01\)00129-1](https://doi.org/10.1016/S0013-7944(01)00129-1).
 - [7] Endo M, McEvily AJ. Prediction of the behavior of small fatigue cracks. *Mater Sci Eng A* 2007;468–470:51–8. <https://doi.org/10.1016/j.msea.2006.09.084>.
 - [8] Maierhofer J, Kolitsch S, Pippan R, Gänser H-P, Madia M, Zerbst U. The cyclic R-curve – Determination, problems, limitations and application. *Eng Fract Mech* 2018;198:45–64. <https://doi.org/10.1016/j.engfracmech.2017.09.032>.
 - [9] Pourheidar A, Patriarca L, Madia M, Werner T, Beretta S. Progress in the measurement of the cyclic R-curve and its application to fatigue assessment. *Eng Fract Mech* 2022;260:108122. <https://doi.org/10.1016/j.engfracmech.2021.108122>.
 - [10] Zerbst U, Vormwald M, Pippan R, Gänser H-P, Sarrazin-Baudoux C, Madia M. About the fatigue crack propagation threshold of metals as a design criterion – A review. *Eng Fract Mech* 2016;153:190–243. <https://doi.org/10.1016/j.engfracmech.2015.12.002>.
-

4.8 References

- [11] ASTM E647 - 15e1, Standard Test Method for Measurement of Fatigue Crack Growth Rates 2015. <https://doi.org/10.1520/E0647-15E01.2>.
 - [12] ISO 12108:2018 Metallic materials - Fatigue testing - Fatigue crack growth method 2018.
 - [13] ASTM E1820-20b: Standard Test Method for Measurement of Fracture Toughness 2020. <https://doi.org/10.1520/E1820-20B>.
 - [14] ISO 12135:2021 Metallic materials - Unified method of test for the determination of quasistatic fracture toughness 2021.
 - [15] Si Y, Rouse JP, Hyde CJ. Potential difference methods for measuring crack growth: A review. *Int J Fatigue* 2020;136. <https://doi.org/10.1016/j.ijfatigue.2020.105624>.
 - [16] Campagnolo A, Bär J, Meneghetti G. Analysis of crack geometry and location in notched bars by means of a three-probe potential drop technique. *Int J Fatigue* 2019;124:167–87. <https://doi.org/10.1016/j.ijfatigue.2019.02.045>.
 - [17] Gandossi L, Summers S., Taylor N., Hurst R., Hulm B., Parker J. The potential drop method for monitoring crack growth in real components subjected to combined fatigue and creep conditions: application of FE techniques for deriving calibration curves. *Int J Press Vessel Pip* 2001;78:881–91. [https://doi.org/10.1016/S0308-0161\(01\)00103-X](https://doi.org/10.1016/S0308-0161(01)00103-X).
 - [18] Belloni G, Gariboldi E, Lo Conte A, Tono M, Speranzoso P, Petersen D, et al. On the Experimental Calibration of a Potential Drop System for Crack Length Measurements in a Compact Tension Specimen. *J Test Eval* 2002;30:11149. <https://doi.org/10.1520/JTE12346J>.
 - [19] Bär J. Crack Detection and Crack Length Measurement with the DC Potential Drop Method–Possibilities, Challenges and New Developments. *Appl Sci* 2020;10:8559. <https://doi.org/10.3390/app10238559>.
 - [20] Funk M, Bär J. DCPD based detection of the transition from short to long crack propagation in fatigue experiments on the aluminum alloy 7475 T761. *Procedia Struct. Integr.*, vol. 17, Elsevier B.V.; 2019, p. 183–9. <https://doi.org/10.1016/j.prostr.2019.08.025>.
 - [21] Tada N, Okada M, Iwamoto J. Three-dimensional identification of semi-elliptical surface crack by means of direct-current electrical potential difference method with multiple-probe sensor. *J Press Vessel Technol Trans ASME* 2007;129:441–8. <https://doi.org/10.1115/1.2748824>.
-

-
- [22] Hartweg M, Bär J. Analysis of the crack location in notched steel bars with a multiple DC potential drop measurement. *Procedia Struct Integr* 2019;17:254–61. <https://doi.org/10.1016/j.prostr.2019.08.034>.
- [23] To S, Lambert SB, Burns DJ. A multiple crack model for fatigue in welded joints. *Int J Fatigue* 1993;15:333–40. [https://doi.org/10.1016/0142-1123\(93\)90383-2](https://doi.org/10.1016/0142-1123(93)90383-2).
- [24] Lecsek RL, Yee R, Lambert SB, Burns DJ. A Probabilistic Model For Initiation And Propagation Of Surface Cracks In Welded Joints. *Fatigue Fract Eng Mater Struct* 2007;18:821–31. <https://doi.org/10.1111/j.1460-2695.1995.tb00907.x>.
- [25] Černý I. Measurement of subcritical growth of defects in large components of nuclear power plants at elevated temperatures. *Int J Press Vessel Pip* 2001;78:893–902. [https://doi.org/10.1016/S0308-0161\(01\)00104-1](https://doi.org/10.1016/S0308-0161(01)00104-1).
- [26] Černý I. The use of DCPD method for measurement of growth of cracks in large components at normal and elevated temperatures. *Eng Fract Mech* 2004;71:837–48. [https://doi.org/10.1016/S0013-7944\(03\)00012-2](https://doi.org/10.1016/S0013-7944(03)00012-2).
- [27] Černý I. Estimation of Crack Depth and Profile Using DCPD Method in Full Scale Railway Axle Loaded by Rotating Bending. *Appl Mech Mater* 2015;732:171–4. <https://doi.org/10.4028/www.scientific.net/AMM.732.171>.
- [28] Černý I. Growth and retardation of physically short fatigue cracks in an aircraft Al-alloy after shot peening. *Procedia Eng* 2011;10:3411–6. <https://doi.org/10.1016/j.proeng.2011.04.562>.
- [29] Černý I. Measurement of Local Initiation, Early Growth and Retardation of Physically Short Fatigue Cracks Using Amended DCPD Method. *Key Eng Mater* 2013;586:19–22. <https://doi.org/10.4028/www.scientific.net/KEM.586.19>.
- [30] Černý I, Sís J, Mikulová D. Short fatigue crack growth in an aircraft Al-alloy of a 7075 type after shot peening. *Surf Coatings Technol* 2014;243:20–7. <https://doi.org/10.1016/j.surfcoat.2012.06.008>.
- [31] Saka M, Abé H, Oouchi A. NDE of a crack by using closely coupled probes for DCPD technique. *J Press Vessel Technol Trans ASME* 1996;118:198–202. <https://doi.org/10.1115/1.2842181>.
- [32] Ritter MA, Ritchie RO. On the calibration, optimization and use of d.c. electrical potential methods for monitoring mode III crack growth in torsionally-loaded samples. *Fatigue Fract Eng Mater Struct* 1982;5:91–9. <https://doi.org/10.1111/j.1460->
-

4.8 References

- 2695.1982.tb01227.x.
- [33] Campagnolo A, Meneghetti G, Berto F, Tanaka K. Crack initiation life in notched steel bars under torsional fatigue: Synthesis based on the averaged strain energy density approach. *Int J Fatigue* 2017;100:563–74. <https://doi.org/10.1016/j.ijfatigue.2016.12.022>.
- [34] Meneghetti G, Campagnolo A, Berto F, Tanaka K. Notched Ti-6Al-4V titanium bars under multiaxial fatigue: Synthesis of crack initiation life based on the averaged strain energy density. *Theor Appl Fract Mech* 2018;96:509–33. <https://doi.org/10.1016/j.tafmec.2018.06.010>.
- [35] Campagnolo A, Meneghetti G, Berto F, Tanaka K. Calibration of the potential drop method by means of electric FE analyses and experimental validation for a range of crack shapes. *Fatigue Fract Eng Mater Struct* 2018;41:2272–87. <https://doi.org/10.1111/ffe.12856>.
- [36] Aronson GH, Ritchie ROR. Optimization of the Electrical Potential Technique for Crack Growth Monitoring in Compact Test Pieces Using Finite Element Analysis. *J Test Eval* 1979;7:208. <https://doi.org/10.1520/JTE11382J>.
- [37] Antonarulrajah A, Ramos VPS, Fazluddin SB, Rand B. Evaluation of the electrical potential drop technique in the determination of crack growth resistance-curves of Carbon/Carbon composites and carbon bonded refractories. *J Mater Sci* 2005;40:373–80. <https://doi.org/10.1007/s10853-005-6093-3>.
- [38] Singh YP, Panakarajupally R, Presby MJ, Morscher GN. Interlaminar damage detection through the understanding of direct current spreading in continuous fiber reinforced composites. *Compos Part B Eng* 2019;166:722–30. <https://doi.org/10.1016/j.compositesb.2019.03.011>.
- [39] Nayeb-Hashemi H, Swet D, Vaziri A. New electrical potential method for measuring crack growth in nonconductive materials. *Measurement* 2004;36:121–9. <https://doi.org/10.1016/j.measurement.2004.05.002>.
- [40] Barnett WJ, Troiano AR. Crack propagation in the hydrogen-induced brittle fracture of steel. *J Met* 1957;9:486–94. <https://doi.org/10.1007/BF03397905>.
- [41] Ritchie RO, Bathe KJ. On the calibration of the electrical potential technique for monitoring crack growth using finite element methods. *Int J Fract* 1979;15:47–55. <https://doi.org/10.1007/BF00115908>.
-

-
- [42] Ljustell P. The Effect of Large Scale Plastic Deformation on Fatigue Crack Length Measurement with the Potential Drop Method. *J Test Eval* 2011;39:985–1002. <https://doi.org/10.1520/JTE103532>.
- [43] Doremus L, Nadot Y, Henaff G, Mary C, Pierret S. Calibration of the potential drop method for monitoring small crack growth from surface anomalies - Crack front marking technique and finite element simulations. *Int J Fatigue* 2015;70:178–85. <https://doi.org/10.1016/j.ijfatigue.2014.09.003>.
- [44] Tarnowski KM, Davies CM, Dean DW, Nikbin KM. The Influence of Plasticity on Crack Length Measurements Using the Potential Drop Technique. *Eval. Exist. New Sens. Technol. Fatigue, Fract. Mech. Test.*, vol. STP 1584, 100 Barr Harbor Drive, PO Box C700, West Conshohocken, PA 19428-2959: ASTM International; 2015, p. 73–96. <https://doi.org/10.1520/STP158420140055>.
- [45] Tarnowski KM, Dean DW, Nikbin KM, Davies CM. Predicting the influence of strain on crack length measurements performed using the potential drop method. *Eng Fract Mech* 2017;182:635–57. <https://doi.org/10.1016/j.engfracmech.2017.06.008>.
- [46] Wong FMG. Fatigue, Fracture, and Life Prediction Criteria for Composite Materials in Magnets. PhD Thesis, Massachusetts Institute of Technology, 1990.
- [47] Levan A, Royer J. Part-circular surface cracks in round bars under tension, bending and twisting. vol. 61. Kluwer Academic Publishers; 1993. <https://doi.org/10.1007/BF00032340>.
- [48] Carpinteri A, Brighenti R. Circumferential surface flaws in pipes under cyclic axial loading. *Eng Fract Mech* 1998;60:383–96. [https://doi.org/10.1016/S0013-7944\(98\)00036-8](https://doi.org/10.1016/S0013-7944(98)00036-8).
- [49] Meneghetti G, Lazzarin P. Significance of the elastic peak stress evaluated by FE analyses at the point of singularity of sharp V-notched components. *Fatigue Fract Eng Mater Struct* 2007;30:95–106. <https://doi.org/10.1111/j.1460-2695.2006.01084.x>.
- [50] Meneghetti G, Campagnolo A. State-of-the-art review of peak stress method for fatigue strength assessment of welded joints. *Int J Fatigue* 2020;139:105705. <https://doi.org/10.1016/j.ijfatigue.2020.105705>.
- [51] Campagnolo A, Roveda I, Meneghetti G. The Peak Stress Method combined with 3D finite element models to assess the fatigue strength of complex welded structures. *Procedia Struct Integr* 2019;19:617–26. <https://doi.org/10.1016/j.prostr.2019.12.067>.
-

4.8 References

- [52] Meneghetti G, Campagnolo A, Visentin A, Avalor M, Benedetti M, Bighelli A, et al. Rapid evaluation of notch stress intensity factors using the peak stress method with 3D tetrahedral finite element models: comparison of commercial codes. *Fatigue Fract Eng Mater Struct* 2022;accepted.
- [53] Shin CS, Cai CQ. Experimental and finite element analyses on stress intensity factors of an elliptical surface crack in a circular shaft under tension and bending. *Int J Fract* 2004;129:239–64. <https://doi.org/10.1023/B:FRAC.0000047784.23236.7d>.
- [54] Ritchie RO, Garrett GG, Knott JP. Crack-growth monitoring: Optimisation of the electrical potential technique using an analogue method. *Int J Fract Mech* 1971;7:462–7. <https://doi.org/10.1007/BF00189118>.
- [55] Van Minnebruggen K, Hertelé S, Verstraete MA, De Waele W. Crack growth characterization in single-edge notched tension testing by means of direct current potential drop measurement. *Int J Press Vessel Pip* 2017;156:68–78. <https://doi.org/10.1016/j.ijpvp.2017.06.009>.
- [56] Saxena A. Electrical potential technique for monitoring subcritical crack growth at elevated temperatures. *Eng Fract Mech* 1980;13:741–50. [https://doi.org/10.1016/0013-7944\(80\)90005-3](https://doi.org/10.1016/0013-7944(80)90005-3).
- [57] Bakker A. A DC Potential Drop Procedure for Crack Initiation and R-Curve Measurements During Ductile Fracture Tests. *Elastic-Plastic Fract Test Methods User's Exp* 1985:394–410. <https://doi.org/10.1520/STP34537S>.
- [58] Chang F, Markmiller JFC, Yang J, Kim Y. *Structural Health Monitoring. Syst. Heal. Manag.*, Wiley; 2011, p. 419–28. <https://doi.org/10.1002/9781119994053.ch26>.
- [59] Farrar CR, Worden K. An introduction to structural health monitoring. *Philos Trans R Soc A Math Phys Eng Sci* 2007;365:303–15. <https://doi.org/10.1098/rsta.2006.1928>.
- [60] Matelect. Mat-3 handheld probe: datasheet 2021.

CHAPTER 5.

Conclusions

5.1. Conclusions

In the context of fatigue design of welded structures, the Peak Stress Method (PSM) is a rapid technique to estimate the Notch Stress Intensity Factors (NSIFs) at the weld toe and weld root, which are idealised and modelled as sharp notches having null tip radius. Essentially, the PSM takes advantage of the singular, linear elastic, opening, sliding, and tearing peak stresses evaluated at the notch tip using coarse free mesh patterns to estimate the mode I, II, and III NSIF-terms, respectively. By adopting the averaged Strain Energy Density (SED) as a fatigue strength criterion, a PSM-based design stress, i.e. the so-called equivalent peak stress, can be defined as a function of the relevant peak stresses. The validity and efficacy of this method has been extensively verified in the Literature.

In the present work, the PSM has been extended for the first time to variable amplitude (VA) uniaxial as well as in-phase and out-of-phase multiaxial fatigue loadings applied to steel arc-welded joints. The extension to VA loading situations has been based on Palmgren-Miner's linear damage rule (LDR) to account for cumulative damage. The proposed method has been validated against a large bulk of VA fatigue data taken from the literature proving the PSM as an extremely valid technique to design welded joints against CA or VA uniaxial as well as multiaxial fatigue local stresses. The proposed method has also been checked against new experimental results generated by testing non-load-carrying (nlc) fillet-welded double transverse or inclined attachments made of S355 structural steel under pure axial loading. In this case different load spectra, both deterministic and stochastic, have been applied to investigate VA loading conditions.

In the present manuscript, another extension of the PSM has been addressed to estimate the constant amplitude uniaxial fatigue limit of welded structures in the stress-relieved state. A fracture mechanics criterion based on the cyclic R-curve analysis has been considered. The application of the method required the definition of an initial crack size, which value has been accurately calibrated by means of dedicate experimental tests. Among these tests, the experimental determination of the cyclic R-curve was necessary. It has been done on a S355J2+N structural steel both in base metal and in the Heat Affected Zone conditions adopting a new experimental procedure, capable of completely describing the short to long crack regime

by means of a single experimental test. Once performed the calibration of the method, the fatigue limit of a welded structure was possible with different degrees of accuracy depending on the available information. Under certain simplifying assumptions it was possible formulating a new procedure which is substantially based on the definition of a threshold value for the Notch Stress Intensity Factor NSIF. By exploiting the advantages offered by the PSM, the proposed method allows to a rapid and effective design of weld toe failures in the infinite life region, without the need of complex and time-consuming fracture mechanics-based calculations. Finally, the proposed procedure has been successfully checked against experimental data from the Literature.

Finally, the present work has given an insight on some critical aspects relevant to the experimental determination of the cyclic R-curve and, in general, on experimental fracture mechanics tests dealing with short cracks. In particular, the problem of performing real-time in-situ crack growth monitoring of short cracks has been extensively discussed, this aspect being undoubtedly the most crucial when performing fracture mechanic tests on short cracks. Accordingly, the application of the Direct Current Potential Drop (DCPD) method to a single-edge-crack round bars subject to axial fatigue has been investigated. Firstly, 3D electrical FE analyses have been performed to investigate the effect of the current and the potential probes position on the performances of the DCPD method in terms of measurability, sensitivity and reproducibility. The increased sensitivity but decreased reproducibility obtained by injecting the current and by measuring the potential drop as close to the superficial crack tip as possible have been evaluated quantitatively. Secondly, the accuracy of the numerical analyses has been checked against experimental results obtained by fatigue testing round bar specimens with a straight-fronted crack starter notch. The propagating fatigue crack has been monitored with the DCPD technique with the local configuration of the current and potential probes, which were located at the superficial crack tip. To do so, a dedicated clip-on gauge device seating both current and potential probes has been designed and realized. Experimental crack fronts have been beach-marked, digitally acquired and modelled in the FE environment to run electric numerical analyses obtaining a quite good agreement between numerical and measured potential drop values. In the future, the obtained results will be used to perform the experimental determination of the cyclic R-curve on specimen's geometries different from that one usually adopted in the Literature (SENB).

List of Publications

Below, a list of publications taken from this thesis.

a) Journal papers

- [1] Vecchiato L, Campagnolo A, Meneghetti G. Numerical calibration and experimental validation of the direct current potential drop (DCPD) method for fracture mechanics fatigue testing of single-edge-crack round bars. *Int J Fatigue* 2021;150:106316. <https://doi.org/10.1016/j.ijfatigue.2021.106316>.
- [2] Campagnolo A, Vecchiato L, Meneghetti G. Multiaxial variable amplitude fatigue strength assessment of steel welded joints using the peak stress method. *Int J Fatigue* 2022;163:107089. <https://doi.org/10.1016/j.ijfatigue.2022.107089>.

b) Papers published in indexed Conference Proceedings

- [3] Meneghetti G, Vecchiato L, Campagnolo A, Rech P, Cova M. Numerical calibration of the direct current potential drop (DCPD) method in fracture mechanics fatigue tests. *Procedia Struct Integr* 2020;28:1536–50. <https://doi.org/10.1016/j.prostr.2020.10.126>.
- [4] Vecchiato L, Campagnolo A, Besa B, Meneghetti G. The Peak Stress Method applied to fatigue lifetime estimation of welded steel joints under variable amplitude multiaxial local stresses. *Procedia Struct Integr* 2022;38:418–27. <https://doi.org/10.1016/j.prostr.2022.03.043>.

c) Papers published in Conference Proceedings

- [5] Vecchiato L, Rech P. Analisi numeriche per la calibrazione del metodo Direct Current Potential Drop (DCPD) applicato in prove a fatica di componenti criccati. *Atti Del 49° Convegno Nazionale AIAS* 2020.
- [6] Vecchiato L. Calibrazione numerica e validazione sperimentale del metodo “Direct Current Potential Drop” per la misura non distruttiva della dimensione di cricca in prove

sperimentali di meccanica della frattura a fatica. Atti Del 50° Convegno Nazionale AIAS 2021.

- [7] Vecchiato L, Moda G, Meneghetti G. Stima del limite di fatica di giunzioni saldate in acciaio basata sul metodo della curva R ciclica. Atti Del 51° Convegno Nazionale AIAS 2022.

d) Submitted

- [8] Vecchiato L, Campagnolo A, Meneghetti G. The Peak Stress Method for fatigue lifetime assessment of fillet-welded attachments in steel subject to variable amplitude multiaxial in-phase local stresses.
Under revision, Journal: Int J Fatigue.

e) In preparation

- [9] Vecchiato L, Moda G, Madia M, Meneghetti G. Estimating the constant amplitude fatigue limit of welded joints using the cyclic R-curve analysis for the lifetime assessment according to the peak stress method.
Estimated date of submission: December 2022, Journal: Theor Appl Fract Mech.
- [10] Duarte L, Madia M, Vecchiato L, Meneghetti G. A unified experimental procedure for the determination of the crack propagation threshold from short to long crack regime.
Estimated date of submission: December 2022, Journal: Int J Fatigue.

Ringraziamenti

Desidero ringraziare sentitamente il Professor Giovanni Meneghetti che ha saputo incoraggiarmi e supportarmi non soltanto dal punto di vista accademico, ma soprattutto sul profilo personale. A tal proposito, il suo entusiasmo, la sua passione insieme al suo impegno e alla sua dedizione sono stati l'energia necessaria per completare al meglio questo percorso. Lo ringrazio molto per la fiducia che non ha mai mancato di dimostrare nei miei confronti.

Un altrettanto sentito ringraziamento va al Professor Alberto Campagnolo che con la sua energia e il costante supporto è stato per me, non solo una guida nei momenti di lavoro, ma anche un amico sempre presente e disponibile. I suoi consigli e i suoi suggerimenti preziosi, oltre ad essere sempre puntuali, non sono mai mancati.

Allo stesso modo vorrei ringraziare Daniele Rigon per la sua pazienza, la sua disponibilità e la sua compagnia. Lo ringrazio in particolar modo per le nostre chiacchierate scientifiche (e non), sempre spunto di crescita e riflessione.

Un grazie importante va anche ai miei colleghi dottorandi Davide, Alberto, Jacopo, Francesco, Filippo e agli altri ragazzi che hanno lavorato con me: Giovanni M., Pietro R., Giulio P., Stefano B., Beatrice B., Brian M., Alex D., Filippo S., Luca V., Sofia P. e Giulio Z.

Un grazie sentito e profondo lo rivolgo ai miei genitori, che con grande spirito di sacrificio, con fatica e con tanto affetto hanno saputo accettare le mie decisioni, sostenendomi e non smettendo mai di credere in me e di infondermi la loro fiducia.

Infine, il ringraziamento più grande lo rivolgo a mia moglie Federica, per la sua fiducia, la sua costante e preziosa presenza, per la sua pazienza, per la sua comprensione e per il suo amore, che sono stati spunti preziosi per guardare dentro di me, capire me stesso e lavorare sul mio lato migliore.
